



**This electronic thesis or dissertation has been
downloaded from Explore Bristol Research,
<http://research-information.bristol.ac.uk>**

Author:

Ansari, Behjat

Title:

Investigating geometrical and manufacturing effects on the impact performance of UHMWPE composites

General rights

Access to the thesis is subject to the Creative Commons Attribution - NonCommercial-No Derivatives 4.0 International Public License. A copy of this may be found at <https://creativecommons.org/licenses/by-nc-nd/4.0/legalcode> This license sets out your rights and the restrictions that apply to your access to the thesis so it is important you read this before proceeding.

Take down policy

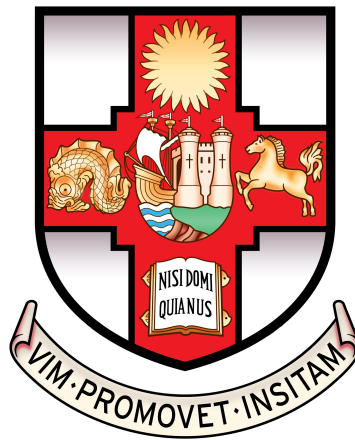
Some pages of this thesis may have been removed for copyright restrictions prior to having it been deposited in Explore Bristol Research. However, if you have discovered material within the thesis that you consider to be unlawful e.g. breaches of copyright (either yours or that of a third party) or any other law, including but not limited to those relating to patent, trademark, confidentiality, data protection, obscenity, defamation, libel, then please contact collections-metadata@bristol.ac.uk and include the following information in your message:

- Your contact details
- Bibliographic details for the item, including a URL
- An outline nature of the complaint

Your claim will be investigated and, where appropriate, the item in question will be removed from public view as soon as possible.

Investigating geometrical and manufacturing effects on the impact performance of UHMWPE composites

PH.D. THESIS BY
BEHJAT T. ANSARI



Department of Aerospace Engineering
University of Bristol

A dissertation submitted
for the degree of Doctor of Philosophy.

May 2020

Abstract

The need to continually enhance the ballistic performance of UHMWPE composite body armour has prompted numerous investigations into the failure mechanisms of these material systems, and the effects of dimensional and manufacturing parameters on their ballistic performance. Past studies have identified the contribution of the fibres to the laminate impact performance, while relatively little attention has been paid to the role of the matrix and its contribution to the overall energy dissipation. Likewise, while flat laminate panels have been studied extensively, in reality, panels used in impact protection are not necessarily flat, with many possessing single or double curvature. Furthermore, modern processing methods such as drape-forming, used in the fabrication of UHMWPE composite shells such as ballistic-grade helmets, induce the geometrical and manufacturing deformations of curvature and in-plane shear. The effects of these deformations on the ballistic impact performance of UHMWPE composites have, however, not previously been investigated. The two features must therefore be studied in isolation, in order to gain an understanding of their effects on impact performance.

In this thesis, cohesive elements are implemented into existing numerical tools to model interlaminar contact in flat laminates. The cohesive elements are used to investigate the in-plane and through-thickness dissipation of energy at sub-laminate interfaces under ballistic impact loading, as well as highlighting the contribution of the matrix to overall energy absorption by the laminate. Curved panels are tested under ballistic impact, demonstrating the geometrical effects of curvature on laminate response. In addition, existing numerical tools are shown to require modifications not previously necessary for flat configurations, to capture the impact response of curved laminates. A process is then developed for manufacturing sheared plates that are tested under ballistic impact, demonstrating the effects of in-plane shear deformation on the ballistic performance of UHMWPE composite plates. Finally, it is shown that current manufacturing standards are unsuitable for promoting uniform impact performance across the surface of doubly-curved components.

Acknowledgements

I am incredibly lucky to have had the fundamental guidance of my academic supervisors, Prof Stephen Hallett and Dr Luiz Kawashita at the University of Bristol. Thank you for your continued support throughout the years, for giving me access to your wealth of knowledge and technical expertise, and thank you for helping me bring everything together in the end. I would like to thank my industrial supervisor, Dr Ulrich Heisserer at DSM, for his unparalleled insight and support, besides the endless supply of Eiskuchen and warm reception during my visits. Special thanks goes to Dr Mark Hazzard, Dr Jan Stolk and Ms Mirre van der Kamp of DSM, for always having the time to discuss the many wonders of Dyneema[®]. Thank you to Dr Antonio Melro and Dr Marco Longana at the University of Bristol, for offering their respective expertise on LS-DYNA UMAT models and digital image correlation measurements. I must also extend my gratitude to Dr Stefano Del Rosso at Imperial College London, for offering his kind support, and access to crucial testing facilities. Likewise, the support of the technical team in the Composites Laboratory at the University of Bristol, particularly from Mr Ian Chorley and Mr Guy Pearn, and the technical team at DSM Dyneema, has been essential to the progress of experimental work in this thesis. This research would not have been possible without the funding provided by the EPSRC, under its ACCIS Centre for Doctoral Training grant EP/L016028/1, and the financial support and material supply provided by the Royal DSM. I would also like to thank Prof Paul Weaver, in his capacity as the Director of the ACCIS CDT, for giving me the opportunity to pursue my studies at the Bristol Composites Institute. Last but not least, thank you to my partner, my family, and my friends, for their unwavering support. I will be forever grateful.

Author's Declaration

I declare that the work in this dissertation was carried out in accordance with the requirements of the University's Regulations and Code of Practice for Research Degree Programmes and that it has not been submitted for any other academic award. Except where indicated by specific reference in the text, the work is the candidate's own work. Work done in collaboration with, or with the assistance of, others, is indicated as such. Any views expressed in the dissertation are those of the author.

SIGNED: DATE:

Contents

Abstract	iii
Acknowledgements	v
Author's Declaration	vii
List of Figures	xiii
List of Tables	1
1 Introduction	3
1.1 Research motivation	3
1.2 Research objectives	4
1.3 Research contribution	5
1.4 Thesis outline	5
2 Literature Review	7
2.1 Background	7
2.1.1 Evolution of personal impact protection	7
2.1.2 Composites in ballistic protection	8
2.1.3 Effect of material properties on ballistic protection	9
2.2 Complex geometries	10
2.3 Curved structures	12
2.3.1 Contact force	14
2.3.2 Stiffness	16
2.3.3 Damage	17
2.3.4 Failure modes	19
2.3.5 Advanced cases	20
2.3.6 Ballistic limit	21
2.4 Modelling impact	24
2.4.1 Finite element methods	24
2.4.2 Matrix contribution	28
2.4.3 Contact modelling	29
2.5 Concluding remarks	34

3	Modelling the laminate interface	35
3.1	Introduction	35
3.2	Methodology	36
3.2.1	Material model	36
3.2.2	Cohesive zone modelling	38
3.2.3	Validating element-based CZM	40
3.2.3.1	Low velocity: drop weight impact	40
3.2.3.2	High velocity: ballistic impact	40
3.2.4	Interface energy dissipation	41
3.3	Global interface energy dissipation	43
3.3.1	Baseline model	43
3.3.2	Parametric studies	47
3.3.2.1	Impact velocity	48
3.3.2.2	Dimensional effects	49
3.3.2.3	Plate length	49
3.3.2.4	Plate thickness	51
3.4	Local interface energy dissipation: out-of-plane	54
3.5	Local interface energy dissipation: in-plane	58
3.5.1	Baseline model	58
3.5.1.1	Energy dissipation in mode I	58
3.5.1.2	Energy dissipation in mode II	60
3.5.1.3	Mode mixity	63
3.5.2	Parametric studies	65
3.5.2.1	Dimensional effects	65
3.5.2.2	Plate length	65
3.5.2.3	Plate thickness	67
3.5.2.4	Maximum cohesive traction	68
3.6	Model versatility and interface element behaviour	70
3.6.1	Experimental validation	71
3.6.2	Evolution of element area	73
3.6.3	Number of interfaces	77
3.6.4	Rate effects	83
3.7	Summary of key findings	85
4	Effect of single curvature on impact performance	89
4.1	Introduction	89
4.2	Geometric considerations	91
4.3	Methodology: Experimental testing	93
4.3.1	Manufacturing curved plates	93
4.3.2	Spherical threat	95
4.3.3	FSP threat	97

4.4	Results and discussion: Experimental testing	100
4.4.1	Spherical threat	100
4.4.1.1	Deflection analysis	100
4.4.1.2	Velocity analysis	112
4.4.2	FSP threat	113
4.4.2.1	Velocity analysis	113
4.4.2.2	Deflection analysis	116
4.4.3	Summary of key findings	150
4.5	Methodology: Numerical modelling	152
4.6	Results and discussion: Numerical modelling	154
4.6.1	Spherical threat	154
4.6.1.1	Deflection analysis	155
4.6.1.2	Velocity analysis	169
4.6.1.3	Off-centre and oblique impacts	172
4.6.2	FSP threat	176
4.6.2.1	Deflection analysis	176
4.6.2.2	Velocity analysis	178
4.6.2.3	Interface studies	183
4.6.3	Further discussions	185
4.6.3.1	FSP deformation	185
4.6.3.2	Manufacturing defects	186
4.6.4	Summary of key findings	188
5	Effect of pre-existing shear on impact performance	191
5.1	Introduction	191
5.2	Methodology	192
5.2.1	Material	193
5.2.2	Material characterisation	193
5.2.3	Manufacturing sheared laminates	200
5.2.4	Impact testing sheared plates	204
5.2.4.1	Specimens	205
5.2.4.2	Test set-up	206
5.3	Results and Discussion	208
5.3.1	Investigating material properties	208
5.3.1.1	The effect of grip pressure and displacement rate	208
5.3.1.2	The influence of temperature	210
5.3.1.3	Primary and secondary loading	216
5.3.1.4	The evolution of thickness	217
5.3.2	Ballistic impact testing	221
5.3.2.1	Ballistic limit velocity	221
5.3.2.2	Analysis of fibre rotation	225

5.3.2.3	Compressive strength	228
5.3.2.4	Fibre scissoring	232
5.3.2.5	Coupling effects	232
5.3.2.6	Visual inspection	237
5.3.2.7	External factors	243
5.3.2.8	A1 specimens	245
5.4	Summary of key findings	248
6	Conclusion	249
6.1	Research outcomes	249
6.2	Future Work	252
6.3	Implications for industry	252
6.4	Concluding remarks	256
	Bibliography	259
	Appendix Appendices	275
	Appendix A Implementing rate-dependence at the sub-laminate interface	277
	Appendix B Implementing plasticity at the sub-laminate interface	281

List of Figures

- 2.1 A hemispherical UHMWPE composite manufactured through drape forming, adapted from [17]. The highlighted zones correspond to (a) a region deformed primarily through curvature, (b) a region deformed primarily through shear, and (c) a region where a combination of both shear and curvature exist. 11
- 2.2 Carbon-fibre/epoxy composite plates after drop weight and airgun-propelled impact: (a) contact force and (b) damage initiation impact energy against plate radius, reproduced from [27]. 15
- 2.3 Glass fibre/epoxy composite plates after gas gun impact by a 30 mm diameter steel ball under opposite directions of impact, reproduced from [36]. 19
- 2.4 Energy dissipated due to damage as a function of impact energy, for laminates with internal curvatures of $R1 = 3.94$ in, $R2 = 4.92$ in, $R3 = 7.87$ in and $R4 = \infty$, without (a)-(b) and with (c)-(d) the addition of internal pressure, reproduced from [40]. 21
- 2.5 Percentage change in V_{50} predictions from flat to curved panels with varying radii of curvature, based on [41]. 22
- 2.6 (a) Percentage difference between numerical and experimental V_{50} predictions for different elastic stiffness values, (b) percentage change in V_{50} predictions from flat to curved panels using an empirically derived elastic stiffness in numerical simulations, based on [41]. 22
- 2.7 The sub-laminate cross-ply homogenisation approach adopted by Hazzard *et al.* [49]. 25
- 2.8 Free surface velocity trace from inverse plate impact test and numerical verification, reproduced from [58]. 27
- 2.9 (a) Modelling the interface between two surfaces S^+ and S^- according to (b) a mixed-mode cohesive law, reproduced from [72]. 31

3.1	Comparison between the implementation of CZM at the interface using (a) surface-to-surface contact and (b) cohesive elements.	39
3.2	(a) Cross-sectional views of the full drop weight impact (top) and ballistic impact (bottom) finite element models, and (b) a comparison of contact force against displacement between surface- and element-based models subjected to drop weight impact.	40
3.3	Comparisons between surface- and element-based models under ballistic impact: (a) Evolution of projectile velocity and (b) Lambert-Jonas ballistic limit predictions.	41
3.4	A visual guide to the labelling of sub-laminates and interface layers, together with the dimensions of the baseline numerical model.	43
3.5	Energy dissipated at interfaces during impact (LHS), and as a percentage of the total energy dissipated (RHS), at $V_I = 350$ m/s and $V_I = 600$ m/s.	44
3.6	Progression of the projectile and deformation of the laminate at discreet points in time after impact, at $V_I = 350$ m/s and $V_I = 600$ m/s.	45
3.7	Internal energy U , of each sub-laminate layer m , under impact at $V_I = 350$ m/s, in terms of absolute values per layer (LHS) and the contribution of each layer to the total energy absorbed (centre and RHS).	46
3.8	(a) Apex deflection and (b) shear hinge progression of sub-laminates at multiple interfaces through the thickness of the laminate, at $V_I = 350$ m/s.	47
3.9	Energy dissipated at interfaces and energy dissipated at interfaces as a percentage of total energy dissipated by laminate over a range of impact velocities, with $V_{50} = 407.8$ m/s.	48
3.10	Dimensions d and h_T demonstrated on schematics of the laminate model.	49
3.11	Finite element models of varying dimension d .	50
3.12	Lambert-Jonas V_{50} approximations for various values of plate length d .	50
3.13	Energy dissipated at interfaces and energy dissipated at interfaces as a percentage of total energy dissipated by laminate for a range of in-plane plate dimensions, at $V_I = 350$ m/s and $V_I = 600$ m/s.	51
3.14	Finite element models of varying dimension h_T .	52
3.15	Lambert-Jonas V_{50} approximations for various values of plate thickness h_T .	52
3.16	Energy dissipated at interfaces and energy dissipated at interfaces as a percentage of total energy dissipated by laminate for a range of plate thicknesses, at $V_I = 350$ m/s and $V_I = 600$ m/s.	53

-
- 3.17 An exploded view of individual interfaces within the baseline laminate model. 54
- 3.18 Energy dissipated at each sub-laminate layer under impact at $V_I = 350$ m/s, through mode I (LHS), mode II (centre), and combined mixed-mode (RHS) delamination. 55
- 3.19 Energy dissipated at each sub-laminate layer under impact at $V_I = 600$ m/s, through mode I (LHS), mode II (centre), and combined mixed-mode (RHS) delamination. 56
- 3.20 The evolution of the contact force between the projectile and the laminate, for a time-step $\Delta t = 10^{-5}$ s. 57
- 3.21 The three interfaces selected for investigations of in-plane distribution of energy release rate. 59
- 3.22 The in-plane variation of mode I energy release rate at different interfaces through the thickness of a laminate under impact, for $V_I = 350$ m/s and $\sigma_{II} = 2.6$ MPa. 60
- 3.23 The in-plane variation of mode I energy release rate at different interfaces through the thickness of a laminate under impact, for $V_I = 600$ m/s $\sigma_{II} = 2.6$ MPa. 60
- 3.24 The in-plane variation of mode II energy release rate at different interfaces through the thickness of a laminate under impact, for $V_I = 350$ m/s and $\sigma_{II} = 2.6$ MPa. 62
- 3.25 The in-plane variation of mode II energy release rate at different interfaces through the thickness of a laminate under impact, for $V_I = 600$ m/s and $\sigma_{II} = 2.6$ MPa. 62
- 3.26 The in-plane variation of fracture energy based mode-mixity at different interfaces through the thickness of a laminate under impact, for $d = 300$ mm, $h_T = 10$ mm, and two cases of strike velocity V_I . 63
- 3.27 The in-plane variation of fracture energy based mode-mixity at different interfaces through the thickness of a laminate under impact, for $V_I = 350$ m/s, $h_T = 10$ mm, and various in-plane dimensions d . 66
- 3.28 The in-plane variation of fracture energy based mode-mixity at different interfaces through the thickness of a laminate under impact, for $V_I = 350$ m/s, $d = 300$ mm, and various laminate thicknesses h_T . 68
- 3.29 The in-plane variation of mode I energy release rate at different interfaces through the thickness of the laminate, for $V_I = 350$ m/s and $\sigma_{II} = 1.8$ MPa. 69
- 3.30 The in-plane variation of mode I energy release rate at different interfaces through the thickness of the laminate, for $V_I = 600$ m/s and $\sigma_{II} = 1.8$ MPa. 69

-
- 3.31 The in-plane variation of mode II energy release rate at different interfaces through the thickness of the laminate, for $V_I = 350$ m/s and $\sigma_{II} = 1.8$ MPa. 70
- 3.32 The in-plane variation of mode II energy release rate at different interfaces through the thickness of the laminate, for $V_I = 600$ m/s and $\sigma_{II} = 1.8$ MPa. 70
- 3.33 (a) The effect of modelling ballistic impact of small plates with and without a base-plate, (b) modelling with and without clamping pressure. 71
- 3.34 Modelled target plates with varying threat and target mesh densities, resulting in different numbers of sub-laminates. 72
- 3.35 Comparison of numerically and experimentally derived Lambert-Jonas V_{50} approximations for numerical models of varying mesh density. 73
- 3.36 Comparison of numerically and experimentally derived Lambert-Jonas V_{50} approximations for varying plate thicknesses. 73
- 3.37 Energy dissipated at each sub-laminate layer under impact at $V_I = 350$ m/s, through mode I (LHS), mode II (centre) and combined mixed-mode (RHS) delamination, calculated using true element area. 74
- 3.38 Energy dissipated at each sub-laminate layer under impact at $V_I = 600$ m/s, through mode I (LHS), mode II (centre) and combined mixed-mode (RHS) delamination, calculated using true element area. 75
- 3.39 A comparison of energy dissipated at interfaces during impact at $V_I = 350$ m/s (LHS) and $V_I = 600$ m/s (RHS), together with energy dissipated at the interfaces as a percentage of the total energy dissipated, between calculations using constant and true element area. 76
- 3.40 A comparison of the combined strain energy release rate mode-mixity at all interfaces during impact at $V_I = 350$ m/s (LHS) and $V_I = 600$ m/s (RHS), between calculations using constant and true element area. 77
- 3.41 Lambert-Jonas V_{50} approximations for varying sub-laminate thickness h_{SL} . 77
- 3.42 Energy dissipated at interfaces and energy dissipated at interfaces as a percentage of total energy dissipated by laminate for a range of sub-laminate thicknesses, at $V_I = 350$ m/s and $V_I = 600$ m/s. 78
- 3.43 Average value of normalised mode I (LHS), mode II (centre), and total (RHS) energy dissipated over time, for $V_I = 350$ m/s and $V_I = 600$ m/s. 79

-
- 3.44 Deviations in mean energy values: (a) the largest deviations shown to exist at the smallest sub-laminate thickness, $h_{\text{SL}} = 0.25$ mm, corresponding to (b) element instabilities under impact loading. 80
- 3.45 Energy dissipated at interfaces and energy dissipated at interfaces as a percentage of total energy dissipated by laminate for a range of sub-laminate thicknesses, using scaled values of G_C , at $V_I = 350$ m/s and $V_I = 600$ m/s. 81
- 3.46 A comparison of mode I (LHS), mode II (centre) and total (RHS) normalised interface energy dissipation between models with and without scaled values of K and G_C . 82
- 3.47 A comparison of maximum BFD at $t = 0.3$ ms for $V_I = 350$ m/s (RHS), projectile velocity v at $t = 0.3$ ms for $V_I = 350$ m/s (centre), and V_R for $V_I = 600$ m/s (RHS), between models with and without scaled values of K and G_C . All values are normalised with data from the baseline model represented by the yellow dot. 82
- 3.48 Fringe plots of the velocity of separation at the inter-laminar interfaces over the duration of impact at $V_I = 350$ m/s, and as viewed from the front and the rear at $t = 0.2$ ms. 84
- 3.49 Parameters for which strain-rate dependence can be implemented, displayed on the mixed-mode bilinear traction-separation law used in the interface elements. 85
- 4.1 Deep-drawn panel of Dyneema[®] [17], together with finite element meshes of a flat panel, a panel with a 15 in radius of curvature, and a panel with a 5 in radius of curvature. 90
- 4.2 Mathematically describing a cantilever beam bending deflection. 91
- 4.3 Variation of curvature around one curved dimension of UHMWPE composite preform drawn to a doubly-curved configuration, adapted from [17]. 92
- 4.4 Specimens of varying degrees of curvature, viewed from above and the side. 94
- 4.5 Schematic demonstrating discrepancy between the radius difference in the moulds and the desired laminate thickness, for an inner panel curvature radius of $r = 5$ in. 95
- 4.6 Specimen dimension parameters, viewed from above and the side. 95
- 4.7 Impact test setup showing the initial (top) and subsequent (bottom) configurations, for a combination of DIC and high speed photography techniques, performed at Imperial College London. 96

4.8	Panel and lamp arrangement inside the impact chamber (inset), shown in relation to the overall test setup.	96
4.9	Impact test configuration for tests performed at DSM Dyneema.	98
4.10	Test setup showing (a) velocity gates in relation to the target, and correcting target position with a spirit level to facilitate orthogonal impact (inset), (b) the high speed video camera and its lens configuration (inset).	99
4.11	DIC strain measurements of out-of-plane displacement, δ_z , on the rear faces of flat and curved panels.	100
4.12	Curvature, κ , (a) along the two in-plane directions across the surface of a specimen, (b) along d_s , showing the longitudinal cross-section, (c) along d_c , showing half of the lateral cross-section, and (d) along both directions showing internal residual strain directions imposed by the curved geometry.	102
4.13	Comparing impact deformation stages of panels under the two different impact directions.	102
4.14	Conceptually comparing back face deformations under impact at V_1 300 m/s ($\pm 10\%$), as viewed from the side for convex (LHS) and concave (RHS) impact.	104
4.15	Maximum out-of-plane deflection progression across the target surface over time, for various curvatures and impact directions.	105
4.16	Percentage change in the maximum bulge height of curved panels relative to flat reference plates.	106
4.17	Identifying impact flashes at the point of first contact by the projectile and surrounding sabot debris with the target surface.	107
4.18	High speed video stills of the impact event from the side (LHS) and the rear (RHS), for $r = \infty$ (convex).	108
4.19	High speed video stills of the impact event from the side (LHS) and the rear (RHS), for $r = 20$ in (convex).	109
4.20	High speed video stills of the impact event from the side (LHS) and the rear (RHS), for $r = 10$ in (convex).	110
4.21	High speed video stills of the impact event from the side in an arrest case, for $r = 5$ in (convex).	111
4.22	High speed video stills of the impact event from the side (LHS) and the rear (RHS), for $r = 5$ in (concave).	111
4.23	Impact and residual velocity of a steel ball threat for flat and curved targets.	112

-
- 4.24 Impact and residual velocity plots of 5.56 mm flat-faced FSP threat onto curved laminates. 113
- 4.25 Impact and residual velocity plots of 5.56 mm flat-faced FSP threat onto curved laminates, grouped according to impact direction and radius of curvature. 114
- 4.26 Experimentally-derived Lambert-Jonas ballistic limit approximations for curved panels. 115
- 4.27 Percentage change in the ballistic limit velocity of curved panels relative to flat reference plates. 116
- 4.28 Impact testing of laminates of varying curvature as viewed from the side for the three instances of pre-impact (convex), post-impact (convex) and post-impact (concave). 117
- 4.29 Impact testing of laminates of the most highly curved laminates as viewed from the rear in convex and concave configurations. 117
- 4.30 Impact testing of laminates of varying curvature in the convex direction as viewed from the front, for the three instances of pre-impact, post-impact (shot 1) and post-impact (shot 2). 118
- 4.31 Impact testing of laminates of varying curvature in the concave direction as viewed from the front, for the two instances of post-impact (shot 2) and post-impact (shot 3). 119
- 4.32 Light table images of tested laminates showing the extent of internal damage on the outer curvature (LHS), corresponding to the back face of concave impacts, and on the inner curvature (centre), corresponding to the back face of convex impacts. The back face deflection in each case is labelled with the shot number. The impact properties are also presented in tabular form (RHS), for $r = 20$ in. 120
- 4.33 Light table images of tested laminates showing the extent of internal damage on the outer curvature (LHS), corresponding to the back face of concave impacts, and on the inner curvature (centre), corresponding to the back face of convex impacts. The back face deflection in each case is labelled with the shot number. The impact properties are also presented in tabular form (RHS), for $r = 10$ in. 121

-
- 4.34 Light table images of tested laminates showing the extent of internal damage on the outer curvature (LHS), corresponding to the back face of concave impacts, and on the inner curvature (centre), corresponding to the back face of convex impacts. The back face deflection in each case is labelled with the shot number. The impact properties are also presented in tabular form (RHS), for $r = 5$ in. 122
- 4.35 Light table images used to detect interaction between multiple damage zones arising from the primary shot and subsequent shots on the same laminate. 126
- 4.36 In-plane back face deflection size of arrest cases as a percentage of total laminate surface area plotted against normalised impact velocity. 127
- 4.37 Light table images of the specimen selected for internal deformation analysis of the cross-section. 128
- 4.38 Cross-sectional inspection of a specimen to analyse post-impact, internal through-thickness damage. 129
- 4.39 Overlaid high speed photographs for analysing projectile path and laminate damage under impact, for varying degrees of curvature under three ranges of impact velocity in the convex direction. 130
- 4.40 Overlaid high speed photographs for analysing projectile path and laminate damage under impact, for varying degrees of curvature under three ranges of impact velocity in the concave direction. 132
- 4.41 High speed images capturing impact flashes at a variety of impact velocities and directions. 132
- 4.42 Overlaid high speed photographs for analysing projectile path and laminate damage under impact, for varying degrees of curvature under three subsequent shots in the convex direction. 133
- 4.43 Montages of high speed photography at 0.025 ms intervals for the most extreme radii of curvature tested. 134
- 4.44 Apex deflection of laminates with varying degrees of curvature, for the three impact cases of concave at low velocity (LHS), convex at low velocity (centre), and convex at high velocity (RHS), over a duration of (a) 1.4 ms and (b) 0.2 ms after impact initiation. 135
- 4.45 Apex deflection of laminates with varying degrees of curvature under convex impact for two ranges of impact velocity, over a duration of (a) 1.4 ms and (b) 0.2 ms after impact initiation. 137

-
- 4.46 Apex deflection of laminates with varying degrees of curvature under concave impact for a single range of impact velocity, over a duration of (a) 1.4 ms and (b) 0.2 ms after impact initiation. 138
- 4.47 Maximum out-of-plane back face deflection plotted as a function of the normalised impact velocity. 139
- 4.48 Maximum out-of-plane back face deflection plotted as a function of the projectile kinetic energy. 141
- 4.49 Shear hinge progression of laminates with varying degrees of curvature, for the three impact cases of concave at low velocity (LHS), convex at low velocity (centre), and convex at high velocity (RHS), over a duration of (a) 1.4 ms and (b) 0.2 ms after impact initiation. 142
- 4.50 Shear hinge progression of laminates with varying degrees of curvature under convex impact for two ranges of impact velocity, over a duration of (a) 1.4 ms and (b) 0.2 ms after impact initiation. 144
- 4.51 Montages of high speed photography at 0.025 ms intervals displaying the stages of bulge formation and in-plane progression, followed by its retraction, its re-emergence and further shear hinge progression at a later point, under convex impact with $r = 20$ in. 144
- 4.52 Shear hinge progression of laminates with varying degrees of curvature under concave impact for a single range of impact velocity, over a duration of (a) 1.4 ms and (b) 0.2 ms after impact initiation. 145
- 4.53 Evolution of the back face bulge at 0.05 ms intervals for different panel curvatures, under low impact velocity (top), $V_I \approx 350$ m/s, and high impact velocity (bottom), $V_I \approx 580$ m/s, convex impact. 147
- 4.54 Evolution of the back face bulge at 0.05 ms intervals for different panel curvatures, under high impact velocity, $V_I \approx 550$ m/s, concave impact. 149
- 4.55 Radially projecting solid element nodes onto the desired radius of curvature using segment theorem to generate meshes of panels with varying radii. 153
- 4.56 Experimentally acquired and numerically generated δ_z distribution on the back face of laminates at maximum deflection under impact, for $r = \infty$. 157
- 4.57 Experimentally acquired and numerically generated δ_z distribution on the back face of laminates at maximum deflection under impact, for $r = 20$ in. 158

4.58	Experimentally acquired and numerically generated δ_z distribution on the back face of laminates at maximum deflection under impact, for $r = 10$ in.	158
4.59	Experimentally acquired and numerically generated δ_z distribution on the back face of laminates at maximum deflection under impact, for $r = 5$ in.	159
4.60	Experimentally acquired and numerically generated δ_z distribution on the back face of laminates at maximum deflection under impact, for $r = -20$ in.	159
4.61	Experimentally acquired and numerically generated δ_z distribution on the back face of laminates at maximum deflection under impact, for $r = -10$ in.	160
4.62	Experimentally acquired and numerically generated δ_z distribution on the back face of laminates at maximum deflection under impact, for $r = -5$ in.	160
4.63	Comparison of percentage change in maximum apex deflection of curved laminates relative to a flat reference, between experimental and numerical data for a range of impact velocities.	161
4.64	Comparing deformation of curved plate under impact between simulated and tested results at 0.1 ms time intervals following impact, at $V_I = 287$ m/s for $r = -20$ in.	164
4.65	(a) Comparing arbitrary examples of linear and non-linear through-thickness shear regimes, (b) combining translational and rotational degrees of freedom to increase the contribution of in-plane stiffness.	165
4.66	Variation in maximum apex deflection with impact velocity, for $\sigma_{II} = 2.6$ MPa.	167
4.67	Variation in maximum apex deflection with impact velocity, for $\sigma_{II} = 1.8$ MPa.	167
4.68	Variation in the depth of penetration with impact velocity, for $\sigma_{II} = 1.8$ MPa.	169
4.69	Numerically-derived Lambert-Jonas V_{50} approximations for curved panels, for $\sigma_{II} = 2.6$ MPa.	169
4.70	Numerically-derived Lambert-Jonas V_{50} approximations for curved panels, for $\sigma_{II} = 1.8$ MPa.	170
4.71	Comparison of percentage change in the V_{50} of curved laminates relative to a flat reference panel, between different values of σ_{II} .	170
4.72	Relating the impact angle λ , non-oblique off-centre impact on a curved surface to the angle of an oblique impact on a flat target.	172
4.73	The variation in impact angle λ , away from the centre of curved panels with varying degree of curvature.	173

4.74	The percentage change in maximum apex deflection with impact angle λ , corresponding to distance away from the centre of a curved panel.	174
4.75	The variation in back face deflection intensity and shape with impact angle λ .	175
4.76	The variation in back face deflection shape and intensity with impact location.	176
4.77	Variation in maximum apex deflection with impact velocity, for $\sigma_{II} = 2.6$ MPa.	177
4.78	Comparison of maximum apex deflection of convex laminates between experimental and numerical results for an FSP threat, under two impact velocities.	177
4.79	Numerically predicted percentage change in maximum apex deflection of curved laminates, relative to a flat reference, over a range of impact velocities.	178
4.80	Numerically-derived Lambert-Jonas V_{50} approximations for curved panels, with $h_t = 6$ mm and a small FSP threat.	179
4.81	Comparison of V_{50} between experimental and numerical data for curved laminates.	179
4.82	Comparison of percentage change in V_{50} between experimental and numerical data for curved laminates, relative to a flat reference panel.	180
4.83	Numerically-derived Lambert-Jonas V_{50} approximations for curved panels, with $h_t = 6$ mm and a large FSP threat.	181
4.84	Numerically-derived Lambert-Jonas V_{50} approximations for curved panels, with $h_t = 10$ mm and a large FSP threat.	182
4.85	Comparison of percentage change in the V_{50} between different laminate and threat dimensions for curved laminates, relative to a flat reference panel.	183
4.86	Energy dissipated at interfaces (top) and energy dissipated at interfaces as a percentage of total energy dissipated by laminate (bottom), for a range of plate curvatures at $V_I = 350$ m/s and $V_I = 600$ m/s, under convex impact.	185
4.87	Energy dissipated at interfaces (top) and energy dissipated at interfaces as a percentage of total energy dissipated by laminate (bottom), for a range of plate curvatures at $V_I = 350$ m/s and $V_I = 600$ m/s, under concave impact.	186
4.88	Comparison of post-impact projectile deformation.	187
5.1	Contour plots of the (a) shear angle on a deformed lamina and (b) thickness change Δt of a 0.148 mm thick lamina due to shearing, as acquired from forming simulations, with (c) showing the suggested filler ply and cut-out pattern. Reproduced from [17].	192

-
- 5.2 The different stages of the process developed for manufacturing sheared plates of Dyneema[®]. 192
- 5.3 The structure of one Dyneema[®] HB26 UD layer, composed of four true UD stacked in a cross-ply formation. Reproduced from [79]. 193
- 5.4 Schematics illustrating (a) the HB26 specimen dimensions, (b) a CAD model of the picture frame fixture prior to any deformation, (c) the same fixture following displacement to achieve a frame angle of 30° , with the arrow pointing in the direction of cross-head displacement. 194
- 5.5 Sheared specimens in the picture frame test rig (a) prior to shearing, (b) sheared by 30° to a frame angle of 60° and (c) sheared by 60° to a frame angle of 30° , together with DIC measurements of the in plane shear strain on the specimen surfaces at a (d) 60° frame angle and a (e) 30° frame angle. 195
- 5.6 Local fibre angles during the shearing process at two intervals of global frame angle (a) $\theta = 75^\circ$ and (b) $\theta = 60^\circ$, before achieving target angle of (c) $\theta = 30^\circ$. 196
- 5.7 Comparison of fibre lengths during the shearing process at three positions across the surface of a sample at 15° intervals. 196
- 5.8 Clockwise from top left: Specimen sheared to $\theta = 30^\circ$ prior to dismounting, close up of the speckle pattern, and a close up of the surface surface deformations accompanying shearing. 197
- 5.9 Four-camera DIC set up to measure change in the out-of plane dimension, (a) top-down view, (b) front view. 198
- 5.10 Contour plot of out-of-plane displacement across the specimen surface (a) on the front side and (b) on the rear side. 199
- 5.11 Thickness across the specimen surface (a) with edge effects and (b) with reduced edge effects. 199
- 5.12 Contour plots of the specimen thickness at shear angle 60° : (a) The surface is rotated to align with the in-plane axes, (b) 10% of the length is eliminated from each edge to minimise edge effects in thickness calculations, giving (c) the final measurement of thickness across the area of interest. 199
- 5.13 The improvements after reducing the AoI, seen in (a) the thickness, with the error bars denoting the standard deviation, in (b) the standard deviation of the data, and in (c) the thickness change. 200

- 5.14 Post-shear spring-back in (a) a square cut-out of a sheared specimen within the space of a few seconds after dismounting from the frame, with out-of-plane deformation seen as a result of the in-plane dimensions of the sample being restricted with cork, (b) a specimen mounted on the frame and sheared to a frame angle of 30° , with a maximum lateral dimension of 10 mm, (c) the same sample immediately after being dismounted from the frame, with the same dimension having increased to 12.4 mm. 201
- 5.15 Calibrating the consolidation cycle of the press at the University of Bristol through empty cycles with and without pre-heating of the press, together with four $100\text{ mm} \times 100\text{ mm}$ trial samples on a pre-heated press. 202
- 5.16 Spring-back of the material as observed through the change in θ from a (a) pre-consolidation state to a (b) post-consolidation state. 203
- 5.17 Manufacturing-induced spring-back was reduced to a range of 0° to 2° : (a) pre-consolidation $\theta = 71^\circ$, (b) post-consolidation $\theta = 71.5^\circ$ to 73° , (c) pre-consolidation $\theta = 51^\circ$ to 52° , (d) post-consolidation θ has remained the same. 203
- 5.18 Highlighted regions demonstrate the in-plane and out-of-plane expansions of the unconsolidated specimens at the edges following cutting. 204
- 5.19 Pressed samples (a) pre-cutting and (b) post-cutting. 205
- 5.20 Demonstrating the fibre length from the centre to the edge of (a) an unsheared reference plate and (b) a sheared plate. 206
- 5.21 Ballistic impact testing: (a) a top-down view of the test apparatus, with the arrow depicting the idealised direction of projectile motion, (b) the testing facility at DSM Dyneema, (c) a sheared plate held loosely in position with four grips in the corners directly before impact, (d) bulging and fibre failure on the back face of a sheared plate following penetration by the FSP upon impact. 207
- 5.22 (a) Normalised global force-strain curves for specimens encountering slippage, and (b) normalised global shear force-global shear angle curves for single and multiple plies. All specimens were sheared at room temperature ($T \approx 25^\circ\text{C}$). 209
- 5.23 The variation of normalised shear force with the global shear angle at different temperature cycles. 210
- 5.24 SEM micrographs of samples sheared at temperature cycles corresponding to the border colour, at 1 mm (top row) and $300\ \mu\text{m}$ (bottom row) length scales. 211

-
- 5.25 Variation of holding force (solid lines) during the shearing process and over the following one hour, for specimens subjected to different temperature cycles (dashed lines). 212
- 5.26 The increase in θ over a two week period following the shearing process, for different temperature regimes. 214
- 5.27 Shearing a 1060 mm square ply using a large picture frame rig: (a) shearing frame mechanism and ply, (b) a ply sheared to a fame angle of $\theta = 30^\circ$, displaying in-plane variation of fibre orientation, and (c) heating the specimen with a heat blanket and an infra-red light. 215
- 5.28 The variation of normalised shear force with the global shear angle at different for primary and secondary loading regimes. 216
- 5.29 Schematics demonstrating the concept of conservation of volume during shear deformation [17]. 217
- 5.30 Thickening of the specimen due to contraction of in-plane dimensions causing fibres to move together, leading to the formation of (a) uniform striations, (b) a combination of striations and ridges, or (c) uneven ridges. 218
- 5.31 Thickness evolution of Dyneema[®] HB26 with increasing shear angle, compared to previous measurements [17]. 219
- 5.32 The thickness change factor, as calculated analytically using $\frac{1}{\sin(\theta)}$, based on conservation of volume, and as acquired from the DIC measurements, equal to the sheared thickness divided by the original thickness, plotted against the fame angle θ . 219
- 5.33 Potted samples for microscopy, from a specimen that was (a) heated during shearing and not pressed afterwards, (b) reloaded in shear after primary loading and not pressed afterwards, (c) sheared at room temperature and pressed afterwards to retain the deformation, (d) not sheared or pressed, representing the material in its original cross-ply form. 219
- 5.34 Optical microscope images of specimen cross-sections under $5 \times$ magnification for (a) an unsheared specimen, (b) a sheared specimen that was not pressed under heat, (c) a specimen that was sheared and pressed under heat. 220

- 5.35 Compound optical microscope images of specimen cross-sections under $5 \times$ magnification from samples that were (a) not sheared or pressed, representing the material in its original cross-ply form, (b) heated during shearing and not pressed afterwards, (c) reloaded in shear after primary loading and not pressed afterwards, (d) sheared at room temperature and pressed afterwards to retain the deformation. 221
- 5.36 Ballistic impact testing data and Lambert-Jonas curve fits for sheared plates (coloured lines) with varying degrees of shear angle and the corresponding un-sheared reference plates (black lines), grouped by the number preforms N_p . 222
- 5.37 Ballistic impact testing data and Lambert-Jonas curve fits for all sheared plates (coloured lines) and corresponding un-sheared reference plates (black lines). 223
- 5.38 Illustrating the dependence of the laminate AD on its other physical parameters. 223
- 5.39 Fibre angles in a standard $0^\circ/90^\circ$ cross-ply layup (top), in an orthogonal layup inclined at angles Θ and $\Theta - 90^\circ$ to the laminate x -axis, and in a non-orthogonal inter-ply angle of ω . 227
- 5.40 The indirect tension mechanism, whereby compressive force F_c introduced upon impact induces a tensile force F_t in the neighbouring lamina for a preform layer of (a) un-sheared and (b) sheared Dyneema[®] HB26. 229
- 5.41 Illustrating the change in inter-ply angle ω of from an un-sheared laminate (LHS) to a sheared one (RHS). 230
- 5.42 (a) The variation in the maximum through-thickness compressive strength σ_c with plate dimension d for multiple ply thicknesses, and demonstrating the variation in percentage change in σ_c with (b) percentage change in ply thickness Δh_p and with (c) shear angle α . 231
- 5.43 The variation in laminate stiffness terms with reducing fibre angle θ for a ply count of $N_p = 24$. 236
- 5.44 Visual inspection of specimens R2 and B2 from stop cases. 237
- 5.45 A closer examination of the BFD of B2 for a strike velocity of 755 m/s, highlighting deformations such separation of the laminate into multiple sublaminates, extensive in-plane shear, as well as out-of-plane wrinkling and twist. 238
- 5.46 Visual inspection of specimens R3 and B4 from stop cases. 240
- 5.47 Visual inspection of specimens R2 and B2 from two perforation cases. 243

-
- 5.48 Numerical predictions of percentage change in V_{50} of laminates with the addition of clamping pressure, relative to a no-clamp boundary condition with $V_{50} = 925.5$ m/s. 244
- 5.49 Comparison of deformed FSPs collected from two arrest cases of R2 and B2 to an unused FSP. 246
- 5.50 Visual inspection of specimens R1 and A1 for one stop and two perforation cases. 247
- 6.1 Top-down view of pre- and post-forming fibre directions across a helmet-shaped surface for a purely cross-ply layup sequence (LHS) and a cross-ply layup sequence with an additional fibre direction at an interlaminar angle ω (RHS). 254
- A.1 Logarithmic linear and exponential curved fitting to determine a strain rate function for yield stress, based on data from [98]. 278
- A.2 Logarithmic linear and exponential curved fitting to determine a global displacement rate function for mode I fracture energy, based on mean average data from [131], inset showing simulation of DCB test using the current modelling technique. 279
- B.1 Implementing effective plasticity in the cohesive interface elements through a trapezoidal traction-separation law in (a) mode II and (b) in the mixed-mode domain, reproduced from [135], or (c) combined with alternative unloading and reloading paths, reproduced from [137]. 282

List of Tables

3.1	MAT162 failure criteria [82].	36
3.2	FSP threat properties used in the MAT098 material model [49].	36
3.3	HB26 properties used in the MAT162 material model [49].	37
3.4	Contact properties used in the cohesive element model [49].	39
4.1	Identifying shape and extent of in-plane back face deflection as a percentage of plate size in arrest cases, presented in ascending order of V_I for $r = 20$ in.	123
4.2	Identifying shape and extent of in-plane back face deflection as a percentage of plate size in arrest cases, presented in ascending order of V_I for $r = 10$ in.	124
4.3	Identifying shape and extent of in-plane back face deflection as a percentage of plate size in arrest cases, presented in ascending order of V_I for $r = 5$ in.	125
4.4	Specifications of specimens with different curvatures.	187
5.1	List of samples manufactured for testing.	205
5.2	HB26 material constants [11, 50].	233
5.3	Comparison of sheared and unsheared shot plates.	241

Chapter 1

Introduction

1.1 Research motivation

The current study is focused on composite materials composed of Dyneema[®], a form of ultra-high molecular weight polyethylene (UHMWPE) fibre, known for its exceptional tensile strength, elastic modulus and very low density. The fibres are typically embedded in a polyurethane matrix to form pre-impregnated composite plies. The high strain to failure of Dyneema[®], arising from the substantial amount of energy required for failure, together with its high specific strength that renders it 15 times stronger than steel and 40% stronger than aramid fibres, give laminates of Dyneema[®] a high energy absorption potential and excellent perforation limit have, which have prompted their use in ballistic armour.

In protective armour applications, it is vital to reduce weight to improve mobility and comfort, and more importantly, to protect wearer. Improvement in protection are derived from increases in the ballistic limit velocity, the impact velocity at which the probability of full perforation is 50%, and from reductions in the back face deflection of components, which determines the degree of damage, in the form of behind-helmet blunt trauma, induced onto the wearer under non-perforating impacts. It is imperative to note the inevitable trade-off between these two parameters, due to the deformation mechanisms of UHMWPE composites under impact loading. Therefore, progress in this field is driven by the need to increase the ballistic limit velocity of components at equivalent values of back face deflection, or aerial density, and alternatively, to maintain the limit velocity while reducing the deflection, or aerial density.

The need to continually enhance the ballistic performance of composite body armour has led to numerous studies on the failure mechanisms of the composite, and the effects of dimensional and manufacturing parameters on the ballistic performance of the material system.

While previous investigations have identified how the fibre system in an UHMWPE composite system contributes to the laminate impact performance, little attention has been paid to the role of the matrix and its contribution to the overall energy dissipation capability of the laminate system. Likewise, flat laminate panels have been studied extensively. In reality however, panels used in impact protection are not necessarily flat, with many possessing a geometry with single or double curvature. Therefore questions still remain regarding the behaviour of hemispherical surfaces under ballistic impact, and the tools that could be developed to effectively predict the behaviour in order to aid the optimisation of design, together with the continual enhancement of ballistic performance. More specifically, modern processing methods such as drape-forming, are used in the fabrication of UHMWPE composite hemispherical shells, as used in the production of ballistic-grade helmets. These methods induce the geometrical and manufacturing deformations of curvature and in-plane shear, respectively, the individual effects of which on the ballistic impact performance of UHMWPE composites have not previously been investigated. In order to gain an understanding of their effects, the two features must be studied in isolation, and independent of one another.

1.2 Research objectives

The work presented in this thesis endeavours to fulfil the following objectives:

- (i) To improve existing macro-scale numerical tools for modelling ballistic impact of flat UHMWPE composite panels, by employing a well-established, element-based cohesive zone method to model the interface of laminates.
- (ii) To use these tools to investigate the in-plane and through-thickness trends in the dissipation of energy that occurs at sub-laminate interfaces under impact loading, and to understand the role of the matrix in terms of contribution to overall energy absorption.
- (iii) To determine whether the existing numerical tools can be extended to curved laminates through experimental validation of the models.
- (iv) To perform experimental impact testing of curved panels to investigate the geometrical effects of curvature on the impact behaviour of the laminate, including the contribution of impact direction and the degree of curvature.
- (v) To develop a representative manufacturing process, for the creation of sheared plates that can be impact tested.

- (vi) To perform experimental impact testing of sheared plates to characterise the effects of the manufacturing-induced deformation of in-plane shearing, on the impact behaviour of the laminate, including the significance of the degree of shear.

Throughout the study, two key parameters are used for evaluating ballistic impact performance; the ballistic limit velocity (V_{50}), a key industry-standard indicator of impact performance, and the back face deflection (BFD), the extent of which determines the degree of behind-armour blunt trauma.

1.3 Research contribution

The main intended research contributions of this thesis can be summarised as follows:

- (i) The contribution of the matrix, as represented by the laminate interface, to the dissipation of impact energy can be used to identify the most significant in-plane and out-of-plane interfaces within a laminate, that can be optimised in terms of matrix and laminate layup design.
- (ii) Insight gained from the modelling and the experimental work on the effects of curvature and shear can, in the future, be used in forming simulations, as well as combined into a single numerical model, capable of predicting the ballistic limit and back face deformation of a hemispherical UHMWPE composite shell. This will allow the identification of a suitable method for reducing the back face deflection of these geometries, and thus the trauma induced in a body armour application, without compromising the ballistic limit velocity of the material
- (iii) Testing data from sheared laminates with varying aerial density and thickness values can be used to evaluate the effectiveness of current manufacturing standards that are based on maintaining these two parameters constant, for the purpose of promoting uniform impact performance across the surface of a doubly curved component.

1.4 Thesis outline

Following this introductory chapter, *Chapter 2: Literature Review* provides an overview of state-of-the-art research in the open literature on the topics explored in this work, while identifying knowledge gaps that the technical chapters subsequently aim to address. The first

technical chapter is *Chapter 3: Modelling the laminate interface*, which tackles objectives (i) and (ii). This is followed by *Chapter 4: Effect of single curvature on impact performance*, based on objectives (iii) and (iv), and *Chapter 5: Effect of pre-existing shear on impact performance*, describing work that addresses objectives (v) and (vi). Final remarks in *Chapter 6: Conclusion* summarise key research outcomes of this work and discuss using these as the basis of potential future investigations, as well as outlining the relevance of current findings to industry.

Chapter 2

Literature Review

This chapter summarises published literature in the field of impact protection, specifically with regards to personal, wearable armour against high velocity projectile impact. Previous studies on topics relevant to the work presented in this thesis are reviewed, with the topics covered falling under the following overarching themes:

- (a) *Composites in ballistic protection*; a brief background on UHMWPE composites used in impact protection.
- (b) *Complex geometries*; an overview of manufacturing doubly-curved UHMWPE composite shells and the geometrical and manufacturing effects arising from this process, as well as an extensive review of the impact behaviour of curved panels.
- (c) *Numerical modelling of impact*; an introduction to the different approaches taken in literature, a note on the contribution of the matrix, and identification of suitable contact modelling methods to capture this contribution.

The chapter concludes by identifying knowledge-based gaps in the literature, and how the technical chapters in this thesis aim to address these.

2.1 Background

2.1.1 Evolution of personal impact protection

Armour has been an integral part of battle throughout the course of history, aiming to provide protection for the user. Its primary functions are to reduce, and ideally prevent, trauma to the body by blocking penetration and diminishing the impact energy. Weaponry has evolved

from premodern combat weapons to high speed projectiles in the form of bullets, grenade fragments and artillery shells, and with it, it has driven the design for more protective gear [1].

Steel shields and wearable steel armour were the main form of combat protection until the use of modern warfare machinery in the first half of the 20th century, which prompted the use of thicker, heavier steel plates for protection. In this era, steel was utilised only in heavily armoured vehicles due to the added weight and the lack of mobility that the steel armour brought with it. Meanwhile, body armour was limited to metal helmets, breastplates and waistcoats, which were not only inconvenient due to their weight and bulk, but also inefficient at providing protection against high speed projectiles [2].

Technological breakthroughs of the second half of the century began with the implementation of nylon in flexible and rigid armour. However, the development that revolutionised the industry was that of aramid fibres in the late 1960s, followed by the development of fibre-reinforced ballistic composites in the 1970s. These have been driven by the need for mobility in modern day applications. Protection for law-enforcement and special operations purposes have been a modern addition to more traditional warfare protection. This has shifted the focus of body armour in particular, from providing protection against explosives to minimising impact from hand-held weaponry. These applications have fuelled the growing demand for more flexible, more lightweight, and more damage-resistant materials for use in armour, a demand which is being fulfilled by the development of ballistic-grade composites.

2.1.2 Composites in ballistic protection

Composites in ballistic protection are composed of a range of materials including fabrics, ceramics, felts and hybrids. Nano-particle reinforcements and natural fibre-filled composites have also been investigated for new-generation body armour systems [3]. Pre-impregnated (prepreg) plies, where an uncured matrix medium reinforced with fibres is consolidated (and cured) to form the final material, are the most advanced form of composites in impact protection [4]. In pre-preg form, defects such as twisting and crimp can be minimised. The composite plies can be categorised into woven and unidirectional. The ratio of fibre to matrix is one of the key determinants of the impact performance of the composite material, whereby a high fibre volume of around 80% gives armour-grade composites their distinctive and defining ballistic properties in comparison with the lower fibre volumes of around 60%, that exist in structural-grade composites [5]. Ballistic impact performance has also been attributed to the physical properties

of the fibre and matrix constituents, and the quality of the bonding between them [1].

Ultra-high molecular weight polyethylene (UHMWPE) fibre composites exhibit exceptional specific strength and stiffness. These provide an excellent perforation limit, a fundamental requirement for protective armour [6]. The current study is focused on composite materials composed of Dyneema[®], an UHMWPE, gel-spun to form fibres that are then embedded within a thermoplastic polyurethane (PU) matrix to form unidirectional prepreg, that is most commonly hot pressed into a cross-ply configuration to form [0,90] plies. Across literature, these [0,90] laminates are referred to as unidirectional (UD), to distinguish them from their woven counterparts. Laminates formed from these UD plies are reported to have extremely anisotropic properties. Applications of the composite vary based on the properties being utilised. The high strain to failure of Dyneema[®] and its high specific strength, combined with poor matrix shear strength, weak fibre-matrix adhesion and a fibre volume fraction of approximately 83%, mean that under impact loading, the fibres absorb energy via extensive elongation, while a smaller extent of energy is dissipated at the interfaces through delamination upon impact. These exceptional properties have rendered Dyneema[®] particularly suitable in ballistic armour applications.

2.1.3 Effect of material properties on ballistic protection

The impact performance of UHMWPE composites is highly dependent on the mechanical properties of the fibres. Their high tensile strength provides the means for resisting deflection, and their high elastic modulus prevents a large back face deflection. The kinetic energy of projectile is converted into potential energy upon impact through strain [7], as the impact wave propagates along primary fibres, *i.e.* the fibres which fall under the path of the threat.

In one of the first steps towards predicting the performance of different fibre composite systems under ballistic impact, Cunniff [8] developed a parametric model encompassing a six-dimensional non-linear regression analysis, based on test data for Kevlar[®]. Cunniff [9] later observed that the ballistic limit velocity of a fibre-reinforced composite scales with the product of the fibre specific toughness and the fibre strain wave velocity. The ballistic limit velocity, V_{50} , is a commonly used measure of impact performance for ballistic components. It is defined as the impact velocity at which there is a 50% likelihood of full perforation of a configuration, specific to the target material, as well as the target and threat dimensions. A dimensional analysis performed by Cunniff [9], captured the relationship between the ballistic limit velocity

and the fibre properties, using the dimensional ratios

$$\Phi \left(\frac{V_{50}}{U^{*\frac{1}{3}}}, \frac{A_d A_p}{m_p} \right) = 0, \quad (2.1)$$

where A_d denotes the areal density of the system, with the properties of the projectile represented by its area, A_p , and mass, m_p . It is assumed that fibre specific toughness, $\frac{\sigma \varepsilon}{2\rho}$, and fibre strain wave velocity, $\sqrt{\frac{E}{\rho}}$, are the only critical mechanical properties that are required for the analysis. These are represented by the so called Cunniff parameter, $(U^*)^{\frac{1}{3}}$, calculated using

$$U^* = \frac{\sigma \varepsilon}{2\rho} \sqrt{\frac{E}{\rho}}, \quad (2.2)$$

with σ equal to the ultimate tensile strength of the fibre, ε the ultimate tensile strain of the fibre, ρ the fibre density, and E the Young's modulus of the fibre, assuming the fibre response is linearly elastic. As the ratios given in Eq. (2.1) can be used to determine the V_{50} ballistic limit of fibre-reinforced armour systems, for any projectile and fibre combination, the work paved the way for advancements in the ballistic performance of armour through direct modifications of the mechanical properties of the fibres. While the approach has been widely used in the literature [10, 11], some authors [12] have questioned the suitability of the Cunniff parameter, as it does not account for the significance of the matrix shear strength. See Section 2.4.2 for a more detailed account of this.

2.2 Complex geometries

In reality, ballistic interactions often involve the impact of projectiles against components that are geometrically more complex than a flat plate, such as curved plates (single curvature) or hemispherical shells (double curvature). Manufacturing more complex geometries from UHMWPE composites calls for suitable processing methods, which tend to be more elaborate than the consolidation of a simple flat plate. To understand the driving mechanisms behind the failure modes that more complex geometries bring about, the deformations induced by these manufacturing techniques will be explored.

In the manufacturing of more complex geometries, the industry is moving away from more traditional cut-and-dart techniques [13] to near-net-shape methods that are adapted to fibre-reinforced composites [14]. In doing so, manufacturers are faced with a trade-off between wrinkling and in-plane shearing, which arise from compression moulding techniques

such as deep-drawing or thermoforming. Dangora *et al.* [15] investigated these two types of deformation. The authors concluded that increasing the binding pressure reduces, and in some cases completely eliminates wrinkling defects, as the material resorts to shearing instead. Figure 2.1 demonstrates how drape-forming of UD layers of Dyneema[®] into a doubly-curved geometry induces curvature and in-plane shear, with each deformation affecting the impact performance of the laminate in its own way [16].

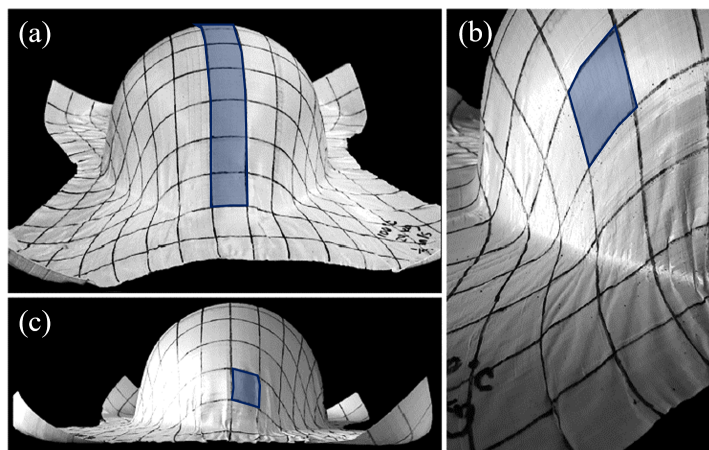


Figure 2.1: A hemispherical UHMWPE composite manufactured through drape forming, adapted from [17]. The highlighted zones correspond to (a) a region deformed primarily through curvature, (b) a region deformed primarily through shear, and (c) a region where a combination of both shear and curvature exist.

The effects of curvature on the impact performance of fibre-reinforced composite panels have been extensively studied and are addressed in the following section. The effects of in-plane shear on the other hand, have not previously been explored with regards to the effect on ballistic impact performance, since large degrees of shear strain are very specific to polymer composites. Shear deformation is a secondary phenomenon that manifests itself in the forming process of doubly-curved configurations. The literature is therefore limited to investigations involving the implications of shearing on laminate behaviour, namely fibre rotation and scissoring, together with studies on the in-plane shear properties of UHMWPE composite laminates.

For example, Nazarian and Zok [12] developed analytical and numerical models that incorporate the large fibre rotations that accompany in-plane shear deformations, the effects of which are not accounted for by the widely used non-dimensional indicator of impact performance, the Cunniff parameter [9]. In a study by Hazzard *et al.* [18], drop weight impact tests were performed to determine how the deformation mechanisms of flat plates of Dyneema[®] differ

with varying fibre orientation, by using stacking sequences ranging from cross-ply [0/90], to quasi-isotropic and helicoidal layups. It was revealed that in the purely cross-ply layup, the combination of extensive in-plane shear and insufficient load transfer from primary fibres, amounted to the largest back face deflection amongst the different types of laminate architectures investigated. These were reportedly an average of 43% larger than the central deflections in the quasi-isotropic panels, the failure mechanisms of which were described as multi-scale levels of panel buckling. The helicoidal laminates exhibited bend-twist and extension-twist coupling behaviour, with maximum values of the back face-deflection and resulting fibre pull-in reported to be significantly less than in the cross-ply laminates, but slightly greater than in the quasi-isotropic laminates. The coupling behaviour in the helicoidal laminates was attributed to their non-symmetry about the mid-plane, leading to buckling and wrinkling deformations in the clamped regions of the panels. With respect to the in-plane shear properties of UHMWPE composites, Russell *et al.* [11] observed a laminate shear strength for Dyneema[®] HB26, that was a hundredfold lower compared to the tensile strength. It was noted that the in-plane shear strength of a laminate is limited by the properties of its matrix, which also determine the rate-sensitivity of the shear response. Likewise, the magnitude of the shear modulus of these composite laminates is three orders of magnitudes lower than the axial modulus, as a result of the low fibre shear modulus arising from the highly drawn nature of UHMWPE fibres [19].

2.3 Curved structures

Previous studies regarding the effects of curvature on the impact performance of fibre-reinforced composites have considered a range of different materials and impact velocities. Although these material systems differ from the UHMWPE system that is the focus of the current work, these remain relevant in the context of isolating the sole effect of curvature on impact performance. Thus, a small selection of previous work is explored here. Quantitative parameters studied for the dependence of impact performance on plate curvature include peak contact force, peak back face deflection (BFD) and impact duration, together with observations of the extent of damage initiation and propagation through intra-laminar cracks and inter-laminar delamination. Boundary effects will not be discussed at length as the boundary conditions in the majority of previous studies are sufficiently similar, and are thus considered to be comparable. Furthermore, previous studies performed on the influence of curvature on the impact behaviour of fibre-reinforced composites are typically distinguished by the thickness of the laminates considered.

Thin laminates, where the in-plane plate dimensions exceed the thickness by at least a factor of 10 are most applicable to the current study where the thickness-to-length ratio stands at $\frac{1}{20}$.

The effects of the addition of positive and negative target curvature, representing convex and concave impacts respectively, were studied by Lindfors *et al.* [20], using a combination of analytical, numerical and experimental approaches. The objective was to examine the ballistic and fragmentation behaviour of thin (1.6 mm and 6.4 mm) steel and aluminium half-cylindrical shells impacted by steel spheres. It was revealed that regardless of target material, the ballistic limit was consistently higher for the convex case, with significant differences between the two directions of impact reported for the thinner set of shells. These differences were much less apparent in the thicker plates.

The authors attributed the higher ballistic limits of the positively curved plates to the higher levels of energy absorption that take place due to dishing, a form of global deformation in metallic targets, which can extend a considerable distance from the impact area [21]. Dishing also contributed to the overall energy absorption of the thinner plates, to a greater extent than in the thicker plates. The authors also noted that concave impacts on the steel shells resulted in a more significant degree of fragmentation upon impact than convex configurations. It was reported that changes in the target curvature corresponded to changes in wave interactions and transfer of momentum upon impact. Since impulse transfer was assumed to vary linearly with curvature, κ , an expression was derived to linearly scale the ballistic limit velocity V_{50} with κ , based on the ballistic limit of a flat plate, V_{50}^F , shell thickness, h_T , and A , an empirically derived dimensionless constant, as follows

$$V_{50} = V_{50}^F (1 + A\kappa h_t) . \quad (2.3)$$

With a shift in focus to curved composite plates, attempts by Ambur [22] to investigate the scalability of the low velocity impact response of thin flat panels to curved laminates, demonstrated that the overall structural behaviour can be scaled, to a degree, in line with the findings of Swanson *et al.* [23]. However, the scaling laws developed for specimens with a geometrically linear response are not applicable to the extent of damage generated through the non-linear response of curved configurations, making further research into this area necessary for the characterisation of this behaviour.

The following subsections review the effects of curvature on the inherently interdependent topics of impact energy and contact force, target stiffness response, damage initiation, and failure modes in curved panels under varying rates of impact loading. These are followed by a brief overview of more advanced cases in terms of geometry and loading condition, together with a dedicated subsection on the ballistic performance of curved laminates.

2.3.1 Contact force

Some of the earliest analytical studies of the effects of curvature on low velocity impact performance of cylindrical fibre-reinforced composites were carried out by Greszczuk and Chao [24]. The calculations compared a flat carbon-fibre/epoxy laminate with two cylindrical shells of the same material, with curvature radii $r = 3$ in and $r = 1.5$ in, all in a cross-ply configuration and subjected to impact by a spherical threat. The predictions revealed that while a reduction in r , equivalent to an increase in the degree of curvature, led to a reduction in the maximum impact load, there was an increase in the maximum surface pressure due to a fall in the area of contact. In addition, the area of contact with the spherical impactor moved from circular in the case of the flat laminate, to a more elliptical configuration as the radius of curvature was increased, as was confirmed through physical testing. However, the placement of strain gauges at the impact site and at the rear face may have affected the impact response and the failure modes respectively.

More recently, Kistler and Waas [25] performed drop weight impact tests on the external curvature of cylindrically curved panels of AS4/3502 carbon-fibre and epoxy resin in a quasi-isotropic layup sequence, for two sets of curvature radius, $r = 60$ in and $r = 15$ in. The study revealed that the effect of decreasing the radius of curvature, thus increasing the intensity of curvature, corresponded to that of increasing panel thickness. Thicker panels brought about higher maximum forces upon contact, while inducing more limited impact durations and peak deflections on the rear face. Analytical and experimental investigations of low speed impact by Ambur and Starnes [26], [27], on thin, cylindrically curved panels of AS4/3502, with a quasi-isotropic stacking sequence and a comparable testing fixture to the one used in [25], showed a similar trend in the response of laminates with varying curvature at a given thickness, as seen in Fig. 2.2(a) [27]. Under drop weight impact, the peak contact force decreased as the radius of curvature was increased from $r = 15$ in to $r = 30$ in, resulting in a reduction in the degree of curvature. However, the peak contact force subsequently recovered, increasing beyond the starting value as the radius was further increased to $r = 60$ in. Beyond this radius of

curvature, the maximum contact force plateaued as the radius approached infinity, resembling the response of a flat plate.

Furthermore, Kistler and Waas [25] noted a drop in the significance of curvature effects with increasing thickness, but a higher prevalence in thinner laminates, in line with the observations made for the impact behaviour of metallic shells by Lindfors *et al.* [20]. Sensitivity to impact energy was also noted by the authors, with a reduction in distinguishable variations between the different curvatures at the highest impact energy levels. Likewise, higher velocity airgun impact testing by Ambur and Starnes [27] visible in Fig. 2.2(a), revealed that the peak contact forces were more than double those of the drop weight impact cases, but with no distinguishable differences visible between the contact force response of different panel curvatures. This effect was attributed to the transient nature of the high-speed impacts, which gives rise to a localised response that is not reflected through the contact load measurements, while at the lower velocity impacts, membrane and bending effects are more dominant than the effects of inertia. Kistler and Waas [28] later investigated the validity of linear and non-linear curved plate theory in the context of quasi-static and low velocity impact response, demonstrating that the non-linear analyses more accurately captured the large deformations arising from bending and membrane effects due to the non-linear softening response.

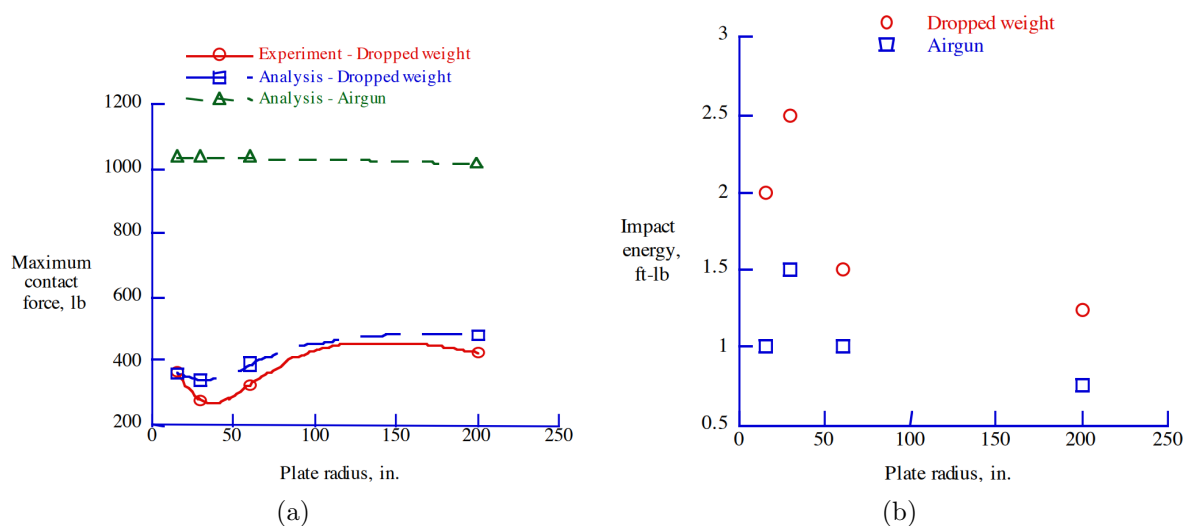


Figure 2.2: Carbon-fibre/epoxy composite plates after drop weight and airgun-propelled impact: (a) contact force and (b) damage initiation impact energy against plate radius, reproduced from [27].

A study by Saghafi *et al.* [29], investigated the combined effects of curvature and pre-loading on impact performance. Using glass fibre/epoxy panels with a quasi-isotropic layup,

flat laminates were pre-stressed in a test fixture, post-cure, prior to testing under drop weight impact. The pre-loaded state was achieved by bending the thin panels under the application of a static load, which incidentally formed curved panels. An increase in the pre-load was synonymous with an increase in the degree of curvature, and therefore a reduction in the radius of curvature. A clear distinction must be made between pre-loaded plates [29] and pre-strained laminates that are fabricated into a curved geometry under pressure and heat, thereby retaining some level of residual strain prior to the initiation of impact. Saghafi *et al.* [29] reported an increase in the maximum contact force together with a reduction in the BFD of the laminates subjected to a higher pre-load. The authors also highlighted that geometrical variations in the degree of curvature were distinctly higher than differences in the strain measurements on the surface of the laminates under pre-loading, rendering the geometrical effects of curvature more dominant than pre-loading. It is worth noting that the pre-stressing of laminates without the generation of curvature, has been shown to also reduce the amount of energy dissipated under impact [30]. Saghafi *et al.* [29] also reported that higher impact energies resulted in an increasingly larger difference between flat plates and curved, pre-stressed plates, attributed to the increase in the tension and the resulting stiffening effect in the outer curvature regions of specimens.

2.3.2 Stiffness

Kistler and Waas [25] observed a stiffer initial force-displacement response in panels with a higher degree of curvature. However, stiffness was reduced as these panels underwent softening due to the buckling of the structure. The response of more highly curved panels resembled the limit-point instability of a clamped arch, subjected to a central transverse point load. The authors noted that the maximum BFD of shallower plates, *i.e.* those with a lower degree of curvature, had almost immediately exceeded their small arch height of 1 mm. In addition to the smaller extents of bending and membrane stretching, the behaviour of the less curved panels was reminiscent of the more stable response of flat laminates. Although the stiffness for both panel curvatures increased again in the later stages of deformation, the recovery of stiffness was much lower in the panels with a higher degree of curvature, making the less curved plates stiffer at larger deformations. This behaviour, where the resultant peak force of the shallower panels overtakes that of the more curved panels, was observed at impact velocities representing static and dynamic impact. However, this was not observed at much higher impact velocities due to the dominance of the effects of inertia.

2.3.3 Damage

Ambur and Starnes [27] investigated the impact energy at which damage was initiated. A peak in initiation energy was observed for a curvature radius of $r = 30$ in, as seen in Fig. 2.2(b). This was the case for both rates of impact considered, where the damage-initiation impact energy level was considered to be a function of the curvature, with airgun impacts requiring half the level of impact energy as the corresponding drop weight impacts for damage to be initiated. Although the peak contact force recorded drops at plates with radius of curvature $r = 30$ in, a more significant impact force was necessary for damage to take place at this curvature. The sensitivity of the damage-initiation impact energy under airgun impact to the plate curvature, given the lack of sensitivity of the contact force to curvature, was explained with the differences in the particular damage modes that occur between the drop weight and airgun impact test.

Further numerical and analytical studies on another form of carbon-fibre/epoxy (T300/976) composite in cross-ply formation by Zhao and Cho [31], also demonstrated that significantly higher impact velocity thresholds were required for damage initiation in curved panels, in comparison to fully flat laminates. The threshold velocity for the two radii of curvature analysed, $r = 1.88$ in and $r = 3.72$ in, exceeded the threshold velocity of a flat plate. The authors assumed that the impact velocity necessary for the initiation of damage scales linearly with the square root of the impact energy required at a given impactor mass, and therefore follows the trend in Fig. 2.2(b) for drop weight impact. Moreover, the findings are in line with the work of Greszczuk and Chao [24], which highlighted the greater extent of crack-growth containment in the curved laminates, relative to flat geometries.

Zhao and Cho [31] also noted a reduction in the size of the damaged area with an increase in the degree of curvature of panels. The more extensive damage in panels with shallower curvatures was attributed to a lower stiffness response compared to the more curved panels. This agrees with previous findings reported by Kistler and Waas [28] and Christoforou and Swanson [32], where laminates with higher degrees of curvature produced stiffer responses under impact, although only during the initial stages of deformation, corresponding to the damage initiation period. In addition, the through-thickness location of the region with the highest severity of damage was shown to be sensitive to panel curvature. The most extensive damage was observed at the interlaminar interface closest to the rear face in flat panels, but closer to the front face in curved panels. Since all cases involving curved laminates only considered a convex impact direction, the panel strike faces would have been under tension upon impact.

The tensioned regions yield a stiffer, more damage-prone response when the panels undergo deformation and bulging in the direction normal to the curvature.

An increase in damage area under larger extents of pre-loading and impact-energy levels, was reported by Saghafi *et al.* [29]. The study demonstrated that although increasing the pre-load leads to more extensive damage, the total amount energy absorbed by the laminate decreases. This follows previous numerical studies on curved panels and cylindrical shells [33], which have shown that a larger degree of curvature, together with the resulting increased stiffness on the strike face, results in a larger contact force and therefore greater damage under impact. When the portion of the impactor kinetic energy transferred to the laminate used in damage initiation and propagation increases, energy absorption via other means is reduced. Hence, an increase in shell curvature can bring about more damage under impact loading and is accompanied by a fall in energy absorption via various mechanisms of deformation.

Moreover, matrix cracking along the direction of pre-loading, aligned with the direction of curvature, was observed by Saghafi *et al.* [29]. The cracks were more prevalent in the front half of the laminates under tension, than in the compressed regions in the vicinity of the back face, suggesting that the compressive state of this region had, to an extent, inhibited crack propagation. While delamination and matrix cracking were considered to be the dominant modes of damage, ply splitting orthogonal to the pre-load direction was also reported, albeit to a much smaller extent. In addition, the resulting bulge shape observed on the back face at lower impact energies resembled an ellipsoid, tending towards a rhombus-like shape at higher impact energies.

The findings are aligned with the work of Lin and Lee [34], who also discovered more severe damage occurring in 0/90 configurations of carbon-fibre/epoxy cylindrical shells, with $r = 4.9$ in, compared to flat laminates of equivalent dimensions under a given velocity of drop weight impact. However, numerical analysis and inspection of the post-impact damage showed the flat plates to possess matrix cracks and delamination close to the rear face of the target, while the cylindrical shells exhibited different modes of damage through the thickness. In the cylindrical shells, more severe fibre cracking was observed in the vicinity of the impact location on the front face, shear cracks in the middle region, and delamination at the interfaces close to the front and rear surfaces. According to Palazotto *et al.* [35] though, fibre failure in curved laminates only becomes relevant at higher impact energies, the threshold of which is reached much earlier than in the case of flat laminates.

2.3.4 Failure modes

As pointed out by Johnson and Holzapfel [36], the majority of studies on the performance of curved composite laminates are carried out with regards to foreign object impact on aircraft skin. While the focus of most studies is limited to convex impact, representing impact on a fuselage or leading edge of a wing, concave impact was also investigated by these authors. This was reported to be representative of engine containment and impact of broken fan blades on nacelle structures. Numerical simulation and experimental high velocity gas gun impact testing of 6 mm thick, curved laminates composed of R-glass and toughened epoxy resin with a quasi-isotropic lay-up, revealed the existence of significant differences in the failure modes undergone by the concave and convex panels at a given impact energy.

The extent of delamination due to impact by a steel ball at a velocity of approximately $V_I = 110$ m/s in plates with a radius of curvature $r = 7.60$ in, was determined from C-scan tests and is outlined in Fig. 2.3. The authors observed vastly different responses between the plates under the two opposite directions of impact. The specimens under concave impact were fully perforated through localised fibre fracture, accompanied by very limited delamination. Under convex impact however, the same structure underwent extensive bending, together with local and distal delamination across the laminate, before the projectile rebounded, leaving the front face with a noticeably large transverse crack. The large bending deformations were attributed to the stored elastic strain energy in the convex face, the release of which prevented localised fibre fracture and led to the rebound of the projectile.

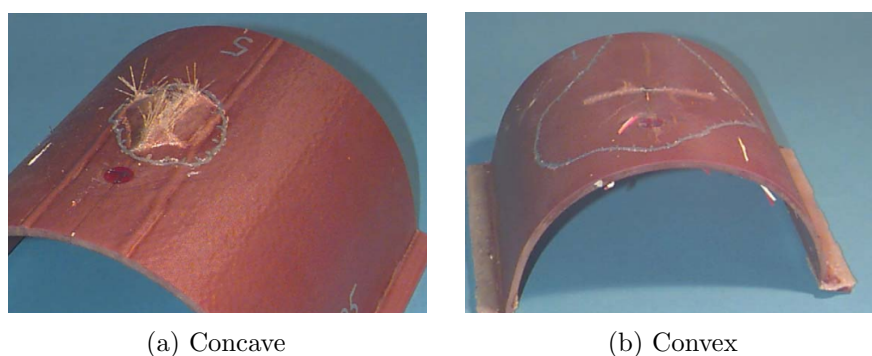


Figure 2.3: Glass fibre/epoxy composite plates after gas gun impact by a 30 mm diameter steel ball under opposite directions of impact, reproduced from [36].

2.3.5 Advanced cases

The ramifications of the presence of curvature have been extended to doubly curved panels in numerous studies, e.g. [37, 38], featuring analyses in the form of compression, crush and buckling tests. In one study, repeated, non-penetrating drop weight impact tests were performed on the external curvature of composite domes composed of short, randomly oriented glass fibres in a polyester resin suitable for crashworthiness applications [39]. It was shown that the domes with a larger degree of curvature, equivalent to a smaller radius of curvature of $r = 2.95$ in, tolerated higher peak loads and more damage, while exhibiting a lower damage propagation energy level and a smaller extent of back face deflection than slightly shallower domes with $r = 3.94$ in.

Another study expanded the notion of a curved geometry to include the behaviour of pressurized vessels. A numerical energy-based failure model developed by Yokoyama *et al.* [40], validated using data from previous studies of physical coupon testing, investigated impact on curved woven carbon fibre-reinforced epoxy laminates subjected to internal pressure. The effect of curvature on energy dissipation due to damage in the laminate is seen in Fig. 2.4, for two different values of plate thickness, h_t , along with two load cases for internal pressure, P_i . The addition of curvature noticeably increased the dissipation of energy for impact energies greater than 4 J and 2 J in the thicker and thinner laminates, respectively. This indicates an increase in the extent of damage caused by the impact load. The divergence of the dissipated energy in the curved laminates from the flat laminates grew with an increase in impact energy, before settling on a constant value at the higher impact energy levels considered for each plate thickness.

At the lowest impact energy tested for each plate thickness, the difference between plates of varying curvature was negligible. With an incremental increase in impact energy, the lower degree of curvature appeared to yield a smaller increase in energy dissipation than the two higher degrees of curvature. However, this difference decreased as the impact energy was raised further. The addition of internal pressure reduced the level of energy dissipated by all laminates, although this was particularly the case for flat plates, which saw the largest drop while the curved panels remained substantially insensitive to the addition of pressure. The fall in dissipated energy levels demonstrated a reduction in the extent of damage in the plates under additional loading in the form of internal pressure. The study also predicted a reduction in plate damage with an increase in thickness, under both pressure loading conditions and for all curvatures considered.

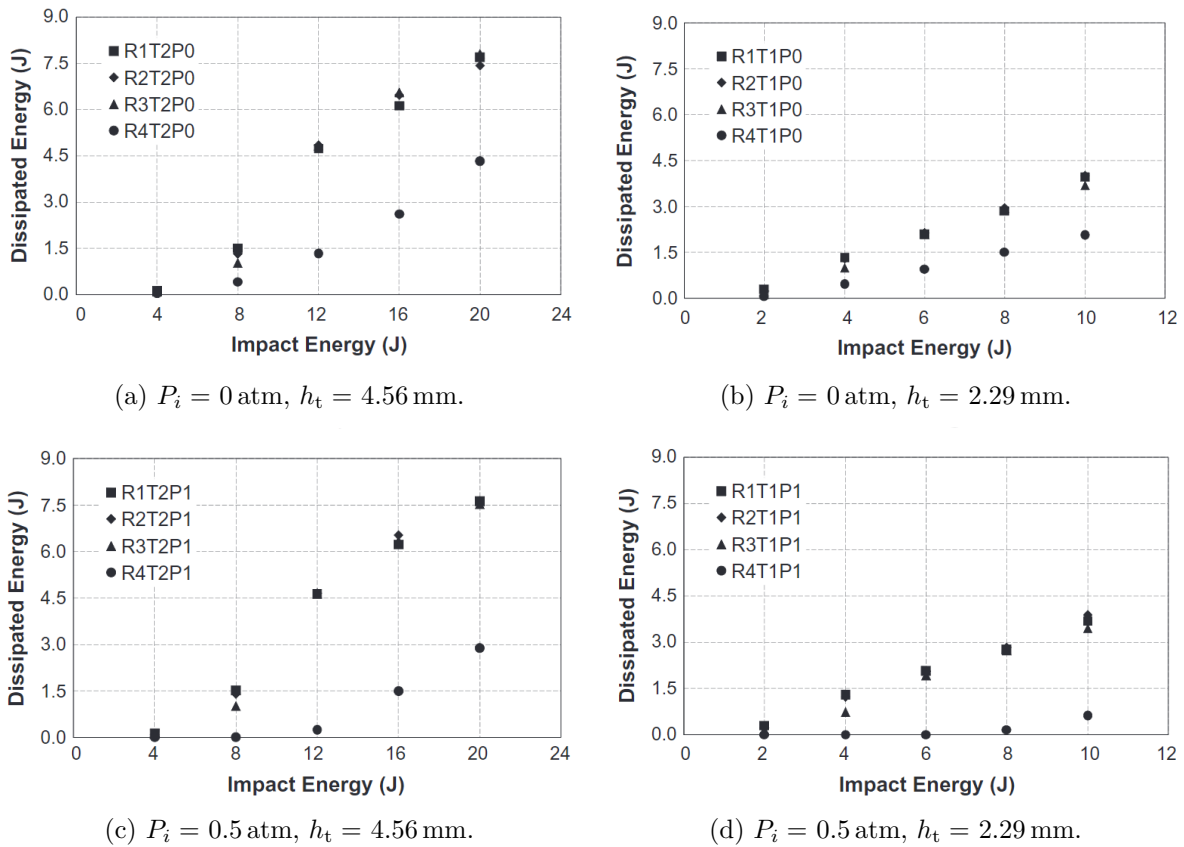


Figure 2.4: Energy dissipated due to damage as a function of impact energy, for laminates with internal curvatures of $R1 = 3.94$ in, $R2 = 4.92$ in, $R3 = 7.87$ in and $R4 = \infty$, without (a)-(b) and with (c)-(d) the addition of internal pressure, reproduced from [40].

2.3.6 Ballistic limit

To investigate curvature effects under ballistic rates of impact, Stargel [41] tested the behaviour of quasi-isotropic carbon-fibre/epoxy AS4/3501-6 plates under the impact of spherical steel projectiles, accelerated with a light gas gun. The testing of curved composite panels was accompanied by testing corresponding aluminium 2024-T3 plates. This was done to identify the role of geometry-induced differences in the impact response of the curved targets made from the two different material systems, for the application to aircraft fuselages and wind turbine blade sections. The specimens were manufactured with multiple curvature radii, and cut to have equal side and arc lengths of 8 in. The curved specimens were held in a fixture along the two straight edges during impact.

The experimental and numerical predictions of the ballistic limit for plates of different radii of curvature, adapted from [41], are presented in Fig. 2.5(a) in terms of percentage change in the V_{50} prediction of the curved panels relative to the flat composite panel. Positive change

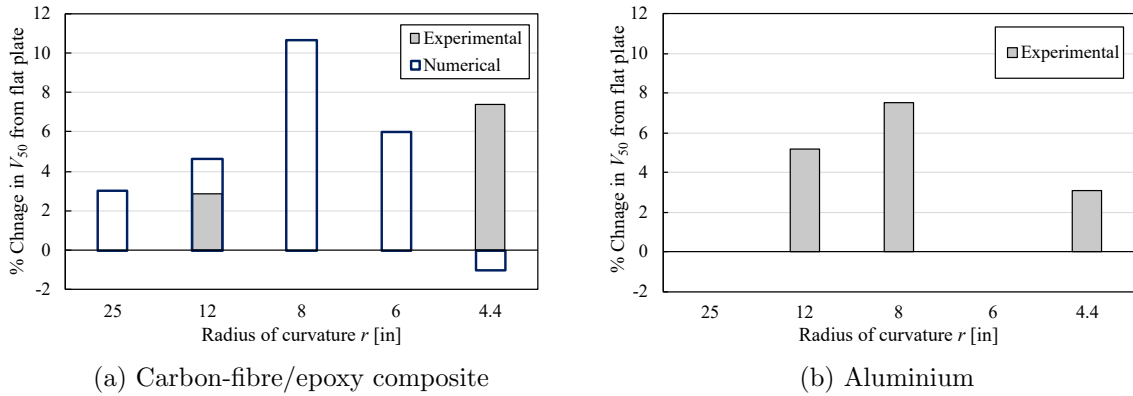


Figure 2.5: Percentage change in V_{50} predictions from flat to curved panels with varying radii of curvature, based on [41].

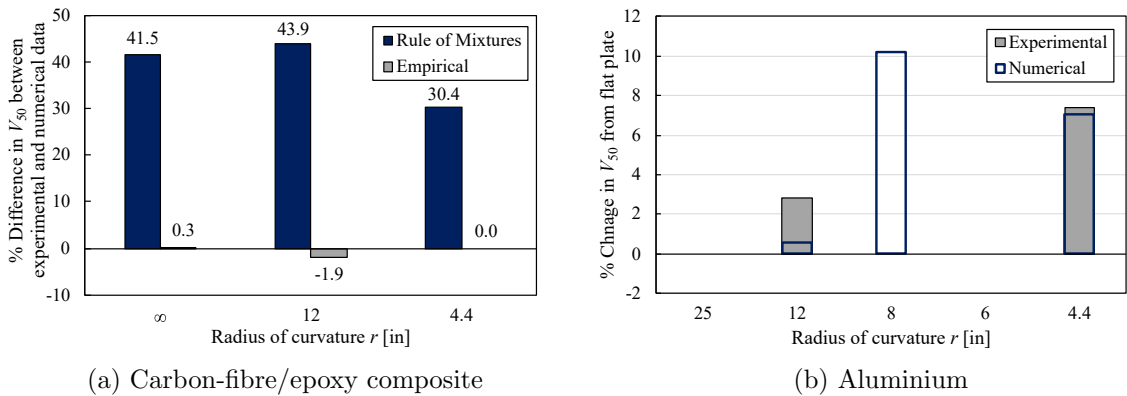


Figure 2.6: (a) Percentage difference between numerical and experimental V_{50} predictions for different elastic stiffness values, (b) percentage change in V_{50} predictions from flat to curved panels using an empirically derived elastic stiffness in numerical simulations, based on [41].

represents better impact performance in curved panels than flat panels, in terms of the V_{50} parameter. Due to the good agreement between experimentally- and numerically-derived data for the aluminium plates, only one set of data is presented for these plates in Fig. 2.5(b). The overall trend visible in these figures indicates a parabolic relationship between the panel curvature and the V_{50} ballistic performance indicator. Since the data for both material systems follows the same trend, it is possible to assume that geometry plays a key role in subsequent impact behaviour. In addition, the data plots suggest the existence of an optimal value for panel curvature that results in peak ballistic performance, the basis for which was justified with an energy-based method.

Due to relatively poor agreement between the computational results and the experimental data for the composite panels, the authors argued the need for an empirical, effective elastic modulus, as an input into the numerical model. Figure 2.6(a) demonstrates the improvements

achieved in the difference between numerical and experimental impact data with the use of an empirical stiffness value, as opposed to the one used initially, calculated using the rule of mixtures. Using the effective stiffness term also resulted in better alignment between numerical and experimental predictions of the change in V_{50} of curved panels relative to flat panels, as demonstrated in Fig. 2.6(b). Moreover, post-impact non-destructive damage analysis of the composite specimens showed a reduction in damage area with increasing impact velocity for a given curvature, and with increasing radius of curvature for a given impact velocity.

Further ballistic testing and modelling performed by Tan [42] on a B4C/Kevlar[®] armour system demonstrated an increase in V_{50} , in combination with a reduction in peak deflection on the rear face of laminates, with decreasing radius of curvature. The values of curvature radii tested were limited to 4.72 in, 6.69 in and 8.66 in, which do not span across a sufficiently large range to capture the complete picture of the effect of curvature on impact performance. The study did, however, reveal maximum out-of-plane deflection to be more sensitive than the ballistic limit velocity to changes in panel curvature.

The curved geometries tested in the literature vary greatly in terms of physical and geometrical attributes such as in-plane dimensions and thickness, in terms of laminate architecture including layup sequence and material composition, and in terms of testing conditions. A wide range of impact velocities and energies are considered from quasi-static to dynamic rates, with some subjected to boundary effects from the test fixture or additional variables such as internal pressure or pre-loading. Nevertheless, the overall trends observed in the findings have been largely congruent.

The difference between the impact response of flat and curved geometries has been shown to be significant for panels with a radius of curvature of $r < 60$ in. Irrespective of the composite material or layup sequence considered, higher contact forces and extents of damage were widely reported for curved composite panels under convex impact, relative to their flat counterparts. Meanwhile, only minimal differences seem to exist amongst specimens of varying degrees of curvature, with trends largely dependent on the range of curvatures investigated, due to the parabolic relationship that exists between the degree of curvature in a panel, and its impact performance. These differences become negligible at sufficiently high impact velocities, where inertial effects prevail over geometric effects, thereby dominating the deformation of the target under impact loading.

2.4 Modelling impact

2.4.1 Finite element methods

Numerical modelling is an integral part of understanding the behaviour of materials under impact loads, or in fact under any kind of load case. It facilitates the prediction of performance, without the costs associated with experimental testing. Accurate numerical models can therefore be used to not only understand existing designs, but also as tools for improving and optimising future designs. A successful model however, must be experimentally validated for a range of input parameters, and must also be computationally efficient to maintain its edge over practical testing, both financially and duration-wise. Impact models of UHMWPE composite laminates have evolved from an array of simpler, yet fundamental, material testing procedures that can be experimentally validated. These include a multitude of in-plane tension, through-thickness shear, short beam shear, and cantilever beam tests that have been employed in the past [19, 43–46]. These mechanical material characterisation methods have aided the development of suitable constitutive material models to represent the behaviour of UHMWPE systems [47]. In addition, they have facilitated the construction of modern numerical models of UHMWPE composites under ballistic impact.

The modelling and prediction of material behaviour under impact loading has been the subject of numerous studies and has been attempted via different approaches. While some have focused on the mechanisms through which the material deforms when subject to a single point of impact, others have placed greater emphasis on the ability to predict the impact performance of the material, as defined by either the back-face deflection (BFD) or by the ballistic limit velocity (V_{50}). Numerical models can be used as a tool for analysing material behaviour under a wide range of impact scenarios. They can be used for predicting new impact scenarios, as well as driving design. Previous studies have investigated this behaviour through the development of multi-scale modelling approaches, from beam bending [19] to hydrocodes [48].

More recently, Hazzard *et al.* [49] proposed a homogenised sub-laminate approach in the explicit finite element code LS-DYNA, as seen in Fig. 2.7, to model laminates of Dyneema[®] over a range of impact rates. Homogenisation of multiple plies at the macro-scale was deemed crucial for keeping the simulation times viable, due to the low ply thickness of approximately 67.5 μm for each unidirectional layer and relatively large panel thicknesses, potentially creating very large models. It is worth noting that although impact performance can be predicted to a

sufficiently accurate degree [49], the sub-laminate approach exhibits inherent limitations, such as the inability to capture deformation of the laminate through the indirect tension mechanism [44], or the contribution of in-plane shear-induced fibre scissoring [50]. Furthermore, investigations that have implemented these features have not addressed varying loading rates [51].

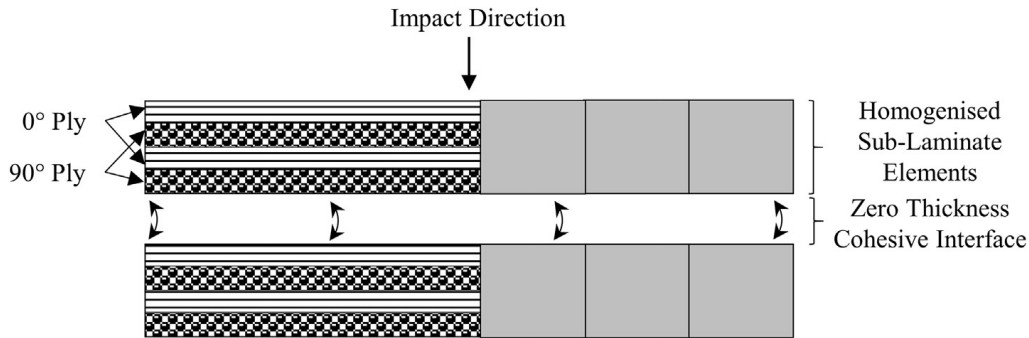


Figure 2.7: The sub-laminate cross-ply homogenisation approach adopted by Hazzard *et al.* [49].

Numerical models can range from the micro- and meso-scales to the macro-scale, equivalent to the fibre and matrix level, the lamina level and the laminate level, respectively. The length scale investigated in each study was selected based on the level of detail required in the output, the objectives of the study and the availability of computational resources. The impact rates investigated in literature vary from quasi-static rates where impact velocity, V_I , is less than 10 m/s, to hyper-velocity impact rates where V_I exceeds 1000 m/s. Likewise, each approach varies in terms of effectiveness in simulating the transfer of energy and the modes of deformation that occur during the different stages of impact. The stages of impact were summarised by Greszczuk and Chao [24] as follows:

- (1) Contact is established between projectile and target.
- (2) The impact of the projectile imposes a time-dependent pressure on the target.
- (3) Stresses arise from the impact pressure through the material medium.
- (4) If significant, the stresses activate various forms of mechanical failure.
- (5) These failure modes interact to induce damage.

As a result, the modelling approach in each study was adapted to capture these failure mechanisms, energy dissipation paths and other phenomena brought about by the magnitude of the impact velocity. One such phenomenon is the appearance of shock waves upon impact at higher ranges of impact velocity [48]. Other factors affecting the modelled impact behaviour

of UHMWPE laminates include laminate thickness and architecture, projectile geometry and dimensions, as well as the boundary conditions imposed upon the laminate during impact.

At much higher impact velocities, namely those approaching 1000 m/s, models must account for the non-linear shock compressibility behaviour of the material. Nguyen *et al.* [48] captured this effect using the Mie-Grüneisen equation of state. This is a non-linear shock formulation equation of state that describes the pressure contribution from volumetric strain $p(\varepsilon_{\text{vol}}, e)$, defined by

$$p(\varepsilon_{\text{vol}}, e) = p_r(v) + \frac{\Gamma(v)}{v} [e - e_r(v)] , \quad (2.4)$$

where v is the volume, $p_r(v)$ is a reference pressure, $\Gamma(v)$ is the Grüneisen coefficient, e is the internal energy and $e_r(v)$ is a reference internal energy, with the empirically derived shock Hugoniot used as the reference [52, 53]. The Grüneisen coefficient of 1.64 for polyethylene was deemed suitable, due to similarities to the shock response of UHMWPE [54].

In general, the stress tensor can be split into volumetric and deviatoric components that are handled separately [55], although this is not the case for anisotropic materials where the two responses are coupled and therefore indistinguishable as separate responses. However, the theory of shock wave propagation through orthotropic materials, which would not trigger significant coupling between volumetric and deviatoric responses, can still be used for anisotropic materials, as demonstrated in [48]. According to Anderson *et al.* [56], total pressure in anisotropic materials can be defined by the pressure contributions from deviatoric strains, in combination with the contributions from volumetric strain, as

$$p = p(\varepsilon_{\text{vol}}, e) - \frac{1}{3} (C_{11} + C_{21} + C_{31}) \varepsilon_{11}^{\text{d}} - \frac{1}{3} (C_{12} + C_{22} + C_{32}) \varepsilon_{22}^{\text{d}} - \frac{1}{3} (C_{13} + C_{23} + C_{33}) \varepsilon_{33}^{\text{d}} , \quad (2.5)$$

with C_{ij} denoting the coefficients of the material stiffness matrix, and the $\varepsilon_{ij}^{\text{d}}$ terms representing the deviatoric strains in the three principal directions denoted by i and j . Nguyen *et al.* [48] used this formulation, together with an empirical linear relationship between the shock wave velocity, U_S , and the velocity of the particle, u_p , where

$$U_S = c_0 + S u_p , \quad (2.6)$$

with c_0 denoting the bulk sound speed, calculated from elastic orthotropic constants, and S

referring to the gradient of the linear curve, the value of which is empirically adjusted to match flyer plate impact test results. Due to the low friction coefficient of UHMWPE composites, clamp slippage was a common occurrence under high velocities of impact, as observed during experimental investigations [57]. This prompted Nguyen *et al.* [48] to refrain from using any form of boundary condition to hold the specimen in place during impact. Likewise, the ballistic impact model developed by Hazzard *et al.* [49] had no boundary conditions applied, due to the limited effectiveness of clamps in holding the HB26 specimens of Dyneema[®] in place.

At impact velocities below 2000 m/s, Nguyen *et al.* [57] demonstrated that material strength plays a vital role in controlling the deformation and penetration behaviour of the material, as evident from poor deformation predictions and under-predictions of the ballistic limit velocity. Premature through-thickness shear failure was identified as the major cause of these effects, attributed to coupling between out-of-plane tension and out-of-plane shear failure modes. This issue was subsequently addressed through sub-laminate discretisation [48], which decouples the two out-of-plane failure modes. The authors note that using this approach, the model can be used to generate data for one-dimensional simulations that compare well to experimental measurements of the free surface velocity in impact tests on UHMWPE composite plates performed by Lässig *et al.* [58]. This is demonstrated in Fig. 2.8, where it was acknowledged that the agreement between the data for initial and subsequent release waves exist for only 0.3 ms to 3.5 ms following impact. Beyond this point, it can no longer be assumed that strain is purely one-dimensional, since the free surface velocity measurements are affected by waves propagating from the lateral edge of the specimen.

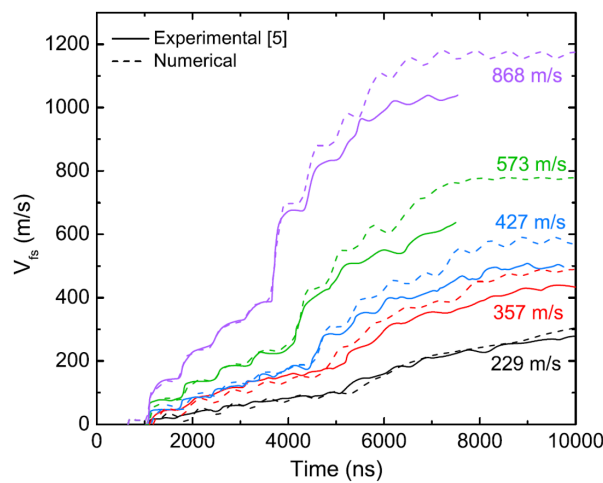


Figure 2.8: Free surface velocity trace from inverse plate impact test and numerical verification, reproduced from [58].

In addition to capturing physical phenomena, modelling features and considerations such as element dimensions and mesh sensitivity of the output have also been the subject of past studies. According to Nguyen *et al.* [48], it was imperative to match the mesh density of the projectile to that of the laminate impact zone, in order to avoid a stiffness mismatch between the two bodies. This approach was also taken by Hazzard *et al.* [49], who also used a single, one integration point element per sub-laminate layer, as beam studies confirmed the accuracy of the approach in achieving near zero bending stiffness in laminate models of Dyneema[®]. A finer mesh density was selected by Hazzard *et al.* [49] for the central impact zone, with a cubic element length of 1 mm following a mesh refinement study, combined with a mesh bias with decreasing mesh density away from this central impact region. The use of cubic elements in the impact zone was an essential feature of both studies, in order to maintain stability and limit non-physical deformation modes under large, impact-induced deflections.

2.4.2 Matrix contribution

Superior fibre properties, namely high tensile strength, high modulus and high strain to failure are traditionally credited for providing UHMWPE composites with exceptional impact performance. Hence the absence of any contribution from the matrix and its properties in ballistic performance indicators such as the Cunniff parameter [9]. However, recent studies have shed more light on the role of the matrix in the behaviour of the composite laminates under impact loading [59]. Karthikeyan *et al.* [50] highlighted the inverse relationship that exists between matrix shear strength and the velocity-based ballistic performance of composite plates. The authors reported higher ballistic velocity limit predictions, but also higher back face deflections, for lower values of matrix shear strength. This was observed in both carbon-fibre-reinforced plastic (CFRP) and UHMWPE composites, furthering the work of Walsh *et al.* [60], in which the necessity of the matrix medium was demonstrated. While through-thickness tensile and shear strengths are known to be predominantly determined by the properties of the matrix material [61, 62], low interlaminar shear strength (ILSS) has been identified as another contributor to increased energy absorption under impact loading. Through the ILSS, failure mechanisms under impact, the most significant of which is delamination [63], can be altered and controlled. The ILSS is typically dominated by matrix shear properties, although it has been shown to be dependent on processing parameters, namely the pressure and temperature cycles used during laminate consolidation [64]. Chocron *et al.* [65] pointed out that matrix properties were fairly insignificant in influencing the impact wave speed, although the study

only considered deformations on the laminate back face. Hence, a more in-depth investigation is required to determine whether this is the case across all interfaces throughout the laminate thickness, as the front and middle regions may react differently.

2.4.3 Contact modelling

Previous attempts to model UHMWPE composites under impact loading have employed a variety of algorithms and modelling tools to define physical contact between elements representing laminate layers. For example, in the model developed by Nguyen *et al.* [48], each sub-laminate layer was one element thick and contact between adjacent layers was achieved with the addition of a small gap, in order to prevent over-penetration of elements. The total thickness of the gaps was less than 5% of the total specimen thickness, and was therefore assumed to impose negligible effects on the performance of the laminate. The sub-laminates were connected through bonded contact, with a failure criterion based on normal stress, σ_N , together with shear stress, σ_S , where

$$\left(\frac{\sigma_N}{S_N}\right)^a + \left(\frac{\sigma_S}{S_S}\right)^b \geq 1, \quad (2.7)$$

with S_N and S_S representing normal and shear strengths, respectively, and exponents a and b assumed to be equal to 1.0. A high strain rate value was used for the tensile strength of the composite, together with a high pressure value for interlaminar shear strength, the nature of which was deemed more suitable for ballistic impact and the subsequent high pressure that propagates through the material.

The cohesive zone model (CZM) approach is deemed most suitable for modelling interlaminar failure of composite laminates, since the energy required for crack propagation can be accounted for, the absence of which is a limitation of a stress-based approach [48]. A stress-based approach assumes that the contribution of delamination to the total amount of energy absorbed is relatively small. According to Peijs *et al.* [66] however, in high-performance polyethylene/epoxy composites such as SpectraTM/AralditeTM LY556/HY917/DY070, energy dissipation through this type of failure accounts for a tenth of the total impact energy, with the rest of the impact energy mostly absorbed through fibre fracture. Impact energy dissipation through delamination is particularly prevalent in low velocity impacts, with a reduction in its significance observed at higher impact velocities.

The CZM method [67, 68] has been developed as a tool to model interfacial fracture.

A damage zone is simulated at the tip of a discontinuity, such as a crack, where there is a continuation in stress transfer across this zone during crack growth. Traction-separation laws for different modes of fracture, as well as the combined mixed-mode response, govern the fracture behaviour of the interface. The simplest form of the traction-separation law is characterised by a bi-linear curve, with an initial stiffness representing the decohesion state. Upon reaching maximum traction, damage is initiated and a softening phase follows where the stiffness is gradually reduced to zero, portraying separation at the interface. Advantages of the CZM method over other fracture mechanics-based methods, such as the virtual crack-closure technique (VCCT), include the ability to predict crack initiation as well as crack propagation [69].

Hazzard *et al.* [49] modelled the behaviour between homogenised sub-laminates using a cohesive surface-to-surface contact definition in LS-DYNA, employing the tiebreak contact option with the DYCOSS algorithm [70], to provide a mixed-mode bilinear traction separation law for capturing the delamination of the composite. The interpenetration of sub-laminates and subsequent negative contact energy values were also reported here. The authors overcame rate effects attributed to a non-automatic contact algorithm, through the implementation of additional automatic surface-to-surface contact. In order to accurately capture the limited load transfer between the sub-laminates, the authors proposed that the traction stiffness values of the interface should be scaled inversely to the sub-laminate thickness. The thickness of each layer was said to implicitly represent the number of interfaces that were present in a homogenised stack. As a result of the homogenisation of individual plies, it was vital to capture the contribution of the interface between each sub-laminate, and the role that the matrix properties play in this. The larger the sub-laminate thickness, the higher the number of interfaces it represents that can deform and dissipate energy. The mode I traction stiffness, K_I , was therefore calculated as

$$K_I = \frac{E_m}{h_{SL}}, \quad (2.8)$$

where h_{SL} is the sub-laminate thickness and E_m is the Young's modulus of the matrix, while the mode II equivalent, K_{II} , is approximated as 60% of K_I . Although this model yields realistic indications of the energy absorbed by the interface through mode I and mode II deformations under impact, the values obtained are of a mixed-mode nature. It would be valuable to isolate the two modes of deformation in order to investigate the effect of different interface fracture parameters, as determined by matrix properties, on the impact performance of the laminate.

One such approach utilises element-based cohesive models to describe the interface between homogenised sub-laminate layers of a fibre-reinforced composite structure [71]. Interface elements are inserted between solid or shell elements representing laminate layers, as displayed in Fig. 2.9(a) [72]. Crack behaviour is governed by a traction-separation law, based on forces per unit area and displacements, as opposed to stresses and strains. The propagation of the crack is recorded by the relative displacement between the top and bottom surfaces of the cohesive elements, interpolated to the Gauss points. As per surface-based cohesive zones, the traction-separation law is based on several interfacial parameters; maximum strength, σ^{\max} , and critical fracture energy, G_C , together with the elastic loading stiffness, K .

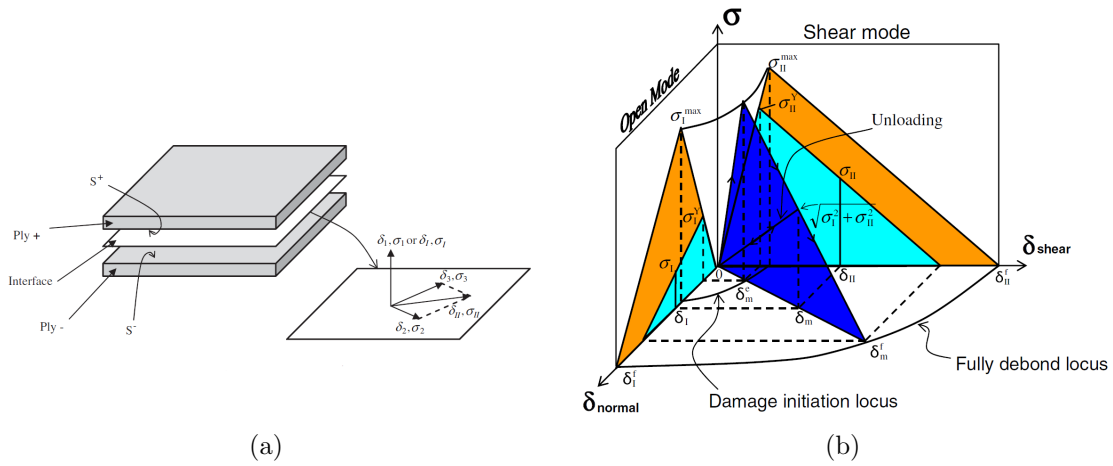


Figure 2.9: (a) Modelling the interface between two surfaces S^+ and S^- according to (b) a mixed-mode cohesive law, reproduced from [72].

Jiang *et al.* [72] proposed an interface constitutive law for the analysis of delamination, an approach currently adopted by the University of Bristol cohesive user-defined material (UMAT) model. This bilinear cohesive law is expressed in terms of mixed-mode behaviour, representing the interactions of mode I normal opening and mode II in-plane shear fracture, as shown in Fig. 2.9(b). Note that here, mode II encompasses both mode II and mode III shear behaviour. The relative displacement components are denoted by δ , and traction components by σ , while σ^{\max} components refer to the maximum interfacial strengths. Subscripts I, II and m correspond to mode I, mode II and mixed-mode fracture, respectively, while superscripts Y and e refer to values at the onset of damage, softening or yield, with f referring to values at the point of total interface failure. The deformations are calculated from relative displacements in the Cartesian coordinate system, with 1 referring to the out-of-plane direction, while 2 and 3 represent the in-plane directions of motion shown in Fig. 2.9(a). The opening, shear, and mixed-mode relative

displacements, δ_I, δ_{II} , and δ_m , are defined as

$$\delta_I = \delta_1 \quad (2.9)$$

$$\delta_{II} = \sqrt{\delta_2^2 + \delta_3^2} \quad (2.10)$$

$$\delta_m = \sqrt{\delta_I^2 + \delta_{II}^2}. \quad (2.11)$$

The mixed-mode damage initiation criterion marking the onset of softening under a multi-axial stress state adapted from previous studies [73, 74], is given by

$$\sqrt{\left(\frac{\max(\sigma_I, 0)}{\sigma_I^{\max}}\right)^2 + \left(\frac{\sigma_{II}}{\sigma_{II}^{\max}}\right)^2} = 1, \quad (2.12)$$

so that the relative mixed-mode displacement at damage initiation can be calculated as

$$\delta_m^e = \left(\left(\frac{K_I \cos \Omega_I}{\sigma_I^{\max}} \right)^2 + \left(\frac{K_{II} \cos \Omega_{II}}{\sigma_{II}^{\max}} \right)^2 \right)^{-1/2}, \quad (2.13)$$

with the initial stiffness values, K_I and K_{II} , possessing significantly high values, since the interface is assumed to be infinitesimally thin. The direction cosines are defined as

$$\cos \Omega_I = \frac{\delta_I}{\delta_m} \quad (2.14)$$

$$\cos \Omega_{II} = \frac{\delta_{II}}{\delta_m} = \sin \Omega_I, \quad (2.15)$$

where Ω_I and Ω_{II} are the angles from the normal and shear planes to the mixed-mode plane. The yield stresses, in other words the maximum traction values, are calculated as

$$\sigma_I^Y = K_I \delta_m^e \cos \Omega_I \quad (2.16)$$

$$\sigma_{II}^Y = K_{II} \delta_m^e \cos \Omega_{II}. \quad (2.17)$$

Following the onset of damage, or softening, the interface strength degrades linearly under further loading, until decohesion occurs due to complete failure of the interface at a critical fracture energy level. The critical energy levels in each mode correspond to the strain energy release rates, given by

$$G_I = \frac{1}{2} \sigma_I^Y \delta_m \cos \Omega_I \quad (2.18)$$

$$G_{II} = \frac{1}{2} \sigma_{II}^Y \delta_m \cos \Omega_{II} . \quad (2.19)$$

Interface failure is modelled by the power law [75, 76], based on the failure criterion

$$\left(\frac{G_I}{G_{IC}} \right)^\alpha + \left(\frac{G_{II}}{G_{IIC}} \right)^\alpha = 1 , \quad (2.20)$$

where α is derived empirically from mixed-mode experimental testing, and has a value in the range of $1 \leq \alpha \leq 2$. These equations are used to derive the relative mixed-mode displacement at failure, in the form of

$$\delta_m^f = \left(\left(\frac{\sigma_I^Y \cos \Omega_I}{2G_{IC}} \right)^\alpha + \left(\frac{\sigma_{II}^Y \cos \Omega_{II}}{2G_{IIC}} \right)^\alpha \right)^{-1/\alpha} . \quad (2.21)$$

Alternatively, the Benzeggagh-Kenane law [77] can be employed to evaluate failure, a criterion that is more suited to modelling the relatively brittle behaviour of epoxy-based composites [78], using

$$G_C = G_{IC} + (G_{IIC} - G_{IC}) \left(\frac{K_{II} \cos^2 \Omega_I}{K_I \cos^2 \Omega_{II}} + K_{II} \cos^2 \Omega_I \right)^\beta , \quad (2.22)$$

where BK is an empirical parameter, with the the relative mixed-mode displacement at failure calculated as

$$\delta_m^f = \frac{2G_C}{\sigma_I^Y \cos \Omega_I + \sigma_{II}^Y \cos \Omega_{II}} . \quad (2.23)$$

Subsequently, Jiang *et al.* [72] introduced a damage parameter, D , for the purpose of recording damage accumulation at the interface, with

$$D(\delta_m) = \frac{\delta_m - \delta_m^e}{\delta_m^f - \delta_m^e} , \quad (2.24)$$

based on a simulation time-step of Δt , for a history variable, d , evaluated at time t as

$$d|_t = \max(d|_{t-\Delta t}, D|_t) . \quad (2.25)$$

Meanwhile, the unloading stresses were assumed to be reduced from the maximum yield stress in the respective direction of loading, by a loading level factor of δ_{ratio} , such that

$$\delta_{\text{ratio}} = \frac{\delta_m}{\delta_m^e + d(\delta_m^f - \delta_m^e)} , \quad (2.26)$$

so that the normal and shear tractions can be defined as

$$\sigma_{\text{I}} = (1 - d)\delta_{\text{ratio}}\sigma_{\text{I}}^{\text{Y}} \quad \text{for } \delta_{\text{I}} \geq 0 \quad (2.27)$$

$$\sigma_{\text{I}} = (1 - d)\delta_{\text{ratio}}\sigma_{\text{II}}^{\text{Y}}. \quad (2.28)$$

These are translated into stresses in the Cartesian coordinate system as normal stress σ_1 , with a penalty contact stress to reduce interpenetration of neighbouring element faces, in the form of

$$\sigma_1 = \sigma_{\text{I}} \quad \text{for } \delta_1 \geq 0 \quad (2.29)$$

$$\sigma_1 = \delta_1 K_{\text{I}} \quad \text{for } \delta_1 < 0. \quad (2.30)$$

The shear stresses are expressed as

$$\sigma_2 = \frac{\sigma_{\text{II}}\delta_2}{\delta_{\text{II}}} \quad (2.31)$$

$$\sigma_3 = \frac{\sigma_{\text{II}}\delta_3}{\delta_{\text{II}}}. \quad (2.32)$$

Note that stress degradation was modelled here as a proportional reduction of the peak stress, in contrast to previous works that have employed initial stiffness values for this purpose.

2.5 Concluding remarks

Studies have been performed on the failure mechanisms of laminates of Dyneema[®] under impact, in a continuous effort to enhance the ballistic performance of modern UHMWPE composite personal and vehicular protection [79]. Most however, have been limited to flat laminates, devoid of any manufacturing effects. In reality, panels used in impact protection are not necessarily flat, with many possessing single or double curvature. Modern manufacturing techniques of doubly-curved surfaces induce the geometrical and manufacturing effects of curvature and in-plane shearing, the implications of which on the ballistic impact performance of UHMWPE composites have not previously been investigated. As a result, these form the basis of the work presented in *Chapter 4* and *Chapter 5*. But first, the contribution of the matrix to the performance of UHMWPE laminates under impact, a topic that is mostly overlooked in literature, is investigated in the first technical chapter, *Chapter 3*, with the development of suitable numerical tools for this purpose.

Chapter 3

Modelling the laminate interface

3.1 Introduction

Generally speaking, delamination is perceived to be one of the most critical modes of failure in laminated composites, as a result of their relatively poor through-thickness and interfacial performance [80]. Characterising the delamination process has therefore been crucial to understanding crack initiation and growth mechanisms, and subsequently, to devising preventative measures. Under high rates of impact, UHMWPE composites can readily deform and delaminate in the normal direction and particularly in the shear direction. The extent of deformation via these mechanisms determines the level of energy absorbed under impact, and hence the impact performance [50]. Since the delamination fracture process is generally dominated by matrix properties and is of a mixed-mode nature, it is imperative to consider the deformation of the composite material in both mode I and mode II. Thus, the purpose of this study is to develop a better understanding of the composite deformation mechanisms by approaching the inter-laminar interface modelling with an element-based (E-B) cohesive zone model (CZM).

This chapter is based on the work presented at the *22nd International Conference on Composite Materials* [81]. Firstly, impact on a panel of Dyneema[®] is numerically simulated and analysed using an element-based cohesive zone method for a range of impact velocities. The models are validated against numerical [49] and experimental [57] data from literature, and subsequently used to explore the dissipation of energy that occurs at the sub-laminate interfaces. This is followed by parametric studies involving a multitude of modelling and physical parameters, at global and local length scales. Finally, a collection of further investigations are presented on a range of topics, including element behaviour, model versatility, and rate effects.

3.2 Methodology

3.2.1 Material model

Table 3.1: MAT162 failure criteria [82].

Failure mode	Failure criterion
Fibre tension-shear (longitudinal)	$\left(\frac{\sigma_a}{S_{aT}}\right)^2 + \left(\frac{\tau_{ca}}{S_{aFS}}\right)^2 - r_7^2 = 0$
Fibre tension-shear (transverse)	$\left(\frac{\sigma_b}{S_{bT}}\right)^2 + \left(\frac{\tau_{cb}}{S_{bFS}}\right)^2 - r_8^2 = 0$
Fibre compression (longitudinal)	$\left(\frac{\sigma_a}{S_{aC}}\right)^2 - r_9^2 = 0$
Fibre compression (transverse)	$\left(\frac{\sigma_b}{S_{bC}}\right)^2 - r_{10}^2 = 0$
Fibre crush (through-thickness)	$\left(\frac{\sigma_c}{S_{FC}}\right)^2 - r_{11}^2 = 0$
Matrix shear (in-plane)	$\left(\frac{\tau_{ab}}{S_{ab}}\right)^2 - r_{12}^2 = 0$
Matrix delamination	$S^2 \left[\left(\frac{\sigma_c}{S_{cT}}\right)^2 + \left(\frac{\tau_{bc}}{S_{bc}}\right)^2 + \left(\frac{\tau_{ca}}{S_{ca}}\right)^2 \right] - r_{13}^2 = 0$

Table 3.2: FSP threat properties used in the MAT098 material model [49].

Property	Symbol	Value	Units
Density	ρ	0.0078	g/mm ³
Young's modulus	E	207×10^3	MPa
Poisson's ratio	ν	0.33	-
Yield stress	A	1030	MPa
Hardening constant	B	477	MPa
Hardening exponent	N	0.18	-
Strain rate constant	C	0.012	-
Effective plastic strain at failure	ε_{PF}	1.0×10^{17}	MPa
Maximum stress before rate effects	σ_x	1.0×10^{20}	MPa
Saturation stress	σ_{SAT}	1.0×10^{20}	MPa
Reference strain rate	$\dot{\varepsilon}_0$	1.0	s ⁻¹

Table 3.3: HB26 properties used in the MAT162 material model [49].

Property	Symbol	Value	Units	Ref.
Density	ρ	0.00097	g/mm ³	[83]
Young's modulus (longitudinal)	E_{aa}	34257	MPa	[11]
Young's modulus (transverse)	E_{bb}	34257	MPa	[11]
Young's modulus (through-thickness)	E_{cc}	3260	MPa	[45]
Poisson's ratio (longitudinal)	ν_{ba}	0	-	[49]
Poisson's ratio (transverse)	ν_{ca}	0.013	-	[45]
Poisson's ratio (through-thickness)	ν_{cb}	0.013	-	[45]
Shear modulus (in-plane)	G_{ab}	173.8	MPa	[46]
Shear modulus (through-thickness)	G_{ca}	547.8	MPa	[62]
Shear modulus (through-thickness)	G_{cb}	547.8	MPa	[62]
Tensile strength (longitudinal)	S_{aT}	1250	MPa	[83]
Compressive strength (longitudinal)	S_{aC}	1250	MPa	[49]
Tensile strength (transverse)	S_{bT}	1250	MPa	[83]
Compressive strength (transverse)	S_{bC}	1250	MPa	[49]
Tensile strength (through-thickness)	S_{cT}	1.0×10^{20}	MPa	[49]
Fibre crush strength (through-thickness)	S_{FC}	1250	MPa	[44]
Fibre mode shear strength	S_{FS}	625	MPa	[49]
Matrix mode shear strength (in-plane)	S_{ab}	1.8	MPa	[46]
Matrix mode shear strength (out-of-plane)	S_{bc}	1.8	MPa	[46]
Matrix mode shear strength (out-of-plane)	S_{ca}	1.8	MPa	[46]
Residual compressive strength factor	S_{FFC}	0.1	-	[49]
Failure model	A_{MODEL}	2 (fabric cross-ply)	-	[49]
Coulomb friction angle	ϕ_C	0	°	[49]
Delamination scale factor	S_{DELM}	1	-	[49]
Limiting damage factor	ω_{max}	0.999	-	[49]
Eroding axial strain	E_{LIMT}	0.06	-	[49]
Eroding compressive volume strain	E_{CRSH}	0.05	-	[49]
Eroding volumetric strain	E_{EXPN}	4	-	[84]
Coefficient of strain rate (fibre strength)	C_{rate1}	0.0287	-	[11]
Coefficient of strain rate (axial moduli)	C_{rate2}	0.1163	-	[11]
Coefficient of strain rate (shear moduli)	C_{rate3}	0.225	-	[11]
Coefficient of strain rate (transverse moduli)	C_{rate4}	0.1163	-	[11]
Coefficient of softening (axial fibre damage)	a_{m1}	20	-	[49]
Coefficient of softening (transverse fibre damage)	a_{m2}	20	-	[49]
Coefficient of softening (crush damage)	a_{m3}	20	-	[49]
Coefficient of softening (matrix failure)	a_{m4}	-0.8	-	[48]

The current study follows on from the work of Hazzard *et al.* [49], that used the LS-DYNA explicit finite element software for impact simulations. LS-DYNA's MAT162 by Materials Science Corporation was selected for representing the homogenised cross-ply sub-laminates of Dyneema[®] HB26, due to its sophistication in modelling composite damage and failure [85]. MAT162 (Composite MSC with Damage) is a rate-dependent progressive damage model for composites, with the ability to incorporate parameters such as cross-ply damage criteria, as well as capturing additional failure modes, non-linear damage and strain rate effects, deeming it most suitable for modelling the behaviour of this material. The fibre failure criteria are based on the Hashin failure criteria. These and the failure criteria for the matrix are presented in Table 3.1, together with the corresponding failure modes. Here, a, b , and c represent local element axes where direction a is aligned with the longitudinal direction along the fibres, b with the transverse direction orthogonal to the fibre length, and c with the through-thickness direction. Subscripts T and C refer to tensile and compressive components, respectively, while FS and FC represent failure in fibre shear and fibre crush modes, while S refers to a delamination scaling factor and r_{7-13} denote cross-ply damage thresholds [82]. The threat and target material model selection, as well as model validation through single element response studies are extensively described in the work of Hazzard *et al.* [49]. The FSP is modelled using MAT098 (Simplified Johnson-Cook) with properties given in Table 3.2. The material properties used in the MAT162 material card in the current work are displayed in Table 3.3. Mesh convergence studies were also performed by Hazzard [86], for a 20 mm diameter fragment simulating projectile (FSP) threat and a square laminate with in-plane dimension $d = 300$ mm.

3.2.2 Cohesive zone modelling

In the current work, cohesive elements based on the Bristol Cohesive UMAT developed from the work by Jiang *et al.* [72] and using LS-DYNA's ELFORM = 19, were implemented at the interfaces of sub-laminates via the attachment of coincident nodes. Interfacial element nodes were shared with elements in the layers above and below, as demonstrated in Fig. 3.1. The interface element behaviour is based on a bilinear traction separation law, with the quadratic mixed-mode delamination criterion and damage formulation discussed in Section 2.4.3. The cohesive elements did not possess a finite thickness, as the sub-laminate interface in the laminates considered in this work is dominated by the existing matrix medium with no additional adhesives. Zero thickness was achieved through the translation of nodes, in order to collapse the interface elements. As the cohesive material laws are displacement-driven, the critical timestep is independent of

thickness [87]. Due to the zero thickness value, the calculation of an individual element's mass is based on its areal density. To ensure negligible mass is added to the model by the interface, a minimal density value approaching zero (1.0×10^{-12} g/mm²) was used. By using this approach, the strain energy release rate of the elements in the two modes of fracture can be extracted and attributed to the total energy released through delamination at the interface. The model was tested initially at quasi-static rates, and subsequently at ballistic impact velocities. The cohesive contact properties are presented in Table 3.4 and are based on [49]. These properties were implemented in the form of material parameters in the user material card of the cohesive elements.

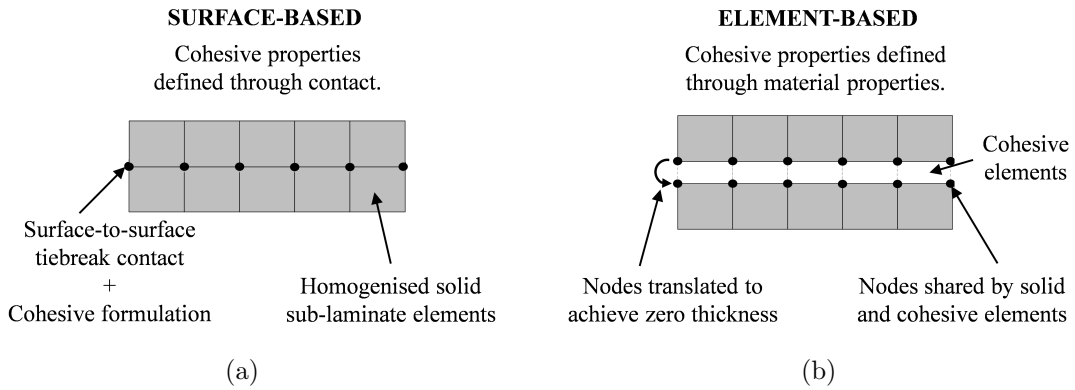


Figure 3.1: Comparison between the implementation of CZM at the interface using (a) surface-to-surface contact and (b) cohesive elements.

Table 3.4: Contact properties used in the cohesive element model [49].

Property	Symbol	Value	Units	Ref.
Mode I critical energy release rate	G_{IC}	0.544	N/mm	[88]
Mode II critical energy release rate	G_{IIC}	1.088	N/mm	[49]
Mode I peak traction	$\sigma_{I \max.}$	1.2	MPa	[45]
Mode II peak traction	$\sigma_{II \max.}$	1.8 (quasi-static) 2.6 (ballistic)	MPa	[50],[46]
Mode I initial stiffness (scaled with thickness)	K_I	60 (1 mm thickness)	N/mm ³	[49]
Initial stiffness ratio	K_{II}/K_I	0.6	-	[49]
Power-law exponent	P^α	1	-	[70]

3.2.3 Validating element-based CZM

3.2.3.1 Low velocity: drop weight impact

Under quasi-static rates representing drop weight impact (DWI) tests performed at 3.37 m/s, illustrated in Fig. 3.2(a), the laminate was modelled between two base plates under a uniform pressure representing clamping pressure, as per the approach described in [49]. Both element-based (E-B) and surface-based (S-B) cohesive zone models were simulated under the same conditions. The E-B cohesive zone approach yields comparable force-displacement results to tiebreak contact with S-B cohesive formulation, as demonstrated in Fig. 3.2(b). The introduction of the cohesive elements with zero volume resulted in the reduction of the simulation timestep, thereby increasing the computation time to some extent. This was counteracted by taking advantage of the symmetric loading and geometry to reduce the model size to a quarter, while scaling the results by a factor of four, as seen in Fig. 3.2(b). Since low impact velocity does not lead to cohesive element failure, no additional contact definition was required between the laminate layers to model interlaminar contact following the erosion of the interface elements.

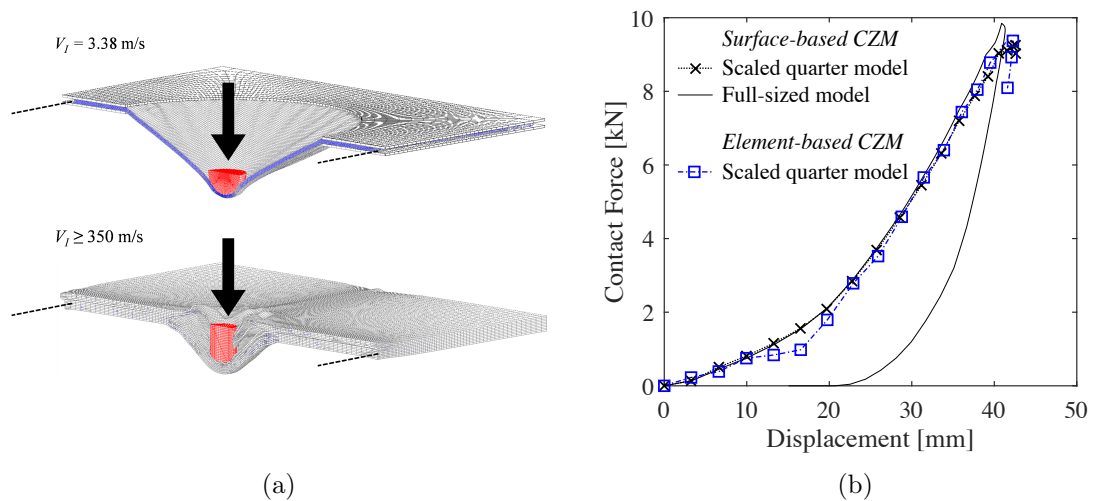


Figure 3.2: (a) Cross-sectional views of the full drop weight impact (top) and ballistic impact (bottom) finite element models, and (b) a comparison of contact force against displacement between surface- and element-based models subjected to drop weight impact.

3.2.3.2 High velocity: ballistic impact

By contrast, under ballistic impact, the failure of cohesive elements leads to their erosion. An additional form of contact was therefore required to maintain the contact definition between sub-laminate layers throughout the simulation. A single-surface eroding contact with SOFT

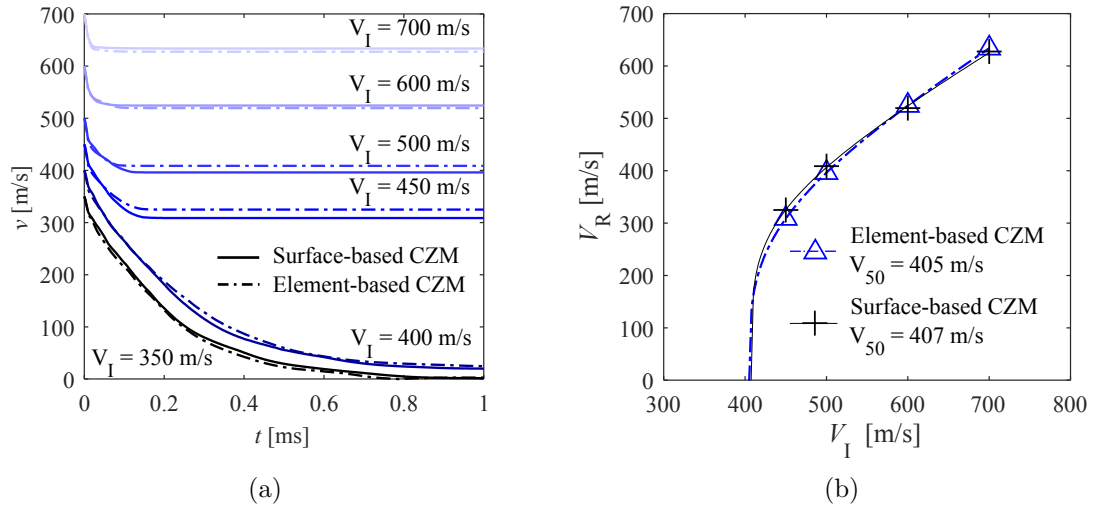


Figure 3.3: Comparisons between surface- and element-based models under ballistic impact: (a) Evolution of projectile velocity and (b) Lambert-Jonas ballistic limit predictions.

option equal to 2 was found to be most suitable for this purpose. Unlike the bucket sort approach used in $\text{SOFT} = 0$ or 1 , where the penetration search algorithm is focused on nodal penetration of segments, the $\text{SOFT} = 2$ option employs a segment-based approach, whereby the contact definition searches for the penetration of segments by other segments [70], resulting in a smaller degree non-physical behaviour such as inter-part penetration.

It must be noted that there is also a requirement for additional contact in the tiebreak contact case under ballistic impact. The purpose of this additional contact definition is to prevent inter-part penetration of sub-laminates and subsequent negative contact energy values, similar to the purpose of gaps between sub-laminate layers in models incorporating bonded contact with stress-based failure criteria [48]. Following the implementation of the two forms of E-B and S-B cohesive contact definition, projectile velocity in the through-thickness direction, v , and Lambert-Jonas curve fits for estimating the ballistic limit velocity, V_{50} , are plotted in Fig. 3.3(a) and Fig. 3.3(b), where the results reveal good agreement between E-B and S-B contact data.

3.2.4 Interface energy dissipation

The overall contribution of the interface to the dissipation of the kinetic energy of a 55 g steel FSP was investigated for a panel with 300×300 mm in-plane dimensions, a 10 mm thickness and a 1 mm sub-laminate thickness, using element-based cohesive interface layers. This was performed for two cases; for a stop (or arrest) case at an impact velocity of $V_I = 350$ m/s, and

for a perforation case at $V_I = 600$ m/s. In addition, the contribution of each individual interface was investigated to demonstrate the variation in energy dissipation, based on proximity to the projectile in the through-thickness and in-plane directions. In order to quantify and visualise the extent of energy dissipation, mode I and mode II strain energy release rates were extracted from the model for every element at each interface. The values extracted are individual element averages that are based on the values at the 4 Gauss integration points of each cohesive element.

These points exist on the element mid-surface, *i.e.* a plane at the mid-point between the top and bottom element surfaces [70]. Since the interface elements (ELFORM = 19) with 4 integration points are connected to solid continuum elements (ELFORM = 1) in the form of constant stress elements with a single integration point, erosion of the interface elements was activated under the premise of setting the number of failed integration points for erosion to take place at 1 and not the recommended 4, to prevent non-physical modes of deformation. Looking at global energy outputs of DWI models, the addition of cohesive elements significantly improves the undesirable hourglass energy in the system, as opposed to using tie-break contacts. However, localised hourglass effects were intensified at the central region of laminates. As hourglass control is typically employed for element stabilisation, the increase in localised hourglass energy was attributed to the mismatch in the number of integration points mentioned. This was addressed by activating the averaging flag under the cohesive material card.

The energy dissipated at each element, E_{el} , at time t , was calculated as the product of the energy release rate, G_{el} , at that element at the respective point in time, and the initial mid-surface area, A_{el} , of the zero-thickness cohesive element. It was initially assumed that the variation in the in-plane dimensions of the interface elements over time are negligible for the purpose of these calculations, allowing the initial area of element el , at $t_0 = 0$, to suffice for the entire impact duration. The total energy dissipated at an interface, n , is denoted by $I_n E$, and can be represented by the sum of the energy dissipated at all the elements, n_{el} , at that interface over time,

$$I_n E(t) = \sum_{t_0}^t \sum_{el=1}^{n_{el}} G_{el}(t) \cdot A_{el} . \quad (3.1)$$

Note that n is the interface number starting at the strike face, so that $n = 1$ represents the interface next to the strike face and thus in closest proximity to the projectile at the point of impact. Moreover, energy dissipated at the interface continually increases over time, and is therefore calculated as a cumulative sum.

3.3 Global interface energy dissipation

3.3.1 Baseline model

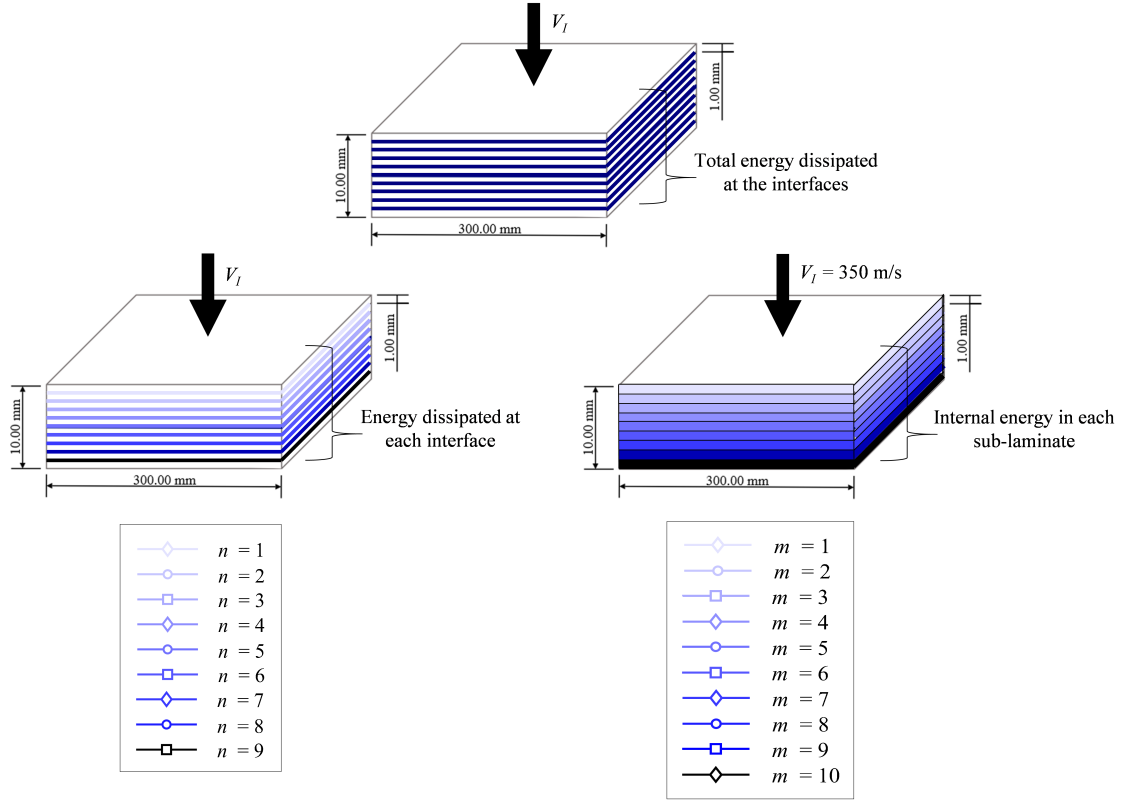


Figure 3.4: A visual guide to the labelling of sub-laminates and interface layers, together with the dimensions of the baseline numerical model.

Figure 3.4 demonstrates the baseline ballistic impact model in relation to the three types of output that are extracted and discussed in this section; the total energy dissipated at all interfaces in the system, the energy dissipated at individual interfaces, and the internal energy in each sub-laminate. To distinguish between different modes of fracture, the term for general energy dissipation at a single interface, $I_n E$, can be represented by the mode I and mode II energy dissipation components, $I_n E_I$ and $I_n E_{II}$. These refer to the energy dissipated at interface n through the mode I and mode II fracture components. The mixed-mode fracture energy, equal to the sum of $I_n E_I$ and $I_n E_{II}$, can be denoted by $I_n E_T$. The sum of the energy dissipated at all interfaces in the entire material system at time t is given by $I_T E(t)$. The kinetic energy of a projectile, $KE_p(t)$, determines the total amount of energy, $TE(t)$, that is dissipated by the entire laminate, such that

$$TE(t) = KE_p(t_0) - KE_p(t) . \quad (3.2)$$

The $I_T E(t)$ term can be normalised with $TE(t)$, to demonstrate how much of the total energy dissipation takes place at the interfaces. In Fig. 3.5, $I_T E$ and $I_T E/TE$ are plotted over the duration of impact, comparing a stop case with $V_I = 350$ m/s (black lines) to a perforation case with $V_I = 600$ m/s (blue lines). There is an equivalent rate of dissipation in both cases until $t = 0.1$ ms, by which point the projectile has either slowed down relative to the target, to a velocity that inflicts no further substantial damage to the sub-laminates, or has fully perforated the laminate, as shown by the corresponding snapshots of the laminate cross-sections in Fig. 3.6, at the highlighted points in time (red crosses). The first 0.1 ms are critical, as they determine whether the laminate is perforated. If fully perforated, the implications of the laminate behaviour will no longer be as relevant. If the projectile is stopped however, the BFD becomes the key indicator of impact performance for the remainder of the impact duration.

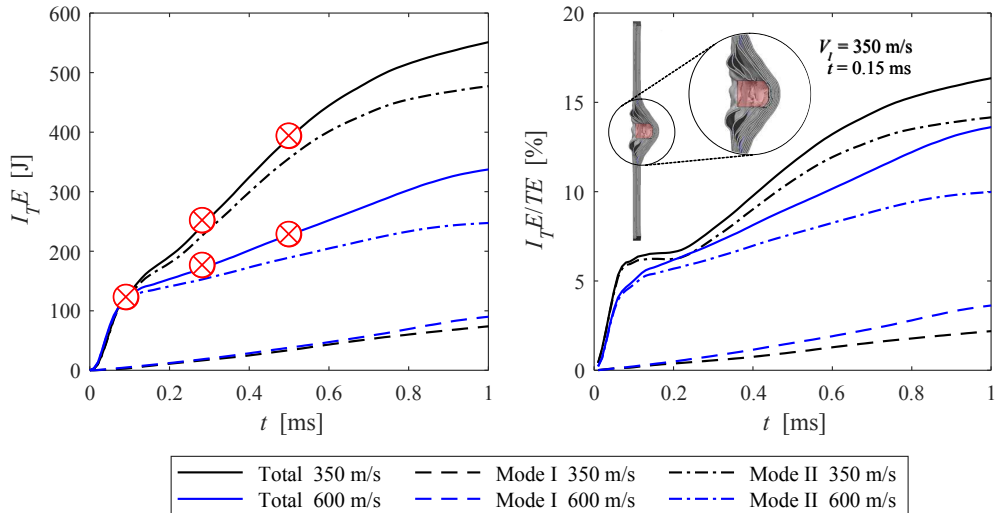


Figure 3.5: Energy dissipated at interfaces during impact (LHS), and as a percentage of the total energy dissipated (RHS), at $V_I = 350$ m/s and $V_I = 600$ m/s.

In both cases, the interfaces continue to dissipate energy after $t = 0.1$ ms, albeit at a lower rate. Membrane bulging is known to contribute to higher levels of energy dissipation than the more localised damage which occurs in the progressive failure regime in the earlier stages of impact [89]. The absolute amount of energy dissipated through in-plane modes continues to rise linearly until the end of the simulation at $t = 1$ ms. Naturally, if the laminate is fully perforated, the rate of dissipation is substantially reduced after $t = 0.1$ ms, whereas in the stop case, the laminate continues to dissipate the kinetic energy of the projectile that it is in contact with, at a similar rate to the earlier stages of impact.

From $t = 0.1$ ms onwards, the contribution of mode II deformations to the total mixed-

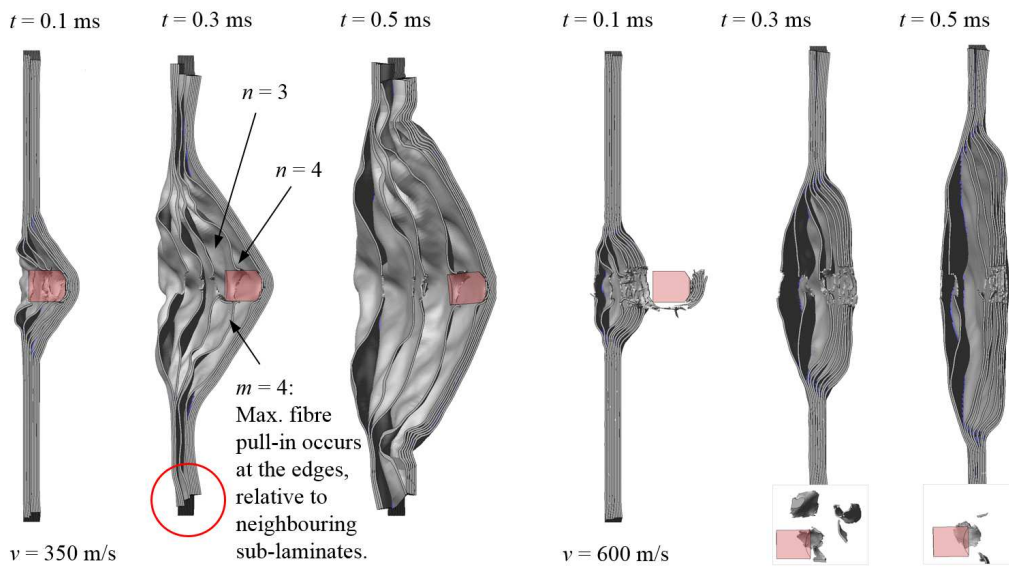


Figure 3.6: Progression of the projectile and deformation of the laminate at discrete points in time after impact, at $V_I = 350$ m/s and $V_I = 600$ m/s.

mode dissipation, displayed in Fig. 3.5, falls by 3% ($V_I = 350$ m/s) and by 4% ($V_I = 600$ m/s) from $t = 0.1$ ms to $t = 0.2$ ms, while the contribution of mode I dissipation grows. Following perforation, while mode II shearing still accounts for most of the energy dissipation, it is the rise in the out-of-plane delamination that is most noticeable in the perforation case, the extent of which exceeds the mode I dissipation of the stop case. This can be attributed to the continued delamination of the sub-laminate layers close to the strike face, as seen in Fig. 3.6, after the projectile has passed through, in addition to the inclusion of the elements that have been disconnected from the laminate during perforation. These elements continue to travel together with the projectile following perforation, until each layer is propelled off course into a different direction, visible in the insets in Fig. 3.6 for $V_I = 600$ m/s. This is verified in the following section, by considering the contribution of each interface separately.

Similarly, the increase in mode I energy dissipation is demonstrated by the increased delamination of the perforated sub-laminates and the progression of the shear hinge on the back face in Fig. 3.6. The mode II, and therefore the mode II dominated total rates of dissipation approach zero, with the curves plateauing over time, as a result of the impactor coming to a complete halt and no longer having any kinetic energy to be dissipated by the laminate. Although the absolute amount of energy absorbed by the stop case is substantially higher after $t = 0.1$ ms, reaching around 60% at $t = 1$ ms, the difference between the two cases is reduced to less than 20% when the values are compared as a proportion of the total energy absorbed by the laminates in Fig. 3.5, over the impact duration considered here.

In addition, energy dissipated at the laminate interfaces, as a proportion of the total energy dissipated by the entire laminate, is seen to continuously rise over the course of impact. Following perforation, no more energy can be transferred from the projectile to the laminate. Inside the laminate however, energy can be redistributed from momentum transfer and internal energy through the interface, which continues to absorb energy during this transfer. This results in the increase in the contribution of the interfaces to the total energy dissipation, that occurs in the laminate in both arrest and perforation cases. While the sub-laminates absorb most of the projectile's energy through fibre elongation and crushing [49], this is most significant at the initial moments following impact, coinciding with the spike in internal energy seen in Fig. 3.7. In these plots, the internal energy, U , is plotted for each sub-laminate, identified by m , with $m = 1$ representing the layer on the front face of the target.

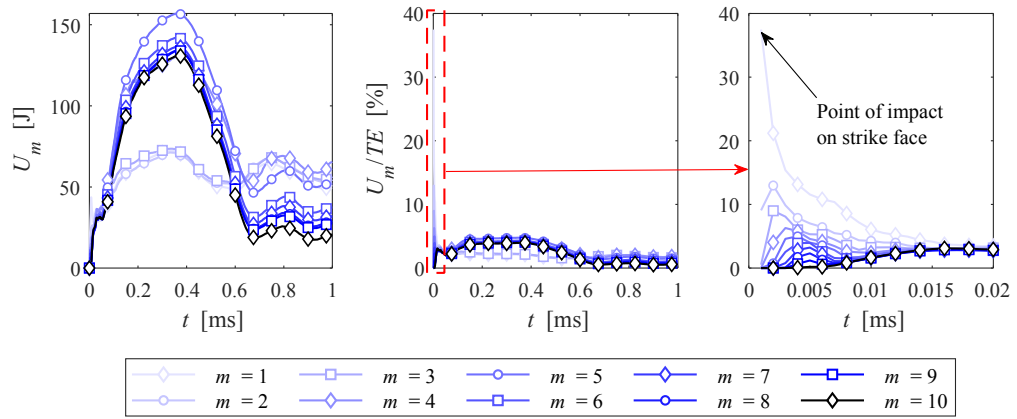


Figure 3.7: Internal energy U , of each sub-laminate layer m , under impact at $V_I = 350$ m/s, in terms of absolute values per layer (LHS) and the contribution of each layer to the total energy absorbed (centre and RHS).

The flat regions of $V_I = 350$ m/s *Total* and *Mode II* curves in Fig. 3.5 represent the period during which the projectile is slowed down the most, as seen in Fig. 3.3(a), and ceases the penetration of further layers. The sub-laminate layer at which this occurs is under significant strain, as visualised by the cross-section of the model at $t = 0.15$ ms, displayed in the inset in Fig. 3.5. The larger the extent of stretching, the greater the amount of energy that is absorbed through internal energy of the fibres, as demonstrated by the rise in the internal energy of sub-laminates in Fig. 3.7, and the contribution of this to the total amount of energy dissipated by the laminate. While the largest percentage of internal energy absorption occurs at the point of contact, as shown in Fig. 3.7, particularly in the sub-laminate layers directly under the path

of the projectile, there is also a rise to almost 4% in the unperforated layers between $t = 0.1$ ms and $t = 0.3$ ms, coinciding with the relatively flat region of the interface energy curves in Fig. 3.5.

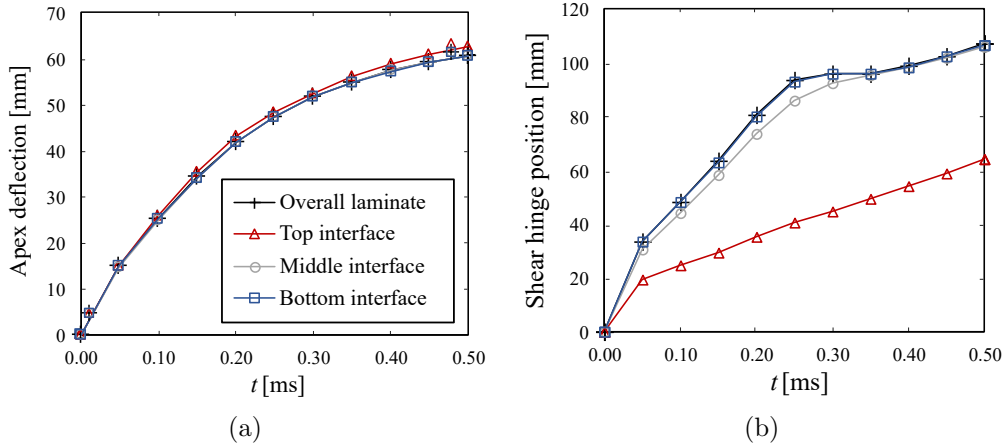


Figure 3.8: (a) Apex deflection and (b) shear hinge progression of sub-laminates at multiple interfaces through the thickness of the laminate, at $V_I = 350$ m/s.

Apex deflection and shear hinge progression can be useful indicators of the evolution of the deformation mechanisms that the material system undergoes during impact, by tracking the dominant modes of deformation, namely delamination, membrane motion and bulging. These analyses were performed at three regions through the thickness of a laminate impacted at $V_I = 350$ m/s, as presented in Fig. 3.8. Although the apex deflection of the different layers appear to be aligned with the overall out-of plane back face deflection of the laminate, the in-plane progression of the shear hinge at $t = 0.5$ ms at the front interface, *i.e.* the region closest to the strike face, is 40% lower than the rest of the laminate. The extent of these deformations and the transition zones are, to some extent, governed by interface properties and the resulting capability of the interface to dissipate energy. Tracking energy dissipation in fracture modes I and II can therefore be used at the sub-laminate interfaces in a similar manner to the way the apex deflection and shear hinge progression have previously been used for studying the back face deflection of the laminate [48, 49], as discussed in the following sections.

3.3.2 Parametric studies

The element-based CZM approach is used to study the effects of several parameters on the energy absorption mechanisms of the laminate. The energy absorbed through mode I and mode II delamination are investigated in terms of the energy dissipated at the interfaces and the contribution to the total energy absorbed by the entire system. These parameters

include physical parameters such as impact velocity, in-plane and out-of-plane dimensions of the laminate, and modelling parameters including the number of plies and interfaces, represented by one homogenised sub-laminate. Subsequently, the ballistic performance of the material is explored in terms of the back-face deformation and ballistic limit velocity, presenting the effect of the aforementioned parameters on these two indicators of ballistic performance.

3.3.2.1 Impact velocity

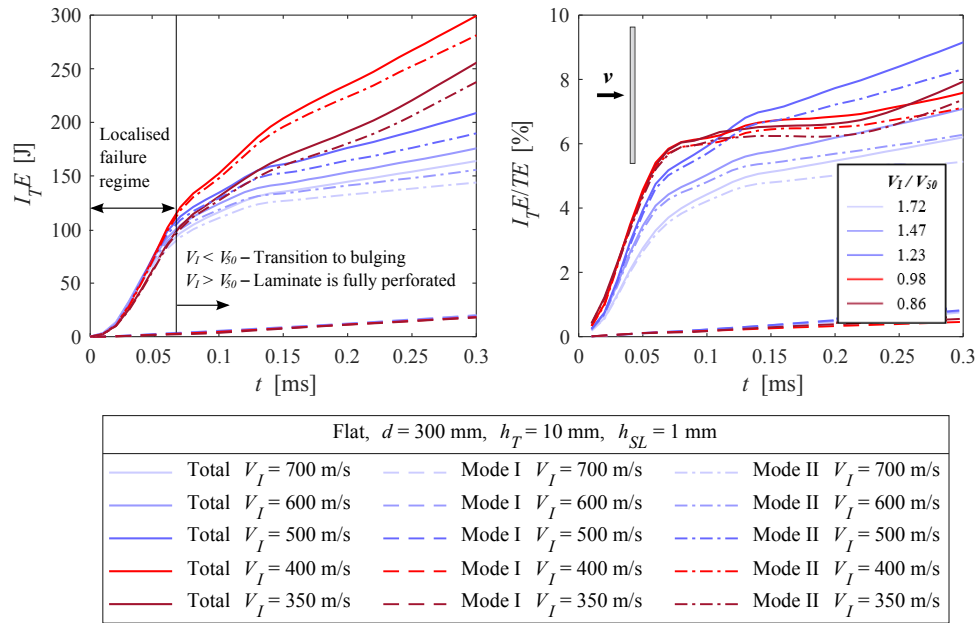


Figure 3.9: Energy dissipated at interfaces and energy dissipated at interfaces as a percentage of total energy dissipated by laminate over a range of impact velocities, with $V_{50} = 407.8$ m/s.

Figure 3.9 demonstrates the consistency in the rate of energy dissipation through delamination across a range of strike velocities up to a point of transition in the penetration mode, or total perforation. This occurs almost entirely in mode II, followed by a gradual increase in the contribution of mode I dissipation. The similarity in the rate of dissipation arises from the local failure regime, the extent of which increases with V_I . In the range of velocities considered, the amount of energy dissipated is highly sensitive to V_I , with an increase of 50 m/s from $V_I = 350$ m/s to $V_I = 400$ m/s, leading to a rise of approximately 50 J in $I_T E$, between $t = 0.1$ ms and 0.3 ms.

It is worth noting that total energy is highest at velocities closest to the laminate V_{50} , equal to 407.8 m/s in this particular case. Meanwhile, impact velocities exceeding the V_{50} result in full perforation, together with the rate of energy absorption falling with increasing values of

V_I . According to Fig. 3.9, however, the trends in $I_T E/TE$ are almost identical for $V_I < V_{50}$, while clear distinctions can be made when $V_I > V_{50}$, even prior to perforation. At the same time, the results indicate that the TE levels are lower for impact cases where $V_I > V_{50}$, hence, giving rise to the more similar levels seen for I_T/TE than in absolute values of $I_T E$ between the cases with impact velocities above and below the V_{50} .

3.3.2.2 Dimensional effects

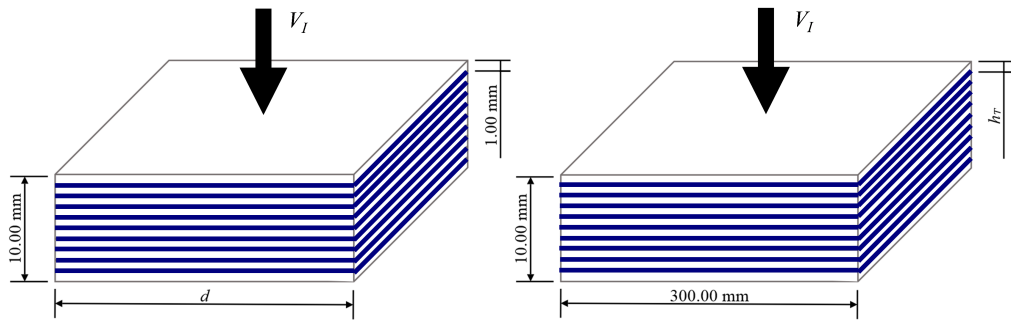


Figure 3.10: Dimensions d and h_T demonstrated on schematics of the laminate model.

The following two sections demonstrate the effects of the in-plane and out-of-plane plate dimensions d and h_T , on the level of energy dissipation that takes place at the interfaces, and on the V_{50} estimate. Dimension d represents the length of the square target, while h_T is the total laminate thickness, as defined in Fig. 3.10. Lambert-Jonas approximations of the V_{50} values for the $300 \times 300\text{ mm}$, 10 mm thick baseline model, as well as various plate lengths and thicknesses, are presented in Fig. 3.12 and Fig. 3.15.

3.3.2.3 Plate length

More extensive pull-in deformation occurs in the primary fibre regions of laminates with smaller in-plane dimensions, seen in Fig. 3.11, due to the smaller distance from the centre of the targets to the edges. This behaviour facilitates higher ballistic limits in targets with smaller in-plane dimensions, as demonstrated in Fig. 3.12. Furthermore, it has previously been reported that in simulations without boundary conditions holding the targets in place, target panels with $d < 300\text{ mm}$ end up accelerating with the projectile rather than undergoing penetration, due to insufficient momentum to hold them in place [49, 90]. Therefore, the simulations of the smaller panels in the current study were performed with frictionless support plates on the back face, that prevent this motion from occurring. The implications of this are discussed in Section 3.6.1.

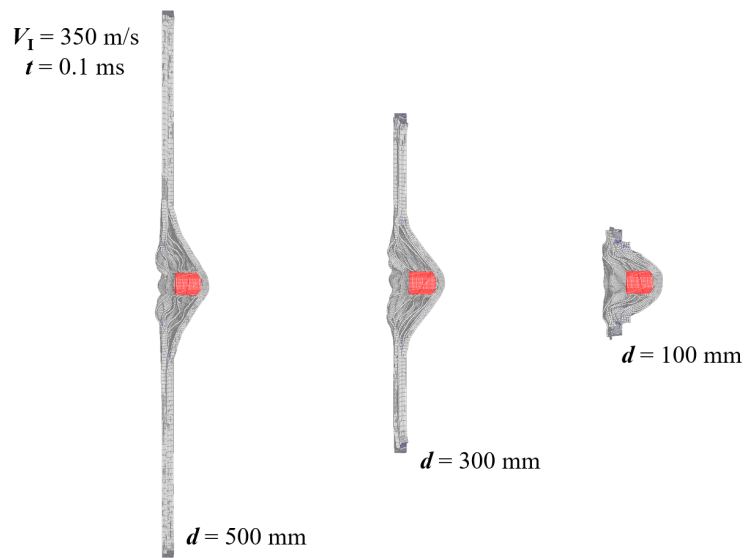


Figure 3.11: Finite element models of varying dimension d .

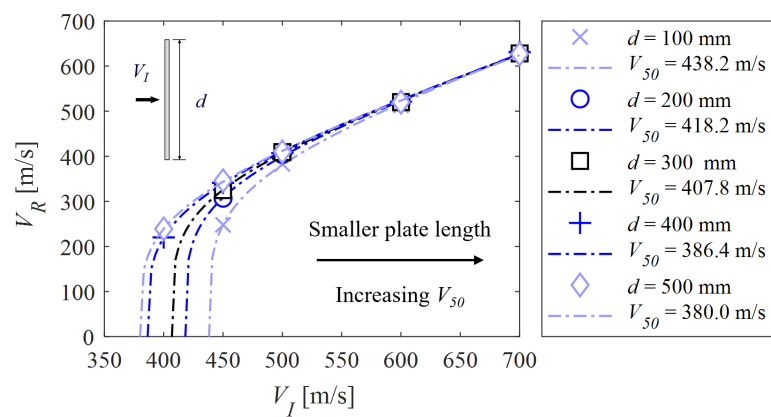


Figure 3.12: Lambert-Jonas V_{50} approximations for various values of plate length d .

Energy plots for different plate lengths at two impact velocities are displayed in Fig. 3.13. The increase in the energy absorbed with increasing d is expected, due to the expansion in the interface area where energy can be dissipated. At both impact velocities explored here, the differences in $I_T E / TE$ become minimal when $d \geq 300$ mm, since the plate is no longer set in motion by the projectile. This effect is much more pronounced in the higher velocity case of $V_I = 600$ m/s, visible in Fig. 3.13, where a smaller extent of the total energy is dissipated at the interfaces due to the absence of the binary bulging mechanism that follows the progressive regime when $V_I = 350$ m/s.

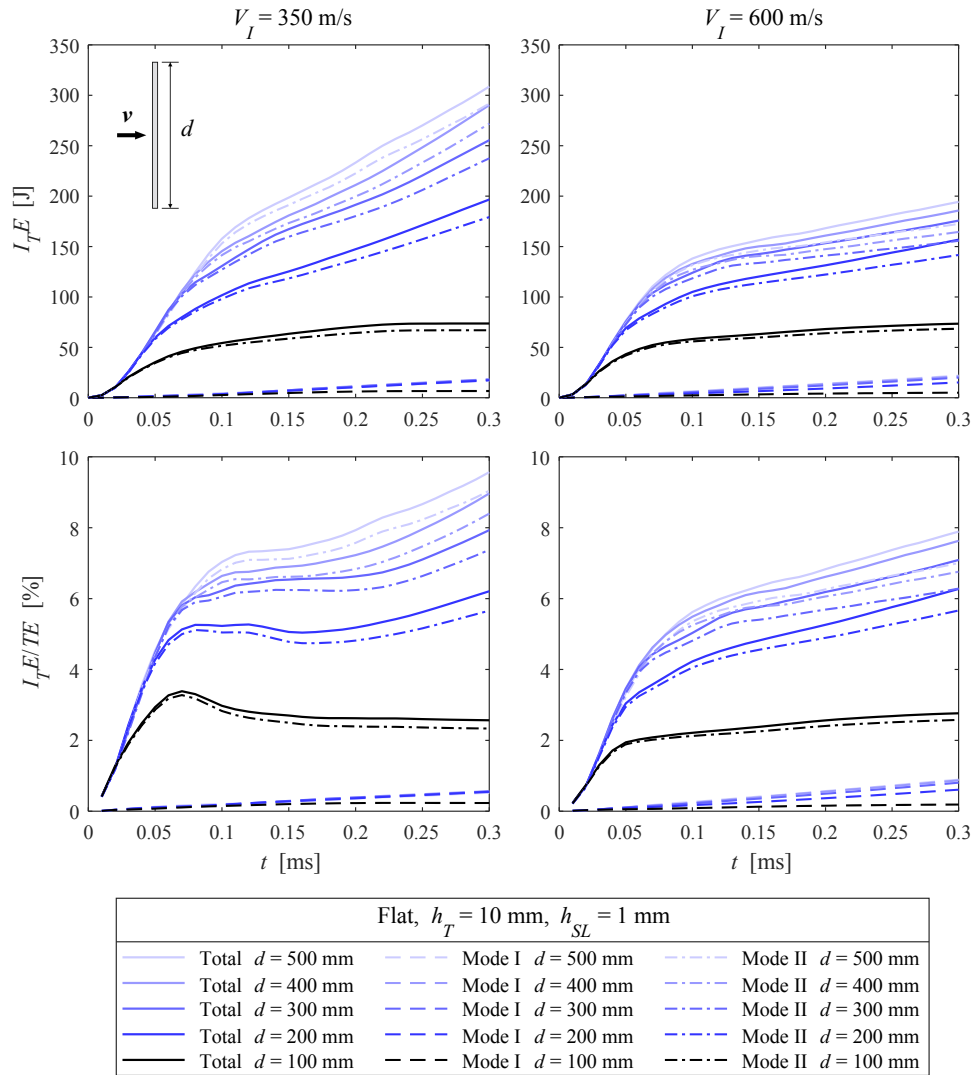


Figure 3.13: Energy dissipated at interfaces and energy dissipated at interfaces as a percentage of total energy dissipated by laminate for a range of in-plane plate dimensions, at $V_I = 350$ m/s and $V_I = 600$ m/s.

3.3.2.4 Plate thickness

The thickness of the modelled laminate was altered by the addition and the removal of entire sub-laminate layers along with the cohesive elements defining contact between them, as seen in Fig. 3.14. This ensured that the 1 mm cubic elements directly under the projectile path, retained their aspect ratio of unity. The effect of varying h_T on $I_T E / TE$ is displayed in Fig. 3.16. The trends reflect what has previously been reported in literature regarding the effect of laminate thickness on impact performance [91, 92], an effect that is also corroborated for this model in Fig. 3.15, showing an increase in V_{50} with increasing thickness h_T . Once again, this disparity in behaviour arises from differences in the penetration mechanisms that take place.

Since these mechanisms [60, 93] and therefore the depth of penetration [94] are determined by V_I and V_{50} , the ratio between the two are given for each plate thickness in Fig. 3.16, thus normalising the impact velocity with the ballistic limit at each laminate thickness.

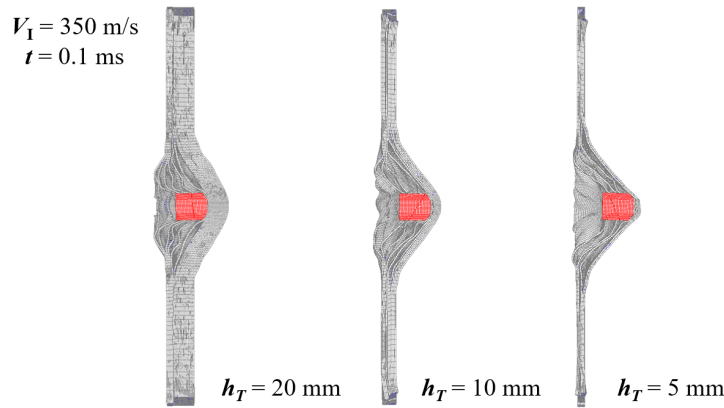


Figure 3.14: Finite element models of varying dimension h_T .

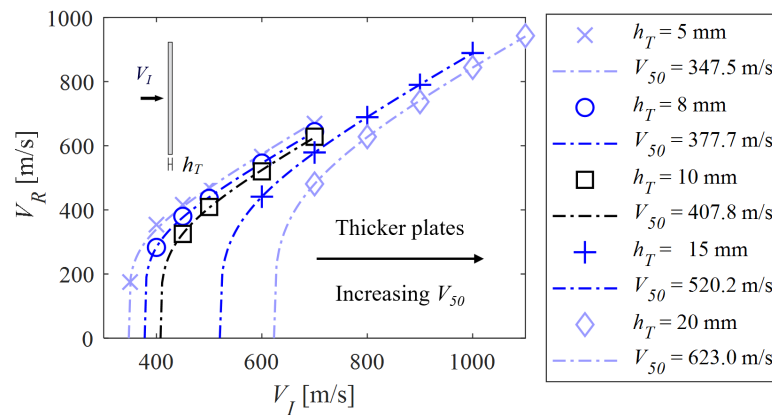


Figure 3.15: Lambert-Jonas V_{50} approximations for various values of plate thickness h_T .

At both impact velocities considered, the impact velocity exceeds the ballistic limit of the thinnest plate ($h_T = 5$ mm), while not reaching the ballistic limit of the thickest target ($h_T = 20$ mm). However, the influence of the ballistic limit on the rate of energy absorption of the laminate does not explain the large differences that exist between plates with $8 \text{ mm} \leq h_T \leq 15$ mm, and those with the minimum and maximum thickness values, under both impact velocities. Likewise, questions remain regarding the exact thickness values below and above which the interfaces see a drastic rise or fall in terms of their contribution to the overall energy dissipation, warranting further investigation into this matter.

At the lower end of the thickness spectrum, these differences have previously been attributed

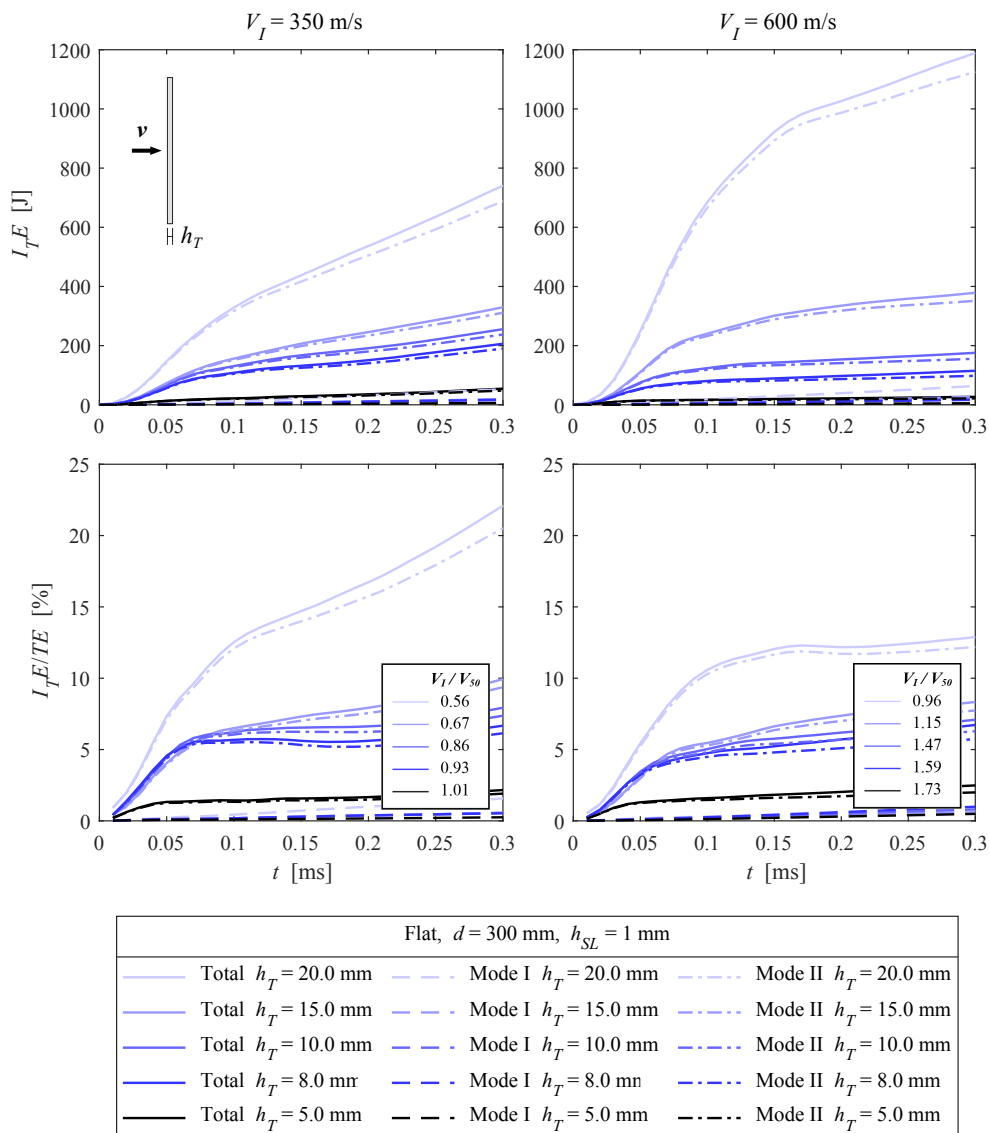


Figure 3.16: Energy dissipated at interfaces and energy dissipated at interfaces as a percentage of total energy dissipated by laminate for a range of plate thicknesses, at $V_I = 350$ m/s and $V_I = 600$ m/s.

to the sole action of the binary failure regime in laminates with low areal densities [89], compared to the multi-stage failure regimes of higher areal density laminates. In the case of thicker laminates however, ductile tensile failure has previously been observed at the back face of targets, believed to have been a result of shock induced temperature increase [93]. Thus, the applicability of the current model could be limited for laminate thicknesses above 15 mm, as any temperature effects have been neglected. Furthermore, capturing local failure mechanisms such as indirect tension becomes increasingly important with increasing laminate thickness, as a larger portion of the laminate fails in this manner due to the different Poisson expansion

between the 0° and 90° cross-ply layers in the through-thickness direction [92, 94]. It is also worth noting that the homogenisation approach does not account for ply thickness, which is known to affect performance.

3.4 Local interface energy dissipation: out-of-plane

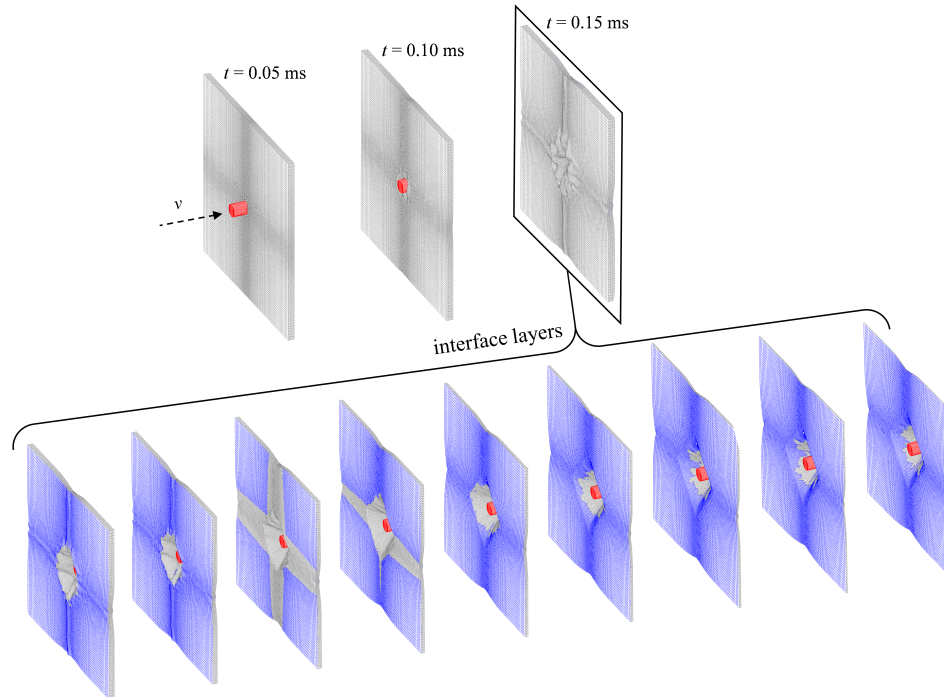


Figure 3.17: An exploded view of individual interfaces within the baseline laminate model.

Individual interfaces through the thickness of the laminate, depicted by the blue regions, are visualised in Fig. 3.17 for $V_I = 350$ m/s at $t = 0.15$ ms. The blue colour indicates the regions where the interface elements have not yet failed. The contribution of each interface to the total energy dissipated at the interfaces is presented in Figs. 3.18 and 3.19 for the partially- and fully-perforated cases, respectively. The lighter the colour of the curve, the closer the proximity of the interface it represents to the strike face. The subplots demonstrate the energy absorbed through mode I, mode II and mixed-mode (total) deformations. As per the overall interface results, the local mixed-mode behaviour at the sub-laminate level is dominated by mode II deformations for all layers, at both strike velocities. Descriptions of the mode II behaviour will therefore also reflect the overall deformation of each layer.

In Fig. 3.18, mode I energy dissipation is consistent across all interfaces, until $t = 0.2$ ms. From this point onwards, there is substantial reduction in the rate of mode I dissipation at

the third interface. As previously discussed for Fig. 3.6, the projectile is arrested after having fully perforated the first three sub-laminate layers. From the fourth sub-laminate layer onwards, the laminate undergoes extensive amounts of in-plane shear, as a result of pull-in of primary fibres from the edges. The effects are captured by the corresponding interfaces above and below the fourth sub-laminate layer ($n = 3$ and $n = 4$), portraying the large mode II deformations experienced by these elements, relative to the elements in neighbouring sub-laminates. This is most visible at the edges of the plate, highlighted at $t = 0.3$ ms in Fig. 3.6.

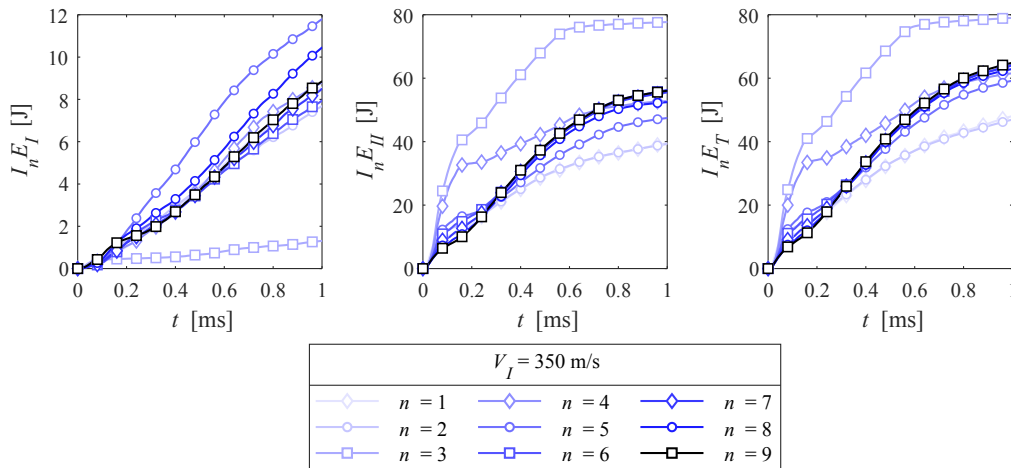


Figure 3.18: Energy dissipated at each sub-laminate layer under impact at $V_I = 350$ m/s, through mode I (LHS), mode II (centre), and combined mixed-mode (RHS) delamination.

Beyond $n = 3$, slightly higher levels of energy are absorbed at the interface following transition to the membrane/bulge mode, which is in line with previous observations reporting on the prevalence of membrane deformation, particularly interlaminar shear in laminates thinner than 20 mm, impacted at velocities below 600 m/s [11, 89]. At $n = 3$, around twice as much energy is dissipated in mode II than at the other interfaces throughout the length of the simulation, as shown in Fig. 3.18. One exception is the fourth interface, at which the laminate switches from a local failure regime to a membrane bulging phase. At $n = 4$, mode II energy dissipation increases rapidly until reaching 33 J, after which point the projectile is caught by the laminate and therefore restricts membrane motion in the surrounding interface. This leads to the following reduction in the rate of mode II energy dissipation at the fourth interface, seen in Fig. 3.18. While energy continues to be dissipated at all interfaces, the layers below the projectile continue to do so at a constant rate until after $t = 0.6$ ms. By contrast, the layers above the projectile move towards total delamination and separation, due to the complete failure of these interface layers and tear-off action from the rear face of the laminate. This limits

further potential dissipation at these locations, thereby slowing the rate of energy dissipation towards the end of the simulation.

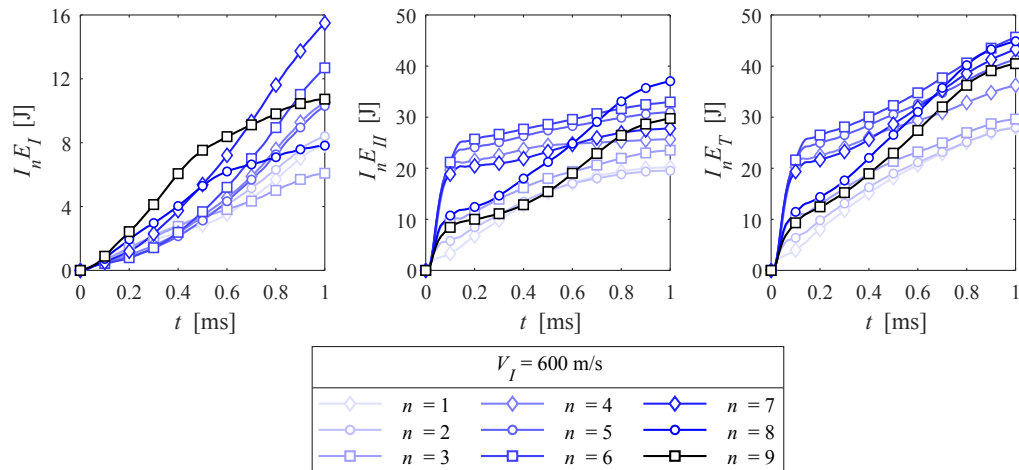


Figure 3.19: Energy dissipated at each sub-laminate layer under impact at $V_I = 600 \text{ m/s}$, through mode I (LHS), mode II (centre), and combined mixed-mode (RHS) delamination.

In the total perforation case ($V_I = 600 \text{ m/s}$) depicted in Fig. 3.19, mode I dissipation of energy is seen to play an increasingly larger role in the overall energy dissipation at the interfaces compared to the lower impact velocity, while the contribution of the interfaces in mode I dissipation remains relatively consistent, with $I_n E_I$ ranging from 0.4 J to 0.9 J until the point of total perforation of the laminate at $t = 0.1 \text{ ms}$. Beyond this point, there is an increase in the rate of dissipation at the interfaces closest to the back face. It was found that the further progression of the shear hinge towards the back face of the panel results in a larger area of the interface dissipating energy in mode I. The closer the layers are to the rear face, the larger the area covered by the shear hinge and therefore the larger the mode I energy at the interfaces between them, as a result of the redistribution of absorbed energy within the laminate. At $t = 0.5 \text{ ms}$, failure occurs in a significant proportion of the two interfaces closest to the back face at $n = 8$ and $n = 9$, hence giving rise to the drop in the rate of dissipation visible in Fig. 3.19.

Figure 3.19 also displays the corresponding mode II dissipation at each layer for $V_I = 600 \text{ m/s}$. Upon impact, there is an immediate rise in the mode II energy dissipated at all interfaces, including those not in contact with the projectile. This is likely due to shock-induced delamination upon impact [57], as the transverse shock arrives at the last interface after $2.66 \mu\text{s}$. This

shock arrival time is calculated analytically using the elastic wave speed, c , defined as

$$c = \sqrt{\frac{E}{\rho}}, \quad (3.3)$$

where E is the through-thickness Young's modulus and ρ the density, assuming a constant wave speed that depends on the wave speed of the material, and linearly elastic material behaviour [95]. This is a valid assumption in the case of UHMWPE composites such as Dyneema[®], as laminate behaviour is dominated by elastic fibre properties [11] due to the high fibre volume fraction [79]. The arrival of the shock is also visualised through the evolution of the contact force, displayed in Fig. 3.20. For simplicity, it was assumed that the shock velocity is not dependent on impact velocity.

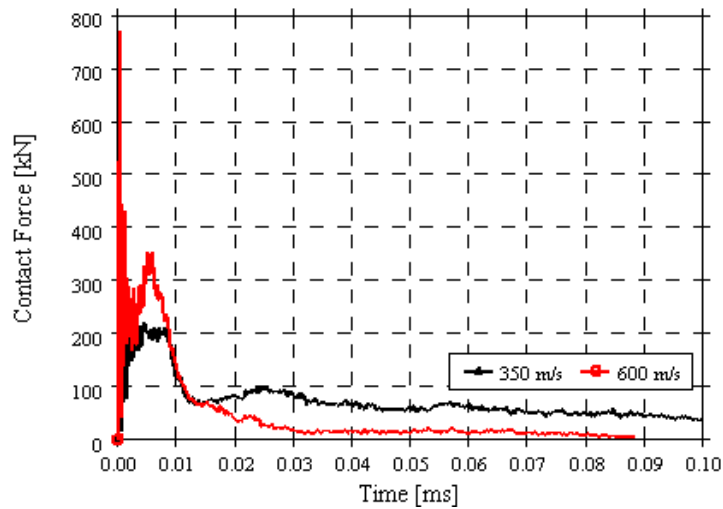


Figure 3.20: The evolution of the contact force between the projectile and the laminate, for a time-step $\Delta t = 10^{-5}$ s.

Furthermore, in Fig. 3.19, the progressive nature of failure in the first three sub-laminates is visible in the mode II energy dissipation at their neighbouring interfaces ($n = 1$ to $n = 3$). In a similar manner, for $I_n E_{II} = 10$ J, the final two interfaces ($n = 8$ and $n = 9$) contribute to around half as much mode II energy dissipation as the middle interfaces at the point of full perforation. The sub-laminates towards the rear face of the panel have failed through fibre tensile failure [11, 93], following the arrival of the transverse pressure wave at the back face and the subsequent pull-in action under the path of the projectile, thus leaving less potential for energy absorption through delamination. Interfaces $n = 4$ to $n = 7$ are therefore responsible for the bulk of mode II interface energy dissipation. These interfaces are adjacent to the sub-laminates with the largest shear pull-in of primary fibres. Upon perforation, the rate of dissipation is rapidly

reduced at the interface below the relevant sub-laminate. Following perforation, all interfaces continue to dissipate energy in mode II, through energy exchange within the laminate. The rate at which this occurs depends on the extent of energy dissipated prior to perforation; the smaller and more localised the failure, the larger the rate of dissipation following perforation.

3.5 Local interface energy dissipation: in-plane

For the first time, cohesive elements have been employed to visualise the behaviour of the interface in a laminate of UHMWPE composite under ballistic impact. The results shed light on the dissipation of energy at different regions of the interface, with respect to the in-plane and out-of-plane locations of the threat. Unlike the results presented in Section 3.4, the in-plane data is presented in terms of strain energy release rate, G [N/m], rather than dissipated energy IE [J], due to the non-uniform mesh density, and therefore the complexity involved in the interpretation of the results. In addition, the strain energy release rate can be evaluated against the critical values for each fracture mode, G_{IC} and G_{IIC} , to analyse the interface regions following the onset of damage and the growth of this up to the point of failure, implied by the erosion of the interface elements. Due to the sheer dominance of mode II deformation over mode I, the mixed-mode (total) strain energy release rate contour plots have been omitted as a result of close resemblance to the mode II plots. Nevertheless, to evaluate the interaction of the two modes of fracture, a mode-mixity parameter is used in Section 3.5.1.3.

3.5.1 Baseline model

The two impact velocity cases discussed in Section 3.3 are explored here in terms of the in-plane distribution of energy dissipation through delamination. A comparison is also provided between interfaces of varying through-thickness proximity to the location of the projectile. For brevity, only three interfaces are selected for presentation, to represent three levels of through-thickness proximity to the projectile. These are at the front face ($n = 1$), the middle ($n = 5$) and at the back face ($n = 9$) of the baseline model, as illustrated in Fig. 3.21.

3.5.1.1 Energy dissipation in mode I

For both the arrest case of $V_I = 350$ m/s, shown in Fig. 3.22, and the perforation case of $V_I = 600$ m/s, displayed in Fig. 3.23, the dissipation of energy through mode I delamination is predominately localised and limited to the region directly below the strike path. In both

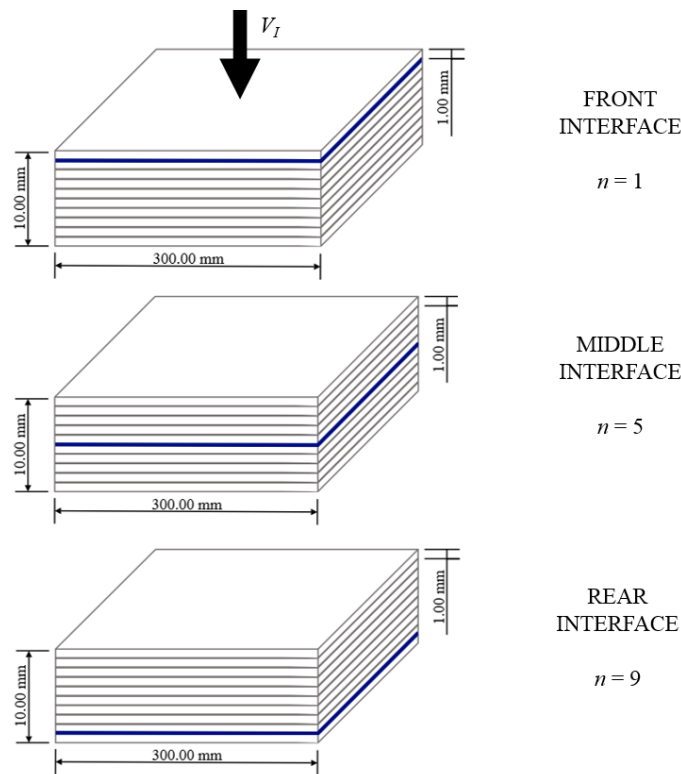


Figure 3.21: The three interfaces selected for investigations of in-plane distribution of energy release rate.

instances, the elements in this region of the front interface are deleted due to immediate failure upon impact due to their proximity to the projectile, as the adjacent solid elements separate and diverge in the out-of-plane direction. Mode I delamination is mostly responsible for the growth of the opening over the course of impact, as shown by the elements surrounding the opening ahead of the “crack-tip”, which are approaching the critical mode I fracture energy required for failure in this mode.

The middle and rear interfaces demonstrate the variation in deformation that stems from a change in strike velocity. While in the earlier stages of impact, up to 0.04 ms for $V_I = 350$ m/s and 0.02 ms for $V_I = 600$ m/s, the fracture process zone in the middle and rear interfaces is enclosed in a circular region below the projectile path. This evolves to a distinctive pyramid shape under the lower velocity, see Fig. 3.22, reminiscent of the pyramid-shaped BFDs that have been previously reported [18]. Meanwhile, under the higher impact velocity seen in Fig. 3.23, the opening continues to grow. Although the interface elements below the projectile in Fig. 3.22 and adjacent to the opening in Fig. 3.23 demonstrate signs of damage, the mode I fracture energy is not in the vicinity of the critical value, thereby suggesting a much more significant mode II contribution.

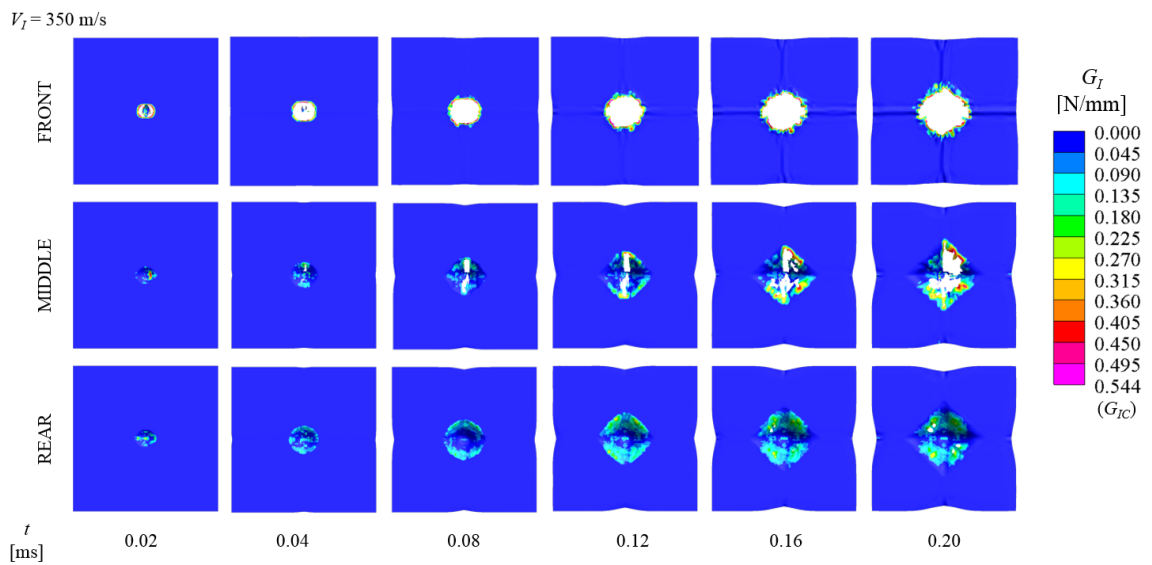


Figure 3.22: The in-plane variation of mode I energy release rate at different interfaces through the thickness of a laminate under impact, for $V_I = 350$ m/s and $\sigma_{II} = 2.6$ MPa.

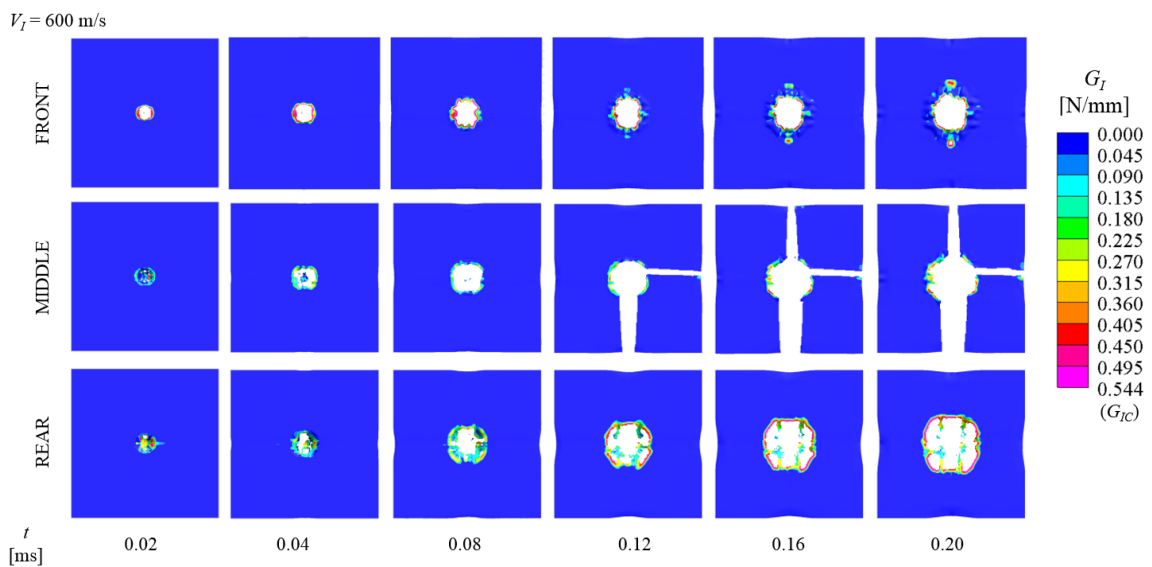


Figure 3.23: The in-plane variation of mode I energy release rate at different interfaces through the thickness of a laminate under impact, for $V_I = 600$ m/s $\sigma_{II} = 2.6$ MPa.

3.5.1.2 Energy dissipation in mode II

While mode I damage is more localised around the projectile, Figs. 3.24 and 3.25 illustrate a more extensive mode II presence across the interfaces due to in-plane pull-in of the elements representing the primary fibres towards the location of impact. The dominance of mode II activity and its greater contribution to the total mixed-mode dissipation of energy at the interface was established in Section 3.3, as was the dependence of the level of interface energy dissipation on the impact velocity. Variations in the distribution of the energy release rate are

therefore expected between the two velocity cases, particularly since the majority of the energy is dissipated through this mode of fracture.

At the front interface of the lower impact velocity in Fig. 3.24, the zone of failed elements is visible in the centre, directly below the path of the projectile, which is progressing at this stage through the first sub-laminate layer in a localised manner. The mode II fracture process zone of this interface begins to radiate from the centre towards the edges, attributed to the drawing in of the primary fibre regions and the disparity that exists for this action between the first and the second sub-laminate layers. As the opening in the interface grows, the strain energy release rate remains considerably uniform in pattern and in magnitude until at least 0.2 ms past the point of impact.

The middle and rear interfaces, despite their distance from the projectile upon impact, experience significant mode II activity at the centre. This region of mode II damage increases in radius with progression through the laminate, demonstrating the interaction of the transverse shock wave with the sub-laminates. As previously pointed out, the sub-laminates initially undergo localised failure as the projectile punctures each layer, followed by more distal in-plane shear once the projectile is caught. The interface elements away from the projectile however, undergo both modes of fracture, albeit mostly mode II, even at the earlier stages of impact as seen in Figs. 3.22 and 3.24, before the projectile is caught at around 0.10 ms.

The fracture process zone of the middle interface is the most expansive. This is the region with the greatest in-plane shear experienced by neighbouring sub-laminates. The damage zone however, is limited to the centre, and is enclosed by the shear hinge. A similar pattern is visible across the rear interface. By contrast, there appears to be very little pull-in action between the primary regions of the adjacent sub-laminates and a lower degree of strain energy release rate directly under the projectile. This pattern of mode II activity can be visualised by referring back to Fig. 3.6, where the close attachment of the sub-laminate layers below the projectile explains the lack of mode II activity across the rear interface, as well as directly below the projectile. With the progression of the shear hinge however, the sub-laminate elements undergo in-plane shear in the deformation region enclosed by the hinge, causing mode II damage to prevail across the interface at the back face, as seen in Fig. 3.24.

Under the higher impact velocity case in Fig. 3.25, the front interface experiences a very small extent of mode II fracture, limited to only one in-plane direction of the primary fibre

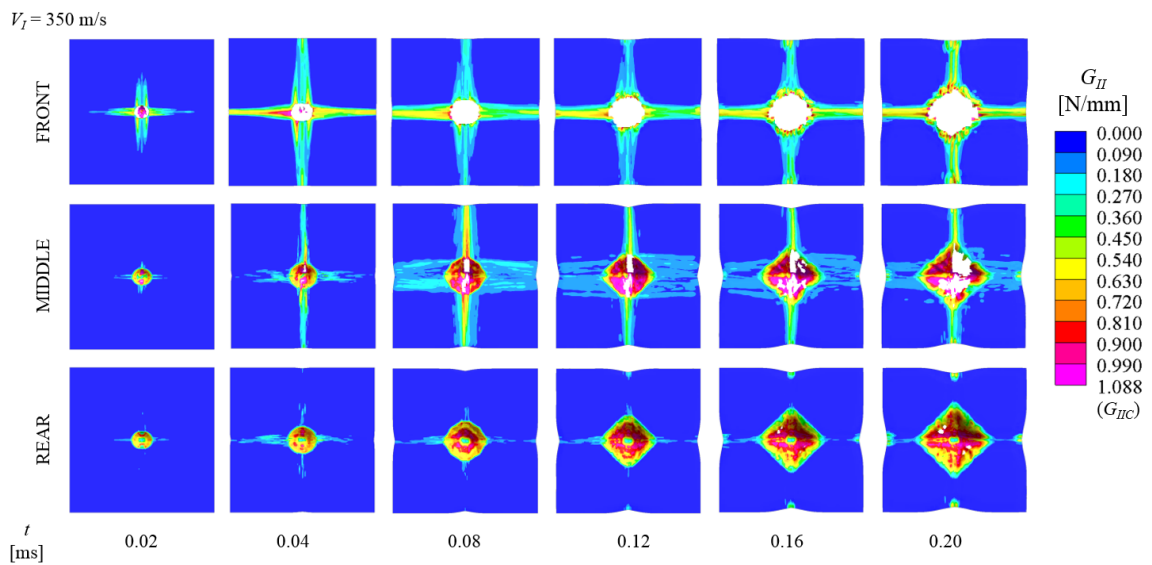


Figure 3.24: The in-plane variation of mode II energy release rate at different interfaces through the thickness of a laminate under impact, for $V_I = 350$ m/s and $\sigma_{II} = 2.6$ MPa.

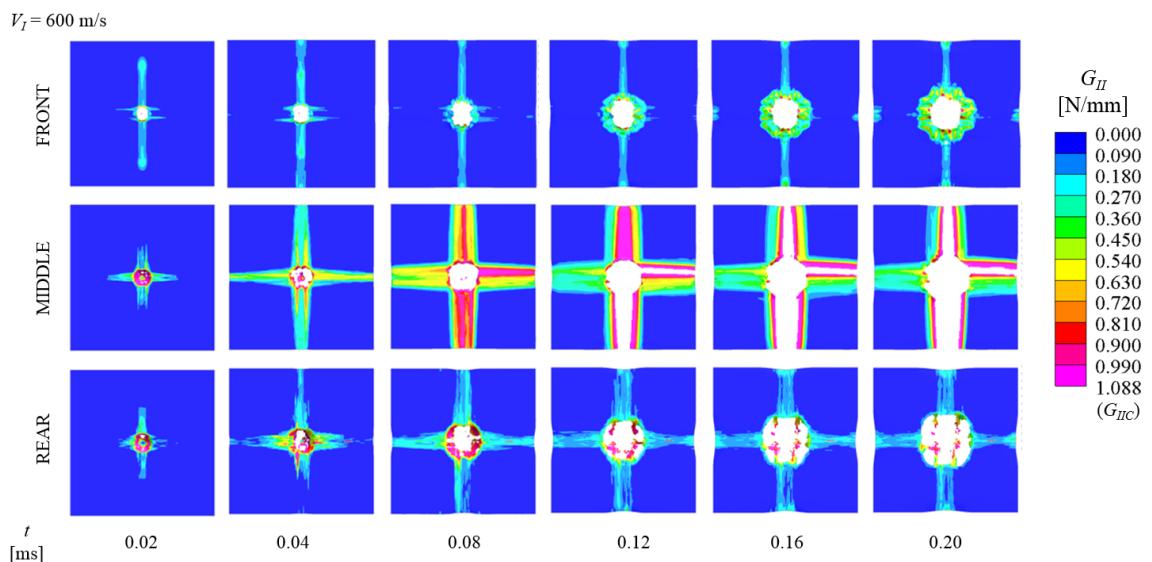


Figure 3.25: The in-plane variation of mode II energy release rate at different interfaces through the thickness of a laminate under impact, for $V_I = 600$ m/s and $\sigma_{II} = 2.6$ MPa.

region. The fracture zone grows in the region surrounding the opening due to mode I damage. The middle interface undergoes much more extensive mode II fracture and damage, where damaged elements contained by the shear hinge zone at the lower impact velocity are eroded with the increase in impact velocity. The damage progressing to the edges in the primary zones after 0.04 ms, also leads to element erosion. The middle interface undergoes more extensive levels of pull-in, relative to the other two interfaces at $V_I = 600$ m/s, making its behaviour comparable to the front face interface at $V_I = 350$ m/s. Thus, it is shown that for the same

impact conditions, a higher impact velocity has forced the regions with the greatest amount of membrane shearing to move deeper into the laminate. A similar pattern is displayed across the rear interface, although the damage zone is limited to the central region only. This confirms the findings of Section 3.4, where it was established that the bulk of mode II fracture energy is dissipated in the middle interfaces rather than at the front ($n = 1$) or the rear ($n = 9$) interfaces, irrespective of the impact velocity.

3.5.1.3 Mode mixity

The fracture energy based mode mixity is used as an indication of the interaction of two modes of fracture, with respect to the total amount of energy dissipated, and is defined as

$$G' = \frac{G_{II}}{G_T}. \quad (3.4)$$

The evolution of the mode mixity at three interfaces through the thickness of the laminate are illustrated as fringe plots in Fig. 3.26, for four time intervals over the first 0.12 ms of impact. The legend colours increase from light to dark, representing the transition of mode I to mode II dominant delamination. Note that the darkest shade represents regions without damage or failure.

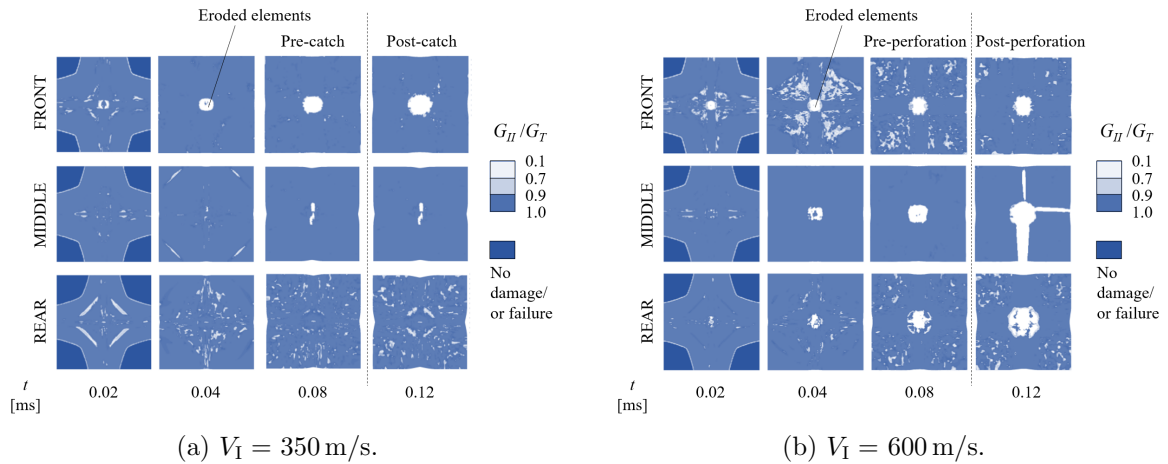


Figure 3.26: The in-plane variation of fracture energy based mode-mixity at different interfaces through the thickness of a laminate under impact, for $d = 300$ mm, $h_T = 10$ mm, and two cases of strike velocity V_I .

For $V_I = 350$ m/s, the sub-laminate elements representing the primary fibres are drawn inwards from the sides upon impact. Figure 3.26(a) shows the behaviour of the interface, corresponding to this effect. A cross-shaped region, with a mode mixity of 90% and above,

expands to cover the entire interface with the progression of the projectile through the thickness. The edges enclosing this region however, are subjected to a larger degree of mode I deformation. At $t = 0.02$ ms, all three interfaces of interest are deforming in a similar fashion, with mode II domination over mode I fracture, and naturally, an increase in the area of energy dissipation with increased proximity to the projectile. Some elements are deleted in the centre of the interface directly beneath projectile due to partial perforation of adjacent sub-laminates, with a small degree of higher mode I activity occurring in a diamond shape outlining the shear hinge.

This effect is replaced by total mode II domination with the progression of the projectile through the layers. The middle interface shows a similar behaviour, with fewer elements deleted as the projectile is caught before reaching this layer. The middle interface does however show some signs of mode I activity in the corners at $t = 0.04$ ms, in a pattern which signifies the expansion of the hinge from the previous time-step, on the front layer. The interface at the back face of the laminate has a more noticeable region of low mode-mixity, which again outlines the diamond-shaped hinge created by the pyramid-like deformation of the back-face, possibly highlighting the progression of the impact wave to the back face. Unlike the first two interfaces, as the projectile progresses through the layers and decelerates, the low mode-mixity region grows outwards, towards the edges of the laminate. It encloses an area inter-dispersed with regions of high (0.9–1) and a relatively lower (0.7–0.9) mode-mixity range. Upon catching the projectile, the diamond shape pattern seems to repeat again, radiating outwards from the laminate centre.

Similarly, when the plate is struck by the projectile at $V_I = 600$ m/s, a mode II dominated cross-shaped region grows outwards from the impact region and the primary fibres. In contrast, the interface closest to the front face experiences a much lower mode-mixity in the regions not connected to the elements representing the primary fibres post perforation, compared to the lower impact velocity case, suggesting a larger extent of energy redistribution following impact at a higher strike velocity. The total domination of mode II deformation at the middle interface is in line with the lower impact velocity, confirming the plots in Section 3.4, which highlighted the higher contributions of the middle interfaces to the total dissipation of energy through delamination, irrespective of whether any, partial or full, perforation occurs. The interface at the back face exhibits fewer regions of low mode-mixity, both prior to and following perforation, relative to the lower impact velocity case.

It is clear that across the surface of an interface, mode II delamination is much more

prevalent than mode I, regardless of the location of the interface through the thickness of a laminate, or the velocity of impact. This behaviour is amplified in the middle interface where there is little to no mode I activity, as the bulk of the total energy is absorbed here. In the arrest case, the most visible mode I activity occurs towards the back face of the laminate, modelling the interaction of the final sub-laminate with the laminate-to-air interface, and thereby the reflected shock waves after the projectile is caught. In the perforation case, a similar behaviour is observed post perforation, signifying the redistribution of energy in the laminate.

3.5.2 Parametric studies

3.5.2.1 Dimensional effects

The following sections investigate dimensional effects on the level of energy dissipation at three interfaces through the thickness of the laminate, for a stop (arrest) case under an impact velocity of $V_I = 350$ m/s.

3.5.2.2 Plate length

Figure 3.27(a) displays mode-mixity fringe plots at the interfaces of laminates with varying in-plane dimensions under impact at $V_I = 350$ m/s. For the smallest plate size ($d = 100$ mm), the most noticeable difference is the shorter distance from the centre of the plate to the edges, which contributes to the presence of delamination across the entire surface of each interface by $t = 0.02$ ms. Element deletion in the interfaces beyond the front face interface occurs in a belt, surrounding elements that are directly under the path of impact. These are not eroded since contact between the sub-laminates is maintained, while they travel with the projectile. The excessive shear pull-in motion of primary fibres towards the centre captured at the edges of the middle and rear interfaces is responsible for the erosion of these elements, which have not failed due to perforation by the projectile, but due to extreme levels of shear strain and the disparity of this in the sub-laminate layers above and below the cohesive zone, leading to failure via mode II fracture.

As the aperture of the failed cohesive zone increases, so do the lower mode-mixity regions around the opening. Likewise, at the back face interface, the corners of the interface see a rise in the contribution of mode I deformation at $t = 0.04$ ms, corresponding to the drop in the rate of energy absorption seen in Fig. 3.13, which implies near complete perforation of the laminate with a ballistic limit of $V_{50} = 438.2$ m/s, according to Fig. 3.12. Although reducing the in-plane

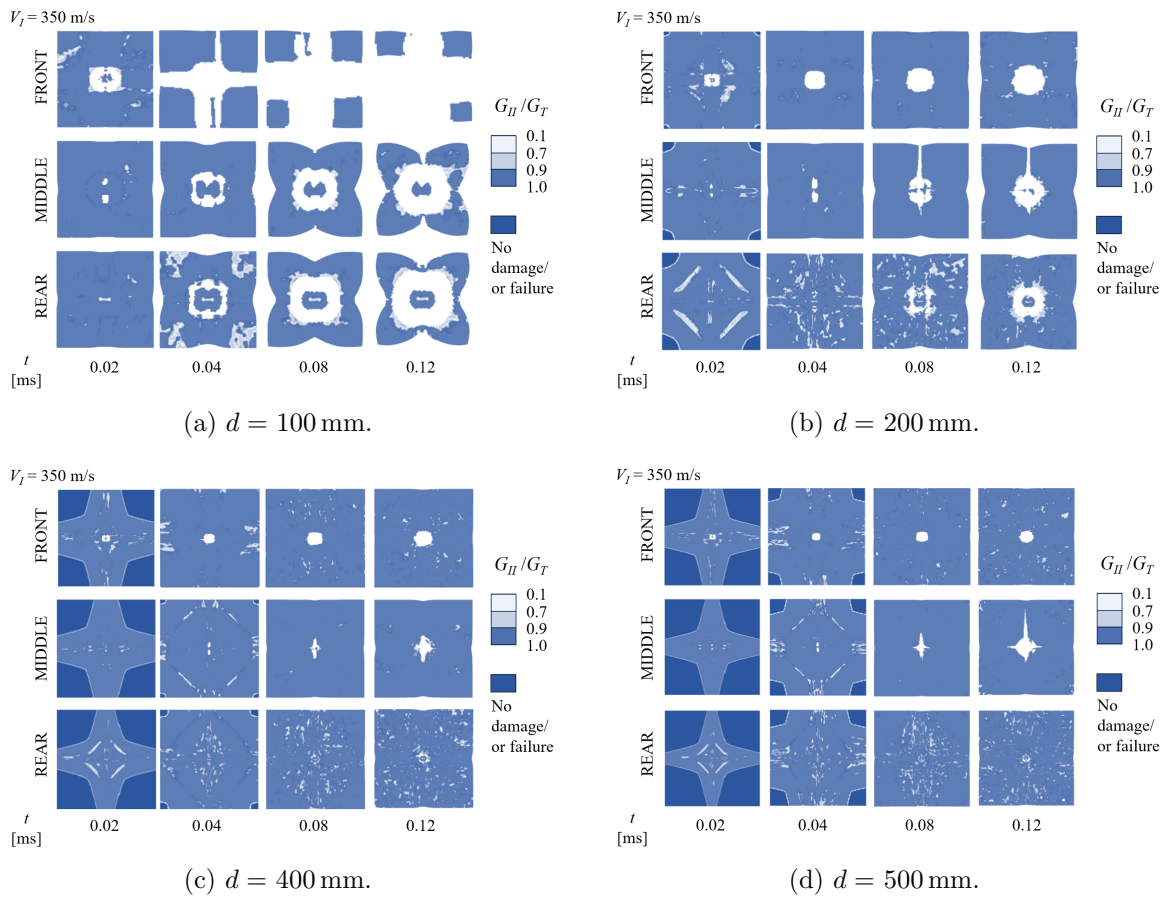


Figure 3.27: The in-plane variation of fracture energy based mode-mixity at different interfaces through the thickness of a laminate under impact, for $V_I = 350$ m/s, $h_T = 10$ mm, and various in-plane dimensions d .

plate dimensions yields an improved ballistic limit, this comes at the expense of the interfaces undergoing much larger deformations and failure, leading to the large levels of BFD discussed previously in Section 3.3.2. In this situation, although longer fibres exhibit higher strengths and strain-to-failure ratios, the smaller the plate dimensions, the more readily energy can be dissipated at the interfaces through in-plane shear. Therefore, as observed in the simulation, the larger the failure experienced by the interface elements, the smaller the extent of failure undergone by the sub-laminate layers.

As the dimensions of the plate are increased to $200 \text{ mm} \times 200 \text{ mm}$, the distribution of the mode-mixity visible in Fig. 3.27(b), moves closer towards the patterns seen for the baseline model ($d = 300$ mm) in Fig. 3.26(a), but with slightly higher levels of mode I activity present across the back face interface than seen for $d = 300$ mm. Further increasing d to 400 mm, see Fig. 3.27(c), and to 500 mm, see Fig. 3.27(d), present similar in-plane distributions of mode I and mode II deformations, compared to the smaller plates. The key difference is the delay in

the arrival of damage and subsequent failure at the interfaces, the extent of which grows with plate dimension d . The limitations of in-plane shear deformation due to larger plate areas leads to more limited mode II delamination at the interface, and the subsequent fall in the ballistic limit velocity observed in Fig. 3.12.

3.5.2.3 Plate thickness

Figure 3.28 displays mode-mixity fringe plots at the interfaces of laminates with varying thicknesses under impact at $V_I = 350$ m/s. Damage is initiated to the same extent across the front interface, irrespective of the plate thickness. However, a variation in the plate thickness does lead to differing distances between the front, middle and rear interfaces. This translates into a varying amount of damage at the middle and rear interfaces, with a variation in the plate thickness. Similar patterns of strong mode II deformation is present between corresponding interfaces (front, middle and back), suggesting that energy dissipation is scaled with the thickness so that the different levels of interfaces contribute equally to the overall amount of dissipation, irrespective of the total thickness and therefore the number of interfaces modelled.

Reducing the plate thickness from 10 mm to 8 mm in Fig. 3.28(b), does not affect the in-plane mode-mixity by a significant amount. Halving the thickness to 5 mm in Fig. 3.28(a) however, slightly reduces the domination of mode II deformation. Towards the edges and the corners across the front and rear interfaces in particular, more dispersed regions with a mode-mixity in the range of 0.7–0.9 are visible, with less concentration around the central zone of impact seen in Fig. 3.26(a) for the 10 mm plate. This is likely to be a result of reduced ballistic limit and increased depth of penetration, due to the reduced overall thickness of the plate.

In contrast, increasing the thickness of the plate to 15 mm in Fig. 3.28(c), and to 20 mm in Fig. 3.28(d), noticeably increases the contribution of mode I delamination to the overall energy dissipation. In both instances, following the perforation of the front layer, there is enhanced mode I activity under the regions not associated with primary fibres, represented by the lighter shaded regions. Increasing the laminate thickness modelled with a constant sub-laminate thickness of 1 mm, increases the ballistic limit of the plate as seen in Fig. 3.15, while Fig. 3.28(d) demonstrates an increased mode I contribution to delamination, particularly in the corners of the four quadrants of each interface, as the sub-laminates undergo relatively more out-of plane separation to in-plane shearing than in the thinner specimens.

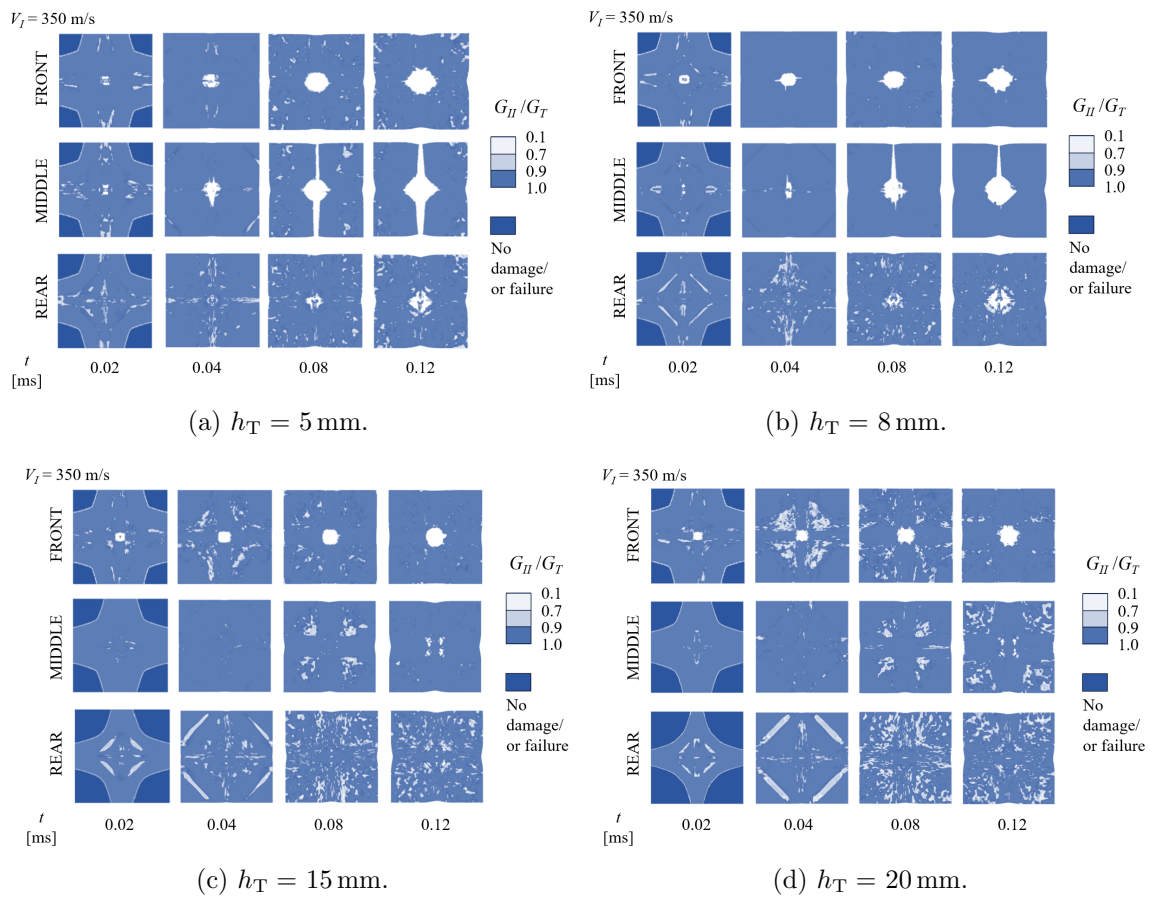


Figure 3.28: The in-plane variation of fracture energy based mode-mixity at different interfaces through the thickness of a laminate under impact, for $V_I = 350$ m/s, $d = 300$ mm, and various laminate thicknesses h_T .

3.5.2.4 Maximum cohesive traction

Due to the dominance of mode II energy dissipation, the effect of altering the peak mode II traction, σ_{II} , in the mixed-mode bilinear cohesive traction-separation law, on the in-plane distribution of energy dissipation at the interfaces was investigated. The high strain rate value of $\sigma_{II} = 2.6$ MPa was reduced to the quasi-static value of $\sigma_{II} = 1.8$ MPa reported in the literature [89]. Reducing the peak traction while retaining a constant critical strain energy release rate, G_{IIC} , increases the separation distance at failure, as the area under the mode II traction-separation curve, representing G_{IIC} , must remain constant. Naturally, reducing maximum traction leads to more extensive damage at the interface under the same impact load. This is demonstrated by the increased number of failed interface elements, as seen by the growth in the aperture in Figs. 3.22 to 3.23, as well as in Figs. 3.29 to 3.30. While the distribution of G_I has remained broadly the same for the lower impact velocity case shown in

Fig. 3.29, the concentrations of mode I fracture energy around the opening have visibly reduced at the higher impact velocity case, as illustrated in Fig. 3.30.

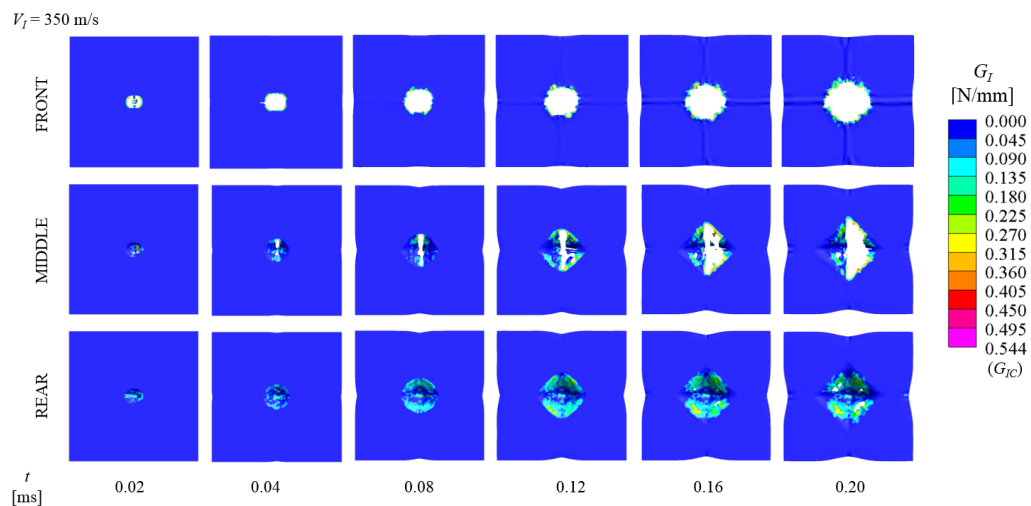


Figure 3.29: The in-plane variation of mode I energy release rate at different interfaces through the thickness of the laminate, for $V_I = 350$ m/s and $\sigma_{II} = 1.8$ MPa.

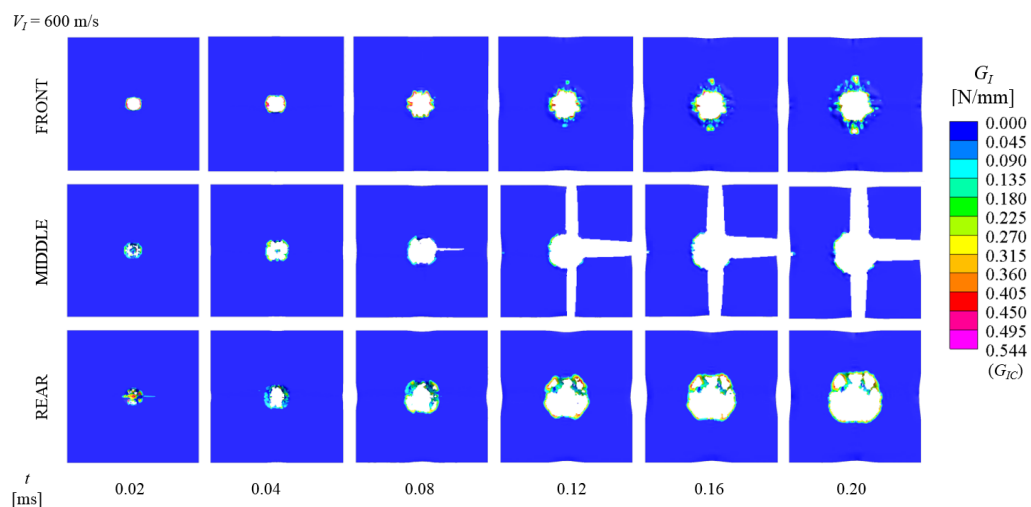


Figure 3.30: The in-plane variation of mode I energy release rate at different interfaces through the thickness of the laminate, for $V_I = 600$ m/s and $\sigma_{II} = 1.8$ MPa.

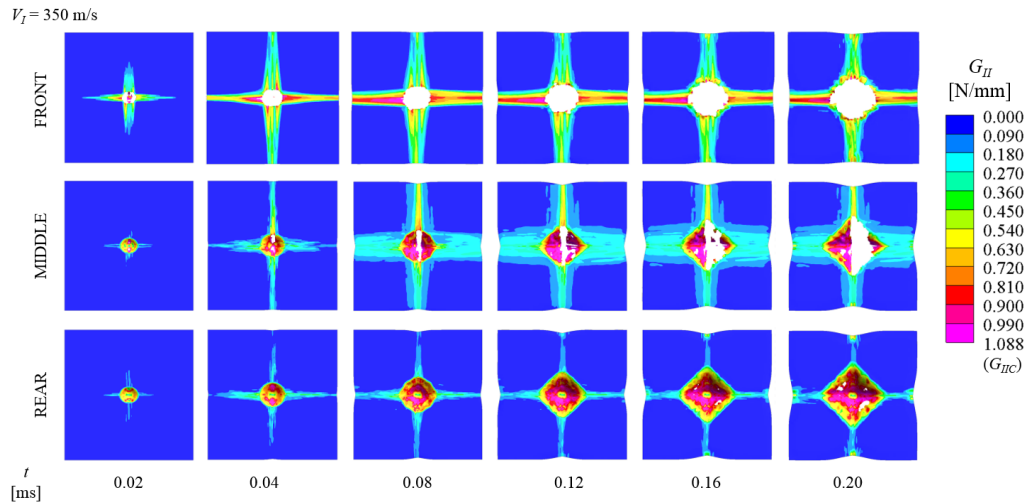


Figure 3.31: The in-plane variation of mode II energy release rate at different interfaces through the thickness of the laminate, for $V_I = 350$ m/s and $\sigma_{II} = 1.8$ MPa.

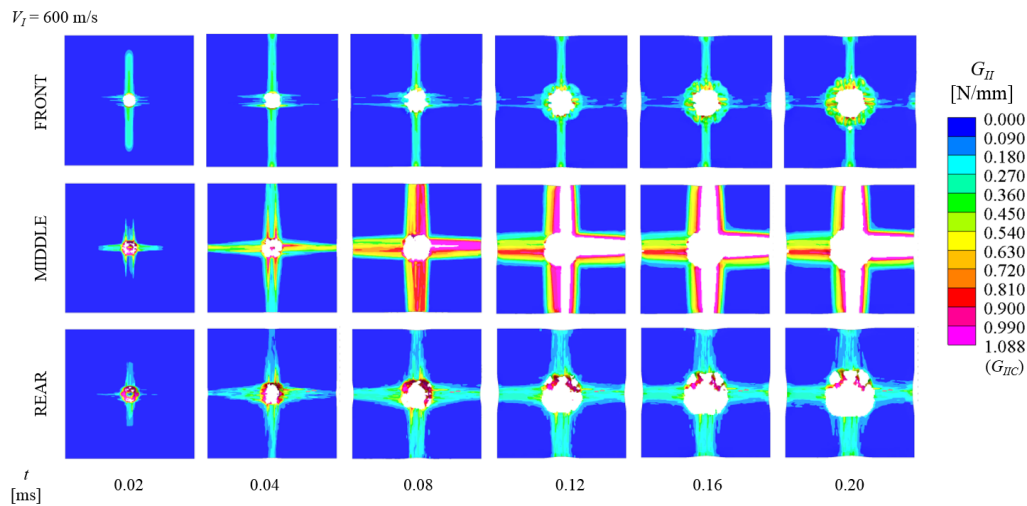


Figure 3.32: The in-plane variation of mode II energy release rate at different interfaces through the thickness of the laminate, for $V_I = 600$ m/s and $\sigma_{II} = 1.8$ MPa.

3.6 Model versatility and interface element behaviour

In this section, the versatility of the current CZM model is explored through experimental validation against test data for flat panels of varying thicknesses. In addition, modelling features such as the evolution of element area used in energy dissipation calculations, the sensitivity of the output to the number of interfaces, as well as the significance of rate effects, are investigated further.

3.6.1 Experimental validation

To validate the flat plate model used in the current study for the target and threat dimensions used in the experimental testing performed in Chapter 5, the in-plane dimensions of the modelled plate were reduced to $d = 100$ mm, the threat was replaced by a 5.56 mm diameter FSP, and a rigid backing plate with a frictionless surface was added at the rear to prevent whole plate movement as a result of the reduction in the plate length, as previously demonstrated in Fig. 3.33 and discussed in Section 3.3.2.3. Clamp pressure applied onto the laminate, as seen in Fig. 3.33, to more accurately recreate testing conditions described in Chapter 5, was deemed unnecessary after an analysis of the effect of applying a range of pressures, 0.1, 1, 2 and 10 MPa, revealed only a small change in V_{50} towards the experimental data. This change was the same for all the magnitudes of clamp pressure investigated, equal to a value of approximately 4%.

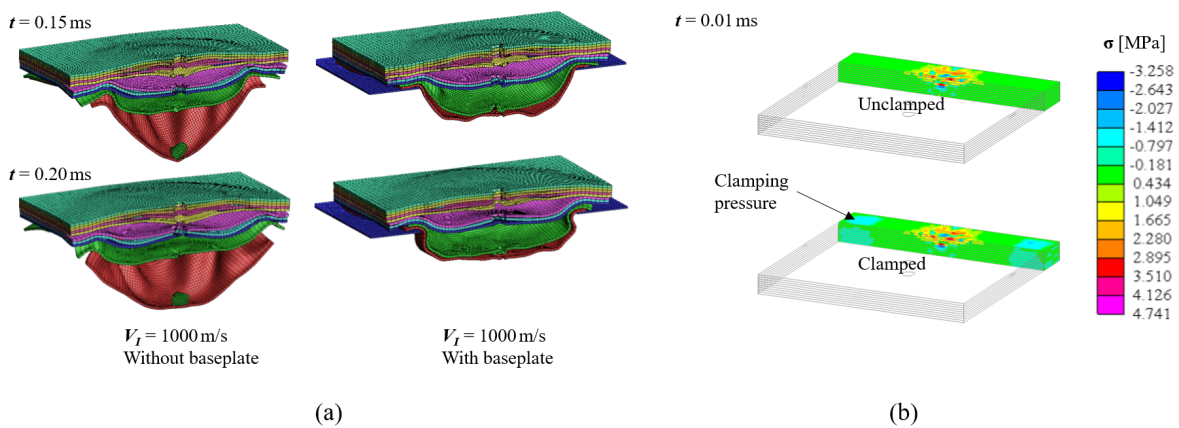


Figure 3.33: (a) The effect of modelling ballistic impact of small plates with and without a baseplate, (b) modelling with and without clamping pressure.

The ratio between the elements on the flat face of the projectile and the target mesh was kept constant, giving an approximate element size of 0.5 mm. To investigate the effect of the projectile mesh density relative to that of the plate, two further scenarios were modelled. One used a refined FSP mesh with the element size almost halved (0.275 mm) and the target mesh density maintained, while the other employed a refined projectile mesh with a refined target mesh of matching element dimensions in the impact zone, visible in Fig. 3.34. Due to the necessity of maintaining cubic element dimensions in the refined impact zone [86], the sub-laminate thickness, h_{SL} , was also adjusted to match the in-plane element dimensions, thereby increasing the number of interfaces to maintain the single element sub-laminate thickness.

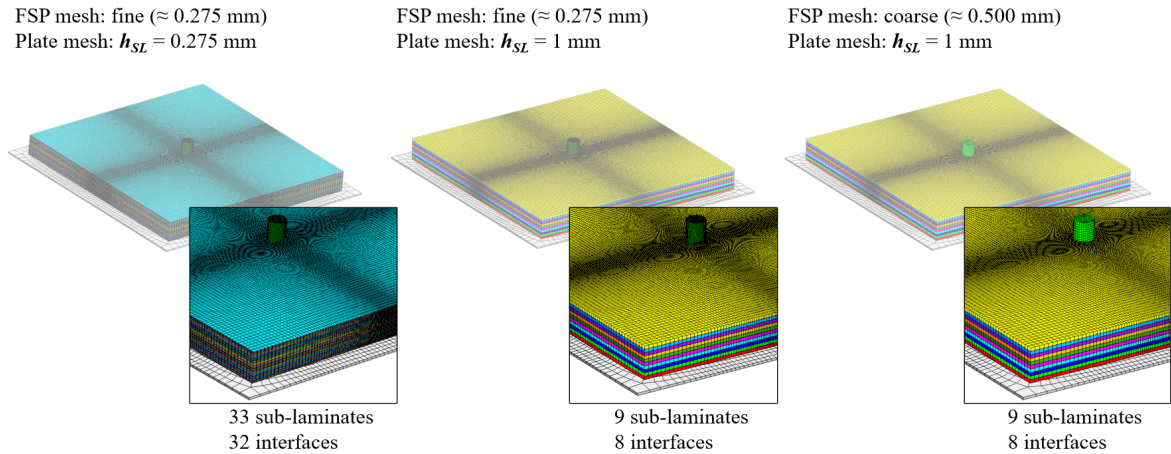


Figure 3.34: Modelled target plates with varying threat and target mesh densities, resulting in different numbers of sub-laminates.

The resulting Lambert-Jonas V_{50} curve fits are plotted in Fig. 3.35, together with corresponding experimental data. In addition, the velocity data from two 10 mm thick panels are plotted with and without a backing plate, to highlight the necessity of having a backing plate to prevent whole plate movement and the accompanying improvements in the V_R data. The velocity plot that most closely resembles the experimentally acquired data points, obtained from Chapter 5, belongs to the model with the least refined mesh. It is hypothesised that further mesh refinement from this point does not improve the accuracy of the numerical predictions based on the experimental data, as the composite material model is governed by stressed-based failure criteria, leading to premature failure as a result of higher levels of stress being captured by smaller elements. Since the stress gradient across an element is linear, with only a single integration point, the smaller elements in the refined mesh collectively fail earlier. Considering the plate with the most refined mesh density and sub-laminate thicknesses approaching the thickness of a UD HB26 layer, it is worth noting that this model was not intended for capturing the laminate constituents and their deformations on a micro-scale level. Therefore, due to the reasonable run time and good fit of results, the unrefined projectile and target mesh were deemed suitable for the purpose of the current work.

To evaluate the versatility of the model for various target thicknesses, numerical V_{50} estimations for $h_T = 6.00$ mm to 9.00 mm are compared against experimental data obtained from testing carried out in Chapter 5, in Fig. 3.36. Since sub-laminate thicknesses were limited to $h_{SL} = 1$ mm, the tested plate thicknesses were not perfectly matched in simulations. However,

the data trends are still in line with what is expected from the effects of varying the laminate thickness, as was previously discussed in Section 3.3.2.

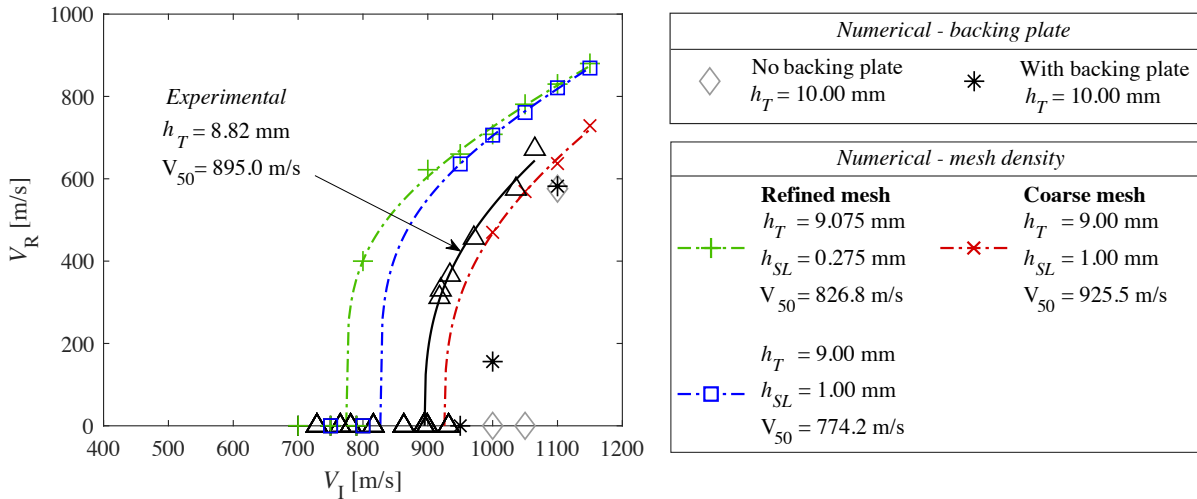


Figure 3.35: Comparison of numerically and experimentally derived Lambert-Jonas V_{50} approximations for numerical models of varying mesh density.

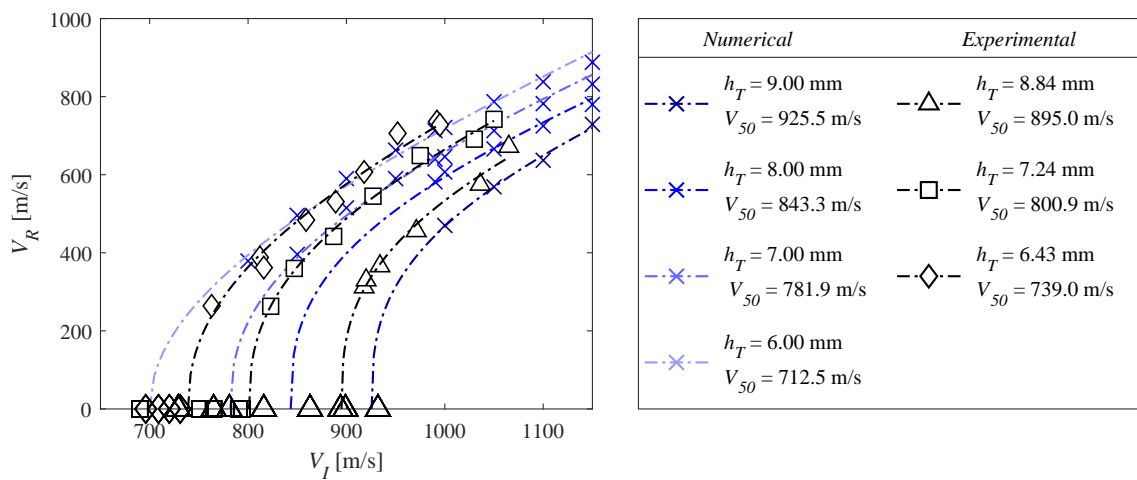


Figure 3.36: Comparison of numerically and experimentally derived Lambert-Jonas V_{50} approximations for varying plate thicknesses.

3.6.2 Evolution of element area

Firstly, it is worth noting that extracting strain energy release rate values directly from LS-DYNA yields falling energy levels over time. Although some elements move back down the elastic region of the traction-separation curve over time, the contribution of this is negligible due to a limited elastic regime, with a smaller energy contribution over the course of impact.

The falling interface energy levels were attributed to the deletion of some cohesive elements, the energy absorption levels of which are then not recorded in the output. To account for this, a for-loop was written in the post-processing MATLAB script, to replace the null energy output of deleted elements, with their last recorded non-zero value. In the methodology section of this chapter, it was assumed that the mid-surface area of the interface elements remained constant throughout the duration of impact. In reality, large deformations might take place in the element areas over time. This may need to be corrected for, by updating the element area for energy calculations. The user material sub-routine was altered to calculate the real-time, true mid-surface area of each interface element, from which the energy dissipation was derived.

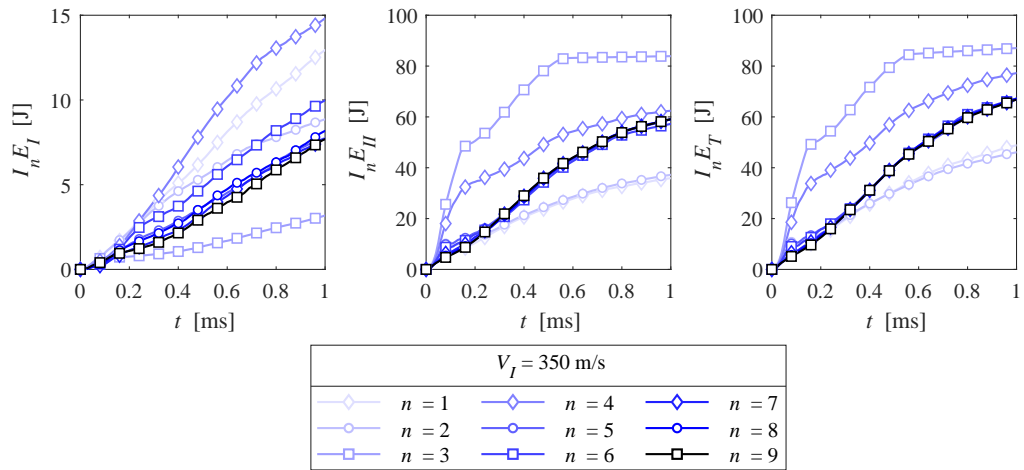


Figure 3.37: Energy dissipated at each sub-laminate layer under impact at $V_I = 350 \text{ m/s}$, through mode I (LHS), mode II (centre) and combined mixed-mode (RHS) delamination, calculated using true element area.

The energy dissipation at individual interfaces from Figs. 3.18 and 3.19 is replotted in Figs. 3.37 and 3.38, respectively. In the stop case in Fig. 3.37 for $V_I = 350 \text{ m/s}$, it can be seen that accounting for the change in element area has altered the distribution of mode I energy dissipation through the thickness of the laminate, with the 4th and the 2nd layers overtaking the 5th interface as the interface with the highest contribution to the total mode I energy dissipated at the interface, implying a prevalence of large deformations in the out-of-plane mode in these layers. This is in line with the in-plane analysis of the interfaces, displayed in Fig. 3.22, where failure and thus erosion of interface elements, particularly due to penetration of neighbouring sub-laminate layers and subsequent mode I failure of the cohesive elements, continued to grow over time in the front interface. Mode II deformations on the other hand, have remained largely the same after accounting for the change in element area, since the layers

with the largest amounts of dissipation are also the layers accommodating the greatest extents of mode II separation of sub-laminates.

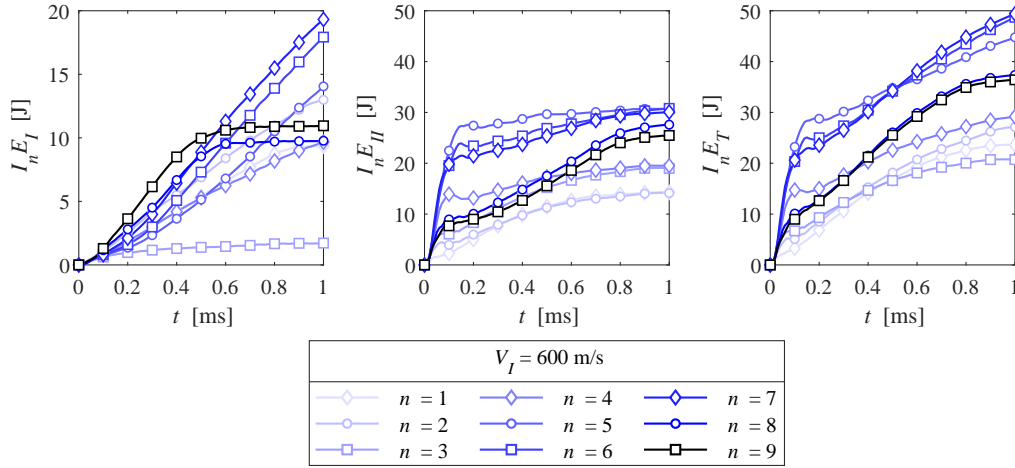


Figure 3.38: Energy dissipated at each sub-laminate layer under impact at $V_I = 600 \text{ m/s}$, through mode I (LHS), mode II (centre) and combined mixed-mode (RHS) delamination, calculated using true element area.

In the perforation case in Fig. 3.38 for $V_I = 600 \text{ m/s}$, the contribution of individual interfaces to the total interface energy dissipation has remained largely the same, as the extent of element deformation is less relevant due to the higher velocity and smaller overall extension the sub-laminates undergo as a result of this. For both modes of deformation in the lower impact velocity case, together with mode II deformation at the higher impact velocity, there has been an increase in energy dissipation most notably in the interfaces with the largest contributions, due to the change in the element area as the sub-laminates separate from one another. In effect, this has led to a small net increase in the overall dissipation of energy at the interfaces for $V_I = 350 \text{ m/s}$, while there has been minimal change in the combined mixed-mode energy levels for $V_I = 600 \text{ m/s}$. This stems from the rise in mode I energy, which has been offset by the drop in mode II energy dissipation, as reflected in the plots presented in Fig. 3.39. For both impact velocity cases, the change in the total mixed-mode energy levels and the contribution to total energy arising from the inclusion of the true element area, is negligible and therefore previously analysed parametric data based on the total mixed-mode interface energy remains valid.

Considering the combined strain energy release rate mode-mixity for all interfaces in Fig. 3.40, the domination of mode II over mode I energy dissipation is clear for both impact velocities. Under the lower velocity, the mode-mixity plot follows the same pattern but is slightly lower when the true element area is used in energy calculations due to the aforementioned

significance of this for mode I deformations. The level of mode II domination drops from above 95%, to approximately 90% following the arrest of the projectile at around $t = 0.1$ ms. Mode II domination, as represented by the mode-mixity parameter, continues to fall as energy redistribution takes place in the laminate, slowly transitioning toward higher levels of out-of-plane separations. By contrast, under the higher impact velocity, mode-mixity at the interface rises from approximately 90%, to more than 95% at the point of full perforation of the laminate. Following this, the mode-mixity begins to drop rapidly, as mode I separation at the interfaces grows at a higher rate than in-plane stretching of the membranes, which was restricted prior to perforation due to the presence of the projectile. The mode-mixity parameter reduces at a slightly more rapid rate in the earlier stages of impact, when the true element area is accounted for.

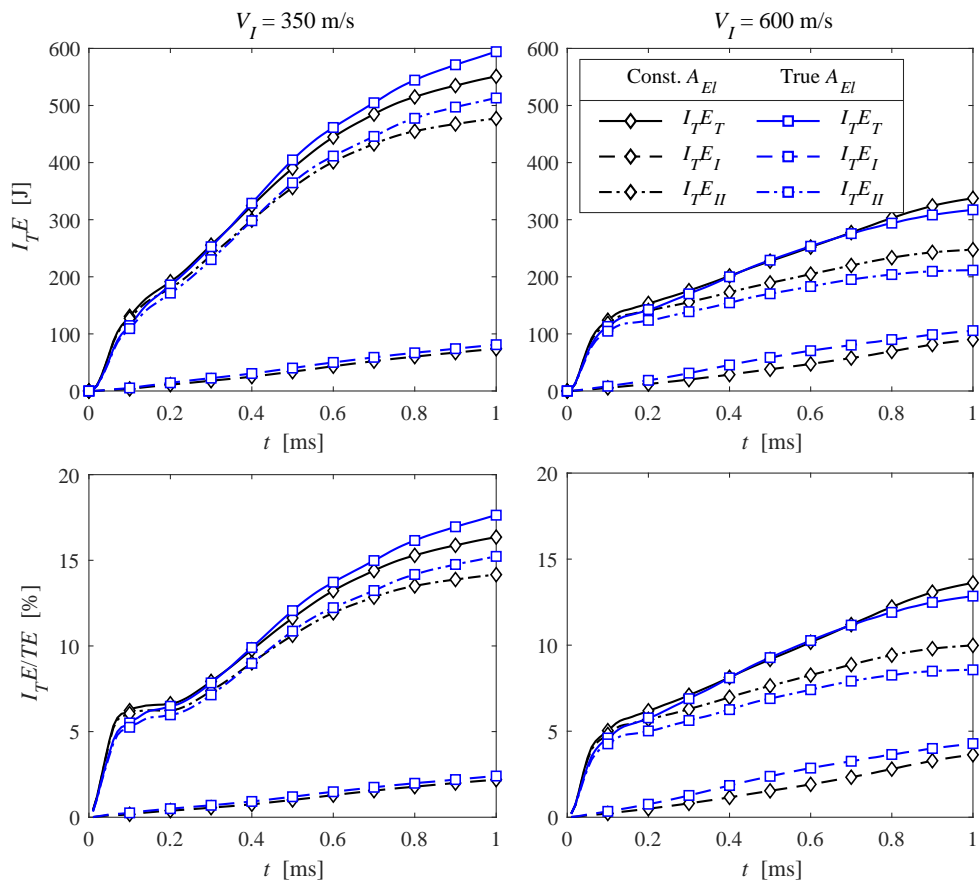


Figure 3.39: A comparison of energy dissipated at interfaces during impact at $V_I = 350$ m/s (LHS) and $V_I = 600$ m/s (RHS), together with energy dissipated at the interfaces as a percentage of the total energy dissipated, between calculations using constant and true element area.

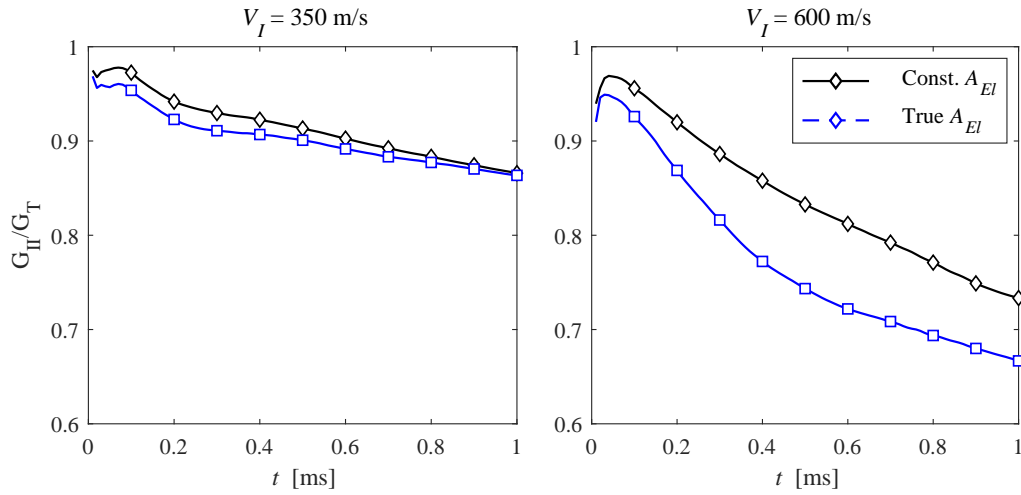


Figure 3.40: A comparison of the combined strain energy release rate mode-mixity at all interfaces during impact at $V_I = 350$ m/s (LHS) and $V_I = 600$ m/s (RHS), between calculations using constant and true element area.

3.6.3 Number of interfaces

Another numerical parameter worthy of consideration is the sub-laminate thickness, which is inversely related to the number of interfaces modelled in a single panel. To investigate the effect of this on the ballistic velocity limit predictions of the panel, five values of h_{SL} were selected, ranging from 0.25 mm to 5.00 mm, and were simulated under impact while maintaining an overall plate thickness of $h_T = 10$ mm. Note that the interface stiffness was also scaled accordingly, using Eq. (2.8) [49]. The velocity results and corresponding Lambert-Jonas fits are presented in Fig. 3.41. Following changes in h_{SL} , deviations of the V_{50} from the baseline model range from 2.1 % to 5.9 %, which is acceptable considering the significant reduction in the simulation time that is achieved by reducing the number of sub-laminates modelled.

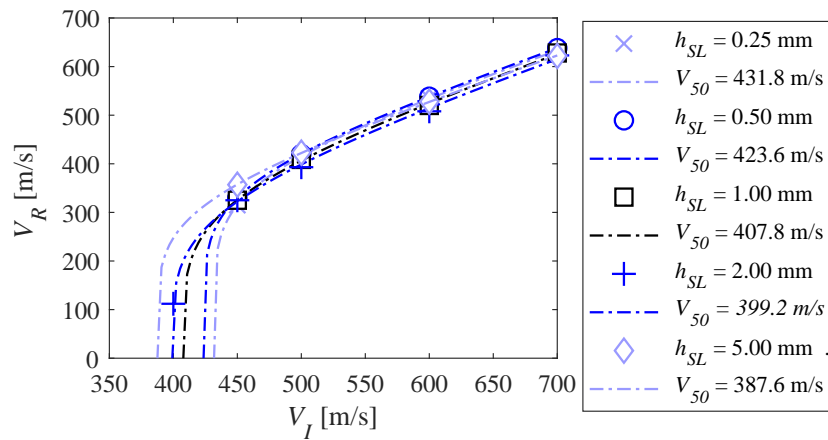


Figure 3.41: Lambert-Jonas V_{50} approximations for varying sub-laminate thickness h_{SL} .

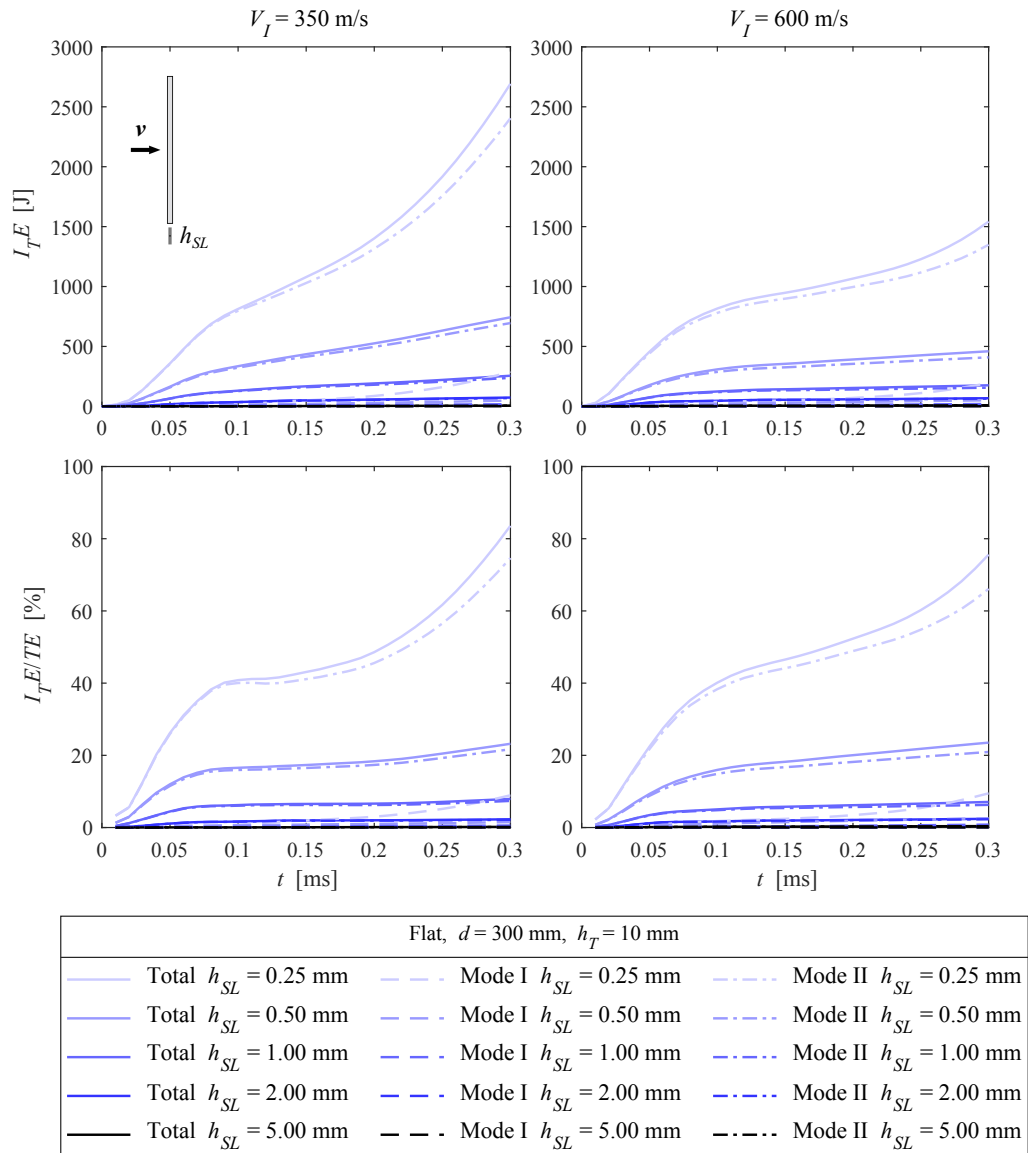


Figure 3.42: Energy dissipated at interfaces and energy dissipated at interfaces as a percentage of total energy dissipated by laminate for a range of sub-laminate thicknesses, at $V_I = 350$ m/s and $V_I = 600$ m/s.

Although the furthest deviation of the Lambert-Jonas V_{50} approximate belongs to the model with the smallest sub-laminate thickness, $h_{SL} = 0.25$ mm, it is in fact the model with the thickest sub-laminates, $h_{SL} = 5.00$ mm, that present the largest deviations in the residual velocity, V_R , at a given impact velocity. This is particularly noticeable at the lower range of velocities tested here. Nevertheless, these deviations are only marginal, which was not expected, given the large variation in mesh size. It is possible that more variation exists at lower impact velocities, close to the ballistic limits.

It is clear that the V_{50} parameter is not particularly sensitive to variations in the sub-

laminate thickness at a given plate thickness. Nevertheless, the plots in Fig. 3.42 reveal that the total level of energy dissipated at the interfaces is dependent on sub-laminate thickness. This effect is anticipated due to the change in the number of interfaces that accompanies the change in sub-laminate thickness at a constant total thickness. It was assumed that scaling the initial stiffness of the interface [49] is sufficient to maintain the response of the interface over a variation of sub-laminate thicknesses. However, the energy dissipation results in Fig. 3.42 indicate otherwise, especially in the most extreme cases of thickness change, irrespective of impact velocity. While increasing the number of interfaces from the baseline model yields a drastic increase in energy dissipation, reducing the number of interfaces results in a significant loss in capturing the same levels of energy dissipation.

To address this variation, the mode I and mode II critical strain energy release rate values at the interface were investigated, to determine whether the scaling of these parameters would yield more comparable levels of energy dissipation at the interfaces of laminates with varying interface numbers. To this end, the mean interface energy level, normalised against the baseline model of $h_{SL} = 1.00$ mm, is first plotted in Fig. 3.43 for the different h_{SL} values considered here. It can be seen that mode I, mode II and the total energy values follow the same pattern. Due to the high convergence of the smaller values of h_{SL} from the data mean presented in Fig. 3.44(a), these were not considered in the following calculations to determine G_C as a function of sub-laminate thickness. The spread of the data in the model with the thinnest sub-laminates was attributed to instabilities in the simulation as a result of the reduced thickness, as demonstrated in Fig. 3.44(b).

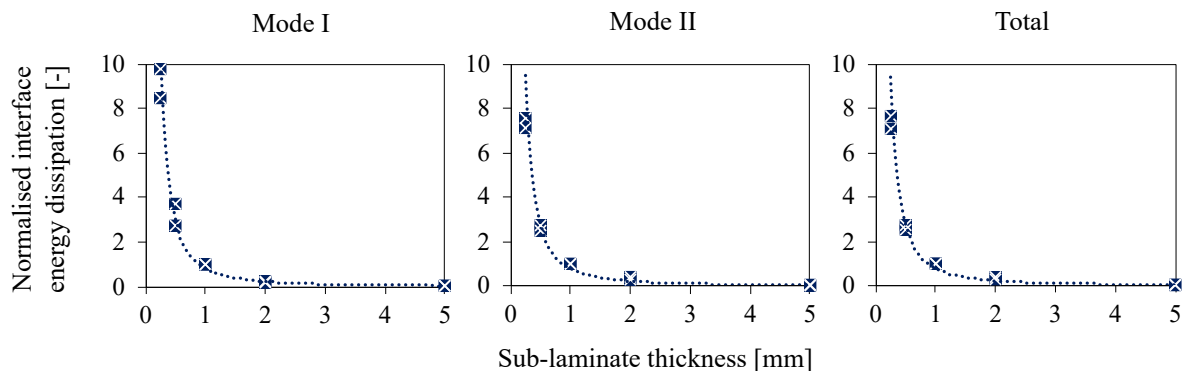
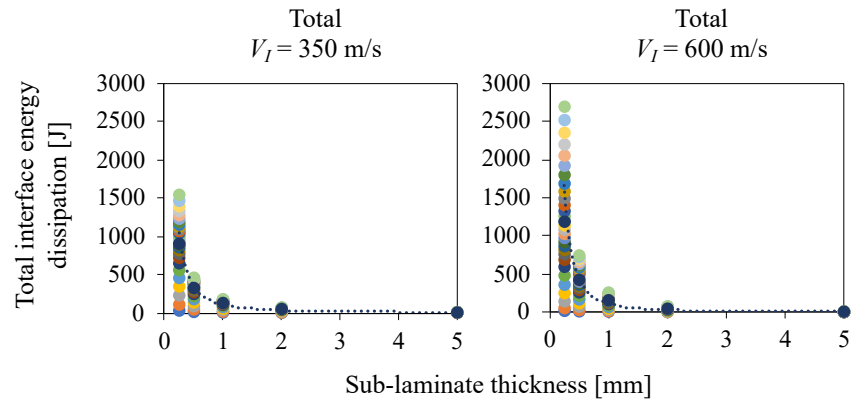
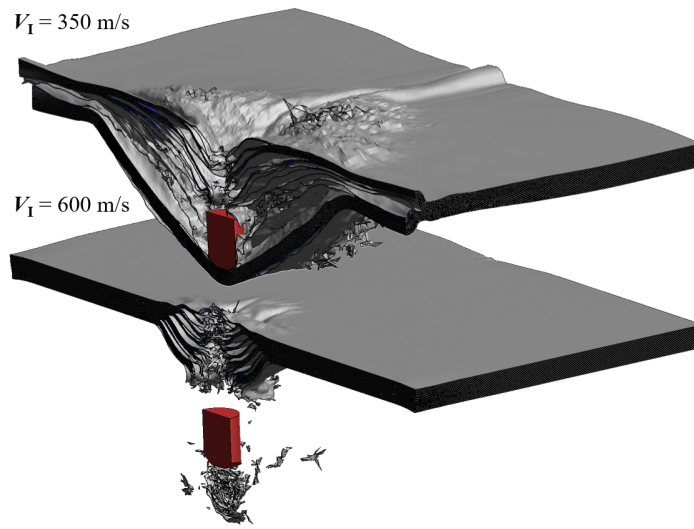


Figure 3.43: Average value of normalised mode I (LHS), mode II (centre), and total (RHS) energy dissipated over time, for $V_I = 350$ m/s and $V_I = 600$ m/s.



(a)



(b)

Figure 3.44: Deviations in mean energy values: (a) the largest deviations shown to exist at the smallest sub-laminate thickness, $h_{SL} = 0.25$ mm, corresponding to (b) element instabilities under impact loading.

Regression analysis of mode I and mode II critical fracture energy terms as a function of h_{SL} was used to generate the following relationship,

$$G_C = \frac{1}{h_{SL}^a}, \quad (3.5)$$

with a being a constant where $a_I = 1.60$ and $a_{II} = 1.44$, for mode I and mode II respectively, giving a ratio of 0.9 between the shear and normal mode constants. The goodness of fit, R^2 , for this regression model stands at 0.988 and 0.998 for the mode I and mode II terms, respectively. Since R^2 represents the amount of variation in the G_C terms, explained by the h_{SL} in these regression models, the model encompasses almost all the variability for these two cases.

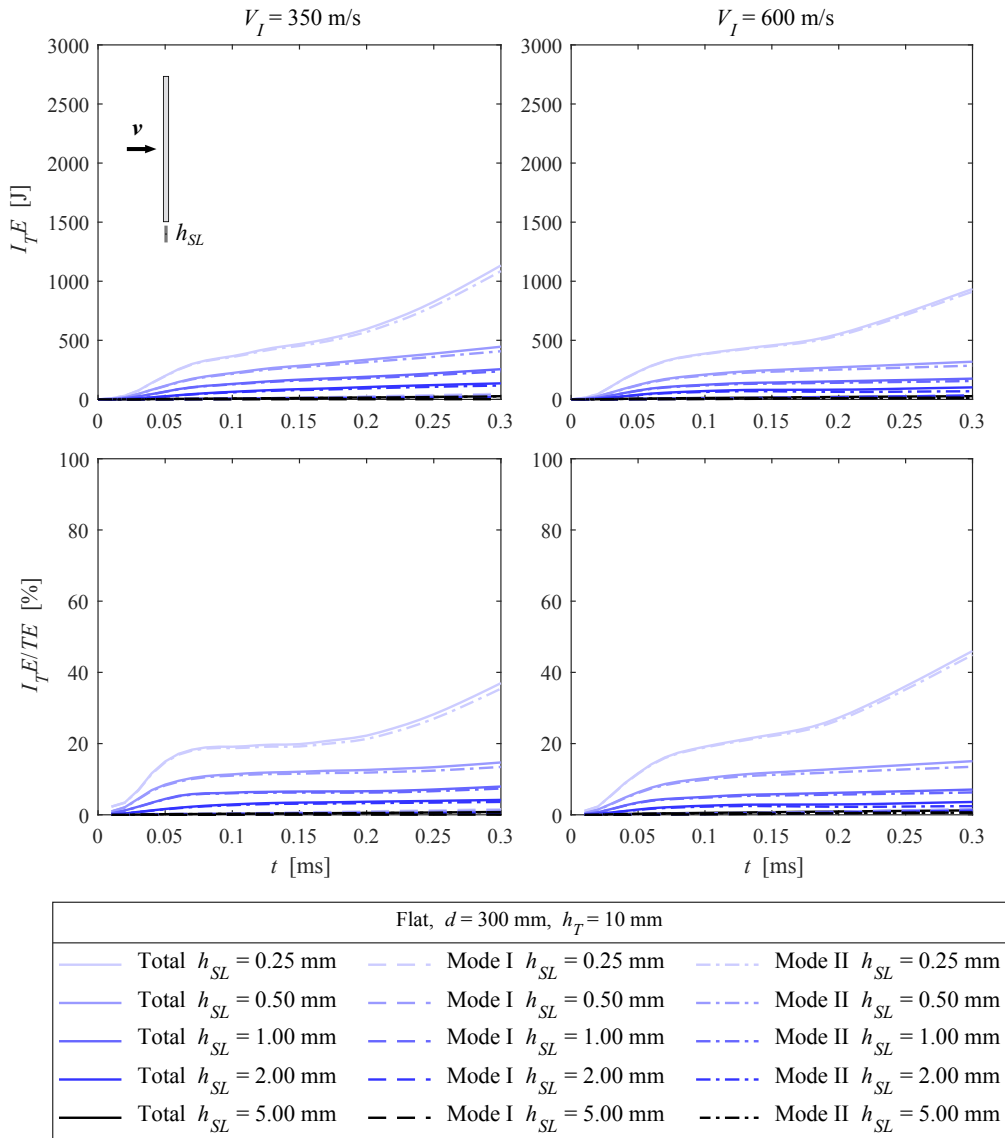


Figure 3.45: Energy dissipated at interfaces and energy dissipated at interfaces as a percentage of total energy dissipated by laminate for a range of sub-laminate thicknesses, using scaled values of G_C , at $V_I = 350$ m/s and $V_I = 600$ m/s.

As h_{SL} tends to 0, a scaled interface stiffness, K , tends to infinity, while a scaled G_C tends to 0. Both represent non-physical behaviour and are only used as tools in numerical modelling. In addition, note that K was scaled, according to Eq. (2.8), based on the quasi-static short-beam shear simulations performed by Hazzard *et al.* [49].

In the pursuit of achieving uniform levels of energy dissipation at the interfaces of plates with a varying number of interfaces, the models were rerun with the appropriately scaled values of G_C^* , where

$$G_C^* = G_C h_{SL}^a . \quad (3.6)$$

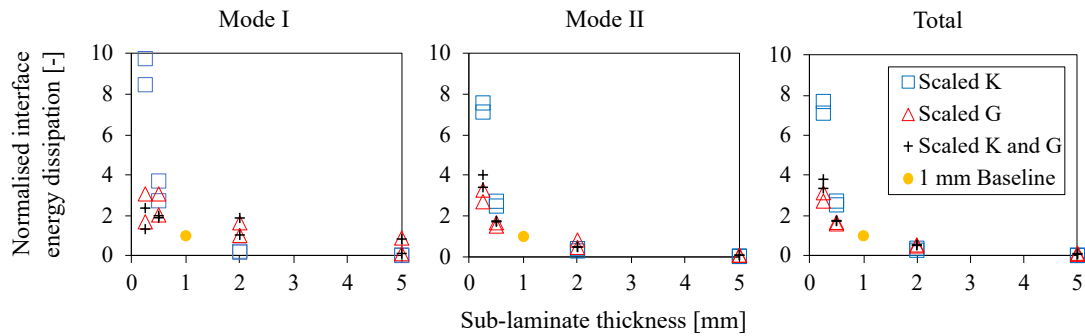


Figure 3.46: A comparison of mode I (LHS), mode II (centre) and total (RHS) normalised interface energy dissipation between models with and without scaled values of K and G_C .

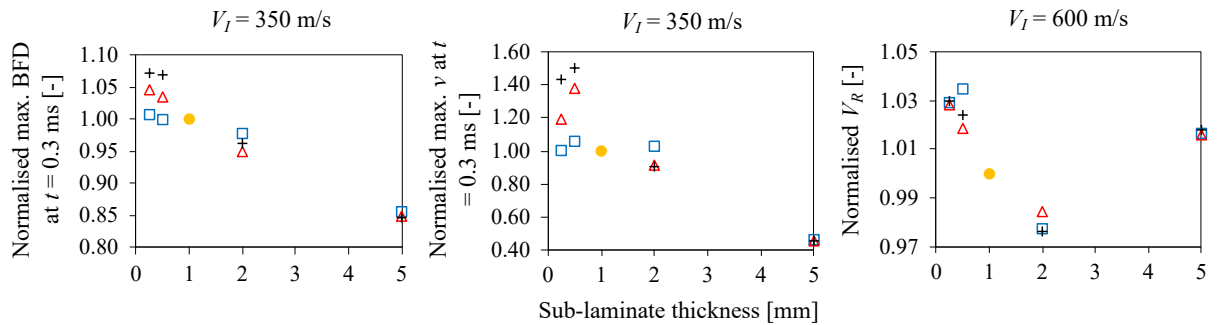


Figure 3.47: A comparison of maximum BFD at $t = 0.3$ ms for $V_I = 350$ m/s (RHS), projectile velocity v at $t = 0.3$ ms for $V_I = 350$ m/s (centre), and V_R for $V_I = 600$ m/s (RHS), between models with and without scaled values of K and G_C . All values are normalised with data from the baseline model represented by the yellow dot.

The interface energy for the scaled critical energy release rate models in Fig. 3.45, showing signs of convergence of the data from the models possessing a range of sub-laminate thickness values towards $h_{SL} = 1$ mm, *i.e.* the baseline thickness. The average disparity of each curve is quantified and normalised with results of the $h_{SL} = 1$ mm model in Fig. 3.46. The data points for the different values of h_{SL} are compared for when K , G_C , and both terms are scaled. For all modes of fracture, the largest improvements achieved in converging the level of dissipated energy towards the baseline model are observed in the cases with the thinnest sub-laminates, and therefore the highest number of interfaces.

While improvements were seen in energy levels, displacement- and velocity-based impact performance parameters analysed for an arrest case at $V_I = 350$ m/s and a perforation case at $V_I = 600$ m/s have been adversely affected by the sub-laminate thickness-based scaling of G_C , as demonstrated in Fig. 3.47. Nevertheless, the differences in the back face deflection and projectile velocity between various sub-laminate thicknesses and the 1 mm baseline remain extremely marginal relative to the data points from models with unscaled values of G_C . Since each sub-laminate had to remain a single element thick, the element aspect ratio in the impact zone

was no longer maintained at unity, as the thickness of the cubic elements was changed in line with the increase or decrease in h_{SL} . As the model was previously shown to be mesh-sensitive, it is possible that the remaining discrepancy in the amount of interface energy dissipation, back face deflection and projectile velocity, can be attributed to skewed element geometry, which can be investigated through the re-meshing of the models to maintain the same aspect ratio in the impact zone as exists in the baseline model.

3.6.4 Rate effects

Rate-dependent material property formulations are typically implemented for continuum elements to capture strain-rate effects on the deformation of laminates under transient impact loads. Strain rate-dependence of strength, axial moduli, shear moduli, and transverse moduli are already incorporated into the non-linear stress-strain response of MAT162 [85], via the coefficients $C_{rate 1}$, $C_{rate 2}$, $C_{rate 3}$, and $C_{rate 4}$, respectively, in accordance to a logarithmic rate-dependent function,

$$X_R = X_0 \left[1 + C_{rate} \ln \left(\frac{\dot{\varepsilon}}{\dot{\varepsilon}_0} \right) \right], \quad (3.7)$$

where X_R is the rate-adjusted material property, X_0 is the quasi-static value of the property, $\dot{\varepsilon}$ is the average strain-rate of interest, while $\dot{\varepsilon}_0$ is the reference unit strain-rate. For the models used in this work, $\dot{\varepsilon}_0 = 1$ ms. The MAT162 formulation does not, however, account for the rate-dependence of through-thickness tensile strength S_{cT} , or for shear strengths S_{ab} , S_{bc} , and S_{ca} [96]. Likewise, rate-dependence is not considered in the cohesive element formulation representing the sub-laminate interface. From preliminary studies of the baseline model for an arrest case at $V_I = 350$ m/s, the velocity of separation at the interface of an UHMWPE laminate under ballistic impact loading can, for the first time, be visualised in Fig. 3.48, as facilitated by the implementation of an element-based cohesive zone. These fringe plots display the variation in velocity, in other words the displacement rate, that exists in the of opening (mode I) and sliding (mode II) modes of separation between neighbouring sub-laminates, represented by all the interfaces modelled in the system, viewed from the front (LHS) and rear (RHS) faces.

Naturally, similarities can be drawn between the regions exhibiting the highest rates of separation, and those where the largest extent of energy dissipation occurs, see Fig. 3.22 and Fig. 3.24. From Fig. 3.48 it can be seen that at 0.2 ms following impact, mode II separation at velocities ranging from 10 m/s to 50 m/s dominates the regions directly below the path of the projectile, extending to the laminate edges along the primary fibres, in addition to the zone enclosed

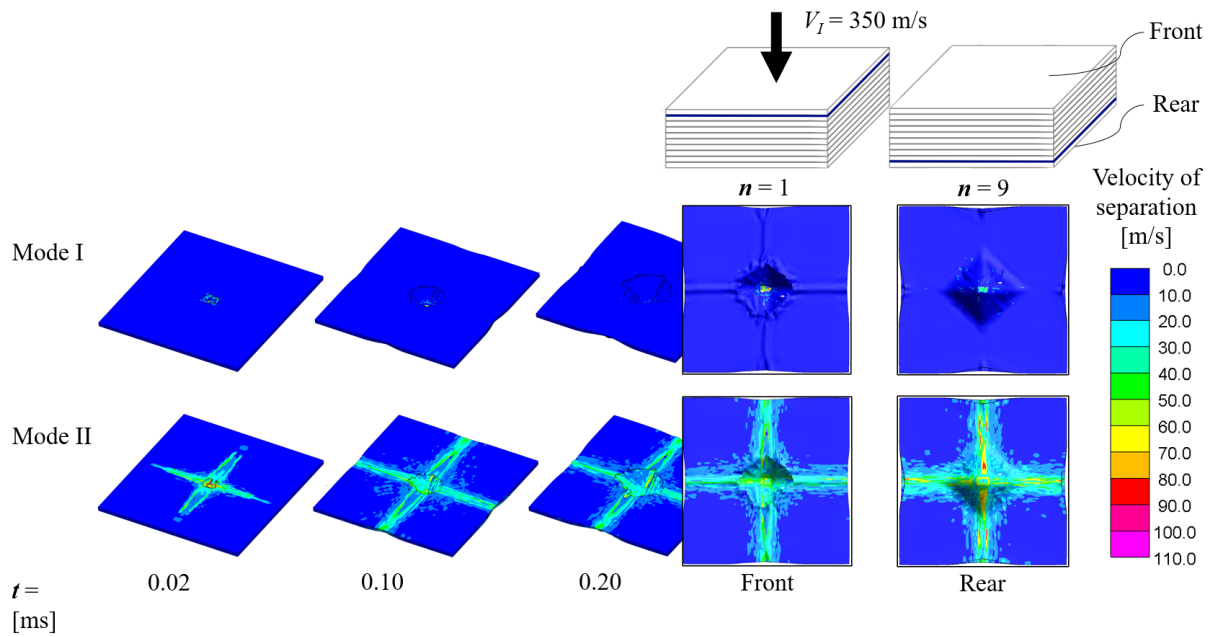


Figure 3.48: Fringe plots of the velocity of separation at the inter-laminar interfaces over the duration of impact at $V_I = 350$ m/s, and as viewed from the front and the rear at $t = 0.2$ ms.

by the shear hinge of the back face bulge. In line with the higher energy dissipation levels at the interface closest to the back of the laminate, separation velocities in some small primary regions towards the back also reach values of 60 m/s to 110 m/s. This variation in velocity rate across the surface of the interfaces highlights the need for implementing rate-dependence at the interface, due to the inherently rate-dependent nature of polymers, such as polyurethane, which typically comprise the matrix in UHMWPE fibre composites like Dyneema[®] HB26 [50]. As explained in Section 3.1, the behaviour of the interface is primarily governed by the properties of the matrix.

Mechanical properties of amorphous polymers that have been shown to be affected by the strain-rate at which they are loaded include strength σ^{\max} , elastic stiffness E , and fracture toughness G_C [97]. The contribution of each parameter to the traction-separation algorithm of the cohesive zone is illustrated in Fig. 3.49. The rate-dependent behaviour of the two modes of σ^{\max} can be used as the peak traction values, while the G_C rate-dependent behaviour can be used for the critical strain energy release rate. Similarly, the rate-dependent properties of E_I and E_{II} , can be used to inform on the cohesive stiffness terms, K_I and K_{II} .

Strength, stiffness, and fracture toughness of these material systems have been shown to be sensitive to changes in loading strain-rate [50, 98, 99]. Alterations of these properties in turn directly influences the back face deflection and V_{50} approximations, as demonstrated for

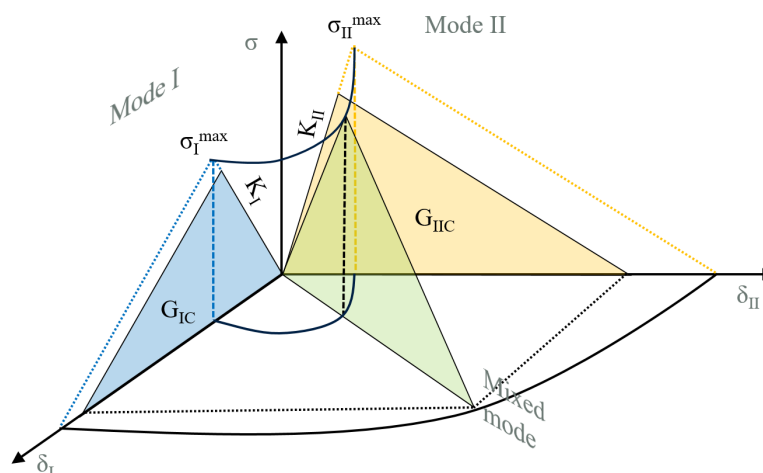


Figure 3.49: Parameters for which strain-rate dependence can be implemented, displayed on the mixed-mode bilinear traction-separation law used in the interface elements.

example, by the parametric studies of the maximum cohesive traction value in Section 3.5.2. On the bi-linear traction-separation curve displayed in Fig. 3.49, increasing the peak traction alters the shape of the cohesive curve, reducing the failure strain to maintain the mode I and mode II values of K and G_C .

In the current study, mesh sensitivity was reported to have more significant effects than marginal changes to interface parameters resembling the effects of rate, thereby rendering the implementation of rate-dependence at the sub-laminate interface futile without increasing the fidelity of the model, in combination with considering shock effects by virtue of an equation of state. A method for incorporating strain-rate effects at the interface in future studies of UHMWPE composite materials is outlined in Appendix A.

3.7 Summary of key findings

A finite element model was developed, to predict energy absorption at the interfaces of flat UHMWPE composite laminates, under varying rates of impact. Cohesive elements were successfully employed to model the behaviour of interface regions between sub-laminates at low strain rates. Upon validation, the model was extended to ballistic impact rates, to facilitate a better understanding of mode I and mode II delamination, both locally, across a single interface, as well as globally, through the thickness of a laminate. Parametric studies were also performed to analyse the sensitivity of the energy dissipated at the interface to several physical and modelling variables.

Regarding energy dissipation at the interface, it was shown that in the earlier stages of impact, over 90% of deformations occur in fracture mode II, as seen by the dominant contribution of energy dissipated through mode II delamination to the mixed-mode total. Energy is dissipated at the same rate in partial- and full- perforation cases, until the deformation mode switches from localised failure to distal membrane bulging or until full perforation. Beyond this stage, in both cases the panel continues to dissipate energy at the interfaces, although at a much higher rate when not fully perforated, since the un-perforated layers continue to deform through in-plane shear via bulging. In terms of contribution to overall energy absorption, the two cases of partial- and full- perforation yield comparable results, both dominated by mode II deformation.

The role of the interface grows over time, until the kinetic energy of the projectile is fully absorbed or the interfaces have failed completely, causing the sub-laminates to become completely detached. This is particularly significant when $V_I < V_{50}$, as the ability of the laminate to dissipate energy following the arrival of the transverse relief wave at the front face of the projectile will determine the extent of trauma caused to the wearer in body armour applications. At $V_I = 600$ m/s, the contribution of mode I energy dissipation to the mixed-mode total is higher than at $V_I = 350$ m/s, suggesting that mode-mixity is influenced by V_I . The contribution of individual interfaces through the thickness of the laminate was examined, and the following observations were made. In both fracture modes, V_I determines the proportion of energy dissipated through delamination at each interface relative to the other interfaces. Naturally, the behaviour of the interfaces mimics the deformation of neighbouring sub-laminate elements, thus leading to a dependency of energy dissipation at individual interfaces on V_I . For $V_I < V_{50}$, the interface at which the penetration mode transitions from local failure to membrane bulging accounts for four times as much mode II energy dissipation than almost all the other interfaces at the point when the mode switches, closely followed by the interface directly below the sub-laminate layer that is not perforated. The same interface accounts for the smallest contribution to mode I dissipation, likely due to extensive delamination damage in mode II at the periphery of the projectile body.

For $V_I > V_{50}$, the interfaces with the largest contribution to mode II energy dissipation are the middle interfaces, where interaction with the shock wave occurs. Therefore, irrespective of the impact velocity or whether or not the target is fully perforated, considering the out-of-plane direction, it is the middle interfaces that are responsible for the bulk of mode II and therefore

total energy dissipation at the interfaces, albeit through different deformation mechanisms. This was confirmed by fringe plots of the separation energy across the surface of each interface. Considering the in-plane distribution of energy dissipation, the majority of the dissipation in mode II and hence mixed-mode delamination occurs in regions adjacent to primary fibres, with some transfer to secondary fibre regions where the peak energy dissipation takes place in the secondary regions enclosed by the shear hinge.

Parametric studies have revealed that for velocities below the V_{50} of a target, $I_T E$ increases with V_I , with larger increases seen for V_I values approaching the V_{50} . However, the trend reverses beyond the V_{50} , where an increase in the strike velocity leads to a reduction in the level of energy dissipated. The reduction in the energy levels converge at higher values of V_I , reflecting the shift in failure modes and rate of energy dissipation of the laminate as a whole. The contribution of the interface as a percentage of total energy dissipation is relatively insensitive to V_I values below the ballistic limit, remaining almost constant. By contrast, for impact velocities above the ballistic limit, an increase yields a reduction in the level of $I_T E/TE$. Targets with larger in-plane dimensions demonstrated higher levels of $I_T E/TE$, as a result of the increased interface area. The increase was, however, less significant at the higher velocity and even less so with increasing plate size, since larger plate dimensions lead to more energy being absorbed via other means. The value of $I_T E/TE$ is not as sensitive to laminate thickness as it is to other parameters, particularly at the lower impact velocity, unless considering extreme changes such as doubling or halving of the baseline laminate thickness of 10 mm. The extensive differences in the extreme cases are to some degree down to modelling deficiencies, but also highlight the differences in the failure mechanisms of laminates of varying thickness. To summarise, the contribution of energy absorbed through delamination in a laminate of Dyneema[®] can be predicted with an element-based cohesive approach in finite element analyses.

Chapter 4

Effect of single curvature on impact performance

4.1 Introduction

In this chapter, the effect of curvature in UHMWPE composite panels is characterised, as it has not been thoroughly investigated before under ballistic impact conditions. The degree of curvature is of particular interest as it corresponds to the location of impact on a hemispherical surface. Thus, understanding its effect on the impact performance of the material can be informative for design and development for example, by highlighting regions that need to be reinforced with filler plies. To quantify this effect, two well-established measures of ballistic impact performance are studied; the ballistic limit velocity, V_{50} , to identify the velocity at which the certainty of full perforation occurring is at 50%, and the maximum back face deflection (BFD), to determine the extent of trauma that is expected from the deformation of the material preceding full perforation.

In the context of helmet applications, the direction of impact is naturally convex, as the target is subject to threats on the external surface of the doubly curved geometry. However, to expand on our fundamental understanding of geometrical effects and for applications of cavity protection, in this study two directions of impact are considered, convex and concave, referring to impact on the external and internal surfaces of the curved plates, respectively. In addition, the application of curved laminate is not limited to helmets, as curved body armour plates are being increasingly employed to optimise fit and enhance comfortability for the wearer [42].

The direction of impact is expected to be a determining factor, as it specifies which face

of the curved laminate, front or rear, is under tension and which is under compression. This is crucial as impact introduces a pressure wave, a form of compressive load, so that when the material bulges outwards on the back face, if the bulge is already under compressive strain it will be more compliant to deforming further. However, if the back face is under tension prior to impact, then as the material deforms, it moves from a state of tension to flat and not stressed to a compressive stress state.

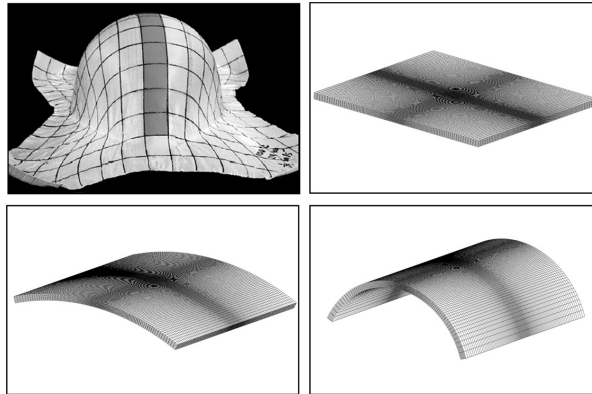


Figure 4.1: Deep-drawn panel of Dyneema[®] [17], together with finite element meshes of a flat panel, a panel with a 15 in radius of curvature, and a panel with a 5 in radius of curvature.

The aim of the current work is to analyse this behaviour numerically and experimentally, in order to understand the effect of curvature on the performance of an UHMWPE composite system. Impact testing data is used to verify existing numerical models demonstrated in Fig. 4.1 that are subsequently used to conduct parametric studies on the effects of several physical and modelling features on the penetration-resistance and deformation of the panels. The parameters of interest include the degree of curvature determined by the radius of curvature r , impact direction, target dimensions, threat shape and size, together with modelling inputs for simulating the deformation of the interface. The effects of these parameters on laminate behaviour under impact are studied through the comparison of observations in bulge shape, delamination and the path of the projectile through the thickness of the laminate. The effects are quantified by measurements of the maximum BFD and the depth of penetration (DoP) in stop-cases, estimations of the V_{50} in perforation cases, and the contribution of the interface to the overall kinetic energy dissipation of the threat, $I_T E / TE$. Note that throughout the chapter, the terms plate, panel, laminate and shell are used interchangeably to refer to the target, which, for structural analysis purposes acts like a solid element, capable of carrying biaxial membrane forces in the normal direction, shear forces in the in-plane and transverse directions, together with bending and twisting moments. Likewise, the terms dome and hemisphere will be used to

refer to a doubly-curved laminate configuration.

4.2 Geometric considerations

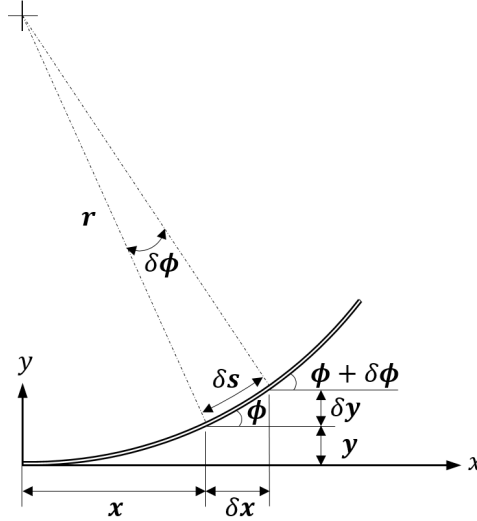


Figure 4.2: Mathematically describing a cantilever beam bending deflection.

In order to understand the geometrical implications of adding single curvature to a structure through bending deformation, first consider the simple two-dimensional case of a cantilever beam subjected to a point load. Assuming the deflection is relatively small and small angle approximations can be used, where $\tan(\phi) \approx \phi$, the deformation can be mathematically described as seen in Fig. 4.2, where r is the radius of curvature, ϕ is the slope of the curve at point x and s is the arc length. Using the definitions in Eqs. (4.1) and (4.2), and that the curvature, κ , is the reciprocal of r , it is shown in Eq. (4.3) that κ is the second derivative of the y position with respect to the x location,

$$\delta\phi = \frac{\delta s}{r} \quad (4.1)$$

$$\lim_{\delta \rightarrow d} \phi = \frac{dy}{dx} \quad (4.2)$$

$$\lim_{\delta \rightarrow d} \kappa = \frac{d\phi}{dx} = \frac{d^2y}{dx^2} \quad (4.3)$$

Expanding this further, the curvature on the surface of a doubly curved shell can be defined by surface curves, the direction of which at a given point is defined by the tangent to the surface at that point. The curvature in two orthogonal directions at that point can then be used to calculate the curvature in all arbitrary directions. For the sake of simplicity in quantifying the variation in curvature across the surface of a hemispherical shell, the doubly curved geometry

will be simplified to a singularly curved section. The approach chosen here is just a first step into the direction of considering doubly curved laminates, as a deeper analysis was beyond the scope of this thesis. On account of this, certain geometrical effects are neglected. For example, a singly curved panel represents an open cylinder, for which the Gaussian curvature is zero, in contrast to a doubly curved surface that has a Gaussian curvature greater than zero. This means that instability and buckling are more significant for a hemispherical configuration, due to high buckling resistance.

In reality however, helmet configurations formed from armour-grade composite systems, such as UHMWPE fibre composites, are not perfectly hemispherical due to fitting constraints. Thus, the doubly-curved structure does not possess a constant geometric radius across its entire surface. To simplify this, consider a two-dimensional plane with only a single direction of curvature on the structure, as presented in Fig. 4.3. It can be seen that towards the sides of the dome-shaped configuration, r tends to infinity, equal to the maximum radius of curvature and the minimum degree of curvature. Approaching the crown, the value of r tends to 0, the lowest radius of curvature and the highest degree of curvature. Meanwhile, the tangential angle, ϕ , moves from a peak value at the highest curvature towards 0 when the degree of curvature reduces down the side of the hemispherical shell.

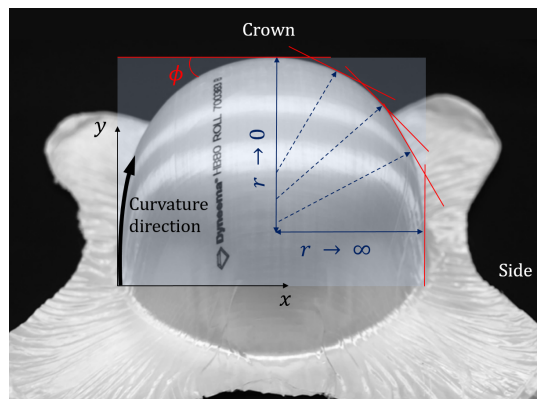


Figure 4.3: Variation of curvature around one curved dimension of UHMWPE composite preform drawn to a doubly-curved configuration, adapted from [17].

To examine the internal stress state induced by the addition of curvature, first consider the case of a flat plate with isotropic, homogeneous properties, together with a linear elastic response. When the flat plate is deformed to induce curvature in a single direction, this results in static loading of the structure in tension on the outside curvature and compression on the inside

curvature, by internally balancing the external bending moments. These bending moments induce internal axial stresses, making the plate pre-stressed prior to any impact event taking place. When a composite laminate is subjected to bending moments, a similar state ensues, with the addition of radial stresses that arise in the inter-laminar regions once curvature has been achieved. This occurs particularly at the interface between the tensile and compressive stress states, which is assumed to coincide with the through-thickness centre-line of the laminate. The exact value of the radial stress, σ_r , depends on a multitude of factors including stacking sequence, the radius of curvature at that point in time, and the loading conditions. It can be simplified and approximated using

$$\sigma_r = \frac{3M}{2rdh_t}, \quad (4.4)$$

where M is the applied bending moment, while d and h_t represent the plate width and height, respectively.

However, it must be noted that the drape-forming of pre-impregnated plies into a curved geometry takes place during the consolidation stage. Due to the presence of elevated temperatures during consolidation, the matrix is partially melted and therefore does not retain residual stresses upon cooling and re-solidification. The fibres are, however, a discontinuous medium and do not reach their melting point through this process. When pressed between curved male and female tooling, the fibres with layup angles that have a directional component aligned with the direction of curvature will become deformed. The half of the laminate on the external section of the curvature will undergo stretching, while the other half of the laminate close to the inner radius undergoes compression, to accommodate the change in the laminate geometry. The fibres that are fully- or even partially-aligned with direction of curvature are therefore pre-strained in tension or in compression, depending on their through-thickness location.

4.3 Methodology: Experimental testing

4.3.1 Manufacturing curved plates

To investigate the effect of curvature on the performance of UHMWPE fibre composites, three degrees of curvature were selected. These comprised panels with a radius of curvature of 20 in, 10 in and 5 in, to cover the range of curvatures that exist across the surface of a standard helmet-like geometry. It is imperative to consider multiple curvatures, covering a sufficiently large range of values [42] for a given configuration, given the parabolic nature of the effect

that curvature was shown to impose on ballistic performance indicators in previous studies [26, 41]. The degrees of curvature considered in this study are higher than what has typically been investigated in the past, due to the nature of the application for helmet components.

The panels, displayed in Fig. 4.4, were fabricated from Dyneema[®] HB26 preforms using curved moulds, as demonstrated by the schematic in Fig. 4.5, and were consolidated under heat and pressure following the recommended manufacturing cycle from DSM Dyneema. The flat, pressed plates measured $300\text{ mm} \times 300\text{ mm}$ with an average thickness of $\bar{h}_t = 6\text{ mm}$, formed from a stack of 20 HB26 cross-ply preforms of $[0/90/0/90]$ plies at an individual thickness of $67.5\text{ }\mu\text{m}$. The dimensions of the panels formed into curved geometries are illustrated in Fig. 4.6(b), and compared to flat reference plates that were manufactured of the same thickness and original in-plane dimensions, illustrated in Fig. 4.6(a), and pressed at the same temperature and pressure cycle. Note that dimension d_c is the in-plane length of the panel from one outer edge to the other, along the direction of curvature.

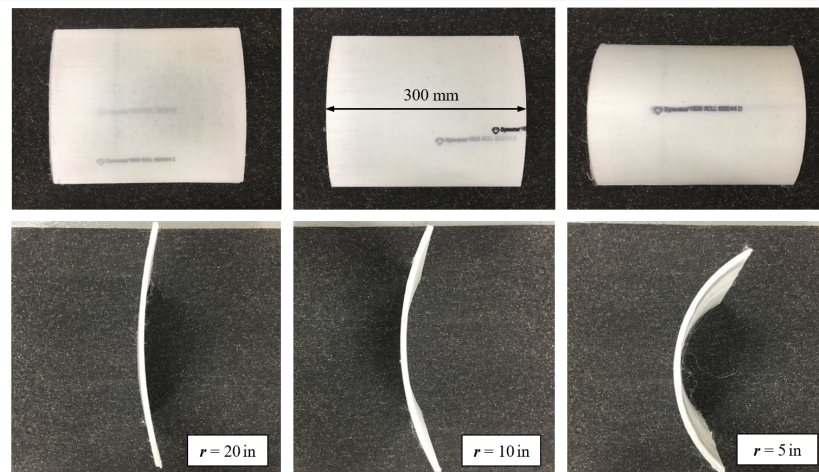


Figure 4.4: Specimens of varying degrees of curvature, viewed from above and the side.

For the panels with a radius of curvature $r = 5\text{ in}$, for example, a female mould with $r = 5.2\text{ in}$ and a male mould of radius $r = 5\text{ in}$ were fitted to a press. The female mould naturally has a larger radius of curvature, as this varies through the thickness of the laminate. The value of r therefore refers to the inner radius of curvature. In addition, a press pad was placed on top of the material during consolidation to even out the pressure across the surface of the laminate, due to the high bulk modulus of the material. The panels were then impact tested in a number of different ways. Some panels were tested in collaboration with and at the facilities of Imperial College London using a steel ball as the threat, while the remainder were tested with a fragment-simulating projectile (FSP) at the DSM Dyneema shooting range in the Netherlands.

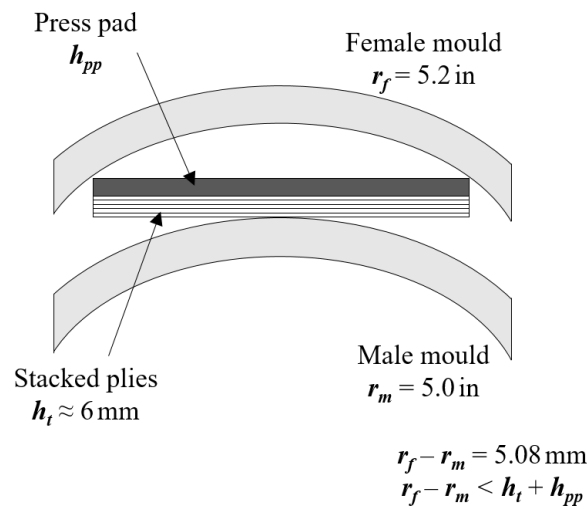


Figure 4.5: Schematic demonstrating discrepancy between the radius difference in the moulds and the desired laminate thickness, for an inner panel curvature radius of $r = 5$ in.

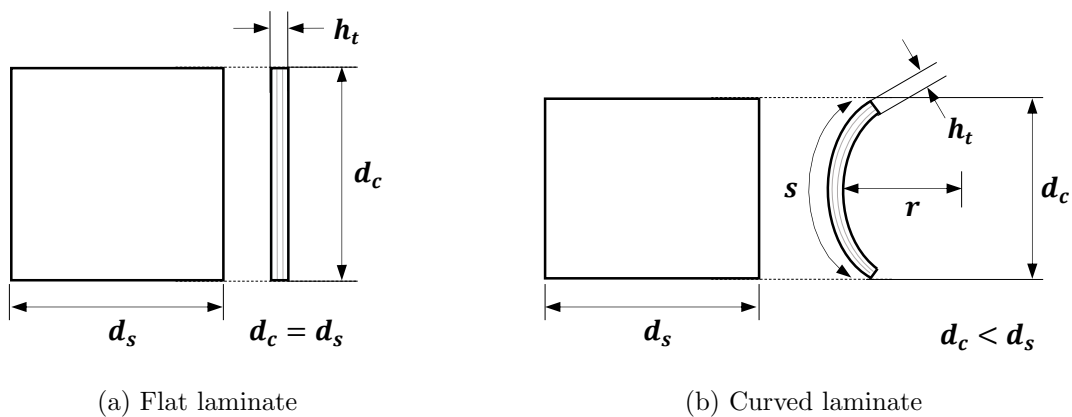


Figure 4.6: Specimen dimension parameters, viewed from above and the side.

4.3.2 Spherical threat

The specimens tested in collaboration with Imperial College London were subjected to impact by a spherical steel threat of diameter 10 mm, weighing approximately 4 g, and placed in a custom-made plastic sabot. The specimens were tested with two gas guns, providing a combined range of impact velocities spanning 270 m/s to 500 m/s. The deflection of the material under impact was initially recorded at three different regions, the front face, the rear face and the side of the laminate, using three Phantom high speed video cameras.

Subsequently, a pair of specimens from each curvature including the flat reference plates, were tested under equal conditions, with the strain distribution on the back face and out-of-plane displacement measured with a GOM Correlate two-camera digital image correlation (DIC)

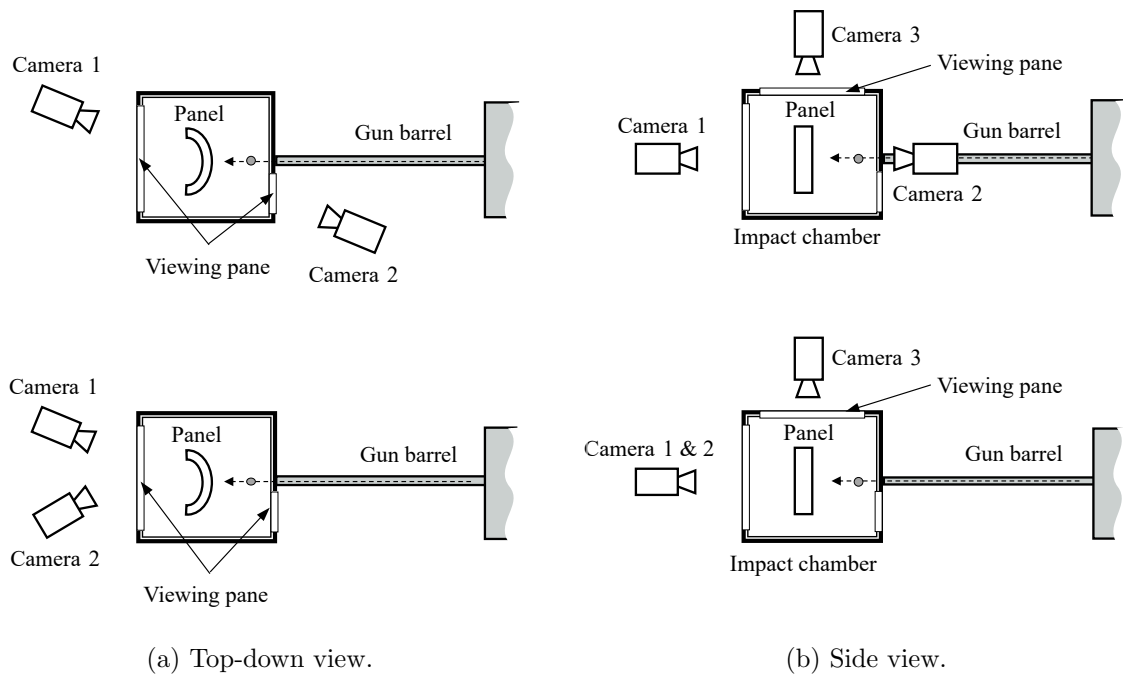


Figure 4.7: Impact test setup showing the initial (top) and subsequent (bottom) configurations, for a combination of DIC and high speed photography techniques, performed at Imperial College London.

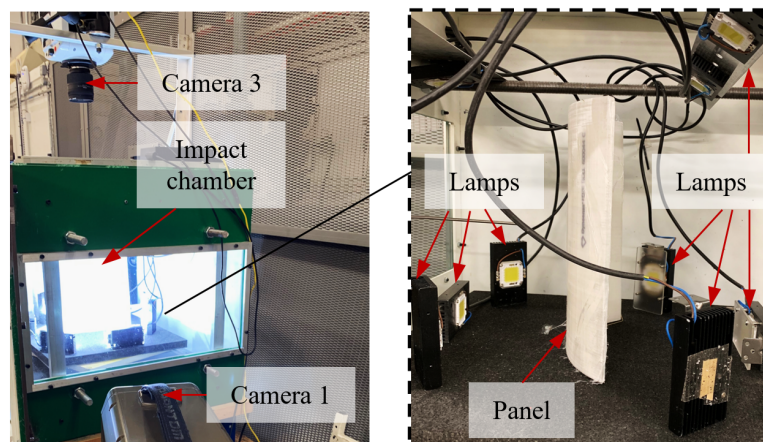


Figure 4.8: Panel and lamp arrangement inside the impact chamber (inset), shown in relation to the overall test setup.

system. The two setup configurations are illustrated in Fig. 4.7. In both cases the projectile velocity before and following impact were measured via high speed photographs captured by a camera facing the specimen side, placed above the test chamber.

For each radius of curvature, one plate was shot on the inside of the curvature, while the other was shot on the outside surface, with the direction of impact naturally making no

difference to the flat reference plates. For the DIC measurements, the regions of interest were marked on the rear face of each specimen, while a single camera recorded high speed footage of the impact event from the side of the panel to determine the velocity of impact V_I and the residual velocity, V_R in the event of projectile exit due to full perforation of the target.

The panels were placed on their sides in the shooting chamber, and were loosely secured to the floor of the chamber with tape, in order to delay the movement of the plate with the oncoming projectile for as long as possible. The chamber was lit up with six lamps to enable a clearer view of the deformation of the specimens, see Fig. 4.8. Since the perforation of laminates could not be achieved with the first gas gun, a second, more powerful gas gun was used. With the more powerful gas gun, it was possible to accelerate the projectile to higher velocities, in a barrel and chamber under vacuum, with high speed video cameras at the side of the plate used as a means of measuring the projectile velocity as before.

4.3.3 FSP threat

Ballistic impact testing using an FSP threat was performed at DSM Dyneema, with the testing arrangement visible in Fig. 4.10. A powder gun was used to shoot the curved panels using a 1.1 g fragment-simulating projectile with a 5.56 mm diameter. The targets were loosely attached to a support frame with strips of tape, adjusted with the aid of a spirit level to ensure an orthogonal impact angle (Fig. 4.10(a)). The support frame was hollow, with no backing plate supporting the projectile at the rear.

A pair of velocity screens installed between the gun barrel and the target were used to measure the initial velocity of the projectile. Assuming that the projectile velocity remains relatively constant until the point of contact, the initial velocity is deemed equal to the impact velocity. As the test is not carried out in a vacuum chamber however, realistically, the FSP will be subjected to aerodynamic drag effects to some extent. A second set of velocity screens measured the residual velocity of the projectile, if present, beyond the position of the target. It must be noted that the screens measure only the horizontal component of the resultant projectile velocity, in this case neglecting the effects of gravity and alteration of the projectile direction in three-dimensional space. While the effects of drag on obtaining an accurate velocity measurement will be consistent at specific velocity ranges across all trials, the effects of changing direction are not, due to variations in plate geometry, deformation and perforation mechanisms.

A laser pointer was used to aim at the front surface of the target. Since the actual location of impact was almost perfectly aligned with this in a large majority of all trials, the effects of

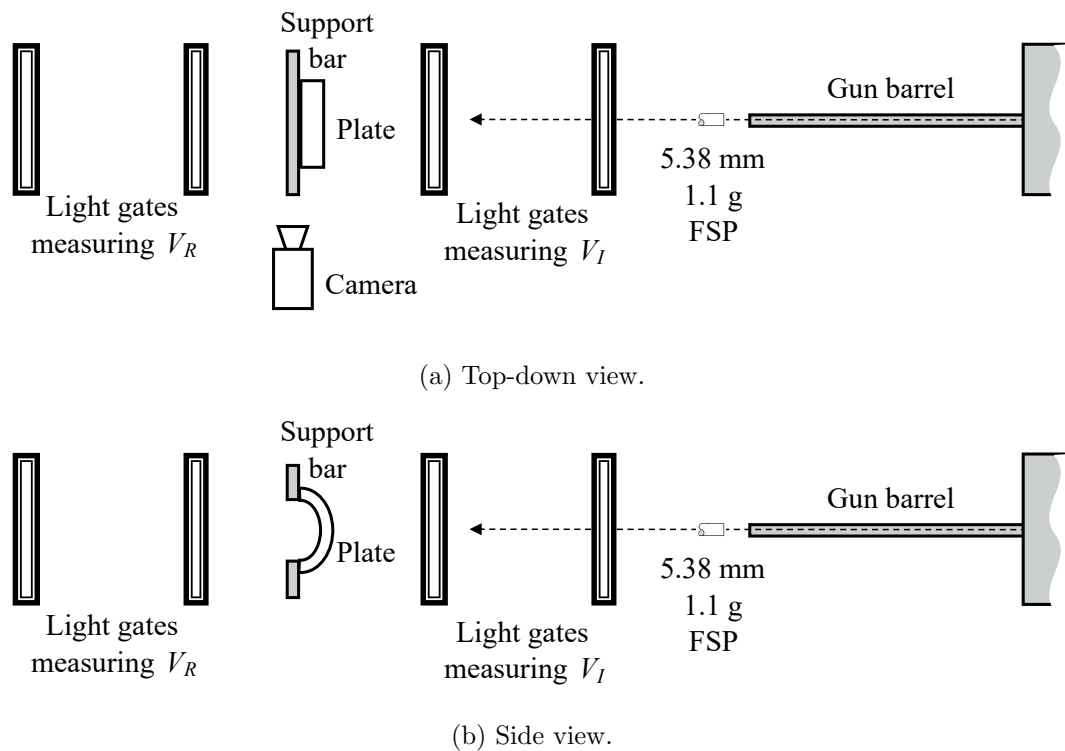


Figure 4.9: Impact test configuration for tests performed at DSM Dyneema.

drag and direction change were considered to be limited. However, to confirm this, a Photron high speed photography camera was installed to capture the impact event as viewed from the side, see Fig. 4.10(b). This helps to assess the deformation of panels over the duration of impact, as well as to obtain more accurate readings of the strike velocity directly before contact and the exit velocity directly following perforation of the laminate. The images also provide insight into the angle of impact, and whether the effect of an oblique impact also needs to be accounted for. The camera was operated at 4000 fps, with the stopping down technique employed to increase the depth of field by reducing the aperture diameter of the camera lens as much as the lighting conditions allowed for. This ensured that both the projectile and the area of impact on the target were in focus and appeared sharp in the recordings. It was noted that sharper images could have been achieved with additional lamps, to counter the restriction in the amount of light entering the lens, which accompanied the reduction in aperture.

To initiate impact, the projectile was placed inside a sabot, together with the desired amount of propellant. This amount determined the approximate launch velocity of the projectile from a smooth gun barrel. Naturally, this was not always precisely as expected, due to limitations in the assumptions that the barrel was perfectly smooth, the projectile experienced no air resistance, or that there were no changes in the travel direction. Each target plate was impacted

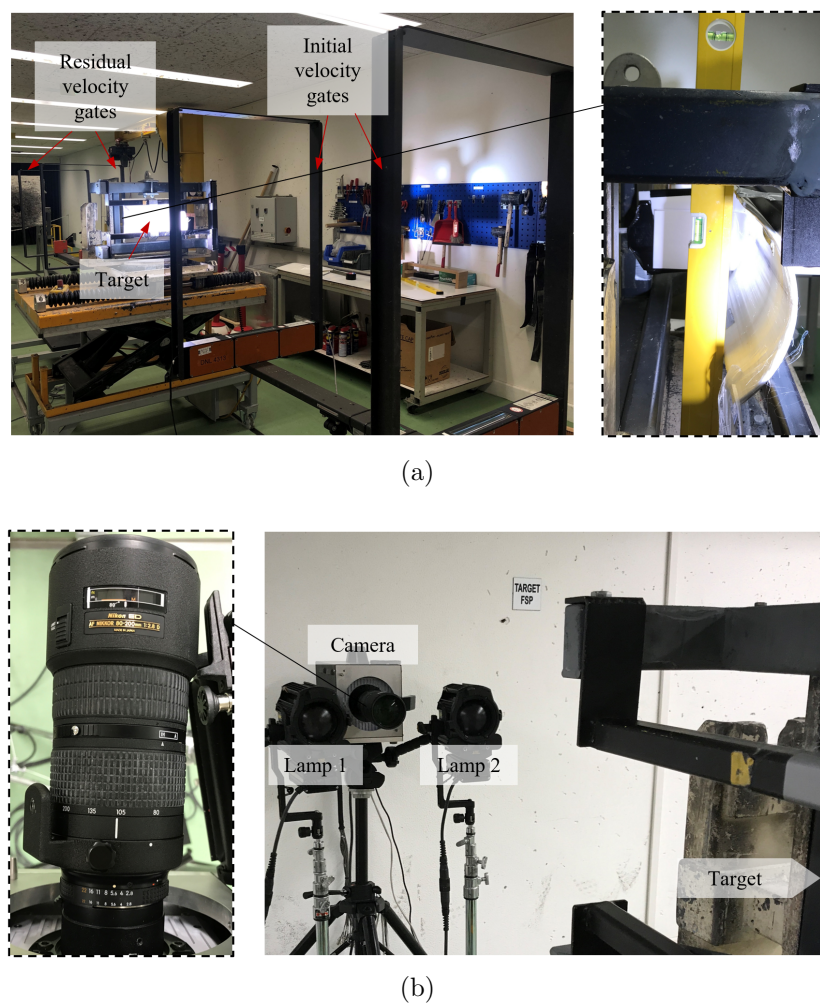


Figure 4.10: Test setup showing (a) velocity gates in relation to the target, and correcting target position with a spirit level to facilitate orthogonal impact (inset), (b) the high speed video camera and its lens configuration (inset).

three times, with the primary shots all taken on the outside surface of the curvature due to the relevance and applicability of this to curved armour plates and helmets. The secondary and tertiary shots were taken on two diagonal quadrants of the panels, ensuring that the primary fibres from the different shots, which take the bulk of the loading and damage such as internal delamination, did not overlap and interact significantly, while maintaining a close proximity between the impact location and the central in-plane axis of the plate. The impact velocity was gradually increased for each set of plates until sufficient velocity measurements had been taken to give an indication of the ballistic limit velocity, amounting to at least three cases with residual velocities, with one preferably lying very close to the predicted V_{50} . Subsequently, tested plates were dissected at the location of impact to facilitate measurement of the depth of penetration, defined here as the original plate thickness subtracted by the thickness of the rear

portion that was not penetrated by the projectile. In addition, the plate cross-section provided a more detailed view of impact-induced damage and failure within the laminates.

4.4 Results and discussion: Experimental testing

The results from the experimental impact testing of the curved laminates is presented and discussed in the following sections, for both types of projectile. Starting with the spherical threat, deflection- and velocity-based analyses of the tests are provided, followed by velocity and deflection studies for the FSP threat.

4.4.1 Spherical threat

4.4.1.1 Deflection analysis

Fig. 4.11 provides a comparison of the out-of-plane displacement, δ_z , on the rear faces of the curved specimens and that of a flat reference plate. The black dotted lines outline the general shape of the back face deflection observed in each specimen. All specimens display BFD profiles with a quadrilateral base, which arises from the anisotropic nature of the laminate response brought about by the cross-ply architecture, since the diagonals of the 4-sided bulges are aligned with the stiff fibre directions, as has been previously reported [50].

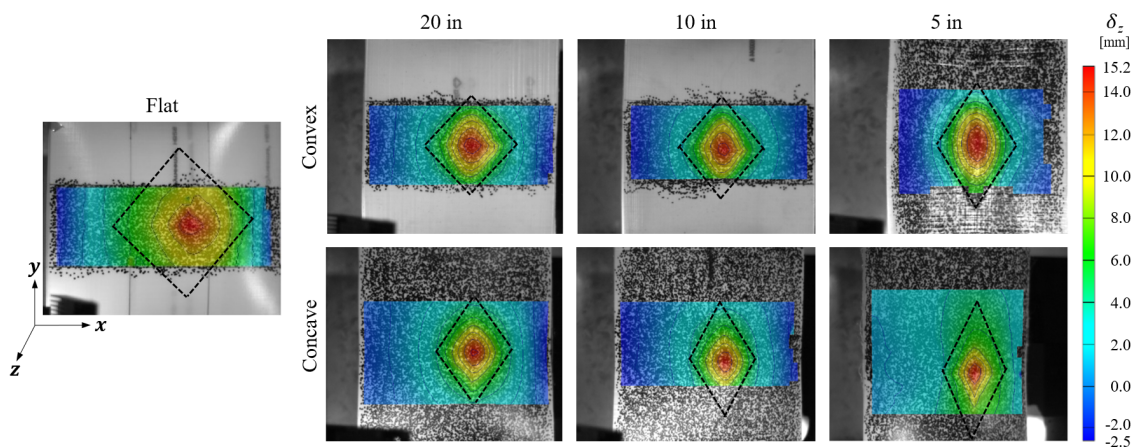


Figure 4.11: DIC strain measurements of out-of-plane displacement, δ_z , on the rear faces of flat and curved panels.

Under convex impact, the images are looking into the panel cavity. As the degree of curvature increases with a reduction of r , the pyramid-shaped back face bulge transforms from a rhombus in the flat laminate, into a rhomboid-shaped bulge in the curved panels. As a result,

the deformation is less spread out in the curved panels and more concentrated around the point of impact, with larger regions of peak displacement of around 15.2 mm present, compared to the flat plate. The regions exhibiting negative δ_z values depict the motion of the plate edges as the material is drawn inwards towards the path of the projectile. As a bulge forms in the positive z -direction, the curved extremities move in the opposite direction, before the projectile is arrested and the plate, in its entirety, is set into motion by the remainder of the incoming projectile's kinetic energy.

The BFD in the case of $r = 20$ in is largely reminiscent of the deformation of the flat plate. Differences between the various curvatures become apparent when observing the deformations for $r = 10$ in, and even more strikingly, on the rear of a panel with $r = 5$ in. The smaller the radius of curvature, the more pronounced these effects are. For example, the panel with $r = 5$ in shows the most skewed bulge deformation and the most elongated BFD peak, together with the most extensive out-of-plane displacement in the opposite direction to the projectile path of motion. The sharp changes in curvature in this panel inhibit the movement of the shear hinge towards the curved sides, thereby expanding the bulge towards the edges in the longitudinal in-plane direction, as displayed in Fig. 4.12. Deformation in the longitudinal direction is more favourable, due to an absence of geometrical resistance imposed by the presence of curvature, as illustrated by the post-impact laminate cross-sections along the d_s and d_c directions represented by the respective blue and red arrows in Fig. 4.12. This is later confirmed in post-impact visual inspections and bulge width measurements shown in Fig. 4.38, showing a larger expansion of the bulge along the flat dimension. Internal strain, ε_c , due to the deformation of the laminate into a curved geometry, exists along the curved dimension of the plate, d_c , acting in the out-of-plane direction when viewed from the cross-section along the flat dimension, d_s , in Fig. 4.12(b).

Considering concave impact scenarios, divergence away from the bulge shape of the flat plate is apparent for all three curvatures, forming even more skewed bulges with increasing degree of curvature. By contrast, the extent of negative out-of-plane displacement at the curved edges of the plate reduces with increasing degree of curvature in the concave cases, to the point of elimination when $r = 5$ in. This can be explained by considering the different stages of physical deformations undergone by the various plate configurations during impact, as visualised in Fig. 4.13. Simplified schematics of the convex impact show the reversal of plate curvature when the projectile moves through the panel, by inducing a flat region around the impact point in the second stage, before the curvature direction is fully reversed from the third stage

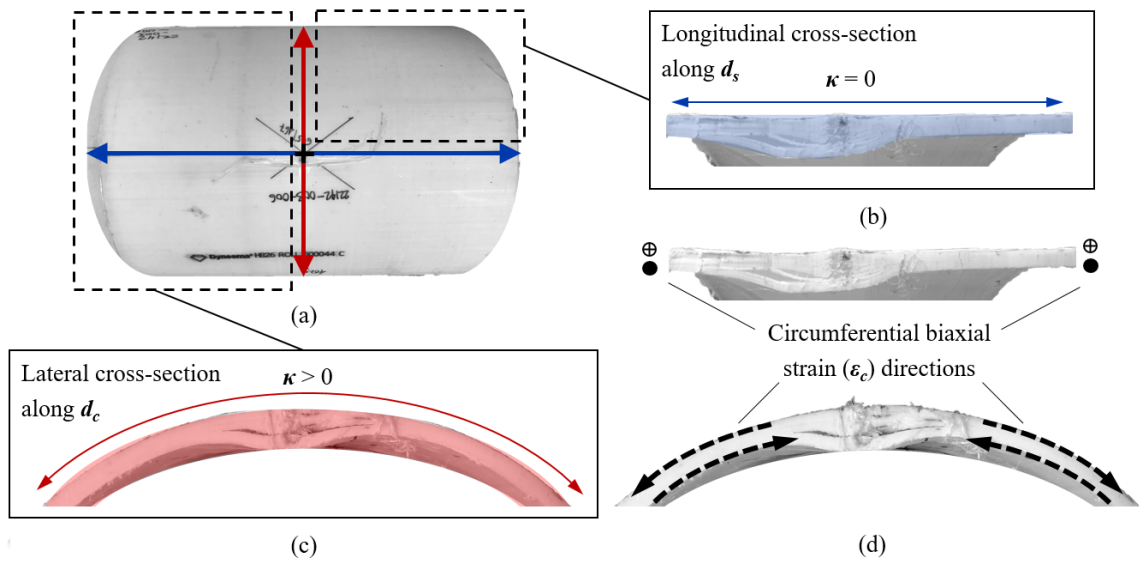


Figure 4.12: Curvature, κ , (a) along the two in-plane directions across the surface of a specimen, (b) along d_s , showing the longitudinal cross-section, (c) along d_c , showing half of the lateral cross-section, and (d) along both directions showing internal residual strain directions imposed by the curved geometry.

onwards, as the flattened plate deforms through in-plane shear and bulging. In comparison, under concave impact the initial state of the plate resembles the shape developed under convex impact between stage 3 and 4. Note that in the second stage of deformation under convex impact, although the laminate region in the vicinity of impact is flat at that particular point in time, the plate possesses excess fibre length along the curved dimension, relative to a fully flat laminate of comparable dimensions. Johnson and Holzapfel [36] noted how convex panels underwent much more extensive bending than concave panels, as a result of the release of the stored elastic strain energy in the convex face.

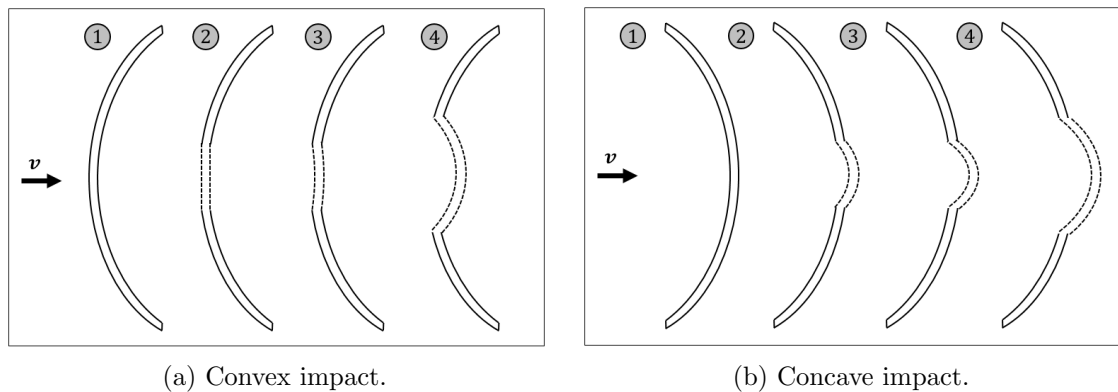


Figure 4.13: Comparing impact deformation stages of panels under the two different impact directions.

The high speed DIC snapshots in Fig. 4.11 also demonstrate how the edges of plates under concave impact move away from the direction of projectile motion during the pull-in activity in those regions that accompany in-plane membrane deformation of the plate. Under convex impact, the region enclosed by the shear hinge is pre-deformed curvature-wise in the opposite direction to subsequent bulging, first evolving into a flat entity, before springing into a cavity shape with the motion of the projectile through its thickness. In contrast, under concave impact, the plate is already pre-deformed in the direction of the bulge-formation, with little to no resistance to further deformation in this direction, resulting in the lack of reaction forces that in turn lead to the motion of the edges in the negative z -direction.

The emergence and retraction of the back face bulge captured by high speed photography over a time-frame of 0.02 ms to 1.30 ms is displayed in Fig. 4.14. The deflections of the panels with varying curvatures and directions of impact are compared. Note that due to difficulties in achieving consistent impact velocities, the comparison is made for tests at similar ($\pm 10\%$) impact velocities. Due to the variations in strike velocity, it is not possible to quantify the effect of curvature and impact direction to the highest degree of accuracy, as velocity must be a controlled variable, based on its influence on the behaviour of the laminate as reviewed in Chapter 3. It is possible, however, to discuss the effects of curvature and impact direction in broad terms. The deformations of a single flat plate are presented twice for ease of comparison in each of the two columns representing convex and concave impact. In some cases, a closer look is required to provide better understanding of the images, due to the reduction in contrast and visibility against the dark background as a result of the black speckle pattern that was applied on the rear surface for the purpose of DIC measurements.

At $V_1 = 300$ m/s, the projectile kinetic energy is not sufficient for complete perforation, resulting in rebound off the front surface of the flat panel, as seen in the majority of cases in Fig. 4.14. It was not possible to reliably acquire a measurement of the rebound velocity due to projectile-sabot interaction, as the sabot coincided with the projectile during rebound. Prior to this occurrence, the projectile rebound velocity ranged from 8 m/s to 14 m/s. Rebound was observed in all cases other than under $r = 5$ in convex and concave impacts, during which the 10 mm steel ball was captured by the panels.

For a given radius of curvature, an increase in the strike velocity corresponds to the capturing of the projectile, until a further increase in the projectile velocity passes a threshold and results in perforation. The projectile was arrested for both $r = 5$ in and $r = -5$ in plates.

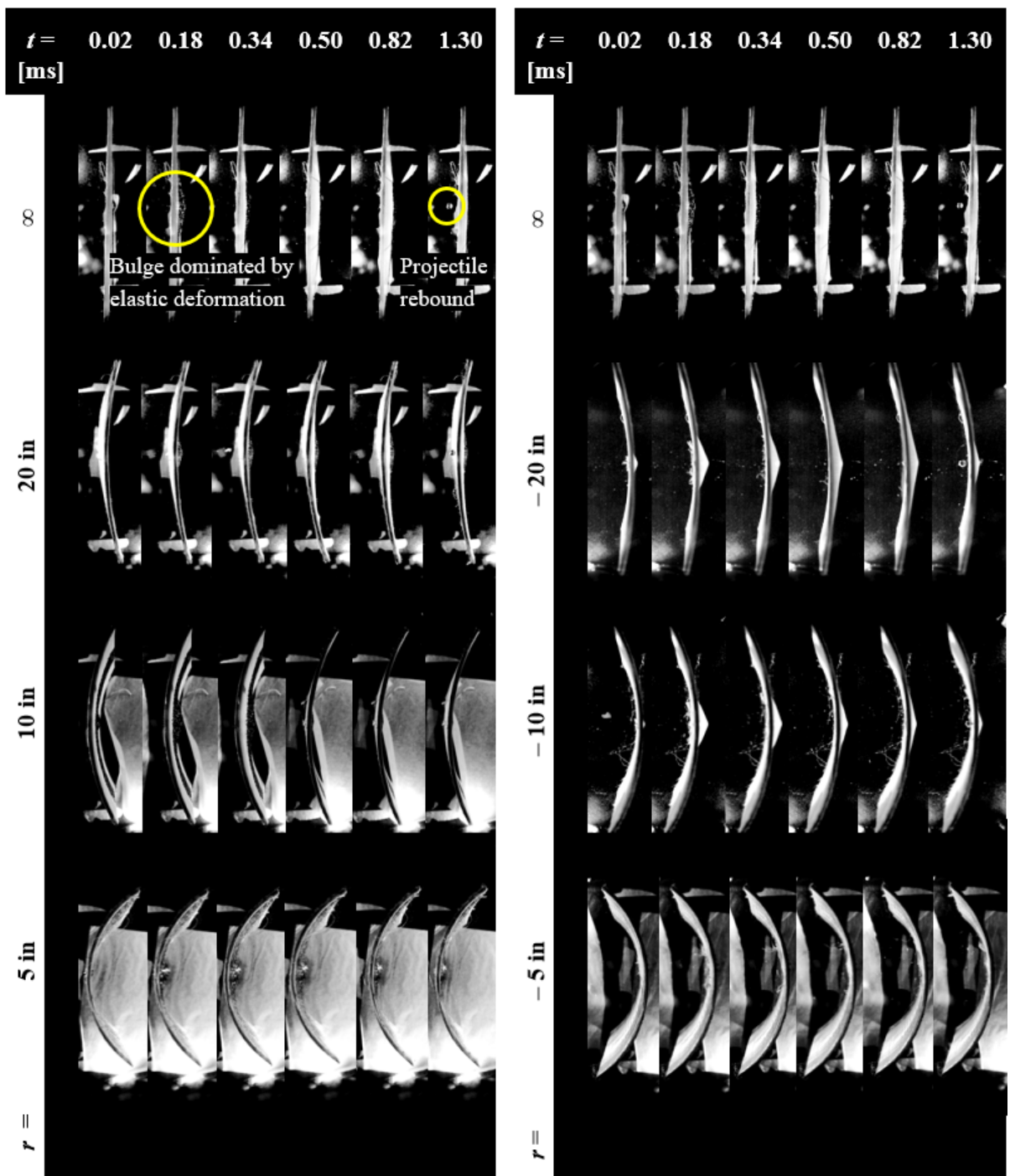


Figure 4.14: Conceptually comparing back face deformations under impact at V_I 300 m/s ($\pm 10\%$), as viewed from the side for convex (LHS) and concave (RHS) impact.

This suggests the possibility that the existence of a high degree of curvature, irrespective of direction, can govern the deformation of the plate and thus the penetration mechanism of the projectile. It is clear from Fig. 4.14 that in all cases of target curvature, projectile energy is not sufficient to impose significant lasting damage on the target, as elastic deformation dominates

the deformation on the back face. Hence, the maximum BFD that occurs during impact does not correspond to the final size of the out-of-plane deformation visible on the rear surface of the panels. The greatest extent of inelastic deformation, composed of a combination of plastic deformation, microcracking, delamination, sliding and reattaching action, was observed in the most highly curved panels $r = 5$ in and $r = -5$ in.

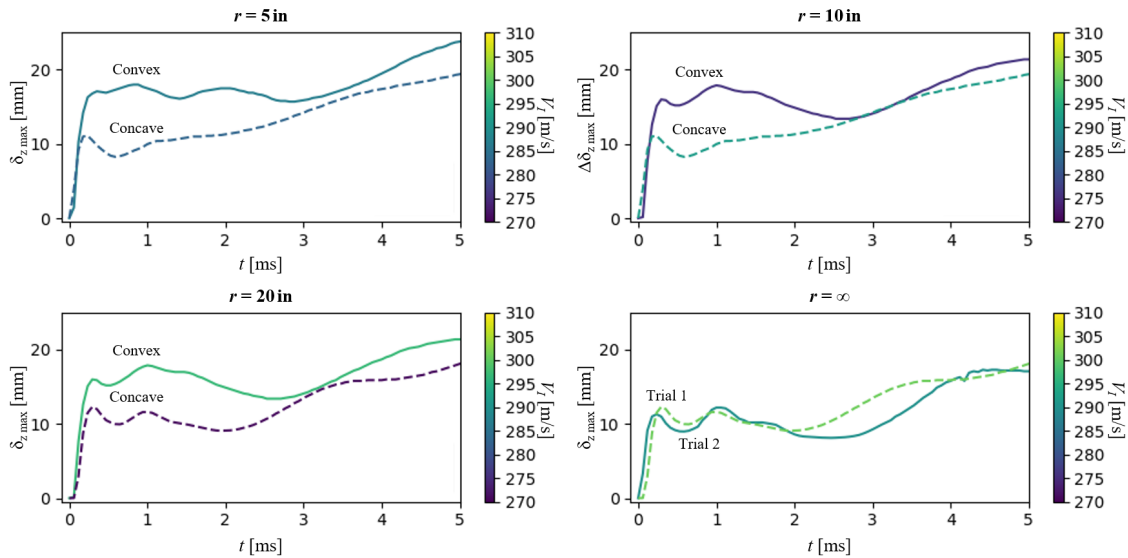


Figure 4.15: Maximum out-of-plane deflection progression across the target surface over time, for various curvatures and impact directions.

In Fig. 4.15, the BFD is reduced to a single parameter. The maximum BFD across the laminate surface, is plotted over the course of the impact, with the colour of the plot corresponding to the strike velocity. The two flat reference plates, tested at impact velocities within a range of 10 m/s of one another, produced comparable displacement profiles. Peak BFD is reached within 10 ms of impact, after which point the projectile bounces back. There is a lot of tumbling and plate rotation as the projectile rebounds since the plate is free-standing and the rebound velocity is not high enough to occur faster than the plate movement due to the effects of inertia. This is followed by the movement of the whole plate in the positive z -direction and in the opposing direction to the retracting projectile. This results in an increase in the out-of plane displacement over time, particularly after 1 ms, that does not correspond to the maximum bulge height. The behaviour is captured in the DIC measurement visible in Fig. 4.15, where a similar trend is also observed for the curved panels. The data for the curved panels is split into individual graphs based on radius of curvature, differentiated by the direction of impact between plots. Despite minor differences between the V_I values of different cases, from

the flat plate data it can be deduced that a small variation in the impact velocity does not yield noticeable changes in the maximum δ_z value. Likewise, previous studies have shown that increasing V_I in arrest cases tends to yield more extensive back face deformation.

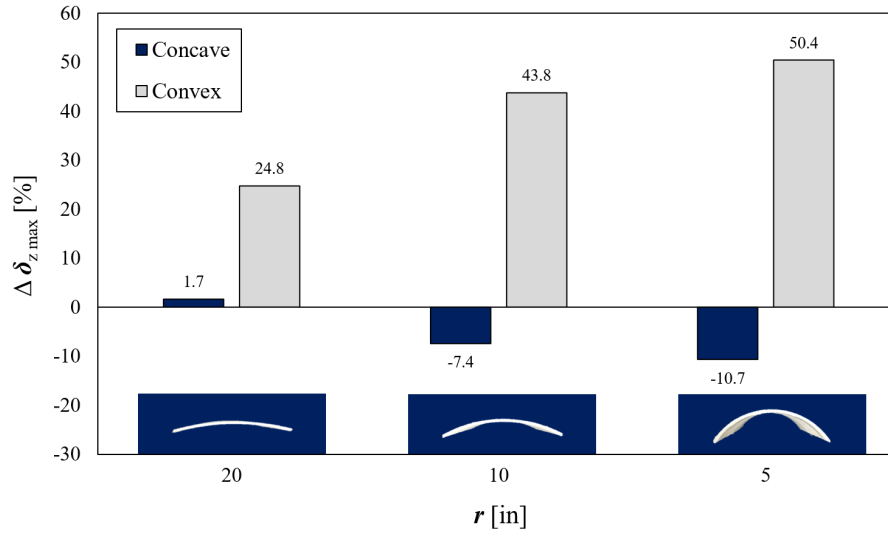


Figure 4.16: Percentage change in the maximum bulge height of curved panels relative to flat reference plates.

For all the degrees of curvature presented in Fig. 4.15, convex impact produces consistently higher values of peak BFD than corresponding concave cases. Amongst different curvatures of the same direction of impact, there is a clear rise in BFD with curvature for convex impacts, and a less dramatic reduction with curvature in the case of concave impacts. These differences are illustrated in Fig. 4.16 as percentage change in the maximum out-of-plane BFD of the curved plates, $\Delta\delta_{z,max}$, with respect to the mean maximum BFD of flat plates. In summary, for all values of curvature radius, the maximum BFD measurements of convex laminates exceed BFD measurements of concave and flat laminates by 20% to 50%, with a significant increase in the magnitude of $\Delta\delta_{z,max}$ for an increasing degree of curvature. Comparing the peak BFD data for a reduction in r from the shallowest convex curvature of $r = 20$ in to $r = 10$ in, to the evolution of its BFD shape in Fig. 4.14, it can be seen that although an almost 25% rise is recorded in the maximum out-of-plane deflection on the rear, the panel exhibits less bending and membrane stretching than other curvatures. The maximum BFD almost immediately exceeds its arch height, $l = 15.5$ mm, upon impact, unlike the other two arch heights of $l = 29.7$ mm and $l = 57.1$ mm for $r = 10$ in and $r = 5$ in, respectively, that were never approached. This is in line with the findings for the shallowest curvature, $r = 60$ in, tested in [25] where the behaviour of the curved panel mimicked that of the more stable response of a flat laminate.

To achieve perforation, a more powerful gas gun was employed with a set-up arrangement similar to the one displayed in Fig. 4.7. This impact chamber, however, had the added benefit of enabling impact to take place under a vacuum, eliminating drag effects on the projectile and achieving even higher strike velocities than was previously attainable. As a result, the projectile impact energy was sufficient for initiating penetration in all cases. This was followed by either the arrest of the projectile, or at higher impact velocities, full perforation of the laminate. No projectile rebound was observed in any of the higher velocity impact cases. The higher ranges of impact velocity and the removal of air resistance, had the effect of propelling the sabot debris much further than before. This can be seen in Fig. 4.17, which displays the impact flash that occurs upon contact of the projectile and debris particles with the surface of the target. The influence of the debris on the impact is assumed to be negligible due to the small size and momentum of these particles relative to the steel ball.

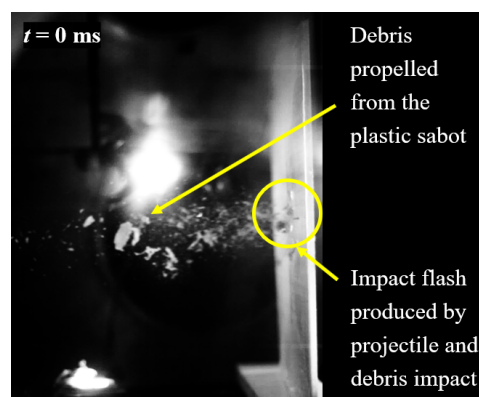


Figure 4.17: Identifying impact flashes at the point of first contact by the projectile and surrounding sabot debris with the target surface.

The impact chamber for this set-up did not possess an observation window at the rear face of the target, thus preventing the possibility of obtaining three-dimensional DIC strain measurements of the out-of-plane deflection. Instead, three high-speed cameras were used to capture the impact event with two from the side and one diagonally facing the rear face of the target. Images of the side view were used to calculate impact and residual velocities. While the progression of the back face bulge could not be accurately estimated, the images provided a comparison of bulge shape development between different degrees of plate curvatures. These are displayed in Figs. 4.18 to 4.22. In Figs. 4.18 to 4.20, convex impact for the two cases of projectile arrest and target perforation are presented, spanning panels with $r = \infty$ to 10 in. A convex impact arrest case is presented for $r = 5$ in, in Fig. 4.21, due to the limited availability of test specimens, along with $r = 5$ in concave impact arrest and perforation cases in Fig. 4.22.

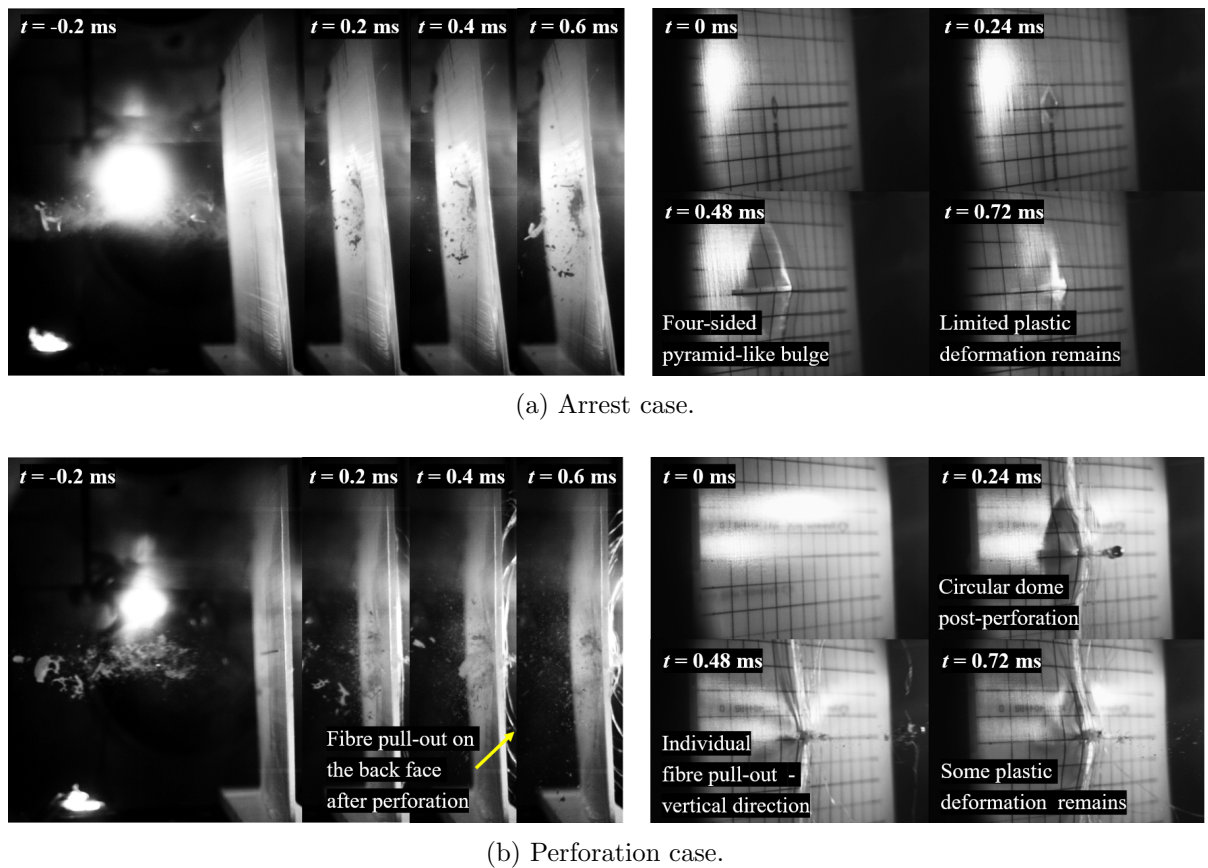
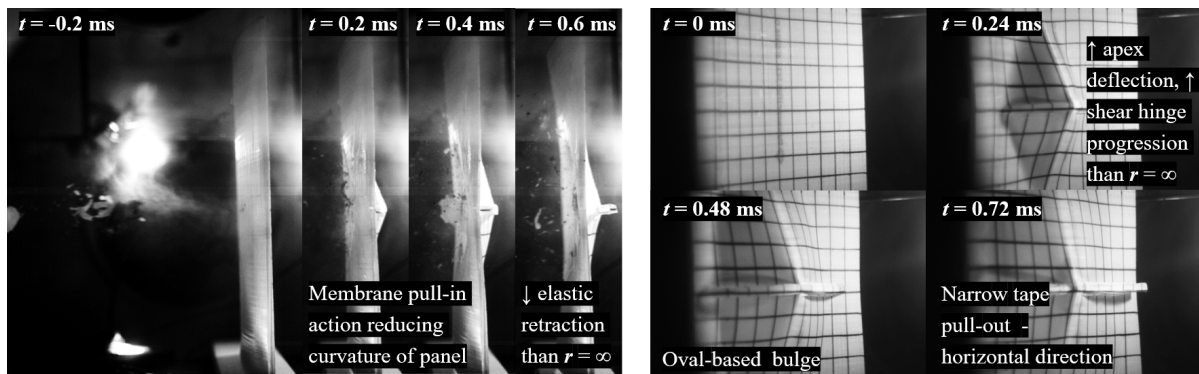


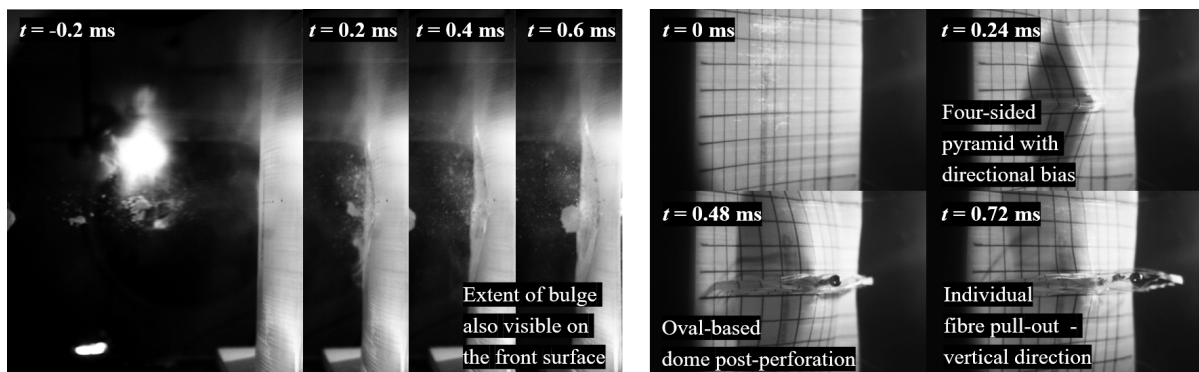
Figure 4.18: High speed video stills of the impact event from the side (LHS) and the rear (RHS), for $r = \infty$ (convex).

The high speed video stills captured from the impact on the flat reference plates can be seen in Fig. 4.18. In the arrest case, the bulge on the rear face develops into a four-sided pyramid, as has been reported in previous work [57]. Although the maximum height of the bulge retracts back as the impact event proceeds, following the capture of the projectile beyond $t = 0.72$ ms, a much more extensive level of inelastic deformation due to damage remains, than was observed earlier in the lower impact energy cases. In the perforation case however, the four-sided pyramid transforms into a circular-based dome upon projectile escape from the material, followed by its collapse and further internal energy dissipation through the thickness of the laminate, as discussed in Chapter 3. As a result of perforation, pull-out of individual fibres is initiated at the site of perforation, extending towards the edges in the form of a crescent in the vertical direction on the back face of the laminate.

The corresponding arrest and perforation cases for panels with a radius of curvature $r = 20$ in, are presented in Fig. 4.19. In both cases, the panels undergo much more extensive in-plane shear deformation, yielding more expansive bulge formation on the back face. The



(a) Arrest case.

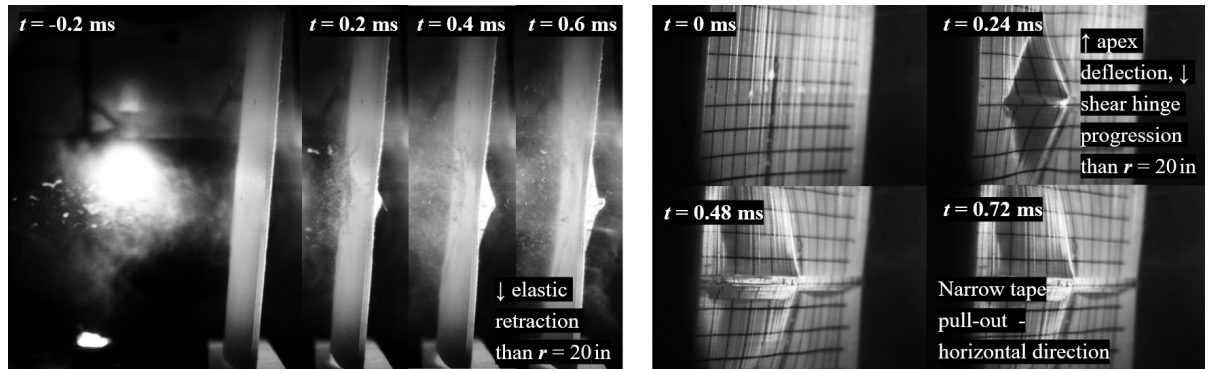


(b) Perforation case.

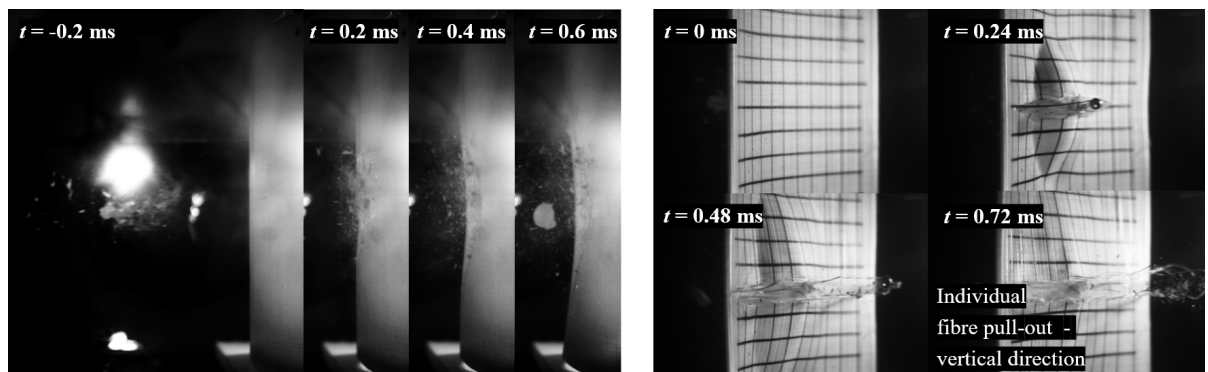
Figure 4.19: High speed video stills of the impact event from the side (LHS) and the rear (RHS), for $r = 20$ in (convex).

drawing in action of the material at the edges towards the site of impact has the effect of reducing curvature in the region of primary fibres, visible in the side view stills in Fig. 4.19(a). When the projectile is caught, the presence of curvature promotes a back face deformation with a more dominant inelastic behaviour, a larger apex deflection and a greater shear hinge progression than for the flat laminate. In the first 0.24 ms of both the arrest and the perforation case, the familiar four-sided pyramid bulge shape appears on the rear face. In contrast to the flat plates, this bulge shape exhibits a bias in the form of further hinge progression in the longitudinal direction, normal to the curvature, due to the absence of geometric constraints in this direction. Between $t = 0.24$ ms and 0.48 ms, the shape of the bulge transforms into an elliptical dome as the shear hinge travelling in the longitudinal direction arrives at the laminate edge. While the hinge may not have achieved the same reach in the lateral direction, the primary fibres that have become detached in the region between the peak BFD and the shear hinge on the back face, continue to detach further towards the edges in the direction of the curvature. This mimics the progression of the shear hinge in the longitudinal direction. In the arrest case,

the fibres move together as a narrow band of tape. When the projectile perforates the rear face at the higher impact velocity, damage and breakage of the fibres prevents them from coherently progressing towards the edge as before in the form of a tape, but rather as bundles of fibres.



(a) Arrest case.



(b) Perforation case.

Figure 4.20: High speed video stills of the impact event from the side (LHS) and the rear (RHS), for $r = 10$ in (convex).

Figure 4.20 displays similar behaviour for plates with $r = 10$ in under convex impact. In the arrest case, the increase in the degree of curvature corresponds to a greater degree of inelastic deformation, larger apex deflection and further shear hinge progression than was seen in laminates with $r = 20$ in. With a further increase in the degree of curvature for the convex arrest case, corresponding to a lower radius of curvature of $r = 5$ in, even more extensive membrane pull-in action is observed to the degree that anticlastic bending is clearly visible on the surface of the singularly curved panel in Fig. 4.21.

The effect of reversing the direction of impact to concave for the most extreme curvature case of $r = 5$ in, is presented in Fig. 4.22. The deformations on the rear face are more

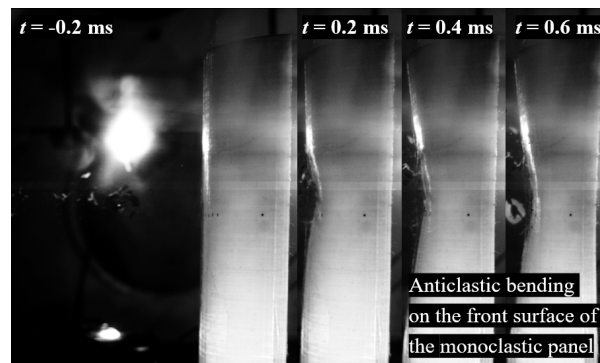
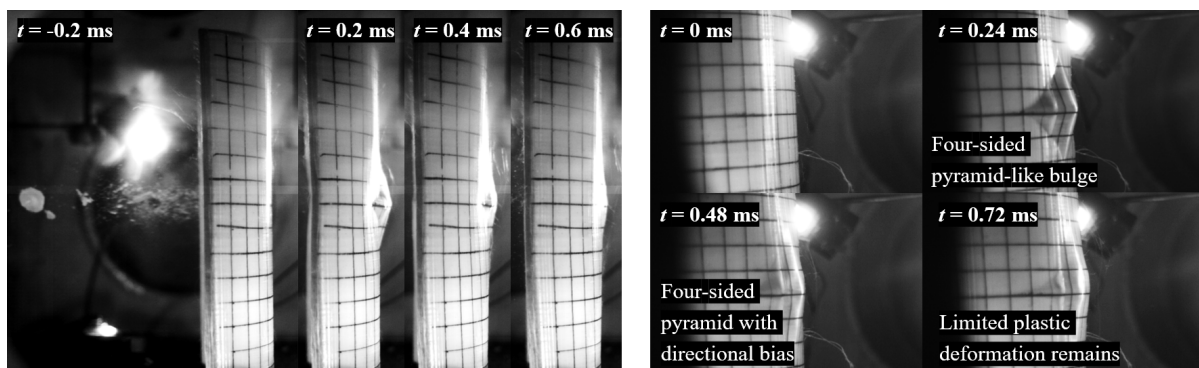
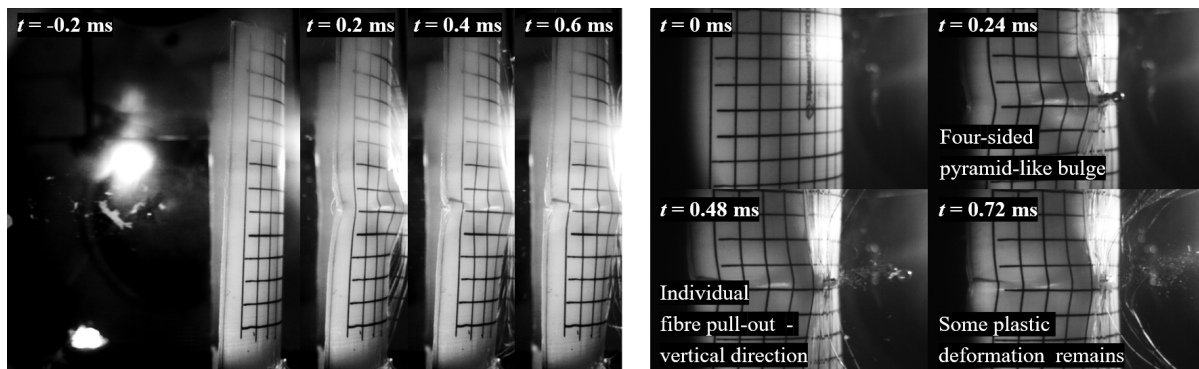


Figure 4.21: High speed video stills of the impact event from the side in an arrest case, for $r = 5$ in (convex).



(a) Arrest case.



(b) Perforation case.

Figure 4.22: High speed video stills of the impact event from the side (LHS) and the rear (RHS), for $r = 5$ in (concave).

reminiscent of the flat panels than they are of the convex curved impact cases, in terms of limited inelastic action, the emergence and retraction of four-sided pyramid shaped bulge, in addition to individual fibre pull-out along the longitudinal direction following perforation. In both arrest and perforation cases however, the directional bias of the shear hinge progression occurs in the direction of the curvature, as opposed to the normal direction which was observed

in the convex cases. This arises from the direction of axial residual strain in the back face region. While this is of a compressive and reactionary nature in the convex case, for concave impact, the rear face is under tensile strain, thereby making it more compliant to outward movement away from the impact site. Since the kinetic energy of the projectile is dissipated in this direction, the maximum apex deflection is reduced. Likewise, the nature of shear hinge progression in the direction of curvature means that the shear hinge does not travel far before the impact event is concluded.

4.4.1.2 Velocity analysis

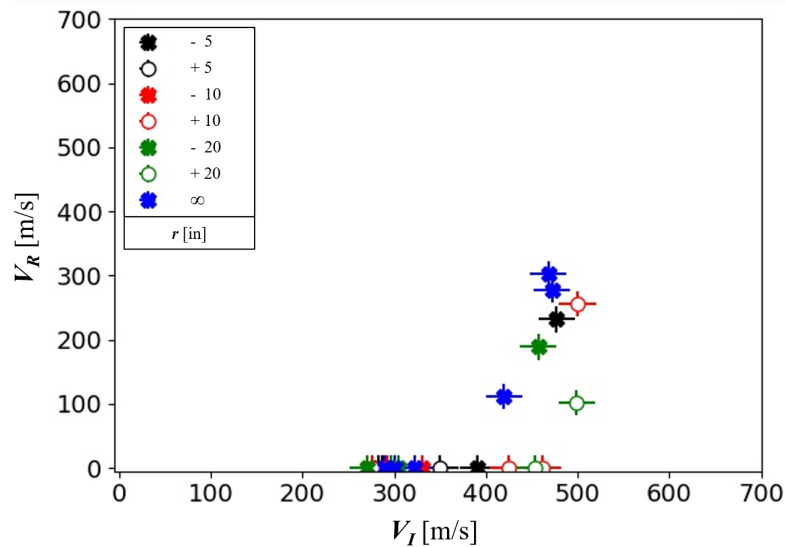


Figure 4.23: Impact and residual velocity of a steel ball threat for flat and curved targets.

Residual velocity (V_R) terms for the different plates are plotted against impact velocity (V_I) terms in Fig. 4.23. Some of the higher impact velocities reached using the more powerful gas gun managed to achieved perforation in the laminates. The range of data is small due to the limited availability of panels, however, it can still provide useful insight into the velocity-based impact performance metric. For instance, consider the velocity data for the flat plate. It is clear that perforation has taken place for a V_I of just above 400 m/s. Meanwhile, for convex impact of curved plates with $r = 20$ in and $r = 10$ in, stop cases have been recorded at V_I values of just below 500 m/s. The same cannot be said for the two data points representing concave impact for $r = 20$ in and $r = 5$ in. However, both data points demonstrate a reduction in V_R at similar V_I values, as compared to a flat plate. This is worth investigating further as previous investigations have shown that improvements in the ballistic limit velocity are accompanied by

larger bulges and therefore poorer BFD performance. Caution must be exercised in drawing comparisons, as previous studies were conducted on flat laminates and may not be applicable to curved panels due to variations in the deformation mechanism under ballistic impact. On the whole, the dataset is not sufficiently large to establish trends or solid relationships between the different degrees of plate curvature. It does however confirm the existence of the effect that the direction of impact has on the residual velocity of the projectile.

4.4.2 FSP threat

4.4.2.1 Velocity analysis

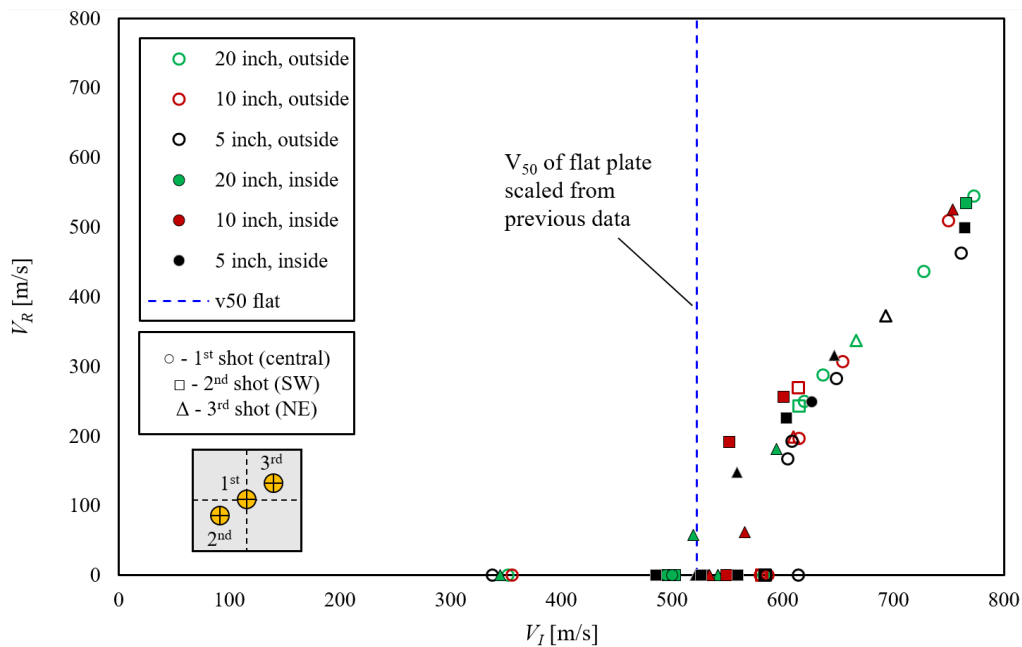


Figure 4.24: Impact and residual velocity plots of 5.56 mm flat-faced FSP threat onto curved laminates.

Data from the ballistic impact testing performed at DSM Dyneema is presented collectively in Fig. 4.24, with V_I plotted against V_R in a similar manner to Fig. 4.23. The different curvatures are distinguished by the different colours of the markers, with the hollow markers representing convex impact and the filled markers denoting concave impact. The shape of the marker depicts the order in which the shot was taken, with the laminate becoming more compliant and therefore easier to deform as the number of shots progress. Since a greater level of energy is dissipated through more extensive deformations, the exit velocity in the event of perforation is likely to be slightly lower in secondary and tertiary shots than in a primary shot, for the same strike velocity. Although care was taken to ensure that the three impact regions did not overlap greatly,

complete avoidance of interaction between the deformed regions is not practically achievable. Thus, the relative reliability of the data points is considered to be based on the chronological order of the shots. The interaction between the deformation regions of the multiple shots on one plate is investigated in more depth in the following section.

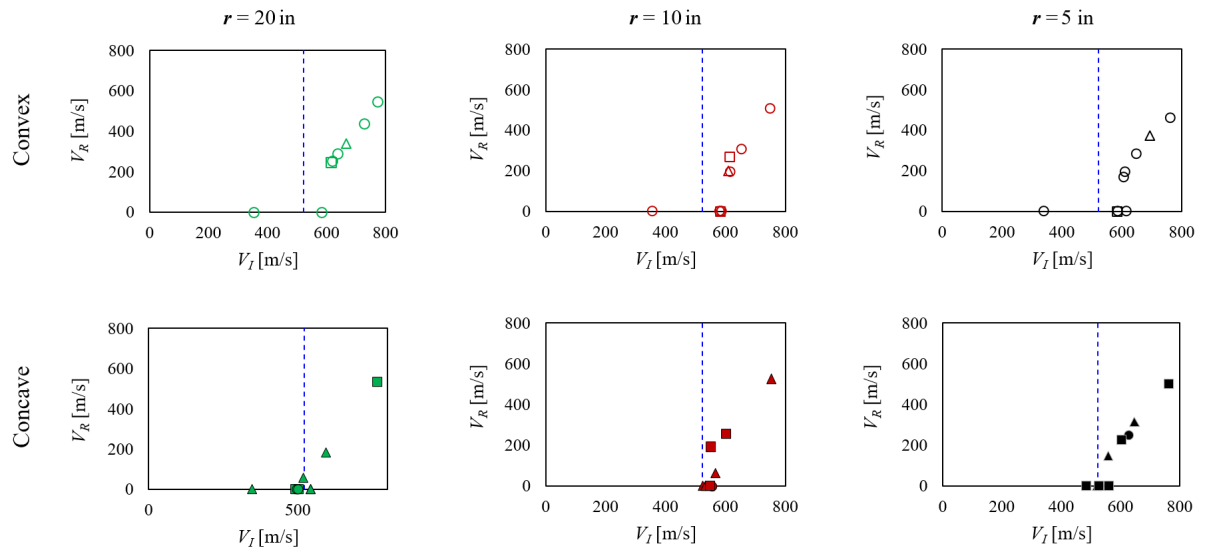


Figure 4.25: Impact and residual velocity plots of 5.56 mm flat-faced FSP threat onto curved laminates, grouped according to impact direction and radius of curvature.

The dashed blue line in Fig. 4.24 represents the V_{50} estimate of 522 m/s for flat plates of matching aerial density (AD), scaled from previous tests. For greater clarity and easier comparison to the flat reference plate, the datasets are grouped by radius of target curvature and direction of impact in Fig. 4.25. It can clearly be seen that while for convex impact the arrest cases are consistently above the ballistic limit of the flat reference plate, for concave impact these arrest cases are aligned with or lie very close to the V_{50} of plates without any curvature. As noted earlier, all concave cases are based on secondary and tertiary shots. It is therefore possible that the velocity at which total perforation occurs, and any residual velocities following this, are over-estimated. It is worth noting that multi-shots are the norm in industry for approximating the ballistic limit velocity of armour material for certification. A 400 mm square panel is typically tested with eight shots. The flat reference panel ballistic velocity limit was derived and scaled from this standard procedure. It would be beneficial in future work to have reference panels tested in the same manner as the curved plates, with their V_{50} also calculated using the same method. Likewise, the effects of impact location proximity to the panel edge should be explored further.

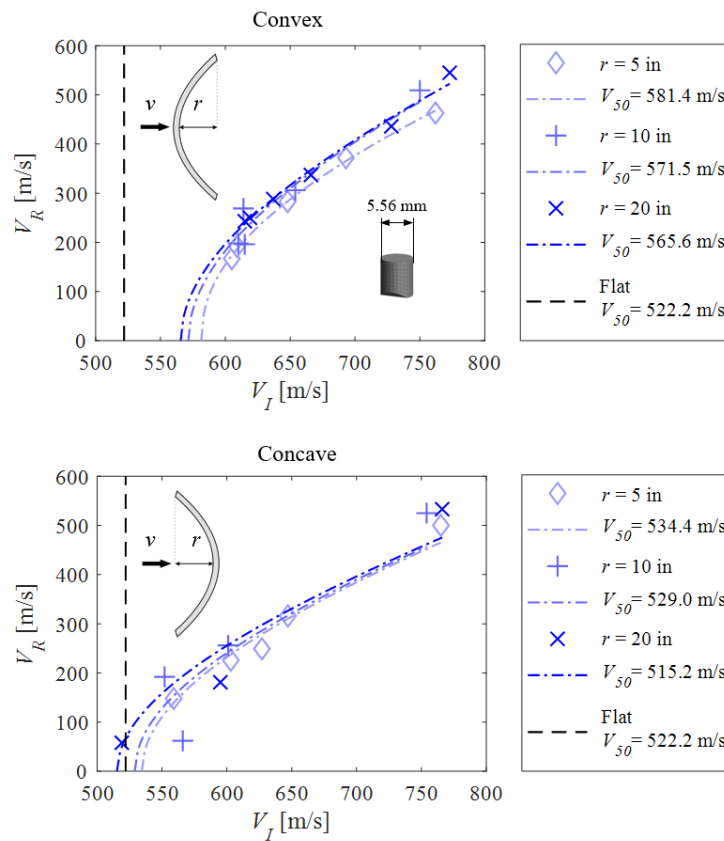


Figure 4.26: Experimentally-derived Lambert-Jonas ballistic limit approximations for curved panels.

In order to examine the effect of curvature and impact direction on the ballistic limit velocity, the Lambert-Jonas equation,

$$V_R = a [(V_I)^p - (V_{50})^p]^{\frac{1}{p}}, \quad (4.5)$$

was employed to fit curves to the velocity data points, in order to estimate the ballistic limit velocity, V_{50} , of each laminate. This was done by means of a least square fit of the results, where a , p and V_{50} are curve fit parameters for V_I input values and V_R output values. The resulting V_{50} approximations for convex and concave impacts of varying radii of curvature are presented in Fig. 4.26. The black dashed line illustrates the flat reference plate ballistic limit, scaled from previous testing, as shown in earlier figures. To facilitate an easier comparison, the percentage change in the ballistic limit relative to a flat plate, ΔV_{50} , is visualised in Fig. 4.27 for each radius of curvature and direction of impact. As expected, the addition of curvature for a convex impact direction yields V_{50} estimates that are 8.3% to 11.3% higher than that of a flat plate (Fig. 4.27). Meanwhile, for a concave impact direction, the addition of curvature

does not change the V_{50} significantly, with the difference ranging from -1.3% to 2.3% . The large spread of data that is visible in the concave cases is likely down to contributions from the interactions of multiple impact regions and the lack of data from primary shots. It is therefore clear that an increase in the degree of curvature noticeably improves the V_{50} prediction of the plate by approximately 10% , when plate is shot on the outside surface.

Meanwhile, when shooting into the cavity of curved plates, the addition of curvature has very little effect on the ballistic limit. Although the V_{50} predictions for the different radii of the same impact direction do not vary greatly, there is a trend indicating that regardless of impact direction, the ballistic limit velocity rises with an increasing degree of curvature. Compared to the changes in the maximum BFD that are brought about by the addition of curvature to a flat laminate, as seen in Fig. 4.16, the changes in the V_{50} of the plates are much smaller in magnitude. This is in agreement with the findings of [42], where the maximum BFD was more sensitive to changes in the curvature than the ballistic limit velocity. The authors also recorded an increase in the V_{50} of the plates accompanying a decrease in the radius of curvature.

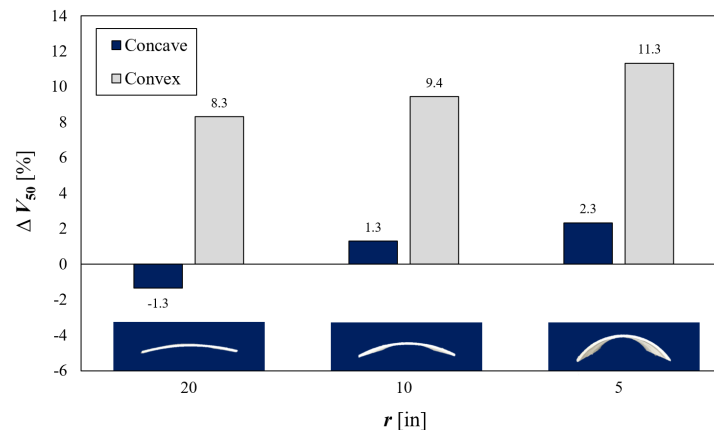


Figure 4.27: Percentage change in the ballistic limit velocity of curved panels relative to flat reference plates.

4.4.2.2 Deflection analysis

In Fig. 4.28, laminates of varying curvature are viewed from the side for the three instances of pre-impact (convex), post-impact (convex) and post-impact (concave). The most striking observation is the increase in the number of fibres that are drawn out and away from the surface of the laminate, yet still remain attached at the edges. This is visible for both convex and concave impact, for a range of impact velocities. This effect is more prevalent than was observed

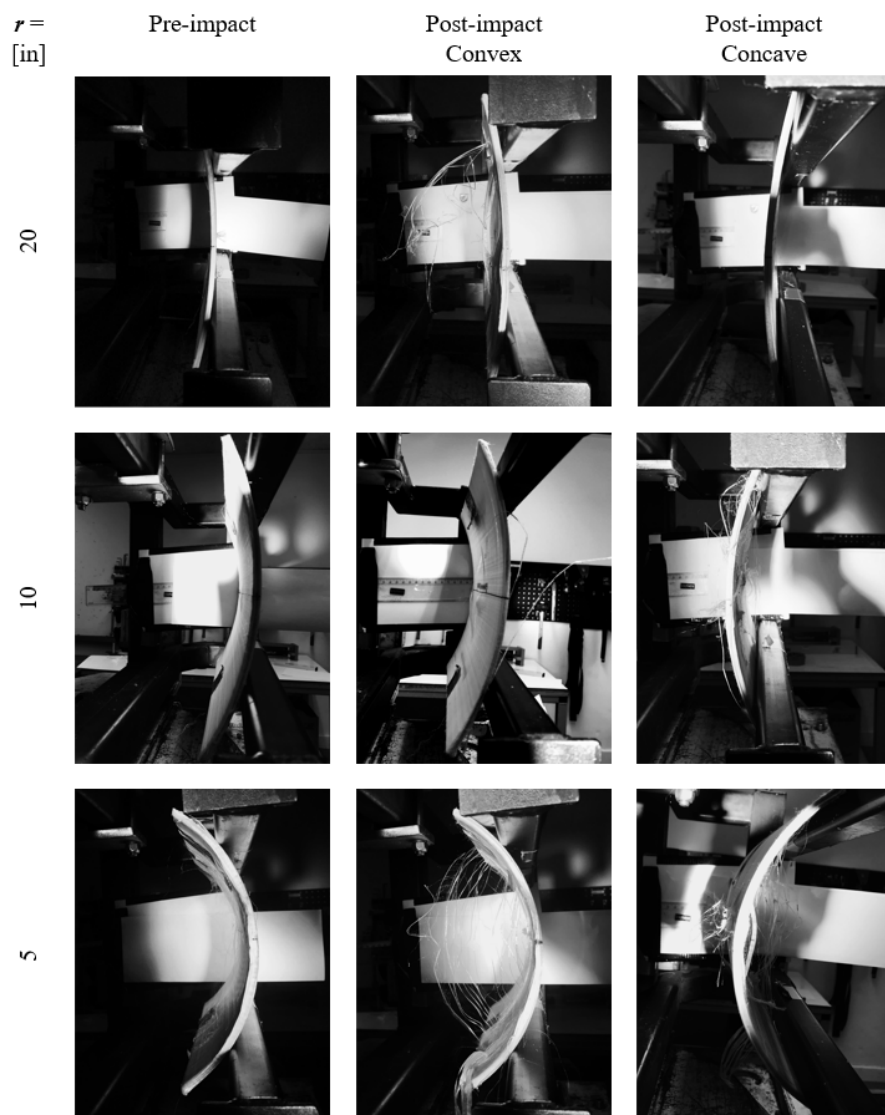


Figure 4.28: Impact testing of laminates of varying curvature as viewed from the side for the three instances of pre-impact (convex), post-impact (convex) and post-impact (concave).

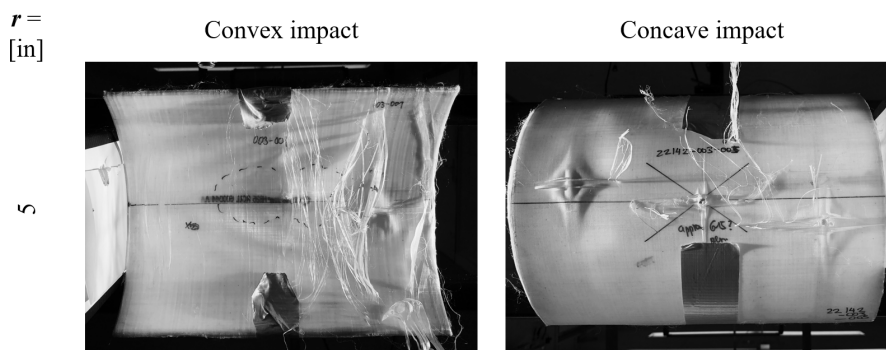


Figure 4.29: Impact testing of laminates of the most highly curved laminates as viewed from the rear in convex and concave configurations.

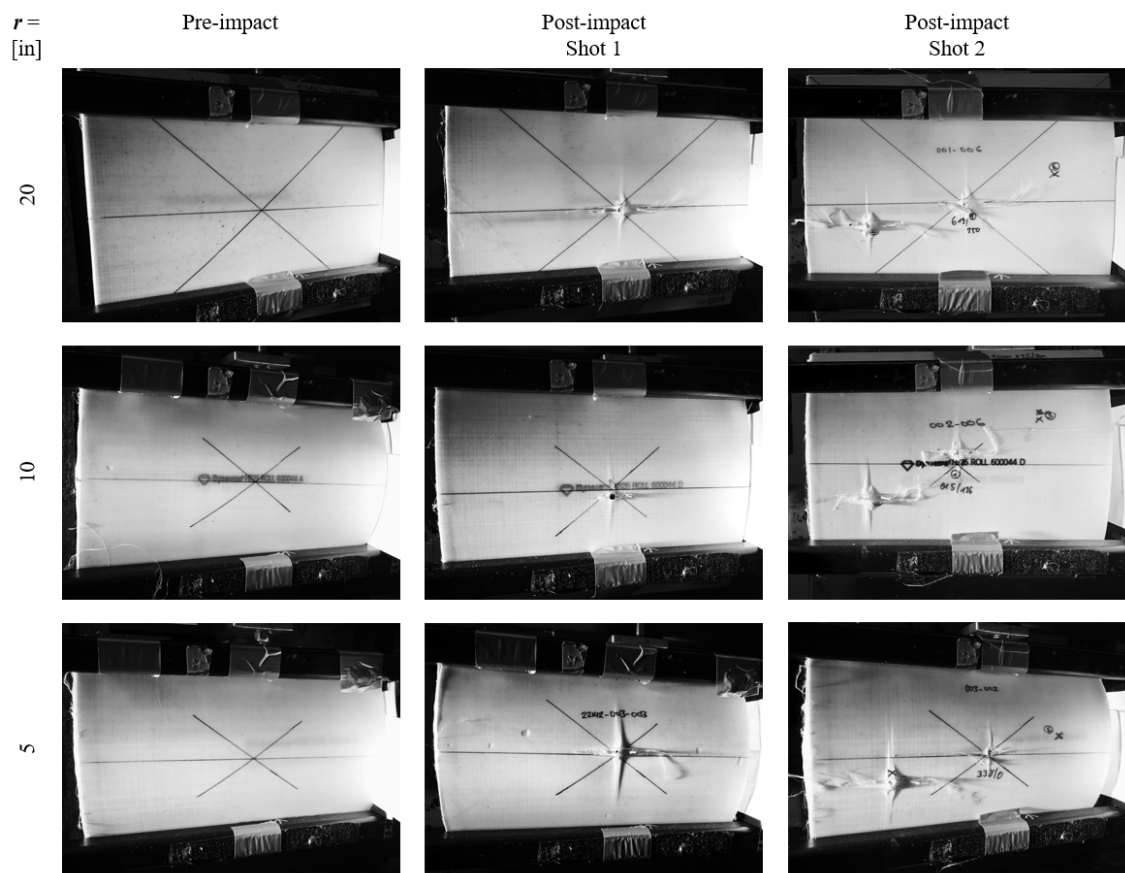


Figure 4.30: Impact testing of laminates of varying curvature in the convex direction as viewed from the front, for the three instances of pre-impact, post-impact (shot 1) and post-impact (shot 2).

previously in Section 4.4.1, due to the higher range of impact velocities investigated, together with the nature of the flat-faced FSP shape which, unlike the spherical projectile, possesses sharp edges and corners. A closer look at the rear faces of the most highly curved laminates in Fig. 4.29, reiterates the presence of the variation that exists in resulting BFD on the rear faces of curved laminates subjected to convex and concave impact, warranting a more detailed focus on this area.

A selection of specimens shot on the outside curvature is presented in Fig. 4.30, where the laminates of different curvatures are shown prior to impact, following primary impact, and following secondary impact. In all of these cases, upon penetration of the first lamina, a bulge is formed on the front surface of the panel, engulfing the incoming projectile and growing in size to extend the out-of-plane deformation along primary fibres. The effect is visible for a range of impact velocities and for both primary and secondary shots. With an increasing degree of curvature however, the bulge and the out-of-plane deformation along the path of primary fibres

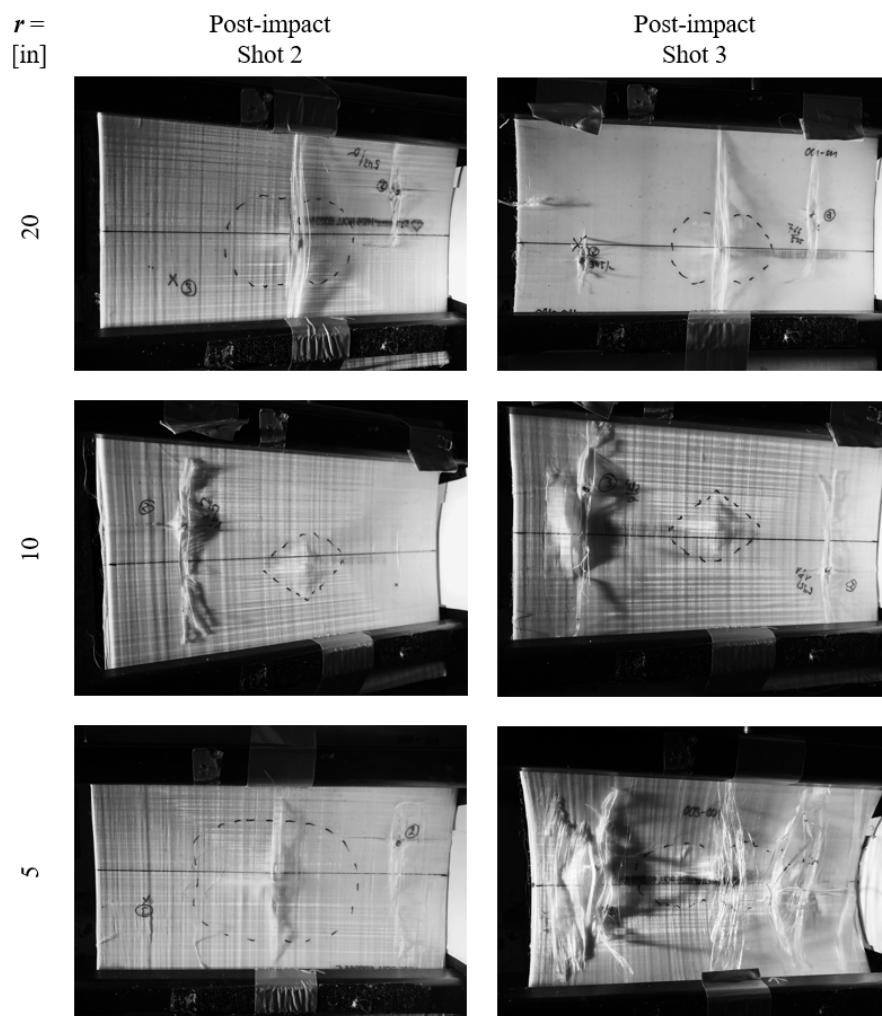


Figure 4.31: Impact testing of laminates of varying curvature in the concave direction as viewed from the front, for the two instances of post-impact (shot 2) and post-impact (shot 3).

grow in size. Similarly, the images in Fig. 4.31 present the plates that were shot on the inside curvature, following the second and third shots, since no initial shots were taken in the concave direction. While in this direction of impact front face bulging is visibly reduced, the extent of fibre pull-out increases with reducing radius of curvature, similar to the damage visible on the rear face of panels subjected to convex impact.

The extent of the internal damage in tested panels was examined on a light table and can be seen in Figs. 4.32 to 4.34 for $r = 20$ in to 5 in, respectively. The dashed lines outline the extent of internal damage visible on the rear face, and are numbered according to the order in which the shots were taken. Hence, the surface which is labelled with a number represents the rear side of a given impact case. As back face deflection undergone by the laminate is determined by

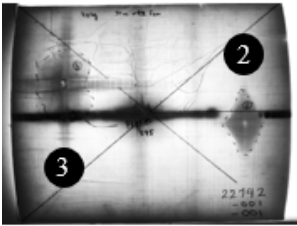
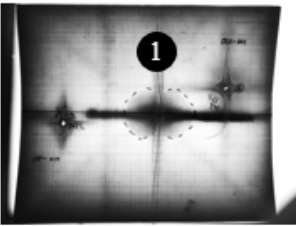
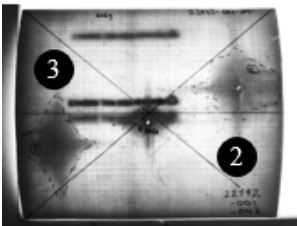
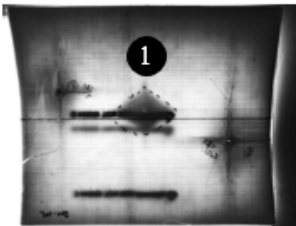
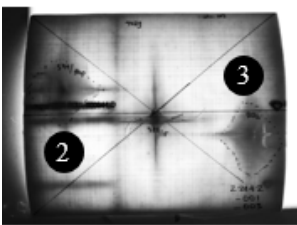
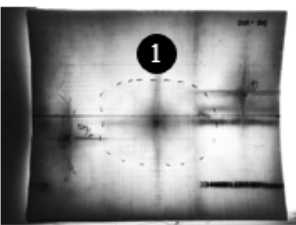
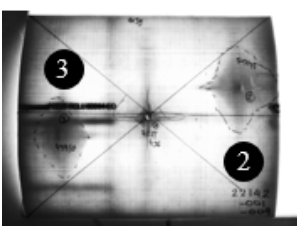
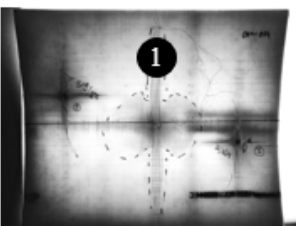
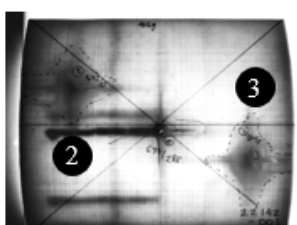
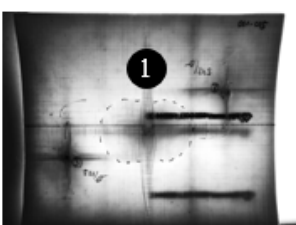
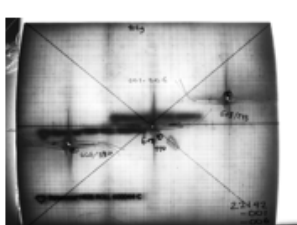
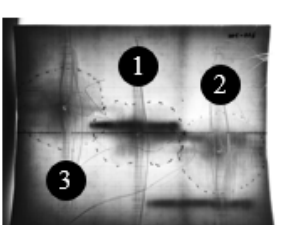
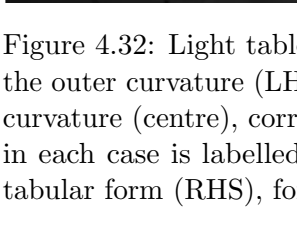
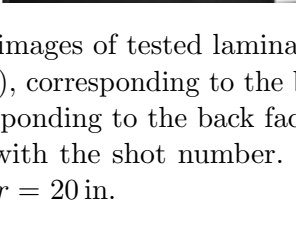




Outer curvature, Concave impacts	Inner curvature, Convex impacts	$r = 20$ in Direction	V_I [m/s]	V_R [m/s]
		1 Convex	773.0	545.0
		2 Concave	345.0	0
		3 Concave	766.2	534.6
		1 Convex	351.7	0
		2 Concave	594.5	181.4
		3 Concave	491.8	0
		1 Convex	582.9	0
		2 Concave	541.5	0
		3 Concave	503.0	0
		1 Convex	727.6	436.5
		2 Concave	519.4	57.5
		3 Concave	494.3	0
		1 Convex	636.6	287.8
		2 Concave	541.6	0
		3 Concave	500.1	0
		1 Convex	619.4	250.0
		2 Convex	666.5	337.3
		3 Convex	614.7	243.2

Figure 4.32: Light table images of tested laminates showing the extent of internal damage on the outer curvature (LHS), corresponding to the back face of concave impacts, and on the inner curvature (centre), corresponding to the back face of convex impacts. The back face deflection in each case is labelled with the shot number. The impact properties are also presented in tabular form (RHS), for $r = 20$ in.

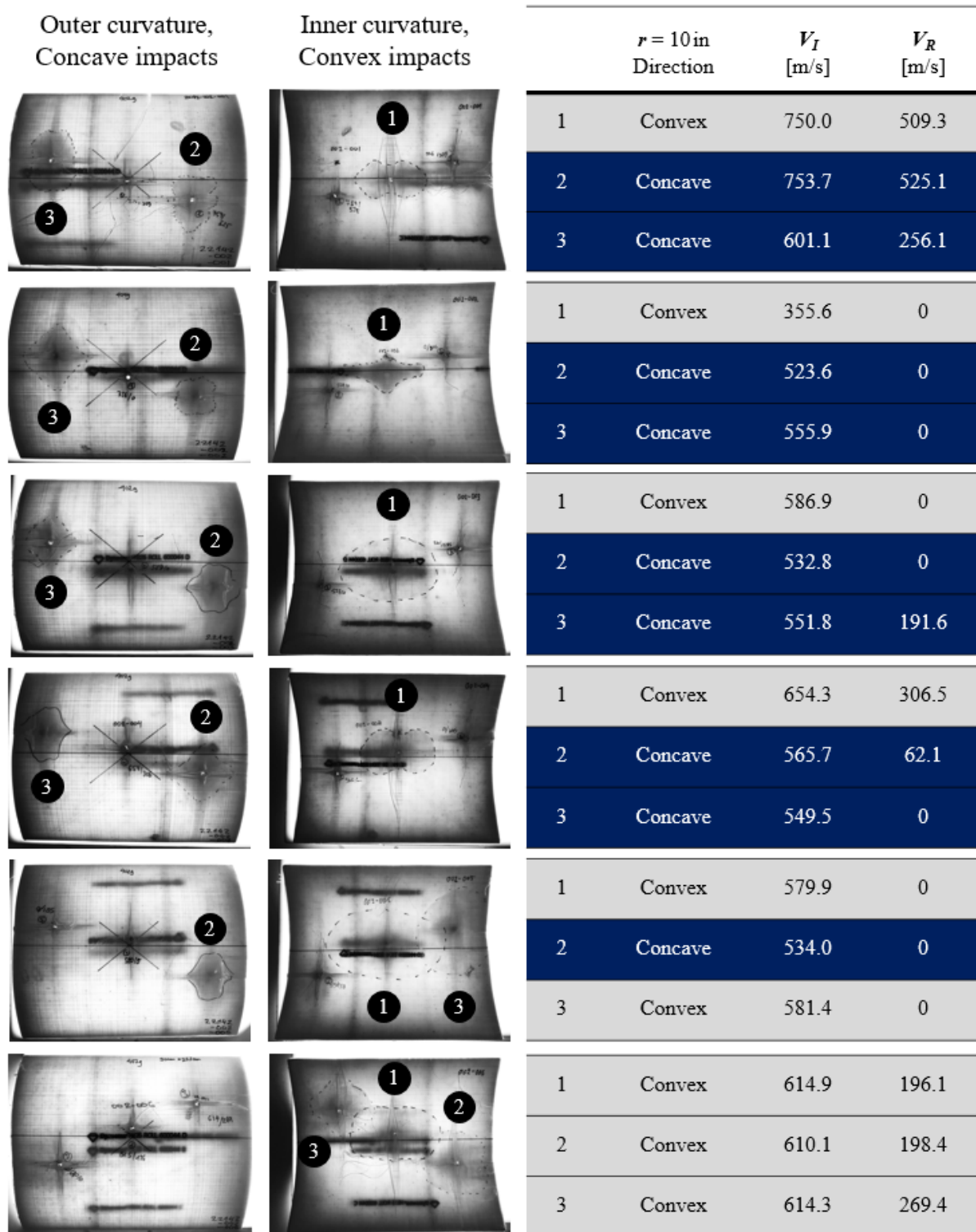


Figure 4.33: Light table images of tested laminates showing the extent of internal damage on the outer curvature (LHS), corresponding to the back face of concave impacts, and on the inner curvature (centre), corresponding to the back face of convex impacts. The back face deflection in each case is labelled with the shot number. The impact properties are also presented in tabular form (RHS), for $r = 10$ in.

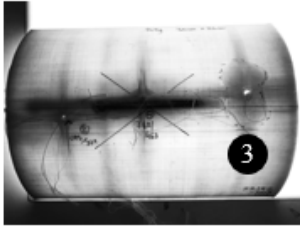
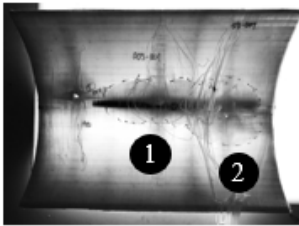
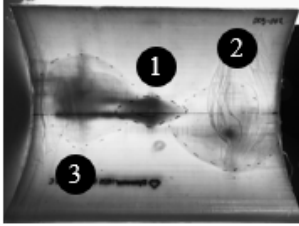
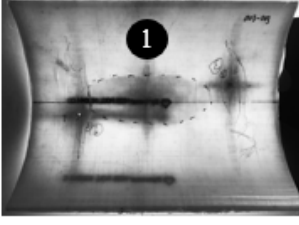
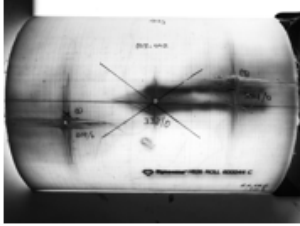
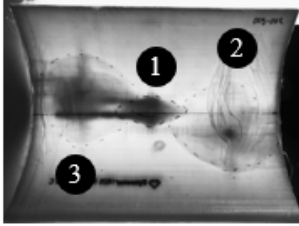
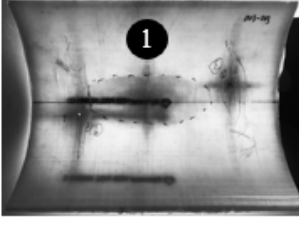
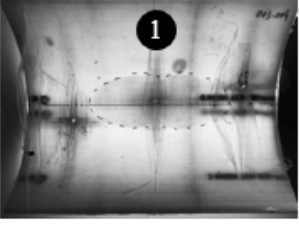
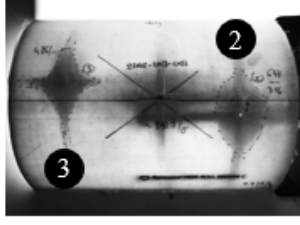
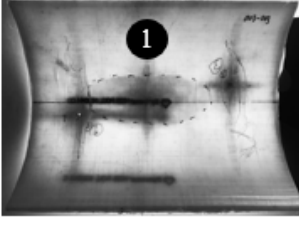
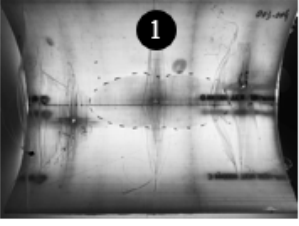
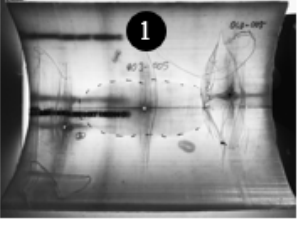
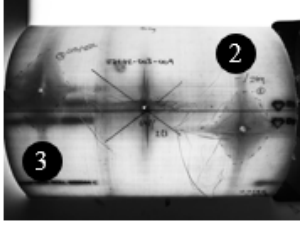
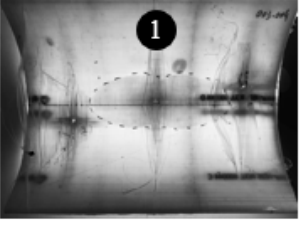
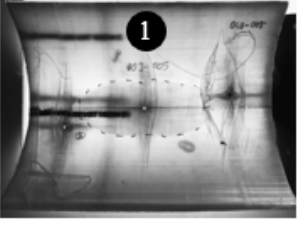
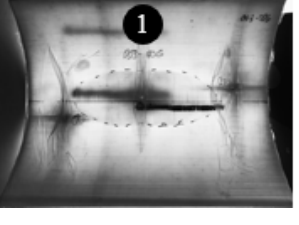
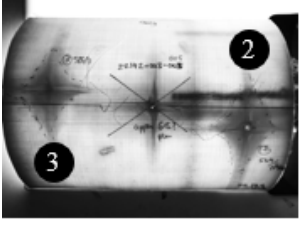
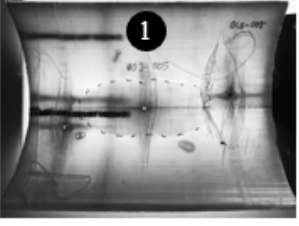
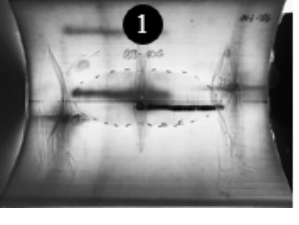
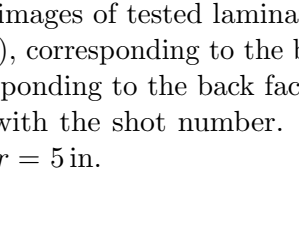
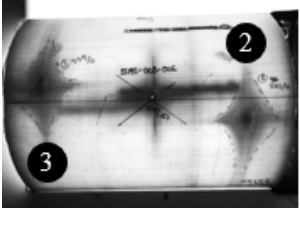
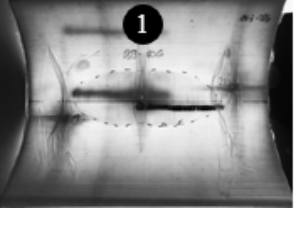
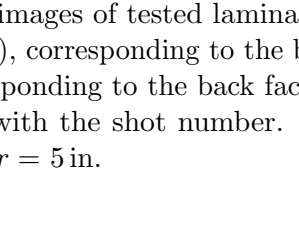

Outer curvature, Concave impacts	Inner curvature, Convex impacts	$r = 5$ in Direction	V_I [m/s]	V_R [m/s]
		1 Convex	761.5	463.0
		2 Convex	693.5	372.3
		3 Concave	764.6	499.5
		1 Convex	337.7	0
		2 Convex	614.1	0
		3 Convex	584.1	0
		1 Convex	585.0	0
		2 Concave	646.7	315.9
		3 Concave	485.5	0
		1 Convex	648.3	282.7
		2 Concave	626.6	249.4
		3 Concave	603.1	226.0
		1 Convex	608.7	192.2
		2 Concave	558.7	148.3
		3 Concave	526.4	0
		1 Convex	604.6	167.1
		2 Concave	520.9	0
		3 Concave	559.4	0

Figure 4.34: Light table images of tested laminates showing the extent of internal damage on the outer curvature (LHS), corresponding to the back face of concave impacts, and on the inner curvature (centre), corresponding to the back face of convex impacts. The back face deflection in each case is labelled with the shot number. The impact properties are also presented in tabular form (RHS), for $r = 5$ in.

the extent of the damage zone, the terms BFD and damage zone will be used interchangeably in the following analysis to refer to the area under the impact zone that is highlighted on the light-table inspections. This excludes the primary fibre zones that are affected in every one of these cases, due to the general deformation mechanisms of the plate under impact. Since the behaviour of the laminate subjected to impact varies through the thickness, for each curvature both the front and the rear face are presented. The tables to the right of the images display the corresponding impact direction and associated velocities for each strike case.

Table 4.1: Identifying shape and extent of in-plane back face deflection as a percentage of plate size in arrest cases, presented in ascending order of V_I for $r = 20$ in.

$r = 20$ in $d_s = 300$ mm $s = 255$ mm									
Shot number	Direction	V_I [m/s]	V_R [m/s]	V_I/V_{50}	Perforation	BFD shape	BFD size [mm ²]	BFD size [%]	Notes
1	Convex	351.7	0.0	0.62	no	Rhombus	1835.8	2.4	-
1	Convex	582.9	0.0	1.03	no	Elliptical - d_s	13614.8	17.8	-
3	Convex	614.7	243.2	1.09	yes	-	-	-	-
1	Convex	619.4	250.0	1.09	yes	-	-	-	-
1	Convex	636.6	287.8	1.12	yes	-	-	-	-
2	Convex	666.5	337.3	1.18	yes	-	-	-	-
1	Convex	727.6	436.5	1.29	yes	-	-	-	-
1	Convex	773.0	545.0	1.37	yes	-	-	-	-
2	Concave	345.0	0.0	0.67	no	Rhombus	1961.7	2.6	-
3	Concave	491.8	0.0	0.95	no	Rhombus	4752.4	6.2	-
3	Concave	494.3	0.0	0.96	no	Rhombus	4943.3	6.5	-
3	Concave	500.1	0.0	0.97	no	Rhombus	5103.9	6.7	-
3	Concave	503.0	0.0	0.98	no	Rhombus	4652.6	6.1	-
2	Concave	519.4	57.5	1.01	yes	-	-	-	-
2	Concave	541.5	0.0	1.05	no	Rhombus	5707.2	7.5	-
2	Concave	541.6	0.0	1.05	no	Rhombus	6232.3	8.1	-
2	Concave	594.5	181.4	1.15	yes	-	-	-	-
3	Concave	766.2	534.6	1.49	yes	-	-	-	-

The resulting deformations on the strike face for each shot agree with the observations noted in Figs. 4.30 to 4.31. Considering the rear faces however, the light table highlights the internal damage caused by the impact event that was not previously visible. The darker the appearance of the region, the greater the extent of damage, particularly delamination, in that area. The shape and extent of the BFD measured from these images in arrest cases,

Table 4.2: Identifying shape and extent of in-plane back face deflection as a percentage of plate size in arrest cases, presented in ascending order of V_I for $r = 10$ in.

$r = 10$ in $d_s = 300$ mm $s = 255$ mm									
Shot number	Direction	V_I [m/s]	V_R [m/s]	V_I/V_{50}	Perforation	BFD shape	BFD size [mm ²]	BFD size [%]	Notes
1	Convex	355.6	0.0	0.62	no	Rhomboid	4023.2	5.3	-
1	Convex	579.9	0.0	1.01	no	Elliptical - d_s	16548.7	21.6	Overlap
3	Convex	581.4	0.0	1.10	no	Elliptical - d_c	10702.6	14.0	Overlap
1	Convex	586.9	0.0	1.03	no	Elliptical - d_s	12243.3	16.0	-
2	Convex	610.1	198.4	1.07	yes	-	-	-	-
3	Convex	614.3	269.4	1.07	yes	-	-	-	-
1	Convex	614.9	196.1	1.08	yes	-	-	-	-
1	Convex	654.3	306.5	1.14	yes	-	-	-	-
1	Convex	750.0	509.3	1.31	yes	-	-	-	-
2	Concave	523.6	0.0	0.99	no	Quadrifolium	3129.2	4.1	-
2	Concave	532.8	0.0	1.01	no	Quadrifolium	3350.9	4.4	-
2	Concave	534.0	0.0	1.01	no	Quadrifolium	3550.2	4.6	-
3	Concave	549.5	0.0	1.04	no	Quadrifolium	4561.4	6.0	-
3	Concave	551.8	191.6	1.04	yes	-	-	-	-
3	Concave	555.9	0.0	1.05	no	Rhombus	5520.6	7.2	-
2	Concave	565.7	62.1	1.07	yes	-	-	-	-
3	Concave	601.1	256.1	1.14	yes	-	-	-	-
2	Concave	753.7	525.1	1.42	yes	-	-	-	-

together with the ratio of V_I to the plate V_{50} are noted in Tables 4.1 to 4.3, where the shots are tabulated in ascending order of impact velocity. Shapes that have a bias in a certain direction are listed together with the corresponding direction of bias, d_s or d_c . Since tissue damage caused by the projectile in personal armour applications is of much greater concern than the back face deflection of the laminate in perforation cases, the BFD is analysed only in arrest cases.

Laminates with $r = 20$ in were found in Section 4.4.1 to behave very similarly to flat plates under ballistic impact, with the maximum bulge height and deflection shape of the curved plates corresponding to those with no curvature. Two-dimensional in-plane analysis of the BFD in Fig. 4.32 reveals much of the same post-impact deformations as were observed for the 10 mm diameter steel ball projectile. As summarised in Table 4.1, the majority of shots on the shallowest plate curvature yield rhombus-shaped zones of damage. These zones translate to through-thickness deformations such as delamination and out-of-plane bulging on the rear

Table 4.3: Identifying shape and extent of in-plane back face deflection as a percentage of plate size in arrest cases, presented in ascending order of V_I for $r = 5$ in.

$r = 5$ in $d_s = 300$ mm $s = 260$ mm									
Shot number	Direction	V_I [m/s]	V_R [m/s]	V_I/V_{50}	Perforation	BFD shape	BFD size [mm ²]	BFD size [%]	Notes
1	Convex	337.7	0.0	0.58	no	Rhomboid - d_s	2113.6	2.7	Overlap
3	Convex	584.1	0.0	1.01	no	Rhomboid	8419.7	10.8	Overlap
1	Convex	585.0	0.0	1.01	no	Elliptical - d_s	9287.7	11.9	Overlap
1	Convex	604.6	167.1	1.04	yes	-	-	-	-
1	Convex	608.7	192.2	1.05	yes	-	-	-	-
2	Convex	614.1	0.0	1.06	no	Rhomboid	11002.1	14.1	Overlap
1	Convex	648.3	282.7	1.12	yes	-	-	-	-
2	Convex	693.5	372.3	1.19	yes	-	-	-	-
1	Convex	761.5	463.0	1.31	yes	-	-	-	-
3	Concave	485.5	0.0	0.91	no	Rhomboid - d_c	2716.9	3.5	Overlap
2	Concave	520.9	0.0	0.98	no	Rhomboid - d_c	4578.8	5.9	Overlap
3	Concave	526.4	0.0	0.99	no	Rhomboid - d_c	3658.7	4.7	Overlap
2	Concave	558.7	148.3	1.05	yes	-	-	-	-
3	Concave	559.4	0.0	1.05	no	Rhomboid - d_c	4591.8	5.9	Overlap
3	Concave	603.1	226.0	1.13	yes	-	-	-	-
2	Concave	626.6	249.4	1.17	yes	-	-	-	-
2	Concave	646.7	315.9	1.21	yes	-	-	-	-
3	Concave	764.6	499.5	1.43	yes	-	-	-	-

face. This formation possesses a strong resemblance to the BFD shape of a four-sided pyramid reported in Section 4.4.1 for panels of the same curvature.

In the multiple concave impact cases presented here, an increase in the strike velocity beyond the ballistic limit estimate does not alter the shape of the BFD. However, as V_I approaches the V_{50} , a significant increase is observed in the size of the damage zone, jumping from 2.6 % of the plate area at $V_I/V_{50} = 0.67$ to 6.2 % at $V_I/V_{50} = 0.95$. Fewer arrest cases are available for comparison in the convex case of targets with $r = 20$ in. Although it is worth noting that at lower impact velocities, where $V_I/V_{50} = 0.62$, both the shape and the size of the BFD are comparable to their respective concave counterparts. Nevertheless, a difference does arise with an increase in the strike velocity to $V_I/V_{50} = 1.03$, where a change in the shape of the BFD to an ellipse with a bias in the direction of the longitudinal non-curved dimension of the plate is accompanied by a very notable growth of the BFD coverage, from 2.4 % to 17.8 % of the plate surface area.

Reducing the radius of the target curvature to 10 in demonstrated a similar trend in the BFD shape and size of concave impact cases at comparable strike velocities, as inferred from the images in Fig. 4.33 and alluded to in Table 4.2. The rhombus-shaped BFD referred to previously appears to be more skewed for this radius of curvature. To make a distinction between the two shapes, the more skewed quadrilateral with unequal sides is referred to as a rhomboid shape instead. As before, an increase in the impact velocity causes a leap in the BFD size, accompanied by a transformation of its shape into an elliptical form inclined to deform along the longitudinal direction, and in the case of a third shot, with a bias along the direction of curvature.

Meanwhile, for a given value of V_1/V_{50} , the concave shots demonstrate a similar behaviour in the variation of the damage zone coverage for targets of shallower curvature. At the lower end of the impact velocity range however, the shape of the damage zone takes the form of a quadrifolium, subsequently transforming into a rhombus. In one convex case, an unusually large BFD coverage of 21 % is noted to have also overlapped with a different shot on the same target. Since this was the first shot taken, it is unlikely that the overlap is responsible for the excessively large damage coverage. It was initially hypothesised that the damage zone increased in size following the third impact on the target in the opposite direction to the first. This was investigated and was shown to be incorrect by comparing images taken following the first and the third shots on this plate, visible in Fig. 4.35.

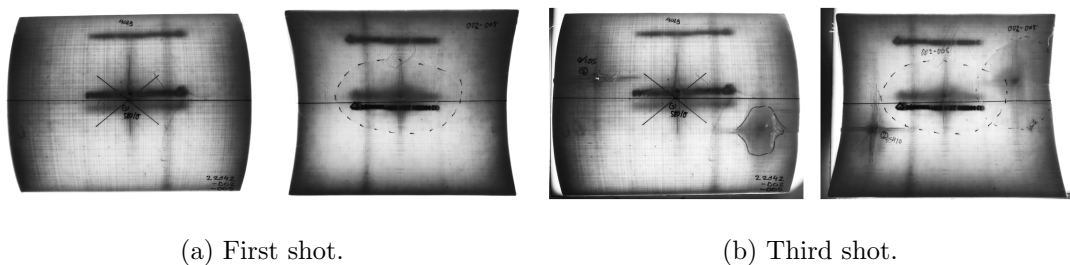


Figure 4.35: Light table images used to detect interaction between multiple damage zones arising from the primary shot and subsequent shots on the same laminate.

In the panels with the highest curvature, every concave and convex arrest case was subjected to overlap of the damage zones caused by multiple shots on a single panel, visible in Fig. 4.34 and listed in Table 4.3. This was not attributed to the sheer size of the damage zones as these remained consistent with the sizes measured in the less curved laminates over the range of impact velocities that were considered. It is instead the nature of the resulting BFD shapes providing the conditions for and promoting overlap between these regions. For example, the

rhomboid or elliptical zones arising from convex impact have a tendency to align with the longitudinal, or straight, dimension of the plate, while all the concave shots favour the lateral dimension that coincides with the direction of curvature. A biased damage zone coverage leads to larger expansions of the zone from the site of impact in one direction, making the overlap of regions more likely to occur.

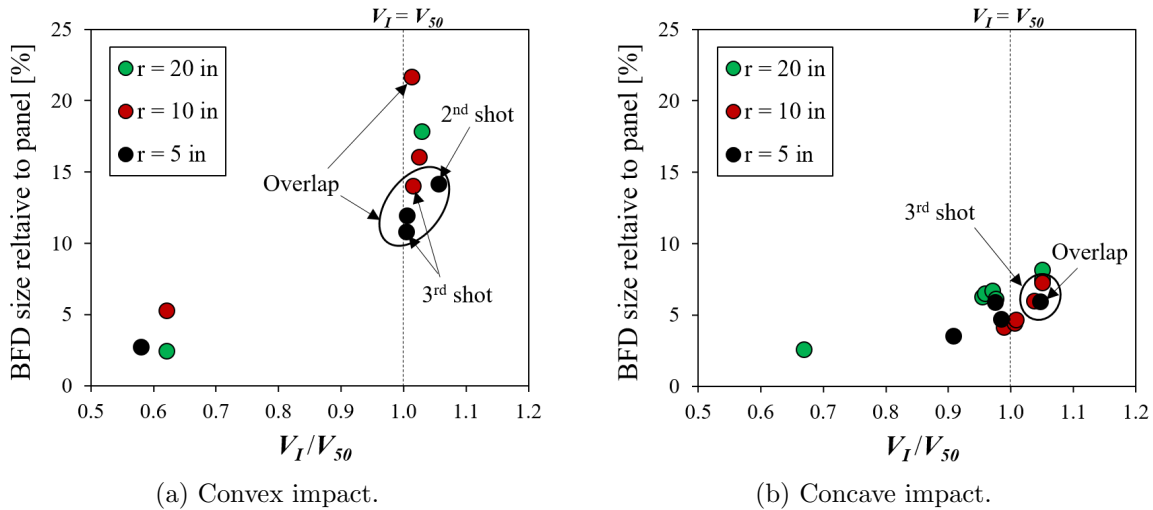


Figure 4.36: In-plane back face deflection size of arrest cases as a percentage of total laminate surface area plotted against normalised impact velocity.

To facilitate an understanding of the relationship between impact velocity, radius of curvature and the subsequent BFD size, represented here by the extent of damage observed on the rear face, the visible damage area is plotted as a percentage of the total panel surface area against impact velocity. The impact velocity is normalised with the V_{50} approximation for each configuration deduced from Fig. 4.26. The data points are plotted in Fig. 4.36, for both the convex and the concave impact cases. In both cases, the shots for which the value of V_I exceeds the target's V_{50} , any observations of overlap between the multiple shots on a single target are labelled. Likewise, secondary and tertiary shots with strike velocities greater than the ballistic limit are noted for convex plots, with the remainder representing primary shots. The same convention is used for the concave cases, although only tertiary shots above $V_I/V_{50} = 1$ are labelled, as the remaining points depict only secondary shots.

The trends in these graphs suggest similar behaviour between concave and convex impact cases at lower velocity ratios of $V_I/V_{50} = 0.6$ to 0.7 . For V_I/V_{50} ratios in the proximity of unity however, the BFD size for the majority of concave cases remains below 10% of panel size, while a coverage of 10% to 20% is predominant in the convex cases around this velocity ratio. In

contrast to the direction of impact, the radius of curvature, the order of shots and the presence of overlap in the damage zones do not appear to be determining factors for the BFD size, as no clear trends can be established from Fig. 4.36 for these variables. Nevertheless, it can be said that although overlapping of damage zones may not significantly affect the size of each zone, the shape of the damage zone was observed to be slightly sensitive to the coalition of deformations, as described in Tables 4.2 to 4.3.

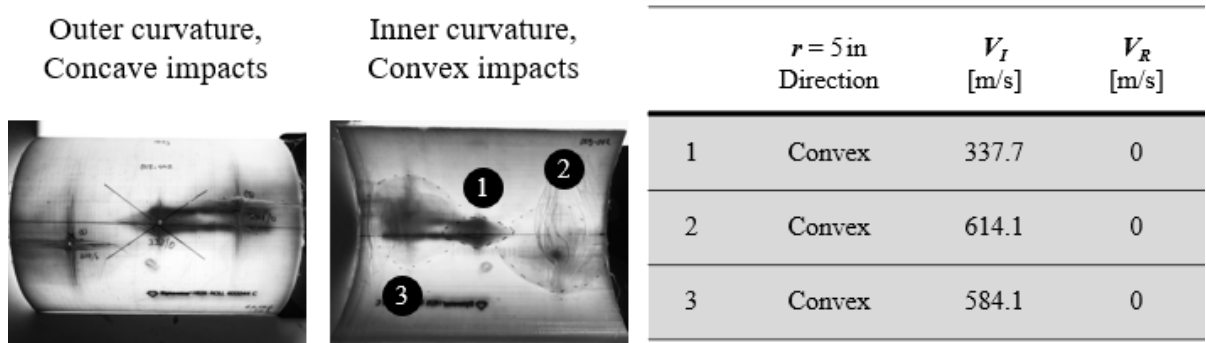


Figure 4.37: Light table images of the specimen selected for internal deformation analysis of the cross-section.

Since it was not possible to distinguish between in-plane and out-of plane deformations, or to determine the actual zones of damage from the overall BFD with the light-table images, some of the laminates were cut open with water-jet cutter at the site of impact, to enable the inspection of the through-thickness dimension. To investigate the interaction of multiple shots in more detail, cross-sectional views of an example laminate of the highest degree of curvature with multiple overlaps, recalled in Fig. 4.37, are presented in Fig. 4.38. However, as the laminate was cut along the sites of impact, damage zone interaction was not visible as these regions of overlap occurred far away from the impact site and the path of the primary fibres, as had been intended. Shots 2 and 3 were selected for comparison due to the similarity in V_I and the resulting BFD. Shot 2 was cut along the non-curved dimension of the plate from A_1 to A_2 , while shot 3 was cut along the curved dimension from C_1 to C_2 , as detailed in Fig. 4.38.

From observations of previous examples of the most highly curved laminates, a greater degree of compliance along the straight dimension gives way for more extensive deformation in this direction, as shown by the 24.1 mm difference in the maximum distance between the shear hinges of the bulges highlighted in Fig. 4.38. Along $A_1 - A_2$, this larger shear progression is accompanied by a bias to one direction. This is the direction with the smallest distance to the edge, and is thus favourable for deformation due to smaller fibre lengths that deform more

readily via membrane action that draws the edges inwards, towards the impact site. However, this asymmetrical deformation is not replicated along $C_1 - C_2$, due to the similar distance from the location of impact to the laminate edge on either side, along the curved length.

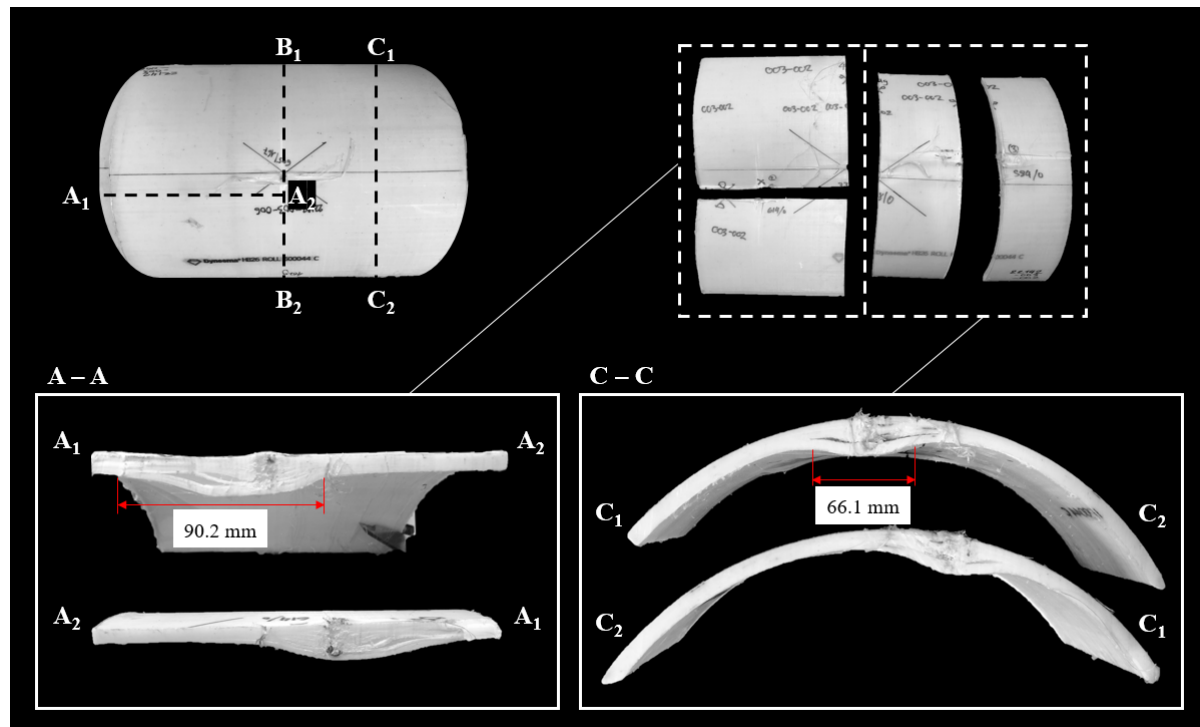


Figure 4.38: Cross-sectional inspection of a specimen to analyse post-impact, internal through-thickness damage.

The following points summarise the deformations observed in the most highly curved convex impact cases, as seen in the cross-sectional inspection in Fig. 4.38, viewed along $A_1 - A_2$, the non-curved dimension, in relation to the deformation along $C_1 - C_2$, the curved dimension of the plate. Along the straight dimension:

- (a) The bulge is one-sided, favouring the direction in the closest proximity to the edge.
- (b) The shear hinge of the bulge has progressed further.
- (c) The apex deflection is larger.
- (d) The BFD peak is spread out over a more extensive area.
- (e) The projectile has travelled further through the thickness of the laminate, resulting in a larger depth of penetration.
- (f) There are more delamination planes with vast extents of mode I deformation.

The cross-sectional views along both dimensions do however demonstrate typical deformation behaviour observed in flat UHMWPE laminate subjected to single-point ballistic impact, showing signs of progressive penetration of layers and their subsequent delamination.

So far, the final state of the laminates post-impact have been investigated. From here onwards, the focus is shifted to the high speed photographs that capture how these deformations evolved over the duration of the impact event. Montages of stills at 0.025 ms intervals demonstrate the development of the back face deformations, while overlays of images provide a tool for analysing the path of the projectile. Subsequently, the development of the bulge on the back face of the target is analysed for multiple arrest cases via apex deflection, shear hinge progression and the trace of the bulge shape. The majority of montages are not provided here due to impracticalities involved with doing so, but are briefly touched upon later in this chapter. The evolution of the back face bulge under impact is quantified using measurements obtained from the high speed images, at a later stage in this chapter. In addition, overlay images of the impact event are provided for a selection of cases for visualisation purposes and for projectile path comparison.

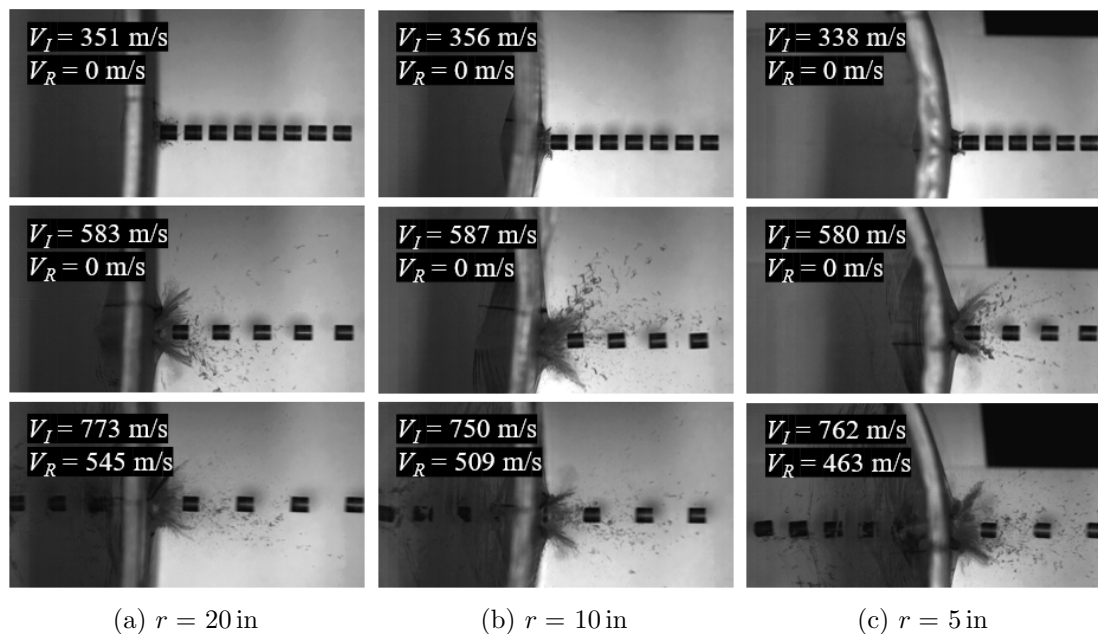


Figure 4.39: Overlaid high speed photographs for analysing projectile path and laminate damage under impact, for varying degrees of curvature under three ranges of impact velocity in the convex direction.

Figure 4.39 displays three ranges of impact velocity cases for the three radii of curvature

investigated under convex impact, in order of increasing impact velocity. The strike face exhibits fibre breakage, with particles propelled outwards as the projectile penetrates the target. The intensity of the scattering of the material increases with higher impact velocities, in cases where the projectile is caught. This effect does not intensify for increasing V_I values beyond the perforation stage, and is observed to a similar extent in all three degrees of curvature. Although at $r = 10$ in and $r = 5$ in, the number of scattered particles, their outward range of expansion, and the distance travelled by them are substantially higher than plates with the lowest degree of curvature. Projectile path prior to impact is reasonably straight, unaffected by external factors, and can be considered as non-oblique in the majority of shots. Meanwhile, perforation cases show that in the two most curved panels, loosened fibres that have been pulled away from the rear surface of the laminate during the exit stage, in addition to gravity, do play a role in hindering the movement of the projectile while altering its path, albeit to a small degree. Nevertheless, this reinforces the idea that the velocity gate measurements do not fully capture the resultant residual velocity magnitude of the projectile, but only its one-dimensional horizontal component.

From the following images in Figs. 4.40 to 4.42, it can be seen that diversions in the projectile path are minimal in the in-plane direction normal to the impact direction. It is rather the rotation of the projectile about its own axes that is not captured by the light gates, which does not affect the magnitude of the velocity captured by the light gates, rendering these recordings appropriate for use in V_{50} approximations. It must be noted however, that the high speed video captures a very limited range of the projectile path, not covering the full range of motion up to the distances where velocity measurements were recorded. Thus, it is possible that the resultant magnitude of the projectile exit velocity could be slightly higher than the single horizontal component captured, resulting in a small overestimation of V_{50} values and material performance. Nevertheless, this effect is assumed to be consistent over the range of impact cases and hence should not affect measurements of difference between impact cases of varying curvature or impact direction. Analysis of the high speed video revealed that only minimal differences ($\pm 5\%$) exist between these measurements and those obtained by the light gates, confirming the validity of the experimental approach used in the current study.

Corresponding cases for concave impact are presented in Fig. 4.40. These display much of the same behaviour that was observed in convex impacts, except for the perforation of the laminates at the middle range of impact velocities considered. This was anticipated due to the

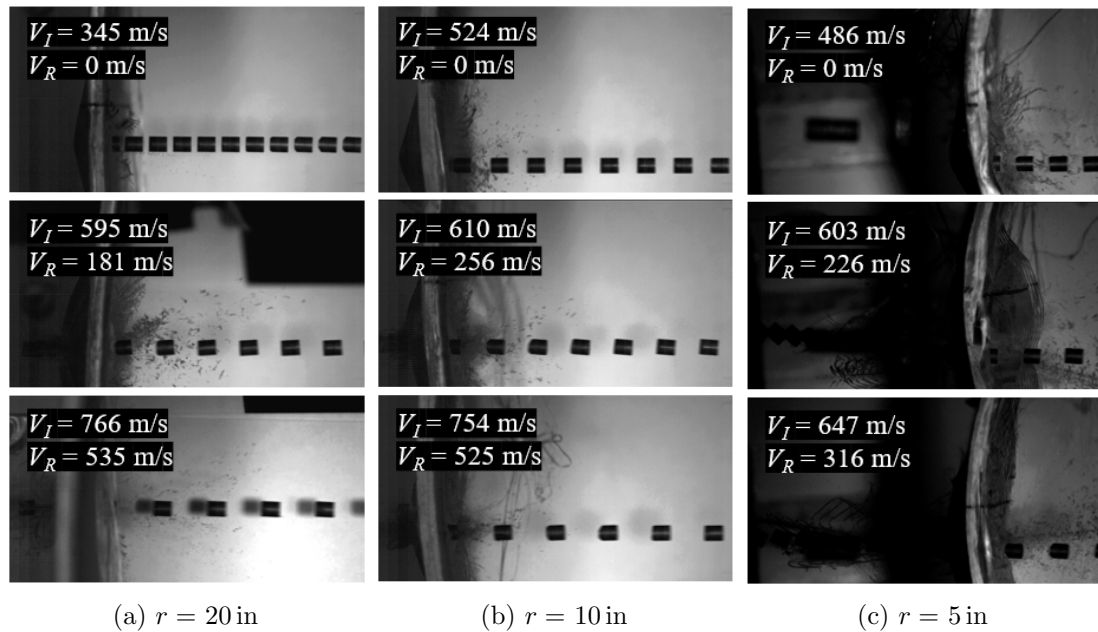


Figure 4.40: Overlaid high speed photographs for analysing projectile path and laminate damage under impact, for varying degrees of curvature under three ranges of impact velocity in the concave direction.

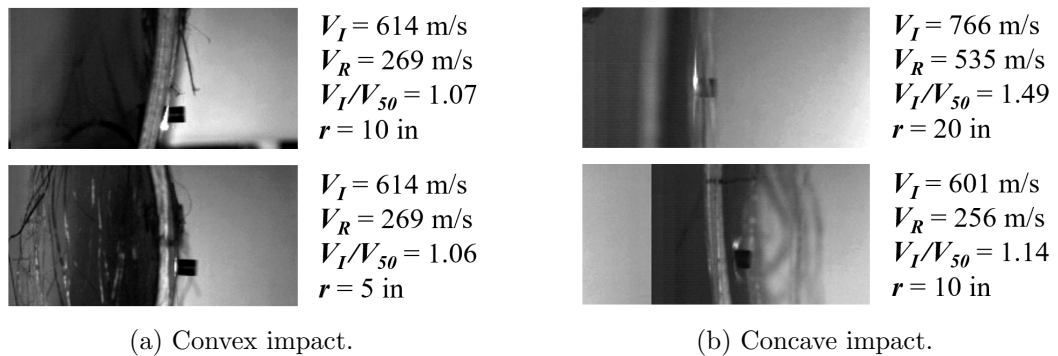


Figure 4.41: High speed images capturing impact flashes at a variety of impact velocities and directions.

significantly lower V_{50} of the plates in the concave direction, as previously shown in Fig. 4.26. The deformation of the target should not be analysed from these images as the convex cases were all taken as secondary or tertiary shots, with likelihood of interactions between the damage zones of the various shots. In addition, impact flashes exhibiting similar characteristics were captured in both directions of impact for all three curvatures tested, as visible in Fig. 4.41.

In a similar manner, the effects of the shot order was checked to determine whether the shot number is a critical factor in the impact deformation of the target, as displayed in Fig. 4.42. The cases inspected include convex cases at two similar strike velocities, considering primary shots on the most extreme curvature cases and at corresponding V_I values for the secondary

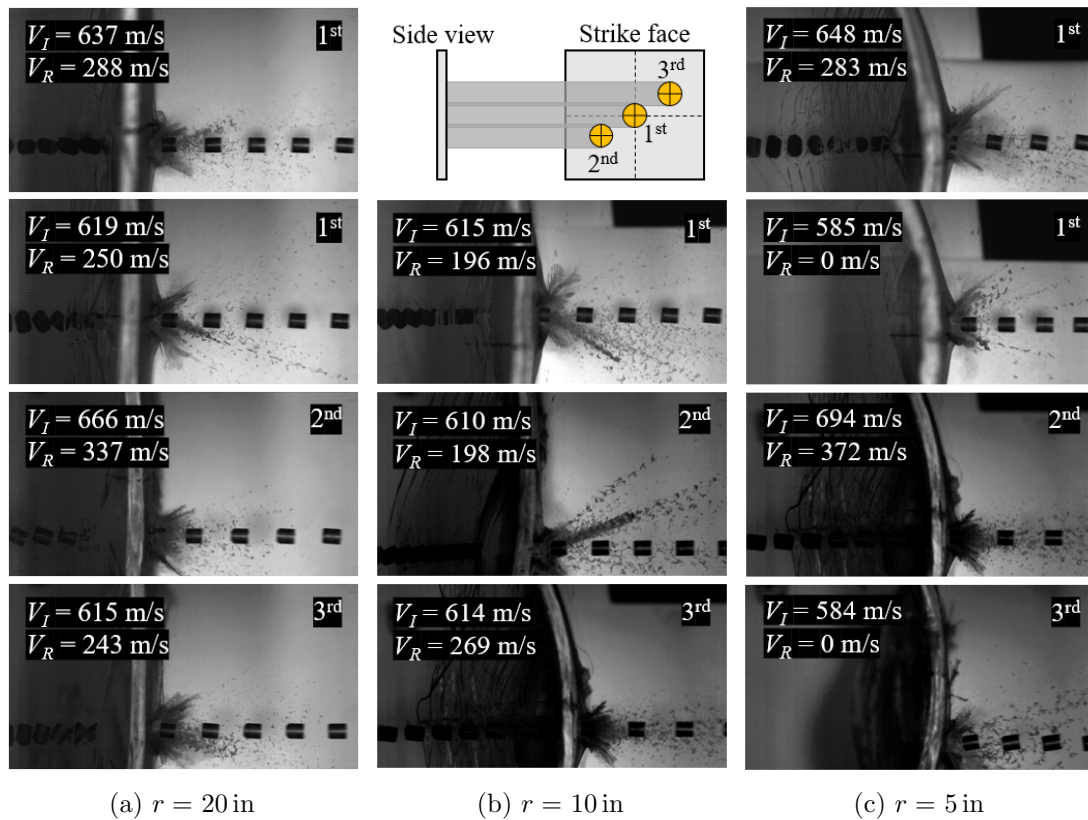


Figure 4.42: Overlaid high speed photographs for analysing projectile path and laminate damage under impact, for varying degrees of curvature under three subsequent shots in the convex direction.

and tertiary shots. Similarities can be drawn between the different shots in terms of particle scatter on the strike face and bulging on the rear face, as well as twisting, rolling and tumbling of the projectile following its exit through the rear face. No discernible variations were identified between the different shot numbers that were not also visible among varying plate curvatures or between cases of preliminary shots.

Furthermore, the evolution of the bulge during projectile arrest is quantified and a comparison is provided for laminates of varying degrees of curvature and impact direction in Figs. 4.44 to 4.52. Apex deflection, representing maximum bulge height, was measured as the distance between the peak of the out-of-plane deformation and the flat, undeformed surface edge of the plate. It is worth noting that the undeformed edge was assumed to be equal to the out-of-plane location of the rear face of the plate prior to impact, accounting for whole-plate motion during the impact event. The shear hinge was defined here as the in-plane distance from the point of impact to the corner of the bulge on the back face. For simplicity, the progression of the

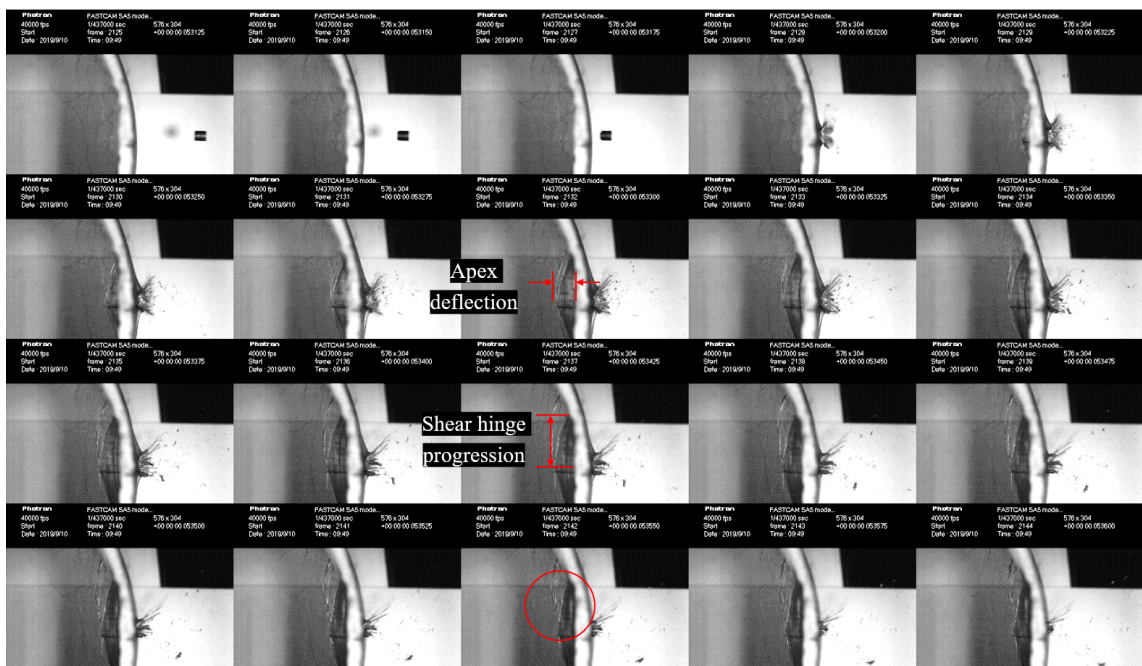
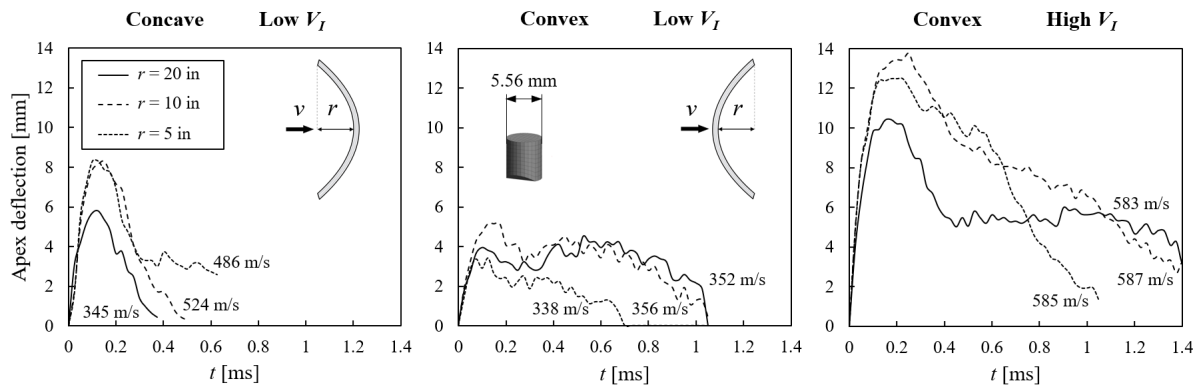
(a) $r = 20$ in(b) $r = 5$ in

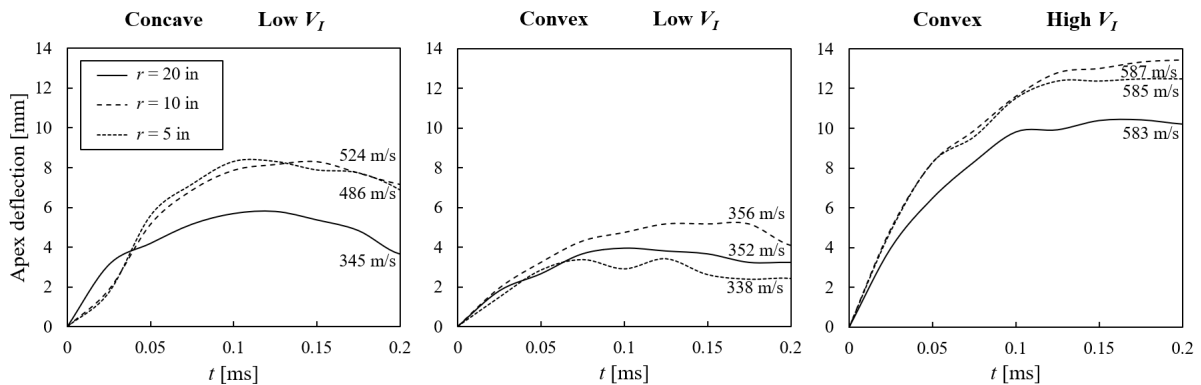
Figure 4.43: Montages of high speed photography at 0.025 ms intervals for the most extreme radii of curvature tested.

shear hinge was assumed to be symmetric about the out-of-plane axis. The measurements were obtained as outlined in Fig. 4.43, for two convex cases of minimum and maximum degrees of curvature. These parameters are evaluated over t , the time after initial contact. To derive

the value of t in each image, the time at impact since the beginning of the recording, t_0 , was calculated and combined with the time interval at each image. The value of t_0 was calculated using the velocity of the projectile directly before impact and the distance remaining to establish contact, neglecting the minimal effects of drag for this short duration.



(a)



(b)

Figure 4.44: Apex deflection of laminates with varying degrees of curvature, for the three impact cases of concave at low velocity (LHS), convex at low velocity (centre), and convex at high velocity (RHS), over a duration of (a) 1.4 ms and (b) 0.2 ms after impact initiation.

To begin with, three impact scenarios are considered as before; concave impact at the lowest strike velocity range that was recorded for each curvature, convex impact at velocities close to V_I 350 m/s and well below the corresponding ballistic limit of each laminate given in Fig. 4.26, together with convex impact at velocities of approximately V_I 585 m/s, closer to target V_{50} estimates. Datasets at a higher range of strike velocities were not available in the concave direction as per the convex case, due to the earlier onset of target perforation under this

direction of impact on curved plates. The apex deflection results are presented in Fig. 4.44(a), up to the point where the projectile has exited the front face through its rebound motion, and can be observed in more detail for the initial stages of impact in Fig. 4.44(b). The following observations are noted:

- (a) In all the cases visible here, the maximum apex deflection representing the bulge peak is reached just before 0.2 ms.
- (b) The profile of the apex deflection over the period of impact for the high V_I convex cases are reminiscent of the low V_I concave shot profiles, with a rapid increase in the deflection followed by an equally rapid decline. The magnitudes of the deflections in the convex cases are almost double the values of those seen in the concave cases, and evolve over durations that are twice as long.
- (c) The low V_I convex profiles peak at significantly lower values and remain at a relatively constant level before slowly retracting over time.
- (d) The majority of the low V_I impact cases for both concave and convex impact display fully elastic behaviour, retracting to the original position over the course of the impact event, while the high V_I case displays some degree of inelastic deformation. The full extent of this deformation cannot be obtained from the data as a longer duration of time needs to be considered for examination of plastic apex deflection.
- (e) A closer look at the initial impact regime in Fig. 4.44(b) reveals the substantial degree of similarity in the behaviour exhibited by the most highly curved plates, with the exception being the low V_I convex cases, where the large gap between the apex deflection profile of the two most highly curved plates can be attributed to the disparity of almost 20 m/s in the V_I values.
- (f) The lower gradient and peak of the target with $r = 20$ in in the low V_I concave cases could also be attributed to the lower impact velocity relative to the other two plate curvatures. Although the difference in strike velocity is minimal in the high V_I convex impact cases, some disparity between the curves still exists.

Due to the large spread of impact velocities, it was not possible to accurately draw comparisons between the concave and convex impact case. To simplify this, the apex deflection

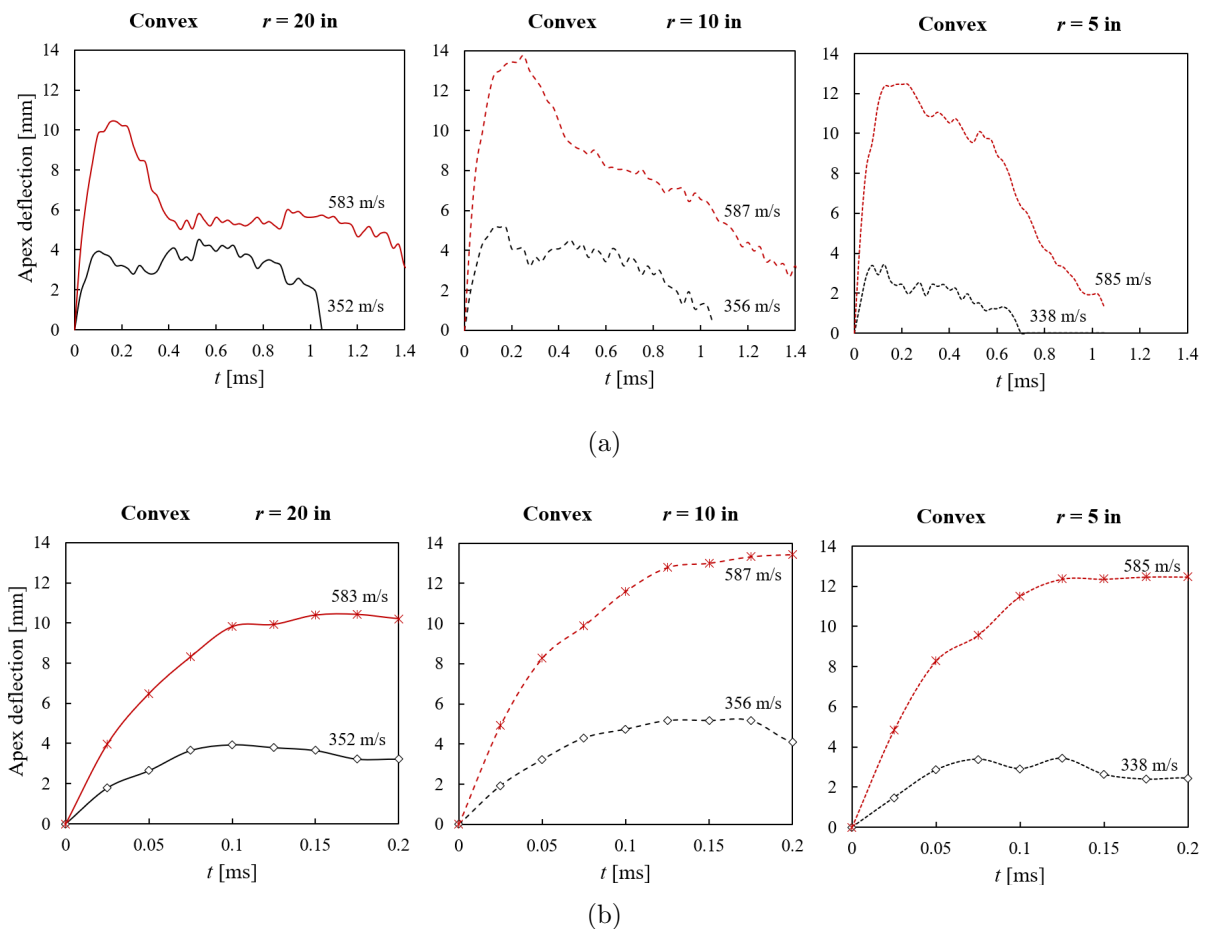


Figure 4.45: Apex deflection of laminates with varying degrees of curvature under convex impact for two ranges of impact velocity, over a duration of (a) 1.4 ms and (b) 0.2 ms after impact initiation.

profiles of two velocity cases are presented in the same manner as was done previously, at each radius of curvature for convex and concave cases in Fig. 4.45 and Fig. 4.46, respectively. The two velocities of impact used in the comparisons were selected based on similarity and availability of data at all target curvatures considered. Under convex impact, the two velocities lie at different positions along the spectrum of impact velocities tested; well below the initiation of perforation and just below the ballistic limit. By contrast, the two velocities of interest in the concave cases are more aligned in terms of magnitude, due to the earlier onset of perforation in this direction, and hence the lack of data at higher impact velocities. These similar velocity cases can, nonetheless, provide a perspective in terms of the repeatability of the acquired data.

Figure 4.45(a) displays similar apex deflection profiles between the three plate curvatures tested in the convex direction, at a lower impact velocity range of 338 m/s to 356 m/s, and at the higher velocity range of 583 m/s to 587 m/s over a 1.4 ms duration. Close-up views of the initial

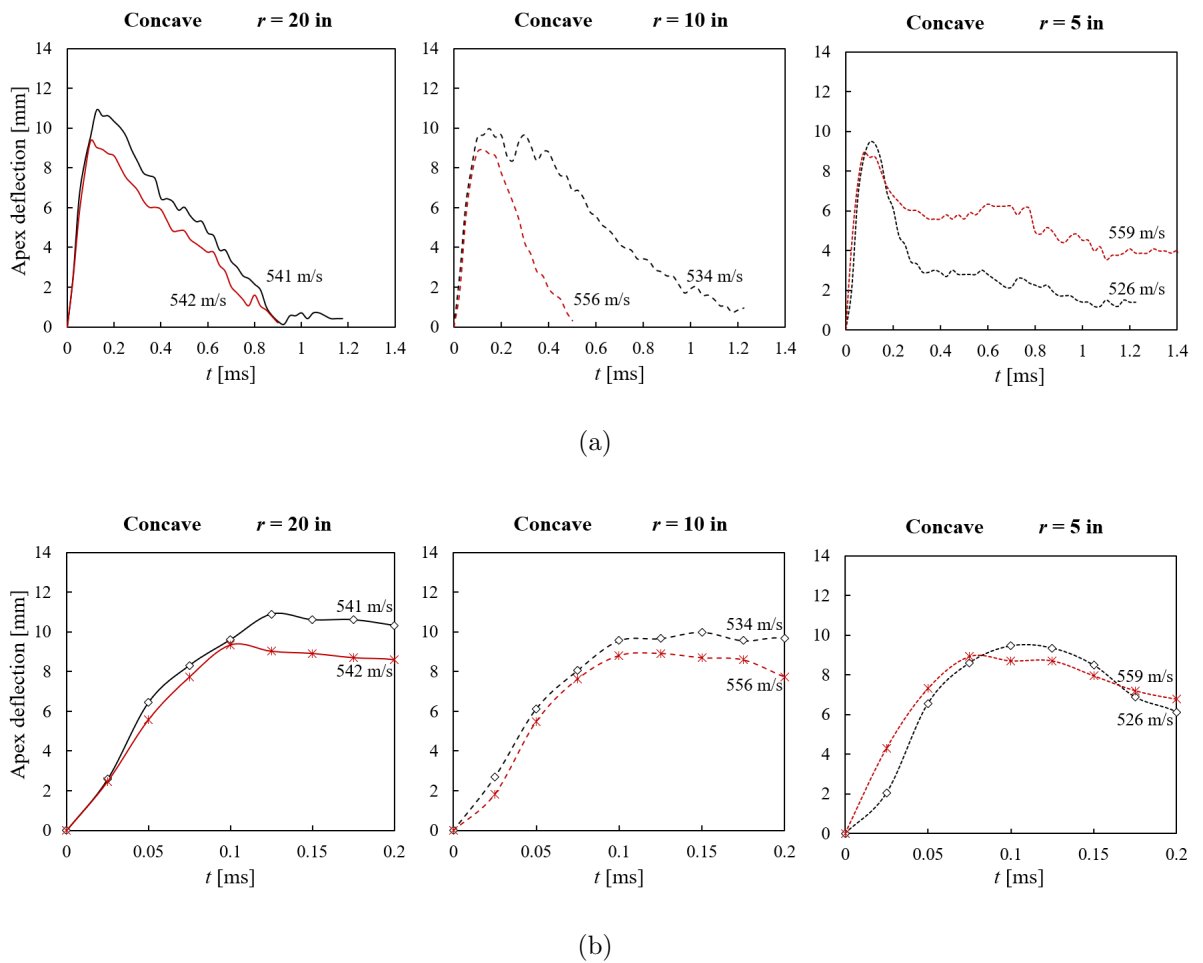


Figure 4.46: Apex deflection of laminates with varying degrees of curvature under concave impact for a single range of impact velocity, over a duration of (a) 1.4 ms and (b) 0.2 ms after impact initiation.

stages of impact in Fig. 4.45(b) reveal that at the lower velocity range, different plate curvatures yield similar maximum values of BFD, ranging from 3.4 mm to 5.2 mm. At the higher impact velocity range however, the 10.4 mm maximum apex deflection of the target with $r = 20$ in is noteworthy compared to 13.8 mm and 12.5 mm for the two higher degrees of curvature. For concave impact, the shots taken at similar velocities display similar deformations in the apex of the back face bulge, most significantly in terms of the peak value and the profile within the first 0.2 ms of impact, visible in Fig. 4.46. For all three curvature cases, the out-of-plane emergence of the bulge is almost identical at the different shots, while its retraction occurs at substantially different rates over the course of the 1.4 ms considered.

To visualise the variation in the relationship between impact velocity and maximum out-of-plane BFD at different plate curvatures, the impact velocity, normalised by the ballistic limit in each case, is plotted against the peak apex deflection, δ_{\max} , for all arrest cases in Fig. 4.47. A dataset for the flat panels from [50] is also included for comparison. Those flat panels were also manufactured from HB26, laid-up in cross-ply formation, and possess comparable thickness and areal density values of $h_t = 6$ mm and $AD = 5.89$ kg/m². In the current study, the nominal laminate thickness and the measured thicknesses are consistent with this. The areal density, AD , of the curved panels ranges from 5.14 kg/m² to 5.28 kg/m², as calculated with the curved length,

$$AD_{\text{curved}} = \frac{m_t}{d_s S}, \quad (4.6)$$

or from 5.61 kg/m² to 5.95 kg/m², considering the straight length, equivalent to the dimensions of a flat plate,

$$AD_{\text{straight}} = h_t \rho, \quad (4.7)$$

with m_t representing the target mass and ρ its nominal material density. However considerable differences do exist between the two studies. These include the BFD measurement technique that was employed; Moiré interference fringe patterns [50] against measurements of the apex deflection from the side in the current work, the projectile used for impact; 8.3 g steel ball [50] versus a 1.1 g flat-faced FSP used here, and the boundary conditions of the target; clamped [50] versus free-standing in the current study.

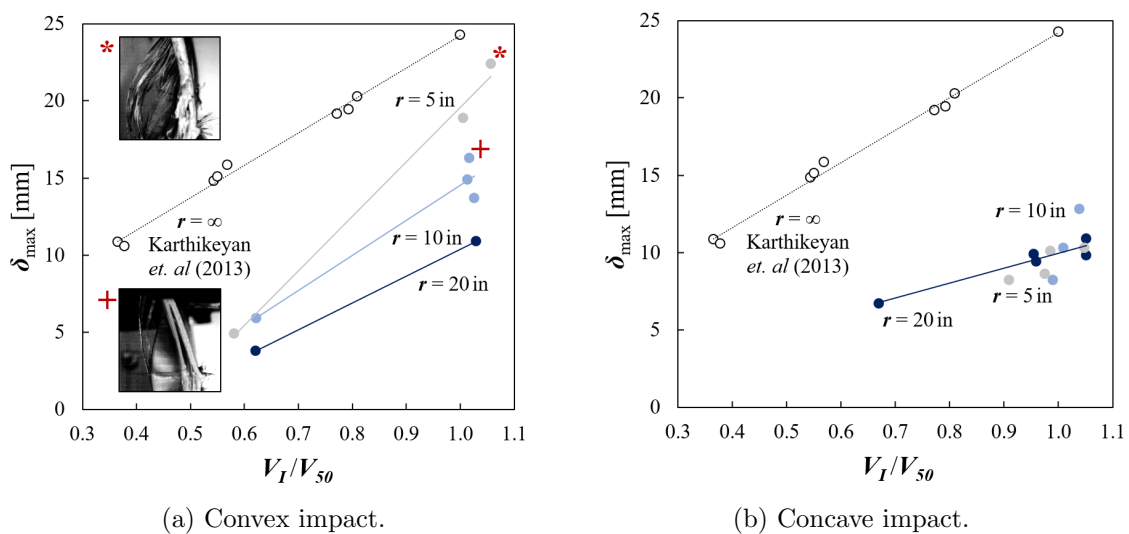


Figure 4.47: Maximum out-of-plane back face deflection plotted as a function of the normalised impact velocity.

The convex cases in Fig. 4.47(a) show a linear increase in δ_{\max} with increasing $\frac{V_I}{V_{50}}$ in all three panel curvatures as the velocity ratio approaches unity, considering a limited range of $\frac{V_I}{V_{50}}$ values. This resembles the behaviour observed for a flat plate, where the maximum BFD scales linearly with the normalised impact velocity. As the radius of curvature is reduced, the gradient of the line increases, so that although plates of varying curvature produce similar degrees of deflection at $\frac{V_I}{V_{50}} = 0.6$, the extents of the peak deflections diverge at $\frac{V_I}{V_{50}} = 1$, with much larger deflections observed in more curved laminates. Accurate measurements of the exact extent of this increase were challenging at the higher degrees of curvature, due to the various deformations induced under impact velocities close to the ballistic limit. Examples of these obstacles are given in the insets in Fig. 4.47(a) and include extensive fibre pull-out and increasing shear hinge angles, as a result of a rapidly expanding bulge face and shear hinge progression towards the edge of the laminate, thereby masking the apex location. The trend in the slope of the different plots is in line with the shallower slope of the flat plate data reproduced from [50], despite differences in the magnitudes which are attributed to the slightly different projectile and different measurement techniques employed.

In comparison, at $r = -20$ in, when the direction of impact is reversed to concave, the rate of increase in δ_{\max} for an increasing velocity ratio is reduced, as displayed in Fig. 4.47(b). A best-fit relationship cannot be established for the higher degrees of curvature in the concave cases, due to the lack of data at lower $\frac{V_I}{V_{50}}$ ratios. Measurements at lower velocity ratios are necessary, in order to establish a relationship over a sufficiently large range of velocities, in light of the spread of data that exists for other configurations and shots at similar impact velocities within close range of one another. To provide a comparison between the different threats employed here and in [50], the impact velocity was normalised with the projectile mass, m_p and subsequently plotted as the initial kinetic energy of the projectile, $KE_p(t_0)$, where

$$KE_p(t_0) = \frac{1}{2}m_p V_I^2 \quad (4.8)$$

to demonstrate its effect on δ_{\max} in Fig. 4.48. From these plots it can be seen that the impact scenarios investigated in [50] are up to 600 kJ higher in terms of the magnitude of the projectile kinetic energy, than the maximum energy levels considered in this study. For comparable impact energy values of around 600 kJ, data for the flat plates tested in [50] display δ_{\max} values that are comparable to the higher degrees of curvature in the convex direction, presented in Fig. 4.48(a), but are more in line with the shallower curvature in the concave direction in Fig. 4.48(b).

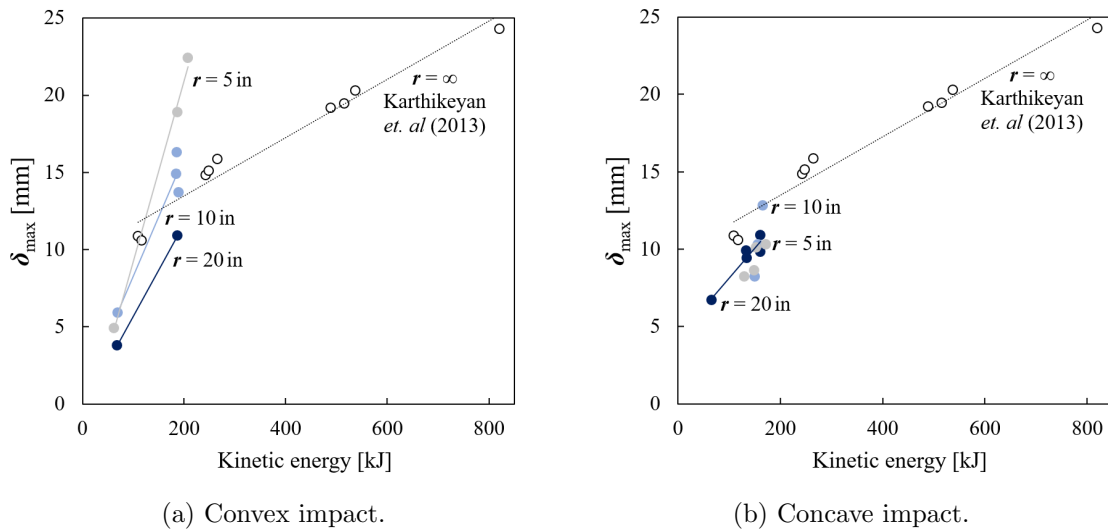


Figure 4.48: Maximum out-of-plane back face deflection plotted as a function of the projectile kinetic energy.

Following on from the out-of-plane deflection analysis of the apex, the in-plane deformation of the back face bulge under impact is analysed via the progression of the shear hinge. The shear hinge progression results are presented in Fig. 4.49(a) for the complete duration of impact, and in Fig. 4.49(b) for the initial stages up to 0.2 ms following the initiation of contact, for the concave and convex impact cases considered earlier for the apex deflection analysis. The following observations are noted:

- (a) The profile of the shear hinge progression over the period of impact is relatively similar for the different curvatures considered, but is nevertheless unique to each combination of strike velocity and impact direction.
- (b) As per the apex deflection regime, the low V_I convex shear hinge progression profiles peak at significantly lower values than the other two cases and remain at a relatively constant level, before slowly retracting over time, while the low V_I concave profiles show abrupt increases and retraction rates. The high V_I convex cases however, display a similarly large rate of increase to the maximum value, which is then followed by a slower retraction, spanning the full course of impact duration considered here. The peak values for these shots are also the highest of the three cases considered, in line with the apex deflection trends.
- (c) The majority of the impact cases considered, particularly at the higher velocities, exhibit a behaviour dominated by elastic deformation. However, a much more significant element

of inelastic behaviour is visible in the shear hinge movement compared to the deflection of the apex. This disparity could be due to the apex deflection measurements only displaying the out-of-plane deformation of the bulge at a single point, therefore not reflecting the true range of motion in the bulge. The out-of-plane displacement of the bulge at the shear hinge in the circled high speed photograph stills in Fig. 4.43(b) provides an example of a situation such as this.

- (d) A closer look at the initial impact regime in Fig. 4.49(b) reveals no considerable trends in the shear hinge progression based on the plate curvature. This relationship is explored in further detail in the following section of this chapter.

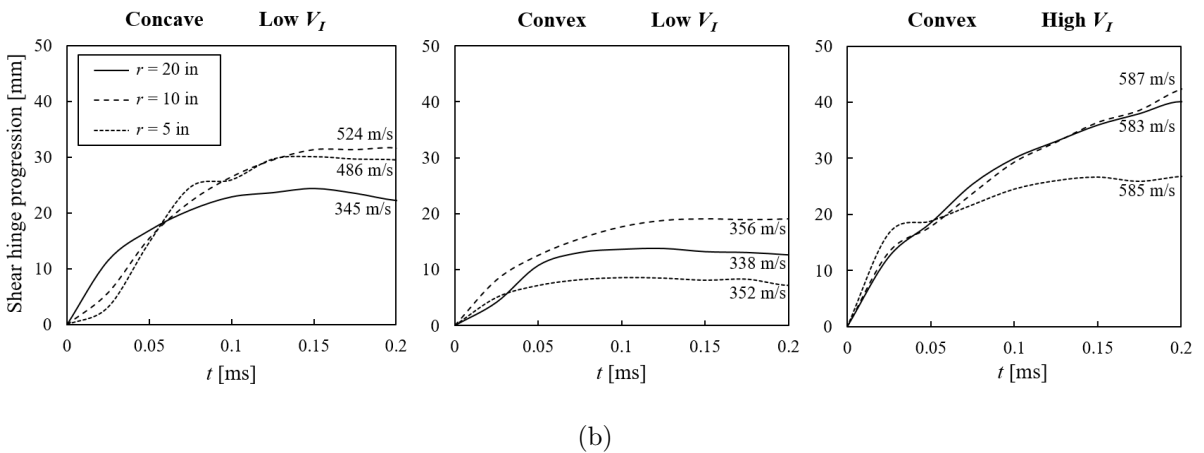
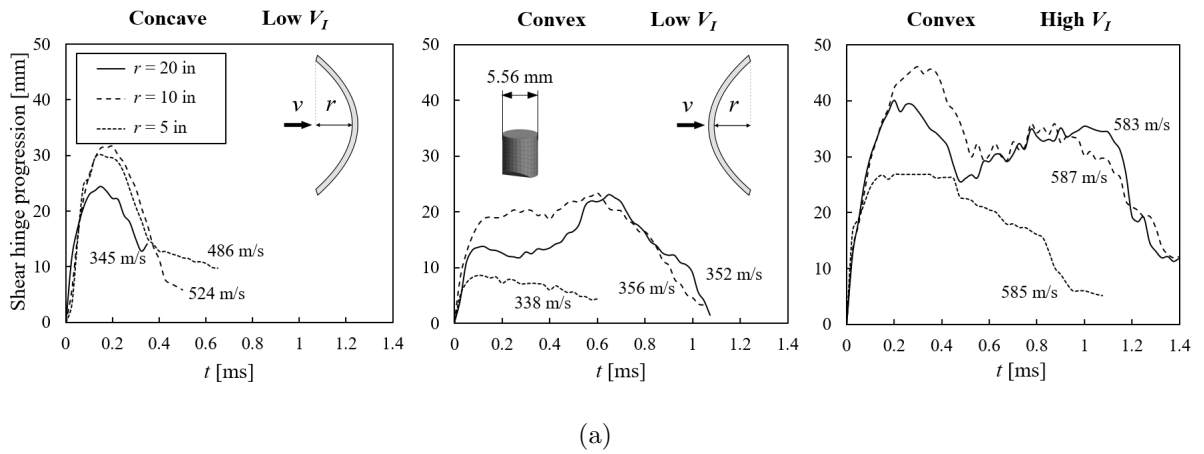


Figure 4.49: Shear hinge progression of laminates with varying degrees of curvature, for the three impact cases of concave at low velocity (LHS), convex at low velocity (centre), and convex at high velocity (RHS), over a duration of (a) 1.4 ms and (b) 0.2 ms after impact initiation.

Figure 4.50(a) displays shear hinge progression profiles for the two shallowest curvatures tested in the convex direction, for both a low and a high range of impact velocities, over the

full 1.4 ms course of impact considered. At the lower velocity range of 352 m/s to 356 m/s, an initial spike in the progression of the shear hinge is followed by a slow ascent to a maximum value at approximately 0.6 ms in both instances, following a similar trend as the apex deflection. This behaviour is attributed to the motion of the projectile with the laminate, where the initial impact velocity is not sufficient for full perforation, causing the projectile to rebound against the surface of plies that have already been penetrated. This results in the retraction of the bulge both in-plane and out-of-plane, from interval 1 to 2 in Fig. 4.51, followed by a second wave of movement in the initial direction of motion, inducing an even larger in-plane expansion of the shear bulge. This is shown by the second expansion of the shear hinge from interval 2 to 3 in Fig. 4.51, before the projectile fully exits the laminate from the front face in a reversed direction of motion. The second outward progression of the shear hinge is more expansive as the laminate has already been delaminated from the primary projectile motion and therefore acts much more compliantly under the secondary loading phase.

At the higher velocity range of 583 m/s to 587 m/s, a similar trend is observed in the shear hinge progression profiles, compared to the lower velocity shots. An exception is the impact velocity, which is sufficiently high so that the maximum value peak occurs at around 0.2 ms, at the first peak in the profile, corresponding to the point of maximum deflection. Unlike the apex deflection however, the target with the highest degree of curvature displays the lowest maximum values out of all three curvatures. For $r = 5$ in, the shear hinge peaks at 8.1 mm and 26.8 mm in the low and high impact velocity cases, respectively. The maximum expansion of the shear hinge at this curvature is at the very least 64 % and 33 % lower than the less curved plates, at the corresponding low and high impact velocity ranges.

Although a small increase is observed in the maximum shear hinge progression of the bulge from $r = 20$ in to $r = 10$ in, amounting to approximately 15 % at the higher impact velocity, further reduction in the radius of curvature to 5 in severely restricts the movement of the shear hinge along the direction curvature, as observed in Fig. 4.43(b). This is reflected in the shear hinge progression graphs through a substantial drop in the maximum values. It is worth noting, however, that previous inspections of the final BFD in Fig. 4.34 revealed a bias in the progression of the shear hinge along the non-curved plate dimension, which was not captured in this arrangement. To enable visibility of the projectile and the target BFD, curved panels were positioned with the curved dimension facing the camera at the side used for high speed video recordings. In future tests, an arrangement of mirrors, as employed by Karthikeyan *et al.* [50], could facilitate the capture of deformations along the non-curved dimension.

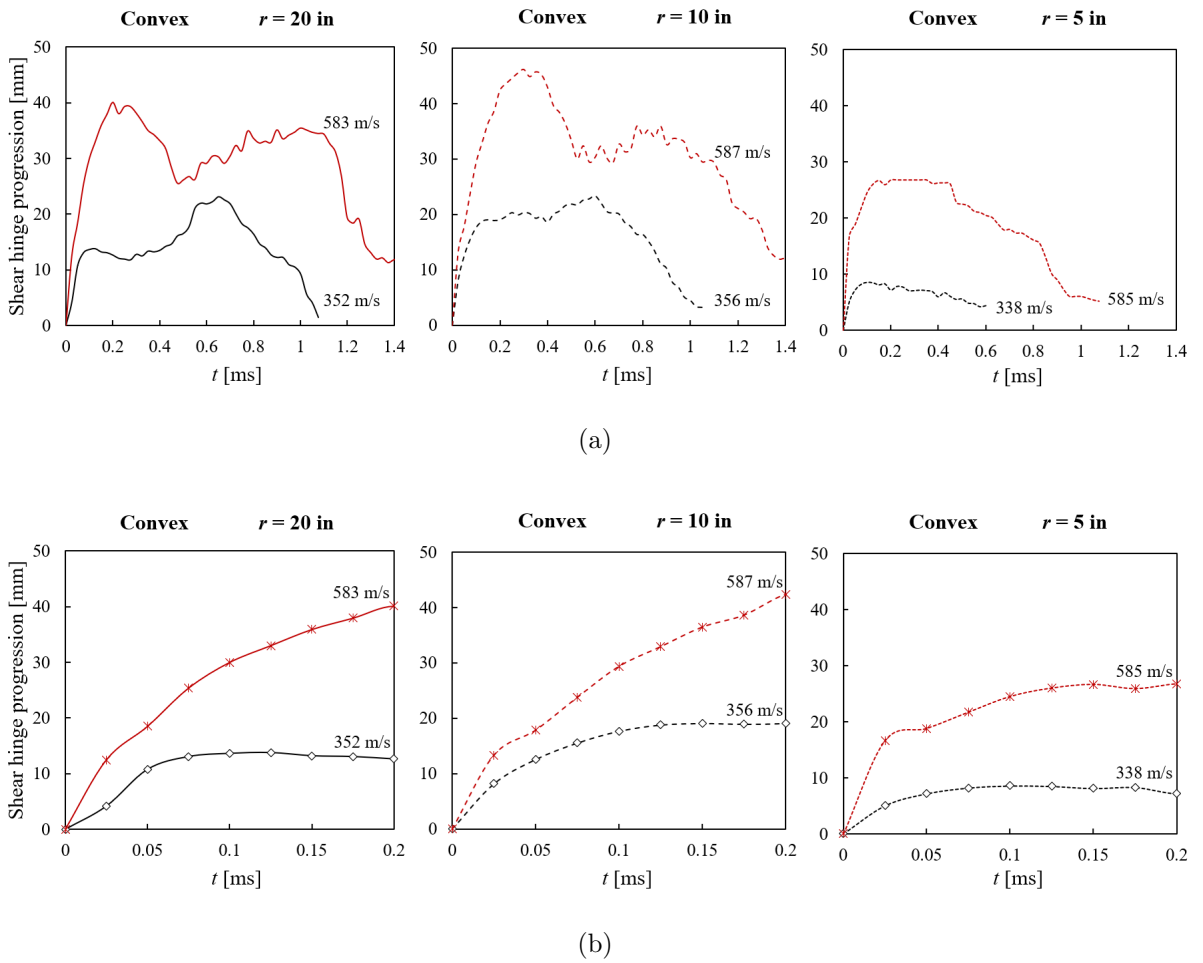


Figure 4.50: Shear hinge progression of laminates with varying degrees of curvature under convex impact for two ranges of impact velocity, over a duration of (a) 1.4 ms and (b) 0.2 ms after impact initiation.

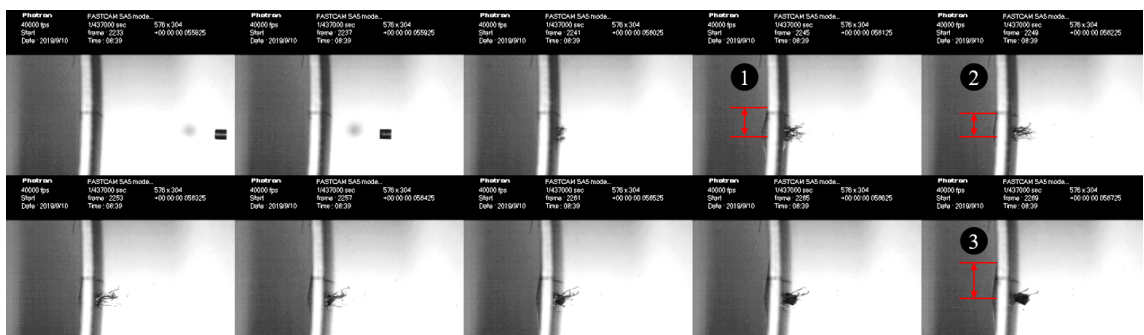


Figure 4.51: Montages of high speed photography at 0.025 ms intervals displaying the stages of bulge formation and in-plane progression, followed by its retraction, its re-emergence and further shear hinge progression at a later point, under convex impact with $r = 20$ in.

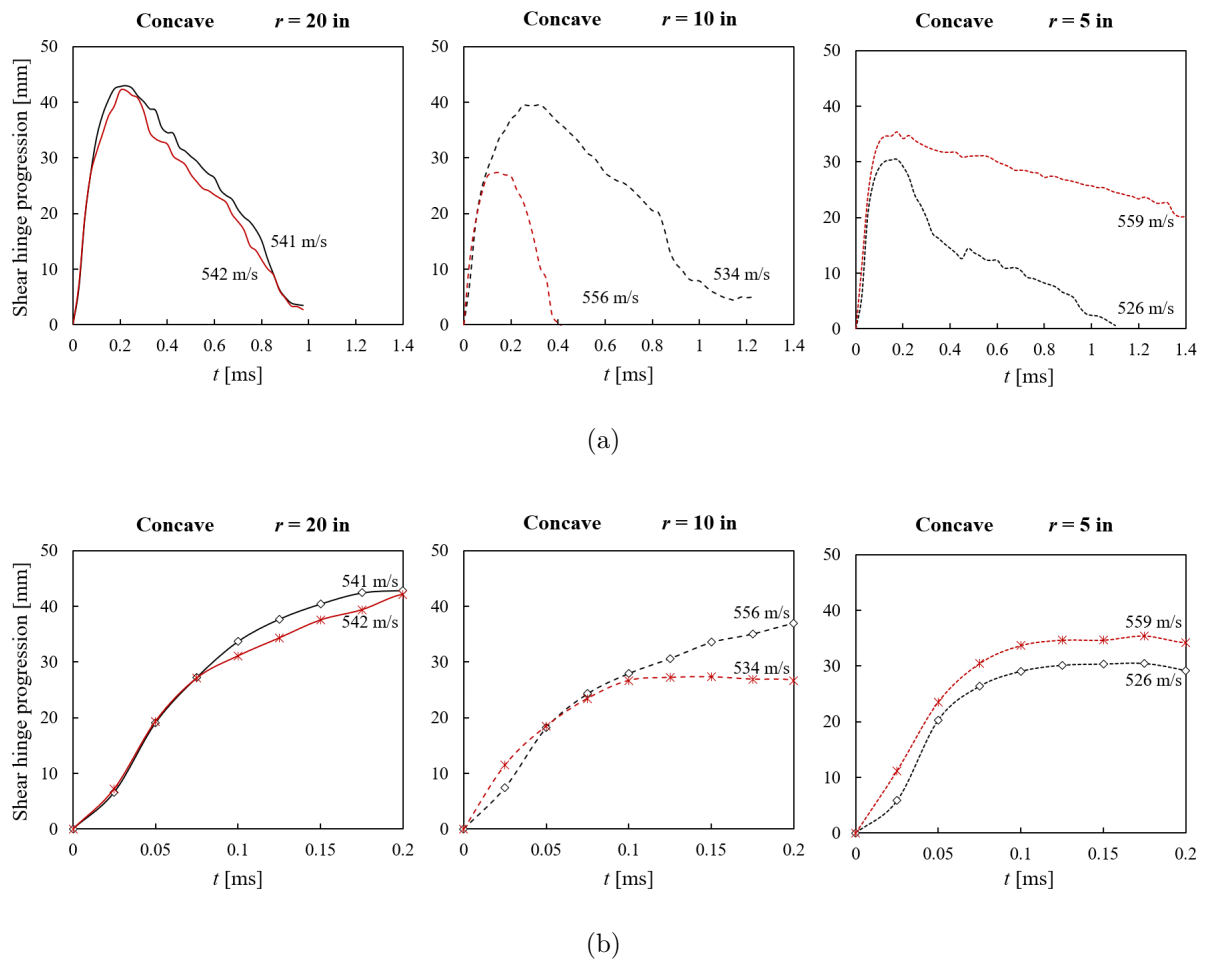


Figure 4.52: Shear hinge progression of laminates with varying degrees of curvature under concave impact for a single range of impact velocity, over a duration of (a) 1.4 ms and (b) 0.2 ms after impact initiation.

Close-up views of the initial stages of impact shown in Fig. 4.50(b) reveal that at both velocity ranges, different plate curvatures yield very similar trends in the progression of the shear hinge within the first 0.2 ms, with the relationship between plate curvature and maximum values aligned with the trend across the full 1.4 ms duration of impact discussed for Fig. 4.50(a). For the concave impact cases presented in Fig. 4.52, the shear hinge profiles seem to follow a pattern corresponding to the apex deflection profiles displayed in Fig. 4.46. However, a notable distinction exists between the two parameters. While the peak values of the apex deflection are consistently around 15% lower in the concave cases than under convex impact, the shear hinge progression restrictions that exist along the curved plate dimension on the back face of convex impact targets are not observed in concave impact, since the outer radius of the back face imposes no such restriction under concave impact. As a result, the maximum shear hinge

progression is of an equivalent value in both concave and convex plates of $r = 20$ in. In plates with $r = 10$ in, concave shots yield lower peak values than their convex counterparts, before rising to equivalent levels again for $r = 5$ in, as geometrical curvature effects on the rear face of the convex plates begin to limit the progression of the shear hinge.

Despite some distinct behaviour in the deformation of laminates emanating from the differences in their degrees of curvature, typical cross-ply oriented UHMWPE composite behaviour alluded to in [50], was observed in all of the tested cases. This behaviour can be summarised as follows:

- (a) For a V_I below a critical value that triggers penetration to commence at a given curvature, the plates demonstrate elastic deformation with a small conical deflection on the rear, together with limited signs of fibre fracture on the front face.
- (b) For a V_I above that critical velocity but below the plate's V_{50} , the plate is only semi-perforated by the projectile, whereby a collection of plies on the front half of the target have undergone fibre fracture and delaminate locally from each other, and also on a much larger scale away from the portion ahead of the projectile, which remains undamaged. This progressive damage through the thickness is accompanied by progressive behaviour of the back-face bulge. This was visible from the apex and shear hinge evolutions of the bulge, which were reported to act progressively with respect to an increasing V_I .
- (c) As V_I approaches V_{50} , a larger number of plies are fractured by the progression of the projectile through the laminate. When $V_I \approx V_{50}$ in the majority of cases, all plies have failed under the path of the projectile and full perforation of the target has occurred.

With high speed photography, it was also possible to trace the shape of the bulge over the duration of impact, for the low velocity ($V_I \approx 350$ m/s) and high velocity ($V_I \approx 580$ m/s) cases in the convex direction, together with the high velocity ($V_I \approx 550$ m/s) impact case in the concave direction, as per the apex deflection and shear hinge analyses. The bulge evolution at $t = 0.05$ ms intervals for different panel curvatures can be viewed in Figs. 4.53 to 4.54. In each graph, the shade of the bulge trace corresponds to the time interval, with the darker tones representing the growth of the bulge in the initial stages of impact, before it begins to retract, as depicted by the lighter shades. In some instances, the entire length of the bulge is not visible due to the limited field of view of the high speed camera lens. The time interval at

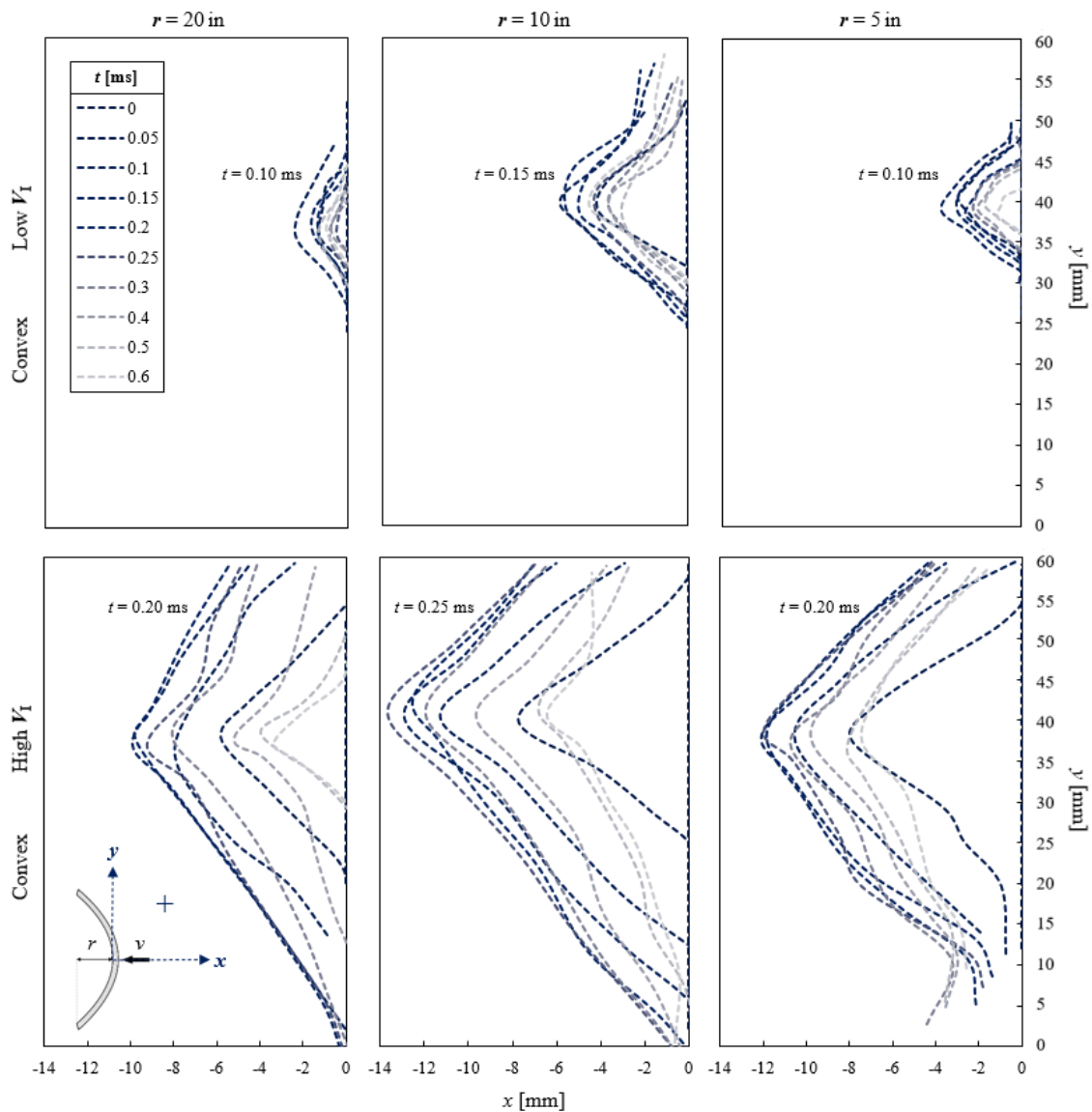


Figure 4.53: Evolution of the back face bulge at 0.05 ms intervals for different panel curvatures, under low impact velocity (top), $V_I \approx 350$ m/s, and high impact velocity (bottom), $V_I \approx 580$ m/s, convex impact.

which the initial apex deflection peak is recorded in this analysis is labelled accordingly on each graph. For the lower velocity range of convex shots and the concave cases, $\delta_{z \max}$ is reached at $t = 0.10$ ms, 0.15 ms and 0.10 ms, for $r = 20$ in, 10 in and 5 in, respectively. By contrast, under higher velocity convex impact, $\delta_{z \max}$ is reached after a 0.1 ms delay relative to the other cases.

The overarching trend in the bulge shape that emerges in the impact cases considered here, is the absence of symmetry in the shape of the bulge about the midspan, which for these cases coincides with a point along the curved length. Note that this length is not necessarily half way along the curved length, as a result of performing multiple shots on a single plate. Earlier in

the shear hinge-progression considerations in this chapter, and also in previous work such as that of the moiré interference fringe patterns observed on the rear face of UHMWPE laminates in [50], the bulge shape was assumed to be symmetric about both in-plane axes.

The BFD traces for convex impact are presented in Fig. 4.53. Bulge formation is very limited at the lower velocity, reaching much smaller extents than the concave cases as the back face is curved in the opposite direction to projectile motion. Since some of the kinetic energy of the projectile is dissipated in the reversal of the direction of curvature, an event not captured here due to the large time steps considered, similar impact velocities do not induce as much deflection in the convex direction of impact. The profile of these deflections over time is distinctly different between the three curvatures. From $r = 20$ in to 10 in, the apex and the shear hinge progress much further. This trend is however not extended to a further reduction in the radius of curvature to $r = 5$ in. In this case, the trend is somewhat reversed, with the shear hinge progression more constricted than was the case in the shallowest curvature, while the apex deflection also sees a significant fall from $r = 10$ in, although it still peaks at a higher value than it did for $r = 20$ in.

Naturally, following an increase in V_I values to the higher velocity range, the increase in impact energy is accompanied by larger deflections characterised by more extensive out-of-plane and in-plane bulge progression. Although the differences in the BFD profiles between each radius of curvature can be described as more subtle than they were for the lower velocity range, the same pattern is observed with respect to changes in the bulge shape over the course of impact. The effects in the convex impact cases are summarised and explained as follows:

- (a) For all curvature configurations, the deformations are progressive at both the lower and the higher velocity ranges.
- (b) At both velocity levels, increasing the curvature from $r = 20$ in to $r = 10$ in results in larger apex deflections and further shear hinge progressions.
- (c) However, when increasing the curvature further, from $r = 10$ in to $r = 5$ in, the previous effect is not replicated. At this stage, curvature effects become apparent by dictating the limits of the bulge shape.
- (d) For lower velocity ranges, the BFD shape is more sensitive to changes in the degree of the curvature of the target, than was observed at the higher ranges of impact velocity.

Regarding point (c), when the degree of curvature is increased from $r = 10$ in to $r = 5$ in, the maximum progression of the shear hinge is confined to a level below that of the shallowest curvature, $r = 20$ in, due to the cavity on the back face in a convex impact case where the panel curvature is reversed to attain bulge growth in the direction of impact. This restricted shear hinge progression is necessarily accompanied by a smaller deflection of the apex than was achieved at $r = 10$ in, due to the membrane deformation mechanism dominating the behaviour of the material. Nevertheless, the geometrical restriction imposed is an in-plane phenomena, thus the apex peaks of the most curved panels still exceed those at $r = 20$ in.

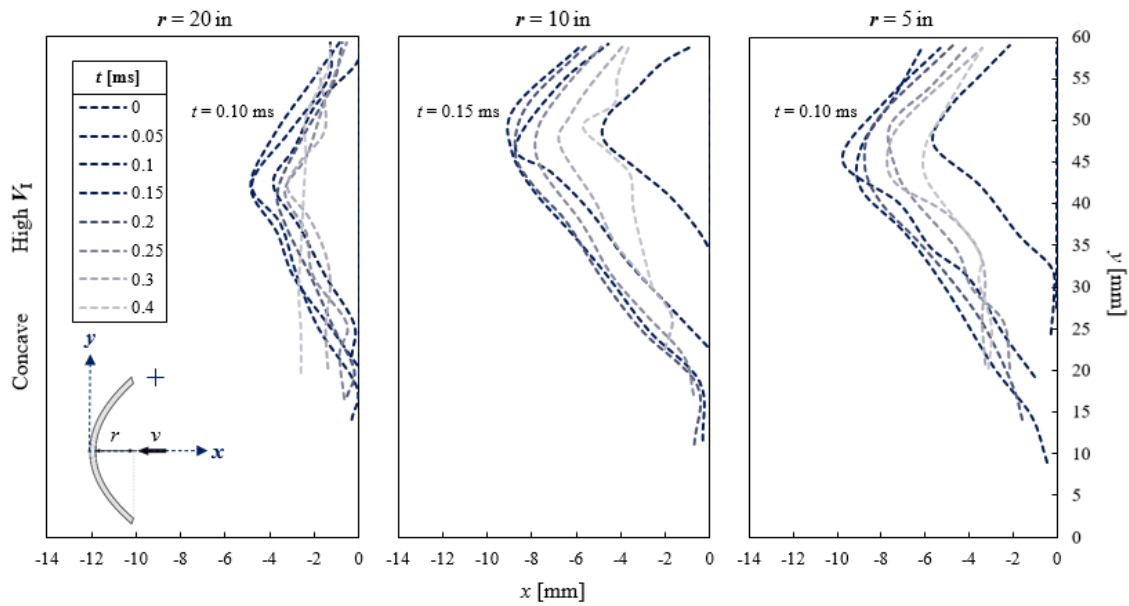


Figure 4.54: Evolution of the back face bulge at 0.05 ms intervals for different panel curvatures, under high impact velocity, $V_I \approx 550$ m/s, concave impact.

For $r = 20$ in under the low V_I concave impact case in Fig. 4.54, the growth of the bulge within 0.05 ms after impact does not vary greatly from its maximum dimensions and furthest reach, achieved after a further 0.05 ms. As the projectile and bulge begin to retract, the laminate starts to travel in the projectile's initial direction of motion, thus resulting in the gradual movement of the traces in the negative x -direction. After 0.4 ms, the bulge has fully retracted back and the laminate back face has recovered its original geometry. By contrast, for the plate curvature of $r = 10$ in, due to the nature of the time intervals at which the shape is traced, there is a jump from a flat configuration to the familiar conical bulge after the first interval. From then on, there is a second jump to the peak apex and shear hinge positions at which the bulge remains before retracting back at a much slower rate. This behaviour is also emulated by the target with $r = 5$ in, where the only difference visible is the time interval at

which the bulge reaches its maximum.

It is worth noting that due to the lower ballistic limits of the plates under concave impact, low V_I concave cases fall in the range of $\frac{V_I}{V_{50}} = 0.9$ to 1.0. This is comparable to the higher velocity range in the convex impacts with an equivalent $\frac{V_I}{V_{50}}$ range, whereas the lower velocities fall in the lower range of $\frac{V_I}{V_{50}} = 0.5$ to 0.7. This explains the close resemblance shown by the BFD profiles under concave impact to the high V_I deformations impacted in the opposite direction. The effects in the concave impact cases are summarised and explained as follows:

- (a) Distinctive differences exist between $r = 20$ in and 10 in panel deformations, although these converge to almost indistinguishable differences between the deformations induced in plates of $r = 10$ in and 5 in.
- (b) The back face is not geometrically restricted in concave impacts. Thus, geometrical effects do not impede or obstruct bulge motion and progression. While an increase in the degree of curvature results in further progression of the shear hinge, the maximum apex deflection increases with an initial increase in curvature, yet remains consistent for a further increase to $r = 5$ in.
- (c) The maximum apex deflection however, does not remain completely unaffected by a reduction of curvature radius from $r = 10$ in to $r = 5$ in. Since the peak value is approximately equal, the velocity of the apex deflection must be higher in the most curved case due to the shorter duration after which the peak value is reached.

Point (b) can be explained by the degree of stored elastic strain energy in the fibres [36], arising from the geometrical deformation into curved panels, which increases with increasing degree of curvature. Since this is a predominantly in-plane feature, the shear-hinge progression, characterising the in-plane motion of the bulge, intensifies.

4.4.3 Summary of key findings

In the first half of this chapter, UHMWPE composite panels were manufactured with three degrees of curvature and were subsequently tested under ballistic impact with a 10 mm diameter spherical projectile, at velocities ranging from 250 m/s to 500 m/s, and with a 5.56 mm diameter FSP threat, at velocities of 300 m/s to 800 m/s. The effect of direction of impact and the radius of curvature, including the very existence of curvature on the panel deformations and residual

velocities, reflecting internal failure modes under impact, were investigated.

For the round projectile, the results confirmed the higher sensitivity of the BFD than the V_{50} , to changes in the plate curvature, in line with previous work [31, 42]. In non-perforating dynamic impact cases at $V_I \approx 300$ m/s, convex panels displayed increases in peak BFD values with increasing degree of curvature. These increases were very substantial, rising from a difference of 25% relative to the flat plate at the lowest degree of curvature, to a difference of 50% for the most highly curved plate. The opposite effect was observed in the concave panels, where only a minimal variation in the peak out-of-plane deflection of curved panels was found, compared to the flat reference panel. Nevertheless, an increasing degree of curvature also led to a further divergence from the BFD of the flat plate, by a maximum of approximately 11% for the highest curvature. At $V_I = 400$ m/s or higher under convex impact, the shear hinge direction of bias was normal to direction of curvature as a result of geometrical restrictions imposed on the laminate, while in concave cases, bulge deformation was biased along the direction of curvature.

At the lowest range of strike velocities of around $V_I = 300$ m/s for the spherical projectile, the impact behaviour of the shallowest convex panel resembled the stable response of a flat plate to a large extent as the arch height was exceeded immediately after impact, resulting in much less bending and membrane shearing than in the more curved counterparts. As the strike velocity was increased beyond $V_I = 400$ m/s, *i.e.* towards the perforation limit, the differences between the responses of curved panels with varying curvature radii became minimal, although the degree of pull-in at the edges and the extent of inelastic deformation continued to increase with increasing degree of curvature. By contrast, deformation of panels under concave impact remained mostly elastic and reminiscent of the flat plate response.

The findings of the velocity-based analysis for spherical projectile impact were in agreement with the residual velocity measurements under FSP impact. While V_{50} estimates were approximately 100 m/s higher than for the round projectile, mostly a result of the smaller FSP mass, the FSP V_{50} predictions displayed improvements of around 10% in curved panels under convex impact, compared to a flat target, irrespective of the degree of curvature. Although the ballistic limit velocity estimate did appear to increase with increasing degree of curvature, the differences were very minimal. Similarly, much smaller changes of 1% to 2% in the V_{50} prediction existed between flat and concave laminates, but were deemed too insignificant to establish a definite pattern for this direction of impact.

Under FSP impact, the existence of curvature induced geometrical effects such as increased bending in convex cases, as stored elastic energy in the fibres was released upon the reversal of the bending direction under impact. In addition, the shape of the back face bulge in non-perforating impact cases, began to transform from a 4-sided pyramid in flat panels, to more skewed geometries with bias in the direction normal to the curvature. As for the FSP threat, geometrical restrictions in the direction of curvature limited the progression of the shear hinge from the site of impact to the edges, and with it the extent of in-plane damage from delamination. Geometrical effects were particularly apparent for $r < 10$ in, giving rise to the parabolic relationship between a panel's impact performance and its degree of curvature that has been reported in literature [26, 41].

Furthermore, the effects caused by the addition of curvature to panels were deemed comparable to patterns seen in curved laminates comprised of various composite materials in previous studies [25, 36, 41], where an increase in curvature has been responsible for an increase in the extent of the maximum out-of-plane deformation on the back face of convex panels, irrespective of material properties. Likewise, the trends in the behaviour of curved laminates with varying layup sequences are consistent with the literature, since the only process through which the layup sequence would have influence on the impact performance is when the site of impact is away from the centre of a curved laminate, or when the direction of impact is non-orthogonal. The main purpose of the next half of this chapter is to identify whether the current macro-scale level numerical tools developed in Chapter 3, can capture the effects of curvature on the impact performance of curved laminates as accurately as they did for flat laminates.

4.5 Methodology: Numerical modelling

The modelling tools developed in Chapter 3 are extended to curved laminates in this section, to determine whether they capture the behaviour observed under physical testing to a sufficient degree of accuracy, with regards to the deflection- and velocity-based performance metrics. The modelling approach is outlined here, followed by a presentation and discussion of the data generated with this approach in the subsequent section.

For the sake of simplicity, the continuous variation in curvature across the surface of the

geometry is represented by adjusting the degree of curvature in the homogenised flat plate model developed in Chapter 3, to a set of discrete values of radius of curvature r , as demonstrated in Fig. 4.1. The set of values is composed of $r = 20$ in, 10 in and 5 in, with the addition of $r = 15$ in also considered in one of the investigations. Likewise, the in-plane reference dimensions were maintained at $300 \text{ mm} \times 300 \text{ mm}$, while the number of 1 mm sub-laminates in the model was reduced to 6, achieving a laminate thickness of 6 mm, to resemble the nominal dimensions of the tested specimens. The mesh was also generated with a reversed direction of curvature, to also account for concave impact cases for the aforementioned values of curvature radii.

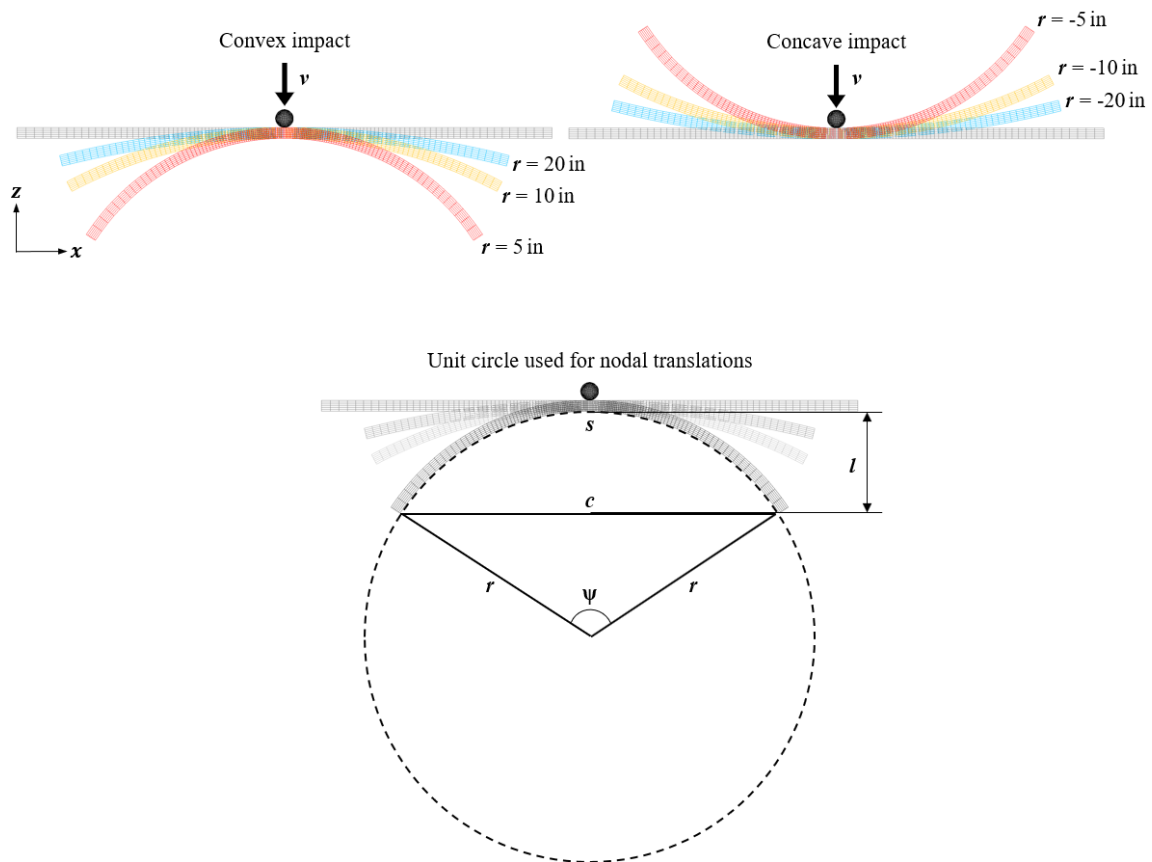


Figure 4.55: Radially projecting solid element nodes onto the desired radius of curvature using segment theorem to generate meshes of panels with varying radii.

The baseline flat model from Chapter 3 was modified and simulated under impact by the tested threats; a 10 mm diameter spherical projectile, and a 5.56 mm diameter FSP. It is imperative to note that since a forming simulation is required to account for pre-strained state of the fibres, these were not considered in the modelling technique employed here.

To transform the fully validated flat plate mesh into the curved geometries demonstrated

in Fig. 4.55, nodal translations were performed using an automated process. MATLAB was used as the interface between the input and output files, whereby the nodal coordinates of the flat plate were extracted from LS-DYNA keyword files, translated, and subsequently rewritten into the keyword files. The nodes were projected radially onto a desired radius of curvature by relating the proportions of the hypothetical circle formed from the desired radius, to those of a unit circle. Nodal displacement was determined using segment and intersecting chord theorems, where

$$s = r\psi \quad (4.9)$$

$$\begin{aligned} c &= 2r \sin\left(\frac{\psi}{2}\right) \\ &= 2\sqrt{l(2r-l)} \end{aligned} \quad (4.10)$$

with parameters ψ , r , c , s , l defined as sector angle, radius, chord length, arc length and segment height, respectively, as illustrated in Fig. 4.55. For each sub-laminate layer, the displacement vector of an individual node was calculated from the Cartesian displacement coordinates, while maintaining the initial thickness value possessed by each layer.

4.6 Results and discussion: Numerical modelling

In this section, numerical modelling results for the two types of projectile are presented. The results are compared against the experimental testing discussed earlier on in Chapter 4, with certain parameters, such as impact location or interface impact energy dissipation, investigated further in each case.

4.6.1 Spherical threat

Due to the lower range of impact velocities tested with the steel ball projectile, both the lower and the higher loading rate values of mode II traction of the interface elements, σ_{II} , were explored in the simulations. This was performed as a continuation of the parametric studies based on the interface, performed in Chapter 3, to determine the effect of altering the rate-dependent value of σ_{II} on the impact behaviour of curved laminates, and to identify the most suitable value for capturing the spherical projectile impact tests that were performed.

4.6.1.1 Deflection analysis

Firstly, a comparison is provided between the rear face out-of-plane displacements of the tested specimens as captured by a DIC system, and the corresponding fringe plots from the numerical simulations, at maximum states of deflection. These are presented in Figs. 4.56 to 4.62 for a flat reference plate, and for plates with increasing degrees of curvature at both directions of impact. Due to small fluctuations in the impact velocity, the impact events were simulated at two velocities that were achieved frequently during testing, $V_I = 280$ m/s and $V_I = 300$ m/s. In addition, at $V_I = 300$ m/s, the two values of cohesive interface mode II peak traction, $\sigma_{II} = 1.8$ MPa and $\sigma_{II} = 2.6$ MPa are considered, as previously done in Chapter 3. The plots of the simulated BFD can be compared against those adjacent to them, with only a single parameter changed in the models of neighbouring fringe plots. Observations of these results are summarised in the following points.

(a) Regarding the shape of the deflected bulge on the rear face:

- i. The shape can be described as a 4-sided pyramid, the base of which represents the shear hinge.
- ii. With an increase in the degree of curvature, the rhombus-based shape of the shear hinge transforms into a rhomboid, while the circular area directly beneath the projectile path exhibiting peak deflection transforms into an oblong-shaped region.
- iii. Both transformations occur with a preferential bias along the straight dimension of the plate, accompanied by a more restricted deformation along the curved length.
- iv. These BFD profiles are reminiscent of the shapes observed during impact testing, consistent across the two values of V_I and σ_{II} considered here.

(b) Concerning out-of-plane deformations:

- i. The out-of-plane motion of the laminate at the edges in the negative z -direction visible in experimental testing is not captured as extensively in the flat and low curvature cases as it is at the higher curvatures.
- ii. In all the simulations, there is an over-representation of the out-of-plane wrinkling of the back face at the edges of the shear hinge in the direction opposite to that of projectile motion.
- iii. The simulations do however capture the wrinkling and folding over of plies that occurs at the edges of the laminate in the vicinity of the primary fibres due to

in-plane shear motion, particularly affecting the specimens with the highest degrees of curvature, as was also seen in the physical testing of laminates in Section 4.4.1.

(c) Comparing the two impact velocities simulated:

- i. In all cases a higher V_I corresponds to a higher $\delta_{z \max}$.
- ii. An increase of 20 m/s in V_I induces an increase of 11 % for the $\delta_{z \max}$ of the flat laminate, 13 %, 13 % and 4 % for the convex plates, and 5 %, 3 % and 0 % for the concave plates, respectively, in order of reducing curvature radius.
- iii. This demonstrates that although convex impacts initially see an increase in $\delta_{z \max}$, from $r = \infty$ to $r = 20$ in, for more highly curved panels this BFD increase levels out before dropping to a mere 3 % for the most highly curved specimen.
- iv. Within the range of concave impact cases considered, a similar trend is observed, whereby higher degrees of curvature are much less sensitive to variations in V_I , to the point that the most highly curved plate is completely insensitive to the change in impact velocity.

(d) Comparing simulated values of $\delta_{z \max}$ with tested results:

- i. The cases simulated with different parameters yield very similar results, which tend to deviate from the tested data by an average of approximately 8 %, within an overall range of 6 % to 12 %.
- ii. The largest deviations were observed at the highest degree of curvature, where $r = 5$ in.
- iii. The concave impact simulated $\delta_{z \max}$ was consistently below measurements from experiments, as shown by absence of the the maximum spectrum values in the fringe plots of the simulated cases. Simulations of the convex cases do however, reach the maximum value of the spectrum ($\delta_{z \max} > 14$ mm) in the regions corresponding to the impact site.
- iv. A more detailed analysis accompanies Fig. 4.64.

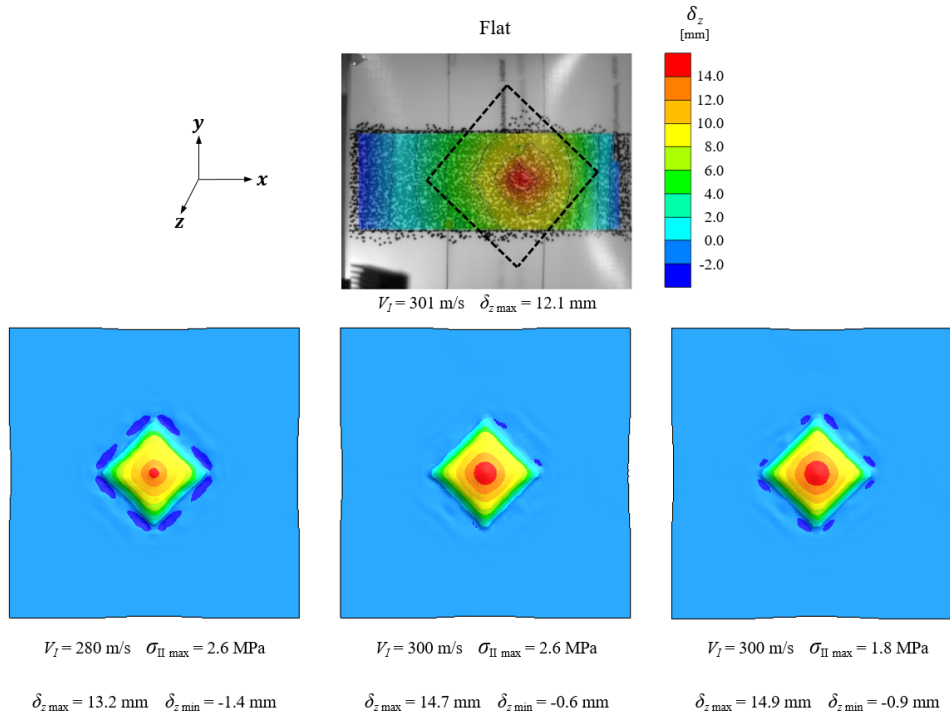


Figure 4.56: Experimentally acquired and numerically generated δ_z distribution on the back face of laminates at maximum deflection under impact, for $r = \infty$.

The percentage change in the peak deflection of a curved plate from that of a flat reference plate, $\Delta\delta_{z \max}$, is recorded against r in Fig. 4.63. The two sets of numerical data, representing sub-laminate interfaces with $\sigma_{II} = 2.6$ MPa and $\sigma_{II} = 1.8$ MPa at discrete values of V_I , are compared against experimentally obtained results for the spherical projectile, at 270 m/s to 330 m/s, the initial range of velocities tested. Under convex impact, the simulated data follow the trend in the experimental results, showing an increase in $\Delta\delta_{z \max}$ with increasing degree of curvature. The magnitude of the increase however, is underestimated in the simulations. In the simulated results for $\sigma_{II} = 2.6$ MPa, the values of $\Delta\delta_{z \max}$ are consistently lower than the experimental data, at both $V_I = 250$ m/s and $V_I = 300$ m/s. Similarly, when $\sigma_{II} = 1.8$ MPa, the simulations underestimate the change in $\delta_{z \max}$ between a flat and a curved geometry, regardless of the intensity of curvature. For instance, consider the median impact velocity, $V_I = 300$ m/s, together with the higher strain-rate σ_{II} value of 2.6 MPa. The trend seen in the experiments is mirrored in the simulations, even though $\Delta\delta_{z \max}$, *i.e.* the relative change in $\delta_{z \max}$, appears to be two- to threefold higher in the experimental data.

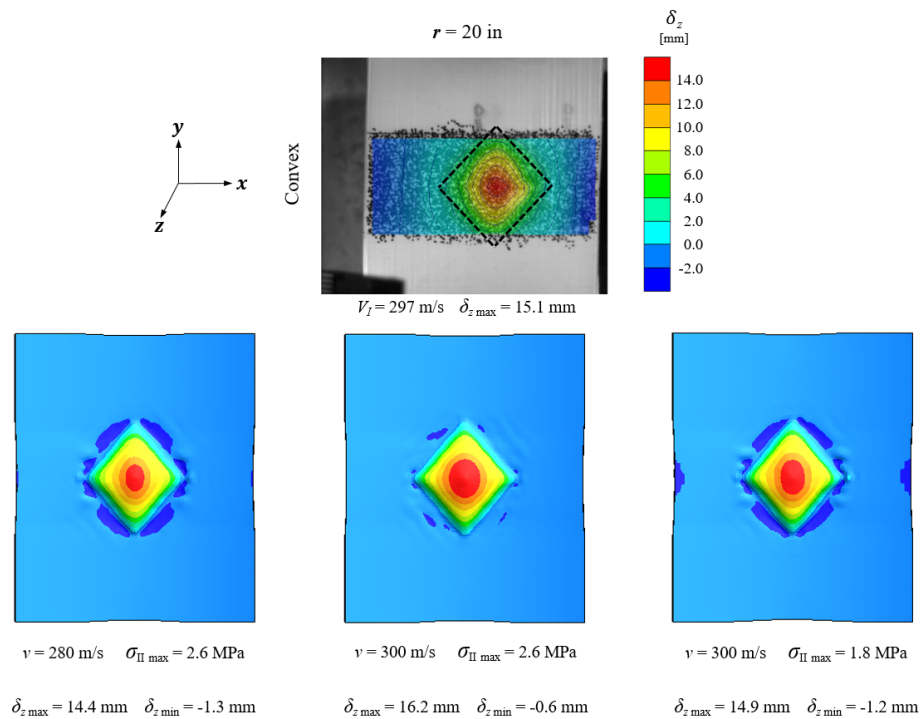


Figure 4.57: Experimentally acquired and numerically generated δ_z distribution on the back face of laminates at maximum deflection under impact, for $r = 20$ in.

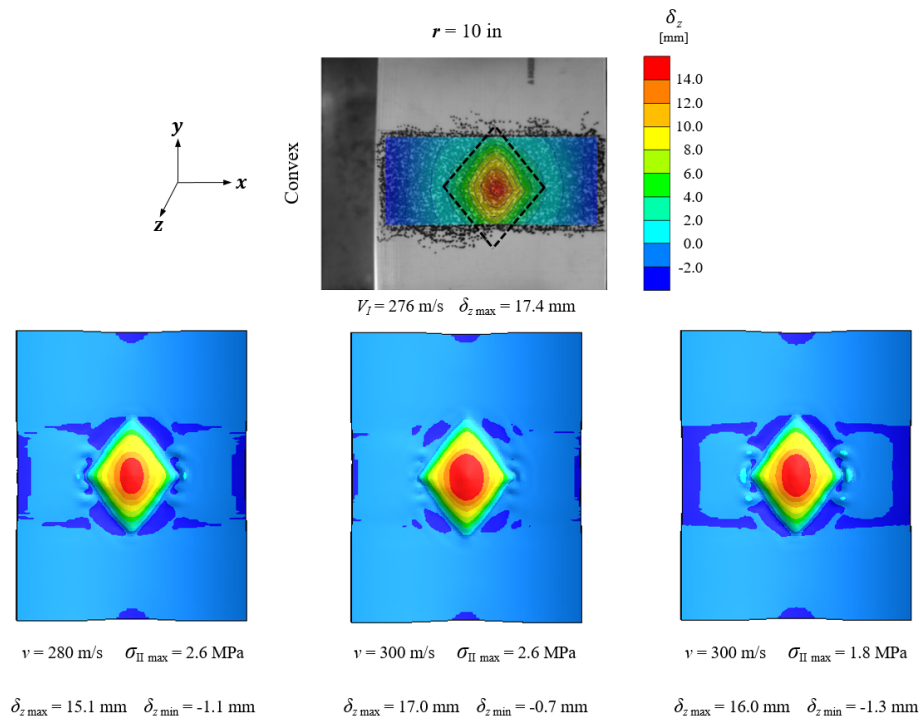


Figure 4.58: Experimentally acquired and numerically generated δ_z distribution on the back face of laminates at maximum deflection under impact, for $r = 10$ in.

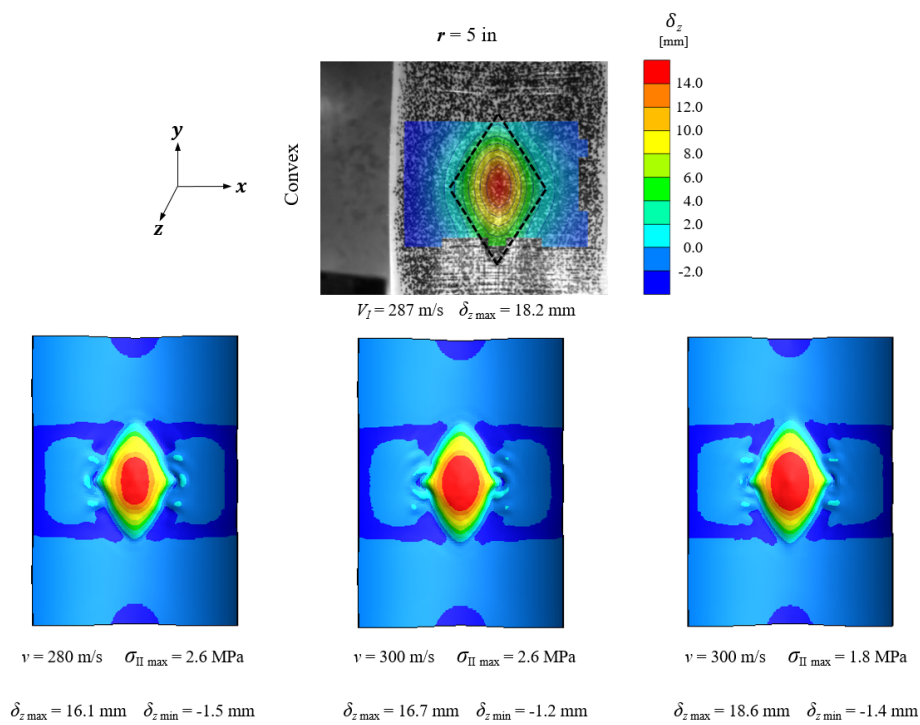


Figure 4.59: Experimentally acquired and numerically generated δ_z distribution on the back face of laminates at maximum deflection under impact, for $r = 5 \text{ in}$.

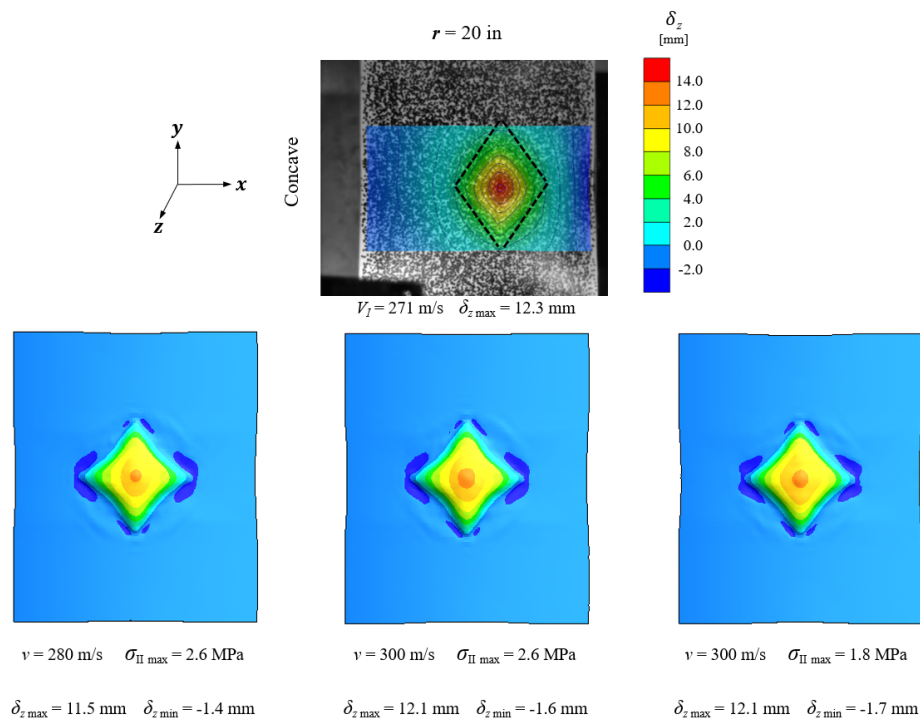


Figure 4.60: Experimentally acquired and numerically generated δ_z distribution on the back face of laminates at maximum deflection under impact, for $r = -20 \text{ in}$.

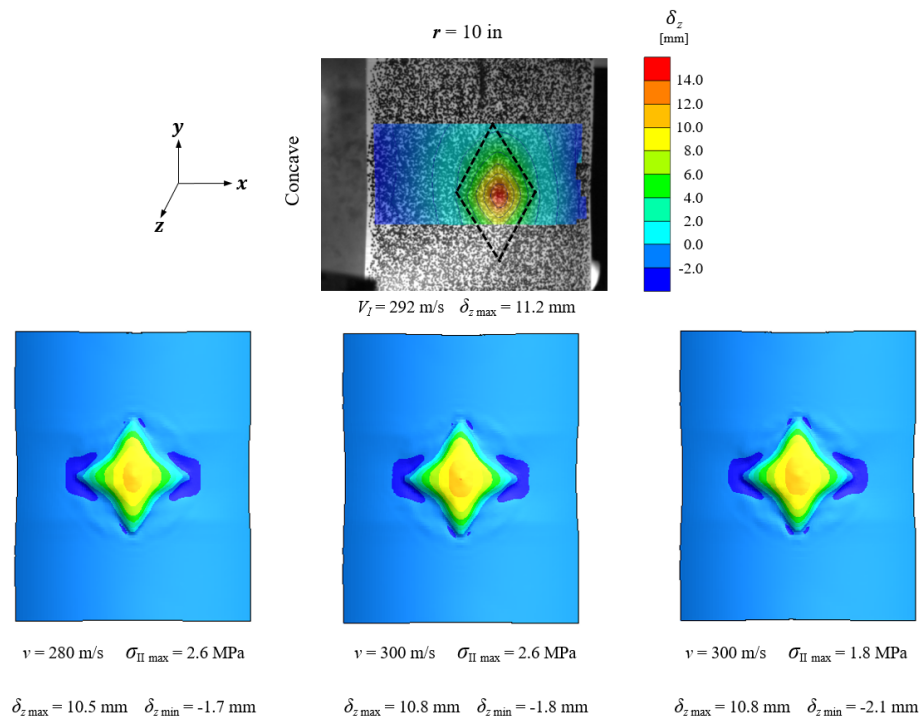


Figure 4.61: Experimentally acquired and numerically generated δ_z distribution on the back face of laminates at maximum deflection under impact, for $r = -10$ in.

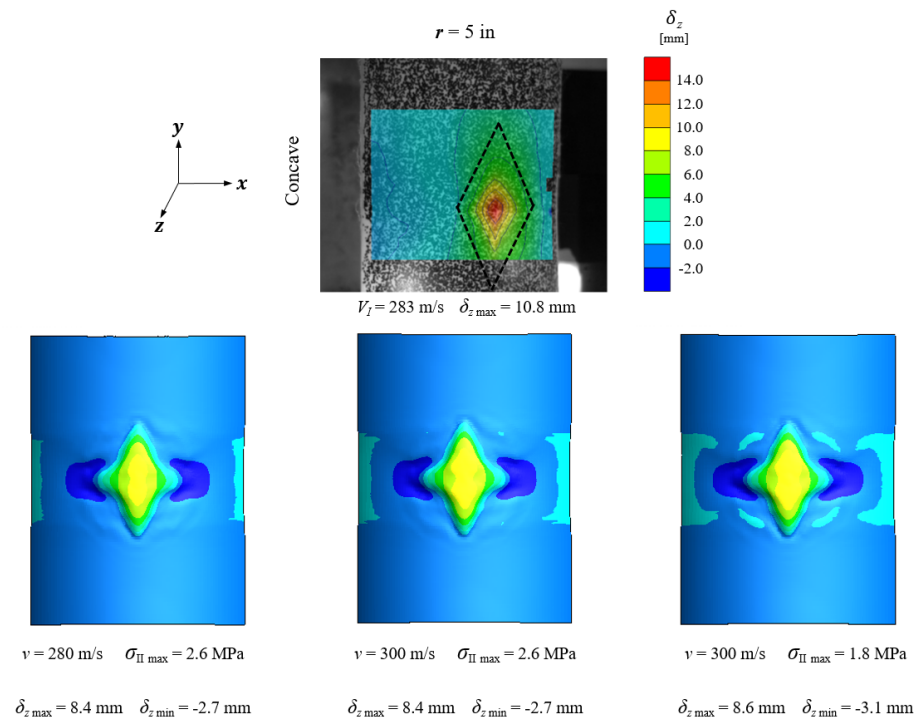
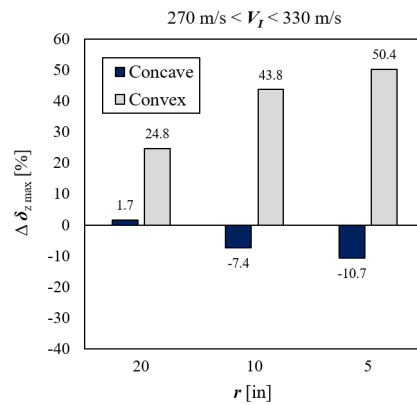
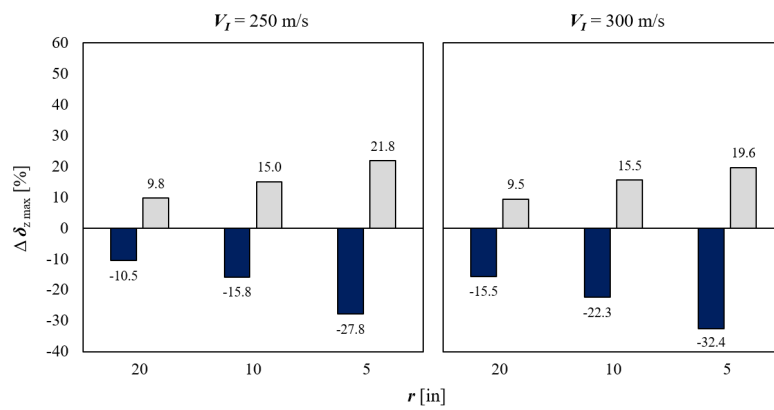


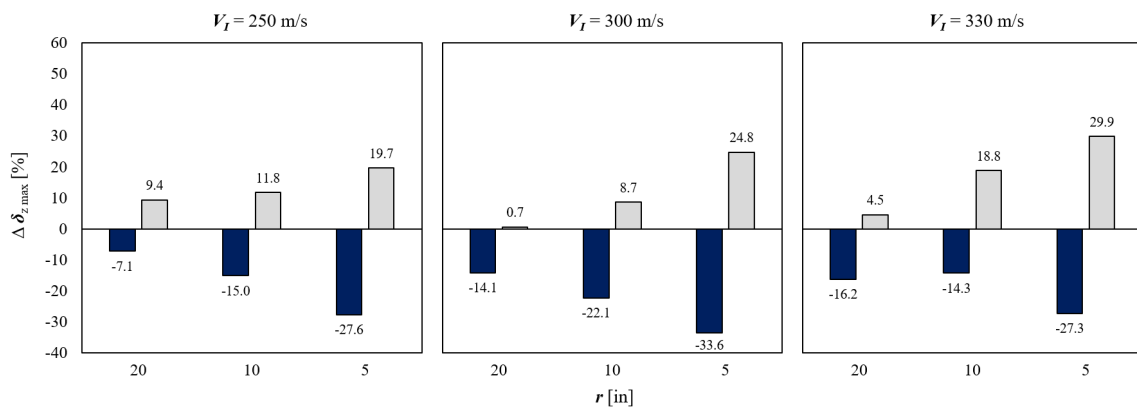
Figure 4.62: Experimentally acquired and numerically generated δ_z distribution on the back face of laminates at maximum deflection under impact, for $r = -5$ in.



(a) Experimental.



(b) Numerical, $\sigma_{II} = 2.6$ MPa.



(c) Numerical, $\sigma_{II} = 1.8$ MPa.

Figure 4.63: Comparison of percentage change in maximum apex deflection of curved laminates relative to a flat reference, between experimental and numerical data for a range of impact velocities.

Under concave impact, while experimental results showed a minor increase in $\Delta\delta_{z \max}$ at the shallowest curvature, $r = 20$ in, increasing the degree of curvature further yielded a decrease in the $\Delta\delta_{z \max}$, relative to a flat plate, as those panels were already bent in the direction of the bulge. The percentage changes in the peak out-of-plane displacement are, however, on a much smaller scale than for convex panels, with the most highly curved panel seeing only a 11% decrease under concave impact, compared to a 50% increase in the convex direction. The simulations also predict a reduction in $\Delta\delta_{z \max}$ with increasing curvature, including a significant decrease even at the shallowest curvature. Contrary to convex impact cases, the simulations overestimate the reductions that occur in $\Delta\delta_{z \max}$ with increasing degrees of curvature. Unlike convex impacts, the results predict an increase in the percentage change for a given panel curvature, when increasing the impact velocity from $V_I = 250$ m/s to $V_I = 300$ m/s, for both values of σ_{II} . This is not replicated however, when the velocity is further increased to $V_I = 330$ m/s, instead showing a drop in $\Delta\delta_{z \max}$ for the two highest degrees of curvature.

The next step is to compare the deformation of the laminate over time, in order to identify the sources of the limitations in the model. A side-by-side comparison of the numerical and experimental deformations is presented in Fig. 4.64 over the duration of impact at 0.1 ms intervals, for a concave impact of the shallowest curvature of $r = 20$ in at $V_I = 287$ m/s. The smallest degree of curvature in the concave direction was selected for this purpose as it was shown to be least affected by the geometrical effects of curvature. This particular case can therefore be used to identify differences that exist even in the most conservative cases, as identified by the lowest level of sensitivity amongst all the configurations. This is based on these specimens showing the smallest extent of change in $\delta_{z \max}$ in Fig. 4.63. Note that snapshots of the simulation display the laminate deformation at the mid-length cross-section, while high speed video images show the side-view of the laminate, without visibility of the internal deformation of the layers.

The key findings are summarised as follows:

- (a) The simulated BFD has good correlation with the measured deflection. The model underpredicts the maximum out-of-plane BFD by only 3%, making it sufficiently accurate. Note that the maximum out-of-plane deflection is considered to be one of the most crucial parameters in determining the impact performance of a laminate.
- (b) The peak deflection occurs at the same time ($\pm 1\%$) in the simulations as it did in the

experiments.

- (c) The most noticeable difference between the simulated and the tested plate responses is the shape of the bulge, which exhibits flatter edges and a sharper peak in reality than is captured by the more curved BFD of the model.
- (d) Fibre damage on the front face of the target is clearly not modelled due to the macroscopic level of the modelling, with homogenisation of plies into sub-laminate layers.
- (e) Out-of-plane wrinkling at the shear hinges is slightly over-predicted in the simulations, although the true extent of this is not perfectly clear from the high speed images taken at the edge of the laminate.
- (f) Likewise, the in-plane progression of the shear hinge is slightly over-predicted in the simulations.
- (g) The model predicts an almost complete retraction of the back face upon projectile rebound. In reality, this retraction does occur, but to a much smaller extent, signifying a region of inelastic deformation.

The differences between the simulation and experiments can be attributed to three factors; homogenisation, non-linear through-thickness shear behaviour, and plastic deformation. These factors are more significant in the deformation of curved geometries due to the increases in the extents of deformation that are undergone, relative to flat laminates, the behaviour of which was captured well with these numerical tools, as demonstrated in Chapter 3. The homogenisation approach, although driven by efficiency, increases the bending stiffness of the composite structure, which can be seen in the shape of the BFD. In the high speed images, the bulge has a straight profile, indicating mostly tension loading, while in the model, the profile has a more curved shape, suggesting more bending behaviour is present. Micro-scale physical deformations such as fibre elongation are not captured, thereby making the structure stiffer in bending than it is in reality. Numerical beam buckling investigations performed by Hazzard *et al.* [49] which were compared against experimental testing by Liu *et al.* [19], revealed some of the limitations of a sub-laminate approach for fully capturing the small radius and high degree of curvature of the deformation. This results in a more rounded bulge on the rear face without the sharp and pointed deflection seen in the high speed images directly ahead of the projectile, also giving rise to extensive wrinkling at the shear hinges in the simulation and could be contributing to the

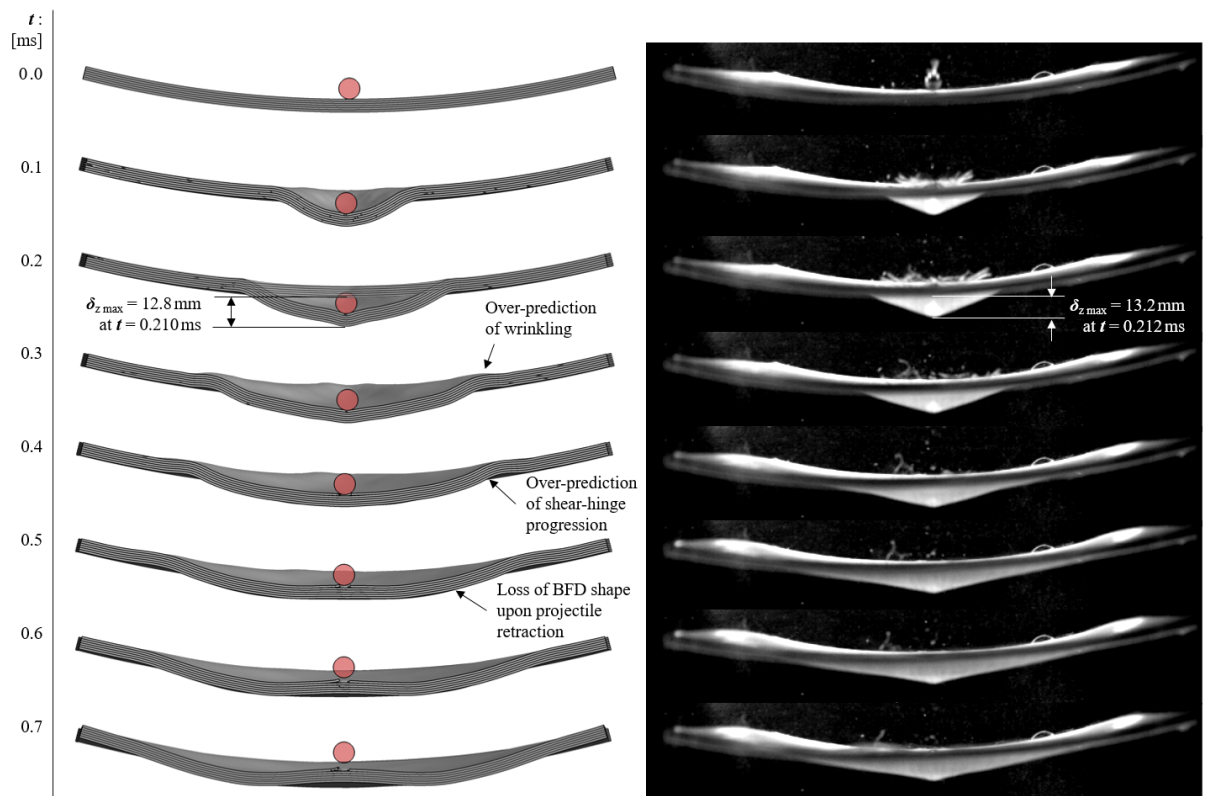


Figure 4.64: Comparing deformation of curved plate under impact between simulated and tested results at 0.1 ms time intervals following impact, at $V_I = 287$ m/s for $r = -20$ in.

small discrepancy in the peak deflection.

The effective bending stiffness of the laminate is exaggerated further due to the absence of non-linear through-thickness shear behaviour in MAT162 [82], for which the linear through-thickness shear damage parameter is identical to the parameter representing the in-plane direction. Adding non-linearity to shearing through the thickness would reduce the effective bending stiffness, as less energy would be dissipated in the first stages of deformation. This would be accompanied by increased sliding action and improved shear hinge-progression, so that a noticeably larger displacement, $\Delta\delta_{NL} \gg \Delta\delta_L$, would be achieved for a given increase in force, ΔF , as illustrated in Fig. 4.65(a). The extent of this increase is naturally dependent on the specific stiffness gradient and ΔF values.

To improve the accuracy of predictions from curved panels models without increasing fidelity, a low stiffness approach can be adopted. Stargel [41] addressed the poor agreement that existed between computational results and the experimental data for the impact performance of

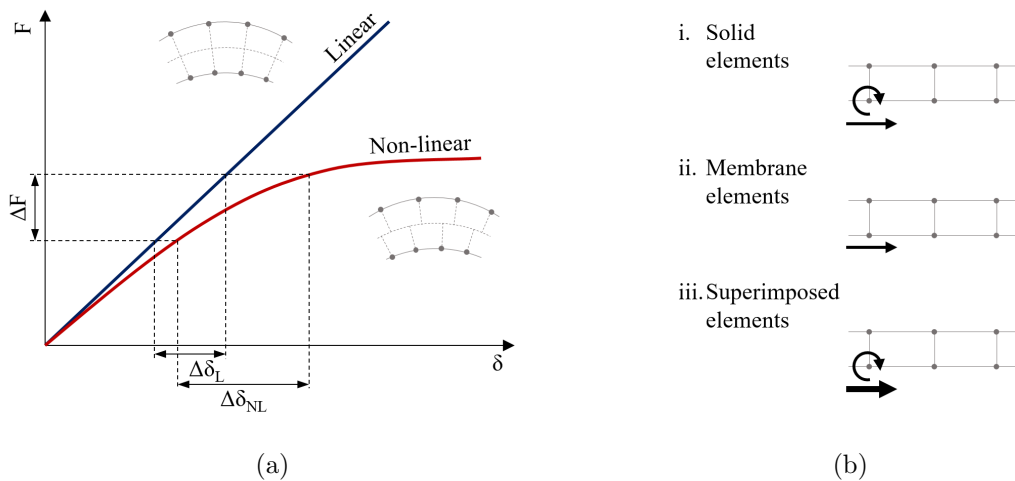


Figure 4.65: (a) Comparing arbitrary examples of linear and non-linear through-thickness shear regimes, (b) combining translational and rotational degrees of freedom to increase the contribution of in-plane stiffness.

curved composite laminates, with the use of an empirically-derived effective elastic modulus (≈ 3.5 GPa) in the numerical model. This effective modulus was more than thirty times lower in magnitude than the value of the parameter calculated using the rule of mixtures (≈ 125.5 GPa). The author's argument for this approach was twofold. Firstly, the elastic modulus is directly proportional to flexural rigidity, and thus a reduction in the modulus of the material would reduce panel stiffness, thereby increasing the maximum out-of-plane BFD. Secondly, the velocity of the impact wave, and therefore the velocity at which disturbances propagate, is also directly proportional to the elastic modulus of the material. A reduction in the modulus of the material would therefore result in slower laminate response to impact. Using the effective elastic modulus in numerical simulations [41] yielded good correlation between experimental and numerical data for the back face deflection, with numerical V_{50} predictions falling within 2% of the experimental estimates. In addition, there was a reduction in the damage area with increasing impact velocity for a given curvature, and with increasing radius of curvature for a given impact velocity.

Alternatively, the coupling behaviour between in-plane and out-of-plane shear could be exploited to overcome the restrictions imposed by MAT162. The contribution of through-thickness shear stiffness could be artificially reduced, by superimposing the solid element nodes onto those of additional membrane elements as illustrated in Fig. 4.65(b), to increase in-plane stiffness, as proposed by Khan *et al.* [100] and performed by Thompson *et al.* [101], to decouple the high tensile stiffness of a fabric from its lower bending stiffness. Since UHMWPE composite preforms deform in a similar manner due to their significantly high fibre volume fraction, this approach

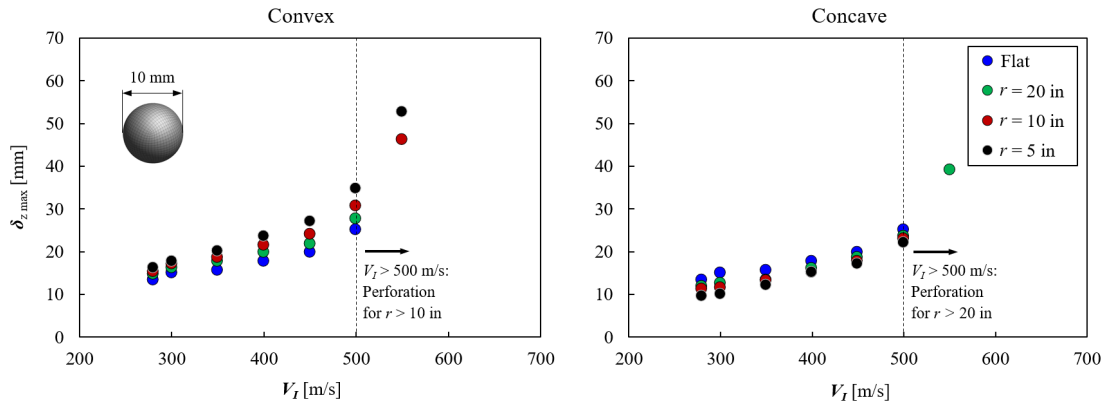
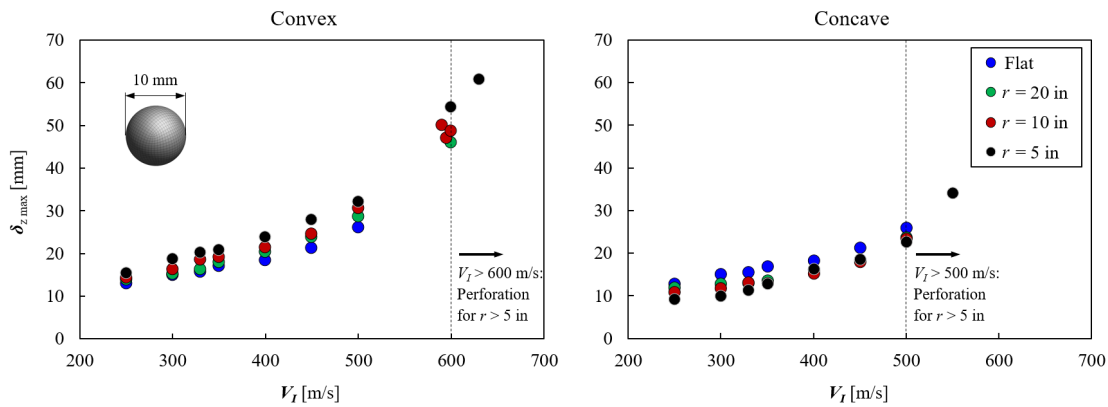
would in turn increase the contribution of in-plane shear stiffness in order to reduce that of the through-thickness shear stiffness.

Furthermore, plastic deformation cannot be captured in these simulations as MAT162 is a purely elastic-damage material model [96]. The material response is modelled by an initial linear elastic region according to the damage functions and damage thresholds. At the onset of damage, the progressive damage model does not account for plasticity. Instead a linear elastic response, bound by updated damage variables, is assumed. The variables are updated to reflect a reduction in the stiffness matrix. In other words, the material exhibits a non-linear response upon damage initiation and growth, not through unrecoverable damage, but through softening behaviour facilitated by a lower elastic modulus. Similarly, plastic deformation is not modelled by the bilinear traction-separation law that dictates the behaviour of the interface elements, as discussed in Chapter 3. Plastic behaviour cannot be added to MAT162. However, it is possible to use the interface to change the effective plasticity, by for example, the use of a trapezoidal cohesive law, or through adding plasticity by having additional unloading and reloading paths. See Appendix B for a more detailed discussion of these options for future work.

The numerical model is therefore deemed reliable in capturing the back face deformations to an extent, particularly at shallower curvatures where geometrical curvature effects have yet to dominate laminate behaviour under impact. Although the shape of the bulge deformation on the back face may not be perfectly achieved in simulations, the most crucial parameter, *i.e.* the peak apex deflection, is predicted to a sufficient degree of accuracy. Since testing laminates at higher velocities required the use of an alternative machine that did not permit DIC measurements of the out-of-plane displacements of the bulge, simulations were used instead to visualise the effects of impact velocity over a more comprehensive range of V_I values. The peak deflection $\delta_{z \max}$ is plotted as a function of V_I for the different curvatures and directions of impact in Figs. 4.66 and 4.67, while also providing a comparison between the outputs based on the two values of σ_{II} considered earlier.

For convex impact, the figures demonstrate the following predictions by the model.

- a) On the relationship between $\delta_{z \max}$ and V_I :
 - (i) A generally increasing value of $\delta_{z \max}$ with increasing V_I .
 - (ii) Higher degrees of curvature display larger BFD profiles. As observed during exper-

Figure 4.66: Variation in maximum apex deflection with impact velocity, for $\sigma_{II} = 2.6$ MPa.Figure 4.67: Variation in maximum apex deflection with impact velocity, for $\sigma_{II} = 1.8$ MPa.

perimental testing at $V_I \approx 300$ m/s, BFD diverges away from the reference flat plate $\delta_{z \max}$ with increasing degree of curvature.

- (iii) The higher the degree of curvature, the greater the extent and the rate of divergence observed, as V_I approaches the perforation threshold velocity when $\sigma_{II} = 2.6$ MPa, and to a smaller degree when $\sigma_{II} = 1.8$ MPa.
- (iv) A more rapid growth rate in $\delta_{z \max}$ with increasing V_I for $\sigma_{II} = 2.6$ MPa than seen in the corresponding relationship for $\sigma_{II} = 1.8$ MPa.

b) On the effect of σ_{II} on $\delta_{z \max}$:

- (i) Although the highest degree of plate curvature shows the greatest level of sensitivity in $\delta_{z \max}$ to changes in the value of σ_{II} , all curved plates are affected in terms of the velocity at which full perforation occurs.

- (ii) For $\sigma_{II} = 2.6$ MPa, perforation is noted in the flat plate and for $r = 20$ in, when $V_I > 500$ m/s, while in the most highly curved cases, it occurs when $V_I > 550$ m/s.
- (iii) By contrast, the behaviour of the flat plate remains consistent at $\sigma_{II} = 1.8$ MPa, while the perforation limit for $r = 20$ in and $r = 10$ in is extended to $V_I = 600$ m/s, and that of $r = 5$ in to $V_I = 650$ m/s.

The deflection of laminates under concave impact follow a similar, yet reversed, trend.

a) On the relationship between $\delta_{z \max}$ and V_I :

- (i) At a given plate curvature, $\delta_{z \max}$ still increases with rising V_I , at faster rates for higher impact velocities, albeit at much slower rates than seen for convex impacts.
- (ii) The value of $\delta_{z \max}$ is generally lower at the higher degrees of curvature at any given impact velocity.
- (iii) Due to the faster rates of increase at higher values of V_I for the most highly curved plates, $\delta_{z \max}$ values converge towards the least curved and non-curved plates, until a minimal level of differences is achieved between the deflections of plates with various curvatures at the $V_I = 500$ m/s perforation threshold.

b) On the effect of σ_{II} on $\delta_{z \max}$:

- (i) In contrast to convex impact cases, the two different values of σ_{II} yield very comparable results in relation to $\delta_{z \max}$, with the same perforation velocity threshold seen in the majority of cases at $V_I = 500$ m/s.
- (ii) This reveals that the geometrical effects imposed on the deflection of the rear face of convex laminates, cause $\delta_{z \max}$ to be much more sensitive to parametric changes, even at the sub-laminate interface.

Figure 4.68 displays the predicted depth of penetration (DoP) at each panel curvature, plotted against impact velocity for $\sigma_{II} = 1.8$ MPa. The overall trends seen here are in line with those witnessed for $\delta_{z \max}$ in Fig. 4.67, yet the small differences between plates of varying curvature are not captured due to the homogenisation of individual laminae into sub-laminate layers. Therefore only discrete outputs can be obtained, since the DoP corresponds to the total number of whole sub-laminate layers that have been fully perforated.

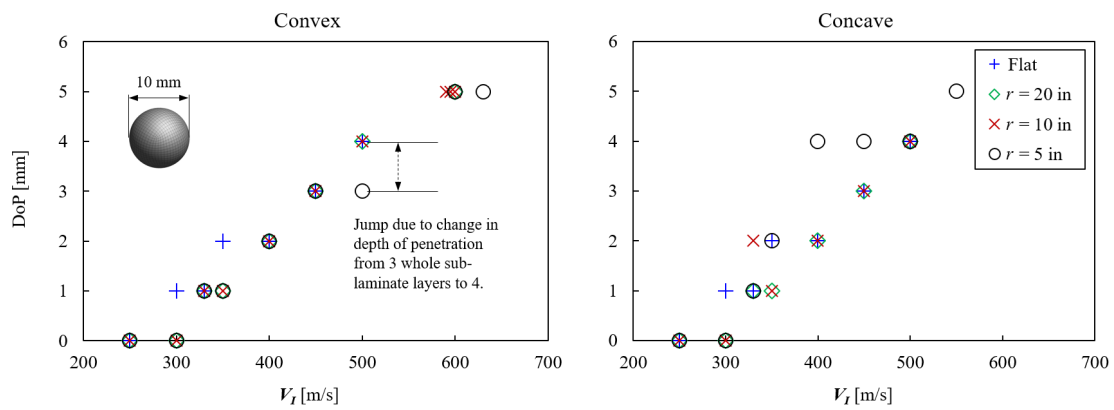


Figure 4.68: Variation in the depth of penetration with impact velocity, for $\sigma_{II} = 1.8$ MPa.

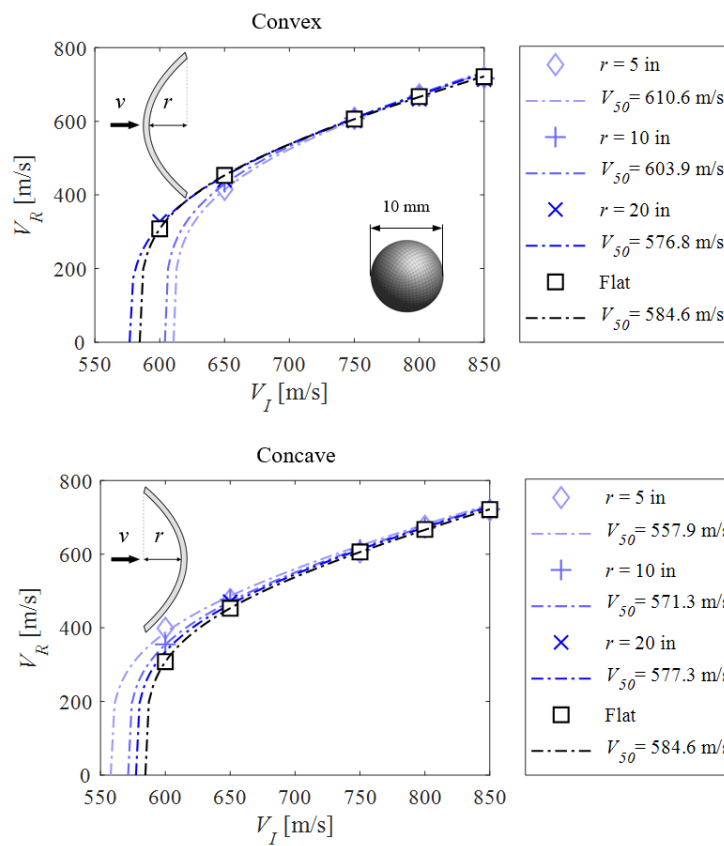


Figure 4.69: Numerically-derived Lambert-Jonas V_{50} approximations for curved panels, for $\sigma_{II} = 2.6$ MPa.

4.6.1.2 Velocity analysis

Ballistic limit predictions of the curved plates subjected to single point impact by the steel ball are presented in Figs. 4.69 and 4.70, for the two different values of σ_{II} considered. The number of data points in Fig. 4.23 are not sufficient for a comparison with numerical

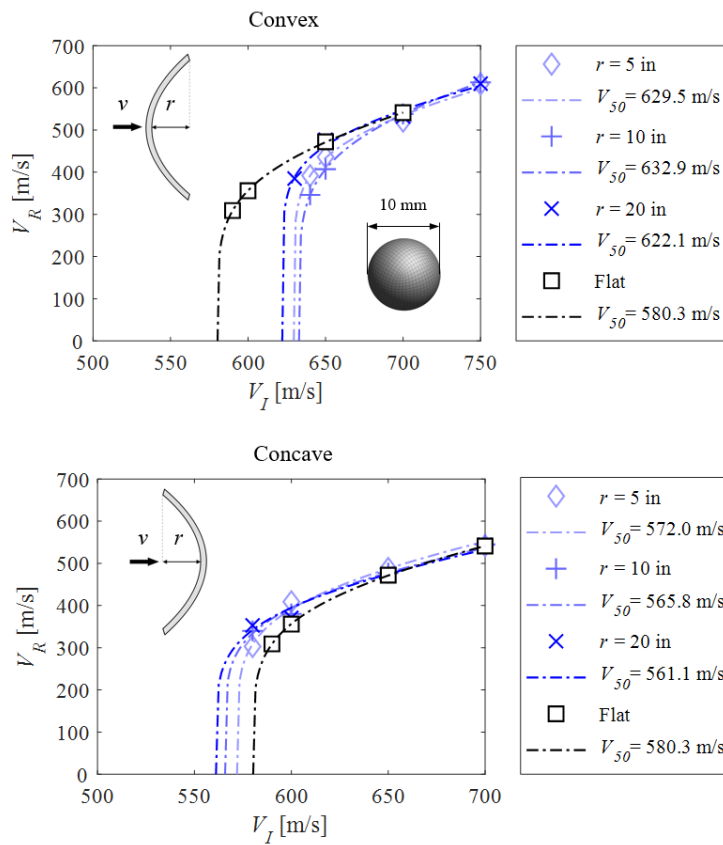


Figure 4.70: Numerically-derived Lambert-Jonas V_{50} approximations for curved panels, for $\sigma_{II} = 1.8$ MPa.

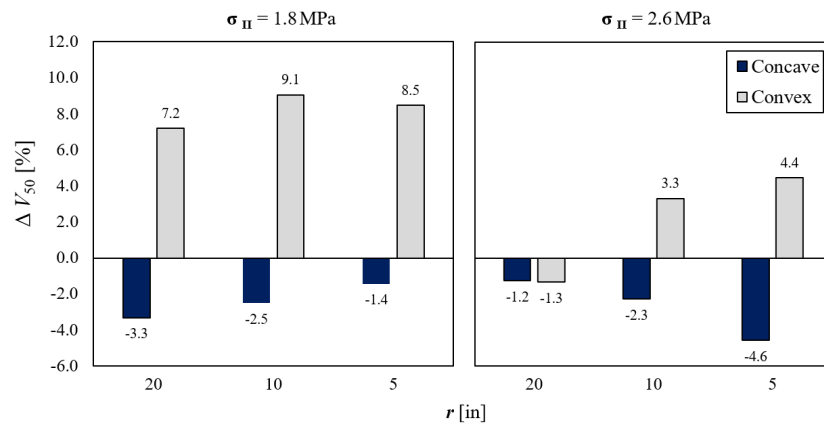


Figure 4.71: Comparison of percentage change in the V_{50} of curved laminates relative to a flat reference panel, between different values of σ_{II} .

results. Nevertheless, the patterns are in line with the experimental observations, where positive curvatures tend to improve the V_{50} predictions and vice-versa for negative curvatures. Using the higher rate value of $\sigma_{II} = 2.6$ MPa (Fig. 4.69), a small degree of positive and negative curvature

act in much the same way, reducing the ballistic limit velocity from a flat reference by no more than around 1.3%. On the other hand, the larger degrees of curvature under both directions of impact generate distinctly different V_{50} predictions relative to flat laminates with an absence of curvature. The maximum changes in the ballistic limit are exhibited by $r = 5$ in, with a rise of 4.4%, and by $r = -5$ in with a drop of 4.6%. Although the true extent of these changes could not be verified, the fall under convex and the increase under concave impact in the V_R value at a given V_I , particularly close to the V_{50} of each target ($V_I = 600$ m/s to 650 m/s), is evident from the modelling output.

Considering the lower rate value of peak traction at the interface, $\sigma_{II} = 1.8$ MPa, the addition of curvature to the target panel produces different predictions of V_{50} than for $\sigma_{II} = 2.6$ MPa. Not only are the V_{50} estimates for the curved panels grouped together, they are also clearly discernible from the flat plate estimate, especially regarding the V_R data points at the lower impact velocities. For example, under convex impact, reducing the value of σ_{II} from 2.6 MPa to 1.8 MPa, results in a 3%, 5%, and 8% increase in the V_{50} estimate for $r = 5$ in, $r = 10$ in, and $r = 20$ in, respectively. Meanwhile, the flat laminate estimate reduces by 1%, which is not considered to be a significant change. This shows that although the addition of curvature from none to a curvature of radius $r = 20$ in makes the velocity output more dependant on the value of σ_{II} , this sensitivity is reduced with an increase in the degree of curvature, as the geometrical effects of curvature become more dominant.

While convex impacts see improvements in the ballistic limit with an increasing degree of curvature, concave impacts result in an initial substantial fall at the shallowest curvature, before also increasing in V_{50} performance as the value of r is reduced further. To aid visualisation, the change in ballistic impact, ΔV_I , for both scenarios is displayed in Fig. 4.71. Since the testing results in Fig. 4.23 show an existing, albeit heavily limited, sensitivity in the residual velocity of the projectile to changes in the plate curvature at given strike velocities, simulations with the low rate σ_{II} value can be deemed less accurate, considering how sensitive the resulting V_{50} predictions are to changes in r . Furthermore, numerical studies and experimental investigations at lower impact velocities of approximately one order of magnitude lower, are required to establish whether the effects of curvature are more prominent at lower rates of impact.

4.6.1.3 Off-centre and oblique impacts

In the impact testing conducted in Section 4.4.1, it was not physically possible to ensure the projectile impacted the target at a perfectly orthogonal direction, due to external factors discussed in that section. Likewise, the location of impact was not necessarily always perfectly aligned with the centre of the target, which was in fact by design in multi-shot cases. As multi-shot tests are a standard way of measuring V_{50} in industry, it is particularly useful to explore the effect of proximity of impact location to the edge. Since the impact cases studied here consider only primary shots aimed at non-central-locations on the target, the interaction of multiple impact damages on a single target are not considered.

The issue with impact locations away from the centre of the target is two-fold. The first problem is of course the proximity to the edge, which changes with divergence away from the centre, affecting the repeatability and comparability of the resulting data. In addition, in curved plates, divergence from the central axis of the plate reduces the angle of impact, further skewing the results due to the oblique nature of the impact, the effects of which were investigated in [8, 102]. Naturally, in armour applications, impact predominately occurs at non-orthogonal angles, with Cunniff [103] demonstrating that only about 6% of total impacts investigated were within 10° of deviation from the normal direction. However, for the sake of investigating the sole effect of curvature, it is necessary to rule out the influence of these additional factors.

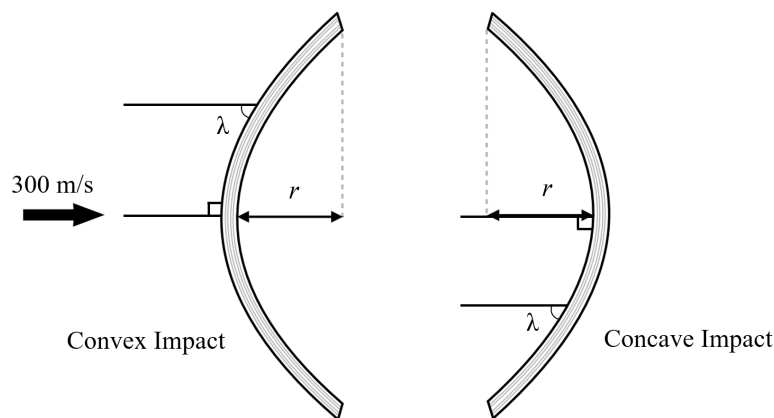


Figure 4.72: Relating the impact angle λ , non-oblique off-centre impact on a curved surface to the angle of an oblique impact on a flat target.

The numerical model of the flat target developed in Chapter 3 was validated against experimental data in literature. It is therefore used here to first decouple the effects of oblique impact from the effects of off-centre impact on the ballistic impact performance of the laminates.

The extent of these effects is then used to inform on whether the effects of curvature can truly be studied in isolation, or whether factors such as off-axis and oblique conditions significantly interact with and alter the effects of curvature. The numerical studies are conducted on a flat plate, at an impact velocity of 300 m/s, with a spherical threat corresponding to the experimental testing discussed in Section 4.4.1.

The angle of impact is represented by λ , equal to the angle of an oblique impact on a flat target, which also corresponds to the impact angle of a non-oblique off-centre impact on a curved surface, as demonstrated in Fig. 4.72. Note that as λ symmetrically converges to 0° , away from the centre of the plate towards the edge in the direction of curvature on the outside surface of a curved target, the trend is replicated on the inner surface the target for concave impact. In Fig. 4.73, the reduction in λ with increasing distance d from the centre of the target, symmetrical at the midline, is plotted at 20 mm intervals from 30 mm to 110 mm, for the three radii of interest.

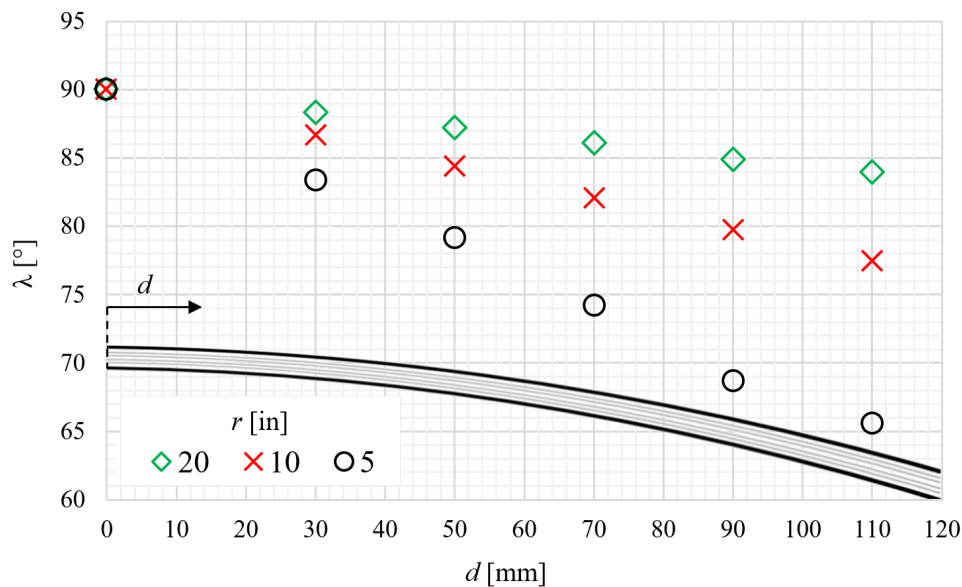


Figure 4.73: The variation in impact angle λ , away from the centre of curved panels with varying degree of curvature.

The percentage change in the peak BFD, $\Delta\delta_{z \max}$, of a flat target subjected to varying angles of oblique impact, is plotted against decreasing values of λ in Fig. 4.74, at 5° intervals, covering the range of impact angles that are brought about by an increase in d , displayed in Fig. 4.73. Since the most extreme case of off-centre impact in the physical testing regime did not exceed $d = 50$ mm, this is taken as the maximum and is thus the most conservative case

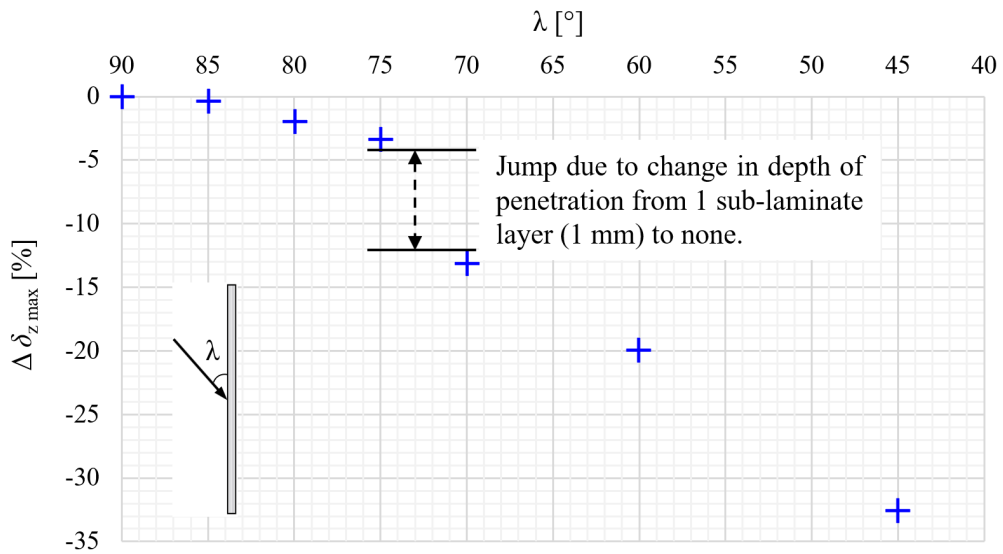


Figure 4.74: The percentage change in maximum apex deflection with impact angle λ , corresponding to distance away from the centre of a curved panel.

considered. For $r = 5$ in, the value of θ lies at 79.2° . From Fig. 4.74, it can be established that for this impact velocity and this projectile, the greatest change in the maximum BFD as a result of off-centre impact on curved targets is limited to 5%, with the majority of cases falling well below this value due to closer proximity to the centre and therefore less deviation from an orthogonal impact angle.

Note that the jump observed between data points at $\lambda = 75^\circ$ and 70° is due to the change in the depth of penetration achieved by the projectile, from 1 mm to no penetration at all, as a result of the homogenisation of individual plies into 1 mm sub-laminates. Changes to the BFD shape are also minimal up to a deviation of 25° , beyond which point the obliquity of impact alters the BFD in a noticeably nonsymmetric manner. This is demonstrated in Fig. 4.75, accompanied by contour plots of the out-of-plane displacement on the back face at $t = 0.2$ ms, which approximately coincides with the time of maximum deflection.

The effect of off-centre impact locations is explored in Fig. 4.76. The bars display the percentage change in $\delta_{z, \max}$ that occurs when the impact location is transferred away from the centre of the target to four alternative locations. The alternative locations are represented by their respective translation vectors, as a percentage of the total plate dimension. Four combinations of 30 mm and 75 mm displacements from the centre in the two in-plane directions were selected. The inset images display corresponding contour plots of δ_z at $t = 0.2$ ms, with the most affected shapes observed in the locations closest to the edge. Proximity to the edge

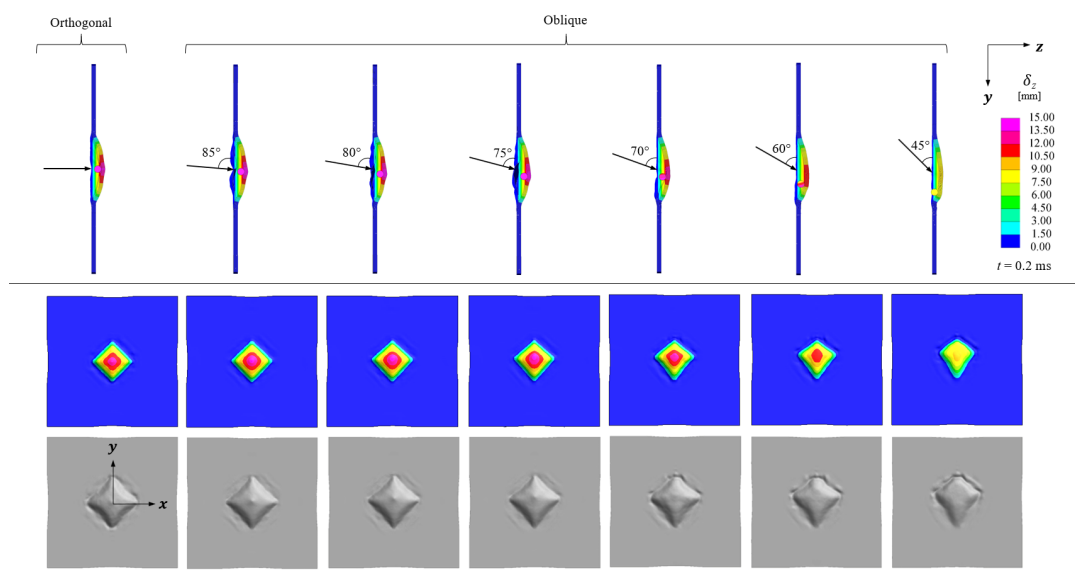


Figure 4.75: The variation in back face deflection intensity and shape with impact angle λ .

results in shorter fibre lengths, which in turn facilitate more extensive pull-in action at the edges, for a given impact duration.

A translation of 30 mm in only one dimension yields a 2.2% increase in δ_z , while the same translation in both directions limits this increase to only 1.2%, as balance is restored in the preferential direction of deformation. The same however cannot be said for a larger deviation of 75 mm from the centre, where translation in both directions generates a larger increase of 2.2% in δ_z . While the majority of cases were below the largest displacement from the panel centre that is considered here, the most extreme cases of off-centre impacts in testing were displaced by a maximum of 50 mm in only one direction, thereby making a 75 mm displacement from the centre a conservative estimate. This corresponds to the 5.2% predicted deviation in the value of δ_z , as compared to a perfectly central impact location, falling below the maximum predicted deviation of 6.7%, and thus within an acceptable threshold.

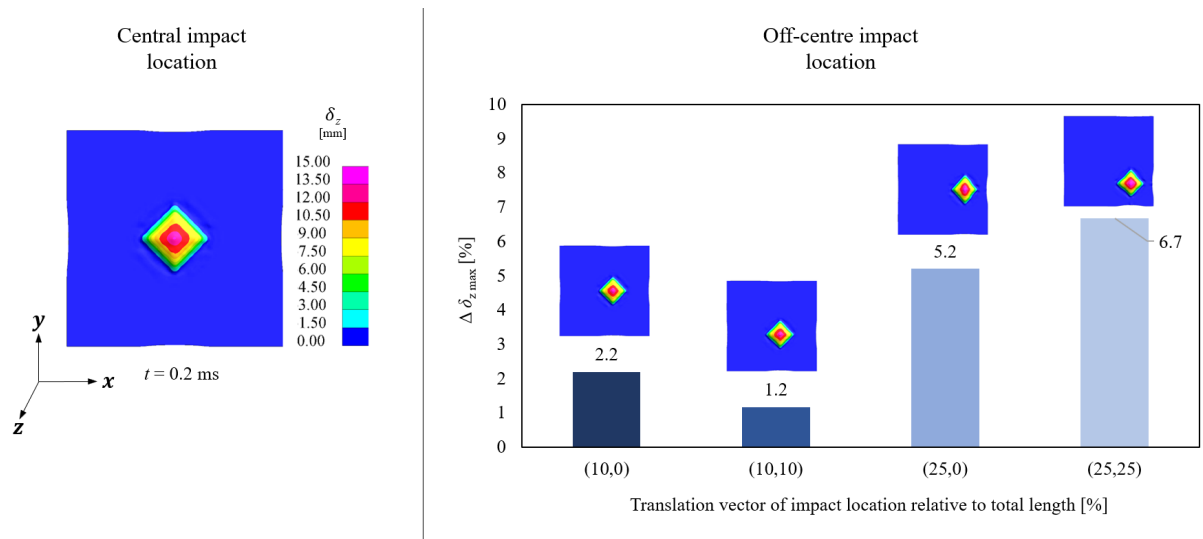


Figure 4.76: The variation in back face deflection shape and intensity with impact location.

4.6.2 FSP threat

Due to the absence of strain measurements and the lack of detailed high speed video captures obtained from the experimental impact testing of the curved laminates with an FSP threat, the deflection analysis is confined to drawing comparisons between plates possessing different degrees of curvature, with the remainder of the numerical comparisons focused on velocity-based analyses.

4.6.2.1 Deflection analysis

In Fig. 4.77, the maximum out-of-plane back face deflection, $\delta_{z \max}$, is presented as a function of V_I , for varying plate curvatures and impact directions. Compared to impact by the spherical projectile and the trends illustrated in Fig. 4.66, for an FSP threat, the relationships between $\delta_{z \max}$ and V_I amongst plates of varying curvature have remained the same, under both concave and convex impacts. The magnitudes of $\delta_{z \max}$ achieved here are however, almost half the values observed for the spherical projectile, while the minimum perforation threshold velocity has seen a rise of 150 m/s, as a result of the change in threat dimensions and geometry. Comparisons can be drawn between these numerical values and the apex deflection profiles extracted from the testing campaign, albeit at specific impact velocities.

The numerical predictions of $\delta_{z \max}$ under convex impact from Fig. 4.77 are compared against corresponding experimental data at impact velocities of approximately $V_I = 350$ m/s and $V_I = 600$ m/s in Fig. 4.78. While the modelling predictions display a linear increase in $\delta_{z \max}$ with increasing degree of curvature at both impact velocities, the experimental results reflect

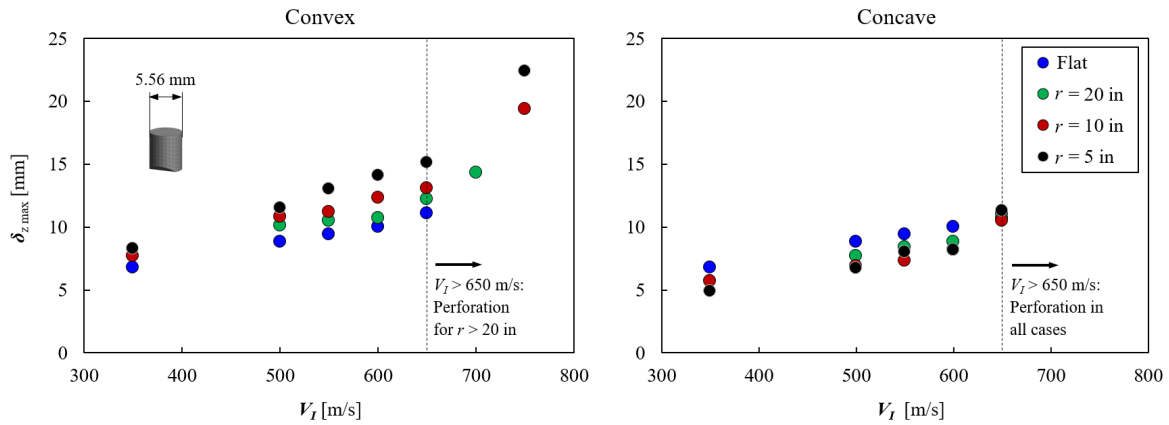


Figure 4.77: Variation in maximum apex deflection with impact velocity, for $\sigma_{II} = 2.6$ MPa.

a parabolic trend, with the peak values among the three curvatures tested lying at $r = 10$ in and 5 in. At both of these impact velocities, the values of the simulated peak apex deflection at a given panel curvature are comparable to the experimental data. The discrepancies that are visible between the numerical and experimental data at $V_I = 350$ m/s become almost negligible at $V_I = 600$ m/s. It was not possible to draw similar comparisons for the concave cases due to the lack of experimental data points.

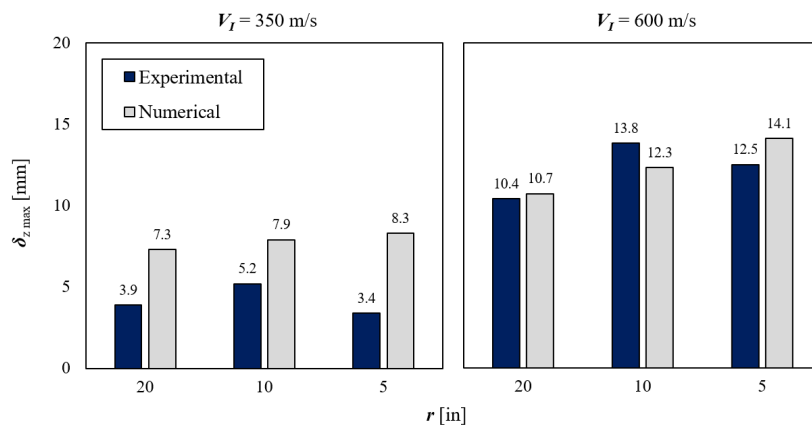


Figure 4.78: Comparison of maximum apex deflection of convex laminates between experimental and numerical results for an FSP threat, under two impact velocities.

In Fig. 4.79, the difference in $\delta_{z,max}$ between a flat reference plate and those of various curvatures is presented over a range of impact velocities. At impact velocities exceeding $V_I = 600$ m/s, the peak apex deflection for $r = 5$ in under convex impact begins to converge towards that of $r = 10$ in. The point of inflection at which a diverging trend in the data points of varying plate curvatures starts to converge, is predicted by the trend lines in Fig. 4.79. A

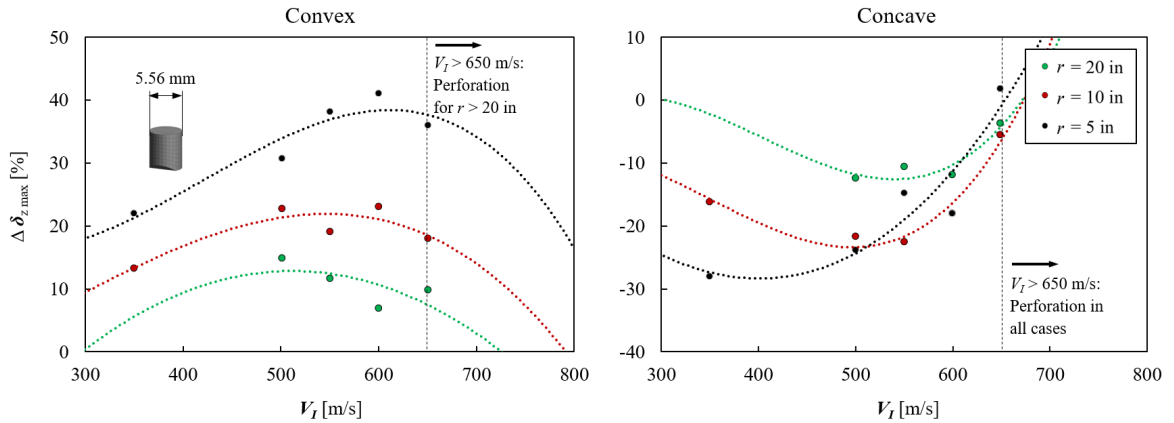


Figure 4.79: Numerically predicted percentage change in maximum apex deflection of curved laminates, relative to a flat reference, over a range of impact velocities.

similar reversal of the trend in the data for the most highly curved panel can be seen under concave impact, albeit at a lower impact velocity of approximately $V_I = 400$ m/s, where the dataset begins to converge towards that of the less curved panels. These trend reversals at higher impact velocities are attributed to the onset of laminate penetration, followed by full perforation. Numerical predictions of the velocity-based impact performance parameter are discussed in the following section.

4.6.2.2 Velocity analysis

In this section, V_{50} approximations based on numerical simulations of the FSP impact are compared to the predictions calculated from the test data presented in Section 4.4.2. Unlike for the round projectile, there are sufficient empirically-acquired velocity data points for calculating V_{50} estimates that the simulation results can be compared against. Subsequently, the effect of laminate thickness and projectile dimensions on the simulated V_{50} performance are evaluated for various plate curvatures.

Numerically-derived V_{50} estimates at different target curvatures subjected to FSP impact are presented in Fig. 4.80. Note that no perforation was achieved in the convex simulations below $V_I = 750$ m/s, around which point the V_{50} approximations revolve. This is followed by a comparison of the numerical estimates with experimental data in Fig. 4.81. Based on the numerical estimates, the effect of target curvature on the V_{50} is explored in Fig. 4.82, which displays the percentage difference in the ballistic limit, ΔV_{50} , between a curved panels and the flat reference plate, in comparison to experimental results.

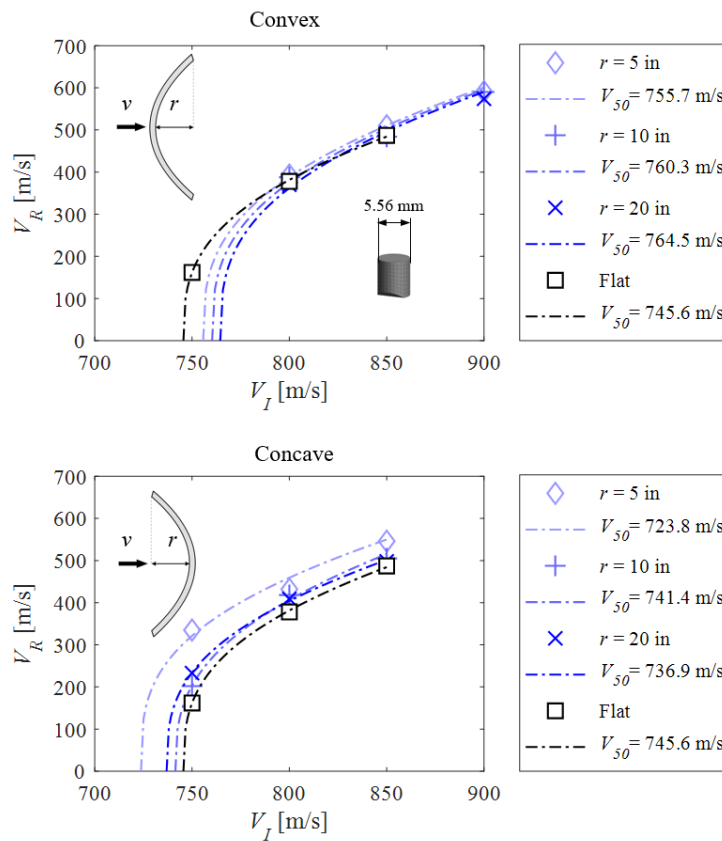


Figure 4.80: Numerically-derived Lambert-Jonas V_{50} approximations for curved panels, with $h_t = 6$ mm and a small FSP threat.

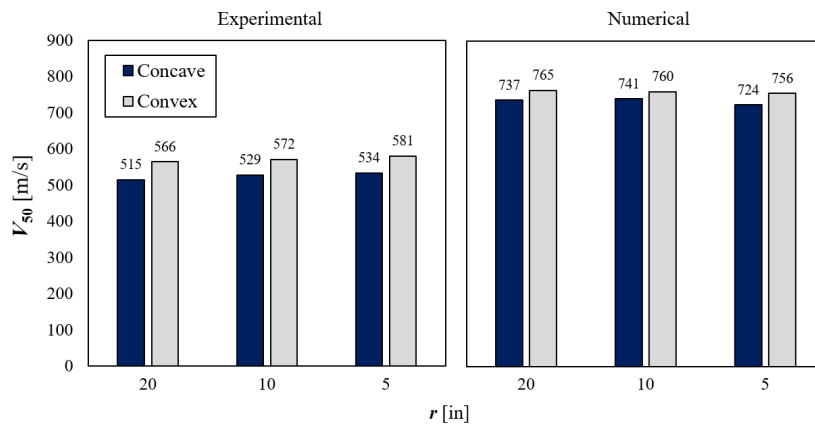


Figure 4.81: Comparison of V_{50} between experimental and numerical data for curved laminates.

Comparing the absolute values of the numerical and experimental V_{50} predictions in Fig. 4.81, the experimental data shows that the ballistic limit of convex laminates with varying degrees of curvature is within a range of 566 m/s to 581 m/s, with the highest V_{50} value belonging to the most highly curved laminate. Concave panel V_{50} estimates are approximately 10% (40 m/s

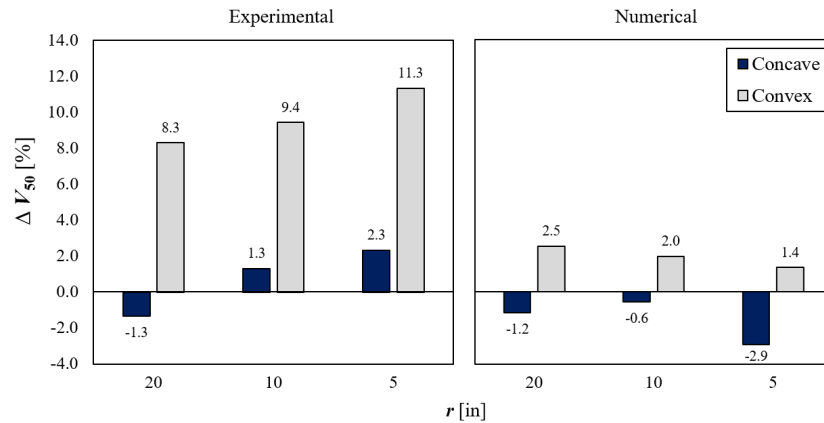


Figure 4.82: Comparison of percentage change in V_{50} between experimental and numerical data for curved laminates, relative to a flat reference panel.

to 50 m/s) lower than the convex panels at a given curvature. This results in a ballistic limit range of 515 m/s to 534 m/s, with the highest V_{50} estimate also belonging to the most highly curved laminate. Numerical predictions are, however, in the order of approximately 200 m/s higher in magnitude than was reported from the experimental testing, with V_{50} estimates in the range of 756 m/s to 765 m/s and 724 m/s to 737 m/s for convex and concave impacts, respectively. In contrast to experimental findings, in numerical predictions, the maximum values of the ballistic limit range for both directions of impact belong to the panel with the shallowest curvature. Nevertheless, the numerically-derived ranges of V_{50} are in line with the experimental observation that V_{50} predictions for concave impact are lower than for convex impact, with an approximately 5% (20 m/s to 30 m/s) difference between concave and convex cases at any degree of curvature.

To investigate the effect of curvature, the difference in V_{50} estimates between curved and flat laminates are considered in Fig. 4.82. Under convex impact, the V_{50} prediction sees an initial increase of 2.5% from a flat target to one with $r = 20$ in, as documented in Fig. 4.82. Following further reductions of the radius of curvature, that trend reverses and V_{50} starts to approach the ballistic limit velocity of the flat reference plate. Concave impact results in similarly small changes to the V_{50} estimate, with the most highly curved plate seeing a reduction of 2.9%. The simulations show similar levels of under-prediction of the effect that curvature has on the V_{50} of curved panels, as was previously shown in Section 4.6.1.2, with regards to the effects on the peak BFD under impact by a spherical threat. Ballistic limit velocity predictions under concave

impact show a much smaller degree of sensitivity to changes in panel curvature, in line with the results obtained experimentally. Under both directions of impact however, the effect of r on ΔV_{50} is reversed between numerical and experimental results.

The V_{50} of the flat reference plate was also found to be significantly over-predicted by numerical simulations at a value of 746 m/s, compared to the empirical estimate of 522 m/s. Hence, it is possible that the addition of curvature to the modelled plate is not the only parameter influencing the disparity between experimental and numerical data; the flat laminate model was validated in Chapter 3 [49, 81], however, the laminate thickness was then reduced from 10 mm to 6 mm by reducing the number of 1 mm thick sub-laminates to 6, while the FSP used for impact testing was also smaller in size than the projectile used in model validation. To evaluate this notion and rule out effects other than that of curvature, parametric changes to the laminate thickness and the FSP dimensions are investigated as follows.

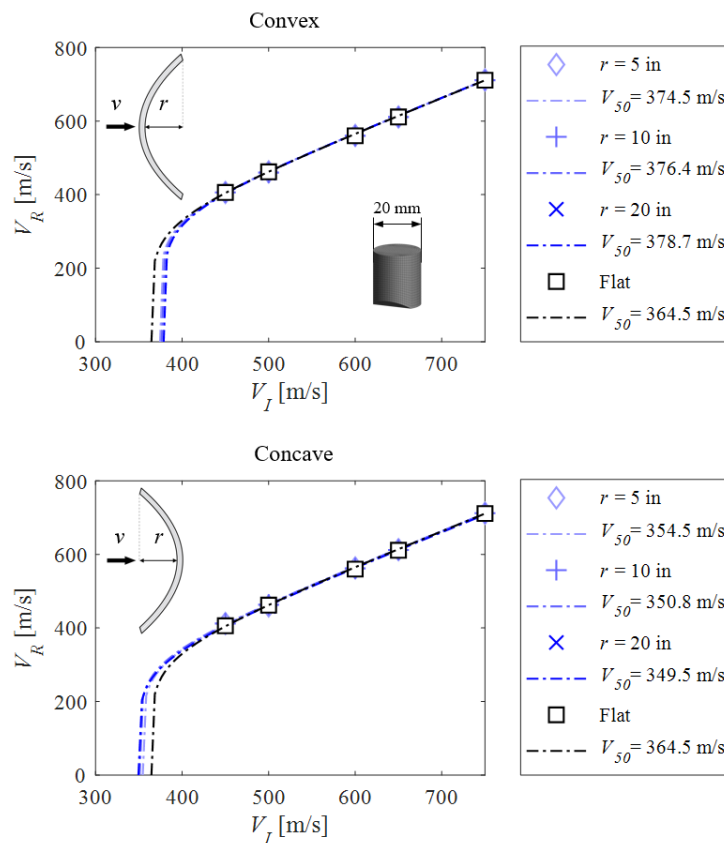


Figure 4.83: Numerically-derived Lambert-Jonas V_{50} approximations for curved panels, with $h_t = 6$ mm and a large FSP threat.

Figure 4.83 demonstrates the effect of increasing the projectile diameter from 5.56 mm,

with a mass of 1.1 g, to the FSP selected for investigations in Chapter 3, with a diameter of 20 mm and a mass of 55 g. Note that the ratio of the projectile mesh density to its overall dimensions was maintained across the two projectiles investigated. The reduction in V_{50} that follows this increase in projectile dimensions is severe. Under the smaller FSP, V_{50} estimates for the different plates revolved around velocities close to 750 m/s. This is reduced to velocities around 360 m/s, with the introduction of the larger FSP. Although in Fig. 4.83, changes in V_{50} with increasing plate curvature appear to be minimal, the bar charts in Fig. 4.85 put these differences into perspective. Here, it can be seen that the extent of changes in V_{50} is similar across laminates of the same thickness, without being very sensitive to the projectile dimensions. Increasing the thickness of the laminate to 10 mm however, visibly alters this trend.

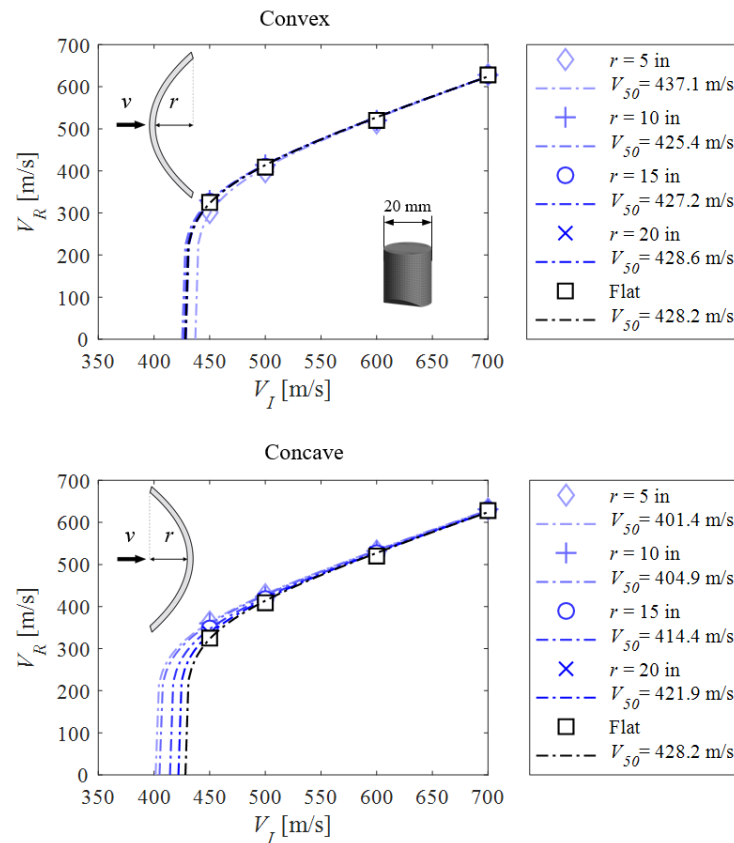


Figure 4.84: Numerically-derived Lambert-Jonas V_{50} approximations for curved panels, with $h_t = 10$ mm and a large FSP threat.

The effect of plate thickness is shown in Fig. 4.84, with the addition of $r = 15$ in to the previous range of curvature radii investigated. While the laminate thickness, h_t , is increased to

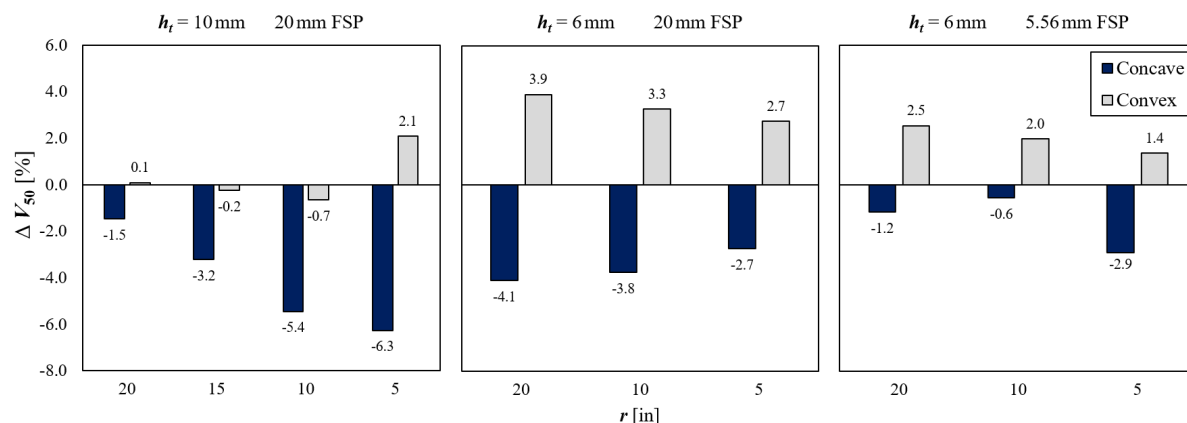


Figure 4.85: Comparison of percentage change in the V_{50} between different laminate and threat dimensions for curved laminates, relative to a flat reference panel.

10 mm, the in-plane dimensions of the curved plates are kept the same. As a result of the increase in thickness for all curvatures, the V_{50} predictions have increased significantly, falling between 400 m/s to 450 m/s, although still well below the values observed for the smaller FSP threat. It can be seen that the addition of curvature in both impact directions has marginal effects on the V_{50} estimate. The increase in thickness is not a determining factor as it is consistent across the different degrees of plate curvature, unlike the reduction in plate length which is slightly larger for more curved panels. Note that concave impact V_{50} predictions that have previously demonstrated very little sensitivity to the degree of curvature display a small dependence on the curvature in Fig. 4.84, resembling of the V_{50} trend seen in Fig. 4.80 for the thinner laminate with the smaller FSP. Further investigations are therefore required to determine the sensitivity of the modelling outcomes to the ratio between projectile dimensions and plate thickness.

4.6.2.3 Interface studies

The element-based CZM models developed in Chapter 3 were used to study the effects of several parameters on the energy absorption mechanisms of the laminate, together with the ballistic performance of the material in terms of back-face deformation and ballistic limit velocity. These parameters included the in-plane and out-of-plane dimensions of the laminate, as well as the number of plies and interfaces represented by one homogenised sub-laminate. The levels of kinetic energy dissipated through mode I and mode II were investigated, together with the overall amount of energy absorbed at different in-plane and out-of-plane locations in the

laminates. This section is a continuation of that work, with a parametric study to investigate the effect of single curvature on the energy dissipation that takes place at the sub-laminate interfaces, using the same modelling parameters and dimensions as the baseline model described in Section 3.3.1, which correspond to the threat and target dimensions investigated in Fig. 4.84.

The graphs in Figs. 4.86 to 4.87 demonstrate the total level of energy dissipated at the interfaces over time in terms of absolute value, $I_T E$, in the top row, and as a percentage of the total amount of energy dissipated by the entire laminate over time, $I_T E / T E$, along the bottom row. The plots are grouped by impact velocity, with $V_I = 350$ m/s on the left-hand side and $V_I = 600$ m/s on the right-hand side. Energy levels of a flat plate are represented by black curves for reference, while the results of curved laminates $r = 20$ in to 5 in are portrayed by the blue-shaded curves, with lighter tones corresponding to smaller radii.

Deformations at the sub-laminate interfaces of curved laminates with varying degrees of curvature follow the same trends that are visible for the flat reference plate, wholly dominated by mode II energy dissipation. As shown in Fig. 4.86, under convex impact, there are no significant disparities between the curved laminates and the reference plate in both absolute and relative energy terms, with the only exception being the most highly curved case. The noticeably lower values for this plate are in line with the findings in Fig. 4.84, where $r = 5$ in was the only case that demonstrated a reduction in exit velocity, particularly at the lower end of the V_I range, consequently leading to a higher V_{50} approximation.

From Fig. 4.87, it can be seen that under concave impact panels of varying curvature show a similar behaviour at $V_I = 600$ m/s, while for $V_I = 350$ m/s the initial rise in the absolute amount of energy dissipated is also identical in all curvature cases. However, beyond $t = 0.05$, the dissipation of energy accelerates faster in the curved laminates than it does in the flat case. More significantly, under concave impact, energy dissipation via mode I drops to zero in all curved laminate cases. This occurs as the laminate is already deformed in the out-of-plane direction of bulging that corresponds to the direction of impact. The implications of this with regards to residual strain and BFD shape progression were examined and reviewed throughout the earlier sections of this chapter.

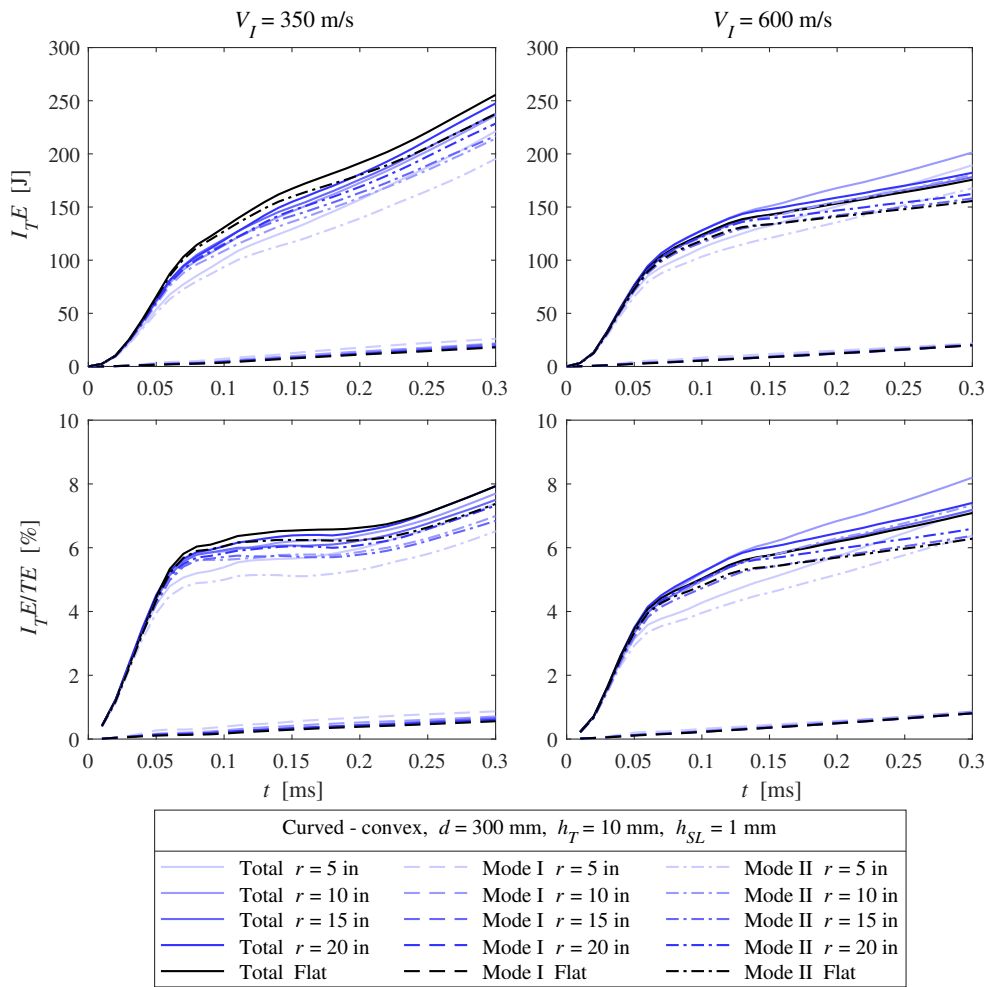


Figure 4.86: Energy dissipated at interfaces (top) and energy dissipated at interfaces as a percentage of total energy dissipated by laminate (bottom), for a range of plate curvatures at $V_I = 350$ m/s and $V_I = 600$ m/s, under convex impact.

4.6.3 Further discussions

In this section, some manufacturing effects and potential sources of discrepancy between specimens and the models are highlighted. These include modelling effects in capturing the FSP deformation, together with manufacturing defects.

4.6.3.1 FSP deformation

Numerical and post-impact physical deformations of the smaller FSP are presented in Fig. 4.88. Tested FSPs for the three impact cases of projectile rebound, partial penetration and full perforation show various degrees of deformation, most of which are not noticeable.

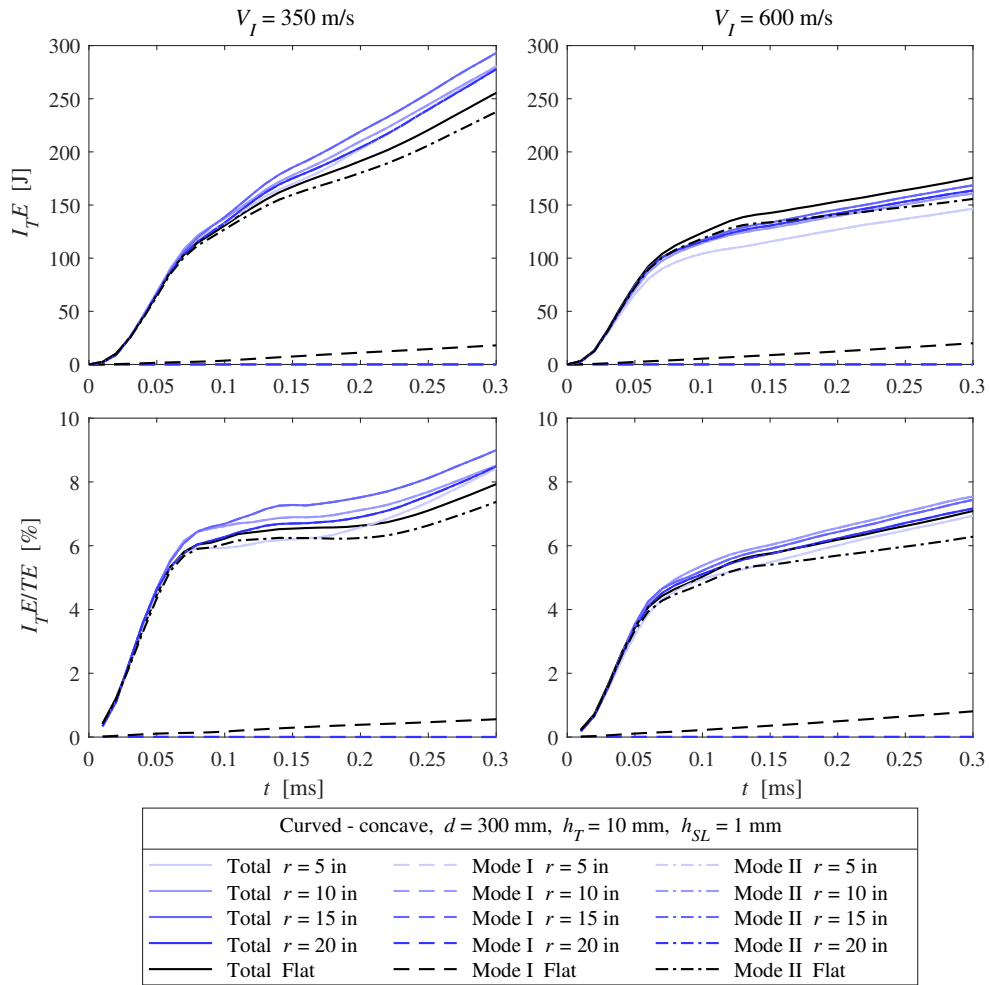


Figure 4.87: Energy dissipated at interfaces (top) and energy dissipated at interfaces as a percentage of total energy dissipated by laminate (bottom), for a range of plate curvatures at $V_I = 350$ m/s and $V_I = 600$ m/s, under concave impact.

Numerical deformations of the projectile on the other hand, are prominent even at the lowest impact velocities considered, from the moment that contact with the target is established and irrespective of the strike velocity considered. Further studies are required to investigate the evolution of the contact force over the duration of impact, and the effect of projectile dimensions on the results.

4.6.3.2 Manufacturing defects

It is also imperative to consider the effect of external factors during the manufacturing and testing regimes of the laminates. Table 5.1 displays the specifications of the specimens with different curvatures, where the areal density (AD) is calculated using the curved dimensions

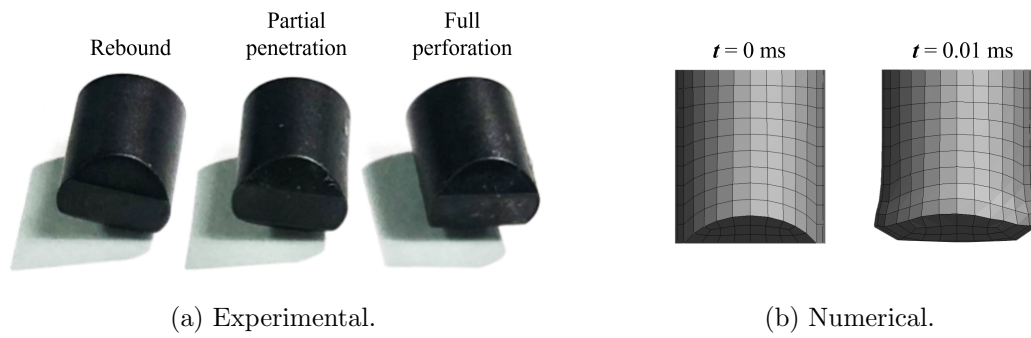


Figure 4.88: Comparison of post-impact projectile deformation.

using Eq. (5.4). The remainder of this section will focus on the potential causes of the disparity in the AD and d_c values between the flat and the curved panels.

Due to the extremely low inter-laminar friction coefficient, the sliding of plies over each other in either direction in the curved dimension was a common occurrence during consolidation under the curved press tooling, as evident by the extra lengths at either end of the manufactured laminates. This explains another observation that was made regarding disparities and mismatches in the laminate length throughout the thickness of each specimen [104]. Note that fibre stretching and shortening [105], can coexist with the sliding of plies during the manufacturing process as the former typically follows the latter, once the consolidation pressure is ramped up. In addition, the curved laminate ends were modelled at an angle to the direction of impact due to the radial translation of nodes, while in reality, prior to consolidation the plies were stacked on top of each other with the edges aligned along the direction of impact.

Table 4.4: Specifications of specimens with different curvatures.

r [in]	\bar{h}_t [mm]	d_s [mm]	d_c [mm]	s [mm]	AD [kg/m ²]	N_p
∞ (flat)	6	300	300	300	4.47	20
20	6	300	252	255	5.26	20
10	6	300	244	255	5.26	20
5	6	300	222	260	5.16	20

Evidence from the BFD images in Section 4.4.2.2, suggests not all laminates were consolidated uniformly across the surface area, and not to the same degree amongst different specimens, as a result of, for example, poorer consolidation away from the central region of the panel when placed between the female and male moulds. The higher the consolidation pressure, up to a

limit of around 165 bar [106], the more transparent the laminate becomes when pressed and the better the resulting V_{50} performance. A press pad was placed on top of the material during consolidation in the press, as displayed in Fig. 4.5, with the potential to cause wrinkling, a defect that was observed in some regions on the surface of laminates. More insight into the behaviour of the press pads under a curved tooling is required to infer the implications of this. Similarly, a more detailed inspection of surface wrinkling and microscopy of untested laminate cross-sections is required to identify and evaluate the effects of manufacturing defects. Note that ultrasound c-scanning is, however, not possible for laminates of Dyneema[®], due to the similarities that exist in the acoustic damping properties of the composite material and that of air, making delamination very challenging to detect due to the low resolution of the images that can be obtained.

Furthermore, the schematic in Fig. 4.5 illustrates the mismatch between the total thickness of the laminate together with the press pad, and the difference that exists between the radius of curvature of the female and male moulds, $r_f - r_m$, for manufacturing a target with $r = 5$ in. This can alter the resulting degree of curvature, away from the desired target curvature. Post-consolidation spring-in effects can also reduce the distance between the ends of the laminate. Spring-in occurs due to discrepancies in the in-plane and through-thickness shrinkage rates of the laminate, as the through-thickness rate is an order of magnitude higher. As a result, the corner angles close up to maintain continuity. This does not result in a change in the curved length, yet it does result in a non-uniform value of r along the curved length of the plate. However, the extent of this is likely to be marginal due to the use of an actively cooled press in the manufacturing process, meaning that laminates were cooled under the geometrical restrictions of the moulds.

4.6.4 Summary of key findings

In the second part of this chapter it was revealed that the modelling tools developed for curved laminates based on previous flat plate models, predicted the maximum BFD of laminates under spherical and FSP threats to a reasonable degree of accuracy. They were, however, limited in their ability to capture the full extent of the in-plane deformations under ballistic impact, as well as the ballistic limit velocity for impact by a fragment simulating projectile. In addition, numerical predictions demonstrated high levels of sensitivity to the ratio between projectile and laminate dimensions. Some of the trends in deformation- and velocity-based parameters presented a parabolic relationship with the degree of curvature, in line with previous

findings in literature [26, 41]. However, improved accuracy of the simulated predictions of these parameters is required in order to utilise these numerical tools in the identification of an optimal panel curvature, to achieve the highest ballistic limit velocity for the lowest back face deflection possible.

Several explanations were found for the discrepancies between numerical predictions and experimental results. Most were focused on the modelling principles and techniques, ranging from limitations in modelling bending deformation and the effects of pre-straining in the fibres, to the presence of rate effects and plastic deformations that are not accounted for. It is thought that some of these effects are more prominent in curved laminates, due to the increased stiffness in the configuration, to the extent that they cannot be neglected as had previously been possible for flat laminates. To improve the accuracy of the modelling predictions in future work, the effective stiffness approach used by Stargel [41] could be adopted. Note that although using this approach will likely improve the correlation between the computational and experimental data in the current study, the sources of error arising from other factors, such as manufacturing defects, will still remain.

The effect of modelling parameters were also investigated in this chapter. These included mesh density in the laminate and the FSP, as well as cohesive peak mode II traction. The simulations performed with these varying parameters over-predicted the ballistic limit velocity to a very similar degree. Although the parametric investigations suggested a high degree of sensitivity to geometrical changes in the model, this is a reflection of the physical behaviour of the laminate in reality. In addition, some sources of discrepancies between the modelling and experimental results were attributed to the manufacturing process. Curved laminates are prone to effects that a flat plate would not be subjected to, and if so, not to the same extent. Examples include poor consolidation and extensive sliding of plies, due to the curved geometry of the tooling. Furthermore, the numerical models were developed based on nominal values of the radius of curvature, whereas the actual radius of curvature may have been affected by ill-matched tooling dimensions, as well as post-consolidation spring-back effects. Components with geometrical complexities that are fabricated through particular manufacturing techniques are best modelled from the manufacturing stage onwards, using process modelling methods such as forming simulations, to incorporate these manufacturing effects into the impact behaviour of the laminate. This approach would account for processing conditions, the internal strain induced in the fibres, as well as post-consolidation cool-down effects. More importantly however, process modelling will capture an essential manufacturing effect; in-plane shear. The consequences of

this shearing deformation and accompanying secondary effects on the ballistic impact behaviour of UHMWPE fibre composites are investigated in the following chapter.

Chapter 5

Effect of pre-existing shear on impact performance

5.1 Introduction

This chapter characterises the behaviour of sheared panels of Dyneema[®] under impact, in order to advance capabilities in predicting the performance of the material subject to such loading cases. Focus will be placed on the effects of shearing on the ballistic limit velocity, V_{50} , of laminates, a key industry-standard indicator of impact performance. Similarly, the effect on the form and extent of the back face deflection will be touched upon, since it is a determining factor for the degree of behind-armour blunt trauma inflicted upon the user.

To begin with, a representative manufacturing process is developed to fabricate sheared plates of Dyneema[®]. In addition, the behaviour of the material and the effects of external factors on the process are investigated. Dangora *et al.* [107] have characterised the in-plane shear stiffness of Dyneema[®] HB26, together with the factors affecting it, forming the basis of the initial methodology steps in this investigation. Subsequently, ballistic impact testing is performed on the specimens to evaluate the effect of the extent of in-plane shear deformation on their impact performance. The degree of shear in a specimen corresponds to the location of impact on a hemispherical surface, as shown in Fig. 5.1(a). The figure illustrates the variation in shear angle across the surface of a laminates, as predicted through forming simulations performed by Dangora *et al.* [17]. For volume to be preserved, in-plane shear of the preform is accompanied by its thickening, demonstrated in Fig. 5.1(b). The authors suggest using

the filler ply pattern in Fig. 5.1(c) in order to achieve a relatively uniform thickness across the hemispherical configuration. The work presented in this chapter will also evaluate the effectiveness of a constant thickness requirement for promoting uniform impact performance throughout the laminate.

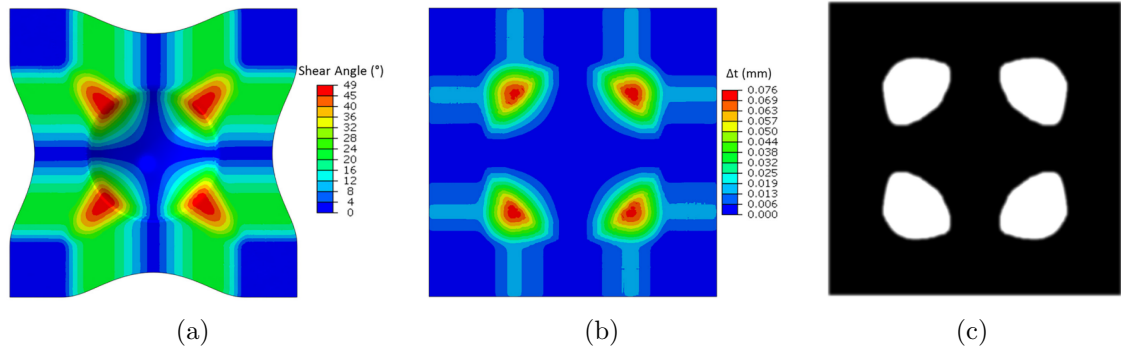


Figure 5.1: Contour plots of the (a) shear angle on a deformed lamina and (b) thickness change Δt of a 0.148 mm thick lamina due to shearing, as acquired from forming simulations, with (c) showing the suggested filler ply and cut-out pattern. Reproduced from [17].

5.2 Methodology

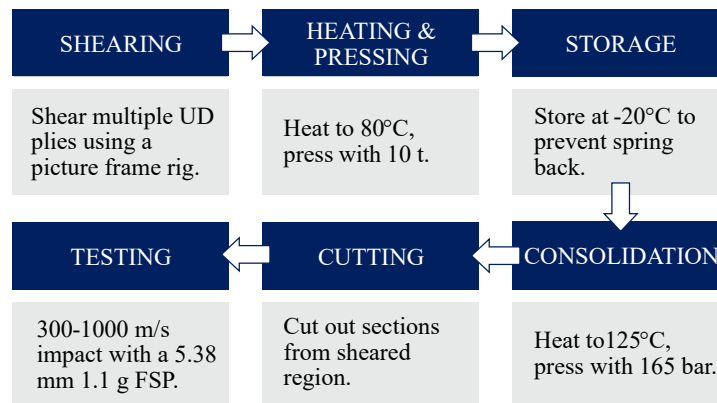


Figure 5.2: The different stages of the process developed for manufacturing sheared plates of Dyneema[®].

It was desired to separately investigate the two deformations that occur in forming a dome shape from a flat laminate, *i.e.* curvature and in-plane shear. In this chapter the focus is on in-plane shear and how the method outlined in Fig. 5.2 was used to manufacture the specimens used in this study, deformed purely through in-plane shear. Batches of the preform were sheared by either 30° or 60° in a picture frame rig that was manufactured for this purpose, and partially

consolidated under a hot press to contain spring-back deformation before full consolidation of an entire stack could take place. It should be noted that the heat and pressure regimes present during the forming of UHMWPE laminates were not mimicked here, due to the need for simplification which led to the separation of the shearing and consolidation processes. Following the shear deformation process, preform layers of the material were consolidated with heat and pressure, as per the recommended manufacturer's cycle adopted in [86].

5.2.1 Material

Dyneema[®] grade HB26 was selected for the purpose of this study. Its prevalence in literature not only provides a comprehensive insight into its behaviour, but also the means for comparison of data from this work. It is worth noting that although the material is referred to as HB26 UD, each layer of the as-received material is made up of four individual true unidirectional layers consolidated in a cross-ply formation of $[0,90]_2$, as illustrated in Fig. 5.3 [79].

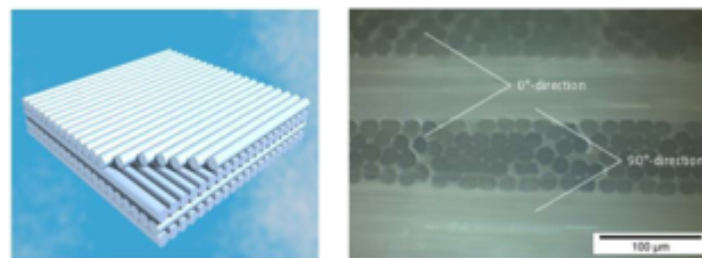


Figure 5.3: The structure of one Dyneema[®] HB26 UD layer, composed of four true UD stacked in a cross-ply formation. Reproduced from [79].

5.2.2 Material characterisation

A picture frame test rig was designed and built to accommodate and induce in-plane shear in square-shaped $200\text{ mm} \times 200\text{ mm}$ Dyneema[®] HB26 specimens, which were then consolidated to form plates with varying degrees of shear. The frame fixture was mounted onto a 100 kN electromechanical tensile test machine by Zwick and a displacement was applied to extend the samples in the $\pm 45^\circ$ direction, as demonstrated in Fig. 5.4(c), until the desired shear angles of 30° and 60° were reached. Due to the ambiguity involved with the term 'shear angle', from now on the angle by which the material was sheared will be referred to as the shear or rotation angle α , and the angle between alternating layers of fibres will be referred to as the frame angle θ , equal to $90^\circ - \alpha$.

Based on the work of Dangora *et al.* [107], slits were introduced to the flange regions of the

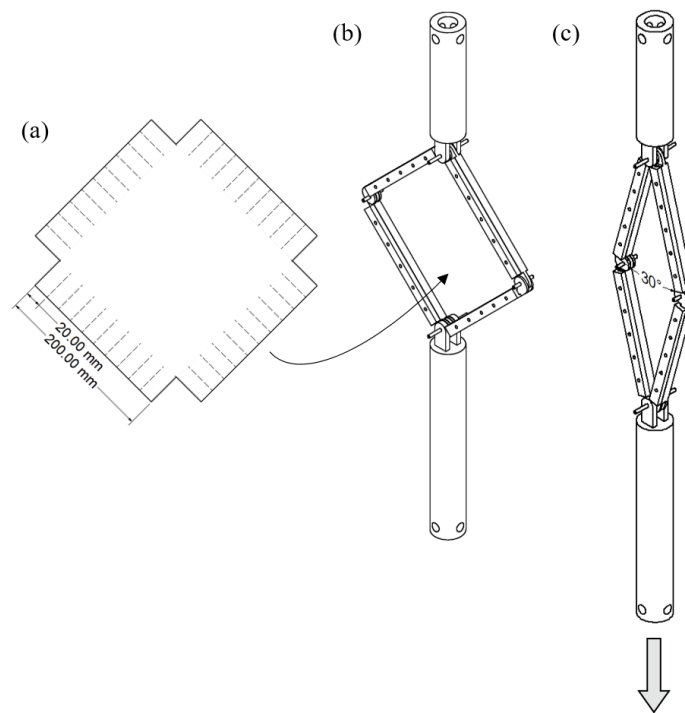


Figure 5.4: Schematics illustrating (a) the HB26 specimen dimensions, (b) a CAD model of the picture frame fixture prior to any deformation, (c) the same fixture following displacement to achieve a frame angle of 30° , with the arrow pointing in the direction of cross-head displacement.

specimen at 5 mm intervals, as illustrated in Fig. 5.4, to enable these flanges to take the bulk of the out-of-plane wrinkling deformation that is induced during shearing, in order to achieve a flat surface in the central regions. According to the authors, the numerically optimised number of slits approaches infinity and is implemented by dissolving the matrix in the flanges until only fibres remain. However, this was deemed impractical and unnecessary for the purpose of this study. The presence of the slits every 5 mm helped to achieve a sufficiently uniform in-plane strain across the surface of the specimen, throughout the shearing process, as verified by digital image correlation (DIC) measurements visible in Fig. 5.5, together with a consistent shear angle in the cross-ply fibre architecture, as shown in Fig. 5.6. In addition, there is little evidence of fibre elongation, with recordings of the length taken at five intervals demonstrating fluctuations of less than 5% throughout the process, seen in Fig. 5.7, pointing to an almost perfect scissoring behaviour of fibres within the domain of the matrix. For the purpose of efficiency, multiple layers of HB26 were sheared simultaneously. As will be demonstrated later in Fig. 5.22, the response of multiple plies is well-aligned with the response of a single ply, when scaled down based on the number of preform layers used. Since the simultaneous shearing of four layers was prone to slippage of plies out of the frame, only three HB26 UD plies were sheared together in

each single step during the manufacture of sheared plates.

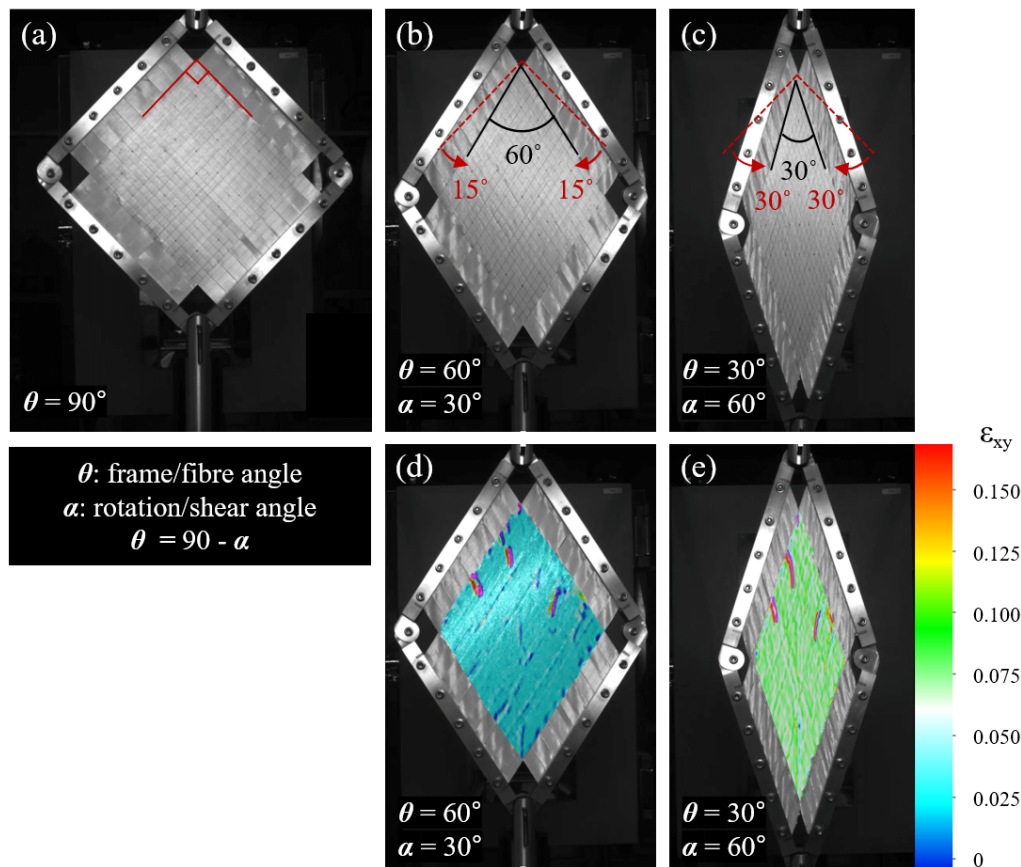


Figure 5.5: Sheared specimens in the picture frame test rig (a) prior to shearing, (b) sheared by 30° to a frame angle of 60° and (c) sheared by 60° to a frame angle of 30° , together with DIC measurements of the in plane shear strain on the specimen surfaces at a (d) 60° frame angle and a (e) 30° frame angle.

An example of a sheared specimen prior to dismounting and close-up images of the sheared material can be seen in Fig. 5.8. Challenges involved with deforming the material to this extent were not limited to the simple slippage of the flanges out of the grip of the picture frame rig. An excessively tight grip resulted in fibre breakage and was therefore reduced to the minimum required to prevent the slippage of plies. Thickening of the material during shearing and the creation of ridges on the front and rear surfaces of the sample visible in Fig. 5.8, displaced thermocouples attached to the surface for trials at elevated temperatures in a thermal chamber. To prevent this, thermocouples were attached instead to the edge of the top corner of the sample, and secured in place with flash tape on both the front and the rear. Another challenge faced was creating a speckle pattern for the purpose of DIC analysis on the surface of the unconsolidated preform, due the dispersion of ink spots along the fibres. To minimise this effect,

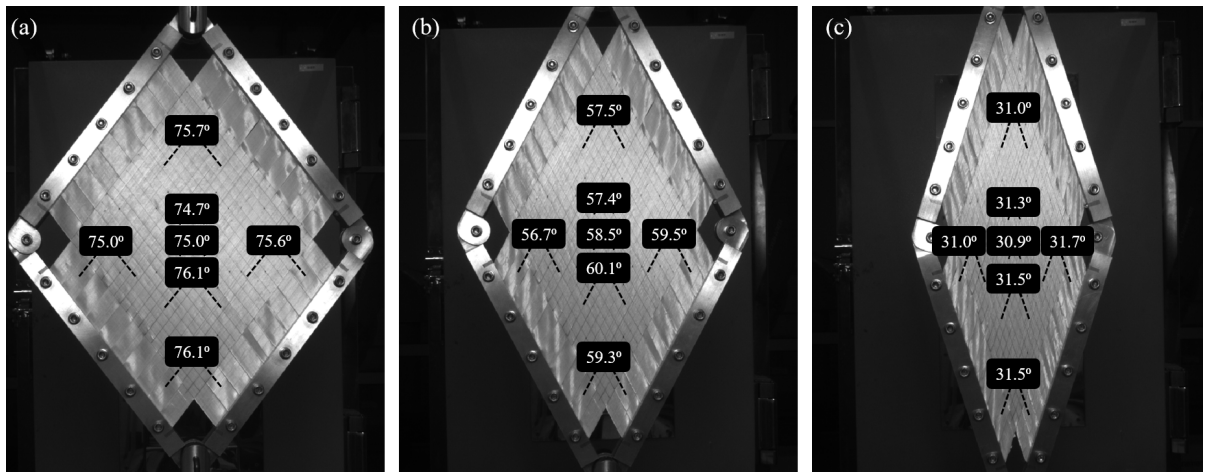


Figure 5.6: Local fibre angles during the shearing process at two intervals of global frame angle (a) $\theta = 75^\circ$ and (b) $\theta = 60^\circ$, before achieving target angle of (c) $\theta = 30^\circ$.

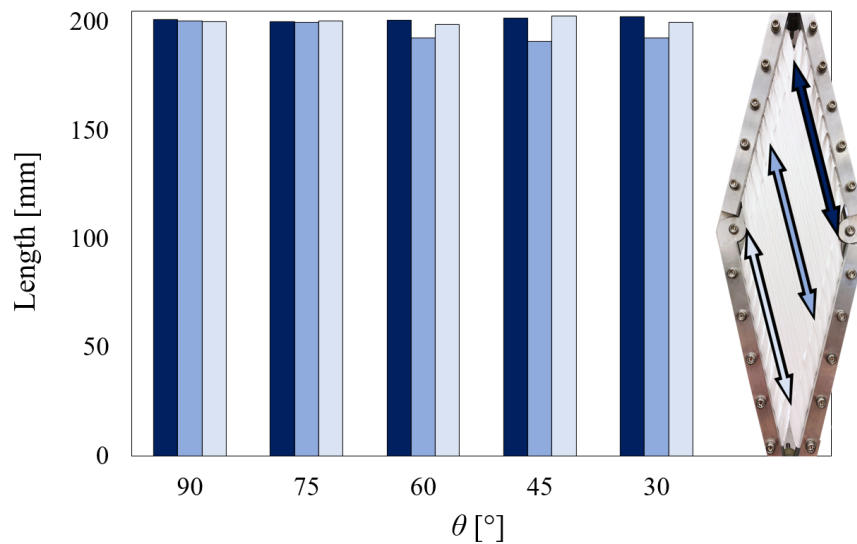


Figure 5.7: Comparison of fibre lengths during the shearing process at three positions across the surface of a sample at 15° intervals.

the sample was not sprayed directly but was placed on a flat surface while the spray can was pointed upwards, facing away from the samples, and then sprayed. The indirect application of ink drops created much smaller spots, thereby containing the dispersion of ink across the surface. This was presumably because the ink had partially dried before becoming attached to the sample surface. The presence of a sufficient quality speckle pattern is vital for calibration of the DIC cameras, as well as subsequent detailed tracking of the material under deformation.

Factors investigated during the shearing process include cross-head displacement rate,



Figure 5.8: Clockwise from top left: Specimen sheared to $\theta = 30^\circ$ prior to dismounting, close up of the speckle pattern, and a close up of the surface surface deformations accompanying shearing.

10 mm/min and 60 mm/min, frame clamping pressure, 0.1 MPa and 0.5 MPa, and temperature, 21 °C and 80 °C. The temperature, T , was controlled using a thermal chamber, while the grip pressure, P_{Grip} , was applied using a mechanical torque wrench, the value of which was calculated from the total bolt force, F_{Total} , and the total area of application on the sample, A_{Total} . The total force is the product of the total number of bolts and F_{Bolt} , the force on an individual bolt, derived from

$$F_{\text{Bolt}} = \frac{T}{K \cdot d}, \quad (5.1)$$

where d is the diameter of one bolt, equal to 6 mm here, and K is the nut factor, a torque variable assumed to be 0.3 for stainless steel on mild or alloy steel [108]. The global load was recorded against global displacement, with local strain values obtained using an Imetrum video gauge extensometer. While a two-camera LaVision DIC system was utilised for checking the uniformity of the in-plane shear strain in the material, a four-camera system was set up as demonstrated in Fig. 5.9, as a non-contact means of monitoring the in-plane evolution of the sample thickness with increasing shear angle. The 5 Megapixel front set of cameras measured the out-of-plane displacement on the front surface of the sample and the 16 Megapixel rear cameras obtained the same measurement for the rear surface of the sample. The difference between the two measurements at each time interval was taken to be the sample thickness at that interval.

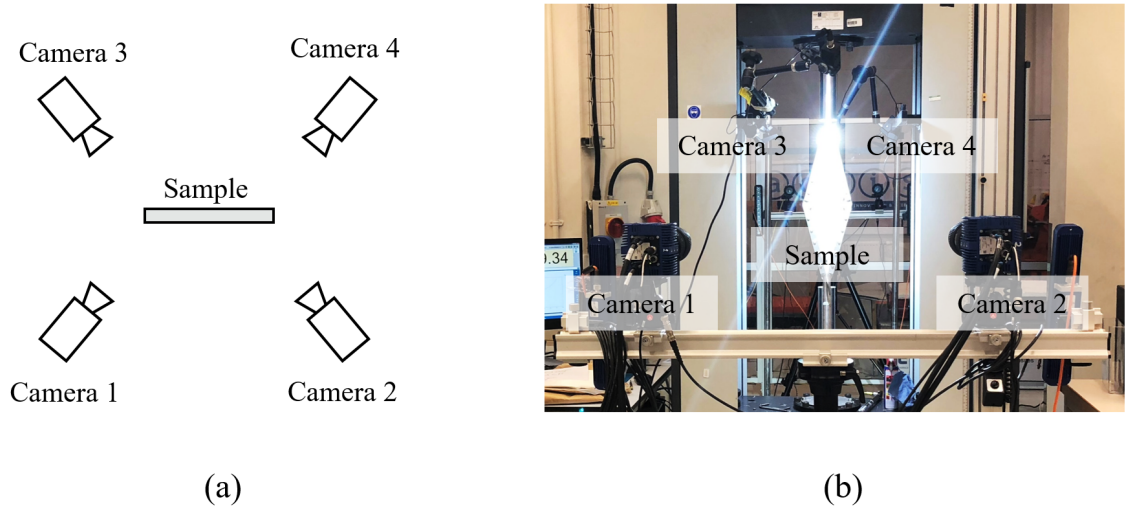


Figure 5.9: Four-camera DIC set up to measure change in the out-of plane dimension, (a) top-down view, (b) front view.

Figure 5.10 displays the out-of-plane deformation of the front and rear surfaces of a specimen sheared by 60° . The specimen thickness was derived from the difference between the two out-of-plane displacement measurements, with thickness $Z_i(t)$ at time t and at position i is calculated as

$$Z_i(t) = U_{z, \text{front}, i}(t) - U_{z, \text{rear}, i}(t) . \quad (5.2)$$

This is subsequently used to determine the mean thickness $\bar{Z}(t)$ across the entire surface at time t . The mean thickness change $\Delta\bar{Z}(t)$ is then calculated at time t with respect to the original thickness at time t_0

$$\Delta\bar{Z}(t) = \bar{Z}(t) - \bar{Z}(t_0) . \quad (5.3)$$

As a result of the mismatch in the resolution between the two pairs of DIC cameras, the results acquired for the front and the rear surfaces were resampled with a custom-written MATLAB script, in order to provide consistent measurement locations that were used to calculate the sample thickness at various locations. The surface thickness at a shear angle of 60° is presented in Fig. 5.11(a). Due to the presence of edge effects, 10% of the surface was removed at each edge, as demonstrated in Fig. 5.12, leaving a more uniform thickness across the central area of interest (AoI), presented in Fig. 5.11(b).

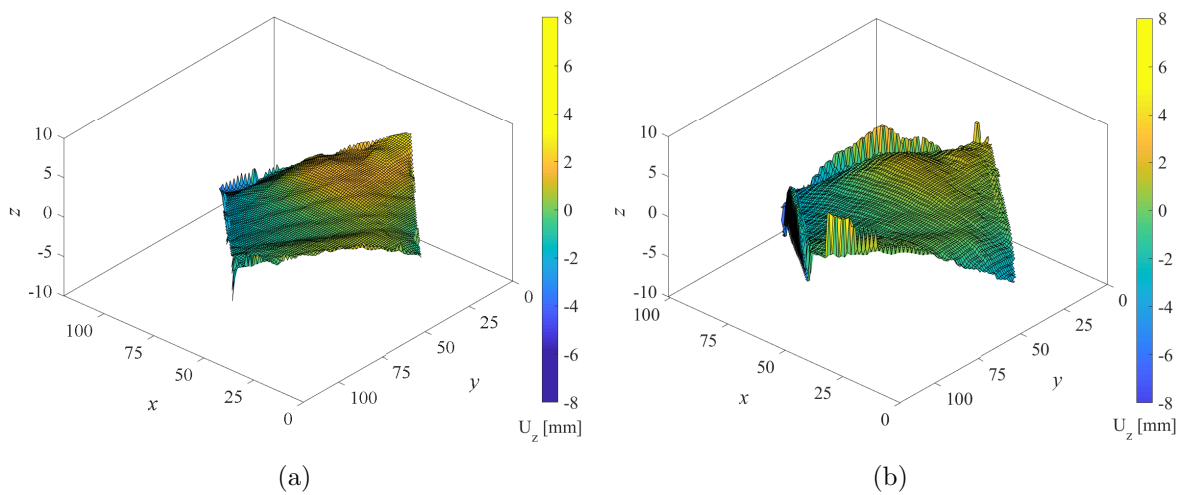


Figure 5.10: Contour plot of out-of-plane displacement across the specimen surface (a) on the front side and (b) on the rear side.

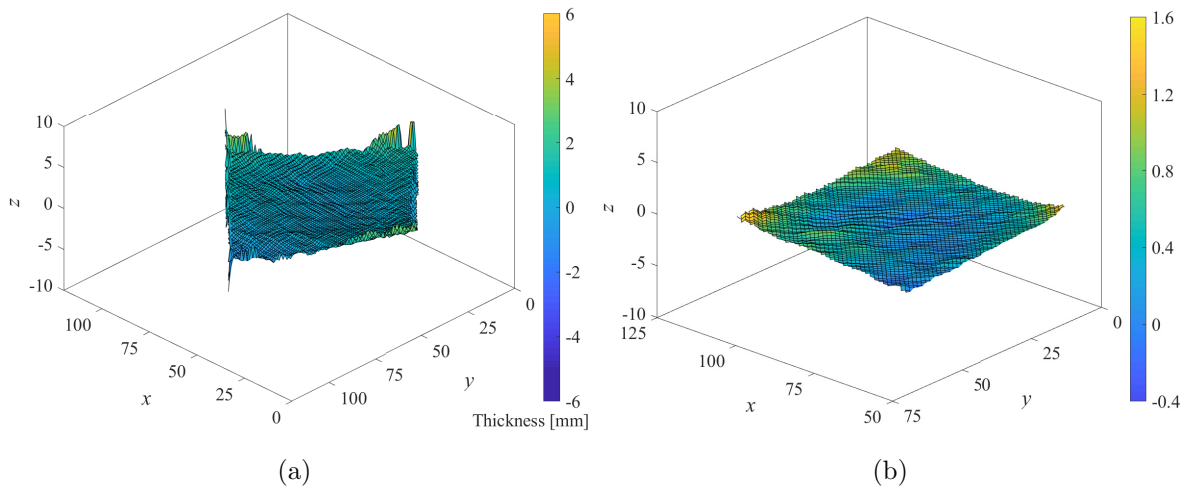


Figure 5.11: Thickness across the specimen surface (a) with edge effects and (b) with reduced edge effects.

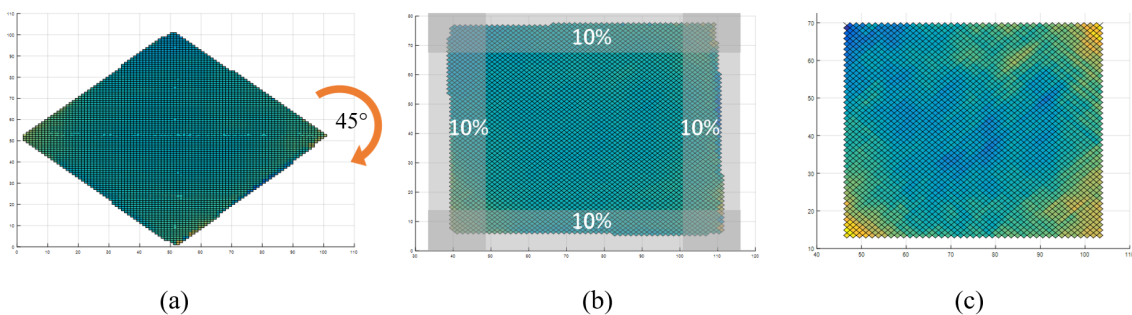


Figure 5.12: Contour plots of the specimen thickness at shear angle 60° : (a) The surface is rotated to align with the in-plane axes, (b) 10% of the length is eliminated from each edge to minimise edge effects in thickness calculations, giving (c) the final measurement of thickness across the area of interest.

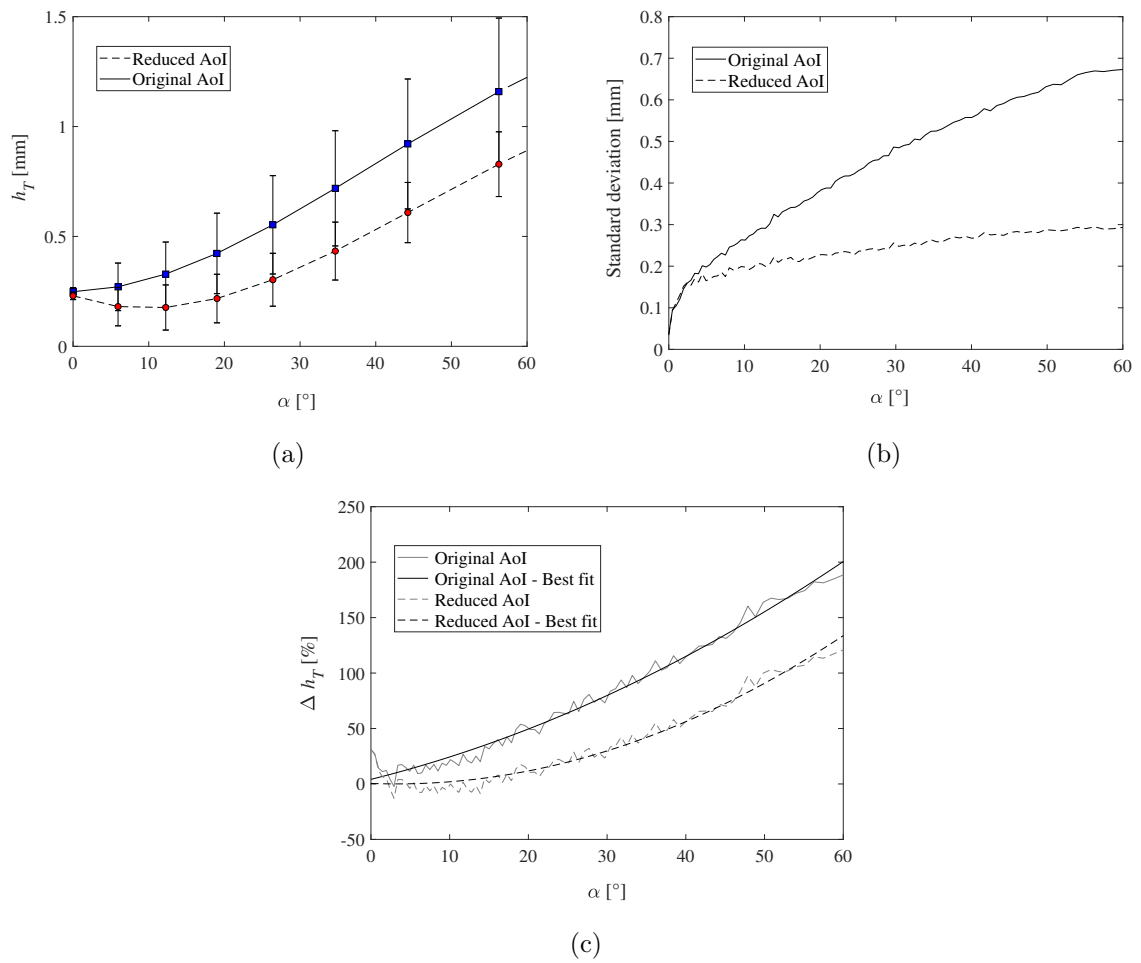


Figure 5.13: The improvements after reducing the AoI, seen in (a) the thickness, with the error bars denoting the standard deviation, in (b) the standard deviation of the data, and in (c) the thickness change.

Figure 5.13 demonstrates the reductions achieved in the measured value of thickness, and the reduction of its standard deviation across the surface of the ply, after limiting the area of interest to the central specimen region. Hence, the plots reinforce the need to remove the edges of the specimen in calculations of the thickness evolution, in order to minimise edge effects on the measurements and to obtain more accurate thickness values, together with a more uniform thickness across the surface.

5.2.3 Manufacturing sheared laminates

Following the shearing process, sets of three plies were pressed at 10 tonnes at a constant temperature of 80 °C for five minutes immediately after being dismantled from the frame, using

a 50 tonne Hare press. This was sufficient to partially consolidate the material, in order to maintain its shape and to prevent post-shear spring-back, demonstrated in Fig. 5.14. The spring-back deformation occurs as a result of residual stresses that exist from the elastic energy stored in the material when it is sheared. It is assumed that the fibres are perfectly rotated in the shearing process causing no fibre elongation. Although some stress may remain at the ends of the fibres where the specimen is gripped in place, the contribution is deemed negligible compared to that of the matrix.

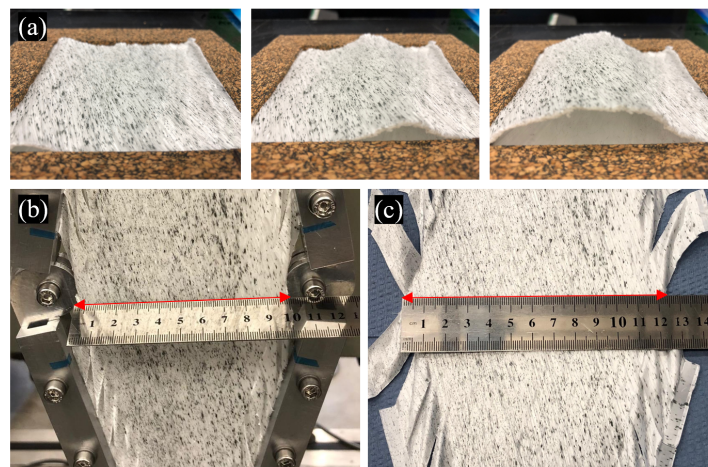


Figure 5.14: Post-shear spring-back in (a) a square cut-out of a sheared specimen within the space of a few seconds after dismounting from the frame, with out-of-plane deformation seen as a result of the in-plane dimensions of the sample being restricted with cork, (b) a specimen mounted on the frame and sheared to a frame angle of 30° , with a maximum lateral dimension of 10 mm, (c) the same sample immediately after being dismounted from the frame, with the same dimension having increased to 12.4 mm.

The batches of three UD plies were stored at -20°C , to further minimise mobilisation of molecular chains responsible for spring-back effects, and were sorted in the order of shear angle achieved post spring-back. The samples were then stacked up and fully consolidated into flat laminates with a hot press. The majority were pressed at the facilities of DSM Dyneema, in line with the manufacturer's recommended cycle, while some samples were pressed at the University of Bristol. Due to the lack of active cooling in the Bristol hot press and the requirement to remove the pressure only after the laminates had cooled down to 60°C , the cycle was much longer in duration than the one used at DSM, while increasing the maximum temperature at a much faster rate. Therefore, the cycles run at the University of Bristol were carried out manually, using thermocouples attached to the material to ensure the core temperature was sufficiently high before progressing to the following step. The consolidation

cycle used for calibration of the hot press at the University of Bristol is demonstrated in Fig. 5.15.

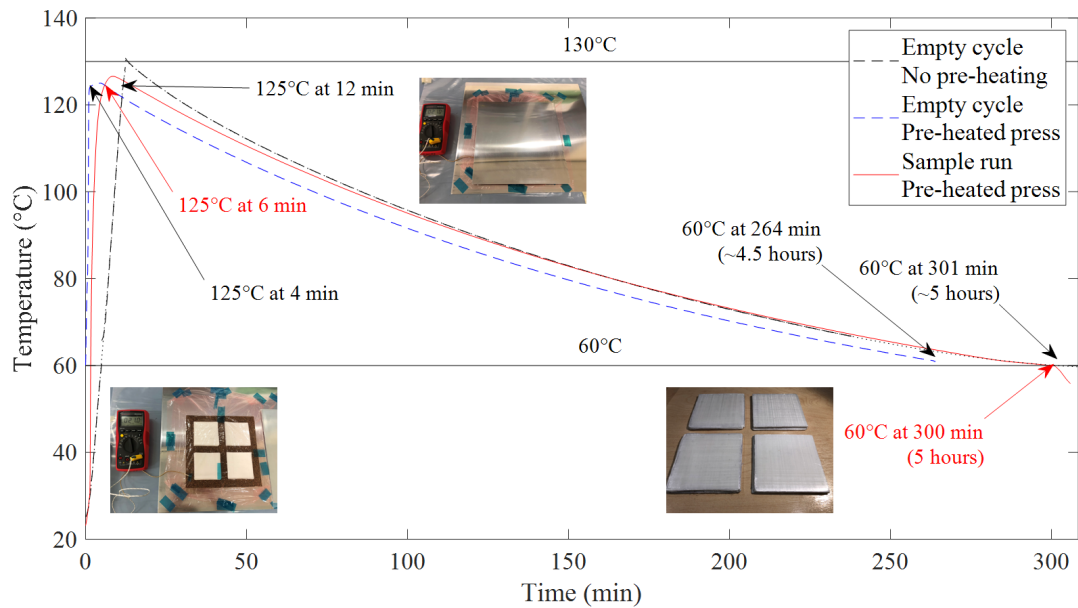


Figure 5.15: Calibrating the consolidation cycle of the press at the University of Bristol through empty cycles with and without pre-heating of the press, together with four 100 mm × 100 mm trial samples on a pre-heated press.

After pressing, the plates had unsheared slightly further towards their original geometry, a selection of which can be seen in Fig. 5.16, resulting in much larger angles than had been planned. To address this issue, the initial degassing step at 10 bar with applied heat was forgone. It was hypothesised that with the increase in temperature, the polyurethane matrix begins to soften. However, the temperature is not high enough to fully melt the matrix at this stage, allowing the residual stresses to prevail and result in the spring-back effect. By forgoing the degassing step, the equivalent of one third to one quarter of the full consolidation pressure of 165 bar depending on the surface area of the sample, would be applied immediately upon installation of samples in the press. In combination with the use of cork to surround the edges, the material would be restricted in both in-plane and out-of-plane movement until the matrix had melted and reformed into the new shape, thereby reducing the likelihood of spring-back. This method was successful when trialled at the University of Bristol, reducing a typical spring-back of over 30° to a mere 0.5° when $\theta = 60^\circ$, and spring-back was completely eliminated when $\theta = 30^\circ$, as visible in Fig. 5.17.

The cycle was initiated by heating the empty press to 60°C , before placing the samples

inside and applying 10 tonnes to prevent any spring-back until the sample core temperature had also reached 60 °C. This occurred in the space of around 3 min. Subsequently, the applied force was increased to achieve an equivalent pressure of 165 bar, while the temperature was ramped up to 110 °C at a rate of 1 °C every 12 s. Upon reaching a core temperature of 110 °C, a second ramp was introduced to increase the temperature to 132 °C, with active heating terminated at 128 °C, while the pressure was maintained at 165 bar. This was followed by the cooling regime that involved sustaining the same pressure until the core temperature of the plate had cooled down to 60 °C, in line with the recommended guidelines, which allow the pressure to be increased in stages. These samples were, however, not impact tested, to maintain as much consistency as possible in the manufacturing method of the tested targets, with only samples pressed at DSM Dyneema being tested.

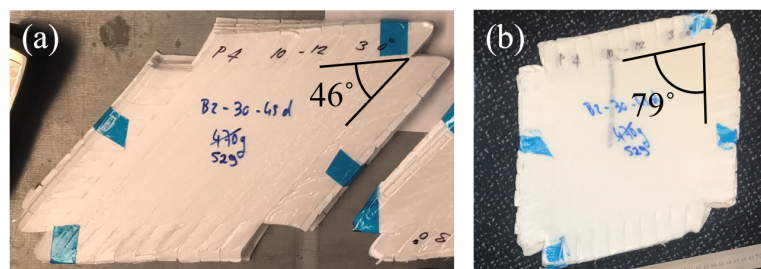


Figure 5.16: Spring-back of the material as observed through the change in θ from a (a) pre-consolidation state to a (b) post-consolidation state.

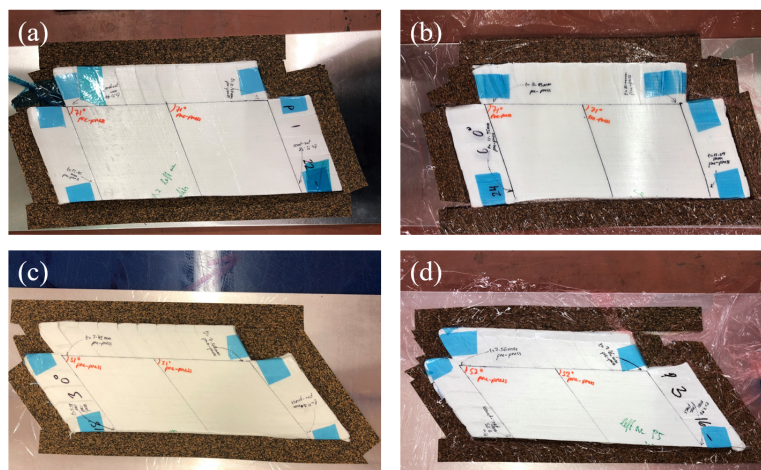


Figure 5.17: Manufacturing-induced spring-back was reduced to a range of 0 ° to 2 °: (a) pre-consolidation $\theta = 71^\circ$, (b) post-consolidation $\theta = 71.5^\circ$ to 73° , (c) pre-consolidation $\theta = 51^\circ$ to 52° , (d) post-consolidation θ has remained the same.

The additional modifications to the consolidation cycle such as forgoing the degassing step and using cork to restrain the samples, nevertheless, proved ineffective in reducing the spring-back deformation when performed at DSM Dyneema. This may have been due to the discrepancies in the temperature cycles that were adhered to, particularly the temperature gradient at the initial stages of the press cycle, where the maximum temperature of the cycle is reached at different rates, within 40 min at DSM Dyneema and within 6 min at the University of Bristol. As a consequence, higher shear angles could not be tested. Cutting the samples prior to consolidation induced local delamination along the cut edges which appeared thicker as a result. After pressing, those regions expanded in-plane, leading to the formation of the extra surface area highlighted in Fig. 5.18. Hence, subsequent samples used in the impact testing were cut following consolidation. They were cut using a band saw along fibre directions, as demonstrated in Fig. 5.19.

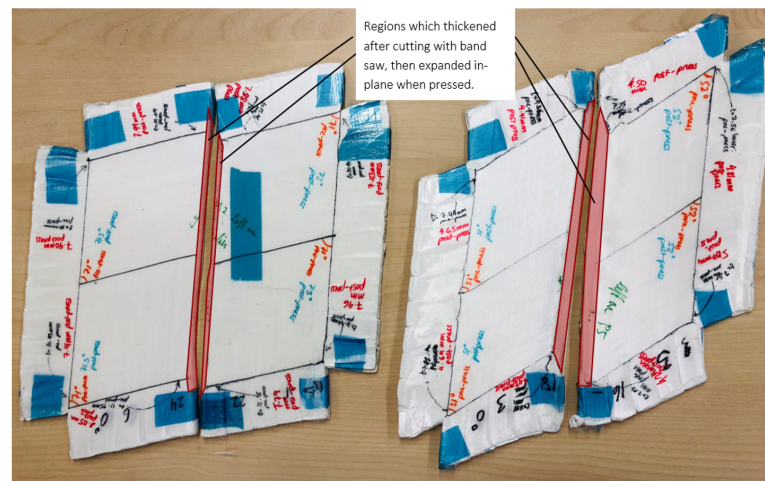


Figure 5.18: Highlighted regions demonstrate the in-plane and out-of-plane expansions of the unconsolidated specimens at the edges following cutting.

5.2.4 Impact testing sheared plates

The sheared plates were tested for ballistic impact performance at DSM Dyneema's shooting range, being compared against reference plates of equivalent aerial density (AD) or number of HB26 preform layers, N_p . Note that unlike the number of plies, the aerial density of laminates does not remain constant throughout the shearing process. The areal density increases with in-plane shearing due to the accompanying thickening of plies. The ballistic performance of protective armour is typically determined through the back face deformation (BFD) of the

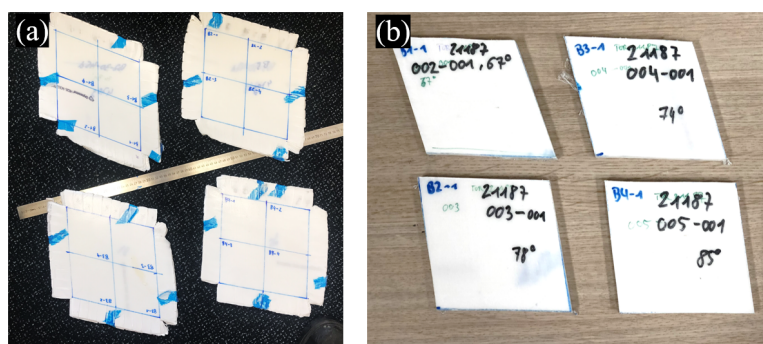


Figure 5.19: Pressed samples (a) pre-cutting and (b) post-cutting.

structure upon impact, or through its ballistic limit velocity, V_{50} . Due to the small in-plane dimensions of the plates, the extent of the BFD is quite limited and therefore not a sufficient measure by itself. In contrast, the V_{50} parameter can be scaled for various in-plane target dimensions and was thus selected as the primary criterion for determining the effect of shear on the impact behaviour of the plates.

5.2.4.1 Specimens

Table 5.1: List of samples manufactured for testing.

Sample ID	AD [kg/m ²]	N_p	θ [°]		
			SP0	SP1	SP2
A1	8.7	33	60	70	90
B1	7.1	27	30	48	84
B2	7.2	27	30	45	80
B3	7.3	27	30	47	74
B4	7.0	24	30	41	68
R1	8.7	33	90	90	90
R2	7.1	27	90	90	90
R3	6.3	24	90	90	90

Table 5.1 outlines the samples that were manufactured for ballistic impact testing, with AD denoting the aerial density of a sample and N_p the number of HB26 layers. The fibre angle θ of each sample is taken as the mean global fibre angle of all the individual layers, and is classified into three columns; the nominal angle SP0, corresponding to the frame angle achieved during the shearing of that sample, the post-shear pre-consolidation spring-back fibre angle SP1, and the subsequent post-consolidation spring-back fibre angle SP2.

Four identical plates were cut from each sample, enabling the plates from the same sample

to be tested at various impact velocities. The plates were cut along fibre directions as opposed to being cut into square laminates, to maintain a constant distance from the central region to the edges, along the fibre length, as illustrated in Fig. 5.20. This variable must be controlled as previous studies in [109] and in Chapter 3 have shown the ballistic performance of the panels to be highly sensitive to their in-plane dimensions.

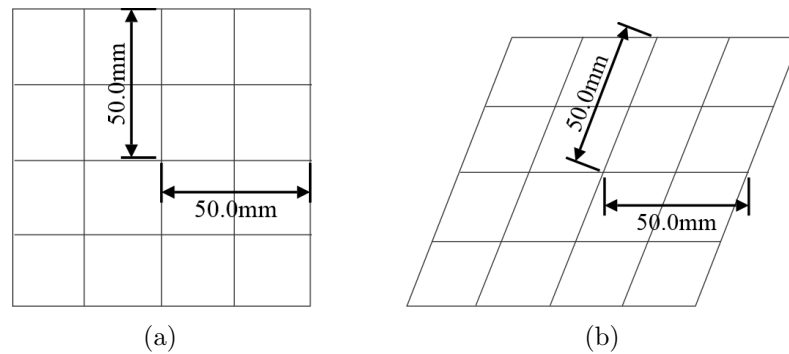


Figure 5.20: Demonstrating the fibre length from the centre to the edge of (a) an unsheared reference plate and (b) a sheared plate.

5.2.4.2 Test set-up

Ballistic impact testing was performed at DSM Dyneema's shooting range in the Netherlands, with the testing arrangement visible in Fig. 5.21. A powder gun was used to shoot a 1.1 g fragment-simulating projectile (FSP) with diameter 5.56 mm at each target plate. The targets were loosely held in place at the corners with clamps, against a support frame. The support frame had a circular aperture of 70 mm diameter to allow bulging to occur in the back face of the plates during impact, and to allow the projectile to pass through following target perforation. A pair of velocity screens were installed between the gun barrel and the target, used to measure the initial velocity of the projectile. Assuming that the projectile velocity remains relatively constant until the point of contact, the initial velocity is deemed equal to the impact velocity. As the test is not carried out in a vacuum chamber however, realistically, the FSP will be subject to drag effects to a small extent. A second set of velocity screens measured the residual velocity of the projectile, if any, beyond the position of the target. It must be noted that the screens measure only the horizontal component of the resultant projectile velocity, in this case neglecting the effects of gravity and alteration of the projectile direction in three-dimensional space. While the effects of drag on obtaining an accurate velocity measurement are small, as shown previously in Section 4.4.2.2 in Chapter 4, the effects of changing direction are not, due to variations in plate geometries, deformation, and perforation mechanisms.

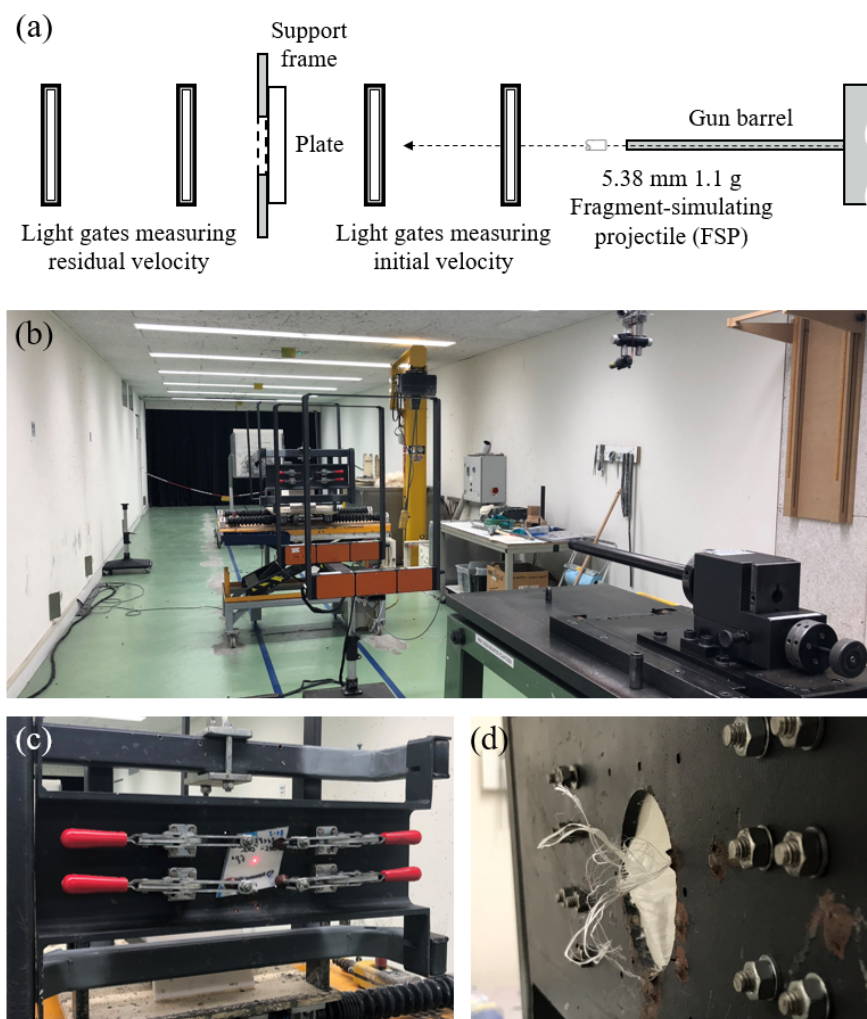


Figure 5.21: Ballistic impact testing: (a) a top-down view of the test apparatus, with the arrow depicting the idealised direction of projectile motion, (b) the testing facility at DSM Dyneema, (c) a sheared plate held loosely in position with four grips in the corners directly before impact, (d) bulging and fibre failure on the back face of a sheared plate following penetration by the FSP upon impact.

A laser pointer was used to aim and since the actual location of impact was almost perfectly aligned with this in the majority of the trials, the effects of drag and direction change were considered to be limited. However, to address this in more extreme cases, high speed video cameras are required to capture the impact event in two planes, in order to obtain a more accurate reading of the resultant three-dimensional strike velocity directly before contact, and the exit velocity directly following perforation of the laminate. The images also provide insight into the angle of impact, and whether the effect of an oblique impact also needs to be accounted for. For the purpose of this study, the angle of impact was assumed to be orthogonal to the in-plane surface of the target. To initiate impact, the projectile was placed inside a sabot,

together with the desired amount of propellant. This amount determined the approximate launch velocity of the projectile from a smooth gun barrel.

Each target was shot at only once, with the impact velocity recorded, together with the residual velocity in perforation cases. The reference samples consisted of 10 plates in each category and were tested first. The impact velocity was gradually increased for each set of plates until sufficient velocity measurements had been taken to give an indication of the ballistic limit velocity, amounting to at least three cases with residual velocities, with one preferably lying very close to the predicted V_{50} . Based on this approach, the sheared plates, which were limited in number, were tested only at velocities close to the estimated ballistic limit velocity of their corresponding reference plates. Subsequently, the tested plates were dissected at the location of impact to facilitate the measurement of the depth of penetration, defined here as the original plate thickness subtracted by the thickness of the rear portion that was not penetrated by the projectile. In addition, the plate cross-section provided a more detailed view of damage and failure within the laminates.

5.3 Results and Discussion

5.3.1 Investigating material properties

This section refers to the shearing process of the unconsolidated preforms, exploring the effect of grip pressure, cross-head displacement rate, and temperature on various aspects of the material's force-displacement response.

5.3.1.1 The effect of grip pressure and displacement rate

In Fig. 5.22(a), the recorded global force is normalised with the sample area. This represents the stress on the samples, while the shear force in Fig. 5.22(b) is normalised with the frame and sample lengths, as has been done in previous work [110]. The presence of a uniform bolt torque of at least 0.1 MPa across the edges of the specimen was paramount to obtaining predictable and scalable results. However, due to the low friction coefficient exhibited by Dyneema[®], slipping was a common occurrence and had to be inhibited through the application of higher gripping pressure. This was therefore increased to 0.5 MPa, without affecting the load-displacement measurements. The curves in Fig. 5.22 demonstrate an expected non-linear response in line

with the findings of [111], characterised by matrix shear and subsequent yielding combined with the rapid effective hardening that occurs with an increasing shear angle. This further stiffening is due to increasing fibre rotations as the fibres reorientate from their original $0^\circ/90^\circ$ formation to align with the $\pm 45^\circ$ loading direction [10, 12].

Unlike the findings of Dangora *et al.* [107] involving Dyneema[®] grade HB80 of the same fibre and matrix composition but half the ply thickness ($30\ \mu\text{m}$), displacement rates higher than $10\ \text{mm}/\text{min}$ were unsustainable as they contributed to the slippage of samples, likely due to the smaller gripping area than was used in [107]. Thus, all following shearing processes were performed at a rate of $10\ \text{mm}/\text{min}$. To counter this slow rate, it was possible to accelerate the process by shearing multiple plies of HB26 at once without affecting the load-displacement curve for one ply, as seen in 5.22(b).

The inherent strain-rate dependency of stiffness and yield stress of polymers such as polyurethane is well-documented [112, 113], the properties of which only become sensitive beyond strain rates of $10^3\ \text{s}^{-1}$, at lower rates than for UHMWPE fibres. However, significant increases in the stiffness and yield stress become visible at strain rates above $10^{-3}\ \text{s}^{-1}$. For a cross-head displacement rate of $10\ \text{mm}/\text{min}$ and sample dimensions of $200\ \text{mm} \times 200\ \text{mm}$, the strain rate amounts to a value in the order of $10^{-4}\ \text{s}^{-1}$.

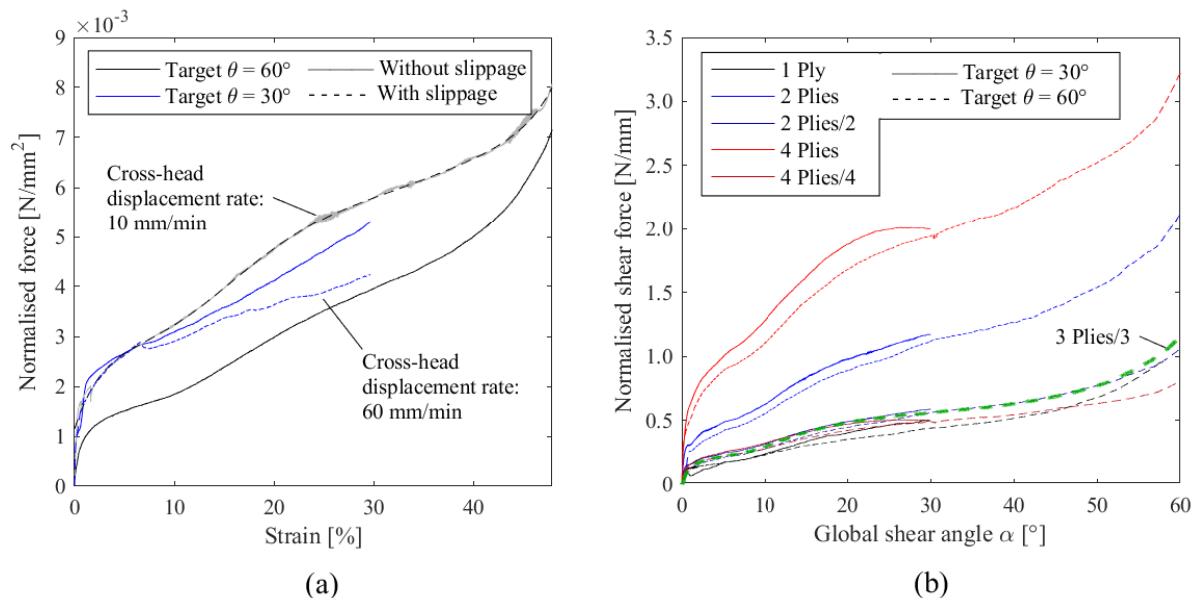


Figure 5.22: (a) Normalised global force-strain curves for specimens encountering slippage, and (b) normalised global shear force-global shear angle curves for single and multiple plies. All specimens were sheared at room temperature ($T \approx 25^\circ\text{C}$).

5.3.1.2 The influence of temperature

The influence of temperature during the shearing process is arguably the most significant effect due to the nature of the polyurethane (PUR) matrix. Figure 5.23 displays the effect of temperature, as applied at various stages of shearing, on the normalised global shear force. The error bars represent the standard deviation. The black curve represents the baseline, where the samples were sheared at room temperature (RT), *i.e.* $T \approx 25^\circ\text{C}$. The amber curve has the same temperature regime as the baseline curve in this graph and lies within the standard deviation boundary. The blue line demonstrates the effect of cooling on the behaviour of the material. These samples were cooled down to -20°C over the period of several days, and were subsequently sheared at RT. It can be seen that although the linear elastic stiffness region of the material is not significantly different, a smaller amount of force is required to deform the material at higher angles of shear than previously, since it is predominantly the linear stiffness behaviour of the specimen that is dominated by the fibre properties.

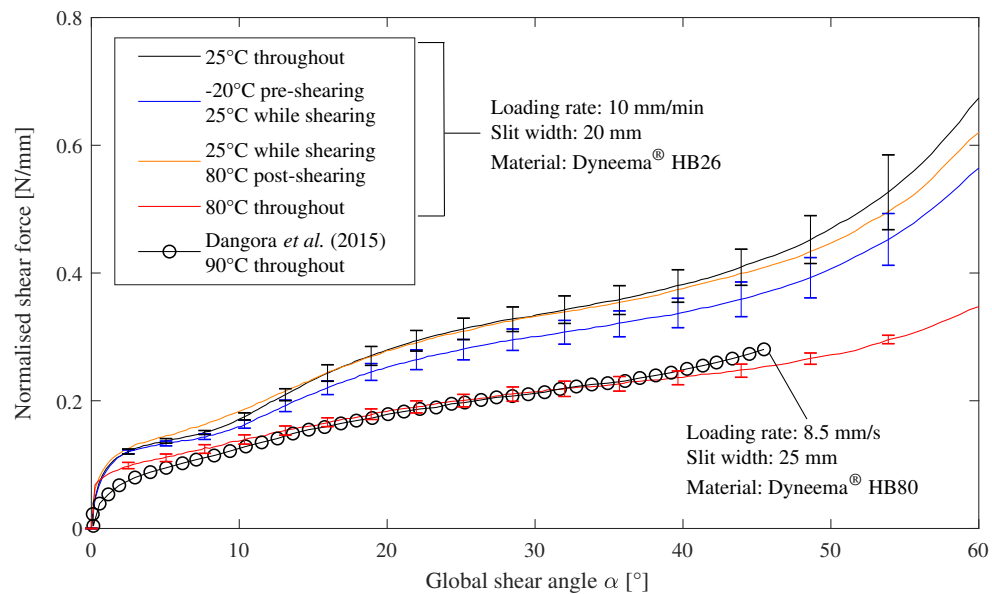


Figure 5.23: The variation of normalised shear force with the global shear angle at different temperature cycles.

This may be attributed to brittle matrix failure occurring as a result of the reduced temperature prior to shearing, which may compromise the quality of samples as result of this. Although UHMWPE fibres tend to have extremely low glass transition temperature (T_g), well below -100°C [114], the PUR matrix T_g is likely to be in the range of -40°C to 20°C at quasi-static strain rates [113]. As the fibres rotate and pile up within the matrix medium,

they leave voids which behave like cracks that induce brittle failure, thereby reducing the peak load required to shear the specimen at higher angles of shear [115]. Iannucci *et al.* [10] also hypothesised that the initial non-linear regions of stress-strain curves of the tensile response of consolidated UD laminates of Dyneema[®] were a result of matrix cracking.

Heating the sample to 80 °C throughout the shearing process significantly reduces the post-elastic stiffness of the material, demonstrated by the much lower non-linear plateau of the red curve, as well as the lower levels of standard deviation throughout. The reduction in the force required to shear the samples to the same angle is a result of matrix softening, whereby a lower matrix viscosity leads to a reduced resistance to deformation. This allows the material system to be deformed more readily, as well as more uniformly, as demonstrated by the reduction in the spread of data. The polymer transitions from a leathery to a rubbery state with increasing temperature, or with reducing loading strain rate [98]. The data obtained here is in line with previous findings [107], with the small differences in the response attributed to slight variations in temperature, ply thickness, number of slits in the flanges, strain rate and grip pressure. Kromm *et al.* [116] also reported falls in the elastic modulus and tensile strength of Dyneema[®] SK75 fibre subject to quasi-static load with increasing temperature levels. Elevated temperatures promote the sliding of long molecular chains of the fibre, resulting in drops of approximately 70 % and 40 % in the stiffness and tensile strength of fibres, respectively, when heated from 20 °C to 80 °C.

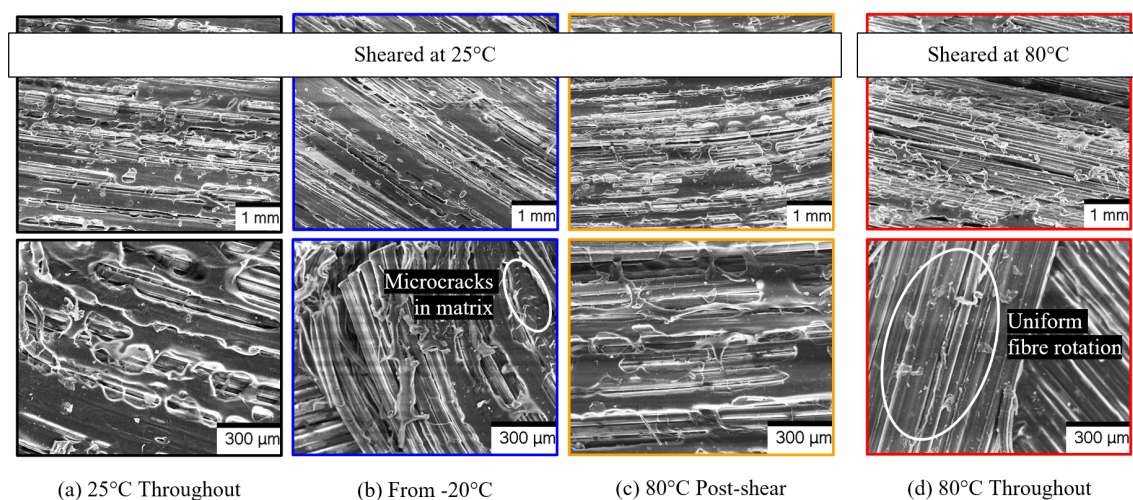


Figure 5.24: SEM micrographs of samples sheared at temperature cycles corresponding to the border colour, at 1 mm (top row) and 300 μm (bottom row) length scales.

Scanning electron microscope (SEM) micrographs of samples sheared by 60° are presented in Fig. 5.24. The images show certain differences between the fibre and matrix structures of the samples exposed to the various temperature regimes. The most notable characteristic is the uniformity of the rotated fibres in the sample that was heated to 80°C throughout the shearing process. This is an expected occurrence due to the lower matrix viscosity, thereby enabling more uniform fibre rotations in the samples as deformations are faced with a smaller degree of resistance. Although a more detailed review is required, the matrix in the specimen that was sheared from -20°C demonstrates evidence of rough paths on the surface resembling previous findings of brittle failure, suggesting that brittle matrix failure may have indeed taken place during the shearing process, as hypothesised earlier and suggested by [117, 118].

The holding force, *i.e.* the force required to maintain the specimens in their deformed state, is displayed in Fig. 5.25 at the corresponding temperature regimes. The initial step, highlighted by the shaded region, represents the loading stage in which the material is sheared by 60° , with the samples reaching their respective peak loads. This is followed by a rest phase in which the maximum displacement is maintained and the load required for this is monitored over the period of approximately one hour, shown by the solid lines for samples at various temperatures. The dashed lines display the core temperature of the specimens over time.

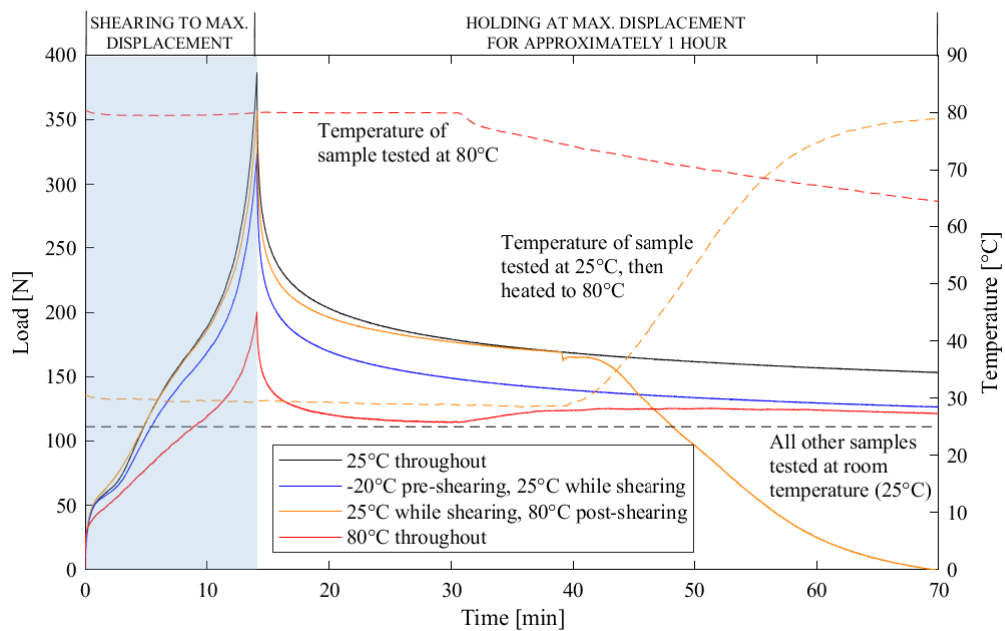


Figure 5.25: Variation of holding force (solid lines) during the shearing process and over the following one hour, for specimens subjected to different temperature cycles (dashed lines).

The time-dependent creep visible in Fig. 5.25 represents typical viscoelastic behaviour exhibited by polymers. A creep model for ultra-high modulus linear polyethylenes proposed by Wilding and Ward [119], split the material response into the two components of viscoelastic behaviour; a linear recoverable component and a non-linear irreversible component. After reaching their peak loads in Fig. 5.25, the samples undergo stress-relaxation where the holding force required to keep the specimen in its deformed state drops to only a fraction of the value at maximum displacement. Testing the samples from a temperature of -20°C reduces the maximum loading and holding force considerably, despite the deformation of the material taking place at RT, since the samples reach ambient temperatures as soon as they are removed from the freezer. Note that the performance of the chilled samples may be affected by the formation of the microcracks discussed earlier. The amber curve shows the behaviour of the material when heat was applied at a temperature of 80°C , after the process of shearing had taken place.

The material experiences further stress relaxation, immediately upon a rise in temperature. This leads to a fall in the holding force, making it negligible 30 min after the specimen was first heated up. On the other hand, heating the sample during and following the shearing process halves the peak load due to the reduced viscosity of the matrix, yet the holding force remains almost constant for the remainder of the time. A slight increase is visible in this curve at 30 min, which coincides with a fall in temperature. However, as the temperature continues to drop, the holding force stabilises at around 125 N and does not drop to zero unlike the amber curve, which displays a much more compliant material behaviour following the application of a significantly higher peak load.

The effect of the holding force on the spring-back of specimens was measured over a two week period and is presented in the bar chart in Fig. 5.26. The amount of spring-back was measured through the increase in θ , the global acute angle between the fibres of alternating layers. Naturally, the greater the rotation angle, the greater the spring-back due to higher residual stresses from the shearing process. As demonstrated by the first two bars in Fig. 5.26, the increase in θ more than doubles in a sample sheared by 60° , compared to one sheared by only 30° . Likewise, the latter undergoes a substantially slower rate of spring-back, with the greatest increase in θ taking place over the period of 24 hours after dismounting. The second and third bars, representing the behaviour of samples sheared at room temperature and from -20°C respectively, display similar levels of spring-back, the large majority of which occurs within the first two hours after dismounting from the frame. The application of heat

throughout and following shearing reduces spring-back to similar levels as a sample that was sheared half as much at RT, while post-shear heating further reduces this increase in θ . In both instances, a significant amount of the spring-back occurs within two weeks following dismounting of the samples, rendering both methods similarly effective in the reduction of spring-back in the immediate aftermath of shearing, particularly for the purpose of manufacturing samples that have been deformed purely through in-plane shear.

Thus, in the context of producing samples with pure in-plane shear, the most optimum method to reduce peak load is the application of heat, whereby a temperature close to but below the melting point of the polymeric matrix enables sufficient softening to significantly reduce the load required to shear the material. This is similar to manufacturing conditions where deformations of the material, partially through in-plane shear, to form it to the desired shape occur under elevated temperatures. However, if the aim is to minimise the holding force to prevent spring-back for the manufacture of sheared samples, it is recommended to shear the specimen at room temperature and follow this with the application of heat.

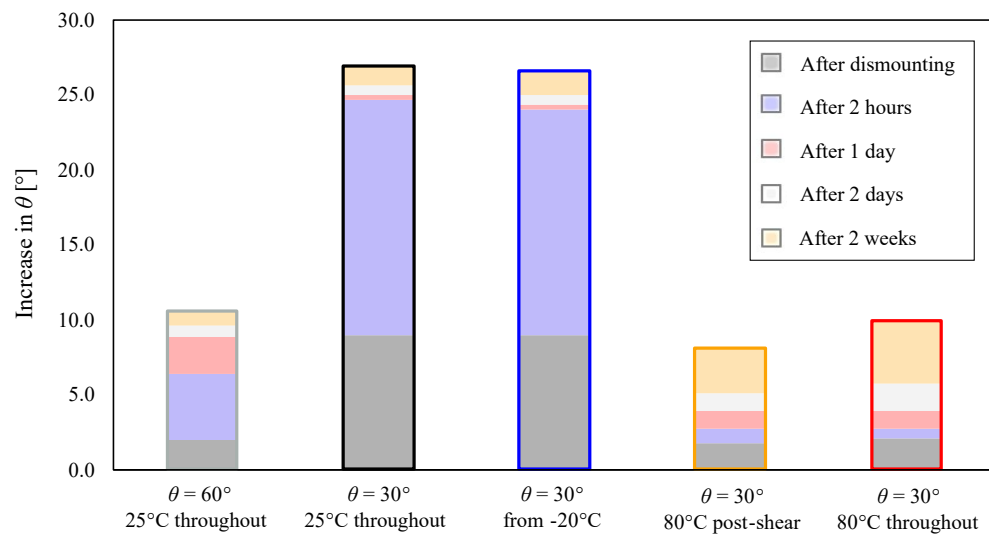


Figure 5.26: The increase in θ over a two week period following the shearing process, for different temperature regimes.

The same principles were applied to a scaled-up picture frame rig to shear much larger samples in a similar manner, as demonstrated in Fig. 5.27(a). The larger frame was manufactured at DSM and can hold square samples of up to 1060 mm in length. The frame was sheared with a hand-held Hitachi drill, achieving uniform in-plane shear in the larger sample without the presence of out-of-plane wrinkles, as shown in Fig. 5.27(b). The central image in Fig. 5.27(b) demonstrates how in-plane waviness was reduced by shearing the frame at the lowest speed

setting of the drill, compared to the higher speed settings that produced the sheared sample seen on the right. Although the shearing process required no additional sources of heat, from the smaller sample trials it was deduced to be the most effective way of forcing the material to retain its shape after dismounting. Subsequently, two sources of heat were compared, a heat blanket and an infrared light, seen in Fig. 5.27(c). While the heat blanket provided a more consistent temperature across the surface of the sample, which was maintained just below 80°C , manually adapting the area covered by the heat blanket proved to be impractical due to the changing shape of the specimen. Meanwhile, the intensity of the infrared light was traded off for its coverage of the entire surface area of the specimen, rendering the temperature of the sample surface well below 80°C . In both instances only one side of the specimen was exposed to heat and as a result, the sheared geometry was retained for a short duration of approximately 10 min before the effects of spring-back started to dominate. This did not allow sufficient time to produce further samples to be sheared for laying up into a laminate. Previously, a thermal chamber was employed for this purpose. However, this was not possible for the larger frame due to its size and the physical limitations imposed by the dimensions of standard thermal chambers. Further trials are therefore required to devise alternative methods to address this.

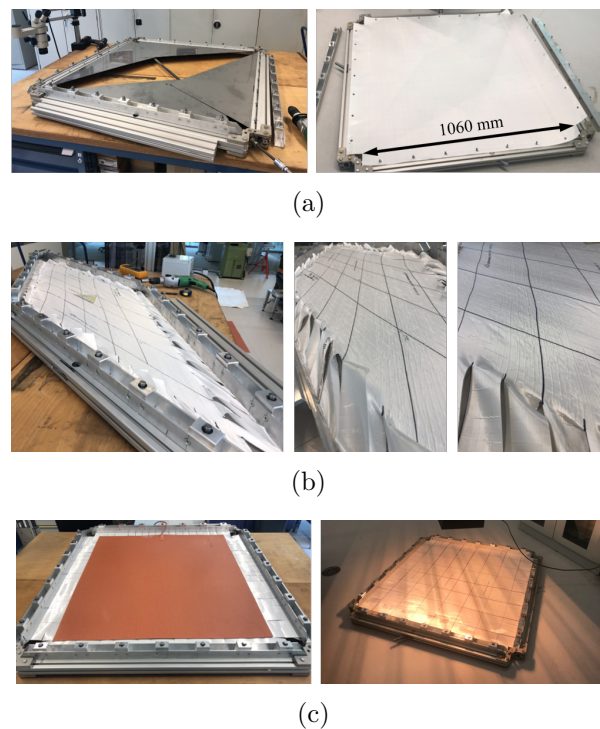


Figure 5.27: Shearing a 1060 mm square ply using a large picture frame rig: (a) shearing frame mechanism and ply, (b) a ply sheared to a fame angle of $\theta = 30^{\circ}$, displaying in-plane variation of fibre orientation, and (c) heating the specimen with a heat blanket and an infra-red light.

5.3.1.3 Primary and secondary loading

The behaviour of the material was investigated under primary and secondary shear loading at temperatures $T = 25^\circ\text{C}$ and $T = 80^\circ\text{C}$, as shown in Fig. 5.28. Both loading steps were performed at 10 mm/min, and the material was also unloaded at a rate of 10 mm/min. At both temperatures, the primary loading phase, represented by the solid lines, produced a stiffer response than the secondary loading phase, represented by the dashed lines. When the primary load is applied, it partially loosens the UD plies in each cross-ply layer of HB26 which occurs readily as a result of the poor inter-laminar strength of the material [120]. In contrast, the true UD layers have already been loosened when secondary loading commences, requiring lower levels of force to be sheared to the same degree, resulting in the drop in stiffness shown by the curves.

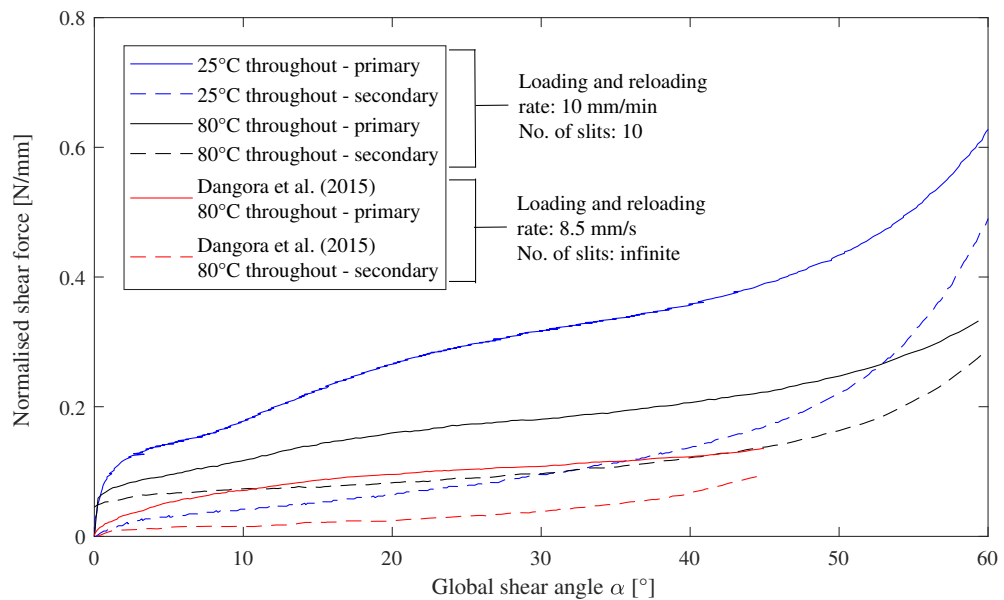


Figure 5.28: The variation of normalised shear force with the global shear angle at different for primary and secondary loading regimes.

Elevating the temperature at which the loading occurs has the effects that were discussed in Section 5.3.1.2, although it can be seen that the temperature effect is much less pronounced during the secondary loading phase in comparison to the primary phase, reducing the gap between the primary and secondary loading responses at the higher temperature. A softer matrix provides better adhesion between the layers of the preform. Hence, at elevated temperatures, the specimen will still be more compliant in the secondary loading phase due to cyclic softening effects [113]. However, there is no reduction in the elastic stiffness due to the improved adhesion

between the individual ply layers. As for Fig. 5.23, a similar trend was observed by Dangora *et al.* [107], although at much lower shear loads due to the lower thickness of the specimen, as HB80 plies are half the thickness of HB26 plies. In addition, Dangora *et al.* [107] used a higher displacement rate, a higher temperature, and an infinite number of slits in the flanges. The higher displacement rate is also responsible for the more linear nature of the red loading curves in Fig. 5.28, as also reported by Russell *et al.* [11] and Hazzard *et al.* [46] for the tensile and shear stress-strain responses of laminates of Dyneema[®]. According to Koh *et al.* [121], higher displacement rates leave less time for plastic slip to occur between inter-chain bonds, thus increasing linearity.

5.3.1.4 The evolution of thickness

The four-camera DIC system facilitated a non-contact, continuous thickness measurement to evaluate the variation in thickness with changing shear angle. The data can be used as input in processing simulations, to include thickness change when modelling in-plane shearing deformation that occurs during forming. This had previously been measured only at discrete points, such as shear angles of 0° , 20° and 60° in a study by Dangora *et al.* [17]. As shown in Fig. 5.29, the conservation of volume dictates that a reduction in acute frame angle, θ , must lead to an increase in the deformed thickness of the material. Owing to their poor adhesion to the matrix, the fibres in Dyneema[®] HB26 roll on top of each other when the in-plane dimensions get constricted during shearing, creating uniform striations, uneven ridges, or both, on the surface of the material, as illustrated in Fig. 5.30.

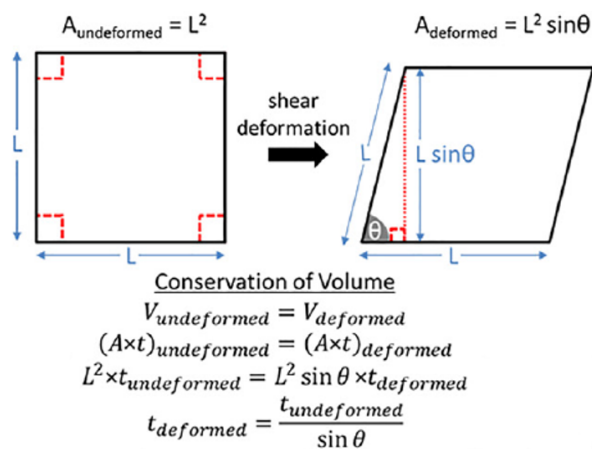


Figure 5.29: Schematics demonstrating the concept of conservation of volume during shear deformation [17].

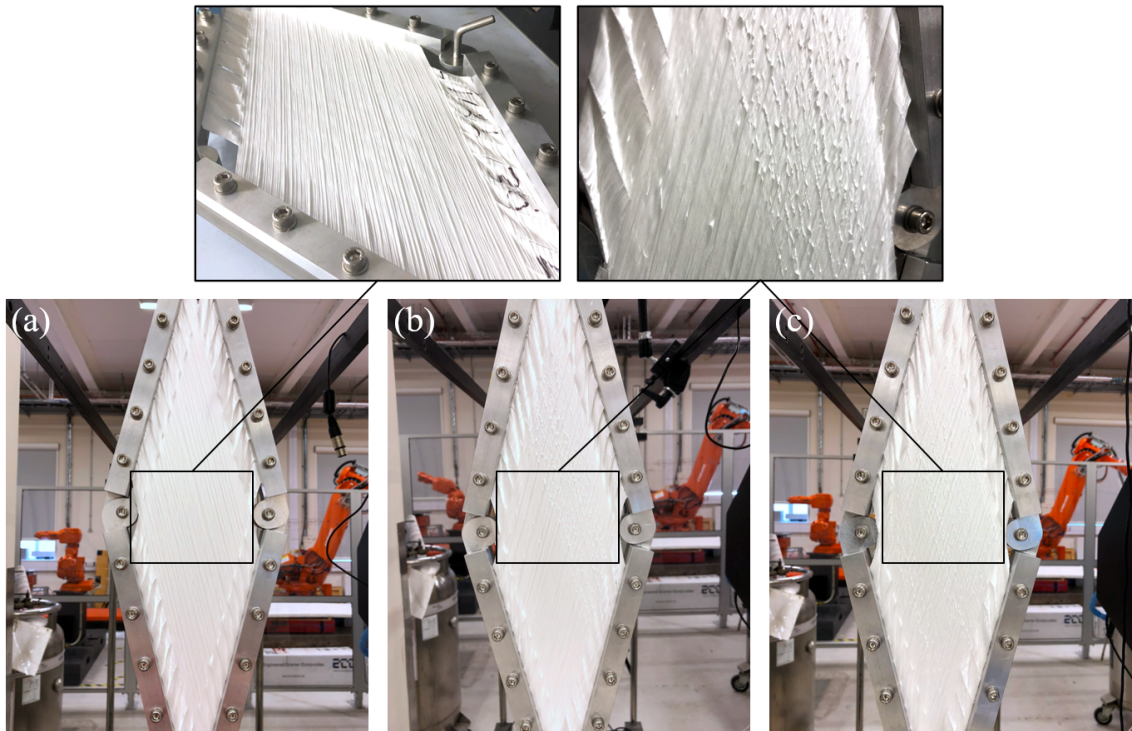


Figure 5.30: Thickening of the specimen due to contraction of in-plane dimensions causing fibres to move together, leading to the formation of (a) uniform striations, (b) a combination of striations and ridges, or (c) uneven ridges.

The results from this work are in line with previous findings, displayed in Fig. 5.31, where an increase in the shear angle leads to an increase in the thickness of the material. The change in thickness is however underestimated by the conservation of volume, in comparison to empirical measurements. To demonstrate this, the thickness change factor is plotted in Fig. 5.32. At a maximum shear angle of 60° , the experimentally acquired measurements report a thickness increase of approximately 135%, while the conservation of volume approach estimates a thickness increase of only 105%. One explanation for this disparity is attributed to the architecture of a HB26 specimen, where each layer of the material is composed of multiple unidirectional plies. This feature, in combination with poor inter-ply strength and the cross-ply fibre formation that allows the fibres to roll into striations, causes the individual layers to delaminate with increasing shear angle. This behaviour creates a phantom thickness, *i.e.* a region where pockets of air created due to delamination of the composite layers have led to additional out-of-plane displacement, unaccounted for in the conservation of volume calculations.

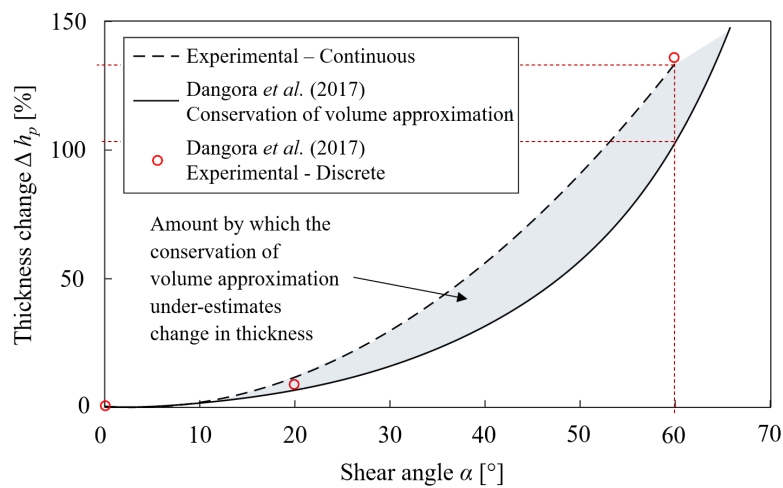


Figure 5.31: Thickness evolution of Dyneema[®] HB26 with increasing shear angle, compared to previous measurements [17].

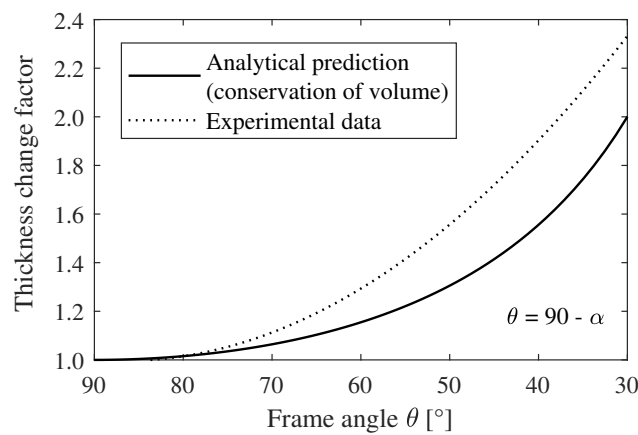


Figure 5.32: The thickness change factor, as calculated analytically using $\frac{1}{\sin(\theta)}$, based on conservation of volume, and as acquired from the DIC measurements, equal to the sheared thickness divided by the original thickness, plotted against the frame angle θ .

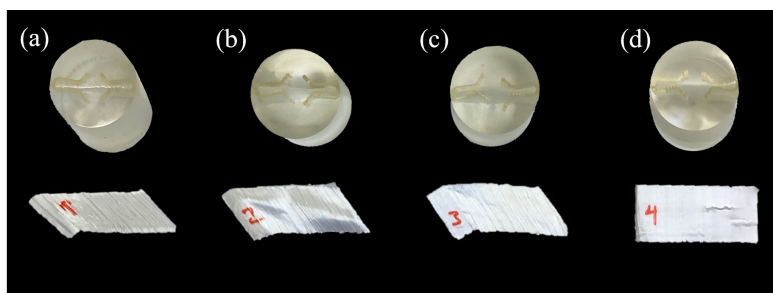


Figure 5.33: Potted samples for microscopy, from a specimen that was (a) heated during shearing and not pressed afterwards, (b) reloaded in shear after primary loading and not pressed afterwards, (c) sheared at room temperature and pressed afterwards to retain the deformation, (d) not sheared or pressed, representing the material in its original cross-ply form.

This hypothesis was verified with optical microscopy, using a ZEISS[®] Axio Imager microscope. Samples of length 25 mm were cut from specimens subjected to various loading conditions, as presented in Fig. 5.33. The sheared samples were cut away along the fibre directions to minimise retraction to the original shape. They were then submerged in a solution of EpoxyCure[™]-2 epoxy resin and epoxy hardener, with two plastic grips holding the samples down to limit buoyancy. These were prepared for microscopy with a Buehler[®] grinder-polisher.

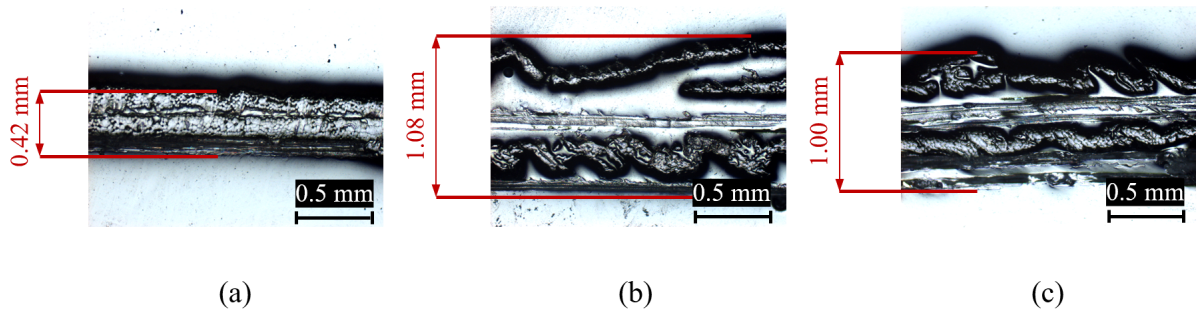


Figure 5.34: Optical microscope images of specimen cross-sections under $5 \times$ magnification for (a) an unsheared specimen, (b) a sheared specimen that was not pressed under heat, (c) a specimen that was sheared and pressed under heat.

As displayed in Fig. 5.34, in a single region of the specimen there is a thickness increase of approximately 157% due to shearing by an angle of 60° . This increase in thickness is reduced to 138% when the sample is pressed under heat to partially consolidate the composite, in order to maintain its deformed geometry. Naturally, the extent of thickness change taken at a single cross-section point does not represent the average value from across the entire surface of the samples presented in Fig. 5.31. They do however, highlight the disparity that exists between the thickness of samples prior to and following partial consolidation in a hot press. The partial consolidation step presses the laminate together, reducing air gaps and voids created through the delamination of the layers during shear deformation, an effect which is unaccounted for by the conservation of volume estimates. Thus, the pre- and post-pressing results correspond to the empirical and analytical curves in Fig. 5.31.

Fig. 5.35 displays the variation in thickness along the cross-section of specimens. Although the conditions under which the samples were sheared do not have noticeable effects, the effect of in-plane shear, *i.e.* thickening of the layers, together with delamination and self-overlapping of the outer-most surfaces, is echoed by all three deformed specimens. Note that the consolidation of the laminate does not compress it to its original thickness, it merely eliminates pockets of air created between the ply layers from the delaminations that occur during shearing.

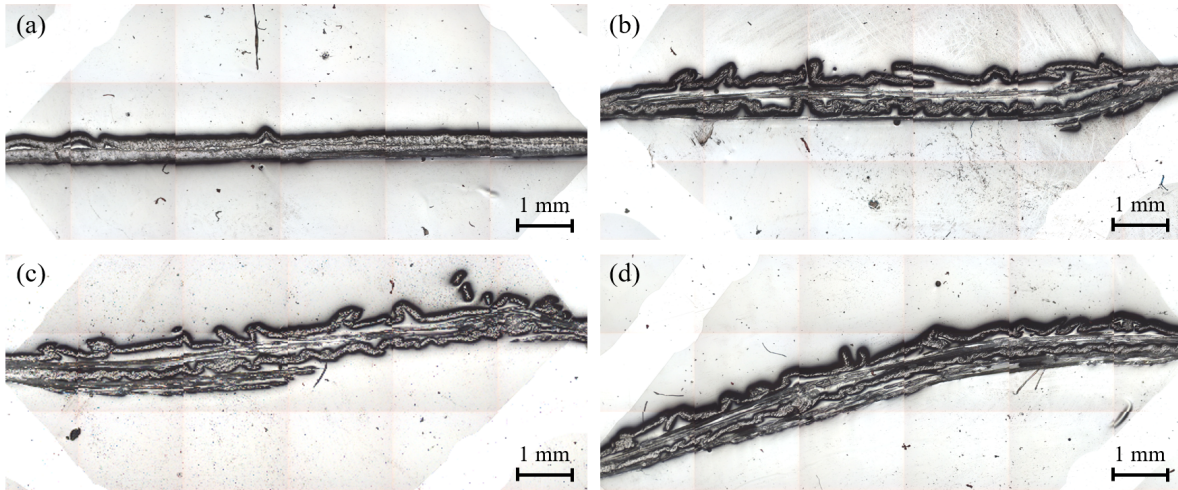


Figure 5.35: Compound optical microscope images of specimen cross-sections under $5\times$ magnification from samples that were (a) not sheared or pressed, representing the material in its original cross-ply form, (b) heated during shearing and not pressed afterwards, (c) reloaded in shear after primary loading and not pressed afterwards, (d) sheared at room temperature and pressed afterwards to retain the deformation.

5.3.2 Ballistic impact testing

5.3.2.1 Ballistic limit velocity

The ballistic impact testing results are presented in Fig. 5.36, where residual velocity V_R of the projectile is plotted against its impact velocity V_I . Coloured data points represent the results from laminates with in-plane shear, with the black data points their corresponding reference plates. The Lambert-Jonas equation given by Eq. (4.5), was used to estimate the ballistic limit velocity, V_{50} , of each laminate, as was done in Chapter 4. It must be noted that although the velocities are recorded on the graph for demonstration in stop cases where $V_R = 0$, these values were not used in the Lambert-Jonas approximations due to the absence of data for the residual velocity.

The velocity datasets are grouped according to the number of preform layers, N_p , in each plate in Fig. 5.36, and combined in Fig. 5.37 for easier comparison. The figures provide a comparison between specimens with three interdependent variables; aerial density (AD), number of plies N_p , and shear angle θ , as defined in Fig. 5.38. The target aerial density, is dependent on h_t , the target thickness post shearing, as

$$AD = \rho_t h_t, \quad (5.4)$$

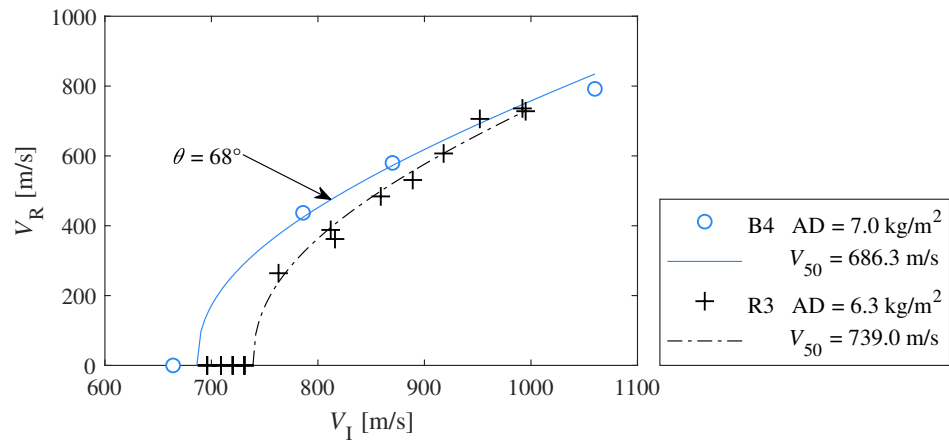
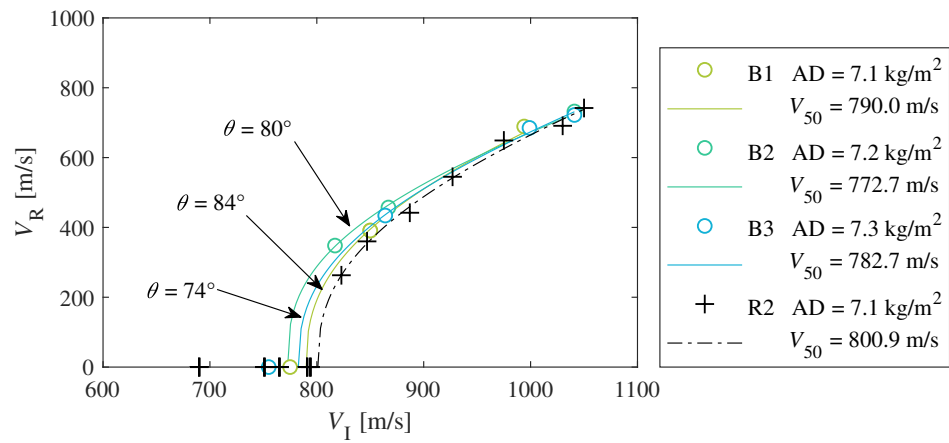
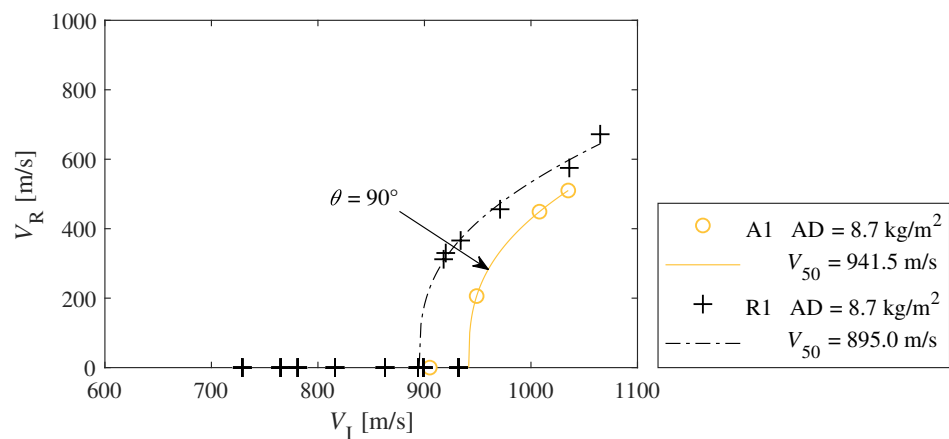
(a) $N_p = 24$ (b) $N_p = 27$ (c) $N_p = 33$

Figure 5.36: Ballistic impact testing data and Lambert-Jonas curve fits for sheared plates (coloured lines) with varying degrees of shear angle and the corresponding unsheared reference plates (black lines), grouped by the number of preforms N_p .

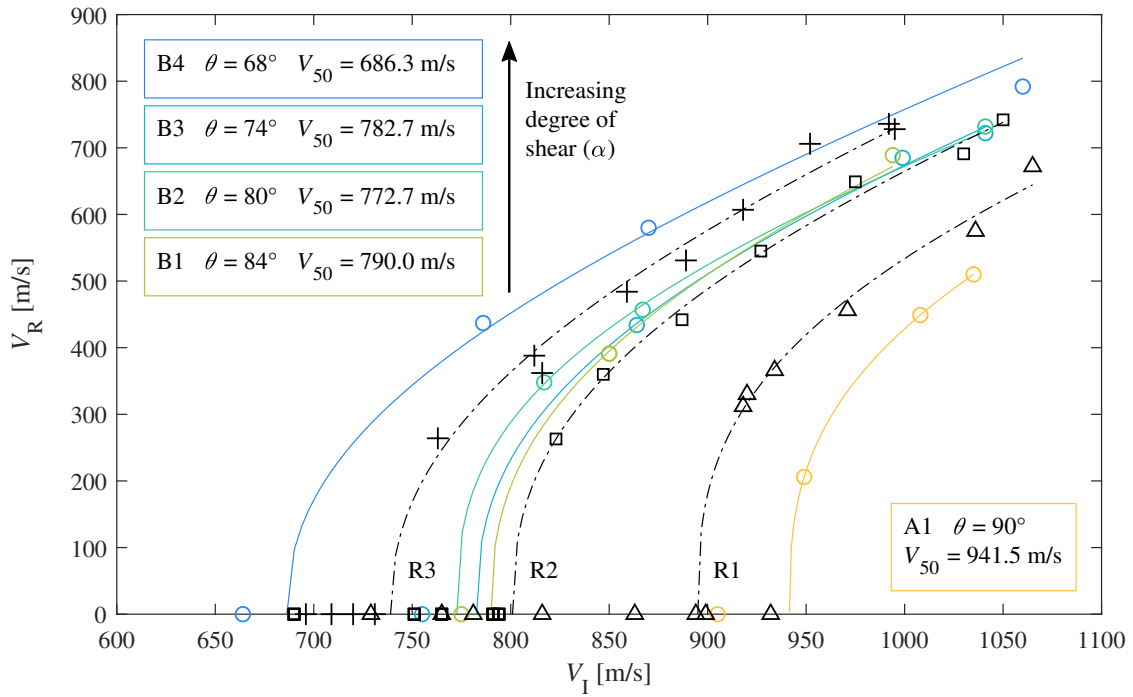


Figure 5.37: Ballistic impact testing data and Lambert-Jonas curve fits for all sheared plates (coloured lines) and corresponding unsheared reference plates (black lines).

and is therefore indirectly dependent on the shear angle θ , through the conservation of volume approximation, where

$$h_t = \frac{h_{t0}}{\sin(\theta)}, \quad (5.5)$$

with h_{t0} denoting the original, *i.e.* unsheared target thickness, equivalent to h_t when no shear deformation has taken place. The original thickness, h_{t0} , is determined by N_p and the thickness of an individual layer h_p , as

$$h_{t0} = N_p h_p. \quad (5.6)$$

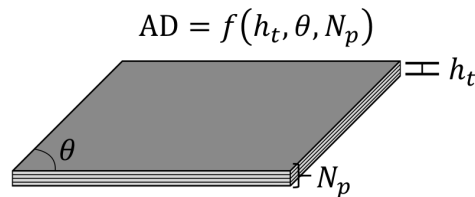


Figure 5.38: Illustrating the dependence of the laminate AD on its other physical parameters.

The data plots demonstrate an expected increase in the estimated V_{50} with increasing AD, as has previously been reported in literature [57, 122]. The following analysis sections will focus on the trends in the plots for specimen sets B1, B2, B3 and B4. The results for specimen set A1, shown in Fig. 5.36(c), will be discussed in Section 5.3.2.8. For $N_p = 24$, shearing by 22° (B4) has led to visibly higher residual velocities compared to the reference plates (R3), with the V_{50} approximation dropping by around 7% in value, as seen in Fig. 5.36. Due to the thickening of the sheared plate, the aerial densities of the plates no longer match those of the corresponding reference, albeit possessing the same number of plies. Instead, the B4 plates match reference plate R2 with a higher ply count of $N_p = 27$, in terms of AD.

Therefore, it must be noted that although the B4 and R3 specimens started with the same ply count and therefore the same thickness, and even though B4 and R2 plates ended up matching in terms of aerial density, neither N_p , h_t , nor AD should be used as indicators of the performance of a plate without accounting for the degradation of performance due to in-plane shear. For instance, from Fig. 5.36, an increase in the AD of unsheared plates caused by the addition of more plies, from 6.3 kg/m^2 (R3) to 7.1 kg/m^2 (R2) and subsequently to 8.7 kg/m^2 (R1), raises the V_{50} approximation from 739.0 m/s to 800.9 m/s and 895.0 m/s , respectively, due to the increase in the number of fibres and interfaces available per unit area for the dissipation of the kinetic energy of the projectile through fibre deformation and in-plane shear. However, an increase in the AD from 6.3 kg/m^2 (R3) to 7.0 kg/m^2 (B4) via ply shearing, does not produce the same effect as this increase in AD does not arise from an increase in the number of UD layers, but from the thickening effect accompanying the in-plane shearing.

For $N_p = 27$, shearing by 6° , 10° and 16° yields similar levels of reduction in the ballistic limit of the plates, albeit to a much smaller degree due to the limited extent of the angles by which they were sheared. Although the range of data is not large enough to establish a well-defined trend, it reinforces the understanding that the presence of in-plane shear in laminates prior to impact degrades their performance, the extent of which is determined by the degree of shear. An additional observation from the data in Fig. 5.37 notes that for the higher impact velocities, particularly beyond 1000 m/s , the effect of in-plane shear in laminates with an equal number of plies becomes almost indistinguishable. At these higher velocities, limitations such as laminate dimensions together with other factors such as shock wave interaction begin to dominate the behaviour of the laminates, making the effect of pre-shearing on impact performance less relevant.

The panels cut from specimen A1 which was originally sheared to 60° and sprang back to 90° , as shown in Table 5.1, not only defy the common trend observed in Fig. 5.37 but instead enhance the performance of the plate relative to an unsheared reference plate of equal ply count ($N_p = 33$) by 5.2%. It is hypothesised that during the spring-back phase, the fibres rotate back to their original positions, having reorientated towards the direction of loading when the plies were sheared. It is possible that this additional step further weakens the fibre-matrix bonding and loosens the interlaminar interface. The data plots from Fig. 5.36(c) are analysed in more detail in Section 5.3.2.8, while the remainder of the following sections are dedicated to discussing the results presented in Fig. 5.36(a) and (b).

5.3.2.2 Analysis of fibre rotation

On the macro-scale level, in-plane shear is accompanied by out-of-plane thickening to maintain the total volume of the specimen Dangora *et al.* [17]. Considering the constituents in the material, it is the rotation of the fibres that leads them to roll on top of each other during the shearing process, as discussed in Section 5.3.1.4. This reorientation of fibres reduces the angle between the original $0^\circ/90^\circ$ layup formation as well as the angle between the two planes of symmetry with isotropic material properties. The effect of the deviation of fibre angles from the standard cross-ply sequence on the impact performance of laminates of Dyneema[®] has previously been explored at a range of impact velocities.

Hazzard *et al.* [18] investigated the effects of reducing the angle mismatch between plies through the thickness of a laminate, and thereby reducing the stiffness mismatch that exists due to the extreme nature of the transverse isotropy of the unidirectional layers of Dyneema[®], on the performance of 2.2 mm thick laminates under low velocity impact, at $V_I = 3.38$ m/s. The authors reported a reduction of 43% in the maximum BFD of impacted helicoidal laminates, compared to an equivalent cross-ply architecture, also noting a reduction of 37.5% in the size of the impact zone between cross-ply and standard quasi-isotropic laminates for a layup sequence of $[0^\circ/90^\circ/\pm 45^\circ]$. These differences were attributed to the deformation mechanisms which occurred under impact as a result of varying stacking sequences. The absence of symmetry in all the laminates was thought to be the largest contributing factor to these effects, through the triggering of extension-bending coupling. The deformation of cross-ply laminates was dominated by primary fibre stretching combined with extensive in-plane shear, as a result of the indirect tension mechanism (ITM) [94].

By contrast, panel buckling was the largest contributor to the deformation of the quasi-isotropic laminates, with bend-twist and extension-twist coupling observed for the helicoidal layups. Earlier investigations by Zhang *et al.* [123] at higher velocities, later numerically confirmed in [93], reported a reduction of 30% in the maximum BFD of a hybrid architecture with a relatively small forfeit of 10% in the ballistic limit velocity, when compared to a standard cross-ply layup. The stacking sequence of the hybrid architecture was three quarters cross-ply at the front face of the laminate, and one quarter helicoidal towards the rear, rotating the fibres by 22.5° after every second ply. Investigations by Karthikeyan *et al.* [124] reported a reduction of 43% in the average ballistic limit velocity of $0^\circ/90^\circ$ cross-ply laminates with the addition of angled plies that introduced a helicoidal stacking sequence. Further reductions of a similar scale were observed moving from the helicoidal laminate with $0^\circ/90^\circ$ plies to the one omitting 90° layers, and from this to a purely unidirectional lay-up. The reduction of the ballistic limit was attributed to the transition of the dominant micro-mechanism of failure from indirect tension to fibre splitting. While macro-mechanical failure mechanisms, such as membrane pull-in of primary fibres and in-plane shear, were increasingly limited, restricted and replaced by wrinkling following a reduction in the plate anisotropy. The triangulation of the fibre directions in laminates with three or more unique fibre directions means that fibre deformation such as wrinkling, folding or stretching is required in addition to overcoming the resistance by the matrix for the laminate to undergo shear deformation [125]. Similarly, pull-in motion at the plate edges becomes increasingly restricted with an increase in the expanse of primary fibres in direct contact with the clamps.

Although the effect of stacking sequence is evident from these studies, previous work has been centred around balanced laminates, where for every lamina with fibres at an angle Θ to the laminate x -direction, there is a lamina with a fibre angle $-\Theta$. Similarly, due to the transversely compliant nature of HB25 and HB26 [126], the preform material comes in cross-ply layers of $0^\circ/90^\circ$. Hence, the angle between immediately adjacent plies in these studies was always maintained at 90° , see Fig. 5.39, other than in some of the specimens manufactured by Karthikeyan *et al.* [124]. Likewise, O'Masta *et al.* [126] endeavoured to investigate the effect of the inter-ply angle on the out-of-plane compressive response, for which laminates with non-orthogonal inter-ply angles were manufactured using a unidirectional precursor to HB26 and HB25. These specimens were also balanced, as the inter-ply angle was maintained throughout the thickness of the laminate. Therefore it is worth pointing out that in this current

study, the fibre reorientation induced through in-plane shearing not only eliminates the inter-ply orthotropy, as demonstrated in Fig. 5.39, but also results in unbalanced laminates. Hence, the work may not be fully comparable to the literature, with the most suitable comparison being an unbalanced lay-up of the unidirectional precursor, with non-orthogonal inter-ply angles.

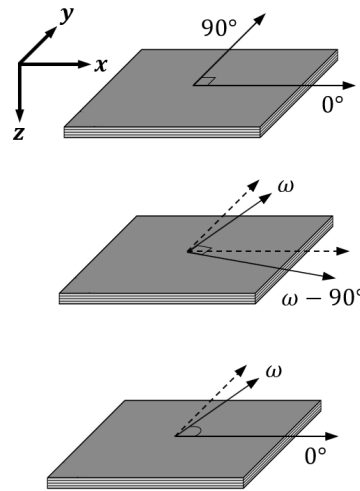


Figure 5.39: Fibre angles in a standard $0^\circ/90^\circ$ cross-ply layup (top), in an orthogonal layup inclined at angles Θ and $\Theta - 90^\circ$ to the laminate x -axis, and in a non-orthogonal inter-ply angle of ω .

The reduction in the ballistic limit of the samples in the present study, induced by the presence of in-plane shear prior to the impact event is attributed to different deformation mechanisms undergone by the laminate during impact. In order to understand these differences, the deformation mechanisms of a reference laminate with a cross-ply architecture are first examined. The key mechanisms through which ballistic-grade composites such as UHMWPE laminates dissipate the kinetic energy of a threat away from the site of a single-point ballistic impact have been investigated in [5, 44, 94, 122, 127–129]. Those that are relevant for a cross-ply laminate are summarised for the following conditions, where V_P is the velocity at which the projectile has sufficient kinetic energy to initiate the penetration of a laminate with a sufficiently high AD so that $V_P < V_{50}$:

- a) $V_P < V_I < V_{50}$ Partial perforation, progressive failure regime:
 - (i) Initiated by fibre fracture as a result of the indirect tension mechanism (ITM), arising from the local compressive force applied by the projectile and the mismatch in the longitudinal and transverse elastic moduli of alternate plies. This also results in small, local delamination in the proximity of the strike face.

- (ii) Complemented by distal fibre and membrane stretching, as well as delamination from through-thickness stress waves travelling ahead of the projectile.
 - (iii) Followed by a regime dominated by inter- and intra-laminar shear. Membrane stretching due to weak inter-ply adhesion [109] promotes the sliding of plies towards the location of impact. This is in combination with an in-plane shear modulus that is three orders of magnitude lower than the longitudinal elastic modulus, see Table 5.2, as well as a low fibre/matrix interface strength, resulting in in-plane shear and further elongation of the primary yarns.
 - (iv) The kinetic energy of the projectile is dissipated away sufficiently so that no further penetration of the laminate occurs.
- b) $V_I \leq V_P$ No perforation, binary failure regime: See Items (iii) to (iv).
 - c) $V_I \geq V_{50}$ Full perforation, binary failure regime: See Items (i) to (ii).

The reduction in the angle between the fibres influences these mechanisms through a combination of the following effects, elaborated on in Sections 5.3.2.3 and 5.3.2.5:

- a) Knock-down of through-thickness compressive strength, reducing the extent of indirect tension.
- b) Imperfect scissoring of fibres during the shearing process.
- c) Coupling of in-plane and out-of-plane deformation mechanisms.

5.3.2.3 Compressive strength

The penetration resistance of UHMWPE laminates has previously been shown by O'Masta *et al.* [130] to be influenced by the compressive strength of the composite material, with a reduction in the work required to activate penetration correlated to a reduction in the through-thickness compressive strength. Hence, it is imperative to understand the effect of fibre rotation as a result of shearing on the compressive strength of the laminate. Attwood *et al.* [44] have previously demonstrated the reduction in peak through-thickness compressive strength following an increase in ply thickness for a range of UHMWPE laminate dimensions. The study also highlighted the gain in out-of-plane compressive strength due to the cross-ply formation of plies

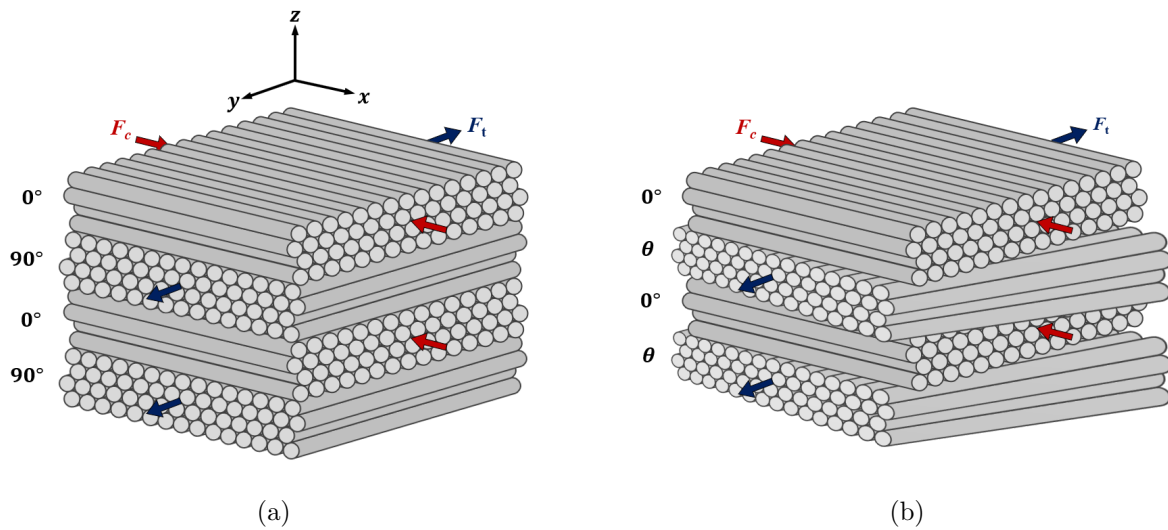


Figure 5.40: The indirect tension mechanism, whereby compressive force F_c introduced upon impact induces a tensile force F_t in the neighbouring lamina for a preform layer of (a) unsheared and (b) sheared Dyneema[®] HB26.

through the utilisation of the indirect tension mechanism, compared to a fully unidirectional stacking sequence failing via ply splitting [122]. In the current study, as the 90° fibres rotate towards the 0° direction and reach an angle θ , illustrated in Fig. 5.40, the mismatch that exists in the longitudinal elastic stiffness of adjacent plies is reduced. Since fibres of alternate plies are no longer orthogonal, indirect axial tension is reduced while in-plane shear stiffness increases. Due to the effects on the micro-mechanical behaviour, namely ITM, and on the macro-mechanical responses such as in-plane shear, there is a knock-down effect on the through-thickness compressive strength of the laminate.

This observation was confirmed by O'Masta *et al.* [126], who reported a fall in the compressive strength of laminates, together with a transition from indirect tensile fibre failure to ply shear failure, with decreasing inter-ply angle ω at constant specimen dimensions. The authors also ensured the fibre lengths remained constant for various layup directions by preparing circular specimens with constant radii. In laminates with a sufficiently large radius, the fall in compressive strength was attributed to the increase in the shear-lag length with the reduction of ω . It must be noted however, that the angle ω referred to the inter-ply angle, uniform through the stack, while in the current work, θ is the frame angle that was defined in Section 5.2.2, as well as the inter-ply angle at every second layer, due to the scissoring deformation of the fibres that occurs during the shearing process, as demonstrated in Fig. 5.41.

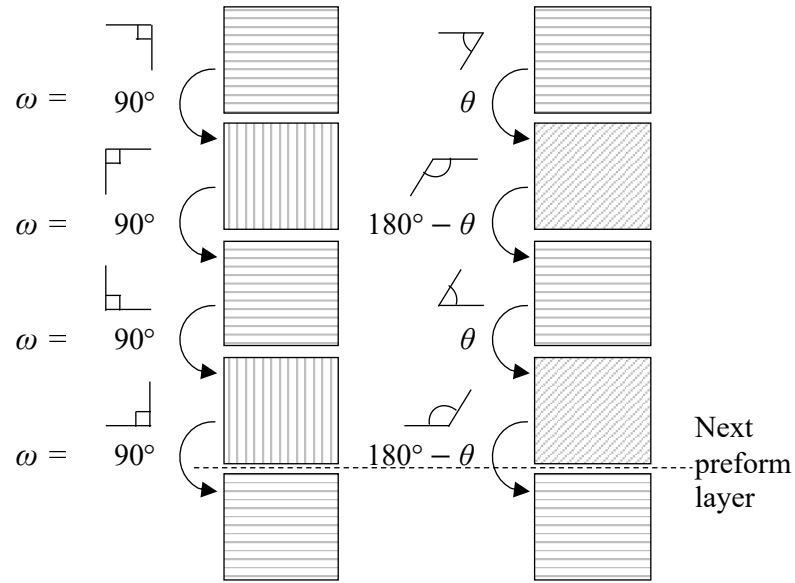


Figure 5.41: Illustrating the change in inter-ply angle ω of from an unsheared laminate (LHS) to a sheared one (RHS).

The shear-lag analysis developed by Attwood *et al.* [44] for orthogonal inter-ply angles derived the critical shear-lag length, y_f , as

$$y_f = \frac{h(1-\mu)}{2\mu} \ln \left(\frac{\sigma_f \mu}{\tau_0} + 1 \right), \quad (5.7)$$

where h is the ply thickness, μ represents a pressure sensitivity coefficient, τ_0 is the zero-pressure shear strength and σ_f is the tensile strength of the ply. The analysis was further generalised by O'Masta *et al.* [126], to account for any interlaminar angle ω , where $\omega < 90^\circ$, using

$$y_f = \frac{h(1-\mu)}{2\mu \sin(\omega)} \ln \left(\frac{\sigma_f \mu}{\tau_0} + 1 \right), \quad (5.8)$$

such that as the interlaminar angle ω is reduced, the shear lag length required for failure through indirect tension increases. As ω approaches 0 for wholly unidirectional plates, the failure length tends to infinity, confirming the absence of ITM in such laminates. Calculations of the compressive strength from these were reportedly in good agreement with experimental observations [126]. For scissored fibres in the sheared laminates of the current study, the inter-ply angle ω is equivalent to θ for an acute interlaminar angle, or $180^\circ - \theta$ for alternating pairs of plies. Since $\sin(180^\circ - \theta) = \sin(\theta)$, the shear lag analysis from [126] holds.

As discussed in Section 5.3.2.2, it is not possible to draw up a direct comparison between the sheared plates in this study and those that have been studied in the past, to determine the

effect of varying stacking sequence on the compressive strength. This is due to the presence of non-orthogonal, non-uniform inter-ply angles in only two unique directions in the current work, that give rise to unbalanced laminates. Instead, data on the change in laminate compressive strength with change in thickness is indirectly used to identify the extent of the knock-down effect on the compressive strength of sheared specimens. Experimentally measured data points from [44] are reproduced in Fig. 5.42, omitting samples with a length-to-thickness aspect ratio (AR) greater than that of the specimens used in this study. In Fig. 5.42(a), third order polynomial best-fit curves of the peak compressive strength σ_c for three different ply thicknesses are plotted against dimension d , the length of a square plate. The highlighted region represents the range of plate dimensions that match the tested samples in the current study in terms of AR. Taking the 30 μm thick plies as the baseline, the mean percentage change in the compressive strength is plotted against the percentage change in ply thickness, h_p , in Fig. 5.42(b). *All ARs* refers to the mean change in σ_c between plies of varying thickness over the entire range of available data, while *Equivalent ARs* refers to the mean change in σ_c for plate dimensions in the *Equivalent AR* range.

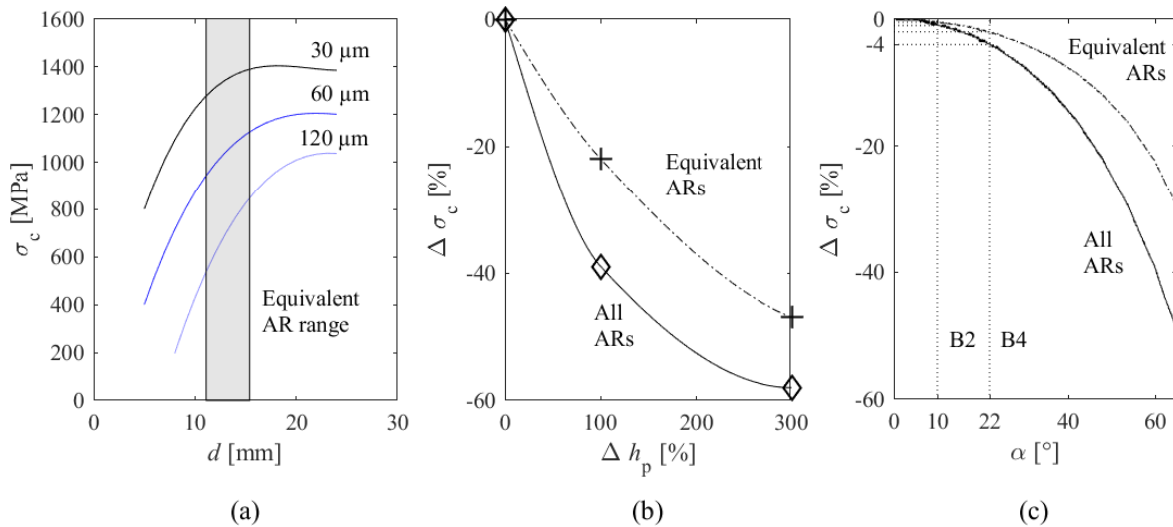


Figure 5.42: (a) The variation in the maximum through-thickness compressive strength σ_c with plate dimension d for multiple ply thicknesses, and demonstrating the variation in percentage change in σ_c with (b) percentage change in ply thickness Δh_p and with (c) shear angle α .

The relationship between the data points is established with second order polynomial curves that, together with the conservation of volume theory discussed in Section 5.3.1.4, are used to predict the percentage change in compressive strength with a changing fibre angle in 5.42(c). Here, sheared specimens B2 and B4 are plotted at their respective shear angles $\alpha = 10^\circ$

and $\alpha = 22^\circ$. Based on the data obtained from the *Equivalent AR* range, the rotation of fibres and subsequent thickening of the laminate can be expected to result in a 0.5% and 2% reduction in the compressive strength, respectively, while more conservative estimates of 1% and 4% are obtained from the *All ARs* data curve. Punch-tests should be performed on the laminates to confirm the extent of the reduction in compressive strength.

5.3.2.4 Fibre scissoring

In Section 5.2.2, footage from video gauge recordings were used to show that fibre extension was limited during the shearing process, as was demonstrated earlier in Fig. 5.7. It is worth noting however, that due to the clamping of the specimens, the fibres were not free to rotate perfectly, thus making it likely for there to be some form of fibre extension present in the specimens prior to impact. Since pre-strained fibres have in fact been shown to improve the V_{50} in the past, the extension in the fibres is not likely to be a detrimental factor in the performance of the laminates, but rather the kink in the yarns at the edges of the laminates where the flanges were cut away. Fractographic investigations need to be carried out to explore this hypothesis. To confirm this, laminate layups of unidirectional plies at the scissored angles of θ and $180^\circ - \theta$, mimicking the sheared laminates, would need to be impact tested to eliminate the effects of fibre rotation and focus solely on the effect of the inter-ply angles on impact performance.

5.3.2.5 Coupling effects

Although classical laminated plate theory (CLPT) is typically used as a tool to evaluate the behaviour of structural composites where large through-thickness forces are assumed to be absent, it can nevertheless be useful indicator of coupling behaviour in a composite laminate. The following assumptions are made for the purpose of analysing the effect of fibre rotation on the mechanical behaviour of a fibre-reinforced laminate. On the constituent level, the fibres and matrix are assumed to have linear elastic behaviour, with the fibres evenly distributed through the matrix domain. Although features such as the absence of voids, perfect bonding between fibres and matrix and perfectly aligned fibres have been shown to be less applicable to UHMWPE composites, the effects are assumed to be limited for the purpose of this analysis. Likewise, macroscopic characteristics were assumed to include strain continuity as a result of perfect bonding between individual plies, linear strain distribution through the thickness, linear elastic and transversely isotropic ply behaviour, together with a small plate thickness relative to its in-plane dimensions. The relationship between in-plane forces and out-of-plane moments

to in-plane strains and out-of-plane curvatures is expressed as

$$\begin{pmatrix} N_x \\ N_y \\ N_{xy} \\ M_x \\ M_y \\ M_{xy} \end{pmatrix} = \begin{bmatrix} A_{11} & A_{12} & A_{16} & B_{11} & B_{12} & B_{16} \\ A_{12} & A_{22} & A_{26} & B_{12} & B_{22} & B_{26} \\ A_{16} & A_{26} & A_{66} & B_{16} & B_{26} & B_{66} \\ B_{11} & B_{12} & B_{16} & D_{11} & D_{12} & D_{16} \\ B_{12} & B_{22} & B_{26} & D_{12} & D_{22} & D_{26} \\ B_{16} & B_{26} & B_{66} & D_{16} & D_{26} & D_{66} \end{bmatrix} \begin{pmatrix} \varepsilon_x^o \\ \varepsilon_y^o \\ \gamma_{xy}^o \\ \kappa_x \\ \kappa_y \\ \kappa_{xy} \end{pmatrix} \quad (5.9)$$

where the x - and the y -axis refer to the in-plane structural axes of the laminate with the x -direction aligned with the 0° fibre direction, while axes 1 and 2 refer to the natural material directions, with the primary direction aligned with the fibres and the secondary direction perpendicular to them. Since the stiffness matrix is constant across the surface of each ply, the stiffness terms populating the [A], [B] and [D] can be simplified as

$$\begin{aligned} A_{ij} &= \sum_{p=1}^P (\bar{Q}_{ij})_p (h_p - h_{p-1}) \\ B_{ij} &= \frac{1}{2} \sum_{p=1}^P (\bar{Q}_{ij})_p (h_p^2 - h_{p-1}^2) \\ D_{ij} &= \frac{1}{3} \sum_{p=1}^P (\bar{Q}_{ij})_p (h_p^3 - h_{p-1}^3) \end{aligned} \quad (5.10)$$

where $i, j = 1, 2, 6$, while P denotes the total number of true UD plies in the laminate, and $(\bar{Q}_{ij})_p$ represents the elements in the stiffness matrix of lamina p , with h_{p-1} and h_p being the distance from the laminate mid-plane to the top and bottom of lamina p , respectively.

Table 5.2: HB26 material constants [11, 50].

E_1	E_2	G_{12}	ν_{12}
[N/m ²]	[N/m ²]	[N/m ²]	[-]
68.06×10^9	2.83×10^9	86.90×10^6	0.30

In Eq. (5.11), a comparison between the [A], [B] and [D] stiffness matrices of an unsheared reference plate with a [0/90]₉₆ layup and a plate with an equal number of plies sheared by 10° , resulting in a layup sequence of [0/80]₉₆, reveals the nature of the coupling behaviour that is introduced, or enhanced, in the sheared laminate as a result of the change in the fibre

orientation. The linear elastic, transversely isotropic material properties used to calculate these terms are given in Table 5.2. Considering the response of in-plane deformations to in-plane forces related by the in-plane stiffness coupling terms in $[A]$, it can be seen that since the $[0/90]_{96}$ laminate is balanced, extension-shear coupling is eliminated ($A_{16}, A_{26} = 0$). The same cannot be said for the $[0/80]_{96}$ laminate, where the A_{16} and A_{26} entries are populated, albeit at a smaller magnitude than the other elements in $[A]$. Thus, in-plane normal forces (N_x, N_y) will yield an in-plane shear strain (γ_{xy}^o) while an in-plane shear force will result in normal in-plane deformations ($\varepsilon_x^o, \varepsilon_y^o$). In addition, the Poisson expansion stiffness term A_{12} has more than doubled in the sheared laminate and the corresponding entry for in-plane shear A_{66} has seen a larger than tenfold increase. The longitudinal stiffness term A_{11} has remained almost the same since there has been no rotation of fibres aligned with the primary material direction, while the in-plane stiffness in the secondary material direction has dropped by almost 13 N as a result of fibre realignment, since the 90° fibres aligned with this direction have now diverged away from it towards the primary direction.

A similar shift is observed in the bending stiffness values that relate the bending moments to resulting curvatures in matrix $[D]$, with changes in the elements following the same pattern as per the in-plane stiffness terms. Likewise, the sheared laminate is now prone to bend-twist coupling since $D_{16}, D_{26} \neq 0$, whereby the application of bending moments (M_x, M_y) will see a twisting deformation in the laminate (κ_{xy}), while a twist moment (M_{xy}) will cause curvatures in the x - z and y - z planes (κ_x, κ_y). In both cases, due to the cross-ply HB26 plies, there is an absence of symmetry in the layups. Hence, $[B] \neq 0$ for both laminates. The in-plane-out-of-plane coupling terms relate in-plane forces to curvatures and moments to in-plane deformations. Since the $[0/90]_{96}$ laminate is orthotropic, $B_{16}, B_{26} = 0$, so there is no extension-twist, bend-shear, or shear-twist coupling. The only type of in-plane-out-of-plane coupling present in this laminate is extension-bending, whereby in-plane forces (N_x, N_y) cause curvatures in the x - z and y - z planes (κ_x, κ_y) and bending moments (M_x, M_y) lead to normal in-plane strains ($\varepsilon_x^o, \varepsilon_y^o$).

$$[A] = \begin{bmatrix} A_{11} & A_{12} & A_{16} \\ A_{12} & A_{22} & A_{26} \\ A_{16} & A_{26} & A_{66} \end{bmatrix}$$

$$[A]_{[0/90], P=96} = \begin{bmatrix} 230.5 & 5.5 & 0 \\ 5.5 & 230.5 & 0 \\ 0 & 0 & 0.6 \end{bmatrix} \times 10^6 \text{ N}$$

$$[A]_{[0/80], P=96} = \begin{bmatrix} 230.4 & 12.1 & 0.1 \\ 12.1 & 217.6 & 36.1 \\ 0.1 & 36.1 & 7.1 \end{bmatrix} \times 10^6 \text{ N}$$

$$[B] = \begin{bmatrix} B_{11} & B_{12} & B_{16} \\ B_{12} & B_{22} & B_{26} \\ B_{16} & B_{26} & B_{66} \end{bmatrix}$$

$$[B]_{[0/90], P=96} = \begin{bmatrix} -716.0 & 0 & 0 \\ 0 & 716.0 & 0 \\ 0 & 0 & 0 \end{bmatrix} \times 10 \text{ N m} \quad (5.11)$$

$$[B]_{[0/80], P=96} = \begin{bmatrix} -716.4 & 22.1 & 0.5 \\ 22.1 & 672.3 & 121.9 \\ 0.5 & 121.9 & 22.1 \end{bmatrix} \times 10 \text{ N m}$$

$$[D] = \begin{bmatrix} D_{11} & D_{12} & D_{16} \\ D_{12} & D_{22} & D_{26} \\ D_{16} & D_{26} & D_{66} \end{bmatrix}$$

$$[D]_{[0/90], P=96} = \begin{bmatrix} 806.7 & 19.3 & 0 \\ 19.3 & 806.7 & 0 \\ 0 & 0 & 2.0 \end{bmatrix} \text{ N m}^2$$

$$[D]_{[0/80], P=96} = \begin{bmatrix} 806.2 & 42.2 & 0.5 \\ 42.2 & 761.4 & 126.4 \\ 0.5 & 126.4 & 24.9 \end{bmatrix} \text{ N m}^2$$

The behaviour of the $[0/80]_{96}$ laminate is heavily dominated by the extension-bending coupling terms (B_{11}, B_{22}). However, the remaining elements of $[B]$ are also now populated, the most significant of which is B_{26} at 1219 N m. This is an extension-twist and bending-shear coupling term, relating in-plane y -direction and shear forces and strains to twist and bending moments and curvatures in the y - z plane. This means that an in-plane normal load N_y will bring about twisting deformation κ_{xy} , an in-plane shear load N_{xy} , a bending curvature κ_y , and a bending moment M_y would cause in-plane shear strain (γ_{xy}^o), and a twist moment an in-plane normal deformation (ε_y^o). The emphasis on the shear coupling in the y -direction is clear from the relatively limited coupling behaviour (5 N m), represented by the other extension-twist coupling term, B_{16} , as it is the 90° fibres originally aligned in this direction that have moved away from the y -coordinate of the laminate. This has also caused a drop in the B_{22} term, as per the other stiffness matrices. Lastly, the sheared laminate will also experience extension-bending (B_{12}) and shear-twist (B_{66}) coupling to the same extent, with an equivalent stiffness of 221 N m.

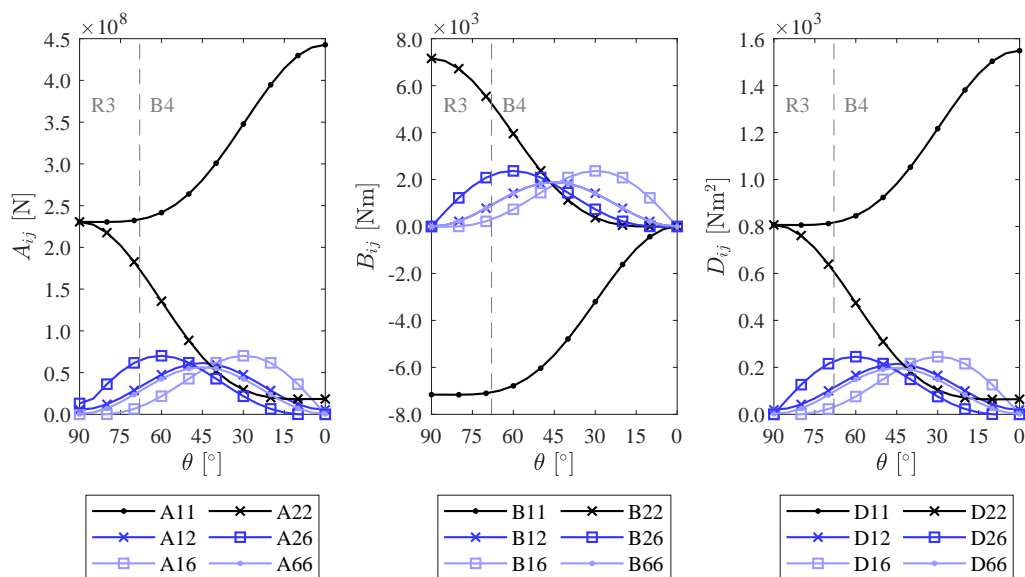


Figure 5.43: The variation in laminate stiffness terms with reducing fibre angle θ for a ply count of $N_p = 24$.

The relationship between a reducing fibre angle θ and the various stiffness terms is characterised and presented in Fig. 5.43, for a laminate with $P = 96$, or in other terms $N_p = 24$. For $ij = 11$, the in-plane $[A]$ and out-of-plane $[D]$ stiffness terms are greatly enhanced through alignment of the secondary fibre direction with the primary material axis, while for $ij = 22$, the terms are reduced to almost zero. In the case of $[B]$ terms $ij = 11, 22$, both converge to zero with the contraction of the fibre angle to zero, since UD laminates do not exhibit in-plane-out-of-plane

coupling behaviour. Other stiffness terms are enhanced until they reach their peak at either 60° ($ij = 26$), 30° ($ij = 16$) or at the 45° diagonal ($ij = 12, 66$). It can also be seen that at $\theta = 45^\circ$, all elements but one (B_{11}) of the [B] matrix are equal in magnitude, with a similar pattern visible for the elements of the [A] and [D] matrices. The implications of the coupling behaviour expected from sheared laminates on impact behaviour is analysed in the following section.

5.3.2.6 Visual inspection

Naturally, weak interlaminar strength is not captured in CLPT, since the plies are assumed to be perfectly bonded to allow for strain continuity. For instance, it has been shown that a bending stress gradient through the thickness of the laminate as a result of the through-thickness pressure wave is relieved through inter-laminar and intra-laminar shear action, and consequent axial fibre strain [50, 89]. CLPT does however offer a comparison of stiffness matrices of laminates with varying fibre angles in a simple bending scenario. Visual inspection of the laminates from two stop cases in Fig. 5.44, reveals the key differences in deformation and impact performance between a sheared specimen (B2) and a corresponding reference plate (R2) of matching ply count and similar AD. These were subjected to comparable impact velocities of 755 m/s and 751 m/s, respectively, both of which were just below the ballistic limit velocity of each plate.

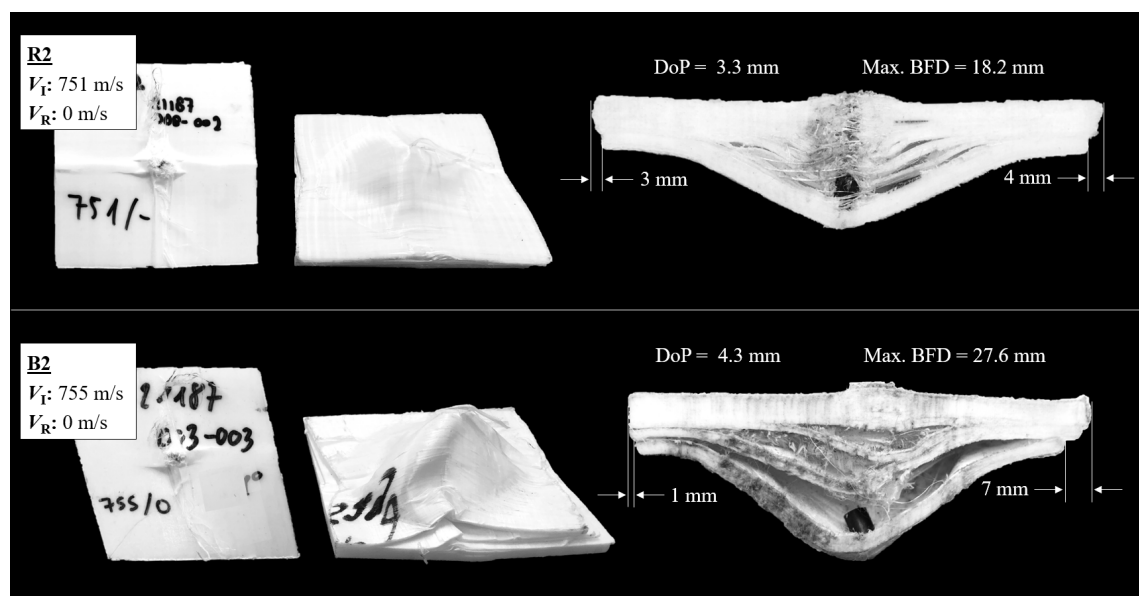


Figure 5.44: Visual inspection of specimens R2 and B2 from stop cases.

Simplifying the impact scenario to plate bending, we can assume the laminate undergoes bending moments M_x and M_y at the point of impact. From the stiffness terms in Eq. (5.11), the laminate is expected to have in-plane normal strains due to bending-extension coupling terms B_{11} and B_{22} , together with curvatures resulting in the first instance from D_{11} and D_{22} , and to a smaller extent from D_{12} . These give rise to a bulge that evolves from spherical to conical, as documented in [129] and [57], also visible in the top row in Fig. 5.44.

The sheared laminate (B2) on the other hand, undergoes a multitude of additional deformation mechanisms and coupling phenomena, ranging in order of significance from bend-shear coupling in the y -direction (B_{26}), to bending-extension coupling (B_{12}), some bending-shear coupling in the x -direction (B_{16}), bend-twist coupling in the y - z plane (D_{26}), increased bending-bending coupling (D_{12}), and a smaller degree of bend-twist coupling in the x - z plane (D_{16}), the results of which are highlighted in more detail in Fig. 5.45. The effect of the twist deformation in the y - z plane is visible at location 1 in Fig. 5.45, where it can be seen that the right corner of the laminate has not only delaminated at multiple stages, but the delaminated regions have lifted up towards the opposite corner. Meanwhile, locations 2 and 3 show evidence of bending-extension and bending-bending coupling in the primary fibre regions, combined with a large degree of bend-shear coupling in the secondary regions.

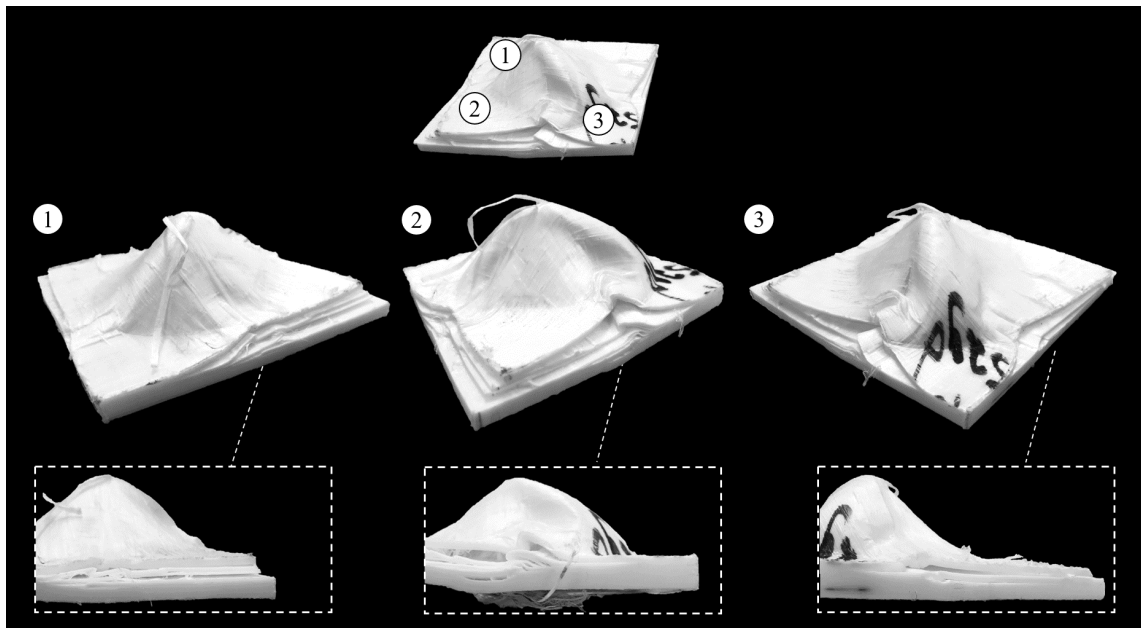


Figure 5.45: A closer examination of the BFD of B2 for a strike velocity of 755 m/s, highlighting deformations such as separation of the laminate into multiple sublaminates, extensive in-plane shear, as well as out-of-plane wrinkling and twist.

On the strike face, the two laminates show a similar degree of damage due to fibre breakage at the site of impact, visible in Fig. 5.44 (LHS). Likewise, in both cases there is evidence of primary fibre stretching and pull-in from the edges, the extent of which increases significantly from the front to the rear surface as fibre breakage develops into fibre straining in the bulge region, seen in Fig. 5.44 (centre and RHS). The effects of this are further exaggerated in the sheared laminate due to the presence of coupling action. Similarly, the bunching effect present at the edges, where primary-fibres are pulled inwards causing the laminate to fold over on itself, is much more prominent in the sheared plate and is biased towards the direction of the diagonal fibres. The presence of in-plane shear and wrinkling is also reminiscent of the macro-mechanisms dominating the deformation of anisotropic and isotropic laminates, respectively. As explained by Karthikeyan *et al.* [124], the stretching and wrinkling deformations are a means of moving from a planar surface to one with a positive Gaussian curvature, accompanied by restrictions in in-plane shear imposed on the isotropic laminates, by the introduction of a third fibre direction. The panels were also inspected in [124] to investigate the effect of the position of the primary fibres, with respect to the clamped boundary, on the shape of the BFD for various lay-ups. This was attributed to the variation in the fraction of the boundary intersected by primary fibres, which determined the overall frictional force of the clamps that had to be overcome by the loading on the primary fibres for pull-in deformation to occur at the edges.

Analysis of the cross-section of the unsheared plate in Fig. 5.44 demonstrates a deformation dominated by a localised, layer-by-layer perforation mechanism, together with a large mode II dominated delamination at the laminate mid-plane. The mid-plane coincided with the arrest plane of the projectile, ahead of which extensive inelastic deformation had taken place, in line with previous observations [64]. On the contrary, the sheared plate has a more localised failure in the penetrated plies, followed by distal delamination of combined multiple layers. The sheared plate has separated into four distinguishable laminates and three bulges, as a result of the major delamination action, with shear hinges that have travelled much further towards the edges. It is worth noting that in the sheared plate, the path of the projectile is affected by the coupling behaviour of the composite, curving its way through the thickness, as visible from the shifting peak of each bulge level from right to left. The differences in the deformation mechanisms indicate that the sheared laminates exhibit limited progressive delamination behaviour, while sustaining more extensive through-thickness damage for a given impact load, thereby rendering them less effective under ballistic impact than non-sheared plates.

As reported previously by Zhang *et al.* [123] and Hazzard *et al.* [18], the introduction of angled plies reduces the maximum BFD noticeably under quasi-static and ballistic impact loads, and to some extent, the ballistic limit velocity. Although those laminate lay-ups were limited to various forms of quasi-isotropic sequences and did not experience extension-shear coupling, *i.e.* A_{16} , $A_{26} = 0$, all other entries in the stiffness matrices of the laminates were populated. In the case of sheared laminates however, the introduction of additional coupling mechanisms reduces their V_{50} compared to their unsheared counterparts, as the coupling behaviour does not allow membrane bulging motion through symmetrical in-plane shear. This is due to weak interlaminar bonds which also allow the fibres to strain to their limit, the mechanism through which the bulk of the impact energy is dissipated. The B2 plate peak BFD increases by 51.6% relative to the unsheared R2 plate, to 27.6 mm, while the DoP rises by 30.3%. The shape of the bulge diverges from a cone to a collapsed one-sided oval-shaped dome, aligned diagonally between the x - and y - axes, generated through the greater levels of pull-in motion at the edges while surrounded by through-thickness wrinkling and bunching of the layers, as can be seen in Fig. 5.45.

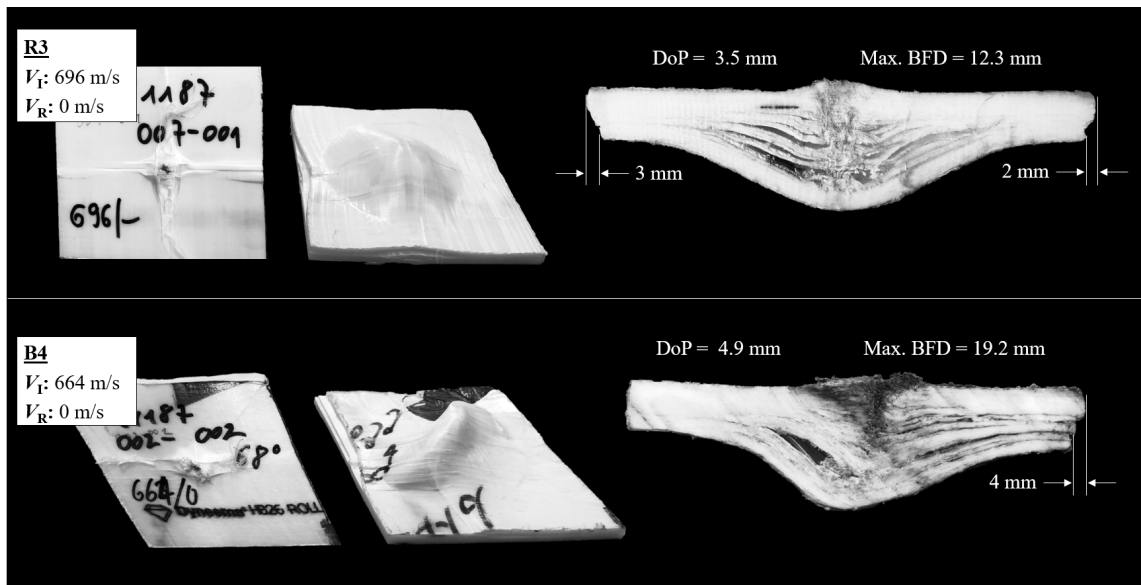


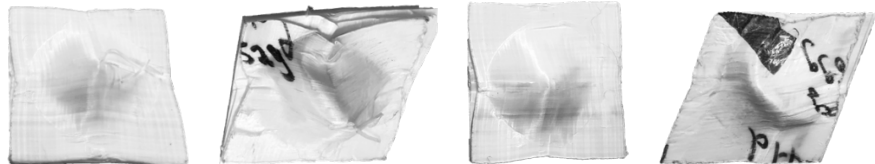
Figure 5.46: Visual inspection of specimens R3 and B4 from stop cases.

To understand the effect of the degree of shear on the impact behaviour of laminates, a specimen with a higher degree of in-plane shear at $\theta = 68^\circ$ (B4) and a reference plate (R3) with a corresponding ply count, $N_p = 24$, were studied and are presented in Fig. 5.46. The plates were considered at non-perforating strike velocities of 664 m/s and 696 m/s, respectively, also falling just below the V_{50} of each target. The deformation of reference plate R3 is consistent

with that of R2, in terms of the shape of the bulge on the rear face, as well as the extent of pull-in motion at the edges. The asymmetric deformation of the B4 sheared plate is also in line with that of plate B2, although the extent of delamination and subsequent inter-ply separation is visibly reduced with an increase in the degree of shear. The two sheared plates are compared against their respective references in Table 5.3. It can be seen that increasing the degree of shear to $\alpha = 22^\circ$ leads to an increase of 56.1% in the maximum out-of-plane dimension of the back-face bulge, relative to the unsheared R3 plate, with a similar pattern observed in the DoP of the sheared laminate. Comparing the sheared plates, an increase of 12° in α from B2 to B4 has led to an approximately 14% higher DoP but a 30% lower maximum BFD, as a result of the reduction in membrane action and delamination in the laminate due to the increase in the degree of in-plane shear.

Table 5.3: Comparison of sheared and unsheared shot plates.

Sample ID	R2	B2	R3	B4
AD [kg/m ²]	7.1	7.2	6.3	7.0
N_p	27	27	24	24
θ [°]	90	80	90	68
V_I [m/s]	751	755	696	664
V_R [m/s]	0	0	0	0
DoP [mm]	3.3	4.3	3.5	4.9
Δ DoP [%]	-	30.3	-	40.0
Max. BFD [mm]	18.2	27.6	12.3	19.2
Δ Max. BFD [%]	-	51.6	-	56.1



It must be noted however, that due to the complexity involved in achieving identical impact velocities, some discrepancy exists between the V_I terms of the plates discussed. While the B2 and R2 cases have comparable strike velocities, as reported in Table 5.3, the impact velocity of the reference for B4 is almost 5% higher. Since higher velocities under the ballistic limit result in a much larger sized bulge due to greater in-plane shear motion [81], for a 5% lower strike velocity, the maximum BFD induced in the R3 reference plate is anticipated to be even lower, which would cause a further increase in the difference in the maximum BFD between R3 and B4. Hence, it is likely that the effect of the increase in the degree of shear on the BFD and the DoP is underestimated. Furthermore, the relatively small in-plane dimensions of the samples

limits the establishment of a relationship between these factors. In Section 5.3.2.2, it was noted that previous studies had reported a reduction in the maximum BFD of laminates exhibiting architectures that varied from the standard cross-ply sequence, contrary to what is observed in the sheared laminates. This is due to inhibited in-plane shear deformation in laminates with more than two fibre directions, a restraint not imposed on sheared laminates with only two fibre directions, allowing further rotations and shearing of the laminate under an impact load.

The effects of increasing the strike velocity on the deformation of B2 specimens and R2 reference plates can be observed in Fig. 5.47. Two perforation cases are investigated; the first at impact velocities just above the V_{50} of each specimen, the second at a much higher value of V_I , in this case above 1000 m/s. For an impact velocity of around 800 m/s, the deformation on the rear faces of B2 and R2 are still substantially distinguishable from one another, and the bulging of both plates reminiscent of the non-perforation cases, with the addition of extensive fibre pull-out and damage on the exit plane of the sheared plate. Observations of the cross-sections, however, display a much greater extent of delamination and resulting bulging in the non-sheared specimen than in the sheared counterpart, giving rise to the lower residual velocity of 263 m/s compared to 348 m/s. While for an even higher V_I , in this case between 1040 m/s and 1050 m/s, the variations in the deformations of the two plates are minimised to the extent that the cross-sections of the two are not distinguishable. This is similar to the deformation on the rear of each plate, with the only noticeable difference being the additional pull-out of primary 0° yarns on the rear surface of the sheared laminate.

The similarity between the V_R values of the two plates confirms the convergence of the deformation mechanisms with increasing V_I , in-line with the trend visible for all specimens in Fig. 5.37. It is hypothesised that as V_I increases, the longitudinal and transverse shear waves travel much faster through the specimen, so that there is much less plate bending to invoke coupling mechanisms that can dominate the deformation, resulting in the reduction of the degradation in the V_{50} performance of the laminates at higher impact velocities. Nevertheless, the cross-sections of all the laminates, irrespective of strike velocity, exhibit extensive fibre damage through the thickness, which have been shown by Greenhalgh *et al.* [64] to highlight regions that have been exposed to compressive stress.

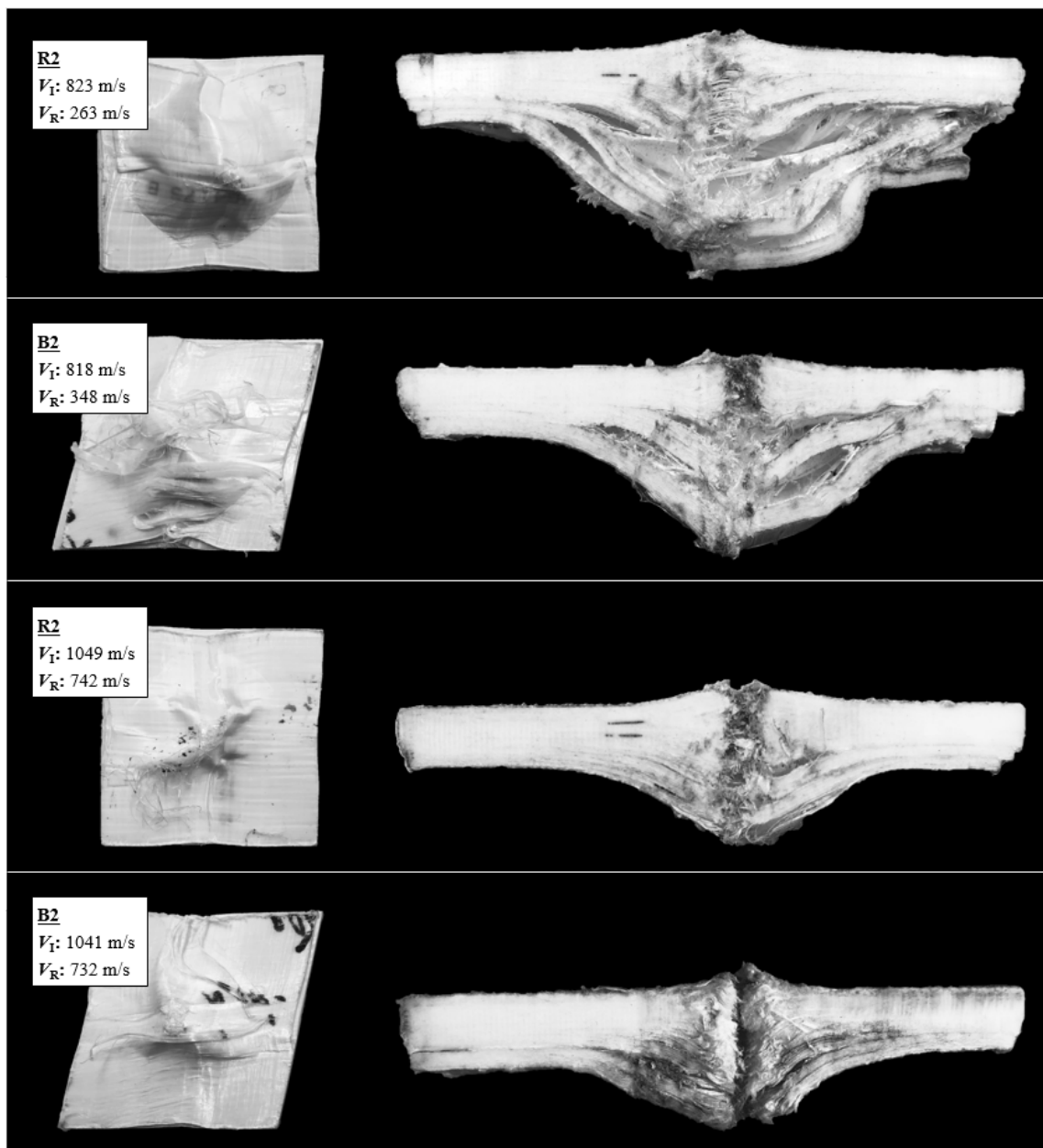


Figure 5.47: Visual inspection of specimens R2 and B2 from two perforation cases.

5.3.2.7 External factors

In this section, external factors affecting impact performance are evaluated. These range from processing conditions during laminate manufacturing and testing boundary conditions, to the physical parameters of the targets.

The processing conditions of laminates have been shown to dramatically influence the failure mechanisms taking place in the panels under impact. Increasing the processing pressure

has been shown to minimise the resin-rich inter-ply interface region [64], enhance the maximum shear strength [46], and improve the ballistic performance of the composite material [106]. Hence, the processing conditions of the sheared laminates were kept as aligned as possible with the non-sheared reference plates. The partial consolidation of the sheared plates to limit spring-back effects prior to the final consolidation of a stack is not expected to influence the behaviour of the material, due to the partial melting and re-solidifying of the matrix during the final consolidation stage.

The presence of the backing plate in the test set-up was deemed necessary in order to prevent the target from being set in motion by the projectile, due to the relatively small dimensions of the plates. Naturally, this restricts the dimensions of the bulge shear hinge expansion to the 70 mm aperture in the 7 mm thick backing plate. However, this was not considered to be significant as the plate dimensions of 100 mm \times 100 mm were considered insufficient for the size of the aperture in the backing plate to be a limiting factor for the extent of the out-of-plane deformation.

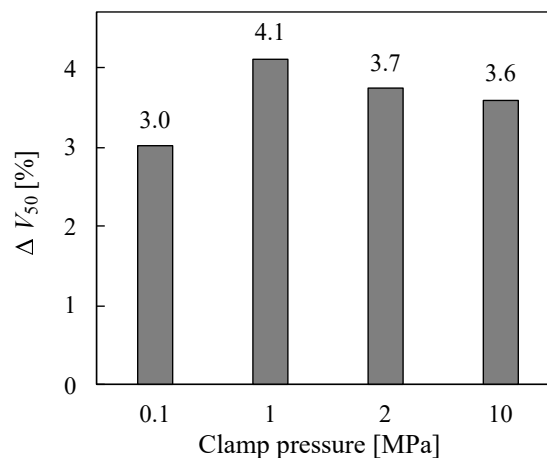


Figure 5.48: Numerical predictions of percentage change in V_{50} of laminates with the addition of clamping pressure, relative to a no-clamp boundary condition with $V_{50} = 925.5$ m/s.

It has previously been reported that the deformations at the edge may be a result of the clamping conditions, whereby some energy is expended in pulling layers out and away from the clamps [129]. This is however not applicable to the current study, due to the smaller target dimensions and therefore the reduced distance from the point of impact to the edges where the target is clamped, together with the fact that the target was only lightly clamped in place. Numerical analysis based on the model developed in Chapter 3 presented in Fig. 5.48, reveals

how the effects of applying an arbitrary clamping pressure on the V_{50} of an unsheared 9 mm thick target are limited. The effects of clamping pressure on the BFD of the laminate were not numerically analysed here due to the small plate dimensions, but it can be assumed they are limited as the ballistic limit of a target is directly influenced by the extent of the BFD. Although the interaction of the primary fibres with the clamped regions of the panels dictated the deformation of panels to a certain degree in [124], in that example the specimens were held in place with steel plates acting as clamps, that caused a substantial portion of the specimens, while the current study employed grips placed only at the corners of the specimens as used in Fig. 5.21.

Specimen parameters including thickness and ply count have been alluded to in Section 5.3.2.1, where it was established that the reference plates were designed to resemble the sheared panels as closely as physically possible. Nevertheless, the shearing process changes the in-plane shape of the plates from squares to parallelograms, consequently changing their surface area. However, the fall witnessed in the V_{50} arising from shearing is not due to a reduction of the strike face area. In fact, this has been shown to have the opposite effect, whereby the smaller distance from the point of impact to the edge of the laminate enables more extensive in-plane shear deformation to take place, accompanied by a larger bulge on the back face, and as a result more energy is absorbed [49, 81, 90, 109]. Likewise, it is not so much the laminate shape but rather the fibre lengths or the distance from the point of impact to the edge that is the determining factor, which could be investigated with circular laminates, as were used in [126].

5.3.2.8 A1 specimens

As discussed in Section 5.3.2.1, the results from A1 specimens oppose the general trend in V_{50} predictions and enhance the performance of the plate relative to an unsheared reference plate of equal ply count ($N_p = 33$). It was hypothesised that during the spring-back phase, the fibres rotate back to their original positions, having reorientated towards the direction of loading when the plies were sheared. This additional step may be responsible for weakening the fibre-matrix bonding and loosening the interlaminar interface. The spring-back effect therefore reduces the in-plane shear strength of the plies, together with the interlaminar shear strength (ILSS). This entails an increase in the compliance of the fibres that are more susceptible to in-plane shearing under through-thickness loading, while the presence of delaminations prior to impact testing is thought to have made the laminates predisposed to subsequent, more extensive delamination upon impact. This is in line with the observations made by Karthikeyan

and Russell [122] for laminates with a ‘pre-delamination’ interface, which outperformed those without any prior delamination.

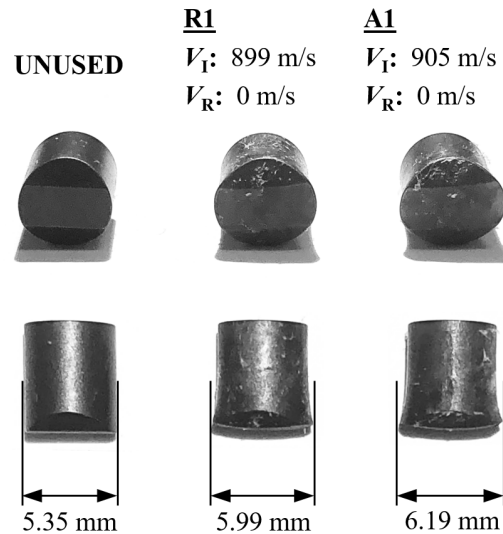


Figure 5.49: Comparison of deformed FSPs collected from two arrest cases of R2 and B2 to an unused FSP.

Meanwhile, the slightly larger extent of deformation of the captured projectile demonstrated in Fig. 5.49 reflects the the increased resistance to penetration that exists in the A1 specimen. Naturally, improvements in the ballistic limit velocity of the plates are accompanied by larger deflections at the rear. This can be observed in Fig. 5.50, where back face deformations of the A1 specimens are compared against those of their corresponding reference R1 plates for one arrest case (LHS) just below the estimated V_{50} , and two perforation cases with one just above the ballistic limit (centre) and the other much higher than the limit (RHS). Significantly larger bulges and more extensive pull-in of the material from the edges can be witnessed for the two impact velocities closest to the V_{50} , to the extent that the A1 stop-case plate has fully separated into two laminates, bar a few yarns still connecting them. The plies ahead of the arrest-plane have been drawn towards the centre through in-plane shearing, together with out-of-plane folding and wrinkling, which has lifted the rear plies off and away from the rest of the laminate, as seen in the inset in Fig. 5.50. Other than the extent of the deflection of the rear face, the shape is largely consistent between the sprung-back sheared plates and the reference ones, whether there is a dome-like bulge at the lower V_I end or a collapsed dome at the higher end of the V_I spectrum. Likewise, A1 and R1 specimens are deformed very similarly under an impact velocity exceeding 1000 m/s, following the trend of all previously analysed cases.

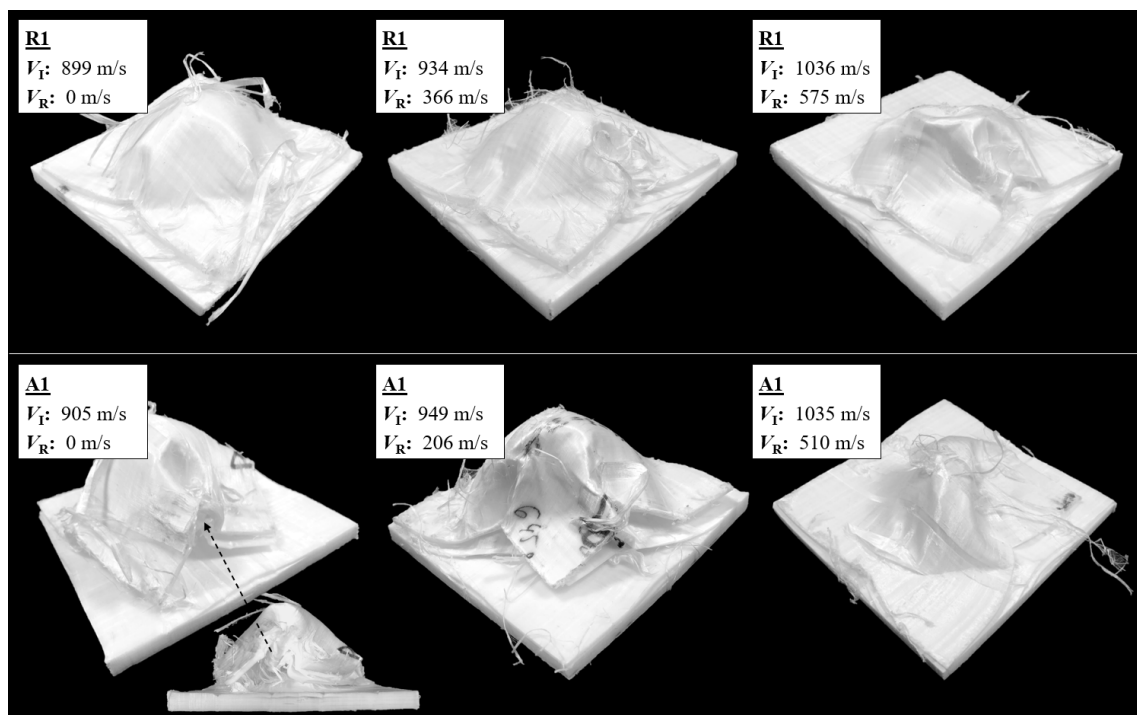


Figure 5.50: Visual inspection of specimens R1 and A1 for one stop and two perforation cases.

Further investigations into the ILSS and the in-plane shear strength using a double notch test shear should be performed to fully confirm this hypothesis, as it implies that all other sheared samples would in fact show improvements in their ballistic limit velocity when compared to specimens of equivalent values of θ , since they all underwent some degree of spring back deformation. This is also necessary, in order to rule out any indication that the V_{50} may actually be enhanced as a result of the inter-ply angle not having fully returned to 90° , suggesting the existence of a sweet spot. This sweet spot may exist for a small range of angles just below a full right-angle, before performance starts to degrade as θ is reduced, similar to the initial increase in shear stress for fibre angles positively deviating from $\pm 45^\circ$, before eventually falling, as reported in [111]. More trials with complete elimination of spring-back are required to confirm this effect. Similarly, further testing of sprung-back 90° specimens is also required to fully confirm the aforementioned effects of spring back, although the data in Fig. 5.37 is still highly significant as all the A1 samples that were impact tested show a reduction in their residual velocity relative to the reference. In practice however, there is no need to consider the effect of spring-back as modern manufacturing techniques prevent this. It may be possible to exploit the spring-back process to enhance the ballistic limit velocity of components, although this is inherently tied to much larger out-of-plane deformations on the back face, increasing the intensity of trauma to the user, and is therefore not a desirable outcome.

5.4 Summary of key findings

In this chapter, the effects of in-plane shear on the ballistic impact performance of UHMWPE fibre composites were investigated. To recreate the shear deformation induced when forming flat UHMWPE preforms into dome-shaped geometries, a manufacturing technique was developed using a picture frame test rig, in order to fabricate panels of varying shear angles. During the shearing process, the effect of external parameters such as temperature, grip pressure, loading rate and sequence were explored, and the continuous evolution of thickness across the surface of a specimen was documented.

After testing the plates under high velocity impact with an FSP threat, it was found that an increase in the degree of shear corresponds to poorer impact performance for the range of impact velocities investigated. The differences were most notable for impact velocities from 600 m/s to 1000 m/s, and were attributed to changes that arise due to the introduction of in-plane shear. Shearing reduces the angle between orthogonal fibres in a cross-ply architecture, thereby influencing the deformation mechanisms of the laminate through a combination of the following. Knock-down effects on through-thickness compressive strength, which reduce the extent of the indirect tension mechanism, and the coupling of in-plane and out-of-plane deformation mechanisms. The imperfect scissoring of fibres during the shearing process, is also thought to be a contributor, albeit to a smaller extent.

Beyond 1000 m/s however, the effects of in-plane shear were negligible. Although it is clear that shearing is detrimental to the ballistic limit parameter of laminates, a larger dataset is required to establish a relationship between the degree of shear and this parameter. Likewise, larger panel sizes are required to minimise the influence of in-plane plate dimensions, and to study the effect of shearing on another key ballistic performance indicator, the back face deflection, in greater detail. Moreover, it was shown that the increase in thickness and aerial density that accompany in-plane shear deformation, render these parameters ineffective for determining the impact performance of a sheared panel. Instead, the laminate ply count, which remains unchanged following shear deformation, is suggested to be a more accurate parameter for comparing the impact performance of sheared and unsheared panels. The implications of these findings for industry are discussed in Section 6.3.

Chapter 6

Conclusion

The final chapter of the thesis provides a brief recap of the research outcomes from Chapters 3 to 5, followed by some topics of discussion for future studies. Contributions of the work carried out in this thesis to the relevant fields are then discussed in the form of implications for industry, before concluding remarks reflect on whether the work has satisfactorily achieved the intended outcomes set out at the beginning of the thesis.

6.1 Research outcomes

The impact behaviour of ultra-high molecular weight polyethylene (UHMWPE) fibre composites was investigated, with the purpose of understanding geometrical and manufacturing effects on the performance of these materials for impact protection applications. Existing numerical techniques for modelling interlaminar contact in UHMWPE composite models under single-point ballistic impact, formed the basis of *Chapter 3*. Subsequently, in *Chapter 4* and *Chapter 5*, the effects of single curvature and in-plane shear on the ballistic performance of UHMWPE laminates were analytically, numerically and experimentally investigated. The key outcomes of the studies from these chapters are summarised as follows.

In *Chapter 3: Modelling the laminate interface*, a finite element model was developed to predict energy absorption at the interfaces of flat UHMWPE composite laminates, under varying rates of impact. Cohesive elements were successfully employed to model the behaviour of interface regions between sub-laminates at low strain rates. Upon validation, the model was extended to ballistic impact rates, to facilitate a better understanding of mode I and mode II delamination, both locally, across a single interface, as well as globally, through the thickness

of a laminate. Parametric studies were also performed to analyse the sensitivity of the energy dissipated at the interface to several physical and modelling variables.

The findings reinforce current understandings that the contribution of the interfaces to overall energy dissipation stands at 10%, and highlight the dominance of energy dissipation through mode II delamination, accounting for over 90% of the dissipated energy levels across all cases investigated. Energy dissipation through both modes of fracture also demonstrated a dependence on the impact velocity, as well as dimensional and numerical parameters. Furthermore, in the projectile arrest cases modelled, the greatest contributions to overall energy dissipation were found to occur at the middle interfaces in the through-thickness direction.

In *Chapter 4: Effect of single curvature on impact performance*, the effects of impact direction and the radius of curvature on the ballistic performance of UHMWPE laminates were experimentally investigated. Panel deformations and residual velocities were studied for three curvature radii, 20 in, 10 in and 5 in, under convex and concave impact by two types of threat; a spherical projectile and a flat-faced, chisel nose fragment-simulating projectile (FSP).

For non-perforating dynamic impact velocities of approximately 300 m/s by the spherical projectile, deflections on the rear laminate face were more sensitive to changes in panel curvature than the ballistic limit velocity of the panel. Under both directions of impact, the introduction of curvature to the panels resulted in deflection increases of up to 50% for convex, and up to 11% for concave panels, at a radius of curvature of 5 in, with larger deflections corresponding to higher degrees of curvature. The least curved convex panel displayed similar behaviour to the stable response of a flat plate, while the highly curved panels displayed more extensive bending, membrane shearing, and inelastic deformation. As the strike velocity was increased beyond 400 m/s, the differences between the response of convex panels of varying curvatures were greatly reduced. By contrast, the deformation of panels under concave impact remained mostly elastic and reminiscent of a flat plate response.

Similarly, under FSP impact, the existence of curvature increased bending in convex cases, thereby releasing stored elastic energy upon reversal of the bending direction under impact. At the higher non-perforating velocities of 500 m/s to 600 m/s, a parabolic relationship was reported between the extent of deflections on the laminate back face and the degree of curvature, both in-plane and out-of-plane. At these higher velocities, and therefore larger deflections, geometrical restrictions in the direction of curvature limited the in-plane progression of the back

face bulge from the site of impact to the laminate edges. Irrespective of the degree of curvature, convex panels displayed increases of around 10% in the ballistic limit velocity, compared to a flat target, while concave panels did not yield any significant differences in this parameter.

Modelling tools developed for curved laminates based on previous flat plate models, predicted the maximum back face deflection of laminates to a reasonable degree of accuracy, but were limited in their ability to predict the full extent of in-plane deformations, and ballistic limit velocity. The discrepancies between numerical predictions and experimental results were attributed to a combination of limitations in modelling bending deformation, the effects of pre-straining in the fibres, and the presence of rate effects and plastic deformations that are not accounted for. These effects are prominent in curved laminates to the extent that they cannot be neglected, as had been possible for flat laminates. The most significant contributor was deemed to be the increased stiffness in the system, as the bending stiffness values used had been validated for flat configurations only. In addition, some sources of discrepancies were attributed to the manufacturing process, as curved laminates are more prone to poor consolidation, extensive sliding of plies and ill-matched tooling curvatures, as well as post-consolidation spring-back effects.

In *Chapter 5: Effect of pre-existing shear on impact performance*, the effects of in-plane shear on the ballistic impact performance of UHMWPE fibre composites were investigated by experimental and analytical means. To recreate the shear deformation induced when forming flat UHMWPE preforms into dome-shaped geometries, a manufacturing technique was developed to fabricate panels with varying shear angles. The sheared plates were tested under high velocity impact with a fragment simulating projectile, and revealed that higher degrees of shear correspond to poorer impact performance. The differences in the laminate response as a result of in-plane shear were most significant for impact velocities of 600 m/s to 1000 m/s. Beyond 1000 m/s, the effects of in-plane shear were negligible.

The effects of in-plane shear on the laminate response were attributed to the reduction in the angle between orthogonal fibres in the cross-ply architecture, influencing the deformation mechanisms of the laminate through a combination of knock-down effects on through-thickness compressive strength, reducing the extent of the indirect tension mechanism, the coupling of in-plane and out-of-plane deformation mechanisms, and to a smaller extent, the imperfect scissoring of fibres during the shearing process. In addition, due to the increase in thickness and aerial density that accompanies in-plane shear deformation, these parameters are deemed inaccurate

and therefore unsuitable for determining the impact performance of a sheared panel. The laminate ply count, which remains unchanged following shear deformation, was identified as a more accurate parameter for comparison of impact performance amongst laminates, irrespective of the degree of shearing deformation.

6.2 Future Work

To build on the outcomes of the work presented in this thesis, future experimental investigations should focus on expanding existing understanding of the effects of curvature and shearing, through further testing of a wider range of impact velocities, threat and target dimensions, as well as degrees of curvature and shear. One particular area of interest would be the effect of in-plane shear on the back face deflection of laminates subjected to impact loads, since the sample dimensions used in the current study were not quite sufficient to investigate this. Meanwhile, future numerical analyses should be geared towards the development of a user-defined material subroutine for the solid sub-laminate elements, to incorporate features that facilitate the capturing of curvature- or shear-induced physical effects.

The implementation of non-linear through-thickness shear, which will reduce the effective bending stiffness in the laminate, together with plastic and rate-dependent behaviour, will improve the modelling predictions of the impact performance in curved panels. Likewise, the implementation of fibre scissoring and ply thickening will be crucial for the modelling of sheared laminates under impact. This approach can be combined with forming simulations, to account for the change in the degree of curvature and scissoring that take place in the manufacturing process. The ultimate aim would be to simulate the ballistic impact of doubly-curved geometries, combining the geometrical effects of curvature and the manufacturing effects of in-plane shear on the impact performance of the material. Considering more immediate future work however, Chapter A and Chapter B provide more details on two topics for improving the current modelling tools; implementing rate-dependence and plasticity at the interface.

6.3 Implications for industry

In this section, the implications of the findings of this thesis for industry are discussed, with suggestions of how the results could be used to improve design in order to enhance the performance of UHMWPE composites used in protective applications.

In *Chapter 3: Modelling the laminate interface*, it was numerically shown that the interfaces of a laminate were responsible for dissipating 10% of the projectile kinetic energy, over 90% of which occurred solely in the sliding mode (mode II) of delamination. A reduction in value of the maximum mode II peak traction of the interface elements, equivalent to the matrix yield strength, displayed higher levels of energy dissipation, implying improved impact performance. These interface modelling tools can therefore be used to optimise impact performance through matrix properties, thereby aiding the matrix design process. Furthermore, in *Chapter 3*, the middle interfaces through the laminate thickness were identified as the largest contributors to the dissipation of impact energy. This insight is essential in the design of hybrid components, to ensure that in the through-thickness regions with the largest energy dissipation contributions, the in-plane shearing action of UHMWPE plies under impact loads is not compromised by the presence of alternative material.

The experimental findings in *Chapter 4: Effect of single curvature on impact performance*, have revealed exceptional increases of up to 50% in the laminate back face deflection with the introduction of curvature, compared to flat UHMWPE laminates, for a convex direction of impact. It was also shown that the increase in the out-of-plane deflection can be significantly reduced by minimising the degree of curvature. For example, component configuration-permitting, the increase in the deflection can be halved by increasing the panel curvature radius from 5 in to 20 in. However, this is only applicable at lower impact velocities of approximately half the ballistic limit, where geometric effects are more dominant than the effects of inertia. It was shown that changes to panel curvature do not yield any considerable changes in the back face deflection at impact velocities approaching the ballistic limit of the laminate, or for the concave direction of impact.

By contrast, the maximum increase achieved in the ballistic limit velocity relative to a flat panel, amounted to approximately 10% for the most highly curved convex panels. The pursuit of a higher ballistic limit with the addition of curvature, is therefore not recommended in body armour applications, as the enhancement of the ballistic limit is accompanied by a much larger penalty in terms of the maximum out-of-plane deflection on the rear face. Furthermore, it was shown that for low fidelity simulations, off-the-shelf modelling tools are not suitable for predicting the response of curved laminates under ballistic impact, due to the increased stiffness and manufacturing effects imposed on laminates with curved geometries. To account for these effects, it is recommended to use processing simulations, followed by impact modelling of the

laminates using the current modelling method with an empirically-derived effective bending stiffness, or a user defined material that accounts for non-linear through-thickness stiffness behaviour.

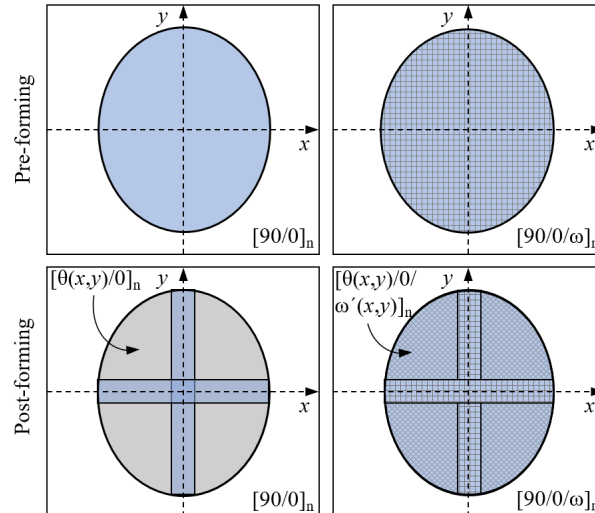


Figure 6.1: Top-down view of pre- and post-forming fibre directions across a helmet-shaped surface for a purely cross-ply layup sequence (LHS) and a cross-ply layup sequence with an additional fibre direction at an interlaminar angle ω (RHS).

Arguably the most relevant implications for industry are based on the findings presented in *Chapter 5: Effect of pre-existing shear on impact performance*. The method developed for manufacturing shear plates can be replicated in future investigations, while the material characterisation results, particularly thickness change with shear angle, can be used in forming simulations for more accurate representations of the material behaviour. More importantly however, the detrimental effect of pre-shearing on the ballistic limit velocity has been documented here. One approach to addressing the loss in the performance of sheared regions is to alter the laminate architecture by alternating $0^\circ/90^\circ$ with another layer of varying interlaminar angle ω . This would ensure that all regions of a deep-drawn hemispherical surface end up with a portion of the laminate formed from $0^\circ/90^\circ$ plies, whether from the original fibre angle or due to fibre rotation post-shear. The latter would occur in the corner regions of each preform quadrant, as demonstrated in Fig. 6.1. Although, the introduction of a third fibre direction to the laminate layup will constrict fibre scissoring and therefore in-plane shearing, which is necessary for the effective dissipation of energy under impact. Improvements would be seen in the maximum back face deflection, yet the ballistic limit velocity of the laminate would suffer. It is therefore a question of to what extent a drop in the ballistic limit is acceptable, for achieving a more uniform performance across the surface of a helmet. Likewise, although a

fraction of the degradation of ballistic performance comes from the inter-ply angle due to the activation of stiffness coupling terms, the rest is due to the very act of fibre rotation and is therefore independent of the resulting inter-ply angle.

To understand the relevance of the findings to industry, it is important to be aware of current manufacturing practices. In recently developed manufacturing methods used in the forming of doubly-curved UHMWPE components, namely combat helmets, attempts have been made to eradicate wrinkling deformation. In doing so, out-of-plane wrinkling has been largely replaced by in-plane shear. The current findings highlight the detrimental effect of pre-shearing on the ballistic velocity performance of UHMWPE fibre laminates. This therefore raises the question of whether under impact loads, in-plane shear is truly preferential over wrinkling, and if so, to what extent, and whether other factors such as user comfort and practicality are also involved. In addition, current manufacturing methods typically employ filler plies in non-sheared regions and cut-outs in sheared regions, to compensate for the increase in thickness during shearing. This is done with the intention of achieving a constant thickness throughout the structure of the component, while considering the physical restrictions of the tooling cavity. Sheared plates possess greater thickness than unsheared plates for the same number of plies, thus effectively increasing the aerial density, the parameter commonly used in comparisons of impact performance. As shown in Section 5.3.2.1, the ballistic limit velocity performance of sheared specimens falls behind those of unsheared reference plates of equivalent aerial density. This makes aerial density a misleading criteria for performance, as the thickness and therefore the aerial density increase in sheared laminates is not due to a higher ply count, but has come about from the thickening of the laminate to conserve its volume. While velocity-based impact performance is typically determined by the aerial density of a panel, in the manufacturing process of UHMWPE composites the emphasis is on achieving uniform thickness across a finished component, as a result of tooling cavity constraints. Current ballistic limit and manufacturing standards across the industry therefore rely on parameters that do not readily account for the secondary effects accompanying in-plane shear, thereby jeopardising the impact performance of sheared regions.

6.4 Concluding remarks

By reflecting on the objectives and intended research outcomes outlined at the beginning of the thesis, the key achievements of this work are summarised as follows:

- a)
 - (i) Numerical tools for modelling ballistic impact of flat UHMWPE composite panels were enhanced by the implementation of cohesive elements to model interlaminar contact.
 - (ii) These numerical models were used to investigate the in-plane and through-thickness dissipation of energy at sub-laminate interfaces under ballistic impact loading, as well as highlighting the contribution of the matrix to overall energy absorption of the laminate.
 - (iii) The contribution of the matrix to the dissipation of impact energy can be used to identify the most significant in-plane and out-of-plane interfaces within a laminate, that can be optimised in terms of matrix and laminate layup design.
- b)
 - (i) Curved panels were tested under ballistic impact and the geometrical effects of curvature on the laminate response, arising from impact direction and the degree of curvature, were demonstrated.
 - (ii) It was shown that existing numerical tools require additional features and modifications not previously necessary for flat configurations, to capture the impact response of curved laminates, due to the geometrical and manufacturing effects arising from the introduction of curvature.
- c)
 - (i) A representative manufacturing process for sheared plates was developed, with the purpose of impact testing.
 - (ii) Ballistic impact testing of sheared plates was performed, and the effects of the manufacturing-induced in-plane shear deformation on the impact performance of the UHMWPE plates were demonstrated, based on the degree of shear.
- d)
 - (i) Modelling and experimental data acquired on the effects of curvature and shear provide insight for forming simulations and pave the way for a numerical model capable of predicting the combined effects of curvature and shear on ballistic impact performance. These can be used in the development of components with lower back face deflection, and thus less trauma induced in body armour applications, without compromising the ballistic limit velocity.

-
- (ii) Testing results highlighted that current aerial density based impact performance comparison criteria and thickness based manufacturing standards do not promote uniform impact performance across the surface of a doubly-curved component, making the case for transforming these standards to suit the latest processing techniques.

Bibliography

- [1] A. Bhatnagar, ed. *Lightweight Ballistic Composites: Military and Law-Enforcement Applications*. 2nd ed. Woodhead Publishing, 2016.
- [2] R. Yadav, M. Naebe, X. Wang, and B. Kandasubramanian. “Body armour materials: from steel to contemporary biomimetic systems”. In: *RSC Advances* 6.116 (2016), pp. 115145–115174. DOI: 10.1039/C6RA24016J.
- [3] N. V. David, X. L. Gao, and J. Q. Zheng. “Ballistic resistant body armor: Contemporary and prospective materials and related protection mechanisms”. In: *Applied Mechanics Reviews* 62.5 (2009). DOI: 10.1115/1.3124644.
- [4] I. G. Crouch. “Body armour - New materials, new systems”. In: *Defence Technology* 15.3 (2019), pp. 241–253. DOI: 10.1016/j.dt.2019.02.002.
- [5] B. A. Cheeseman and T. A. Bogetti. “Ballistic impact into fabric and compliant composite laminates”. In: *Composite Structures* 61.1-2 (2003), pp. 161–173. DOI: 10.1016/S0263-8223(03)00029-1.
- [6] L. Iannucci and D. Pope. “High velocity impact and armour design”. In: *Express Polymer Letters* 5.3 (2011), pp. 262–272. DOI: 10.3144/expresspolymlett.2011.26.
- [7] M. R. O’Masta. “Mechanisms of dynamic deformation and failure in ultra-high molecular weight polyethylene fiber-polymer matrix composites”. PhD Thesis. Charlottesville, VA, USA: University of Virginia, 2014.
- [8] P. M. Cunniff. “A Semiempirical Model for the Ballistic Impact Performance of Textile-Based Personnel Armor”. In: *Textile Research Journal* 66.1 (1996), pp. 45–59. DOI: 10.1177/004051759606600107.
- [9] P. M. Cunniff. “Dimensionless parameters for optimization of textile-based body armor systems”. In: *Proceedings of the 18th international symposium on ballistics*. San Antonio, TX, USA, 1999.

- [10] L. Iannucci, D. Pope, and M. Dalzell. “A Constitutive Model for Dyneema UD composites”. In: *17th International Conference on Composite Materials*. Edinburgh, UK, 2009, pp. 27–31.
- [11] B. P. Russell, K. Karthikeyan, V. S. Deshpande, and N. A. Fleck. “The high strain rate response of Ultra High Molecular-weight Polyethylene: from fibre to laminate”. In: *International Journal of Impact Engineering* 60 (2013), pp. 1–9. DOI: 10.1016/j.ijimpeng.2013.03.010.
- [12] O. Nazarian and F. W. Zok. “Constitutive model for the shear response of Dyneema fiber composites”. In: *Composites Part A: Applied Science and Manufacturing* 66 (2014), pp. 73–81. DOI: 10.1016/j.compositesa.2014.06.012.
- [13] A. L. Alesi, R. P. Ames, R. A. Gagne, A. M. Litman, and J. J. Prifti. *New materials and construction for improved helmets*. Tech. rep. AMMRC MS 75-9. Watertown, MA, USA: Army Materials and Mechanics Research Center, 1975.
- [14] R. Marissen. “Design with ultra strong polyethylene fibers”. In: *Materials Sciences and Applications* 2.05 (2011), pp. 319–330. DOI: 10.4236/msa.2011.25042.
- [15] L. M. Dangora, J. A. Sherwood, J. C. Parker, C. J. Mitchell, and K. D. White. “Temperature dependent tensile and flexural rigidities of a cross-ply thermoplastic for a forming model”. In: *AIP Conference Proceedings* (2016). DOI: 10.1063/1.4963591.
- [16] A. Cherouat and J. L. Billoet. “Mechanical and numerical modelling of composite manufacturing processes deep-drawing and laying-up of thin pre-impregnated woven fabrics”. In: *Journal of Materials Processing Technology* 118 (2001), pp. 460–471. DOI: 10.1016/S0924-0136(01)00987-6.
- [17] L. M. Dangora, C. J. Mitchell, J. Sherwood, and J. C. Parker. “Deep-drawing forming trials on a cross-ply thermoplastic lamina for helmet preform manufacture”. In: *Journal of Manufacturing Science and Engineering* 139.3 (2017). DOI: 10.1115/1.4034791.
- [18] M. K. Hazzard, S. Hallett, P. T. Curtis, L. Iannucci, and R. S. Trask. “Effect of fibre orientation on the low velocity impact response of thin Dyneema composite laminates”. In: *International Journal of Impact Engineering* 100 (2017), pp. 35–45. DOI: 10.1016/j.ijimpeng.2016.10.007.

- [19] G. Liu, M. D. Thouless, V. S. Deshpande, and N. A. Fleck. “Collapse of a composite beam made from ultra high molecular-weight polyethylene fibres”. In: *Journal of the Mechanics and Physics of Solids* 63 (2014), pp. 320–335. DOI: 10.1016/j.jmps.2013.08.021.
- [20] A. J. Lindfors, J. C. Schulz, and S. A. Finnegan. “Plate Curvature Effects on Ballistic Limit and Fragmentation”. In: *12th International Symposium on Ballistics*. San Antonio, TX, USA, 1990.
- [21] M. E. Backman and W. Goldsmith. “The mechanics of penetration of projectiles into targets”. In: *International Journal of Engineering Science* 16.1 (1978), pp. 1–99. DOI: 10.1016/0020-7225(78)90002-2.
- [22] D. R. Ambur. “Scaling the Non-linear Impact Response of Flat and Curved Composite Panels”. In: *46th Structures, Structural Dynamics and Materials Conference*. Austin, TX, USA, 2005. DOI: 10.2514/6.2005-2224.
- [23] S. R. Swanson, N. L. Smith, and Y. Qian. “Analytical and experimental strain response in impact of composite cylinders”. In: *Composite Structures* 18.2 (1991), pp. 95–108. DOI: 10.1016/0263-8223(91)90045-Z.
- [24] L. B. Greszczuk and H. Chao. *Investigation of brittle fractures in graphite-epoxy composites subjected to impact*. Tech. rep. USAAMRDL-TR- 75-15. Fort Eustis, VA, US: U.S. Army Air Mobility Research and Development Laboratory, 1975.
- [25] L. S. Kistler and A. M. Waas. “Experiment and analysis on the response of curved laminated composite panels subjected to low velocity impact”. In: *International Journal of Impact Engineering* 21.9 (1998), pp. 711–736. DOI: 10.1016/s0734-743x(98)00026-8.
- [26] D. R. Ambur and J. H. Starnes. “Nonlinear response and damage-initiation characteristics of curved composite plates subjected to low-speed impact”. In: *38th Structures, Structural Dynamics, and Materials Conference*. Kissimmee, FL, USA, 1997. DOI: 10.2514/6.1997-1058.
- [27] D. R. Ambur and J. H. Starnes. “Effect of curvature on the impact damage characteristics and residual strength of composite plates”. In: *39th Structures, Structural Dynamics and Materials Conference*. Long Beach, CA, USA, 1998. DOI: 10.2514/6.1998-1881.
- [28] L. S. Kistler and A. M. Waas. “On the response of curved laminated panels subjected to transverse impact loads”. In: *International Journal of Solids and Structures* 36.9 (1999), pp. 1311–1327. DOI: 10.1016/S0020-7683(98)00005-5.

- [29] H. Saghafi, G. Minak, and A. Zucchelli. “Effect of preload on the impact response of curved composite panels”. In: *Composites Part B: Engineering* 60 (2014), pp. 74–81. DOI: 10.1016/j.compositesb.2013.12.026.
- [30] C. T. Sun and S. Chattopadhyay. “Dynamic Response of Anisotropic Laminated Plates Under Initial Stress To Impact of a Mass”. In: *Journal of Applied Mechanics* 42.3 (1975), pp. 693–698. DOI: 10.1115/1.3423664.
- [31] G. P. Zhao and C. D. Cho. “Damage initiation and propagation in composite shells subjected to impact”. In: *Composite Structures* 78 (2007), pp. 91–100. DOI: 10.1016/j.compstruct.2005.08.013.
- [32] A. P. Christoforou and S. R. Swanson. “Analysis of simply-supported orthotropic cylindrical shells subject to lateral impact loads”. In: *Journal of Applied Mechanics* 57.2 (1990), pp. 376–382. DOI: 10.1115/1.2892000.
- [33] K. S. Krishnamurthy, P. Mahajan, and R. K. Mittal. “Impact response and damage in laminated composite cylindrical shells”. In: *Composite Structures* 59.1 (2003), pp. 15–36. DOI: 10.1016/S0263-8223(02)00238-6.
- [34] H. J. Lin and Y. J. Lee. “Impact-induced fracture in laminated plates and shells”. In: *Journal of Composite Materials* 24.11 (1990), pp. 1179–1199. DOI: 10.1177/002199839002401105.
- [35] A. Palazotto, R. Perry, and R. Sandhu. “Impact response of graphite/epoxy cylindrical panels”. In: *AIAA Journal* 30.7 (1992), pp. 1827–1832. DOI: 10.2514/3.11143.
- [36] A. F. Johnson and M. Holzapfel. “Influence of delamination on impact damage in composite structures”. In: *Composites Science and Technology* 66.6 (2006), pp. 807–815. DOI: 10.1016/j.compscitech.2004.12.032.
- [37] N. K. Gupta and R. Velmurugan. “Experiments and analysis of collapse behaviour of composite domes under axial compression”. In: *Journal of Composite Materials* 36.8 (2002), pp. 899–914. DOI: 10.1106/002199802023511.
- [38] Z. Cui, G. Moltschaniwskyj, and D. Bhattacharyya. “Buckling and large deformation behaviour of composite domes compressed between rigid platens”. In: *Composite Structures* 66.1-4 (2004), pp. 591–599. DOI: 10.1016/j.compstruct.2004.05.007.

- [39] O. S. David-West, D. H. Nash, and W. M. Banks. “Impact characterisation of doubly curved composite structure”. In: *17th International Conference on Composite Materials*. Edinburgh, UK, 2009.
- [40] N. O. Yokoyama, M. V. Donadon, and S. F. M. de Almeida. “A numerical study on the impact resistance of composite shells using an energy based failure model”. In: *Composite Structures* 93.1 (2010), pp. 142–152. DOI: 10.1016/j.compstruct.2010.06.006.
- [41] D. S. Stargel. *Experimental and numerical investigation into the effects of panel curvature on the high velocity ballistic impact response of aluminium and composite panels*. PhD Thesis. College Park, MD, USA: University of Maryland, 2005.
- [42] P. Tan. “Ballistic protection performance of curved armor systems with or without debondings/delaminations”. In: *Materials and Design* 64 (2014), pp. 25–34. DOI: 10.1016/j.matdes.2014.07.028.
- [43] L. Iannucci and M. L. Willows. “An energy based damage mechanics approach to modelling impact onto woven composite materials-Part I: Numerical models”. In: *Composites Part A: Applied Science and Manufacturing* 37.11 (2006), pp. 2041–2056. DOI: 10.1016/j.compositesa.2005.12.013.
- [44] J. P. Attwood, S. N. Khaderi, K. Karthikeyan, N. A. Fleck, M. R. O’Masta, H. N. G. Wadley, and V. S. Deshpande. “The out-of-plane compressive response of Dyneema composites”. In: *Journal of the Mechanics and Physics of Solids* 70 (2014), pp. 200–226. DOI: 10.1016/j.jmps.2014.05.017.
- [45] T. Lässig, L. Nguyen, M. May, W. Riedel, U. Heisserer, H. Van Der Werff, and S. Hiermaier. “A non-linear orthotropic hydrocode model for ultra-high molecular weight polyethylene in impact simulations”. In: *International Journal of Impact Engineering* 75 (2015), pp. 110–122. DOI: 10.1016/j.ijimpeng.2014.07.004.
- [46] M. K. Hazzard, P. T. Curtis, L. Iannucci, S. Hallett, and R. Trask. “An investigation of the in-plane performance of ultra-high molecular weight polyethylene fibre composites”. In: *20th International Conference on Composite Materials*. Copenhagen, Denmark, 2015.
- [47] R. J. T. Frissen. “Modelling the Ballistic Impact Behaviour of Polyethylene-Fibre-Reinforced Composites”. Masters Thesis. Eindhoven, Netherlands: Eindhoven University of Technology, 1996.

- [48] L. H. Nguyen, T. R. Lässig, S. Ryan, W. Riedel, A. P. Mouritz, and A. C. Orifici. “A methodology for hydrocode analysis of ultra-high molecular weight polyethylene composite under ballistic impact”. In: *Composites Part A: Applied Science and Manufacturing* 84 (2016), pp. 224–235. DOI: 10.1016/j.compositesa.2016.01.014.
- [49] M. K. Hazzard, R. S. Trask, U. Heisserer, M. Van Der Kamp, and S. R. Hallett. “Finite element modelling of Dyneema composites: From quasi-static rates to ballistic impact”. In: *Composites Part A: Applied Science and Manufacturing* 115 (2018), pp. 31–45. DOI: 10.1016/j.compositesa.2018.09.005.
- [50] K. Karthikeyan, B. P. Russell, N. A. Fleck, H. N. G. Wadley, and V. S. Deshpande. “The effect of shear strength on the ballistic response of laminated composite plates”. In: *European Journal of Mechanics - A/Solids* 42 (2013), pp. 35–53. DOI: 10.1016/j.euromechsol.2013.04.002.
- [51] O. Nazarian and F. W. Zok. “Shear-dominated plastic behavior of a cross-ply Dyneema composite”. In: *Composites Part A: Applied Science and Manufacturing* 67 (2014), pp. 316–323. DOI: 10.1016/j.compositesa.2014.09.012.
- [52] S. P. Marsh, ed. *LASL Shock Hugoniot Data*. Berkeley and Los Angeles, CA, USA: University of California Press, 1980.
- [53] M. G. Vigil. *Projectile Impact Hugoniot Parameters for Selected Materials*. Tech. rep. SAND89-1571 UC-704. Albuquerque, NM, USA: Sandia National Laboratories, 1989.
- [54] P. J. Hazell, G. J. Appleby-Thomas, X. Trinquant, and D. J. Chapman. “In-fiber shock propagation in Dyneema”. In: *Journal of Applied Physics* 110.4 (2011). DOI: 10.1063/1.3622294.
- [55] M. L. Wilkins. *Computation of elastic-plastic flow*. Tech. rep. Livermore, CA, USA: Lawrence Radiation Laboratory, University of California, 1963.
- [56] C. E. Anderson, P. A. Cox, G. R. Johnson, and P. J. Maudlin. “A constitutive formulation for anisotropic materials suitable for wave propagation computer programs-II”. In: *Computational Mechanics* 15.3 (1994), pp. 201–223. DOI: 10.1007/BF00375030.
- [57] L. H. Nguyen, S. Ryan, S. J. Cimpoeru, A. P. Mouritz, and A. C. Orifici. “The effect of target thickness on the ballistic performance of ultra high molecular weight polyethylene composite”. In: *International Journal of Impact Engineering* 75 (2015), pp. 174–183. DOI: 10.1016/j.ijimpeng.2014.07.008.

- [58] T. Lässig, W. Riedel, U. Heisserer, H. Van der Werff, M. May, and S. Hiermaier. “Numerical sensitivity studies of a UHMWPE composite for ballistic protection”. In: *WIT Transactions on the Built Environment* 141 (2014), pp. 371–381. DOI: 10.2495/SUSI140321.
- [59] T. A. Bogetti, M. Walter, J. Staniszewski, and J. Cline. “Interlaminar shear characterization of ultra-high molecular weight polyethylene (UHMWPE) composite laminates”. In: *Composites Part A: Applied Science and Manufacturing* 98 (2017), pp. 105–115. DOI: 10.1016/j.compositesa.2017.03.018.
- [60] T. F. Walsh, B. H. Lee, and J. W. Song. “Penetration failure of Spectra polyethylene fiber-reinforced ballistic-grade composites”. In: *Key Engineering Materials* 141-143 (1998), pp. 367–382. DOI: 10.4028/kem.141-143.367.
- [61] H. J. Qi and M. C. Boyce. “Stress-strain behavior of thermoplastic polyurethanes”. In: *Mechanics of Materials* 37.8 (2005), pp. 817–839. DOI: 10.1016/j.mechmat.2004.08.001.
- [62] S. Chocron, A. E. Nicholls, A. Brill, A. Malka, T. Namir, D. Havazelet, H. Van Der Werff, U. Heisserer, and J. D. Walker. “Modeling dyneema and spectra with finite elements by bundling fibers into strips”. In: *28th International Symposium on Ballistics*. Atlanta, GA, USA, 2014.
- [63] I. Meshi, I. Amarilio, D. Benes, and R. Haj-Ali. “Delamination behavior of UHMWPE soft layered composites”. In: *Composites Part B: Engineering* 98 (2016), pp. 166–175. DOI: 10.1016/j.compositesb.2016.05.027.
- [64] E. S. Greenhalgh, V. M. Bloodworth, L. Iannucci, and D. Pope. “Fractographic observations on Dyneema composites under ballistic impact”. In: *Composites Part A: Applied Science and Manufacturing* 44 (2013), pp. 51–62. DOI: 10.1016/j.compositesa.2012.08.012.
- [65] S. Chocron, N. King, R. Bigger, J. D. Walker, U. Heisserer, and H. van der Werff. “Impacts and Waves in Dyneema HB80 Strips and Laminates”. In: *Journal of Applied Mechanics* 80.3 (2013), p. 031806. DOI: 10.1115/1.4023349.
- [66] T. Peijs, H. A. Rijdsdijk, J. M. M. de Kok, and P. J. Lemstra. “The role of interface and fibre anisotropy in controlling the performance of polyethylene-fibre-reinforced

- composites”. In: *Composites Science and Technology* 52.3 (1994), pp. 449–466. DOI: 10.1016/0266-3538(94)90180-5.
- [67] G. I. Barenblatt. “The Mathematical Theory of Equilibrium Cracks in Brittle Fracture”. In: *Advances in Applied Mechanics* 7 (1962), pp. 55–129. DOI: 10.1016/S0065-2156(08)70121-2.
- [68] A. Hillerborg, M. Mod er, and P. E. Petersson. “Analysis of crack formation and crack growth in concrete by means of fracture mechanics and finite elements”. In: *Cement and Concrete Research* 6.6 (1976), pp. 773–782. DOI: 10.1016/0008-8846(76)90007-7.
- [69] S. R. Hallett and P. W. Harper. “Modelling delamination with cohesive interface elements”. In: *Numerical Modelling of Failure in Advanced Composite Materials*. Ed. by P. P. Camanho and S. R. Hallett. Woodhead Publishing, 2015. Chap. 2, pp. 55–72. DOI: 10.1016/B978-0-08-100332-9.00002-5.
- [70] J. O. Hallquist. *LS-Dyna Keyword User’s Manual*. Livermore, CA, USA, 2007.
- [71] Y. Mi, M. A. Crisfield, G. A. O. Davies, and H. B. Hellweg. “Progressive Delamination Using Interface Elements”. In: *Journal of Composite Materials* 32.14 (1998), pp. 1246–1272. DOI: 10.1177/002199839803201401.
- [72] W. G. Jiang, S. R. Hallett, B. G. Green, and M. R. Wisnom. “A concise interface constitutive law for analysis of delamination and splitting in composite materials and its application to scaled notched tensile specimens”. In: *International Journal for Numerical Methods in Engineering* 69.9 (2007), pp. 1982–1995. DOI: 10.1002/nme.1842.
- [73] J. C. Brewer and P. A. Lagace. “Quadratic Stress Criterion for Initiation of Delamination”. In: *Journal of Composite Materials* 22.12 (1988), pp. 1141–1155. DOI: 10.1177/002199838802201205.
- [74] W. C. Cui, M. R. Wisnom, and M. Jones. “A comparison of failure criteria to predict delamination of unidirectional glass/epoxy specimens waisted through the thickness”. In: *Composites* 23.3 (1992), pp. 158–166. DOI: 10.1016/0010-4361(92)90436-X.
- [75] E. M. Wu and R. Reauter Jr. *Crack extension in fiberglass reinforced plastics*. Tech. rep. Urbana, IL, USA: University of Illinois, 1965.
- [76] J. D. Whitcomb. *Analysis of instability-related growth of a through-width delamination*. Tech. rep. Hampton, VA, USA: NASA, Langley Research Center, 1984.

- [77] M. L. Benzeggagh and M. Kenane. “Measurement of mixed-mode delamination fracture toughness of uni-directional glass/epoxy composites with mixed-mode bending apparatus”. In: *Composite Science and Technology* 56.4 (1996), pp. 439–449. DOI: 10.1016/0266-3538(96)00005-X.
- [78] P. P. Camanho and C. G. Dávila. *Mixed-Mode Decohesion Finite Elements in for the Simulation Composite of Delamination Materials*. Tech. rep. Hampton, VA, USA: NASA, Langley Research Center, 2002. DOI: 10.1177/002199803034505.
- [79] H. Van Der Werff and U. Heisserer. “High-performance ballistic fibers: Ultra-high molecular weight polyethylene (UHMWPE)”. In: *Advanced Fibrous Composite Materials for Ballistic Protection*. Ed. by X. Chen. 1st ed. Woodhead, 2016. Chap. 3, pp. 71–108. DOI: 10.1016/B978-1-78242-461-1.00003-0.
- [80] J. K. Kim and Y. W. Mai. *Engineered Interfaces in Fiber Reinforced Composites*. 1st ed. Oxford, UK: Elsevier Ltd., 1998. DOI: 10.1016/B978-0-08-042695-2.X5000-3.
- [81] B. T. Ansari, M. K. Hazzard, L. F. Kawashita, U. Heisserer, and S. R. Hallett. “Numerical modelling of UHMWPE composites under impact loading”. In: *22nd International Conference on Composite Materials*. Melbourne, Australia, 2019.
- [82] B. Z. G. Haque. *A progressive composite damage model for unidirectional and woven fabric:s MAT162 User Manual*. Newark, DE, USA, 2015.
- [83] U Heisserer and H Van Der Werff. “Strength matters: Which strength of Dyneema® fiber composites to use in hydrocode models?-a discussion”. In: *Proceedings - 29th International Symposium on Ballistics, BALLISTICS 2016*. Vol. 2. 2016, pp. 2200–2204.
- [84] B. A. Gama and J. W. Gillespie. “Punch shear based penetration model of ballistic impact of thick-section composites”. In: *Composite Structures* 86.4 (2008), pp. 356–369. DOI: 10.1016/j.compstruct.2007.11.001.
- [85] B. A. Gama and J. W. Gillespie. “Finite element modeling of impact, damage evolution and penetration of thick-section composites”. In: *International Journal of Impact Engineering* 38.4 (2011), pp. 181–197. DOI: 10.1016/j.ijimpeng.2010.11.001.
- [86] M. K. Hazzard. “Composite Armour: From Atoms to Application”. PhD Thesis. Bristol, UK: University of Bristol, 2017.

- [87] T. Graf, A. Haufe, and F. Andrade. “Adhesives modeling with LS-DYNA: Recent developments and future work”. In: *Nordic LS-DYNA Forum 2014*. Gothenburg, Sweden: DYNAmore GmbH, 2014.
- [88] M. Grujicic, G. Arakere, T. He, W. C. Bell, P. S. Glomski, and B. A. Cheeseman. “Multi-scale ballistic material modeling of cross-plyed compliant composites”. In: *Composites Part B: Engineering* 40.6 (2009), pp. 468–482. DOI: 10.1016/j.compositesb.2009.02.002.
- [89] K. Karthikeyan, B. P. Russell, N. A. Fleck, M. O’Masta, H. N. G. Wadley, and V. S. Deshpande. “The soft impact response of composite laminate beams”. In: *International Journal of Impact Engineering* 60 (2013), pp. 24–36. DOI: 10.1016/j.ijimpeng.2013.04.002.
- [90] B. L. Lee, J. W. Song, and J. E. Ward. “Failure of Spectra polyethylene fiber-reinforced composites under ballistic impact loading”. In: *Journal of Composite Materials* 28.13 (1994), pp. 1202–1226. DOI: 10.1177/002199839402801302.
- [91] M. R. O’Masta, B. G. Compton, E. A. Gamble, F. W. Zok, V. S. Deshpande, and H. N. G. G. Wadley. “Ballistic impact response of an UHMWPE fiber reinforced laminate encasing of an aluminum-alumina hybrid panel”. In: *International Journal of Impact Engineering* 86 (2015), pp. 131–144. DOI: 10.1016/j.ijimpeng.2015.08.003.
- [92] U. Heisserer, H. Van der Werff, and J. Hendrix. “Ballistic depth of penetration studies in Dyneema composites”. In: *27th International Symposium on Ballistics*. Freiburg, Germany, 2013.
- [93] C. Grunwald, T. Lässig, H. van der Werff, U. Heisserer, L. Nguyen, and W. Riedel. “Numerical sensitivity study of ballistic impact on UHMWPE composites”. In: *6th International Conference on Design and Analysis of Protective Structures*. Melbourne, Australia, 2017.
- [94] J. P. Attwood, B. P. Russell, H. N. G. G. Wadley, and V. S. Deshpande. “Mechanisms of the penetration of ultra-high molecular weight polyethylene composite beams”. In: *International Journal of Impact Engineering* 93 (2016), pp. 153–165. DOI: 10.1016/j.ijimpeng.2016.02.010.
- [95] J. C. Smith, F. L. Mccrackin, and H. F. Schiefer. “Stress-Strain Relationships in Yarns Subjected to Rapid Impact Loading: Part III. Effect of Wave Propagation”. In: *Textile Research Journal* 25.8 (1958), pp. 701–708. DOI: 10.1177/004051755502500805.

- [96] J. R. Xiao, B. A. Gama, and J. W. Gillespie. “Progressive damage and delamination in plain weave S-2 glass/SC-15 composites under quasi-static punch-shear loading”. In: *Composite Structures* 78.2 (2007), pp. 182–196. DOI: 10.1016/j.compstruct.2005.09.001.
- [97] C. R. Siviour and J. L. Jordan. “High Strain Rate Mechanics of Polymers: A Review”. In: *Journal of Dynamic Behavior of Materials* 2 (2016), pp. 15–32. DOI: 10.1007/s40870-016-0052-8.
- [98] S. S. Sarva, S. Deschanel, M. C. Boyce, and W. Chen. “Stress-strain behavior of a polyurea and a polyurethane from low to high strain rates”. In: *Polymer* 48.8 (2007), pp. 2208–2213. DOI: 10.1016/j.polymer.2007.02.058.
- [99] M. May. “Measuring the rate-dependent mode I fracture toughness of composites - A review”. In: *Composites Part A: Applied Science and Manufacturing* 81 (2016), pp. 1–12. DOI: 10.1016/j.compositesa.2015.10.033.
- [100] M. A. Khan, T. Mabrouki, E. Vidal-Sallé, and P. Boisse. “Numerical and experimental analyses of woven composite reinforcement forming using a hypoelastic behaviour. Application to the double dome benchmark”. In: *Journal of Materials Processing Technology* 210.2 (2010), pp. 378–388. DOI: 10.1016/j.jmatprotec.2009.09.027.
- [101] A. Thompson, J. P. Belnoue, and S. R. Hallett. “Numerical Modelling of Defect Generation During Preforming of Multiple Layers of 2D Woven Fabrics”. In: *17th European Conference on Composite Materials*. Munich, Germany, 2016.
- [102] P. M. Cunniff. “The V50 Performance of Body Armor Under Oblique Impact”. In: *18th International Symposium on Ballistics*. San Antonio, TX, USA, 1999.
- [103] P. M. Cunniff. “The importance of off-normal obliquity impact performance to the casualty reduction potential of ballistic protective helmets”. In: *24th International Symposium on Ballistics*. New Orleans, LA, USA, 2008.
- [104] K. Potter, B. Khan, M. Wisnom, T. Bell, and J. Stevens. “Variability, fibre waviness and misalignment in the determination of the properties of composite materials and structures”. English. In: *Composites Part A: Applied Science and Manufacturing* 39.9 (2008), pp. 1343–1354. DOI: Doi10.1016/J.Compositesa.2008.04.016.

- [105] S. G. Kulkarni, X. L. Gao, S. E. Horner, J. Q. Zheng, and N. V. David. “Ballistic helmets - Their design, materials, and performance against traumatic brain injury”. In: *Composite Structures* 101 (2013), pp. 313–331. DOI: 10.1016/j.compstruct.2013.02.014.
- [106] T. R. Lässig, M. May, U. Heisserer, W. Riedel, F. Bagusat, H. van der Werff, and S. J. Hiermaier. “Effect of consolidation pressure on the impact behavior of UHMWPE composites”. In: *Composites Part B: Engineering* 147 (2018), pp. 47–55. DOI: 10.1016/j.compositesb.2018.04.030.
- [107] L. M. Dangora, C. J. Hansen, C. J. Mitchell, J. A. Sherwood, and J. C. Parker. “Challenges associated with shear characterization of a cross-ply thermoplastic lamina using picture frame tests”. In: *Composites Part A: Applied Science and Manufacturing* 78 (2015), pp. 181–190. DOI: 10.1016/j.compositesa.2015.08.015.
- [108] J. H. Bickford and S. Nassar, eds. *Handbook of bolts and bolted joints*. 1st ed. New York, NY, USA: Taylor and Francis, 1998.
- [109] J. Rockwell. “High velocity impact of Dyneema laminates of varying size”. Masters Thesis. Newark, DE, USA: University of Delaware, 2014.
- [110] J. Cao, R. Akkerman, P. Boisse, J. Chen, H. S. Cheng, E. F. de Graaf, J. L. Gorczyca, P. Harrison, G. Hivet, J. Launay, W. Lee, L. Liu, S. V. Lomov, A. Long, E. de Luycker, F. Morestin, J. Padvoiskis, X. Q. Peng, J. Sherwood, T. Stoilova, X. M. Tao, I. Verpoest, A. Willems, J. Wiggers, T. X. Yu, and B. Zhu. “Characterization of mechanical behavior of woven fabrics: Experimental methods and benchmark results”. In: *Composites Part A: Applied Science and Manufacturing* 39.6 (2008), pp. 1037–1053. DOI: 10.1016/j.compositesa.2008.02.016.
- [111] M. R. Wisnom. “The effect of fibre rotation in 45 tension tests on measured shear properties”. In: *Composites* 26.1 (1995), pp. 25–32. DOI: 10.1016/0010-4361(94)P3626-C.
- [112] S. M. Walley, J. E. Field, P. H. Pope, and N. A. Safford. “A study of the rapid deformation behaviour of a range of polymers”. In: *Philosophical Transactions of the Royal Society of London. Series A, Mathematical and Physical Sciences* 328.1597 (1989), pp. 1–33. DOI: 10.1098/rsta.1989.0020.

- [113] J. Yi, M. C. Boyce, G. F. Lee, and E. Balizer. “Large deformation rate-dependent stress-strain behavior of polyurea and polyurethanes”. In: *Polymer* 47.1 (2006), pp. 319–329. DOI: 10.1016/j.polymer.2005.10.107.
- [114] S. M. Kurtz. *The UHMWPE handbook: Ultra-high molecular weight polyethylene in total joint replacement*. 1st ed. Plastics Design Library. Elsevier Inc., 2004. DOI: 10.1016/B978-0-12-429851-4.X5000-1.
- [115] I. M. Ward and J. Sweeney. *An introduction to the mechanical properties of solid polymers*. 2nd ed. Chichester, UK: John Wiley and Sons, 2004.
- [116] F. X. Kromm, T. Lorriot, B. Coutand, R. Harry, and J. M. Quenisset. “Tensile and creep properties of ultra high molecular weight PE fibres”. In: *Polymer Testing* 22.4 (2003), pp. 463–470. DOI: 10.1016/S0142-9418(02)00127-7.
- [117] M. Ishikawa, H. Ogawa, and I. Narisawa. “Brittle fracture in glassy polymers”. In: *Journal of Macromolecular Science, Part B: Physics* 19.3 (1981), pp. 421–443. DOI: 10.1080/00222348108015312.
- [118] P. C. Powell and A. J. I. Housz. *Engineering with Polymers*. 2nd ed. Oxford, UK: Oxford University Press, 1998.
- [119] M. A. Wilding and I. M. Ward. “Tensile creep and recovery in ultra-high modulus linear polyethylenes”. In: *Polymer* 19.8 (1978), pp. 969–976. DOI: 10.1016/0032-3861(78)90208-2.
- [120] B. D. Heru Utomo. “High-speed impact modelling and testing of Dyneema composite”. PhD Thesis. Delft, Netherlands: Delft University of Technology, 2011.
- [121] A. C. P. Koh, V. P. W. Shim, and V. B. C. Tan. “Dynamic behaviour of UHMWPE yarns and addressing impedance mismatch effects of specimen clamps”. In: *International Journal of Impact Engineering* 37.3 (2010), pp. 324–332. DOI: 10.1016/j.ijimpeng.2009.10.008.
- [122] K. Karthikeyan and B. P. Russell. “Polyethylene ballistic laminates: Failure mechanics and interface effect”. In: *Materials and Design* 63 (2014), pp. 115–125. DOI: 10.1016/j.matdes.2014.05.069.
- [123] T. G. Zhang, S. S. Satapathy, L. R. Vargas-Gonzalez, and S. M. Walsh. “Ballistic impact response of Ultra-High-Molecular-Weight Polyethylene (UHMWPE)”. In: *Composite Structures* 133 (2015), pp. 191–201. DOI: 10.1016/j.compstruct.2015.06.081.

- [124] K. Karthikeyan, S. Kazemahvazi, and B. P. Russell. “Optimal fibre architecture of soft-matrix ballistic laminates”. In: *International Journal of Impact Engineering* 88 (2016), pp. 227–237. DOI: 10.1016/j.ijimpeng.2015.10.012.
- [125] J. C. Maxwell. “On the calculation of the equilibrium and stiffness of frames”. In: *The London, Edinburgh, and Dublin Philosophical Magazine and Journal of Science* 27.182 (1864), pp. 294–299. DOI: 10.1080/14786446408643668.
- [126] M. R. O’Masta, B. P. Russell, and W. Ronan. “Inter-ply angle influence on the out-of-plane compressive response of polyethylene fibre laminates”. In: *Composites Part A: Applied Science and Manufacturing* 110 (2018), pp. 11–20. DOI: 10.1016/j.compositesa.2018.03.032.
- [127] R. G. Shephard. *The use of polymers in personal ballistic protection*. Tech. rep. London, UK: The Plastics and Rubber Institute, 1987.
- [128] R. L. Woodward, G. T. Egglestone, B. J. Baxter, and K. Challis. “Resistance to penetration and compression of fibre-reinforced composite materials”. In: *Composites Engineering* 4.3 (1994), pp. 329–341. DOI: 10.1016/0961-9526(94)90083-3.
- [129] S. A. Taylor and D. J. Carr. “Post failure analysis of 0/90 ultra high molecular weight polyethylene composite after ballistic testing”. In: *Journal of Microscopy* 196.2 (1999), pp. 249–256. DOI: 10.1046/j.1365-2818.1999.00632.x.
- [130] M. R. O’Masta, D. H. Crayton, V. S. Deshpande, and H. N. Wadley. “Indentation of polyethylene laminates by a flat-bottomed cylindrical punch”. In: *Composites Part A: Applied Science and Manufacturing* 80 (2016), pp. 138–147. DOI: 10.1016/j.compositesa.2015.10.015.
- [131] M. May and T. Lässig. “Rate-dependent mode I delamination in ballistic composites - Experiment and simulation”. In: *Composite Structures* 180 (2017), pp. 596–605. DOI: 10.1016/j.compstruct.2017.08.045.
- [132] M. Razmara, S. H. Saidpour, and S. Arunchalam. “DMA investigation on polyurethane (PUR)”. In: *International Conference on Fascinating Advancement in Mechanical Engineering*. Sivakasi, India, 2008.
- [133] C. R. Siviour, S. M. Walley, W. G. Proud, and J. E. Field. “The high strain rate compressive behaviour of polycarbonate and polyvinylidene difluoride”. In: *Polymer* 46.26 (2005), pp. 12546–12555. DOI: 10.1016/j.polymer.2005.10.109.

- [134] G. Czél, S. Pimenta, M. R. Wisnom, and P. Robinson. “Demonstration of pseudo-ductility in unidirectional discontinuous carbon fibre/epoxy prepreg composites”. In: *Composites Science and Technology* 106 (2015), pp. 110–119. DOI: 10.1016/j.compscitech.2014.10.022.
- [135] M. May, H. Voß, and S. Hiermaier. “Predictive modeling of damage and failure in adhesively bonded metallic joints using cohesive interface elements”. In: *International Journal of Adhesion and Adhesives* 49 (2014), pp. 7–17. DOI: 10.1016/j.ijadhadh.2013.12.001.
- [136] S. Marzi, O. Hesebeck, M. Brede, and F. Kleiner. “A rate-dependent, elasto-plastic cohesive zone mixed-mode model for crash analysis of adhesively bonded joints”. In: *9th European LS-Dyna Conference*. Manchester, UK, 2009.
- [137] A. S. M. Al-Azzawi, L. F. Kawashita, and C. A. Featherston. “A modified cohesive zone model for fatigue delamination in adhesive joints: numerical and experimental investigations”. In: *Composite Structures* 225 (2019). DOI: 10.1016/j.compstruct.2019.111114.

Appendices

Appendix A

Implementing rate-dependence at the sub-laminate interface

Strain rate effects can be incorporated into the interface element formulation used in this work, with Eq. (3.7) and the following components:

- The cohesive property as a function of the strain rate.
- The coefficient of this function.
- A minimum strain rate to activate rate adjustment of the property to limit non-physical deformations at lower strain rates.
- An upper cap for the strain rate to prevent instabilities at elevated rates.

The following approach outlines a method for obtaining first approximations of the HB26 matrix properties, as functions of the strain rate, based on a collection of previous experimental, numerical and analytical studies. Deriving the strain rate dependence of:

a) Peak traction

- (i) Derive rate function from the polyurethane yield strength data [98], as demonstrated in Fig. A.1.
- (ii) Primary investigations displayed in Fig. A.1 show a piecewise linear rate-dependence function to best capture the data trend. This can be implemented either using look-up tables in the material input cards or as piecewise functions, as performed in [131].
- (iii) Determine whether the non-linearity in the logarithmic relationship is a result of the differences in measurement techniques employed at different test rates. For instance, determine whether a thermal equilibrium is considered, particularly at higher loading rates.

b) Initial stiffness

- (i) According to the time-temperature superposition effect, temperature is inversely interchangeable with rate, so that increases in the strain rate or the frequency of the applied loading have the same effect on the elastic modulus as decreases in the temperature [132].

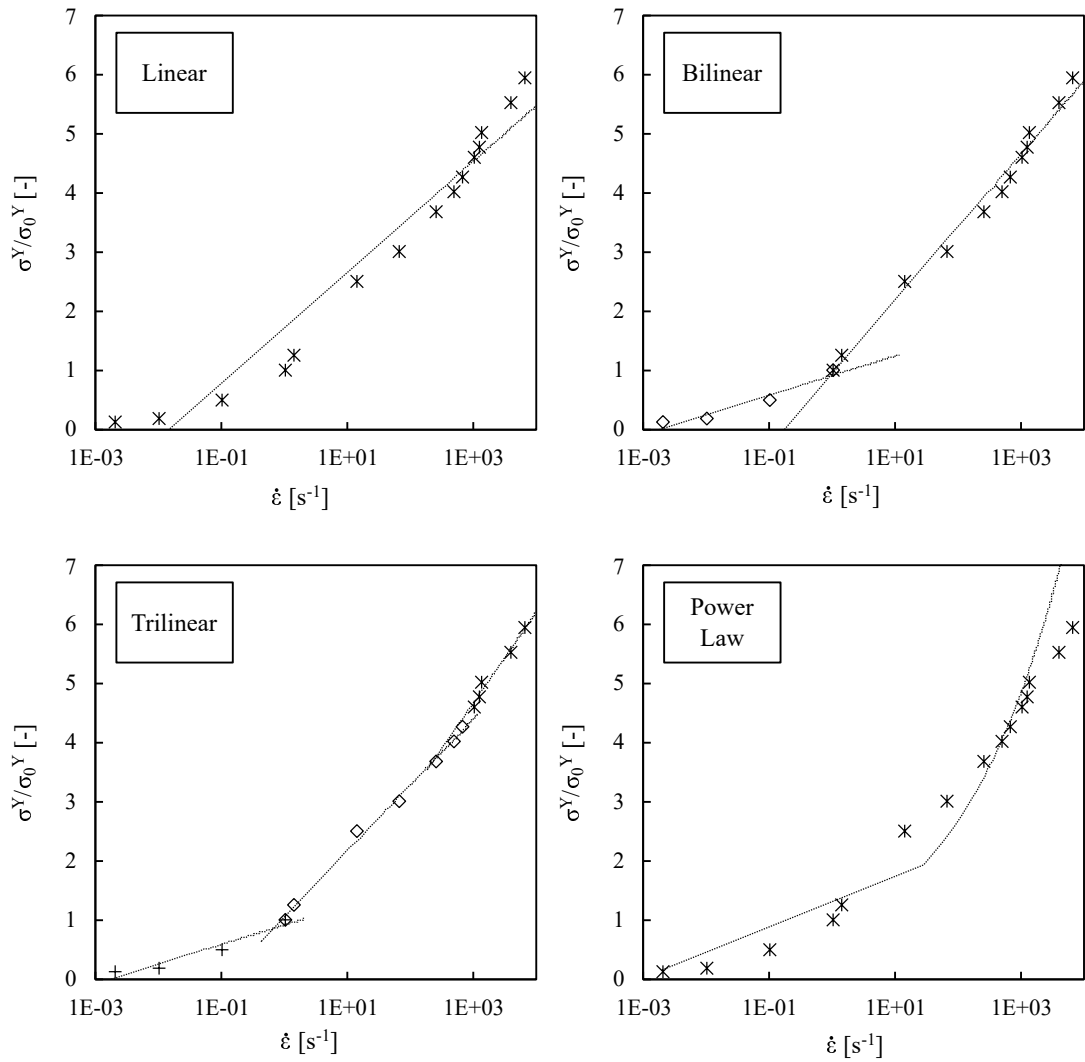


Figure A.1: Logarithmic linear and exponential curved fitting to determine a strain rate function for yield stress, based on data from [98].

- (ii) Thus the relationship $T = T_0 + A (\log \dot{\epsilon}_0 - \log \bar{\epsilon})$, as defined in [133], could be used to map more readily available temperature data, T , to strain rate data, $\bar{\epsilon}$.

c) Fracture toughness

- (i) Implement the piecewise relationship between strain rate and fracture toughness derived by May and Lässig [131], as displayed in Fig. A.2.
- (ii) Since the relationship is based on the global loading rate, obtained from the cross-head displacement rate in double cantilever beam (DCB) tests of mode I fracture toughness, it must be converted into local displacement rate.
- (iii) This can be performed through curve-fitting, with the approach adopted in [131] to back calculate an effective strain rate by assuming a unity proportionality factor between global and local rate dependence coefficients, before adjusting this in DCB simulations to match experimental data. Validation of the model data can be performed for an example rate using the Irwin-Kies equation.

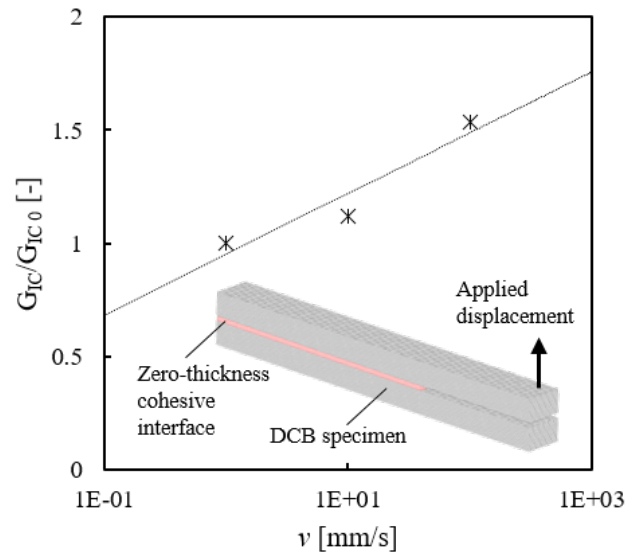


Figure A.2: Logarithmic linear and exponential curved fitting to determine a global displacement rate function for mode I fracture energy, based on mean average data from [131], inset showing simulation of DCB test using the current modelling technique.

For first approximations, the same ratio between rate coefficients for mode I and mode II interface variables can be assumed, as used in the rate coefficients for normal and shear strength and stiffness properties of the composite material model. While data from end-notched flexure (ENF) mode II fracture toughness testing at varying rates of loading is required to derive a rate-dependent function for this material, initial approximations can be based on the rate-dependent behaviour in the normal direction. For all the properties considered, the implementation of rate-dependency should follow a three stage approach, beginning with the use of arbitrary coefficient values of varying orders of magnitude in a standard logarithmic function. This should be followed by determining whether the magnitude of rate coefficients derived from generic polyurethane data available in the literature falls within the range of values that yield noticeable effects on the simulation results. If so, the material rate coefficients and functions should then be refined for the specific matrix used in HB26 [50], since polymers can vary extensively in terms of molecular weight and therefore mechanical properties.

Note that due to variations in the displacement rates reported in the literature, from dynamic mechanical analysis (DMA) loading rates to DCB cross-head velocity, it is advisable to only work in terms of strain rate. This will require converting global rate-dependence to a local level due to the non-uniform strain that exists across a specimen in fracture toughness testing. Subsequently, to convert displacement rate outputs of the separation at the interface with zero-thickness with no reference dimension, an arbitrary thickness of $1\ \mu\text{m}$ to $10\ \mu\text{m}$ can be assumed for analytical purposes. These values represent a resin-rich inter-ply region in laminates, previously measured with optical microscopy as $5\ \mu\text{m}$ by Czél *et al.* [134], for a carbon/epoxy system of substantially lower fibre volume fraction.

Appendix B

Implementing plasticity at the sub-laminate interface

Possible options to address the absence of plasticity in the model are discussed here. MAT162 material behaviour cannot be altered to have plasticity implemented. Under current conditions, alternative parameters such as the bulk modulus of the solid elements or the damage softening parameters can be altered to accomplish a more ductile behaviour. To implement true plastic behaviour however, the material model must be replaced by a user material with the capabilities of MAT162, and additional plastic behaviour. Note that the absence of an equation of state in the model and the accompanying implementation of a Hugoniot elastic limit means that plastic deformations due to strong shocks propagating through the material upon impact are also not captured. The results from simulations performed at the higher ranges of impact velocity are particularly prone to this and must be interpreted with some caution. As a simpler solution, the interface elements can be modified to account for plastic behaviour. Effective plasticity can be achieved at the interface via two approaches; by implementing a trilinear cohesive law for pseudo-plasticity, or by implementing irrecoverable strain paths.

A trilinear, namely trapezoidal, mixed-mode traction-separation curve would mimic plastic behaviour and is therefore considered to only provide pseudo-plasticity. This is done by increasing the area under the traction-separation curve that represents the critical energy release rate, G_C . Under the current bi-linear relationship, adjustments of G_C can also be made, although in vain in relation to increasing plasticity. With a trapezoidal curve however, plastic behaviour can be imitated and increased by introducing a plateau at the point of damage initiation, as performed in [135] and seen in Fig. B.1(a). Cohesive elements were utilised in that study to model adhesively bonded joints. Pseudo-plasticity was implemented in mode II only, and consequently in the mixed-mode behaviour demonstrated in Fig. B.1(b). This is due to the significance of plasticity in the mode II behaviour of soft, ductile materials, such as adhesives [135, 136], metals, and in this case thermoplastic polymer composites, in contrast to the more brittle behaviour exhibited by CFRP laminates. Since it was shown in *Chapter 3* that mode II accounts for above 90% of the total energy dissipated at the interface, implementing effective plasticity in the mode II shear deformation of interface elements could prove to have significant effects. It is possible to implement a trapezoidal cohesive law in the current UMAT, and is also generically available in MAT169, MAT185 and MAT240 on the LS-DYNA platform.

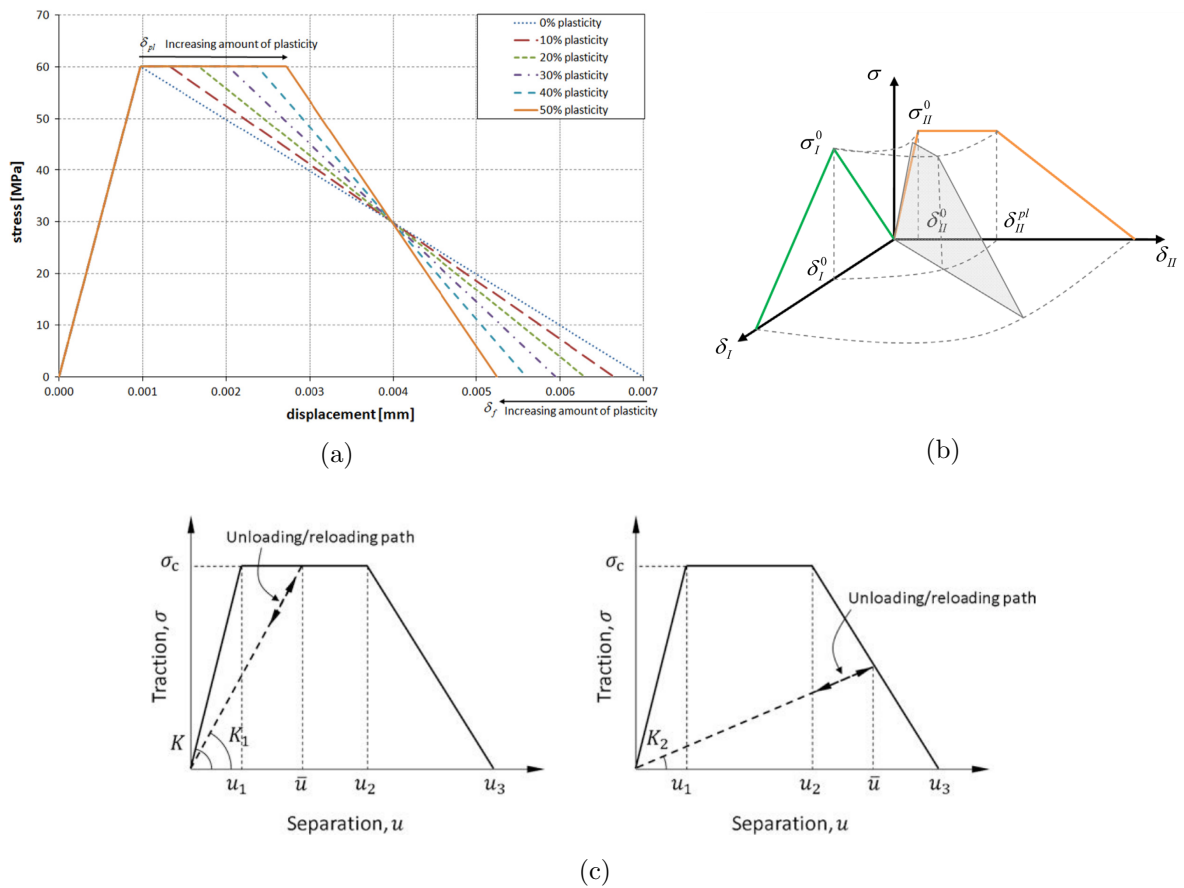


Figure B.1: Implementing effective plasticity in the cohesive interface elements through a trapezoidal traction-separation law in (a) mode II and (b) in the mixed-mode domain, reproduced from [135], or (c) combined with alternative unloading and reloading paths, reproduced from [137].

Nevertheless, a realistic mode II traction-separation curve that captures a trilinear behaviour would require physical values obtained from a custom-made three-point bend end-notched flexure (3ENF) test. In addition, the behaviour of the interface elements can be modified to implement effective plasticity by introducing alternative unloading and reloading paths, as performed in [136, 137] and demonstrated in Fig. B.1(c). This can be extended further to include a truly plastic region, where unloading does not relieve the total stress on an interface element and return the stress levels to zero. For the purpose of the current study, the results generated by the numerical tools with purely elastic behaviour are deemed sufficient as the parameter of interest, maximum BFD, occurs prior to the initiation of laminate and projectile recoil at the lower range of V_I values, and is therefore not dependent on the implementation of plasticity. Likewise, implementation of the plastic phase is not necessary for obtaining reliable estimations of the V_{50} , the other performance parameter of interest in ballistic components. Furthermore, in *Chapter 3*, the interface was shown to account for around 10% of total energy dissipation in the laminate. The effect of implementing plastic behaviour in the solid elements is therefore likely to dwarf that of the interface elements, which is outside the scope of this study.

